

DEVELOPMENT OF A NEW JOINT SYSTEM
FOR A CIRCULAR-SHAPED INFRASTRUCTURE

by

SUGYU LEE

Presented to the Faculty of the Graduate School of
The University of Texas at Arlington in Partial Fulfillment
of the Requirements
for the Degree of

DOCTOR OF PHILOSOPHY

THE UNIVERSITY OF TEXAS AT ARLINGTON

Spring 2017

Copyright © by Student Name SUGYU LEE

All Rights Reserved



Acknowledgements

I am very honored to have had the opportunity to attend the University of Texas at Arlington (UTA), and I wish to thank many people for their helpful assistance and sincere consideration. Most of all, my sincere thanks go to Dr. Ali Abolmaali for his teaching, constant guidance, and kind care throughout my Ph.D. program at UTA. His encouragement and faith in me provided the confidence and motivation I needed to complete the Doctoral of Philosophy degree program. It is a particular pleasure for me to have worked with him on this dissertation.

I also wish to thank the members of my dissertation committee, Dr. Nur Yazdani, Dr. Wen S. Chan, and Dr. Shih-Ho Chao for their advice and constructive criticism of this dissertation.

I am grateful to Dr. Ki-Nam Hong for constant encouragement and well wishes. I would also like to thank to my friends who have supported and believed in me. I especially recognize my thanks to the Drs. Yeonho Park, Swoo-Heon Lee, Jinsup Kim, and Dr. Abolmaali's research members for giving me strength.

Finally, I am sincerely grateful to my parents, older sister, and brother in-law for the inspiration they have given me and for being wonderful role models. Furthermore, I am really grateful for my niece. Thanks to their love, faith, and invaluable support, I was able to endure and overcome the hardships of the past four years.

March 27th, 2017

Abstract

DEVELOPMENT OF A NEW JOINT SYSTEM FOR
A CIRCULAR-SHAPED INFRASTRUCTURE

SUGYU LEE, PhD

The University of Texas at Arlington, 2017

Supervising Professor: Seyedali Abolmaali

This dissertation focused on development of new carbon fiber joint systems for all types of underground gravity and sewer pipe systems. Specifically, the external CFRP wrap and, particularly, the carbon fiber reinforced polymer (CFRP) internal coupler can be used for concrete pipes with regular or reduced wall thicknesses. The concrete pipes with reduced wall thickness are classified as semi-rigid pipe and are referred to as thin-wall (TW) concrete pipe. The performance of the CFRP coupler is presented in this report based on full-scale experimental tests and three dimensional non-linear finite element studies for regular and thin wall pipes. Finally, design equations and contour guidelines are presented for the CFRP internal couplers.

This study was conducted with three Phases: (1) Phase I focused on joint performances of Carbon Fiber Reinforced Polymer (CFRP) sheet externally wrapped with different widths (3, 6, 9, and 12 in.) and curing time of epoxy chemicals in ambient temperature of 72 and 99 Fahrenheit degrees; (2) Phase II focused on experimental tests on the CFRP internal coupler with joint shear and hydrostatic tests in accordance with ASTM C497-16a. This phase also included the development of three dimensional non-linear finite element method (FEM) analyses of CFRP internal coupler for parametric studies. Additionally, a series of material tests with different thicknesses were conducted for obtaining accurate non-linear material properties for the use in the analysis algorithm.

After several experimentations with types of sealants, it was shown that the CFRP internal coupler is water tight based on ASTM C497-16a; and (3) Phase III focused on experimental testing of various inside diameters of TW concrete pipes (48, 54, 72, and 84 in.) with the CFRP internal couplers. Furthermore, the modification of the developed FEM models for the large diameter joint shear tests and derivation of design equations and guidelines of the CFRP internal couplers was one of the main themes in Phase III.

To evaluate structural performance of the joint systems using the CFRP sheet, eight (8) full-scale externally wrapping joint shear tests and eleven (11) full-scale CFRP internal coupler (CFRP Coupler) joint shear tests were performed in accordance with the ASTM C497-16a. The external CFRP wrapping joint of 3 in. width met the aforementioned ASTM standard of shear strengths. The evaluation of epoxy chemical and its curing time indicated that at least 3 hours was required for curing in order to provide bond between the CFRP fabric material and concrete pipe. The effects of various CFRP internal coupler thicknesses (0.0625, 0.125, 0.1875, 0.25, and 0.375 in.) were investigated based on performance evaluations during testing for different internal diameters of TW concrete pipes (36, 48, 54, 72, and 84 in.). It should be noted that since the CFRP internal coupler targets internal diameter for a given pipe, a distinction between regular (conventional) wall thickness concrete pipe and the novel thin wall concrete pipe should not be made. In another word, the CFRP internal coupler can be used for both types of pipes. The joint shear test results showed that an average of 20.5% higher coupler shear strength was obtained by using CFRP internal coupler when compared with the requirements of ASTM C497.

A total of 243 parametric cases was performed by using the experimentally verified FEM analyses in order to develop design equations which could predict the behavior of the joint shear tests for the CFRP internal coupler based on internal diameter, coupler width, and coupler thickness. Finally, Four-dimensional design contour plots for CFRP internal coupler were developed.

Table of Contents

Acknowledgements	ii
Abstract	iii
List of Illustrations	ix
List of Tables	xvi
Chapter 1 Introduction.....	1
1.1 Background.....	1
1.2 Goals	4
1.3 Objectives	5
1.4 Research significance	6
1.5 Outline for dissertation.....	7
Chapter 2 Literature Review	8
2.1 Test methods	8
2.1.1 Material test methods on CFRP composite laminate	8
2.1.2 Joint shear test method	9
2.1.3 Hydrostatic test method.....	10
2.2 Material	11
2.2.1 Dry-mixed concrete material	11
2.2.2 Synthetic-fiber-reinforced concrete	13
2.2.3 Fiber-reinforced polymer	14
2.3 Finite element method (FEM)	17
2.3.1 Material nonlinearity	17
2.3.1.1 Concrete damage plasticity.....	19
2.3.1.2 Yield criteria	23
2.3.2 Contact and contact properties	25
2.3.2.1 Hard contact.....	25
2.3.2.2 Interaction between surfaces.....	27

2.3.2.3 Surface-to-surface contact.....	28
2.3.3 Geometric nonlinearity	30
2.3.4 Newton-Raphson Method.....	31
Chapter 3 Material Test.....	34
3.1 CFRP laminate tensile test	34
3.1.1 Specimen geometry	34
3.1.2 CFRP laminate material properties	36
3.1.2.1 Carbon-Fiber-Reinforced Polymer	37
3.1.2.2 Saturated epoxy resin matrix	38
3.1.3 Manufacturing of material specimen	39
3.1.4 Test setup and procedures.....	41
3.1.5 Material Test Results.....	43
3.1.5.1 0°/90° Fiber direction under pseudo-static loading	43
3.1.5.2 45°/-45° Fiber direction under pseudo-static loading.....	47
3.2 Conclusion	51
Chapter 4 Development of 3D Finite Element Model of Joint Shear Test.....	52
4.1 Numerical Modeling and Analysis Algorithms	52
4.1.1 Parts and geometry	53
4.1.2 Material modeling	55
4.1.3 Assemblage of all parts	58
4.1.4 Boundary and load conditions	58
4.1.5 Contact and contact properties	59
4.1.6 Mesh and element types	61
4.1.7 Analysis algorithm	63
4.2. Results of numerical study	65
4.2.1 Crack pattern	67
4.2.2 Deflection of the CFRP internal coupler.....	68

4.2.3	Relative separation at the bottom of assembled concrete pipes	71
4.2.4	Principal strain value on CFRP internal coupler.....	74
4.3	Conclusion	79
Chapter 5	Experimental Tests	80
5.1	Materials	80
5.1.1	Synthetic-fiber-reinforced concrete material	80
5.1.2	Conventional reinforced concrete pipe.....	80
5.1.3	Thin-walled flexible concrete pipes with synthetic fibers.....	82
5.2	Joint system utilizing carbon-fiber-reinforced polymer fabric	84
5.2.1	External wrapping by CFRP fabric	84
5.2.1.1	Geometry and mechanical properties of specimens.	84
5.2.1.2	Experimental setup and instrumentation	85
5.2.1.3	Procedure of shear test on wrapping joint system.....	86
5.2.1.4	Results of Externally Wrapped Joint System.....	88
5.2.2	Internal CFRP coupler system	98
5.2.2.1	Experimental Joint Shear Test.....	101
5.2.2.2	Geometry and mechanical properties of specimens	102
5.2.2.3	Experimental setup and instrumentation	104
5.2.2.4	Experimental results of CFRP internal coupler.....	106
5.2.3	Hydrostatic test of CFRP coupler system for concrete pipe	126
5.2.3.1	Hydrostatic test setup	127
5.2.3.2	Hydrostatic test result	130
5.3	Conclusion	133
Chapter 6	Parameter Study	135
6.1	Pre-processor	137
6.2	Post-processing.....	139
6.3	Development of CFRP coupler design equation	140

6.3.1 Preliminary model investigation.....	142
6.3.1.1 Correlation analysis	142
6.3.1.2 Residual analysis	144
6.3.2 Best-fitted model selection	146
6.3.2.1 Best subsets selection	147
6.3.2.2 Stepwise regression method.....	148
6.3.2.2.1 Forward selection regression method	148
6.3.2.2.2 Backward elimination method	151
6.3.3 Fitted regression models	152
6.3.4 Design equations.....	153
6.3.4.1 Ultimate Shear Force Equation.....	154
6.3.4.2 Vertical Deflection at CFRP Internal Coupler	156
6.3.4.3 Relative separation at bottom of assembled concrete pipes	158
6.3.5 Three-dimensional contour alignment chart.....	160
6.4 Conclusions of parametric study	165
Chapter 7 Discussion of Results and Recommendations for Future Research	166
7.1 Discussion and Summary	166
7.2 Main Conclusions	173
7.3 Recommended Future Works.....	175
Appendix A Results of uni- and bi- directional material tests.....	176
Appendix B Results of Finite Element Analyses	183
Appendix C Statistical Analysis Results.....	427
REFERENCES.....	455
BIOGRAPHICAL INFORMATION.....	462

List of Illustrations

Figure 2-1 - Joint shear test schematic (ASTM C497-16a, 2016)	9
Figure 2-2 - Hydrostatic testing on 30-inch steel reinforced concrete pipe (Mikhaylova, 2014)	11
Figure 2-3 - Effect of synthetic fiber at different fiber volume fractions (Alhozaimy and Soroushian, 1996).....	13
Figure 2-4 - Performance map of fibers used in structural composite materials (Engineering mechanics of composite materials, 2 nd Ed, 2006)	16
Figure 2-5 - Nonlinear stress-strain relationship	18
Figure 2-6 - Compressive constitutive stress-strain response of concrete material under axial pressure	21
Figure 2-7 - Tensile constitutive stress-strain response of concrete material under axial pressure	21
Figure 2-8 - Post-failure stress-displacement response with fracture energy approach ..	22
Figure 2-9 - Yield surface in principal stress space (ABAQUS, 2016)	24
Figure 2-10 - Hard contact pressure-overclosure relationship (ABAQUS, v6.14)	26
Figure 2-11 - Linear pressure-overclosure relationship with default (ABAQUS, v6.14) ...	28
Figure 2-12 - Schematic of surface-to-surface contact algorithm (ABAQUS, v6.14)	29
Figure 2-13 - The Newton-Raphson method with a load increment (ABAQUS, v6.15)....	32
Figure 2-14 - Process of the second iteration (ABAQUS, v6.15)	33
Figure 3-1 - Dimensions of specimen on pseudo loading scenario.....	35
Figure 3-2 - Coupon specimen under pseudo-static loading scenario on front and side view of unidirectional coupon specimen	36
Figure 3-3 - Carbon fiber reinforced polymer.....	38
Figure 3-4 - Manufacturing of CFRP laminate panel	40

Figure 3-5 - Material Testing Machine (MTS)	41
Figure 3-6 - Layout of the strain gauges on specimen	42
Figure 3-7 - Specimen for unidirectional tensile test.....	42
Figure 3-8 - Poisson's ratio on 0.0625, 0.125, and 0.25 inches uni-directional CFRP laminate thickness.....	44
Figure 3-9 - Tensile loading and corresponding displacement of 0.25 in. thickness specimen	45
Figure 3-10 - Longitudinal stress as function of the longitudinal strain of 0.25 in. thickness specimen	45
Figure 3-11 - Failure mode of unidirectional composite materials	46
Figure 3-12 - No slippages on tab materials for unidirectional CFRP laminates	46
Figure 3-13 - Poisson's ratio on 0.0625, 0.125, and 0.25 inches bi-directional CFRP laminate thickness.....	47
Figure 3-14 - Tension and corresponding displacement of bidirectional composite laminates	48
Figure 3-15 - Shear stress as function of shear strain of bidirectional composite laminates	49
Figure 3-16 - Failure of bidirectional composite materials	50
Figure 3-17 - No slip observed between bidirectional CFRP laminate specimen and wedge grips	50
Figure 4-1 - Schematic of three-dimensional models for joint shear test	52
Figure 4-2 - Configuration of all parts	53
Figure 4-3 - Constitutive laws of synthetic fiber reinforced concrete	56
Figure 4-4 - Stress-Strain curve of steel reinforcement materials	57
Figure 4-5 - Constitutive law of CFRP laminate	57

Figure 4-6 - Applied boundary condition in FEM model.....	58
Figure 4-7 - Contact pairs in joint shear test model.....	61
Figure 4-8 - Schematic of 8-noded linear brick element.....	62
Figure 4-9 - The Newton-Raphson method with a load increment.....	64
Figure 4-10 - Comparison of crack pattern on 48-inch TW pipes with CFRP coupler.....	67
Figure 4-11 - Vertical deflection and shear force plot on 36-inch pipe with three different thicknesses of CFRP coupler.....	68
Figure 4-12 - Shear force vs. vertical deflection on 48-inch concrete pipe with 0.1875 inch of CFRP coupler mid-thickness	69
Figure 4-13 - Shear force vs. vertical deflection on 54-inch concrete pipe with 0.25 inch of CFRP coupler mid-thickness	69
Figure 4-14 - Shear force vs. vertical deflection on 72-inch concrete pipe with 0.375 inch of CFRP coupler mid-thickness	70
Figure 4-15 - Shear force vs. vertical deflection on 84-inch concrete pipe with 0.375 inch of CFRP coupler mid-thickness	70
Figure 4-16 - Relative separation at bottom of assembled concrete pipe	72
Figure 4-17 - Relative separation length at bottom of assembled concrete pipe vs. shear force response on 48-inch concrete pipe with 0.1875 inch thick CFRP coupler	72
Figure 4-18 - Relative separation length at bottom of assembled concrete pipe vs. shear force response on 72-inch concrete pipe with 0.375 inch thick CFRP coupler	73
Figure 4-19 - Relative separation length at bottom of assembled concrete pipe vs. shear force response on 84-inch concrete pipe with 0.375 inch thick CFRP coupler	73
Figure 4-20 - Maximum in-plane principal strain contour of the CFRP coupler at the ultimate shear force on 96-inch ID of TW concrete pipe with a 12 inch wide coupler with 0.25 inch mid-thickness.....	74

Figure 4-21 - Maximum in-plane principal strain value with corresponding angles from crown to invert of the CFRP coupler for 120-inch TW concrete pipes with 12-inch CFRP coupler at 44 kips of the shear force required by ASTM C497-16a.....	75
Figure 4-22 - Strain value vs. shear forces on 48 in. pipe with 0.1875 in coupler thickness	76
Figure 4-23 - Strain value vs. shear force on 54 in. pipe with 0.25 in coupler thickness..	76
Figure 4-24 - Strain values vs. shear forces on 72 in. pipe with 0.375 in coupler thickness	77
Figure 4-25 - Strain value vs. shear force on 84 in. pipe with 0.375 in coupler thickness	77
Figure 4-26 - Shear force vs. strain values obtained by FEM and experimental test on TW72 pipe with 0.375 inch coupler.....	78
Figure 5-1 - Production of thin-wall concrete pipe: (a) Packerhead, (b) Steel mold, and (c) Steam curing.....	81
Figure 5-2 - Production of steel cages: (a) Welding machine (b) Steel cage	82
Figure 5-3 - Hawkeye rising core (Alena, 2014)	83
Figure 5-4 - Setup and schematic of joint shear test	85
Figure 5-5 - Wrapping system process.....	87
Figure 5-6 - Load-deflection plot of TW36-3W-3H.....	89
Figure 5-7 - Flaking of concrete and delamination of CFRP for TW 36-3W-3H	89
Figure 5-8: Load-deflection plot of Second-TW36-3W-3H.....	90
Figure 5-9: Flaking of concrete (Mode I).....	90
Figure 5-10: Load deflection plot of TW36-3W-24H	91
Figure 5-11: Flaking concrete of TW36-3W-24H	91
Figure 5-12: Load deflection plot of TW36-3W-24H-D	92
Figure 5-13: Flaking concrete of TW36-3W-24H with Dirty	92

Figure 5-14: Load deflection of TW36-6W-24H	93
Figure 5-15: Flaking concrete of TW36-6W-24H	93
Figure 5-16: Load deflection of TW60-12W-24H	94
Figure 5-17: Concrete fracture of TW60-12W-24H.....	94
Figure 5-18: Comparison of specimens on dirty or clean environment	95
Figure 5-19: Load deflection plot of TW36-6W-1H	96
Figure 5-20: Slipped out CFRP fabric from assembled pipes on TW36-6W-1H	96
Figure 5-21: Load deflection of TW36-3W-2H	97
Figure 5-22: Slipped out CFRP fabric from assembled pipes on TW36-3W-2H	97
Figure 5-23 - Configuration of internal joint system	99
Figure 5-24 - 36-inch Styrofoam wrapped by the CFRP fabric sheet.....	99
Figure 5-25 - Experimental joint shear test setup for CFRP internal coupler	101
Figure 5-26 - Configuration of joint shear test on TW concrete pipe with the CFRP coupler.....	104
Figure 5-27 - Assembling concrete pipes with the CFRP coupler	105
Figure 5-28 - Joint shear test results on 36-inch inside diameter of TW pipes.....	108
Figure 5-29 - Failure mode of joint shear test.....	109
Figure 5-30 - Propagated crack pattern on springline of pipes at 24 kips for 36-inch RCP	110
Figure 5-31 - Strain gauge installation of the CFRP internal coupler	110
Figure 5-32 - Load vs. displacement curve of RCP-36-0.25.....	111
Figure 5-33 - Local buckling of CFRP coupler and crack pattern on springline	111
Figure 5-34 - Shear force vs. vertical deflection response of TW-36-0.0625	112
Figure 5-35 - CFRP coupler of 0.0625 inch failed; no visible damage on concrete pipe	112

Figure 5-36 - Shear force vs. vertical deflection response of TW-36-0.125	113
Figure 5-37 - Internal joint system failed for TW-36-0.125	113
Figure 5-38 - Shear force vs. vertical deflection response of TW-48-0.125	114
Figure 5-39 - Compressive failure on concrete pipe for TW-36-0.25	115
Figure 5-40 - Shear force vs. vertical deflection response of TW-48-0.1875	116
Figure 5-41 - Shear force vs. vertical displacement response of TW-54-0.1875	117
Figure 5-42 - Shear force vs. vertical displacement response of TW-54-0.25	118
Figure 5-43 - Collapse of the CFRP internal coupler for TW-48-0.1875 specimen	119
Figure 5-44 - Collapse of the CFRP internal coupler for TW-54-0.1875 specimen	119
Figure 5-45 - Collapse of the CFRP internal coupler for TW-54-0.25 specimen	119
Figure 5-46 - Shear force vs. vertical displacement response of TW-72-0.25	120
Figure 5-47 - Shear force vs. vertical displacement response of TW-72-0.375	120
Figure 5-48 - Shear force vs. vertical displacement response of TW-84-0.375	121
Figure 5-49 - Collapse of the CFRP internal coupler for TW-72-0.25 specimen	122
Figure 5-50 - Collapse of the CFRP internal coupler for TW-72-0.375 specimen	122
Figure 5-51 - Collapse of the CFRP internal coupler for TW-84-0.375 specimen	122
Figure 5-52 - Strain value versus shear force on the TW-48-0.25 specimen	123
Figure 5-53 - Strain value versus shear force on the TW-54-0.25 specimen	123
Figure 5-54 - Strain value versus shear force on the TW-72-0.25 specimen	124
Figure 5-55 - Strain value versus shear force on the TW-72-0.375 specimen	124
Figure 5-56 - Strain value versus shear force on the TW-84-0.375 specimen	125
Figure 5-57 - Hydrostatic test setup	126
Figure 5-58 - Hydrostatic test setup configuration	127
Figure 5-59 - Pressure gage and sensor	128
Figure 5-60 - Leakage at the assembled joint	129

Figure 5-61 - Assembled CFRP coupler with sealant.....	129
Figure 5-62 - Pressure vs. time curve for 20 minutes.....	130
Figure 5-63 - The 1 st leakage on the concrete pipe wall.....	131
Figure 5-64 - The 2 nd leakage on the mid-wall of the concrete pipe.....	131
Figure 5-65 - Leakage on wall of the left concrete pipe.....	132
Figure 6-1 - Flow chart of parametric cases for CFRP coupler	135
Figure 6-2 - Parameter study flow chart.....	136
Figure 6-3 - Strategy for building a regression model (Applied Linear Statistical Models, 5th Ed., 2004).....	141
Figure 6-4 - Pearson correlation matrix scatter plot.....	143
Figure 6-5 - Residual plot on inside diameter of concrete pipe	144
Figure 6-6 - Residual plot on thickness of concrete pipe.....	145
Figure 6-7 - Residual plot on width of CFRP internal coupler variable.....	145
Figure 6-8 - Residual plot on mid-thickness of CFRP internal coupler.....	146
Figure 6-9 - Comparison of observed and predicted ultimate shear forces.....	155
Figure 6-10 - Comparison of observed and predicted vertical deflection	157
Figure 6-11 - Comparison of observed and predicted ultimate shear forces.....	159
Figure 6-12 - Contours of normalized shear force as a function of pipe diameter and CFRP coupler thickness with 6-inch width of CFRP coupler	161
Figure 6-13 - Contours of normalized shear force as a function of pipe diameter and CFRP coupler thickness with 9-inch width of CFRP coupler	162
Figure 6-14 - Contours of normalized shear force as a function of pipe diameter and CFRP coupler thickness with 12-inch width of CFRP coupler	163
Figure 6-15 - Contours of normalized shear force as a function of pipe diameter and CFRP coupler volume	164

List of Tables

Table 3-1 - Properties of CF140/45 CFRP fabric sheet.....	37
Table 3-2 - CFRP laminate weight and physical properties (Vectorply, 2015).....	37
Table 3-3 - Material properties of saturated epoxy resin	39
Table 3-4 - Tensile test results of unidirectional composite laminates	44
Table 3-5 - Tensile test results of bidirectional composite laminates	48
Table 4-1 - Geometry properties of all parts for simulation.....	54
Table 4-2 - Tension stiffening damage variable for the plastic displacements.....	56
Table 4-3 - Result summary of numerical analyses and experimental tests of joint shear tests at ultimate shear forces	66
Table 4-4 - Result summary of numerical analyses and experimental test of joint shear tests at the required shear strength	66
Table 5-1 – Failure mode of specimens.....	87
Table-5-2 Maximum shear strengths	88
Table-5-3 Strengths of initial cracks at four regions	88
Table 5-4 - Thin-walled concrete pipe design specifications	103
Table 5-5 - Required shear force computed by ASTM C497-16a	107
Table 5-6 - Summary of joint shear test results	107
Table 5-7 - Summary of trials to prevent leakages	128
Table 6-1 - Input variables for building models.....	137
Table 6-2 - Correlation coefficient matrix of shear force and independent variables	143
Table 6-3 - Results of best subset regression method	147
Table 6-4 - Initial step of the stepwise model selection method	149
Table 6-5 - Second step of stepwise variable selection.....	149
Table 6-6 - Third step of the stepwise model selection method	149

Table 6-7 - 4th step of the stepwise model selection method.....	150
Table 6-8 - Summary of Stepwise model selection method	150
Table 6-9 - Backward elimination method, initial step	151
Table 6-10 - ANOVA result of multiple linear regression for ultimate shear force equation	154
Table 6-11 - The coefficient of the estimators on ultimate shear force equation.....	154
Table 6-12 - Pearson correlation matrix of estimate variable on shear force equation ..	155
Table 6-13 - ANOVA result of multiple linear regression for ultimate shear force equation	156
Table 6-14 - The coefficient of the estimators on ultimate shear force equation.....	156
Table 6-15 - Pearson correlation matrix of estimate variable on deflection equation.....	157
Table 6-16 - ANOVA results of relative separation length equation	158
Table 6-17 - The coefficient of the estimators on relative separation length equation ...	158
Table 6-18 - Pearson correlation matrix of estimate variable on deflection equation.....	159

Chapter 1 Introduction

1.1 Background

Concrete pipelines have been used as representative infrastructural systems since 1842 (Lee, 2010 and Schneider et al., 1999). Because of their low cost, high resistance to corrosion from sewage, and high durability, conventional reinforced concrete pipe (RCP) segments have been widely used to build buried pipelines for the construction of sanitary sewer systems. The RCP is classified as a rigid pipe and is much more brittle than flexible pipes, such as metal and plastic pipes. To improve the brittle failure mechanism, a steel wire mesh is embedded as reinforcement inside the concrete mixture. Due to the corrosion of their steel reinforcements, the RCPs have a crack-width limitation of 0.01 inch under the service load in the United States. The brittle failure mechanism and service-crack-width limitation increase the sensitivity of pipeline installation. Furthermore, buried pipes should have sufficient ductility to soil pressure and live loads. Flexible pipes, made of corrugated metal (CMP), polyethylene (PE), and high-density polyethylene (HDPE), are a possible alternative to RCP. Pipe showing more than 2% deflection without structural damage is classified as flexible (Park et al., 2015).

Within the past few years, 50%-reduced-thickness concrete pipes, also known as semi-rigid concrete pipes or thin-wall (TW) concrete pipes, have been investigated, and it has been found that reduced wall thickness of pipe can lead to greater flexibility, but potential loss of strength. To compensate for the loss of tensile and flexural strength, synthetic fibers were added to the concrete mixture as reinforcement materials. Mixing synthetic fibers within the concrete mixture resulted in lighter, less costly, more durable, and flexible pipe (Park et al., 2015). RCPs are assembled with rubber gaskets or rubber O-rings, with bell and spigot at both ends of the concrete pipe. However, due to the 56%

reduced wall thickness of the thin-wall concrete pipe, the bell and spigot cannot bind to the concrete wall. To overcome this limitation, the development of a new joint system has become essential.

For the past two decades, a fiber-reinforced polymer (FRP) material has been widely used to repair or retrofit damaged concrete of structures. It has extensively been used to confine concrete columns and to strengthen the flexural and shear strength of beams (Bae et al., 2010; Chajes et al., 1996; Hawileh et al., 2015; Sam et al., 2012; Niu et al., 2006; Toutanji et al., 2001; and Yao et al., 2005). It is generally employed as tensile material because of its high strength-to-mass ratio, which enhances a structure without adding dead load. It is easy to install, even in areas of limited access (Hawileh et al., 2015).

A carbon-fiber-reinforced polymer (CFRP) composite material is extremely resistant to various environmental conditions. Because of such an attractive advantage, the CFRP fabric sheet was selected for the joint system and employed to assemble the TW concrete pipes.

This dissertation explores the behavior of the CFRP composite joint system for the RCP and TW concrete pipes manufactured by Forterra, Grand Prairie, Texas. The developed joint system is manufactured of the CFRP fabric sheets and epoxy chemical resin matrices (BASF Corporation Construction Systems, 2014).

Joint shear tests were performed in accordance with the recognized standard of the American Society for Testing and Materials (ASTM) C497-16a. The effects of various thicknesses (0.0625 through 0.375 inches) of the CFRP internal couplers were investigated, and shear forces obtained from joint shear tests were compared with the required shear strength by ASTM C497-16a (ASTM, 2016). All of the results from the

experimental joint shear tests were used to verify a developed finite element method (FEM) model.

A three-dimensional finite element method (FEM) was employed to expand the geometric parameter variables: the wall thickness of the concrete pipe, the inside diameter of the concrete pipe, and the mid-thickness and width of the CFRP internal coupler. The FEM results were used in the post analyses. The nonlinear geometry, interactions, materials, and loading and boundary conditions were considered in the FEM analyses to simulate the experimental joint shear tests. A concrete damage plasticity (CDP) model and eight three-dimensional nodes with reduced interaction (C3D8R) element were employed. A nonlinear constitutive material model and continuum shell (S4R) were used to model the CFRP coupler. To simulate the effect of the deformed system, contact algorithms and surface-based contact were used on two contact pairs: inside the concrete pipe and internal coupler, and wooden cradles and external concrete pipes.

A parametric study was performed to investigate effects of the ultimate shear force, the vertical deflection, and the relative separation length at the bottom of the assembled concrete pipes as functions of the aforementioned geometric parameter variables. Results obtained from the parametric study were used to perform a multiple linear regression (MLR) to build three design equations, and to draw three contour plots of the various inside diameters of the concrete pipes and the mid-thickness of the CFRP internal couplers. Three normalized shear force contour plots for the CFRP coupler width of 6, 9, and 12 inches were drawn with the inside diameter and the wall thickness of the concrete pipe. One normalized shear force contour plot was drawn with the inside diameter of the concrete pipe and the volume of the CFRP internal coupler.

1.2 Goals

The primary goal of this dissertation is to develop design equations for the different sizes of inside diameters of concrete pipes, the wall thickness of the concrete pipe, the width of the CFRP internal coupler system, and the mid-thickness of the CFRP internal coupler system. In order to establish the design equations, a three-dimensional finite element model was developed and verified with the results of the full-scale experimental joint shear tests on different-sized inside diameters of concrete pipes and different thicknesses of the CFRP coupler system. Leakage of the CFRP coupler system was also investigated. Based on the finite element models, parametric studies were performed to develop the design equations of the CFRP coupler system. With the developed CFRP internal coupler, expandability for assemblage of different material pipes, such as assemblage between the concrete pipe and steel pipe, concrete pipe and polypropylene pipe or higher-density polyethylene pipe (HDPE) is possible. A conventional joint system for a conventional reinforced concrete pipe is only applicable to the same conventional RCP, because of an assemblage of bell and spigot debris.

1.3 Objectives

Concrete pipes are vital to infrastructures because they are cost effective, easy to install, and have a higher strength than polypropylene and steel pipes. Extensive research has been done on concrete pipes, and has led to the development of reduced-wall-thickness concrete pipes, which are easier to design, cost effective, and weigh less than conventional concrete pipes. However, as described previously, these pipes require the development of new joint system since bell and spigot cannot be used because of the thinner concrete pipe walls. The objectives of this project were:

- Optimization of geometrical variables: thickness and width of internal joints
- Parametric study of large-diameter-thin-wall concrete pipe's joint system
- Experimental tests of joint system to verify simulation
- Definition of design guideline for internal joint system
- Expandability of connector on different pipe materials

1.4 Research significance

Thin-wall concrete pipes are classified as semi-rigid concrete pipes. They successfully minimize the drawbacks of both rigid pipes and flexible pipes. As described previously, due to their high stiffness and strength, rigid pipes have a 0.01 inch of crack-width limitation of serviceability that can occur before being deflected to 2% of the inside diameter. Such a limitation increases the sensitivity of installation. Flexible pipes, such as steel and plastic pipes, can deflect more than 2% (and up to 5%) of the inside diameter (ASCE 15-98, 2000). Even though flexible pipe can reduce sensitivity without pipe damage, its low stiffness and thinner wall areas are susceptible to local buckling under soil pressure and live loads (Park et al., 2015). Compared with rigid concrete pipes and flexible pipes, thin-wall concrete pipes can deflect more than 2% of the inside diameter without pipe damage for reduced sensitivity of installation, and have sufficient stiffness to resist active soil pressure and live loads by carrying moment and shear in the pipe wall. However, as the wall thickness of the concrete pipe is reduced by 50% of the RCP design specification (ASTM C76, 2013), the conventional joint system, using bell and spigot, is not appropriate. This research validates the reliability of the flexible concrete pipe system which employs a new joint system and forms a continuous pipeline. In addition, the development of the new joint system, which uses CFRP material, can expand the varieties of pipeline system assemblages between different pipe materials. Depending on soil stiffness, neighboring conditions of buried pipe, and/or economic constraints, engineers install the proper types of pipes such as concrete, steel, polypropylene, or high-density polypropylene. Because of the lack of a joint system which can assemble different types of pipes, somewhat over-qualified pipes are sometimes used. This research suggests that the developed joint system of the CFRP internal coupler system be used.

1.5 Outline for dissertation

Chapter 1 represents the introduction of this dissertation, including dissertation goals, dissertation objectives, and the significance of this dissertation.

Chapter 2 presents literature reviews regarding CFRP laminate material tests, experimental tests, and three-dimensional numerical analyses. The history of the concrete pipe system is also described in this chapter.

Chapter 3 describes carbon-fiber-reinforced polymer (CFRP) laminate specimens for coupon material tests. The 0/90 fiber direction stacking and -45/45 fiber direction stacking in balanced and symmetrical CFRP laminate specimens were considered.

Chapter 4 includes numerical analysis techniques and nonlinearity algorithms to define the pre-process of the three-dimensional finite element modeling and post-process of numerical simulation results to analyze data. Analyzed results of some specimens which can be conducted by experimental tests are taken into account in Chapter 3.

Chapter 5 describes details of joint shear tests on thin-walled concrete pipe systems. The assemblage of the TW concrete pipes by the CFRP internal coupler system, and the investigation of the structural performance of the developed internal coupler system by performing experimental tests in accordance with ASTM C497-16a, are detailed in this chapter. The hydrostatic test is also discussed herein.

Chapter 6 deals with the parametric studies on different-sized inside diameters of the concrete pipe, different widths of CFRP internal coupler systems, and various thicknesses of the CFRP coupler system. The analyzed and obtained data was employed to build a design equation for the assemblage of the developed thin-walled concrete pipe system.

In *Chapter 7*, the developed CFRP internal system is summarized, and future researches needed are suggested.

Chapter 2 Literature Review

2.1 Test methods

2.1.1 Material test methods on CFRP composite laminate

Unlike steel and aluminum materials with isotropic material properties, there are several variables, such as different fiber orientations, stacking sequence of fiber fabric sheets, and volume fractions of fiber and matrix resin, that influence the performance of composite materials.

Several test methods have been proposed for determining anisotropic material properties: in-plane shear stress-strain response, bidirectional coupon test, 10° off-axis test, rail shear test, and torsion test. In this research, bidirectional coupon tests were conducted in accordance with ASTM D3518-94 (ASTM, 2013), *Standard Test Method for "In-plane shear response of polymer matrix composite materials by tensile test of a $[+45^\circ/-45^\circ]$ laminate"* and ASTM D3039 (ASTM, 2014). To investigate the in-plane tensile stress-strain response and properties of polymer matrix composite materials, the quasi-static tensile tests were performed on the $-45^\circ/45^\circ$ stacking sequence. The in-plane tensile stress-strain response was determined by ASTM D3518. The constitutive law of CFRP laminate obtained from material tests, ASTM D3039 and ASTM D3518, was applied to the material modeling of a simulation analysis of joint shear test with CFRP internal coupler system.

In order to perform quasi-static material tests on $0^\circ/90^\circ_{is}$ with $i = 3, 6,$ and 12 layers, tab materials were required to prevent clamp failure at the end of the hydraulic grip. The length of the tab was more than 2 inches long, per ISO 527-1, *"International standard for the determination of tensile properties"* and ASTM D3479, *"The Standard Test Method for Tension Fatigue of Polymer Matrix Composite Materials"*. The tab was fabricated of aluminum which has sufficient lateral pressure, and was 3 inches long and

1/8 inch thick. To avoid sudden section geometry of the specimen and slippage, a bevel angle of 7 degrees was applied to one end of the tab. An MTS machine was employed to perform the tensile material test.

2.1.2 Joint shear test method

The purpose of a joint shear test method is to validate the design of joint-connected pipes. The structural capability of external and internal joint systems is investigated by applying a differential shear force to a suspended concrete pipe in accordance with ASTM C497-16a (ASTM, 2016). According to ASTM C497-16a, two test pipes are assembled with three wooden cradles as support. One pipe is fully supported on both ends of the pipe by two wooden cradles; and the second pipe is supported by an installed external and internal joint system, and by a wooden cradle at the far end of the assemblage. The vertical shear force (F) is applied to suspended concrete pipe at a distance of 1 inch for the internal joint system and 6 inches for the external joint system.

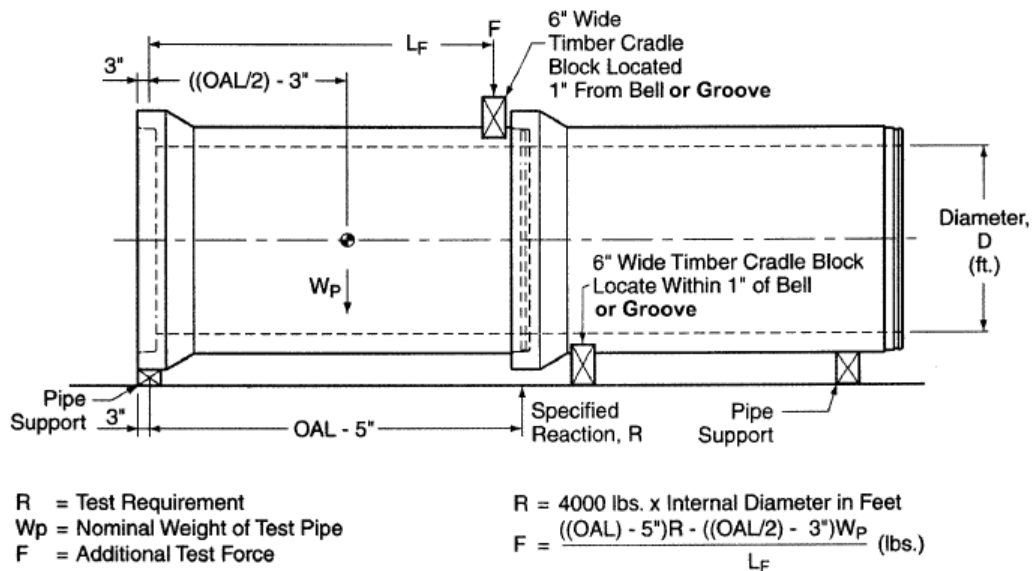


Figure 2-1 - Joint shear test schematic (ASTM C497-16a, 2016)

In the joint shear test for conventional reinforced concrete pipe, the required joint shear strength was computed by using Eq. 2.1, shown below.

$$F = \frac{[(OAL - 5in) \times R - (OAL / 2 - 3in)] W_p}{L_F} (lb) \quad (2.1)$$

where OAL is the overall length of an assembled concrete pipe, W_p is the nominal weight of a test concrete pipe, L_F is the length from end to loading point, and R is computed by 4000 lbs. times the internal diameter in feet.

2.1.3 Hydrostatic test method

The hydrostatic joint test is a key quality control test used to investigate joint system leakage problems. Concrete pipes are widely utilized for drainage, sewage, and irrigation purposes. Buried concrete pipes are subjected to moderate movements due to a failure of backfill or settlement, which makes joint systems vulnerable to failure and leakage. For conventional reinforced concrete pipes (RCPs), the hydrostatic test method is a quality control test that meets the requirements stated in the specification of ASTM C497 and ensures that the RC pipes are ready to be shipped from the manufacturer. The hydrostatic test investigates the flexible watertight seal used, either rubber gaskets, sealing bands, or flexible joint sealants. In accordance with ASTM C497-16a (ASTM, 2016), the hydrostatic test is conducted with 13 psi for 20 minutes. Mikhaylova conducted the hydrostatic test on a 30 in.-diameter wall C steel-fiber-reinforced concrete pipe, as shown in Fig. 2-2. Mikhaylova's test resulted in minor leakage, which started immediately at the joints and lasted throughout the test. Joint seepage was observed on the area where the surface was uneven due to the presence of fiber. In addition, pipes with higher fiber dosages were more venerable to leakage on concrete pipe surfaces than those with a low volume of fiber (Mikhaylova, 2014).



(a) Hydrostatic testing



(b) Ram-nek on tongue and groove

Figure 2-2 - Hydrostatic testing on 30-inch steel reinforced concrete pipe (Mikhaylova, 2014)

2.2 Material

2.2.1 Dry-mixed concrete material

All mixtures used in the production of concrete pipes were of dry-cast concrete, which has a ratio of water-to-cement of 0.34, compared to the normal range of water-to-cement ratio for the wet concrete material of 0.40 to 0.50. For the past ten years, dry-mixed concrete mixture has been widely used in tunnel linings, rehabilitation of marine structures, and repair of damaged structures. Dry-cast concrete mixtures have higher compressive strength and require less curing time than wet-cast concrete mixtures. However, because of the low water-to-cement ratio, the volume of rebounded concrete is greater than that of the wet-cast concrete material. Fiber reinforcement is added to alleviate the amount of rebounded concrete mixture. Steel fiber reinforcement was first employed in a tunnel lining in 1973 at Ririe Dam in Idaho (Banthia et al., 1992). Since

then, researchers have been diligent in their pursuit of the ultimate fiber-reinforced concrete mixture (Shah et al., 1971; Grzybowski et al., 1990; Soroushian et.al, 1990; Toutanji et al., 2000; and Song et al., 2004). The initial use of fiber as reinforcement for concrete material was in the 1960s. In order to improve concrete material properties, Romuldi and Baston used steel-fiber reinforcement to overcome the limited tensile strength of concrete material evidenced by internal holes and micro-cracks (Romuldi et al., 1963). They compared theoretical results and test results, which showed good agreement and increased tensile strength. On the basis of their research, fiber-reinforced concrete materials have been developed by numerous researchers, and interest in using fiber has increased. Fiber reinforcement leads to a plain concrete mixture having benefits such as enhanced toughness, higher ductility, and higher energy absorption. A comparison of failures of structures built of plain concrete mixture and those constructed of fiber-reinforced concrete mixture reveals its benefits more clearly. At peak load, the plain concrete structure fails in a brittle manner. The fiber-reinforced concrete structure, however, supports more load because of a bridge effect. The embedded fiber reinforcement is stretched beyond the peak load, which increases the energy absorption of the structure and maintains its residual strength. Nemkumar's material test shows the fiber-reinforced concrete material, enhanced material properties of strength and flexural toughness, and reduced amount of rebound compared to the plain concrete material (Banthia et al., 1995). However, Fanella and Naaman (1985) found that even though the steel fiber reinforcement enhanced the tensile strength of the concrete material, no significant effect was shown on the compressive strength (Fanella et al., 1985).

2.2.2 Synthetic-fiber-reinforced concrete

The use of synthetic (polypropylene) fibers has been researched less than the use of steel fiber reinforcement in concrete. Alhozaimy and Soroushian investigated compressive, flexural, and impact properties of concrete material (Alhozaimy et al., 1996), and concluded that there were no statistically significant effects on the compressive and flexural strength of the concrete material. However, compressive toughness, flexural toughness, and impact resistance were enhanced, as shown in Fig. 2-3.

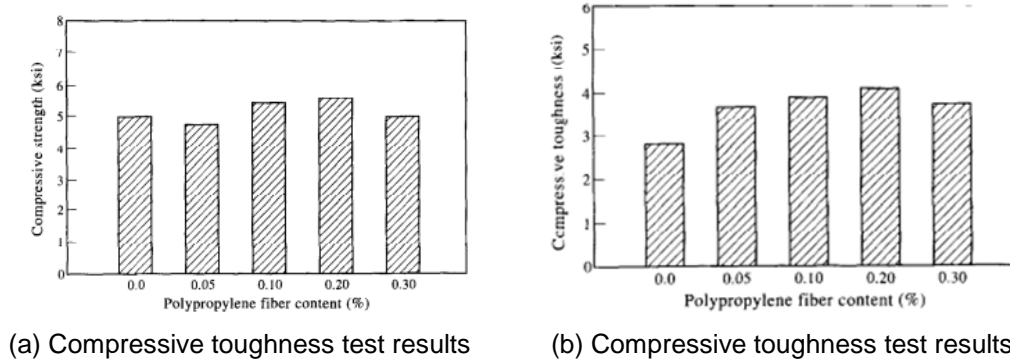


Figure 2-3 - Effect of synthetic fiber at different fiber volume fractions (Alhozaimy and Soroushian, 1996)

According to Alhozaimy and Soroushian's results, the synthetic fibers affected after-peak failure behavior by resisting crack development. For compressive tests, in accordance with ASTM C-39, the compressive strength was recorded when it reached peak.

2.2.3 Fiber-reinforced polymer

For several decades, a combination of steel reinforcement and concrete material was considered the ideal construction material. An advantage of identical thermal expansions between concrete material and steel reinforcement led numerous engineers, designers, and contractors to increase their use of reinforced concrete materials in civil engineering applications. Reinforced concrete materials have been attractive since the 1930s, leading numerous researchers, including Norman de Bruyne, a pioneer in the United Kingdom, to research fiber-reinforced polymers (FRP) (Gutkowski, 2005). FRP was developed for use in the aviation industry. The initial fiber was discovered accidentally when a jet of compressed air was directed at a stream of molten glass and produced fiber (Slayter, 1938). The fiber reinforcement material was widely used after a resin was developed to combine the fiber reinforcements by du Pont (Du Pont, 1936). The resin encapsulates the fiber reinforcement and bonds with the fibers for a suitable curing period to make a matrix called a composite material.

Since the initial stage of FRP development, the materials used have become diversified: (1) glass fiber material, (2) aramid fiber material, and (3) carbon fiber material. For general purposes, glass fiber material is used in various applications in civil engineering, aerospace engineering, and the manufacturing of sports equipment because of low cost, higher strength, light weight, and high chemical resistance compared to conventional steel reinforcement.

Depending on the usage of the glass fiber materials, three different types of fibers are classified: (1) E-Glass for higher electrical resistance, (2) S-Glass for higher strength, (3) AR-Glass for chemical resistance, and (4) ECR-Glass for electrical chemical resistance. The E-Glass fiber material is widely used (90% of the time) as a representative fiber due to its advantages of low cost, high strength, light weight, and

high chemical resistance. Even though the E-Glass fiber has significant disadvantages, such as lower modulus and lower fatigue resistance, high abrasiveness when machined, and susceptibility to stress corrosion, the advantages outweigh the disadvantages, which has led to its widespread use. The S-Glass fiber material, defined as high strength glass, is used in more structurally-demanding applications because it has higher strength and moderately higher stiffness than standard E-Glass fiber material. A slightly lighter density of the S-Glass fiber makes the laminate weight 20-35% lighter than the equivalent made from the E-Glass fiber material (Vectorply, 2016). The AR-Glass and ECR-Glass fiber materials have been used in applications where a higher chemical resistance and electrical chemical resistance was required (Park, 2013).

Aramid fiber materials are crystalline aromatic polyamide and are best used in bullet proof vests, chainsaw pants, and safety gloves because of their higher specific tensile strength and very low density. The Aramid-fiber materials have light weight; high tensile strength, specifically, high impact damage tolerance; excellent vibration damping; and low longitudinal thermal expansion compared to other fiber materials. However, the Aramid fiber materials are not adequate for applications which are exposed to harsh environmental conditions, since they are vulnerable to UV radiation, high moisture absorption, and very low compressive strength.

Carbon fiber materials have the highest strength fiber reinforcement, and are used in high-performance applications such as aerospace, sporting goods, marine, and infrastructures. Carbon fiber materials have excellent stiffness, strength, fatigue resistance, chemical resistance, and light weight, which makes them the ideal reinforcing fiber material except for the manufacturing cost,

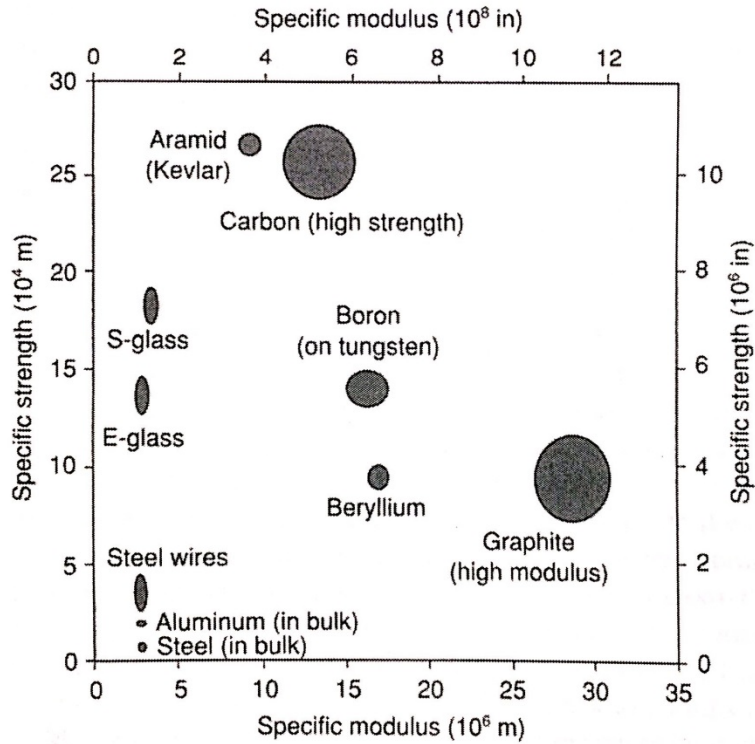


Figure 2-4 - Performance map of fibers used in structural composite materials (Engineering mechanics of composite materials, 2nd Ed, 2006)

Figure 2-4 depicts the modulus and specific strength of some typical fibers such as glass, aramid, and carbon fiber materials that provide higher strength than steel wires. The FRP composite material has been widely used in civil engineering for several decades to retrofit or rehabilitate damaged members of structures. Carbon-fiber-reinforced polymer with a suitable resin is generally used to retrofit damaged columns, slabs, or beams.

2.3 Finite element method (FEM)

Finite Element Method (FEM) is an engineering computational tool that is used to perform engineering analyses and has been widely employed in civil and aerospace engineering. It was developed in the early 1940s by pioneers Alexander Hrenikoff and R. Courant (Anklesaria, 2012). A key characteristic of FEM is that it uses a mesh discretization of a continuous domain entered into a set of discrete sub-domains.

Numerical models regarding performances of a concrete pipe, concrete box culvert, or interaction between the soil and concrete pipe were developed by researchers (Abolmaali et al., 2011, and Kang et al., 2007, Garg et al., 2009). However, little has been published on the joint system of the concrete pipe structure (Rajani et al., 2013; Singhal et al., 1983; Wham et al., 2015; Buco et al., 2008; Garcia et al., 2013; Brockenbrough, 1983; and Wang et al., 2013).

The FEM computes an approximated solution by reducing tolerance error. The nonlinear finite element method can be employed to simulate a more accurate solution than that obtained by the results of experimental tests. The nonlinear algorithms are material nonlinearity, contact nonlinearity, and geometric nonlinearity.

2.3.1 *Material nonlinearity*

Material constitutive law is the basis of numerical analysis. It consists of a relationship between stress and corresponding strain in solid mechanics. Most engineering materials have plastic characteristics that are observed on the stress and strain responses, where the strain value exceeds the yielding strain value.

Concrete and steel reinforcement are representative nonlinearity materials in civil engineering. The material constitutive law is composed of nonlinear elasticity and elasto-plasticity. The nonlinear elasticity is defined as following the same path through loading

and unloading, without change of geometry, which indicates that nonlinear materials have a recoverable deformation and no energy lost, as shown in Fig. 2-5 (a).

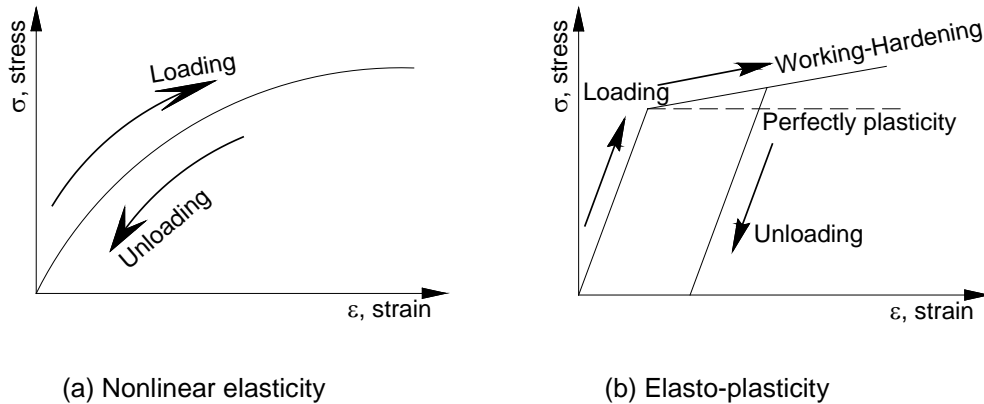


Figure 2-5 - Nonlinear stress-strain relationship

Elastoplastic is material that is permanently deformed after unloading, as shown in Fig. 2-5 (b). Some of them show perfectly rigid plastic behavior, in which elastic strains can be neglected. Work-hardening plastic stress and strain behavior particularly appear in metal materials. The coordinate system of the isotropic material is independently orientated, and the material characteristic is considered under the hydrostatic pressure, influencing the yield point and the flow stress level.

The phenomena of plasticity and associated yield criteria (or failure criteria) should be taken considered for the stabilization of structures. Tresca's and von-Mises's yield criteria took it into account for isotropic materials. The von-Mises criterion was more effective at predicting shear cyclic deformation than the experimental test was.

2.3.1.1 Concrete damage plasticity

Numerous researchers employed concrete damage plasticity (CDP) for a concrete material model designed to capture crack propagation due to loss of tensile strength under tensile or flexural loading (Grassl et al., 2006; Cicekli et al., 2007; Cervenka et al., 2006; Wu et al., 2006; Jason et al., 2006; and Maekawa et al., 2003). The concrete damage plasticity model is included in the ABAQUS material library for the analysis of concrete and quasi-brittle materials (ABAQUS, 2006). The concrete material was used to fail under brittle mechanisms with low confining pressures, and showed that the main failure mechanism was cracking in tension and crushing in compression. The concrete damage plasticity was modeled based on those proposed by Lubliner et al. and by Lee and Fenves (Lubliner et al., 1998). The model is explained with the strain rate decomposition assumed for the rate-independent model. As shown in Eq. 2.2 below, the total strain rate consists of the strain rate inelastic part and the strain rate in the plastic part:

$$\dot{\varepsilon} = \dot{\varepsilon}^{el} + \dot{\varepsilon}^{pl} \quad (2.2)$$

where $\dot{\varepsilon}^{el}$ is strain rate value in elastic part and $\dot{\varepsilon}^{pl}$ is the strain rate in the plastic part.

With the mentioned total strain rate, the stress-strain relation is computed by using an initial elastic stiffness of the material. The stress value is expressed in terms of the total strain rate with the initial elastic stiffness (undamaged material condition) of the material and the scalar stiffness degradation variable which ranges from zero (undamaged material) to one (fully damaged material). The stiffness degradation value influences the reduction of elastic stiffness, depending on how much the material is damaged. With those terms, the effective stress is defined as Eq. 2.3 below:

$$\bar{\sigma} = D_0^{el} \cdot (\varepsilon - \varepsilon^{pl}) \quad (2.3)$$

where $\bar{\sigma}$ is the effective stress and D_0^{el} is the initial elastic stiffness. The Cauchy stress is expressed in terms of the effective stress through the scalar degradation relation as expressed in Eq. 2.4 below:

$$\sigma = (1 - d)\bar{\sigma} \quad (2.4)$$

For the damaged concrete cross section, the factor of (1-d) from the Eq. 2.4 signifies the ratio of the effective load-carrying section, which is computed by substituting the damaged section from the overall area for the overall section area. The material is subjected to damage, and the effective stress is governed by the Cauchy stress because the effective area resists external loads. When the material is damaged, the evolution of the degradation variable, d, is governed by a set of hardening variables and the effective stress, as shown in Eq. 2.5.

$$d = d(\bar{\sigma}, \bar{\varepsilon}^p) \quad (2.5)$$

The degradation damage variables are composed of compressive and tensile damage degradation, d_c and d_t . As shown in Figs. 2-6 and 2-7, the compressive and tension constitutive stress-strain responses are expressed as a function of the compressive and tensile damage variable and initial elastic stiffness and strain values.

$$d_c = (1 - d_c) \cdot E_0 \cdot (\varepsilon_c - \bar{\varepsilon}_c^{pl}) \quad (2.6)$$

$$d_t = (1 - d_t) \cdot E_0 \cdot (\varepsilon_t - \bar{\varepsilon}_t^{pl}) \quad (2.7)$$

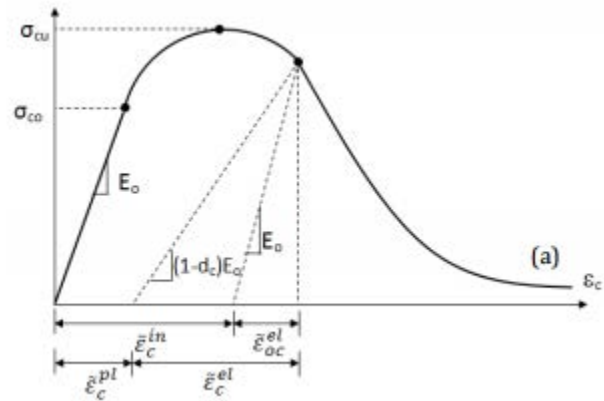


Figure 2-6 - Compressive constitutive stress-strain response of concrete material under axial pressure

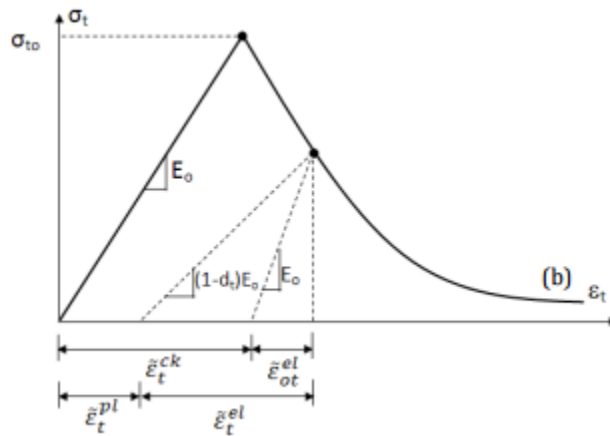


Figure 2-7 - Tensile constitutive stress-strain response of concrete material under axial pressure

Mesh size is a very sensitive factor in numerical analysis and is a challengeable issue on the cracking of a concrete material model. To avoid the mesh size sensitivity issue, Hillerborg suggested a fracture energy approach (Hillerborg et al., 1976). The fracture energy approach is described as the brittle behavior of the concrete material, which is defined by the stress-displacement response instead of the stress and strain responses.

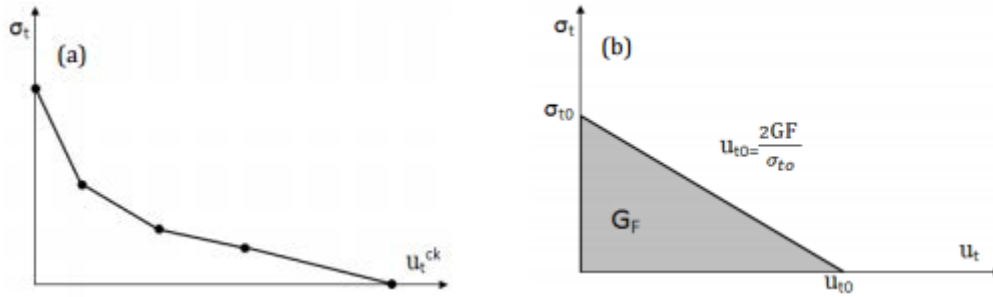


Figure 2-8 - Post-failure stress-displacement response with fracture energy approach

After a crack opening occurs, the linear loss of strength, as shown in Fig. 2-8 (b) is assumed, and the fracture energy, G_f , is employed as a material property and is computed by Eq. 2.8.

$$G_f^l = \int \sigma_t^l du_n \quad (2.8)$$

With the fracture energy and the linear degraded strength, the plastic displacements are computed by using Eqs. 2.9 and 2.10, shown below:

$$u_t^{pl} = u_t^{ck} - \frac{d_t}{(1-d_t)} \frac{\sigma_t l_0}{E_0} \quad (2.9)$$

$$\bar{\epsilon}_c^{pl} = \bar{\epsilon}_c^{in} - \frac{d_c}{(1-d_c)} \frac{\sigma_c}{E_0} \quad (2.10)$$

In the concrete damage plasticity model, plastic flow is assumed as the non-associated plastic flow for dilatancy evaluation. The flow rule is defined by the relationship between the strain rate shown in Eq. 2.11 and the direction of the plastic flow. The strain rate is a function of a non-negative value as the plastic consistency parameter, λ , and a scalar plastic flow potential defined by the modified Drucker-Prager hyperbolic function, ϕ .

$$\varepsilon^p = \lambda \frac{\partial \Phi}{\partial \bar{\sigma}} \quad (2.11)$$

The modified Drucker-Prager hyperbolic function is expressed in Eq. 2.12

$$\Phi = \sqrt{(\varepsilon \sigma_{t0} \tan \psi)^2 + \bar{q}^2} - \bar{p} \tan \psi \quad (2.12)$$

where \bar{p} is a hydrostatic pressure stress, is function of the effective stress as $\bar{p} = -\frac{1}{3} \text{trace}(\bar{\sigma})$, \bar{q} is a Von-Mises equivalent effective stress which is expressed as $\bar{q} = \sqrt{\frac{3}{2}(\bar{S}:\bar{S})}$, \bar{S} is the effective stress deviator, $\bar{S} = \bar{\sigma} + \bar{p}I$, $\psi(\theta, f_i)$ is a dilation angle which is measured in p-q plane at high confining pressures, $\sigma_{t0}(\theta, f_i)$ is an uniaxial tensile stress at failure, and $\varepsilon(\theta, f_i)$ is an eccentricity.

2.3.1.2 Yield criteria

The material modeling is based on three-dimensional tensors of stress and strain, as shown in the following Cartesian tensor notations, 2.13 and 2.14.

$$\sigma_{ij} = \begin{pmatrix} \sigma_{xx} & \sigma_{yx} & \sigma_{zx} \\ \sigma_{yx} & \sigma_{yy} & \sigma_{yz} \\ \sigma_{zx} & \sigma_{yz} & \sigma_{zz} \end{pmatrix} \quad (2.13)$$

$$\varepsilon_{ij} = \begin{pmatrix} \varepsilon_{xx} & \varepsilon_{yx} & \varepsilon_{zx} \\ \varepsilon_{yx} & \varepsilon_{yy} & \varepsilon_{yz} \\ \varepsilon_{zx} & \varepsilon_{yz} & \varepsilon_{zz} \end{pmatrix} \quad (2.14)$$

The isotropic material has the same intensity regardless of the direction, which means the yield criterion is composed of invariant stress components in the coordinate system. Furthermore, the von-Mises yield criterion is employed to suggest yielding in ductile and brittle materials. The yielding begins when the second deviatoric stress

invariant, J_2 , which is a function of principal values, σ_1 , σ_2 , and σ_3 , reaches a critical value identified as the yield strength, σ_y .

$$J_2 = \frac{1}{6} [(\sigma_1 - \sigma_2)^2 + (\sigma_2 - \sigma_3)^2 + (\sigma_3 - \sigma_1)^2] \quad (2.15)$$

The von-Mises yield criterion, in terms of the effective stress, is defined as Eq. 2.16.

$$\sigma_{eff} = \sqrt{3J_2} = \sqrt{\frac{1}{2} [(\sigma_1 - \sigma_2)^2 + (\sigma_2 - \sigma_3)^2 + (\sigma_3 - \sigma_1)^2]} \quad (2.16)$$

In terms of the rectangular components of stress, the effective stress for the von-Mises criterion is expressed as written as Eq. 2.17.

$$\sigma_{eff} = \sqrt{\frac{1}{2} [(\sigma_{xx} - \sigma_{yy})^2 + (\sigma_{yy} - \sigma_{zz})^2 + (\sigma_{zz} - \sigma_{xx})^2] + 3(\sigma_{xy}^2 + \sigma_{yz}^2 + \sigma_{zx}^2)} \quad (2.17)$$

The yield function of F can be defined in terms of the effective stress and the critical value of Y , which is obtained by the uniaxial tension material tests, as shown in Eq. 2.18.

$$F = \sigma_{eff} - Y \quad (2.18)$$

The yield surface of the von-Mises yield criterion forms a cylinder as shown in Fig. 2-9.

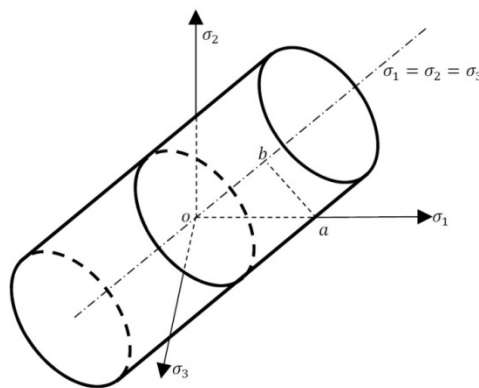


Figure 2-9 - Yield surface in principal stress space (ABAQUS, 2016)

2.3.2 Contact and contact properties

Contact is a critical part of the numerical simulation in FEM, and simulating more accurate models is a challenging process that numerous engineers and researchers have faced. When two bodies touch each other, the normal force to the contacting surface acts on the two bodies, and is transmitted from one part of the model to another. Furthermore, by finite sliding or small sliding motion, shear force can be created to resist the tangential motion of the bodies. The contact algorithm requires specification of the properties between the contacted surfaces: (1) interaction property and (2) contact pressure.

Two components influence the interaction between contacting surfaces: (1) the normal vector to the surfaces, which makes the normal force; and (2) tangential vector to the contacting surfaces, which makes shear force by friction. Hard or soft contact is chosen as the interaction property that defines the normal vector contact to the contacting surface.

2.3.2.1 Hard contact

Hard contact follows the surface constitutive model, which is the definition of the contact pressure between two surfaces at a point, P , as a function of the overclosure, h , of the surface which is the interpenetration of the surfaces. The surface constitutive model is described as Eq. 2.19.

$$p = p(h) \tag{2.19}$$

The hard contact has linear pressure-overclosure relationships and is shown in Fig. 2-10. When two surfaces are in contact, the contact pressure is transmitted between the two surfaces. A dramatic change in contact pressure occurs when the clearance

between two separated surfaces comes in contact. In other words, when the contact condition changes from “open” to “closed,” the contact pressure vertically goes up, as shown below in Eq. 2.20.

$$\begin{aligned}
 p &= 0 \text{ for } h < 0 \text{ (open), and} \\
 h &= 0 \text{ for } p > 0 \text{ (closed)}
 \end{aligned}
 \tag{2.20}$$

A Lagrange multiplier, to represent the contact pressure, is applied to the contact constraint. The virtual work contribution is shown in Eq. 2.21. The linearized form of the virtual contribution is shown in Eq. 2.22.

$$\delta\Pi = \delta p h + p \delta h \tag{2.21}$$

$$\delta\delta\Pi = \delta p \delta h + \delta p \delta h \tag{2.22}$$

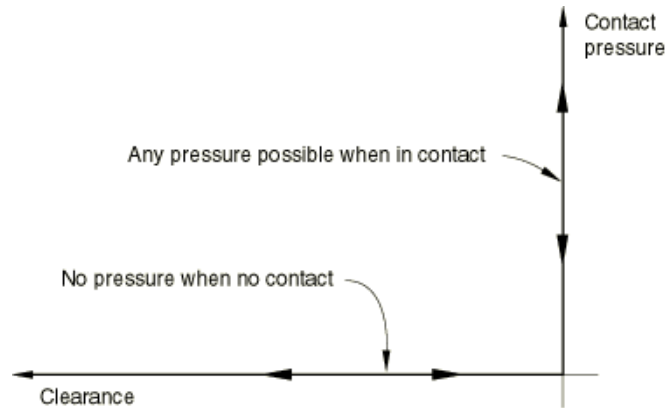


Figure 2-10 - Hard contact pressure-overclosure relationship (ABAQUS, v6.14)

2.3.2.2 Interaction between surfaces

The penalty method is one of contact constraint and is used for surface-to-surface contact. Under the hard contact condition, the penalty method can approximate the hard pressure-overclosure behavior. It is a function of penalty stiffness, which can be increased when contact penetrated distance is increased. Advantages of the penalty enforcements are described below:

- Numerical softening associated with the penalty method can mitigate over-constraint issues
- Less computational time by reducing the number of iterations required in an analysis
- Improved solver efficiency because of no Lagrange multipliers.
- No issues due to conflicts with other types of constraints

The ABAQUS simulation program offers linear and non-linear variations of the penalty method. In a contact pressure-overclosure relationship, the penalty stiffness shows constant as a linear line, as shown in Fig. 2-11. The ABAQUS program defines the linear penalty method as a default method and sets the penalty stiffness to 10 times the representative underlying element stiffness.

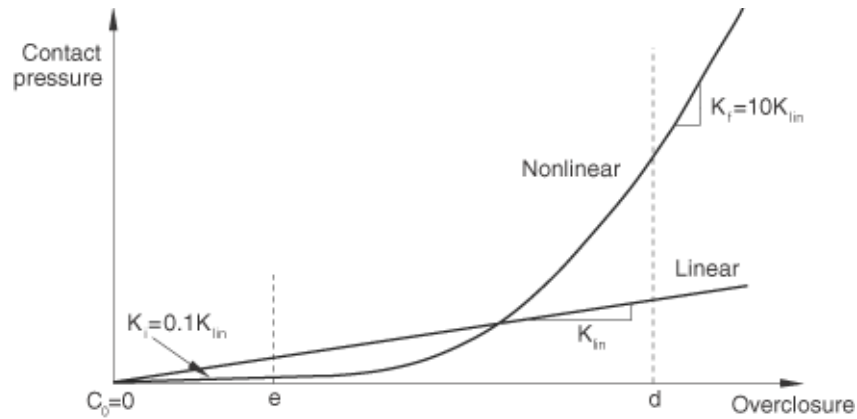


Figure 2-11 - Linear pressure-overclosure relationship with default (ABAQUS, v6.14)

Contact is used to define interactions between surfaces of bodies in mechanical simulations. A pair of rigid or deformable surfaces can be formed by contact interaction. In the finite element analysis, there are two types of contact offerings: node-to-surface and surface-to-surface. In node-to-surface discretization, the interaction between a single slave node and a master surface can be established. Generally, a smaller surface contacts a larger surface. The smaller surface of the element should be defined as a slave surface. For a master surface, the stiffer body, or the coarser mesh, should be assigned as the master slave.

2.3.2.3 Surface-to-surface contact

The surface-to-surface contact algorithm is defined as master and slave surfaces, which are activated when two separated surfaces come in contact with one another. The surface-to-surface contact algorithm is shown in Fig. 2-12. Depending on mesh size, the stiffness of the body, and the deformable or rigid body, the master surface or slave surface is defined to make a contact interaction. The contact modeling in the ABAQUS program follows surface constitutive models, using hard contact properties.

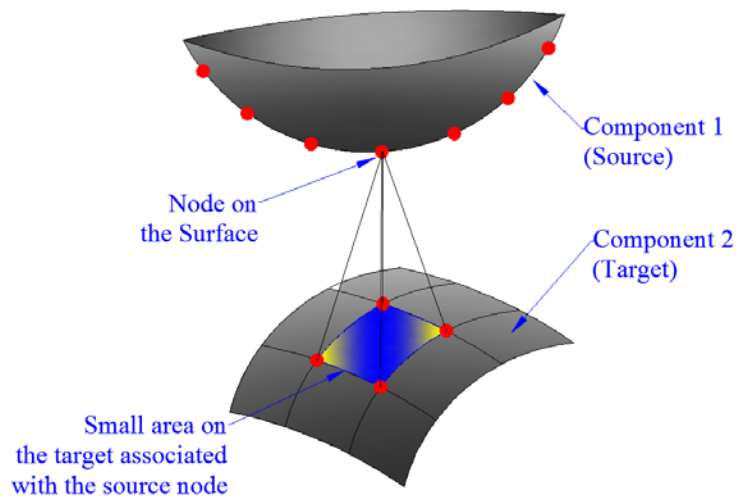


Figure 2-12 - Schematic of surface-to-surface contact algorithm (ABAQUS, v6.14)

The surface-to-surface discretization formulation is employed in terms of slave and master surfaces to simulate contactable parts at the interface of two contacting surfaces. The surface-to-surface contact discretization is more accurate for stress and pressure results, and less sensitive to master and slave surface designations than the node-to-surface contact discretization (Burlayenko, 2012).

As well as employing the hard contact property, a relative motion of the contacting surfaces is calculated by the ABAQUS program in the contact simulation. The relative motion with a finite sliding kinematic transmits shear force on the interface of contacting surfaces. The friction forces are calculated to resist the relative sliding motion of the surfaces. Generally, the *Coulomb friction* model, based on the assumption that no relative motion occurs when the equivalent frictional stress is less than the limited shear stress, is used to describe the relative sliding motion. The standard Coulomb friction model is.

$$\gamma_{equiv.} = \sqrt{\gamma_1^2 + \gamma_2^2} \quad (2.23)$$

where γ_i are the tangential slip velocities derived the local coordinates. The Coulomb friction model is function of a coefficient of friction, μ , and contact pressure between contacting surfaces, p as shown in below Eq. 2.24.

$$\gamma_{crit} = \mu p \quad (2.24)$$

where μ is the coefficient of friction and p is the contact pressure between two surfaces in contact. The critical shear stress is a minimum value of either user-defined maximum shear stress or critical shear stress. If the equivalent shear stress is the critical shear stress, slip between two contacting surfaces can occur.

2.3.3 Geometric nonlinearity

Two concrete pipes assembled with a CFRP coupler system as a connector were analyzed by the ABAQUS commercial numerical simulation program. As mentioned in section 2.2 on contact nonlinearity, these joint shear test models had three different contact pairs, which caused large deformations. If the large deformations are considered, geometrically nonlinearity should be accounted for. The geometric nonlinearity depends on the material constitutive model. For the formulation of small strains and rotations, the linear geometrical model can be employed; for large strain and rotation formulations, geometrically nonlinear models should be employed (Bertram, 2003). The CFRP coupler system is modeled by a shell element and is subjected to uniform pressure from an applied shear force. The large pressure shear can cause rapid straining of the CFRP laminate, or make large deformations.

2.3.4 Newton-Raphson Method

Newton-Raphson's solution procedure is an incremental-iterative technique for solving nonlinear equilibrium equations employed by researchers (Enochsson et al., 2006; Boot et al., 2003; Lee et al., 2014; and Tian et al., 2010). The Newton-Raphson solution is mainly expressed as shown below in Eq. 2.25

$$[F] = [K_T][u] \quad (2.25)$$

where $[F]$ is a force vector, $[K_T]$ is the tangential stiffness matrix, and $[u]$ is a corresponding displacement vector. The specified loads are gradually and incrementally applied to obtain a final solution.

An initial increment, u_0 , of loading of either displacement or force is applied to obtain corresponding force or displacement by employing the tangential stiffness matrix, K_{T0} .

The increment of ΔF is computed by the structure's initial stiffness K_0 configured at u_0 , as shown in Fig. 2-13. The displacement correction, C_a is updated by u_0 . The forces corresponding with the initial tangential stiffness, K_0 reaches P . To perform convergence, the ABAQUS software forms a new stiffness, K_a . Based on the updated tangential stiffness, K_a , I_a is updated at the tangential point across K_a and U_a . A force residual for the interaction between the total applied force, P , and interactive I_a can be calculated as shown below in Eq. 2.26.

$$R_a = P - I_a \quad (2.26)$$

If the structure stays in equilibrium, the residual force, R , should be close to zero at every degree of freedom in the linear problem. However, with nonlinear simulation models, due to different tangential stiffness, K_i , it is almost impossible to make the residual force zero. The ABAQUS program defaults the tolerance value of 0.5% of an average force in a structure. If the residual force is less than the defined tolerance error, the numerical model is in equilibrium. The updated configuration of the incremental force can be accepted as the equilibrium solution (ABAQUS, 2014).

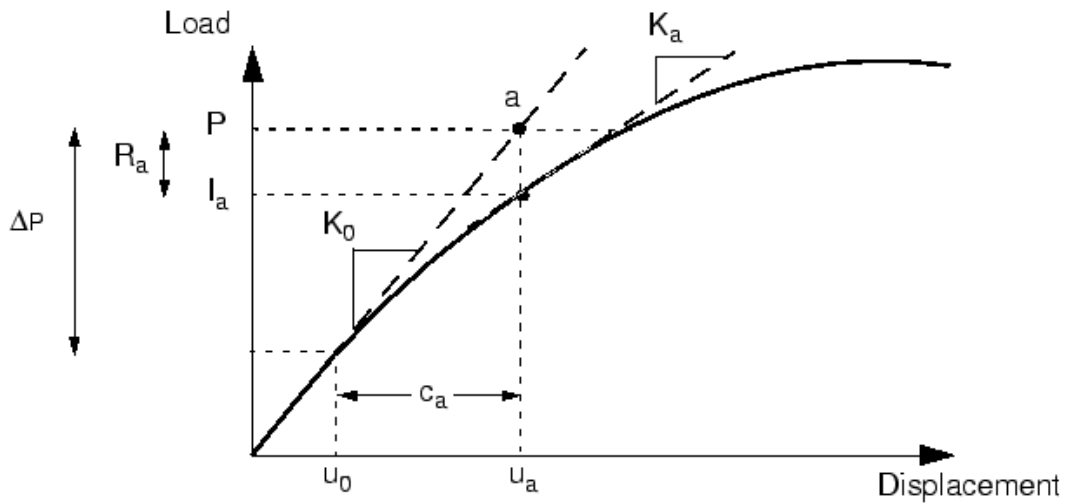


Figure 2-13 - The Newton-Raphson method with a load increment (ABAQUS, v6.15)

ABAQUS checks a displacement correction, C_a which is small, relative to the total incremental displacement, $\Delta u_a = u_a - u_0$, shown in Fig. 2-13. If the C_a value is greater than 1.0% of the incremental displacement, the ABAQUS program accepts this iteration and makes the numerical solution.

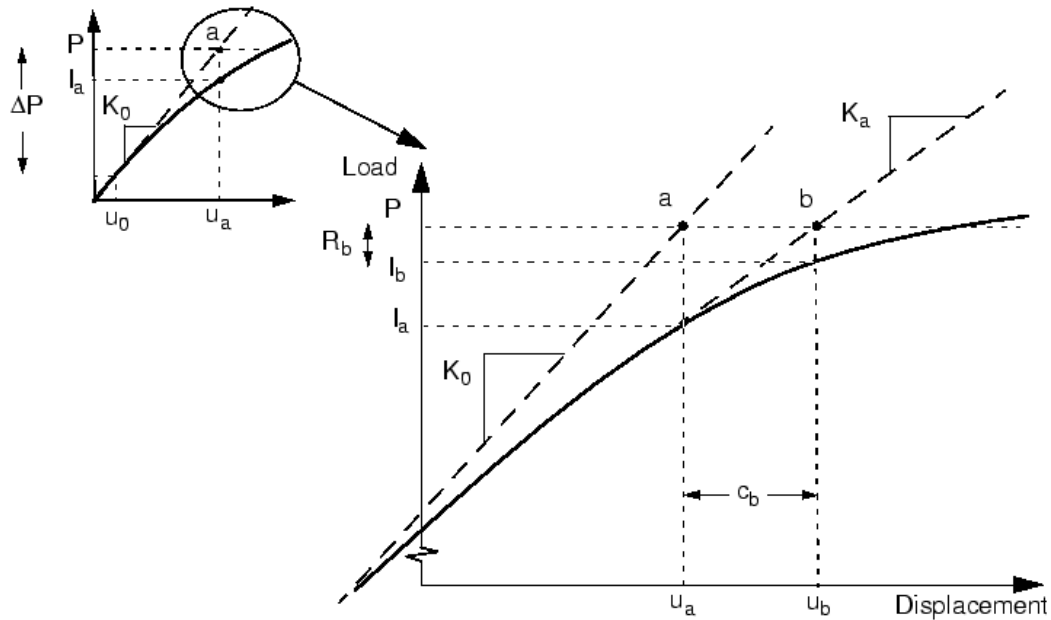


Figure 2-14 - Process of the second iteration (ABAQUS, v6.15)

However, if ABAQUS program's trial of convergence fails, ABAQUS performs iteration with $\frac{1}{4}$ reduced incremental of applied force to try to bring the internal and external forces into balance. As shown in Fig. 2-14, the 2nd iteration is conducted with the 2nd tangential stiffness, K_a which is calculated at the end of the previous iteration with the residual force, R_a from the previous iteration for another displacement correction, C_b . For the numerical solution convergence, the 2nd residual force is computed with the updated force, I_b shown in Fig. 2-14 from the structures' new configuration, u_b . The new force residual R_b is calculated by using the internal forces. The largest force residual, R_b , is compared to the residual force tolerance, and the displacement corrosion is compared to the incremental displacement, $\Delta u_b = u_b - u_0$. Several iterations will be performed up to the solution convergence by comparing the satisfactions of the two conditions of the less residual force than the residual force tolerance and the greater updated displacement than the incremental displacement.

Chapter 3 Material Test

3.1 CFRP laminate tensile test

3.1.1 Specimen geometry

The test specimens were composed of two parts, depending on orientated fiber directions. One was the unidirectional fiber directional CFRP laminate, which means that the CFRP fabric sheets were piled in order of $[0^\circ/90^\circ]_s$ a sequence with $s = 3, 6, \text{ and } 12$. The other was the bidirectional fiber direction; its CFRP sheet was made of $[+45^\circ/-45^\circ]$ oriented fibers. In addition, in order to eliminate bending and torsion moment effects and in-plane deformation, stacking sequences of specimens were symmetric and balanced. In a symmetric laminate, each layer is stacked on top of a layer of identical thickness, orientation, and properties on a reference plane, defined as the middle surface. The laminate is symmetric in both geometry and material properties. Based on coupling stiffness B_{ij} ,

$$B_{ij} = \frac{1}{2} \sum_{k=1}^n \left(Q_{ij}^k (z_k^2 - z_{k-1}^2) \right) = \frac{1}{2} \sum_{k=1}^n \left(Q_{ij}^k (z_k - z_{k-1})(z_k + z_{k-1}) \right) = \sum_{k=1}^n Q_{ij}^k \bar{z}_k t_k \quad (3.1)$$

$$\text{Since } \bar{z}_k = \frac{1}{2}(z_k + z_{k-1}) \text{ and } t_k = z_k - z_{k-1}$$

With respect to the conditions of symmetric laminate, the terms which compose Eq. 3.1 have absolutely equal value and opposite signs. The summation of all of the terms of Eq. 3.1 on laminate should be equal to zero, which indicates that the laminate is symmetric.

The dimensions of the test specimens are shown in Fig. 3-1. Specimen length, width, and thickness were chosen as per ASTM D3039 (ASTM, 2014). The specimen names are denoted by using the X-123-456 label in unidirectional and bidirectional result Tables 3-4 and 3-5. The first character of "N" denotes the fiber direction, either

unidirectional or bidirectional; the second number term indicates the CFRP laminate's thickness; and the third number term denotes the width of the CFRP laminate.

For the unidirectional coupon test, aluminum tabs were utilized at both ends of the specimen to avoid stress concentration at the end of the hydraulic pressure wedge grips. The aluminum tabs were manufactured in accordance with ASTM D3039 Section 8.2.2.3. The ASTM D3039 recommends the use of tabs having lower bevel angles (7 to 10°) and a feathered smooth transition into the coupon when wedge-operated grips are used to conduct the unidirectional material test (ASTM, 2014). The employed tabs' geometries are shown in Fig. 3-1. Specimens conducted are shown in Fig. 3-1.

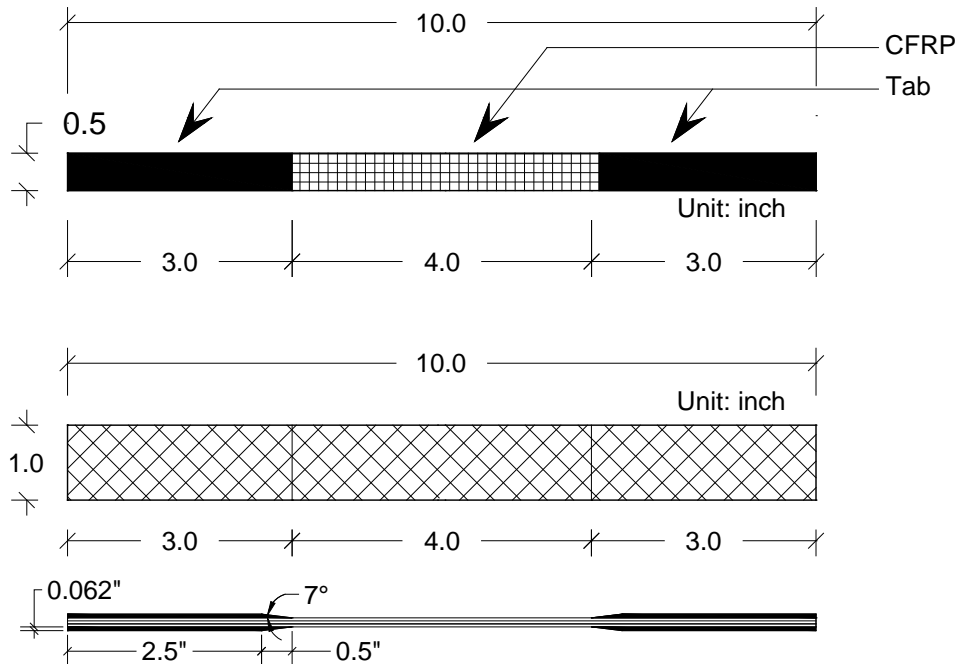


Figure 3-1 - Dimensions of specimen on pseudo loading scenario



(a) Front view of coupon specimen



(b) Side view of coupon specimen

Figure 3-2 - Coupon specimen under pseudo-static loading scenario on front and side view of unidirectional coupon specimen

A pseudo-static loading scenario was employed in the material coupon test, in accordance with ASTM D3518. As shown in Fig. 3-1, the specimens had two different fiber directions: (1) unidirectional and (2) bidirectional. Aluminum tabs were attached on both ends of the specimen and at the end of the grip wedge to prevent failure due to stress concentration.

3.1.2 CFRP laminate material properties

Carbon fiber reinforced polymer (CFRP) laminates are generally composite materials composed of two parts: reinforcement as a fiber, and a polymer chemical matrix. They serve as reinforcement as the fiber carries all of the applied loading; the polymer matrix resin (epoxy) binds the reinforcement together. The strength of CFRP laminate depends on the volume fractions of the two components. For this research, the fiber reinforcement, the CFRP fabric, and the saturated epoxy resin used were

manufactured by the Vectorply company which, is located in Phenix City, AL, and BASF, which is a chemical-manufacturing company.

3.1.2.1 Carbon-Fiber-Reinforced Polymer

The CFRP fabric sheet. *C-BX 1200*, is produced by the Vectorply company. Its material properties are given in Table 3-1. The CFRP fabric is woven with +45° and -45° direction reinforcements.

Table 3-1 - Properties of CF140/45 CFRP fabric sheet

Physical Properties			Tensile Properties		
Fiber Material	Area Weight (lb/ft ²)	Thickness (in/ply)	f_{tu} (ksi)	E_f (ksi)	ϵ_{fu} (%)
Carbon	0.083	0.0043	550	33,000	1.67

The actual cured thickness of a single-ply laminate, the CFRP fiber combined by the saturating chemical resins, is 0.02 in. The specified laminate properties are given in Table 3-2.

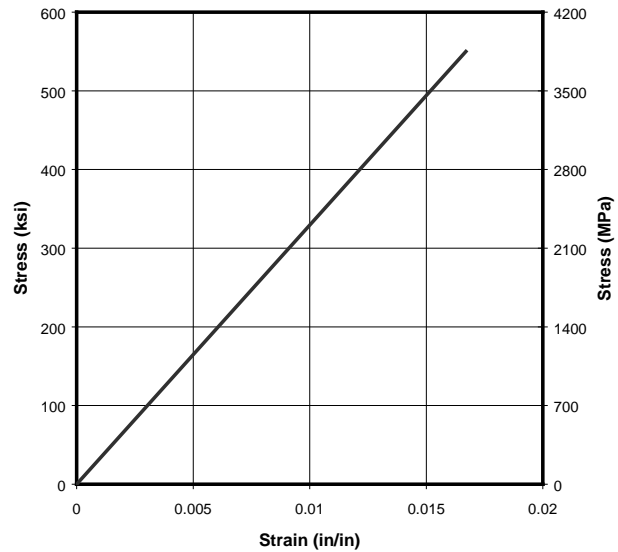
Table 3-2 - CFRP laminate weight and physical properties (Vectorply, 2015)

Laminate weight (C-BX 1200 Resin Infused)					
Fiber	0.08 lb/ft ²	Density	0.88 oz/in ³	$E_x=E_y$	8.40 msi
Resin	0.05 lb/ft ²	Fiber Content	64% by Wt.	$E_x=E_y$, Flex	7.98 msi
Total	0.13 lb/ft ²	Thickness	0.016 in	G_{xy}	0.59 msi

The CFRP fabric used in this dissertation is shown in Fig. 3-3 (a). The stress and corresponding strain value response are shown in Fig. 3-3 (b).



(a) CFRP fabric



(b) Stress and strain response in either +45° or -45° direction

Figure 3-3 - Carbon fiber reinforced polymer

3.1.2.2 Saturated epoxy resin matrix

Saturated epoxy resin matrix is utilized to encapsulate CFRP fiber fabrics. It is a 100% solid and low-viscosity epoxy material, and can be applied to any substrate such as concrete, masonry, steel, and even wood. Structural elements encapsulated by fiber fabric provide additional strength to themselves. Material properties of epoxy resin matrices are summarized in Table 3-3.

The saturated epoxy resin consists of two parts: epoxy resin (Part A) and hardener (Part B). The two components are mixed with a volume ratio of 3:1. The saturated epoxy resin is pre-mixed before adding the hardener, by using a low-speed paddle (600 rpm). The paddle should be kept below the surface of the material to avoid entrapping air.

Table 3-3 - Material properties of saturated epoxy resin (BASF, 2016)

Properties	Tension	Flexure	Compression
σ_{yield} (psi)	7,900	200,000	12,500
$\varepsilon_{\text{yield}}$ (%)	2.5	3.8	5.0
E (ksi)	440	540	380
σ_{ult} (psi)	8,000	200,000	12,500
ε_{ult} (%)	3.5	5.0	5.0
ν	0.4	-	-

3.1.3 Manufacturing of material specimen

Specimens were manufactured in a room with ambient temperature, and two flat wooden plates were used to evenly apply the distributed pressure. ASTM D3039 and D3518 note that unidirectional and bidirectional tensile specimens should be symmetrical, with balanced stacking sequence with respect to the test direction. All CFRP coupon specimens used in this research were manufactured using the procedures shown in Fig. 3-4:

1. The flat wooden plate was covered by a film thickness of 5 mils.
2. The MasterBrace saturant resin epoxy was applied to the filmed wooden plate, using a nap roller.
3. The desired MasterBrace CFRP fabric was attached to the saturated film by epoxy resin.
4. The second layer of MasterBrace saturant resin was painted onto the CFRP fabric by using a painting knife and exerting pressure on the fabric to fully encapsulate the saturant resin into the interface between two CFRP sheets.
5. A second layer of the CFRP sheet was attached to the second layer of saturant resin epoxy.

6. The last layer of saturant resin was painted on the second layer CFRP sheet.
7. Stacked CFRP fabrics with saturate epoxy resin were enclosed by another filmed wooden plate.
8. CFRP laminate panel was cured at ambient room temperature (23°F) for at least 24 hours.

Depending on the thickness of the specimens, steps 4 and 5 were repeated if additional layers of the CFRP fabric sheet were required. After curing for at least 24 hours, specimens were cut off by utilizing a diamond cutter.

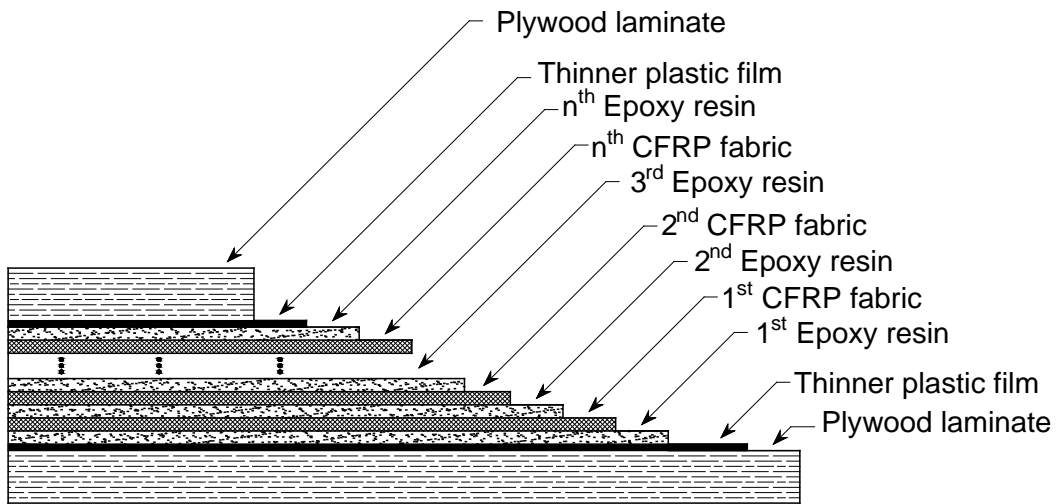


Figure 3-4 - Manufacturing of CFRP laminate panel

3.1.4 Test setup and procedures

Two types of uniaxial tensile tests were conducted in accordance with ASTM D3039 and ASTM D3518 for unidirectional and bidirectional fiber orientation. For this material test, a 50 kips Material Testing Machine (MTS) was employed, as shown in Fig. 3-5.



Figure 3-5 - Material Testing Machine (MTS)

Tensile tests were displacement-controlled in ambient room temperature, with a heading speed of 0.05 inch/min. The specimens were loaded up to failure under uniaxial loading with a pseudo-static loading scenario. Both load and displacement were measured and recorded by the MTS machine and the data acquisition system. Specimens were placed in hydraulic mechanical wedge-type grips which were used to engage the specimens by applying a uniform pressure at the top and the bottom of the MTS machine. In order to obtain the axial and transverse strains from the quasi-static

tensile tests of unidirectional $[0^\circ/90^\circ]_s$ and bidirectional $[+45^\circ/-45^\circ]_s$ laminates, all specimens were instrumented with two separate strain gauge rosettes at middle height, on both sides of the specimens, as shown in Fig. 3-6.

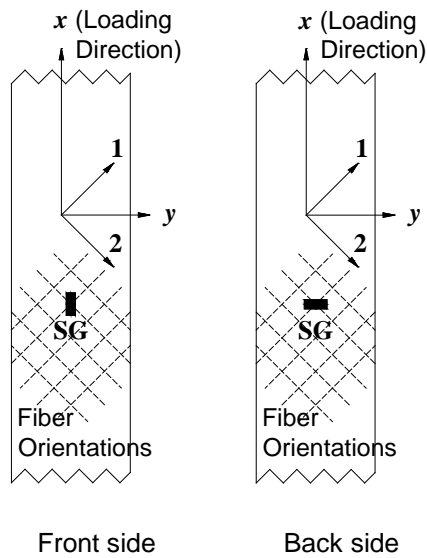


Figure 3-6 - Layout of the strain gauges on specimen

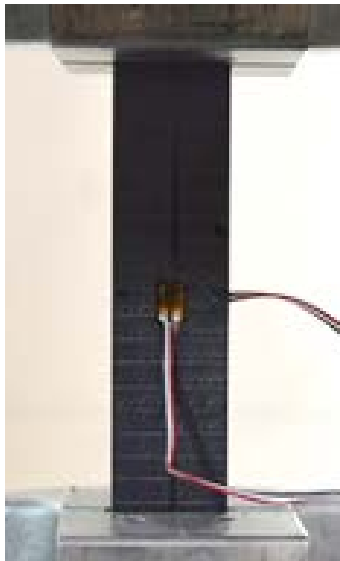


Figure 3-7 - Specimen for unidirectional tensile test

The following properties can be determined from uniaxial tensile tests on unidirectional laminates:

E_1, E_2 = longitudinal and transverse Young's Modulus, respectively

ν_{12}, ν_{21} = major and minor Poisson's ratios, respectively

F_{1t}, F_{2t} = longitudinal and transverse tensile strength, respectively

$\epsilon_{1t}^u, \epsilon_{2t}^u$ = longitudinal and transverse ultimate tensile strain, respectively

3.1.5 Material Test Results

3.1.5.1 0°/90° Fiber direction under pseudo-static loading

The results of the unidirectional fiber direction tensile tests are presented in Table 3-4. The ultimate tensile loads and corresponding displacements at failure are given in Table 3-4. Figure 3-9 shows the failure load and corresponding displacements, which indicate an increased tendency of the failure tensile forces; however, corresponding tensile displacements were constant. The measured tensile forces were increased proportionally to the thickness of the specimens. Specimens in $[0/90]_s$ stacking sequences showed no visible or audible cracks during increased loading. The unidirectional CFRP laminate composite specimens failed simultaneously in fiber fracture and matrix splitting, with cracking sound at the ultimate tensile forces. As seen in Table 3-4, the unidirectional tensile test showed a highly linear load and displacement performance.

Table 3-4 shows the ultimate tensile forces and corresponding displacements. A table depicting the load vs. displacement response is shown in Fig. 3-8. Failure tensile forces were equal to 2.6 kips, 5.2 kips, and 10.4 kips, and Poisson's ratios of 0.078, 0.045, and 0.026, respectively. The strain values, obtained by the strain gauge installed mid-height of the CFRP laminate specimens, showed that the strain and stress

responses from three unidirectional CFRP laminate specimen material tests were identical: 84.0 ksi of failure stress and 0.014 in./in of corresponding strain value, as shown in Fig. 3-10.

Load vs. displacement and stress vs. strain response curves of 0.0625 and 0.125-inch thickness specimens are shown in the appendix A.

Table 3-4 – [0/90°] Tensile test results of unidirectional composite laminates

Specimen	Ultimate force (lb)	Displacement (in.)	Poisson's Ratio	E (ksi)
N-0.0625-0.5	2,615.68	0.088	0.078	7,064.9
N-0.1250-0.5	5,237.46	0.077	0.045	8,438.4
N-0.2500-0.5	10,413.87	0.094	0.026	6,386.4

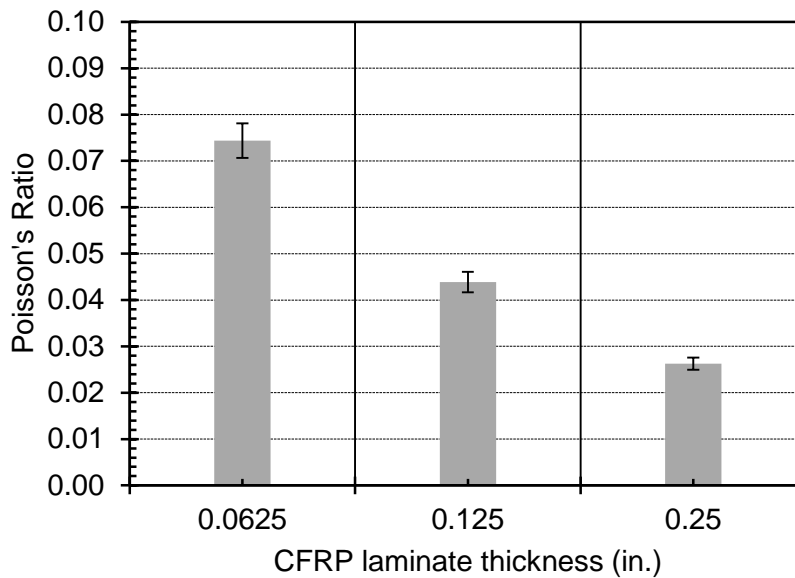


Figure 3-8 - Poisson's ratio on 0.0625, 0.125, and 0.25 inches uni-directional CFRP laminate thickness

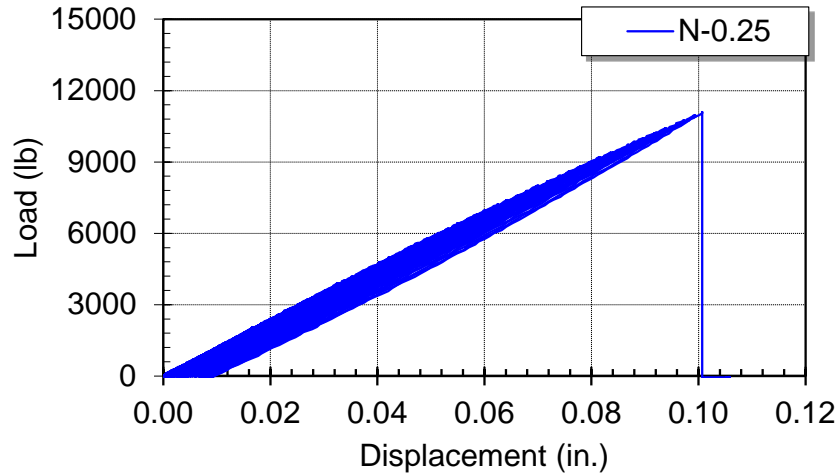


Figure 3-9 - Tensile loading and corresponding displacement of 0.25 in. thickness specimen

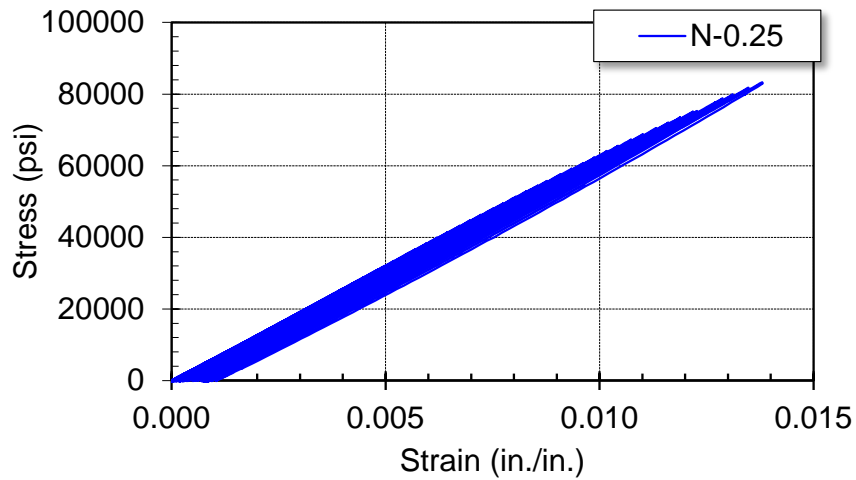


Figure 3-10 - Longitudinal stress as function of the longitudinal strain of 0.25 in. thickness specimen

The strain gauges of unidirectional composite laminates were damaged at ultimate force, as shown in Fig. 3-11. Failures were observed at the bottom of the 0.0625

in. and 0.25 in. thickness specimens. The 0.125 in. thickness specimen failed at mid-height of the specimen, as shown in Fig. 14. No failure was observed at the tab material, as shown in Fig. 3-12.

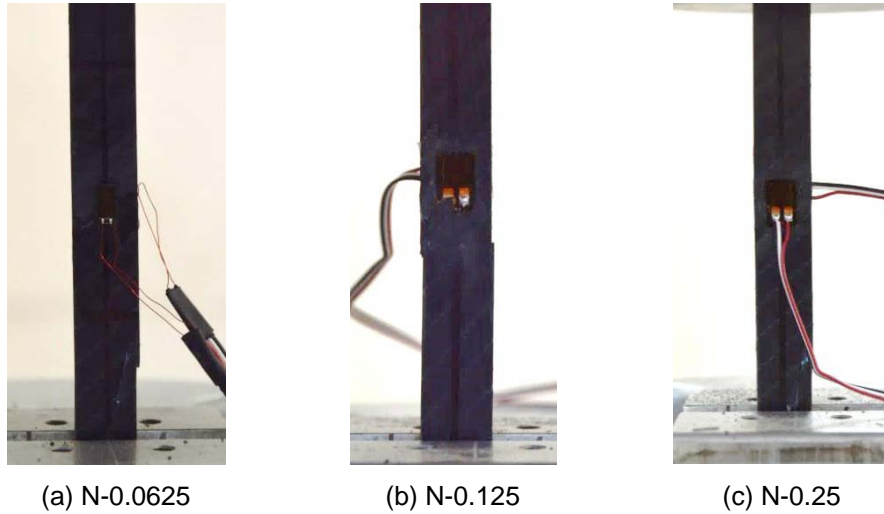


Figure 3-11 - Failure mode of unidirectional composite materials

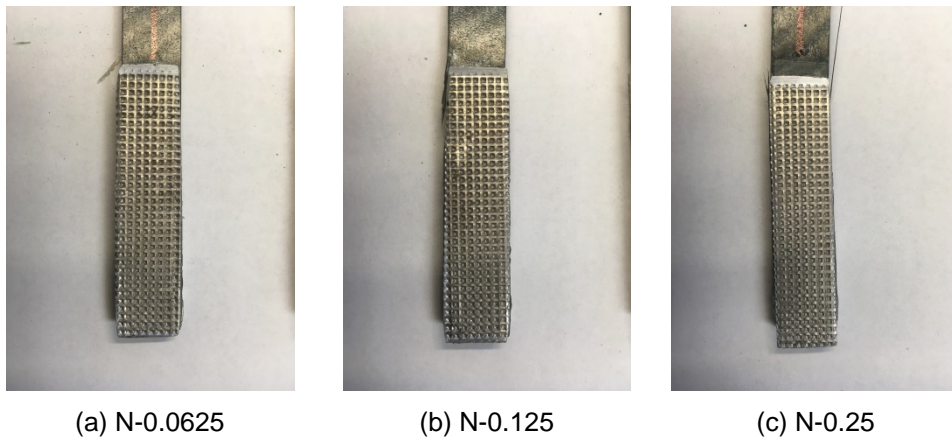


Figure 3-12 - No slippages on tab materials for unidirectional CFRP laminates

3.1.5.2 45°/-45° Fiber direction under pseudo-static loading

Material test results: The ultimate tensile force and corresponding displacement of bidirectional fiber direction specimens under pseudo-static loading are given in Table 3-5. As shown, the measured tensile forces proportionally increased with the thickness of the specimen. During testing, the specimen geometry of the bidirectional composite laminates changed from a rectangular shape to a dumbbell shape due to realignment of the fibers along the loading direction, as shown in Fig. 3-16. When the bidirectional CFRP laminate shape changed, the longitudinal strain value reached around 0.01 in. /in, which was defined as the failure strain value of the CFRP laminate.

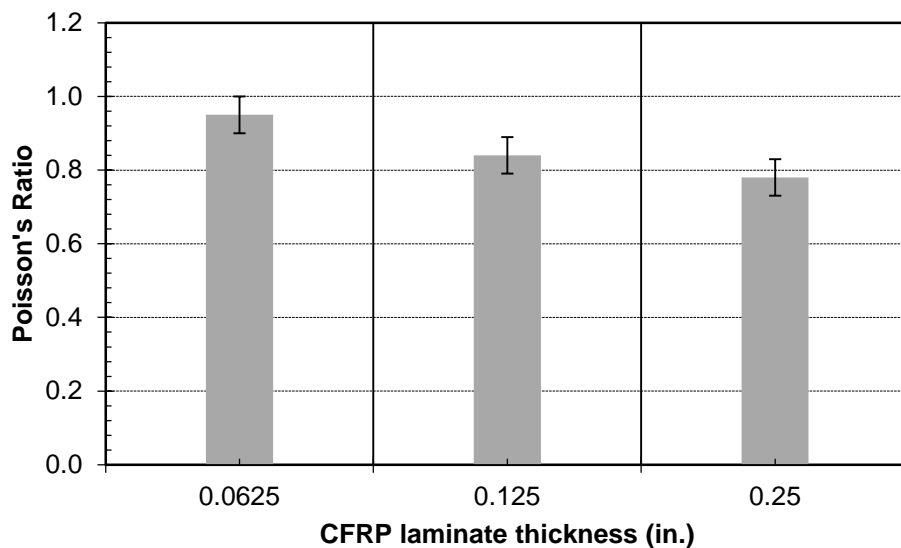


Figure 3-13 - Poisson's ratio on 0.0625, 0.125, and 0.25 inches bi-directional CFRP laminate thickness

Table 3-5 – [+45/-45°] Tensile test results of bidirectional composite laminates

Specimen	Ultimate force (lbf)	Displacement (in.)	Poisson's Ratio	E (ksi)
B-0.0625-1.0	929.37	0.64	0.94	1,654.84
B-0.1250-1.0	1,907.20	0.60	0.83	1,616.96
B-0.2500-1.0	4,077.65	0.54	0.79	1,459.09

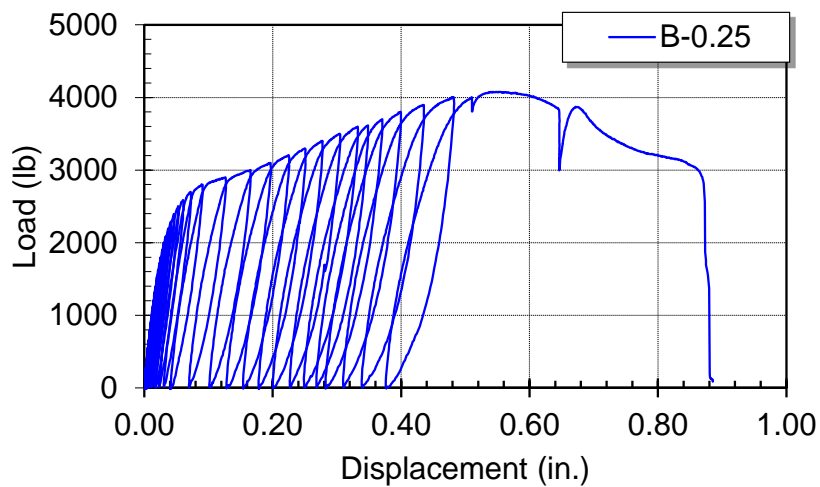


Figure 3-14 - Tension and corresponding displacement of bidirectional composite laminates

As seen in Fig. 3-14, the bidirectional tensile test showed a highly nonlinear load and corresponding displacement curve. Table 3-5 shows a comparison of the loads and corresponding displacements for 0.0625, 0.125, and 0.25 inches of specimen thicknesses. The ultimate loads were 0.93, 1.91, and 4.07 kips, respectively. Corresponding displacements were 0.64, 0.60, and 0.54 inches.

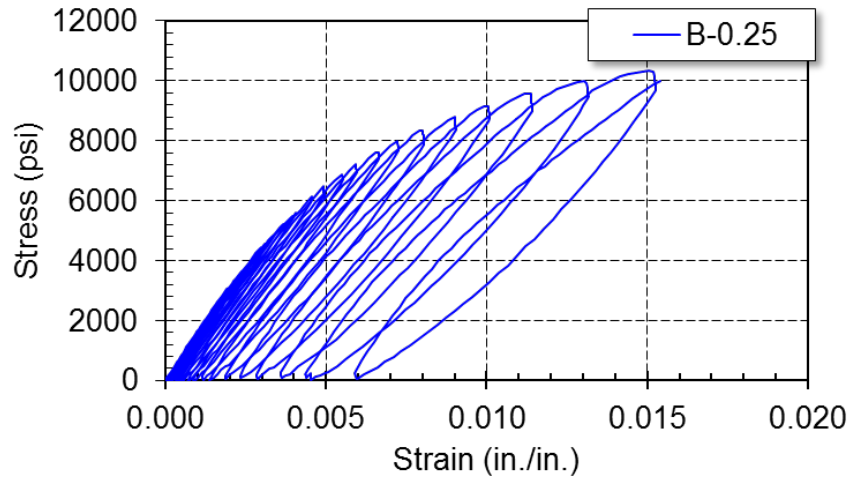
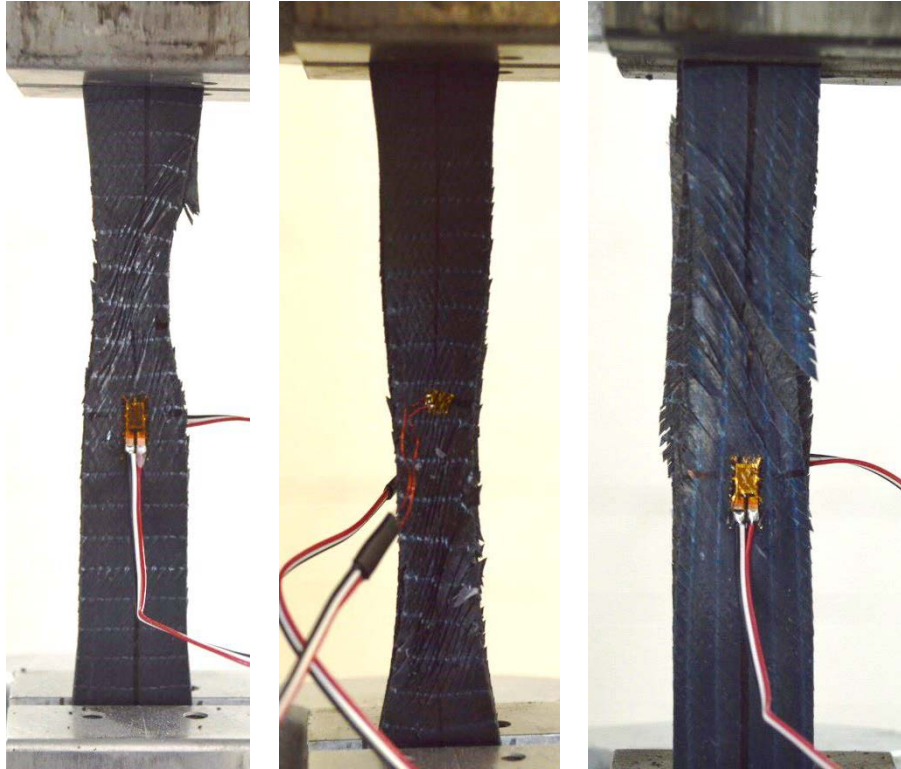


Figure 3-15 - Shear stress as function of shear strain of bidirectional composite laminates

For bidirectional composite laminates, the tests were stopped once all the strain gauges debonded or failed when the strain value reached at 0.015 (in./in.). As shown in Fig. 3-15, stress vs. strain response showed bilinear curves at the point where stiffness degradation started at strain value of 0.004 (in./in.). The failure mode of composite laminate should be considered in the elastic region up to the strain of 0.004; after that, the strain value CFRP laminate is in plastic behavior.



(a) B-0.0625

(b) B-0.125

(c) B-0.25

Figure 3-16 - Failure of bidirectional composite materials

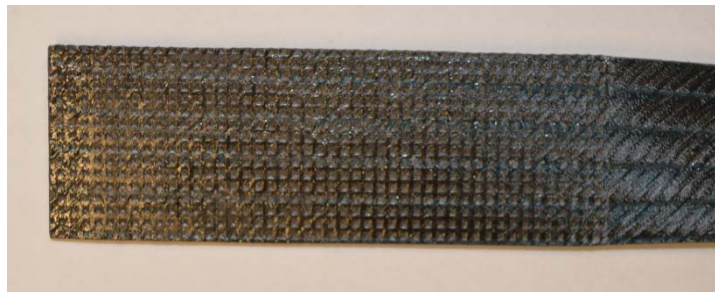


Figure 3-17 - No slip observed between bidirectional CFRP laminate specimen and wedge grips

3.2 Conclusion

In order to characterize the tensile strength of the CFRP laminate, the coupon material tests were conducted in accordance with ASTM D3039 for unidirectional fiber 0/90 laminate and ASTM D3518 for bidirectional -45/45 laminate. Strain values were measured by two strain gauges which were installed on the front and back sides of the CFRP laminate specimens to obtain the Poisson's ratio. Both directional laminates were stacked in symmetric and balanced sequence, and manufactured with thicknesses of 0.0625 inch, 0.125 inch, and 0.25 inch, respectively, to eliminate the bending and torsion. The stress-strain response of the unidirectional laminate was shown as linear behavior with 2% of residual displacement. The ultimate strain value was equal to 0.015 in. /in., with center specimen failure, the ultimate stress was equal to 84 ksi, and the Poisson's ratio shows an average of 0.042. Aluminum tabs were attached on both ends of the CFRP laminate, which protected the CFRP laminate specimen from the serrated surface of the wedge grips and introduced the gripping pressure more smoothly by having lower bevel angles (7 to 10°). The bidirectional CFRP laminate specimens showed the nonlinear behavior of the stress and strain relationship. The material properties of the bidirectional CFRP laminate specimen are the ultimate stress of 14 ksi, the corresponding strain value of 0.015 in. /in., and the Poisson's ratio of 0.853. Matrix failure was observed with stiffness degradation. From 0.010 in. /in. of strain value, the rectangular shape of the laminate specimens began to change to a dumbbell shape at the mid-length of the bidirectional fiber laminate. When the matrix failure was observed, the fiber reorientations occurred at the mid-length of the CFRP laminate specimens. The nonlinear response of the stress and strain on the -45/45 stacking sequenced laminate was modeled as bilinear constitutive law to make better stable convergence under the Newton Raphson solution in the ABAQUS program.

Chapter 4 Development of 3D Finite Element Model of Joint Shear Test

4.1 Numerical Modeling and Analysis Algorithms

The three-dimensional finite element method (FEM) analysis has been widely utilized to predict the behavior of structures and to conduct a parametric study for a design equation of the CFRP internal coupler system. The three-dimensional finite element model was developed by the ABAQUS commercial numerical simulation program, as shown in Fig. 4-1. The FEM analysis algorithms consider material nonlinearities, geometric nonlinearities, and contact nonlinearities. In the joint system analyses, the material non-linearity was composed of elastoplastic and tension-stiffening constitutive law for steel cages and thin-walled concrete pipes. Thin-walled concrete pipes and wooden cradles were modeled with a three-dimensional solid brick element of C3D8R to optimize the mesh size. For considering the small sliding deformation between concrete pipes and the CFRP coupler, surface-to-surface contact nonlinearity was implemented. Circumferential and transverse steel cages were embedded inside the thin-walled concrete pipe, using tie contact nonlinearity.

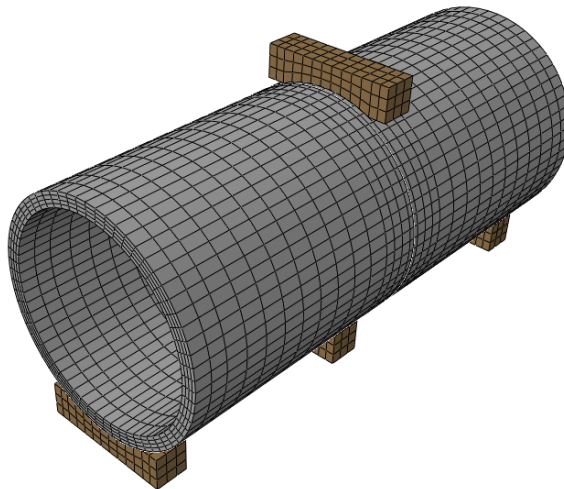


Figure 4-1 - Schematic of three-dimensional models for joint shear test

4.1.1 Parts and geometry

The shear test setup of an internal joint system consists of several parts: thin-walled concrete pipes, four wooden cradles, circumferential and transverse steel cages, and CFRP couplers. Figure 4-2 illustrates all of the parts modeled for joint shear test simulation.

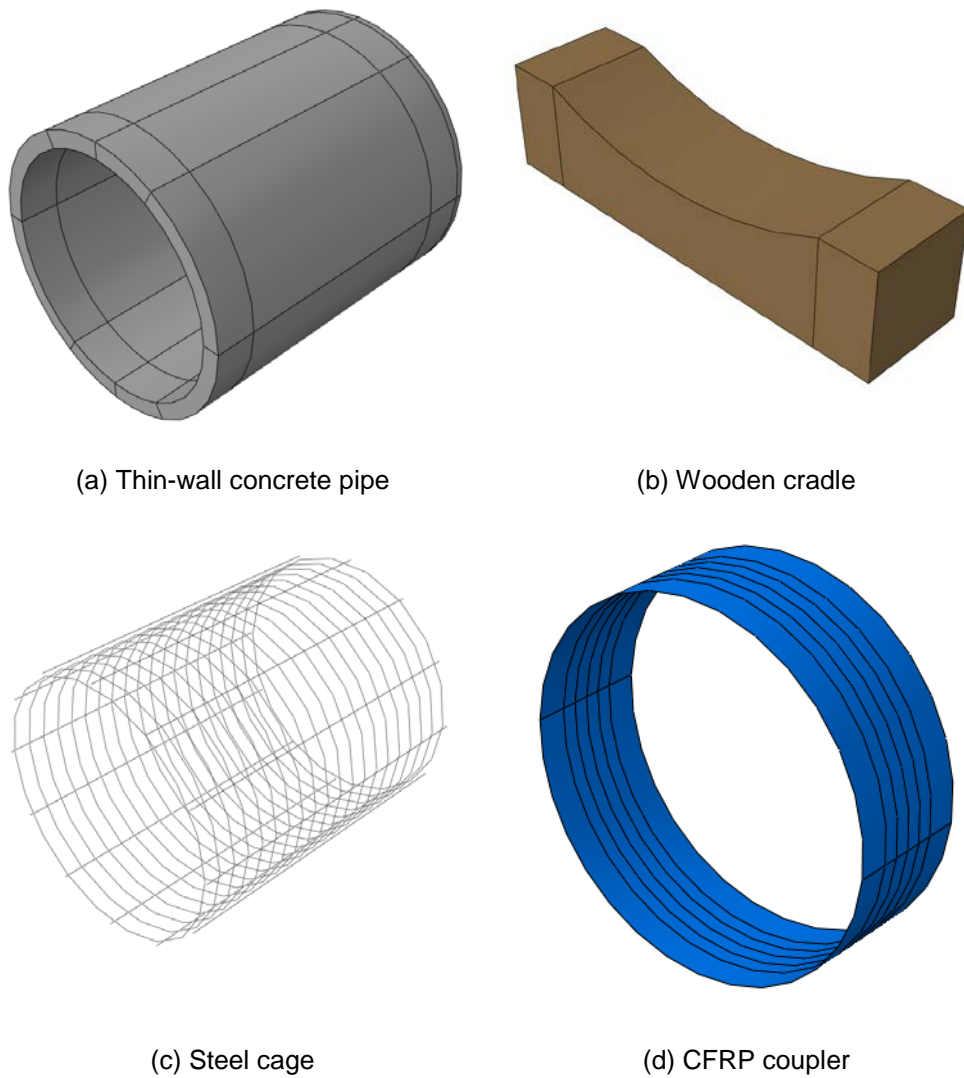


Figure 4-2 - Configuration of all parts

- Geometry properties of all of the parts are summarized as follows:
 - Thin-walled concrete pipe reinforced synthetic fiber
 - Geometry properties of concrete pipes are in given in Table 4-1.
 - Steel cages
 - Areas of circumferential steel reinforcements are given in Table 4-1, according to ASTM C76.
 - Longitudinal steel area of 0.031in^2 with 8-inch intervals, according to ASTM C76
 - Wooden cradle
 - Dimensions of 6 inches by 6 inches by 20 inches, with rounded top surface
 - CFRP coupler
 - Coupler thickness ranging 0.0625 through 0.375 inches and length of 12 inches.

Table 4-1 - Geometry properties of all parts for simulation

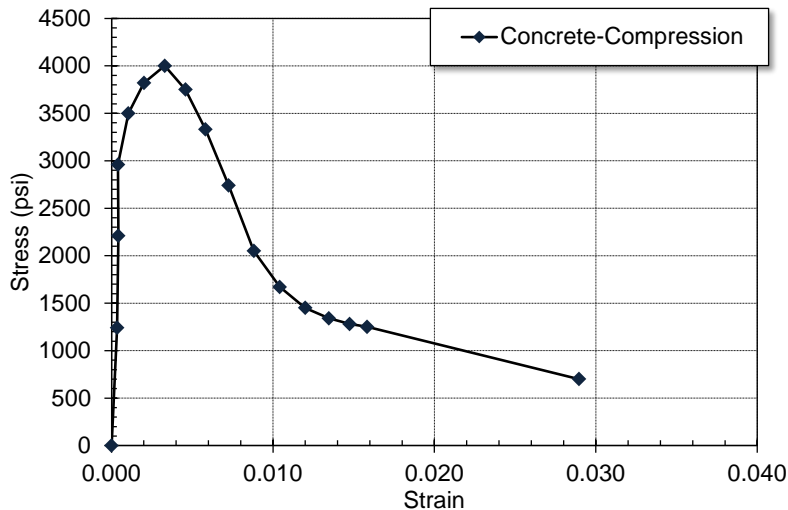
Specimen	Concrete Pipe			Steel	CFRP Coupler	
	I.D. (in.)	t (in.)	L (in.)	A_s (in ² /ft.)	w (in.)	t (in.)
TW36-12-0.0625	36	2.25	48	0.17	12	0.0625
TW36-12-0.1250	36	2.25	48	0.17	12	0.1250
TW36-12-0.2500	36	2.25	48	0.17	12	0.2500
TW48-12-0.1250	48	2.50	48	0.24	12	0.1250
TW48-12-0.1875	48	2.50	48	0.24	12	0.1875
TW54-12-0.1875	54	5.00	48	0.29	12	0.1875
TW54-12-0.2500	54	5.00	48	0.29	12	0.2500
TW72-12-0.2500	72	5.50	48	0.49	12	0.2500
TW72-12-0.3750	72	5.50	48	0.49	12	0.3750
TW84-12-0.3750	84	7.50	48	0.64	12	0.3750

4.1.2 Material modeling

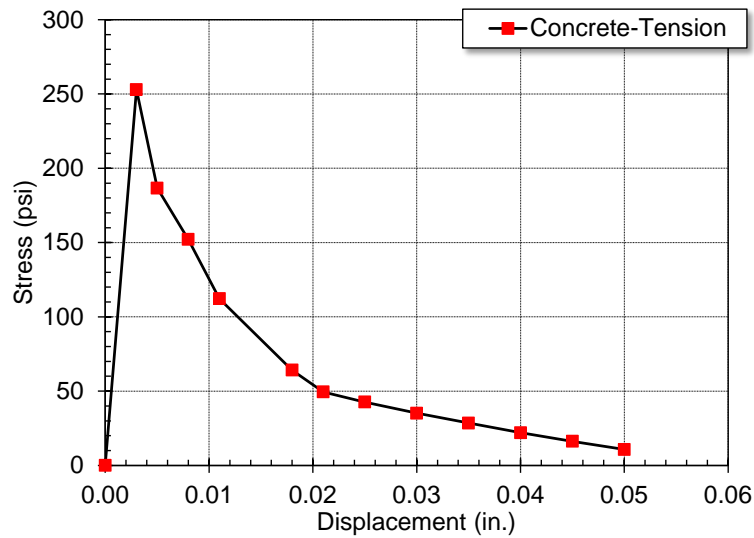
Numerical modeling of the joint shear test was composed of four parts: the concrete pipe, the wooden cradle, the steel cage, and the CFRP internal coupler. Three material properties were defined for each of the parts, separately.

A concrete damage plasticity (CDP) model was utilized for the thin-walled concrete pipe to simulate smeared and discrete crack initiation and propagation. The concrete damage plasticity is composed of tension stiffening and compressive hardening. Abolmaali and Wilson developed a tension-stiffening constitutive law for concrete material reinforced by synthetic fiber (Wilson, 2013).

Figure 4-3 shows applied compressive-hardening and tension-stiffening constitutive laws based on the material tests by Wilson (Wilson, 2013). The maximum compressive strength of synthetic-fiber-reinforced concrete material was 4,000 psi. The maximum tensile strength was calculated by $4.0\sqrt{f'_c}$ (ACI-318). The plasticity parameters for used dry-mixed concrete pipe are given in Table. 4-3.



(a) Compressive-hardening constitutive law



(b) Tension-stiffening constitutive law

Figure 4-3 - Constitutive laws of synthetic fiber reinforced concrete

Table 4-2 - Tension stiffening damage variable for the plastic displacements

Plastic stress (psi)	Displacement (in.)	Damage parameter	Displacement parameter
252.99	0	0	0.000
243.44	0.003	0.2815	0.003
229.12	0.005	0.4238	0.005
210.03	0.008	0.5863	0.008
171.84	0.014	0.7888	0.014
143.20	0.018	0.8642	0.018
95.47	0.025	0.9373	0.025
76.38	0.030	0.9639	0.030
38.19	0.040	0.9881	0.040
23.87	0.050	0.996	0.050

The elastic modulus and yielding strength of steel materials were 29,000 *ksi* and 60 *ksi*, respectively, for circumferential and longitudinal steel cages. In addition to steel

reinforcement, the CFRP coupler was modeled by a composite continuum shell element. The material model of the CFRP coupler was observed through the unidirectional coupon material tests, as shown in Fig. 4-5.

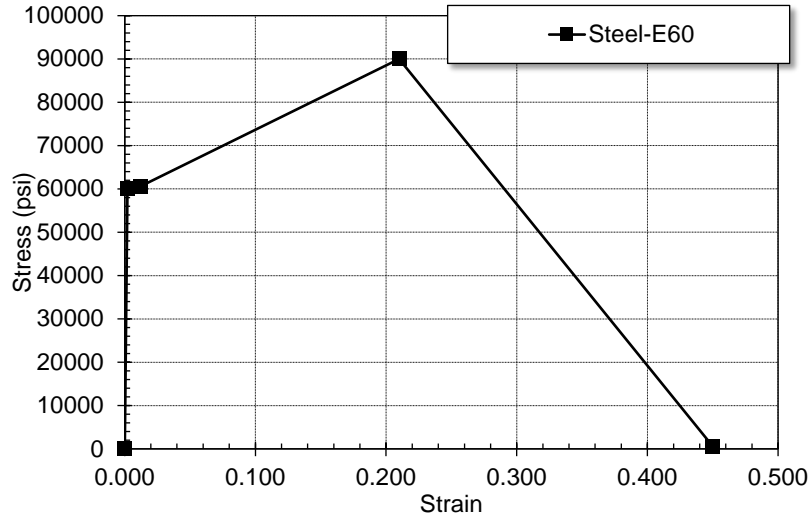


Figure 4-4 - Stress-Strain curve of steel reinforcement materials

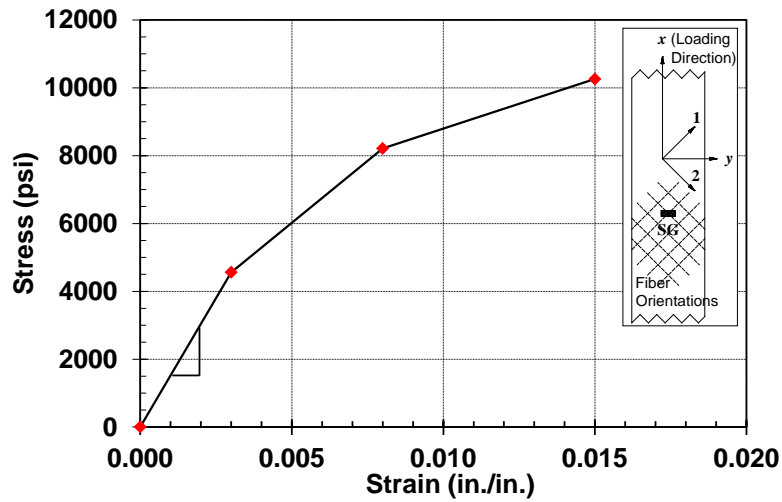


Figure 4-5 - Constitutive law of CFRP laminate

4.1.3 Assemblage of all parts

All of the parts assigned the proper material properties were created independently and assembled in the FEM program in the initial stage of modeling. Two inside cradles were placed 1-inch from the assembled surface of the concrete pipes. To facilitate the definition of interaction and tie contact, all of the surfaces and instances were defined as sets or surfaces after completing the assembly.

4.1.4 Boundary and load conditions

The boundary conditions of the joint shear test were defined to simulate the same conditions as in the experimental tests. Figure 4-6 illustrates the boundary conditions of the cradle supports for the concrete pipes.

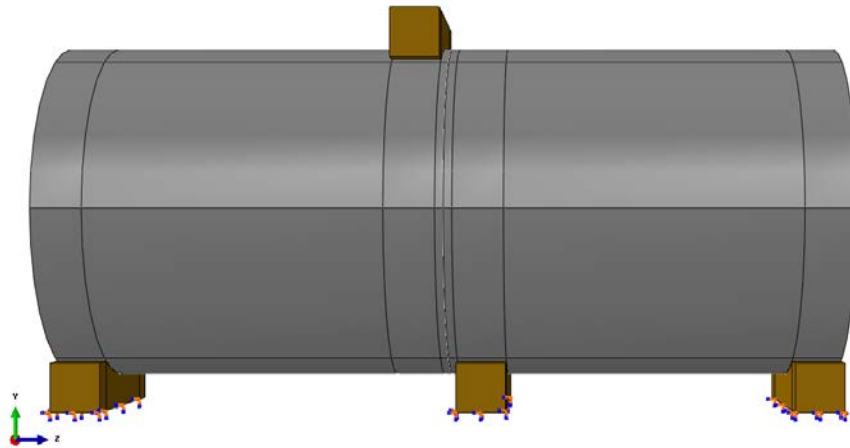


Figure 4-6 - Applied boundary condition in FEM model

In the experimental test, all three cradles supporting concrete pipes were connected to each other. Thus, in the FEM modeling, movement of the three supporting cradles in the x, y, and z directions was prevented. Moreover, due to the weight of concrete pipes, the three support cradles could not be rotated. Boundary conditions of rotating x, y, and z axes were prevented as well.

There are two types of loading cases: the self-weight of the pipe and the loading acting on the upper cradle. Self-weight is activated on concrete pipes by applying a gravitational constant of 386 in/s^2 during the initial stage. In the step defined, pressure loading acted on the top substrate of the upper cradle for the additional shear force.

4.1.5 Contact and contact properties

The surfaces between the thin-walled concrete pipes and the CFRP coupler, contacted surfaces at the assemblage of concrete pipes, and the outside concrete pipe and the wooden cradles were modeled by defining a surface-based contact interaction with suitable coefficients.

When two surfaces touch each other, a normal force acts on the two bodies, stress is transmitted to both surfaces, and contact pressure is generated. All of the contacted surfaces are under uniform pressure loading caused by an applied shear force, and have motions. The surface-based approach, defined on the region on which distributed surface loads are prescribed, can be employed on deformable, rigid, or partially deformable and partially rigid bodies. Surface-based contact is defined as two or more distinct bodies in mechanical contact, with the two bodies defined as master and slave. The master surface should be rigid, and a slave surface has an interaction property. If a small surface contacts a large surface, the best way to reduce computational time is to define the smaller surface as the slave surface. However, if the two surfaces are not distanced, the surface of the stiffer body or coarser mesh body should be chosen as the master surface. In this joint shear test model, because the four wooden cradles were stiffer than the concrete pipe, the surface of the wooden cradles was defined as the master surface, and the concrete pipe surface, which contacts the wooden cradles, was defined as the slave surface, as shown in the green boxes in Fig. 4-

7. The mesh element of the CFRP coupler inside the concrete pipe was smaller than the inside of the concrete pipe. Therefore, the surface of the CFRP coupler was defined as the master, and the inside concrete pipe was defined as the slave surface, as shown in the blue boxes in Fig 4-7.

Three surface-based contacts were designed for the joint shear test simulation: surface interaction contact between the concrete substrate and wooden cradles, surface interaction contact between assembled surfaces of each end of the concrete pipe, and surface interaction contact between the inside of the concrete pipes and the outside CFRP coupler. For creating three different interaction contacts, the pairs of surfaces that contact each other have to be pre-defined, as do the constitutive models governing the interactions between the various surfaces. Relative sliding behavior could occur between the contacted surfaces. To simulate the same conditions in the experimental tests, nonlinear contact properties were designed in two perpendicular directions of normal and tangential behaviors. Hard contact of normal behavior prevented overclosure of each of the contacted surfaces. Tangential behavior was defined by a friction coefficient. The friction coefficients between soft wood and concrete were considered between 0.4 and 0.57 by AMPG Dias (Dias, 2005). Frictionless contact was defined for surfaces of assembled concrete pipes. There was no restraint of the concrete pipe along the longitudinal axis, which means that the assembled surfaces of two concrete pipes did not match perfectly.

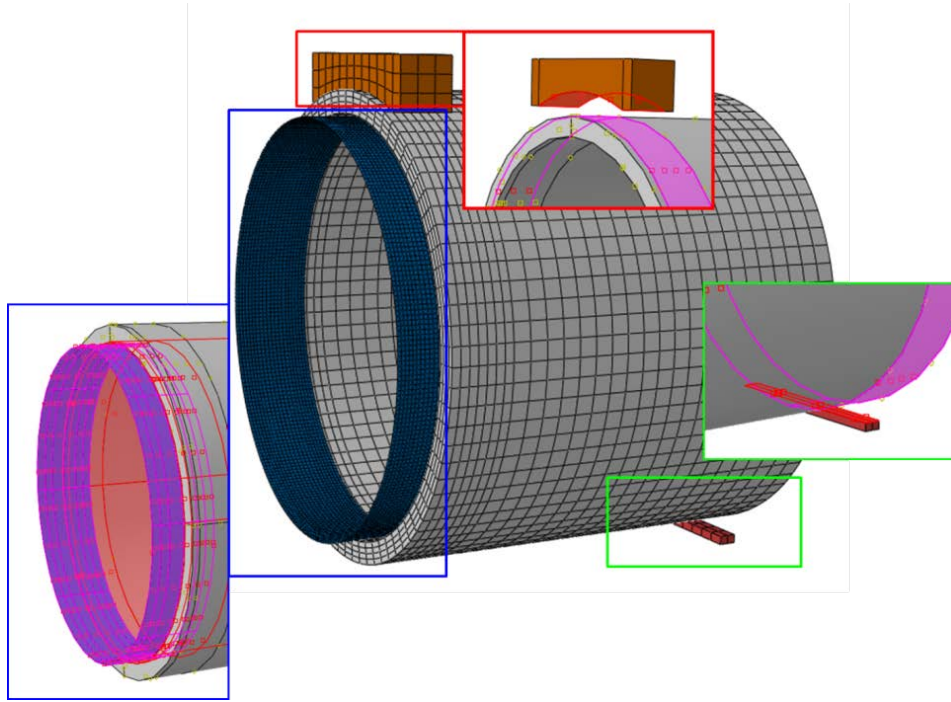


Figure 4-7 - Contact pairs in joint shear test model

4.1.6 Mesh and element types

The completed models, with applied load and defined boundary conditions, were seeded to make the meshing, and the proper element was assigned to each part. Four wooden cradles were defined as rigid bodies, which were seeded with large mesh. For steel wire reinforcements, truss elements were seeded with 1-inch transitional mesh. In the case of concrete pipes, the contacted surface of the concrete pipe was seeded with fine mesh with 0.5-inch mesh to save computational time and enable a better convergence solution. The other surfaces of the concrete pipes were seeded with 2-inch mesh.

In this study, the 8-noded linear brick element with reduced integration was used for the concrete pipe and wooden cradle elements, as seen in Fig. 4-8. Reduced integration (lower-order integration of the stiffness matrix) was used to alleviate the intrinsic model stiffness due to the finite element approximation. Hourglass control was also used to improve mesh distortion due to large deformation and to enhance the nonlinear response.

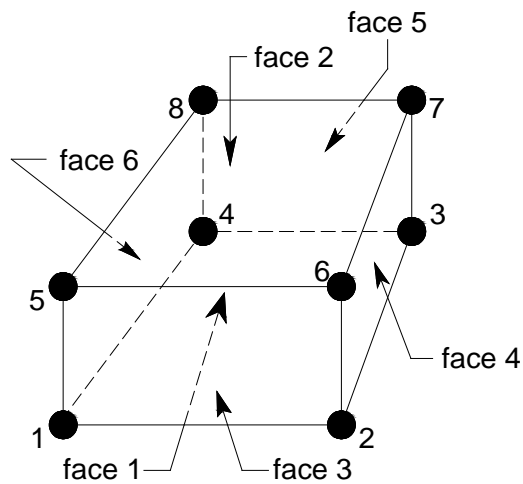


Figure 4-8 - Schematic of 8-noded linear brick element

Two-node linear 3D truss elements (T3D2) were used for the circumferential and longitudinal steel cages. Truss elements are one-dimensional bars or rods that are assumed to deform by axial stretching only. Truss elements are pin jointed at their nodes, and so only translational displacements and the initial position vector at each node are used in the discretization.

A 4-node doubly-curved thin shell (S4R) with hourglass control was used to improve mesh distortion due to large deformation.

4.1.7 Analysis algorithm

Newton-Raphson's solution procedure is an incremental-iterative technique for solving nonlinear equilibrium equations. It was used by Bijian in 1995 to solve nonlinear equilibrium equations on a flat shell plate (Bijian 1995). Bijian employed the Newton-Raphson method as applied force on each step to analyze large deformation problems and to consider nonlinearity due to a change in geometry. Results obtained by the numerical analysis for a cantilever fabric bending showed good agreement with the actual experimental tests in terms of bending angle value. Cui et al., in 2016, published the numerical analysis paper regarding composite connections for an underground structure. The Newton-Raphson iteration method was employed to analyze the mechanical behavior and performance of the connections with concrete-filled steel tubular (CFST) columns with steel H-beams.

The Newton-Raphson solution is expressed as Eq. 4.1.

$$[F] = [K_T][u] \quad (4.1)$$

where $[F]$ is a force vector, $[K_T]$ is the tangential stiffness matrix, and $[u]$ is a corresponding displacement vector. An initial increment, u_0 , of loading of either displacement or force, is applied to obtain corresponding force or displacement by employing the tangential stiffness matrix, K_{T0} . To solve the numerical finite element model, the numerical solution program compares two conditions: (1) residual force and (2) an incremental displacement. The repeated residual force is reduced as the number of iterations increase. The numerical solution can be accepted when the final residual force is less than the residual force tolerance pre-defined, and when the incremental displacement is greater than 1.0% of total applied displacement.

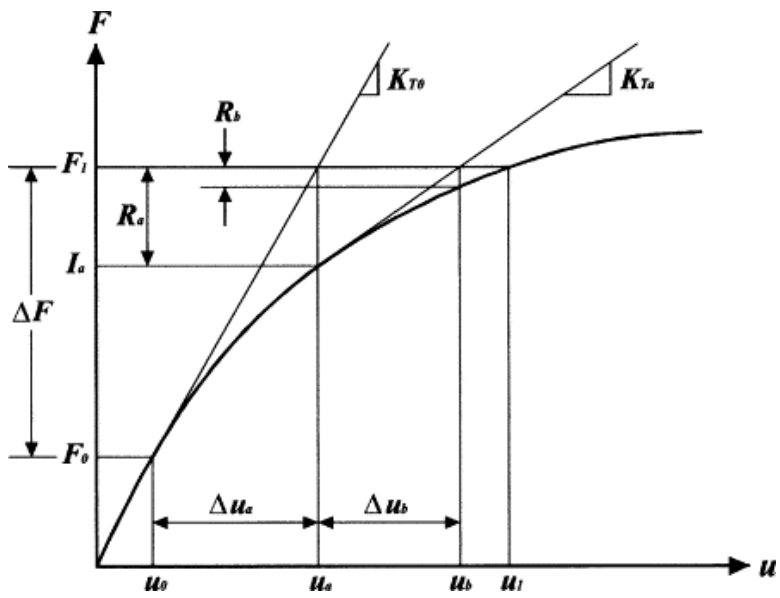


Figure 4-9 - The Newton-Raphson method with a load increment

4.2. Results of numerical study

Numerical results are explained as a basis of global behavior, the ultimate shear force, corresponding vertical deflection, and corresponding relative separation at the bottom of the TW concrete pipes. In addition, strain values are taken accounted to decide failure mode either in the concrete pipe or the CFRP internal coupler system. Three-dimensional numerical models were analyzed to conduct parametric studies and optimize each variable for the coupler system. While conducting the experimental tests, trendy crack patterns were observed, which were shown in the numerical models.

A total of 12 joint shear test numerical models were developed to predict global behavior of the joint shear tests. They were used to investigate the structural performance of the CFRP coupler system and to determine governed failure mode. The models were verified with the experimental joint shear test results. The numerical and experimental test results are given in Table 4-4, and show good agreement. Table 4-3 includes ultimate shear forces, corresponding vertical deflection, and separated relative distances at the bottom of the assembled concrete pipes on different inside diameters of concrete pipes and different CFRP coupler thicknesses. The vertical deflections and the separated relative distances at the bottom of the assembled concrete pipes at the shear strength required, computed by Eq 2.1 by the ASTM specification, are given in Table 4-4. The results obtained by the numerical analyses and experimental tests showed an average of 1.6% and 3.5% for the vertical deflection and the separated relative distance, respectively. Based on the vertical deflection and separated relative length at the bottom of assembled concrete pipes, the numerical models accurately predicted the full-scaled experimental test.

The relative separation lengths for 36-inch inside diameter TW concrete pipes were not measured during the experimental joint shear tests. The calibrated nonlinear

parameters, such as material constitutive laws, friction coefficient of contacted pairs, and geometric parameters were used to perform expanded parametric studies.

Table 4-3 - Result summary of numerical analyses and experimental tests of joint shear tests at ultimate shear forces

I.D. (in.)	t_{coupler} (in.)	FEM joint shear test			Experimental joint shear test			Pass /Fail
		F_{ult} (kip)	Deflection (in.)	Relative separation (in.)	F_{ult} (kip)	Deflection (in.)	Relative separation (in.)	
36	1/16	7.26	0.39	-	7.0	1.0	-	Fail
36	1/8	18.85	1.25	-	17.0	1.1	-	Pass
36	1/4	19.1	0.75	-	20.0	0.7	-	Pass
48	1/8	14.0	1.4	1.42	13.0	1.8	1.39	Fail
48	3/16	15.0	1.2	1.25	21.0	2.6	0.9	Pass
54	3/16	21.6	1.55	1.10	20.97	1.76	0.65	Pass
54	1/4	26.65	1.68	1.31	25.38	1.57	1.36	Pass
72	1/4	30.45	1.54	1.60	27.65	1.30	1.03	Pass
72	3/8	34.11	1.61	1.47	34.55	2.08	2.08	Pass
84	3/8	31.45	1.18	1.08	36.84	1.79	1.24	Pass

Table 4-4 - Result summary of numerical analyses and experimental test of joint shear tests at the required shear strength

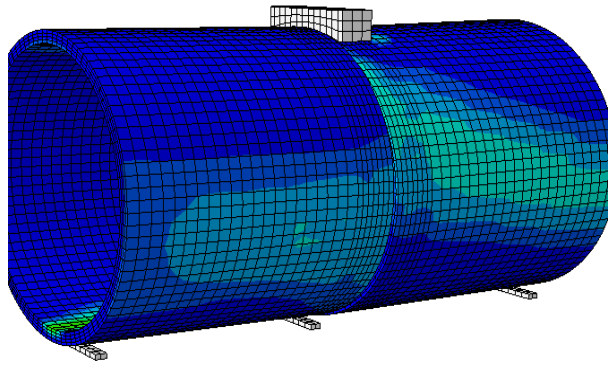
I.D. (in.)	t_{coupler} (in.)	FEM joint shear test			Experimental joint shear test			Pass /Fail
		F_{ult} (kip)	Deflection (in.)	Relative separation (in.)	F_{ult} (kip)	Deflection (in.)	Relative separation (in.)	
36	1/16	13.0	-	-	13.0	-	-	Fail
36	1/8	13.0	0.43	-	13.0	0.49	-	Pass
36	1/4	13.0	0.43	-	13.0	0.30	-	Pass
48	1/8	16.2	1.43	1.62	15.1	1.72	-	Fail
48	3/16	17.3	1.30	0.83	17.3	1.42	0.80	Pass
54	3/16	20.0	1.42	0.88	20.0	1.53	0.64	Pass
54	1/4	20.0	1.07	0.70	20.0	1.56	0.62	Pass
72	1/4	26.0	1.01	1.11	26.0	1.05	1.04	Pass
72	3/8	26.0	0.76	0.79	26.0	0.78	0.77	Pass
84	3/8	30.0	1.04	0.98	30.0	0.96	0.97	Pass

4.2.1 Crack pattern

During the joint shear test, four major cracks were observed at the invert, crown, and both spring lines on the concrete pipes. Figure 4-10 shows the comparison of crack patterns on the experimental test and numerical analysis.



(a) Full-scale experimental joint shear test on 48-inch pipe



(b) Numerical joint shear test model on 48-inch pipe

Figure 4-10 - Comparison of crack pattern on 48-inch TW pipes with CFRP coupler

During the three-edge bearing test, administered in accordance with ASTM C497-16a, hairline cracks developed on the thin-walled concrete pipes, and four major longitudinal cracks developed along the length of the pipe, on the top and bottom of the

inside concrete pipe and two mid-height exterior surfaces (Park et al., 2015). Similar crack patterns were shown during the joint shear tests.

The initial crack opening developed at the invert of the suspended concrete pipe's end support because the concrete materials' modulus of rupture was exceeded. Stiffness degradation on the vertical deflection and shear force response was also observed. The initial crack propagated up the assembled concrete pipes and transferred to another concrete pipe which was not loaded by the CFRP coupler system. The crack patterns are shown in Fig. 4-10 (b). The lighted region indicates the developed crack opening. The crack patterns were well predicted, as compared with the crack patterns from the experimental joint shear tests. At the peak shear forces, the widest cracks were detected at the invert of the concrete pipe subjected to the shear force.

4.2.2 Deflection of the CFRP internal coupler

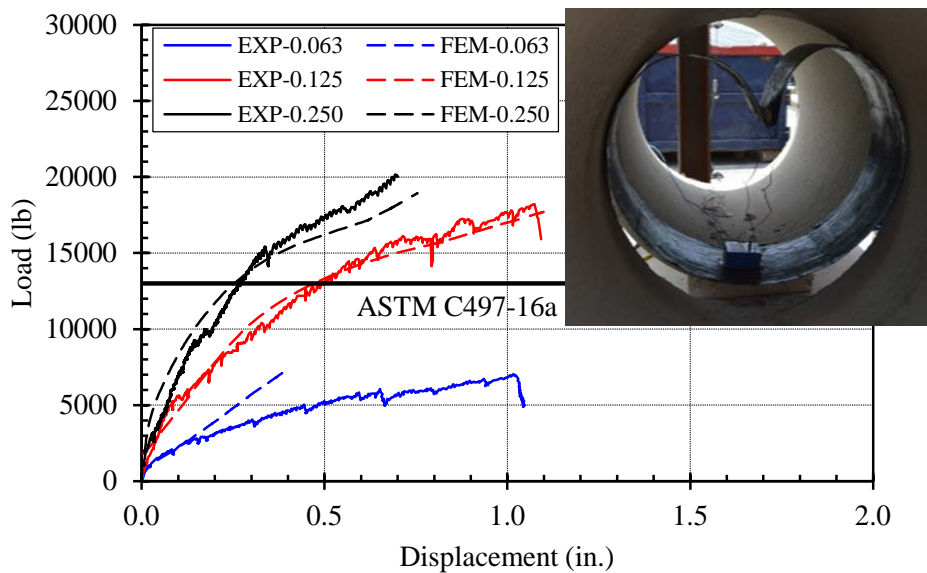


Figure 4-11 - Vertical deflection and shear force plot on 36-inch pipe with three different thicknesses of CFRP coupler

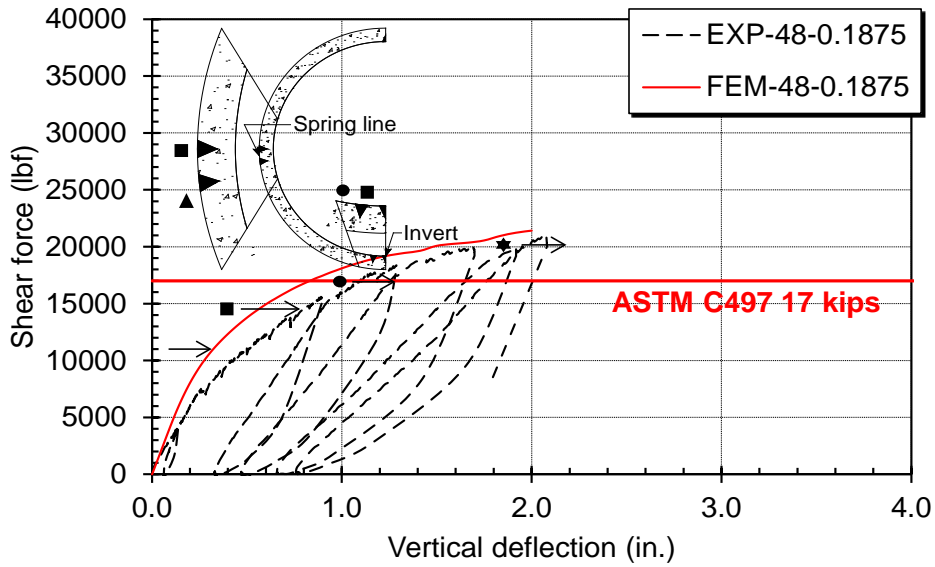


Figure 4-12 - Shear force vs. vertical deflection on 48-inch concrete pipe with 0.1875 inch of CFRP coupler mid-thickness

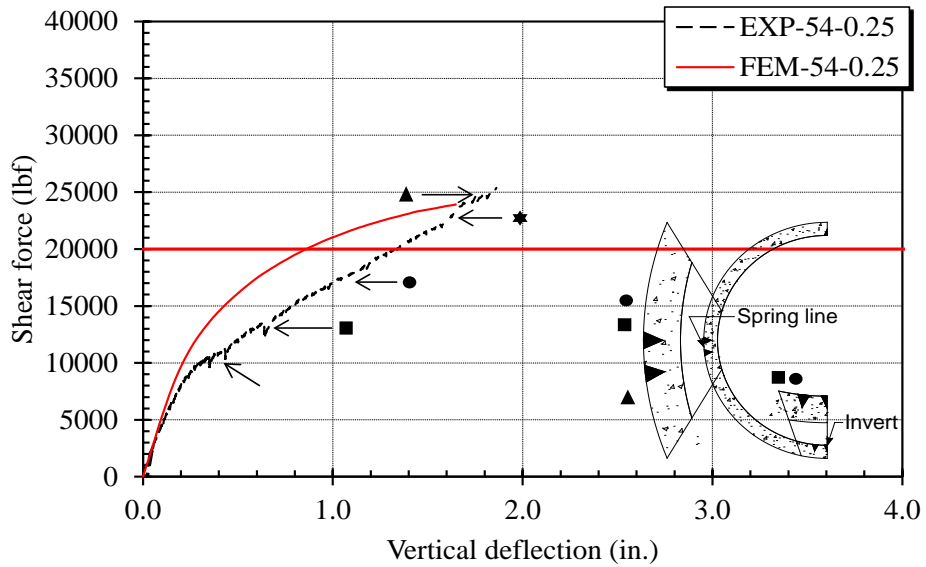


Figure 4-13 - Shear force vs. vertical deflection on 54-inch concrete pipe with 0.25 inch of CFRP coupler mid-thickness

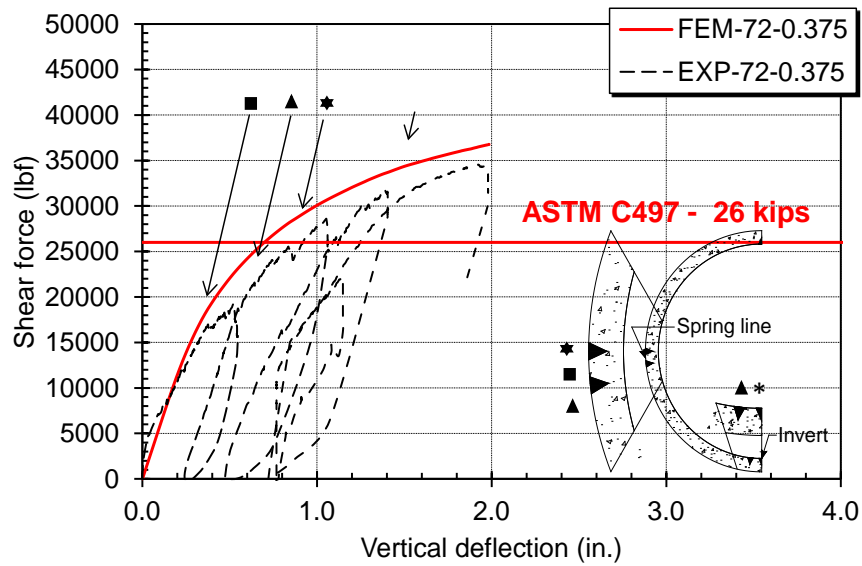


Figure 4-14 - Shear force vs. vertical deflection on 72-inch concrete pipe with 0.375 inch of CFRP coupler mid-thickness

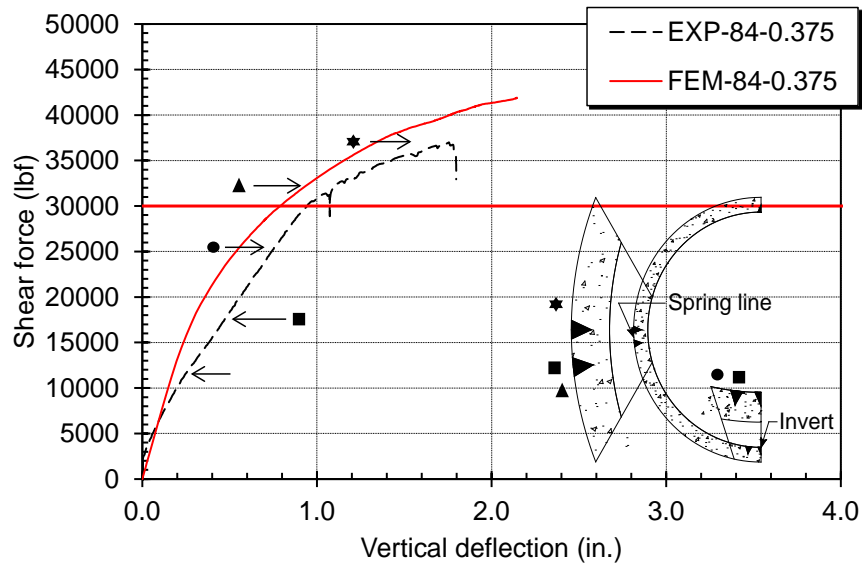


Figure 4-15 - Shear force vs. vertical deflection on 84-inch concrete pipe with 0.375 inch of CFRP coupler mid-thickness

Figures 4-11 through 4-15 show the vertical deflection at the crown and invert of the CFRP coupler vs. corresponding ultimate shear forces on different sizes of inside diameters (ID) of the concrete pipes, including 36 in., 48 in., 54 in., 72 in., and 84 inches. On the 36-inch ID TW pipes, 0.125 inch and 0.25 inch mid-thicknesses of the CFRP coupler showed 23% and 53 % higher ultimate shear forces than the shear force required by ASTM C497-16. However, 0.0625 inch mid-thickness of the CFRP coupler failed at 7 kips which is less than the required shear force of 13 kips. Furthermore, for 48-inch ID pipes, the CFRP coupler system with the mid-thickness of 0.125 inch had slightly less shear strength than the required shear force of 17 kips, and the CFRP coupler system with the mid-thickness of 0.1875 inch had 23% higher shear strength compared to the ASTM C497-16a required shear force of 17 kips. The CFRP coupler with 0.25 inch of mid-thickness supported a higher shear force than is required as 25 kips, but the 0.1875 inch of the mid-thickness coupler failed at 16 kips compared to the required shear force of 20.0 kips on a TW pipe with a 54-inch ID. On the 72-inch and 84-inch concrete pipes, the CFRP couplers mid-thicknesses of 0.375-inch supported the ultimate shear forces of 34.6 kip and 37.2 kips rather than the required shear forces of 26 kips and 30 kips.

4.2.3 Relative separation at the bottom of assembled concrete pipes

The CFRP internal coupler was placed between the insides of two concrete pipes to connect them to each other. During the joint shear tests, a relative separation at the bottom of the assemblage occurred due to the applied shear force. Because of the separation, groundwater or backfill material could infiltrate the pipes, and sewage or storm water could exfiltrate the surrounding soil. The CFRP internal coupler system cannot support applied external shear force or moment. In this research, the relative separation length was limited to 1.5 inch.

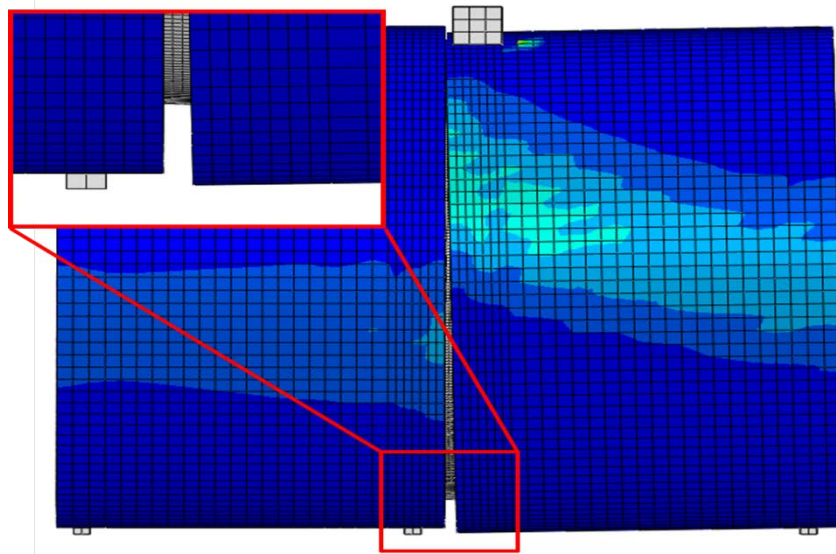


Figure 4-16 - Relative separation at bottom of assembled concrete pipe

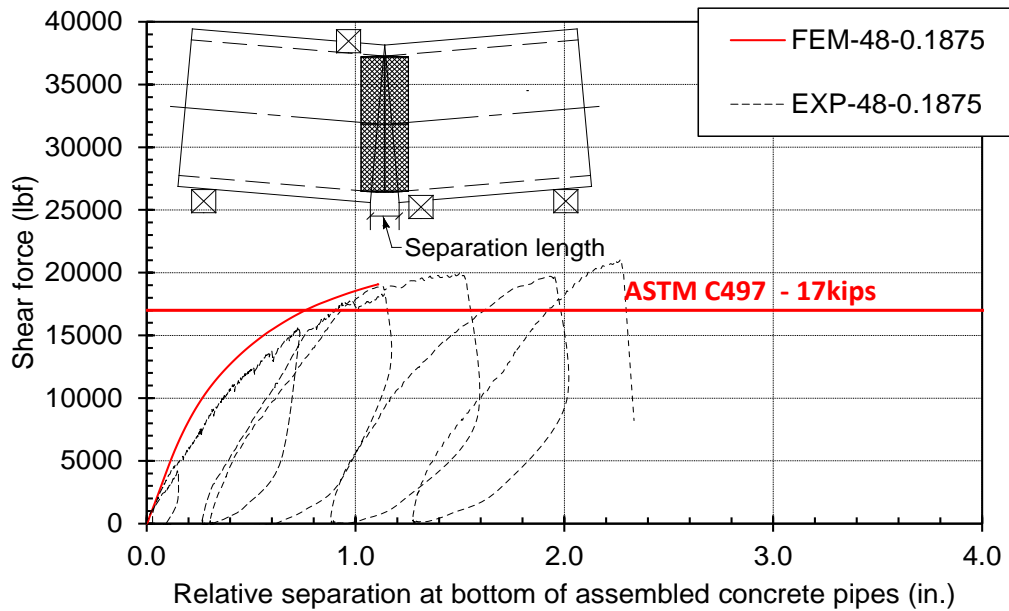


Figure 4-17 - Relative separation length at bottom of assembled concrete pipe vs. shear force response on 48-inch concrete pipe with 0.1875 inch thick CFRP coupler

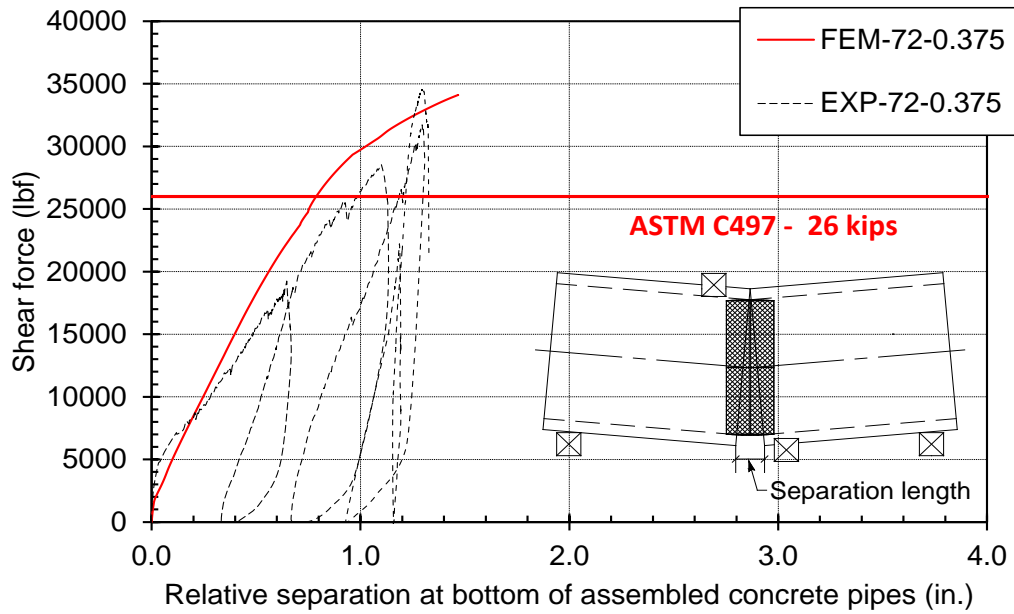


Figure 4-18 - Relative separation length at bottom of assembled concrete pipe vs. shear force response on 72-inch concrete pipe with 0.375 inch thick CFRP coupler

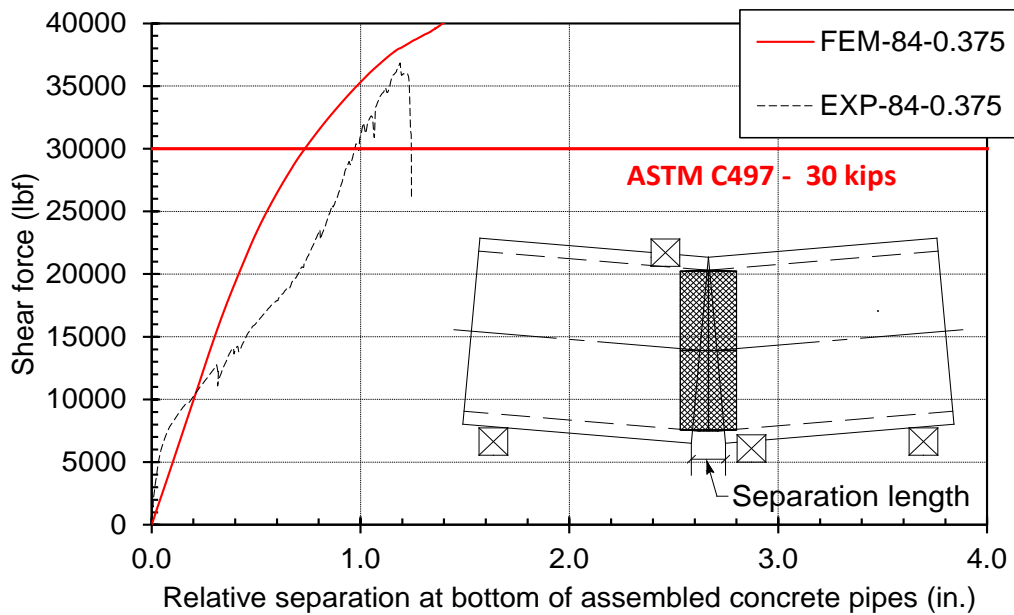


Figure 4-19 - Relative separation length at bottom of assembled concrete pipe vs. shear force response on 84-inch concrete pipe with 0.375 inch thick CFRP coupler

Figures 4-17 through 4-19 show responses between the relative separation lengths at the assembled bottom of the concrete pipes and the applied shear forces obtained by the experimental tests on the 48 in., 72 in., and 84 inch concrete pipes. To simulate sliding of the concrete pipes on the wooden cradles in the FEM models, a friction coefficient of the concrete pipe and wooden cradle was defined as 0.4. The comparison between results obtained by the numerical FEM analyses and the experimental tests indicated that the defined coefficient of friction between the concrete pipe and the wooden cradle calibrated well, and that FEM models are capable of predicting the relative separation length between the concrete pipes at the bottom.

4.2.4 Principal strain value on CFRP internal coupler

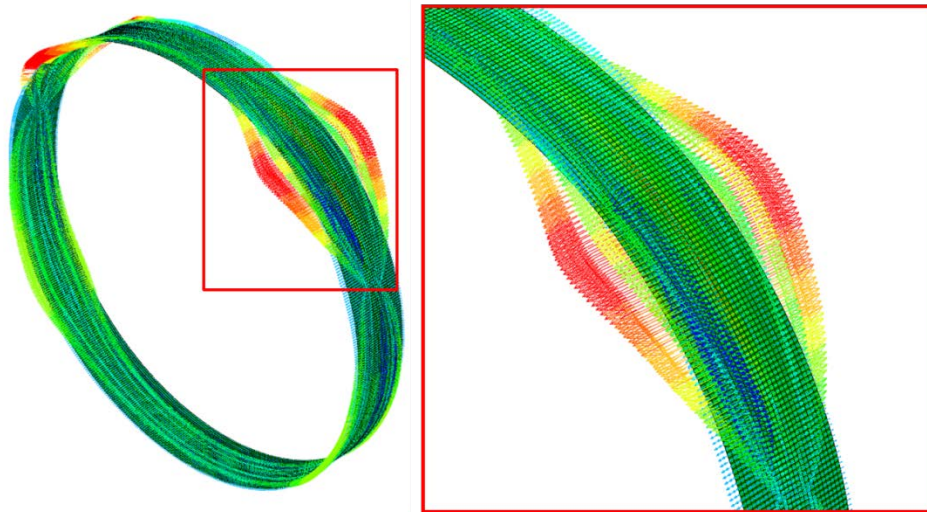


Figure 4-20 - Maximum in-plane principal strain contour of the CFRP coupler at the ultimate shear force on 96-inch ID of TW concrete pipe with a 12 inch wide coupler with 0.25 inch mid-thickness

In Fig. 4-20, the maximum in-plane principal strains are shown as red colored arrows which are expanded in transverse directions from the CFRP coupler. Depending on the mid-thickness of the CFRP couplers, the locations of the maximum-principal strain change. As the mid-thickness increases, the region showing the maximum principal strain gets lower, up to the invert of the CFRP coupler. Figure 4-21 shows maximum in-plane principal strain value responses with different mid-thicknesses of the CFRP couplers, 0.125 inch through 1.0 inch. As illustrated with a dashed line referred to as “THK-0.125” in Fig. 4-21, the maximum principal strain value is shown 45 degrees from the crown of the CFRP coupler. Strain value responses converged to an average of 0.002 in./in., as the mid-thickness of the CFRP coupler increased. According to the ultimate strain value obtained by the CFRP laminate coupon test, the CFRP coupler with a mid-thickness greater than 0.375 inch will not fail at the CFRP coupler system in a TW concrete pipe with a 120-inch inside diameter.

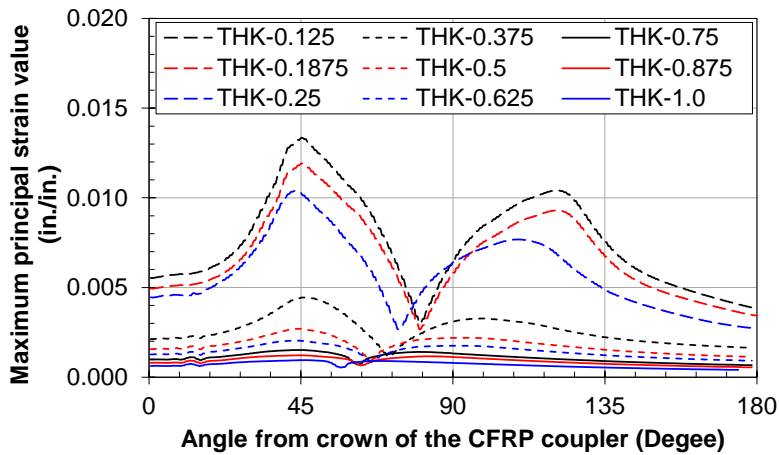


Figure 4-21 - Maximum in-plane principal strain value with corresponding angles from crown to invert of the CFRP coupler for 120-inch TW concrete pipes with 12-inch CFRP coupler at 44 kips of the shear force required by ASTM C497-16a

Figures 4-22 through 4-25 show the strain value vs. ultimate shear force responses on 48 in., 54 in., 72 in., and 84 inch TW concrete pipes with CFRP couplers. As shown in Figs. 4-22 to 4-25, failure strain values for the CFRP internal coupler systems are an average of 0.01 in./in. in transverse direction of the CFRP coupler.

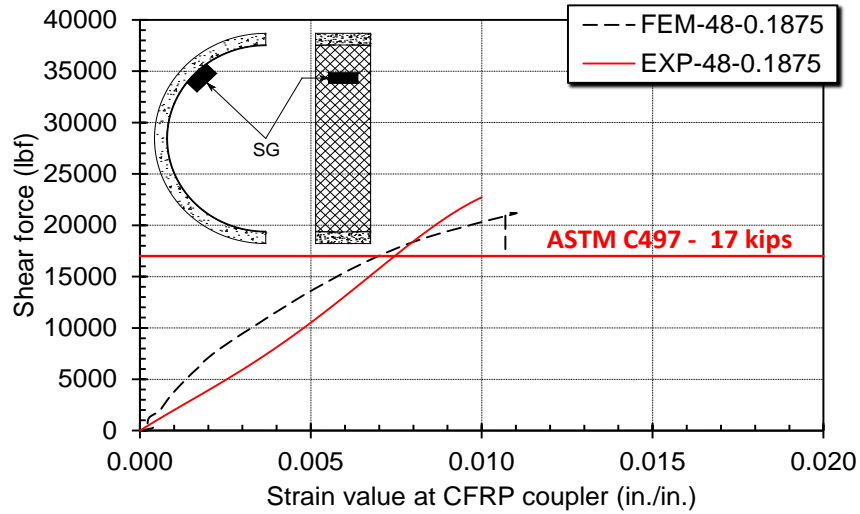


Figure 4-22 - Strain value vs. shear forces on 48 in. pipe with 0.1875 in coupler thickness

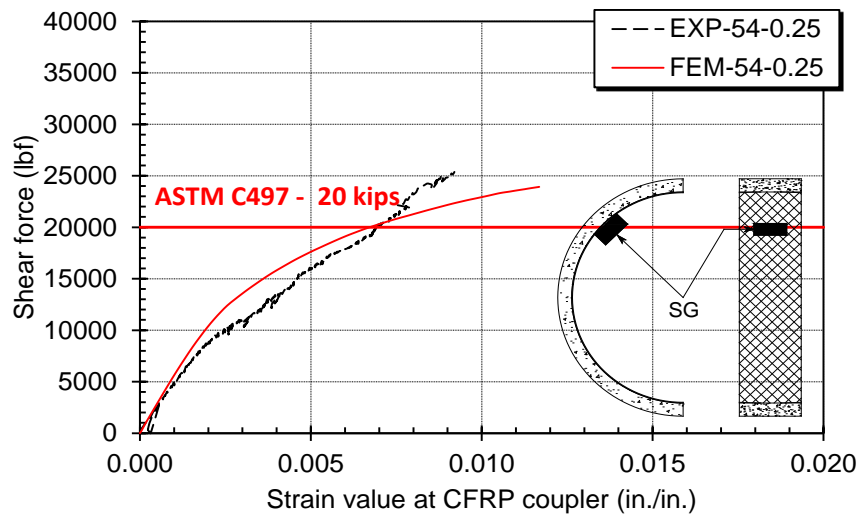


Figure 4-23 - Strain value vs. shear force on 54 in. pipe with 0.25 in coupler thickness

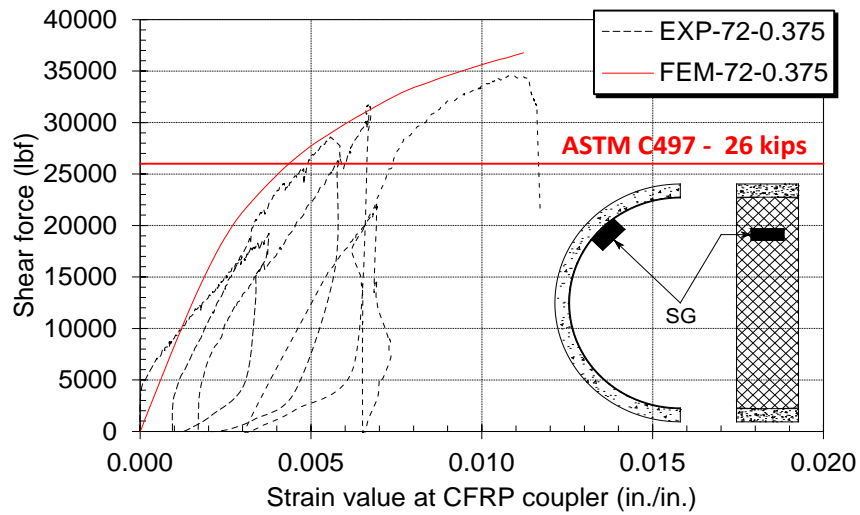


Figure 4-24 - Strain values vs. shear forces on 72 in. pipe with 0.375 in coupler thickness

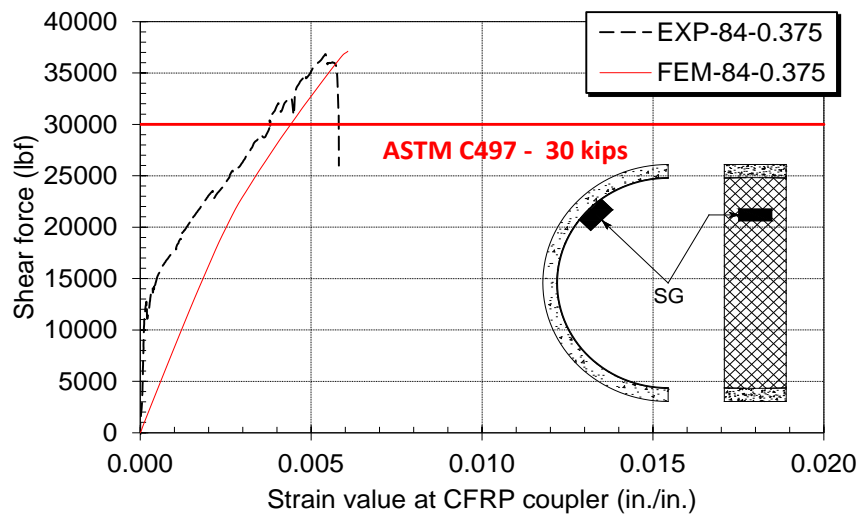


Figure 4-25 - Strain value vs. shear force on 84 in. pipe with 0.375 in coupler thickness

Figure 4-26 shows the response of shear force and corresponding strain values obtained by the experimental test and finite element method analysis of a 72-inch concrete pipe with a CFRP internal coupler with a mid-thickness of 0.375 inch. As shown in Fig. 4-26, the FEM method accurately predicted the strain values and global behavior

of the joint shear test. The results from the experimental joint shear test and the numerical analysis were within 10% of each other in the somewhat offset areas shown in Fig. 4-26.

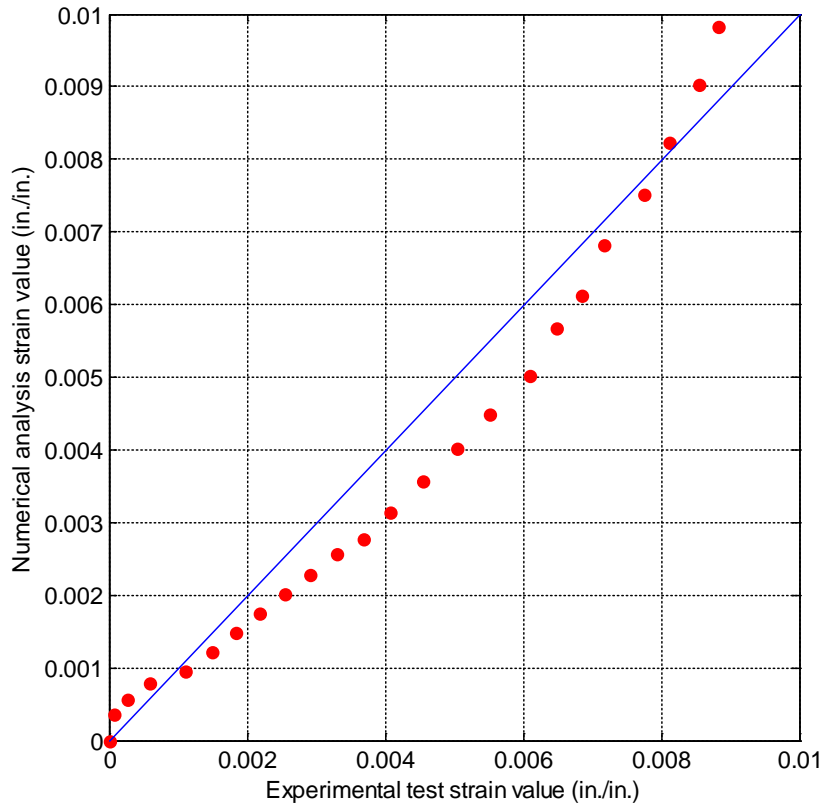


Figure 4-26 - Shear force vs. strain values obtained by FEM and experimental test on TW72 pipe with 0.375 inch coupler

The difference was due to an imperfect alignment of the strain gauge on the circumferential CFRP coupler surface. As aforementioned in the CFRP laminate material test, the strain value of 0.01 in. /in. is a limitation of the CFRP laminate, caused by fiber-reorientation that occurs after the strain value is exceeded. When the critical strain value reached 0.01 in. /in., the CFRP internal coupler failed at the top of the coupler.

4.3 Conclusion

The three-dimensional nonlinear finite element models were developed and utilized to predict the behavior of joint shear tests on concrete pipes assembled by the CFRP internal coupler system. Shear forces, corresponding vertical deflections, and maximum principal strain values at specified points of rotations of vectors around the y-axis by 45 degrees were used to verify the numerical model by comparing it with the results obtained from the experimental joint shear tests conducted under real conditions. It was concluded that the FEM models were capable of predicting the behavior of the CFRP internal joint system on the concrete pipe under static loading conditions. The margin of difference between the results of the FEM method and the actual experimental tests was less than 5%, which is an acceptable range for concluding that the FEM models predicted the experimental tests well. The verified FEM models served as a basis for the parametric study to expand various geometric properties of the CFRP internal coupler and concrete pipes.

Chapter 5 Experimental Tests

5.1 Materials

5.1.1 Synthetic-fiber-reinforced concrete material

A dry-mixed concrete material with synthetic fiber reinforcement was used to manufacture concrete pipes having an enhanced toughness property. Water and cement were mixed at a ratio of 3 to 4, respectively.

For a thin-wall synthetic-fiber-reinforced concrete pipe, 8 pounds per cubic yard of synthetic fibers were added to the concrete mixture. The synthetic fibers were made of a blend of 100% virgin polypropylene resin, had tensile strength of 84.85 ksi, were 2.12 inches long, and had a diameter of 0.03 inches (Park et al., 2014). The volume fraction was calculated based on the relative density of water (1.0) as 8 pounds per cubic yards (0.52%) (Wilson et al., 2014). They were manufactured in compliance with ASTM C1116 (ASTM, 2006).

5.1.2 Conventional reinforced concrete pipe

Conventional reinforced concrete pipes (RCP) were utilized to investigate the performance of newly developed joint system. RCP pipe is produced based on ASTM C76, "*Standard Specification for Reinforced Concrete Culvert, Storm Drain, and Sewer Pipe*" (ASTM, 2014). The concrete mixtures were cast by Packerhead equipment, using the same procedure that the Forterra plant used to produce RCP pipes, as shown in Fig. 5-1 (a), and the steel mold shown in Fig. 5-1 (b). Packerhead equipment is comprised of a three-piece jacket and steel mold, as depicted in Fig. 5-1 (a). The three-piece jackets rotate simultaneously, introducing dynamic forces and radial compaction, and force the concrete mixture to the inside of the steel mold. The movement of the Packerhead along

the length of the pipe creates the inside diameter of the pipe. While moving along the length of the pipe, the vibrating Packerhead compacts the dry-mixed concrete material.

The steel mold was pre-fabricated in a bell and spigot shape to fabricate the bell and spigot on the concrete pipes. Either single layer or double layers of steel wire reinforcements were embedded in the steel mold. After casting, the concrete pipes were steam cured at atmospheric pressure, which was important for the formation of early strength, as shown in Fig. 5-1 (c).



Figure 5-1 - Production of thin-wall concrete pipe:
(a) Packerhead, (b) Steel mold, and (c) Steam curing



Figure 5-2 - Production of steel cages: (a) Welding machine (b) Steel cage

5.1.3 Thin-walled flexible concrete pipes with synthetic fibers

Joint shear tests were performed on concrete pipes with reduced wall thickness, hereinafter called thin-wall (TW) concrete pipes. The conventional concrete pipes reinforced with synthetic fibers were developed by Wilson et al. by adding synthetic fibers to the concrete mixture, which enhanced the strength and resistance of crack growth up to 1 inch of crack width when the pipe was deflected over 10% of the diameter of the pipe (Wilson et al., 2014). Park et al. further developed the TW flexible concrete pipes with synthetic fibers (Park et al., 2015). The main reinforcement was circumferential and longitudinal steel cages that were installed inside the steel mold. However, the area of the circumferential reinforcement reduced proportionally as the wall thickness reduced. In

addition, one important difference between the conventional RCP and TW pipe is the presence of the bell and spigot as the connector. Because the walls of TW concrete pipes are so thin, the conventional bell and spigot cannot be fabricated on the ends of the TW pipe. TW concrete pipes with 36-inch inside diameters were manufactured by Forterra, Grand Prairie, Texas without the bell and spigot, and other diameter concrete pipes were produced by the Northern Concrete Pipe (NCP) plant located in Lansing, Michigan. NCP employs the Hawkeye equipment shown in Fig. 5-3, with a rising core and descending jackets, which vibrates and consolidates the dry-mixed concrete mixture up to the steel mold to produce the wall thickness of concrete pipes (Alena, 2014).



Figure 5-3 - Hawkeye rising core (Alena, 2014)

5.2 Joint system utilizing carbon-fiber-reinforced polymer fabric

Carbon Fiber Reinforced Polymer (CFRP) fabric sheets were employed as connectors for the joint systems of the thin-walled concrete pipes. The CFRP fabric sheet, selected because of its high chemical resistance and tensile strength, was bonded to the two thin-walled concrete pipes. The externally wrapped joint system, a pre-fabricated joint system made of the multiple layers CFRP laminate, was employed to assemble the two thin-walled concrete pipes.

5.2.1 External wrapping by CFRP fabric

With developed flexible concrete pipe, a new joint system by wrapping carbon fiber reinforced polymer (CFRP) fabric fiber used to enhance seismic performance of structures has been conducted. This dissertation aims to evaluate joint capacity of wrapping system subjected to shear force. The specific objectives are as follows: (1) to determine the idealized width of CFRP fabric fiber and (2) to investigate behavior of joint shear capacity depending on curing time of epoxy resin matrix. Shear tests of wrapping system were performed according to ASTM C497-16a, as shown in Fig. 5-4.

5.2.1.1 Geometry and mechanical properties of specimens.

The strength capacity of the joint system was investigated, with the width of the CFRP sheets as the variable. Three CFRP sheet widths (3 inches, 6 inches, and 12 inches) were considered. The thin-walled concrete pipe was manufactured by using a head-rotating method, as aforementioned in the conventional concrete pipe manufacturing. The pipes used in the experimental tests had diameters of 36 inches and 60 inches, and were 48 inches long, with 2.25 inches and 2.5 inches of wall thicknesses. After casting, the concrete pipes were steam cured at atmospheric pressure, which was important for early strength gain.

5.2.1.2 Experimental setup and instrumentation

Joint shear tests were conducted on the concrete pipes and carried out in accordance with the ASTM C497-16a standard (ASTM, 2016). Single lay-up CFRP sheets, with widths of 3 inches, 6 inches, and 12 inches, were used to connect two concrete pipes with inside diameters of 36 inches and 60 inches.

Figure 5-4 shows the experimental setup with four cradles and two concrete pipes, assembled by externally-bonded CFRP sheets. One pipe was fully supported by two timber cradles, which were placed 6 inches from the surface of the assembled concrete pipes. Another was suspended and subjected to applied load. Shear force was applied through the loading cradle of the assembled joint system, between the two concrete pipes' end surfaces. Tests were conducted by controlling the forces of the hydraulic cylinder and pressure pump. Two-kip incremental pseudo cyclic forces were loaded to simulate the worst possible scenario for the joint system.

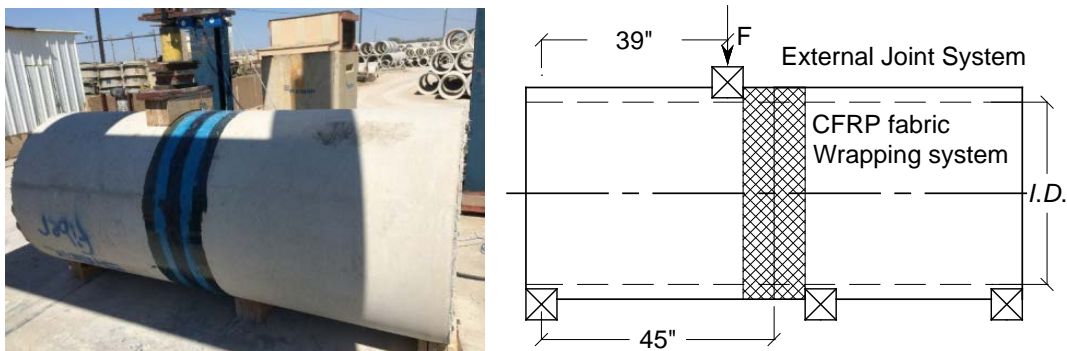


Figure 5-4 - Setup and schematic of joint shear test

Load cell was used for obtaining the applied forces during the testing. Two cable displacement sensors (CDS) were also employed to measure the relative displacement of the two concrete pipes.

5.2.1.3 Procedure of shear test on wrapping joint system

To simulate more critical circumstances, vertical cyclic load acting on pipe increases by 1000lbf per cycle. There are three variables; (1) width of CFRP fabric: 3, 6, and 12 inch, (2) curing time of epoxy matrix: 1, 3, and 24 hours, and (3) exposure on dirty environmental condition. Shear strength of all of tested specimen pipes should be over the required shear load from ASTM C497-16a as Eq. 2.1 in Chapter 2.

1. With same internal diameter pipe, test is performed by reducing width of fabric fiber as order of 12 inch, 6 inch, and 3 inch until failure occurs on either concrete or CFRP wrapping system.
2. Idealized width of fiber on the 1st step is used to find sufficient curing time of MBACE epoxy for CFRP fiber as wrapping system. Unlike with test for idealized width of fabric, test for sufficient curing time extends curing time from 1 hour to 24 hours.
3. In pipes expose on dirty environment, the shear joint test is performed with minimum width of fabric fiber and the most sufficient curing time.

Two individual pipes are assembled with three different chemicals and the CFRP fabric fiber. These chemicals include (1) putty for identical surface level on two pipes (Chemical I), (2) primer to fill the void and make even surface of concrete pipes (Chemical II), and (3) MBACE epoxy to stick and harden the fabric on pipes (Chemical III). As shown in Fig. 5-5, the wrapping system is made. It is noted that the epoxy should permeate inside the CFRP fabric fiber to perfectly bond the CFRP fiber on concrete pipes. Test will be interrupted at observation of either failure of concrete or MBACE epoxy matrix.

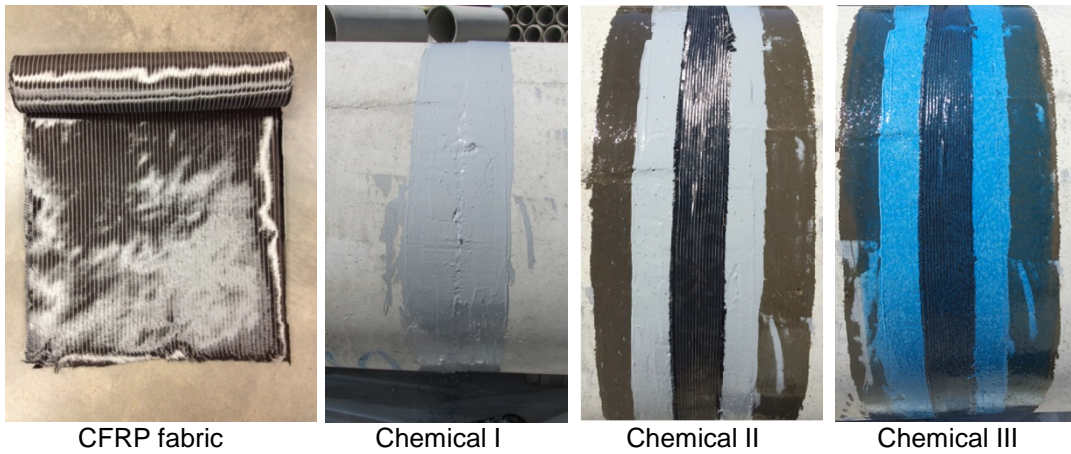





Figure 5-5 - Wrapping system process

Eight joint shear tests were performed as order: TW36-6W-24H, TW36-3W-24H, TW36-3W-3H, TW36-3W-1H, TW36-3W-2H, TW36-6W-1H, and TW36-3W-24H with dirty. The name of specimen is denoted that TW is thin-wall concrete pipe, the number of 36 means internal diameter (inch), 3W means width of CFRP fabric fiber, 24H means curing time for wrapping system after completing wrapping process. As mentioned in test set-up, all of shear strengths in joint shear tests is compared to the serviceability load from ASTM C497-16a.

Table-5-1 shows three types of failure modes; (1) surface flaking concrete by MBRACE epoxy, (2) delamination of CFRP fabric fiber, (3) fracture of concrete.

Table 5-1 – Failure mode of specimens

Surface flaking concrete	Delamination of CFRP	Fracture of concrete
		

5.2.1.4 Results of Externally Wrapped Joint System

Table-5-2 shows maximum shear strengths depending on different variables. Furthermore, Table-5-2 appears shear strength at initial cracks on four critical regions; crown, invert, and right and left springlines.

From results of joint shear tests, the minimum width of CFRP fabric fiber is 3 inch, which can support the required shear load from ASTM C497-16a. In the respect of curing time, all of joint specimens cured over 3 hours were satisfied with the required shear load. In case of less than three hours curing time, the MBRACE epoxy matrix did not hardened, which resulted in slipping out the CFRP fabric fiber from assembled pipes.

Table-5-2 Maximum shear strengths

Specimen	3W-3H	3W-3H-2	3W-24H	3W-3H-D	6W-24H	12W-24H
Max. Load (kip)	23.0	22.0	24.0	18.0	17.0	28.0
Failure mode	Mode II	Flaking concrete	Flaking concrete	Flaking concrete	Flaking concrete	Fracture of concrete
* D denotes exposed pipe on dirty environment						

Table-5-3 Strengths of initial cracks at four regions

Specimen	V_u (kip)	Crown (kip)	Invert (kip)	Left Spring line (kip)	Right Spring line (kip)	Pass/Failed
TW36-3W-3H	23	10	6	9	10	Pass
TW36-3W-3H-2 nd	22	10	10	10	12	Pass
TW36-3W-24H	24	8	12	12	11	Pass
TW36-3W-24H-D	18	9	9	10	10	Pass
TW36-6W-24H	17	7	8	8	10	Pass
TW60-12W-24H	28	9	9	10	10	Pass
TW36-3W-2H	5	-	-	-	-	Failed
TW36-6W-1H	3	-	-	-	-	Failed
* D denotes exposed pipe on dirty environment						

TW-3W-3H

As shown in Figure 5-6, the maximum shear strength reached 23kips with surface flaking concrete at crown and invert (Mode I) and fabric delaminating at both side springlines of wrapping system (Mode II). Maximum loading induced 0.6inch of deflection at crown. Crack on crown of concrete pipe was observed at 10kips load. When crown crack occurred, both sides concrete brittle also happened at 10kips.

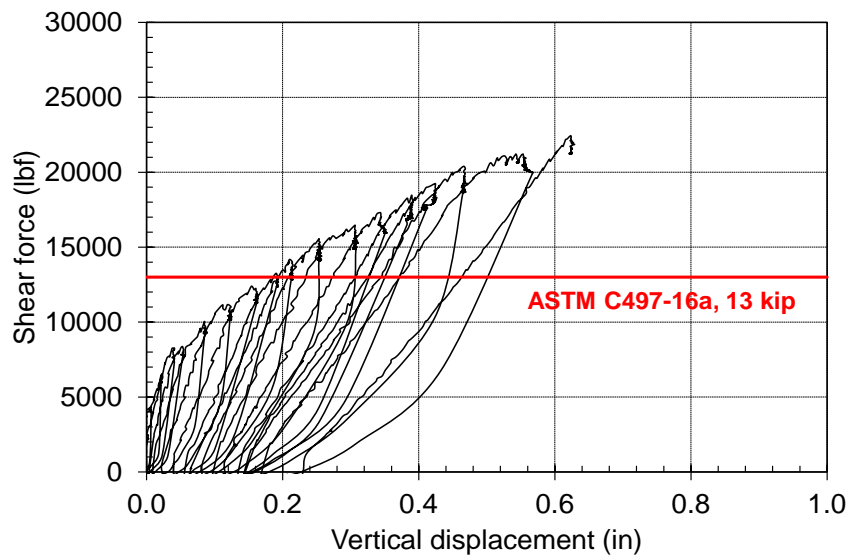


Figure 5-6 - Load-deflection plot of TW36-3W-3H

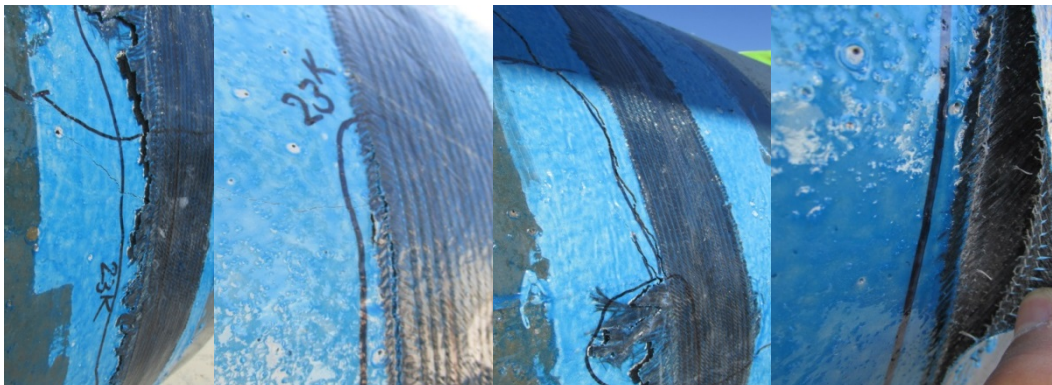


Figure 5-7 - Flaking of concrete and delamination of CFRP for TW 36-3W-3H

TW-36-3W-3H-Second

As shown in Figure 5-8, the maximum shear strength reached 22kips with surface flaking concrete at both side of assembled portion. When loading is 22kips, deflection of crown suspected is 0.9inch. 10kips load made an initial crack on invert of considered pipe. Crack on crown of concrete pipe appeared at 10kips load. Crack at both spring lines of concrete also was observed at 10kips and 12kips.

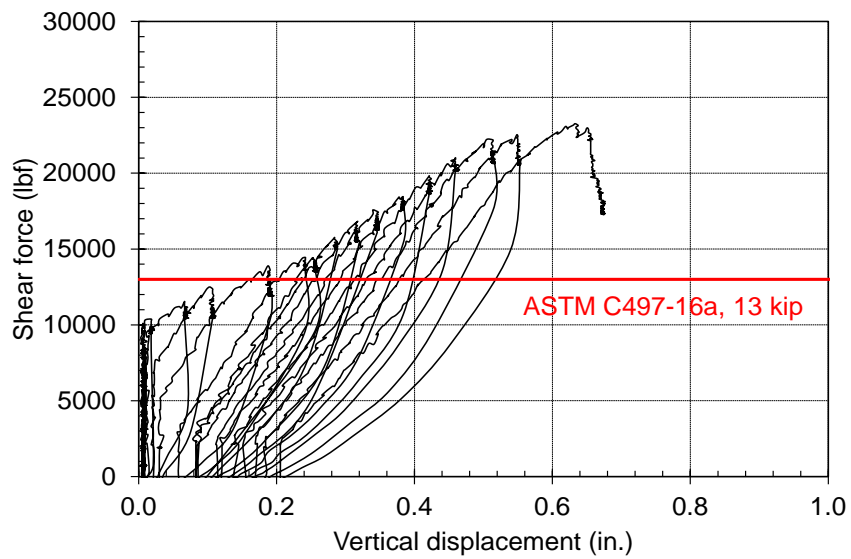


Figure 5-8: Load-deflection plot of Second-TW36-3W-3H



Figure 5-9: Flaking of concrete (Mode I)

TW 36-3W-24H

As shown in Figure 5-10, the maximum shear strength reached 24kips with surface flaking concrete (Mode I) at both spring lines of assembled portion. When loading is 24kips, deflection of crown considered pipe is 0.67inch. 8kips load made an initial crack on invert of considered pipe. Crack on crown of concrete pipe appeared at 10kips load. When crown crack occurred, crack at spring lines of concrete also was observed at 10kips and 12kips.

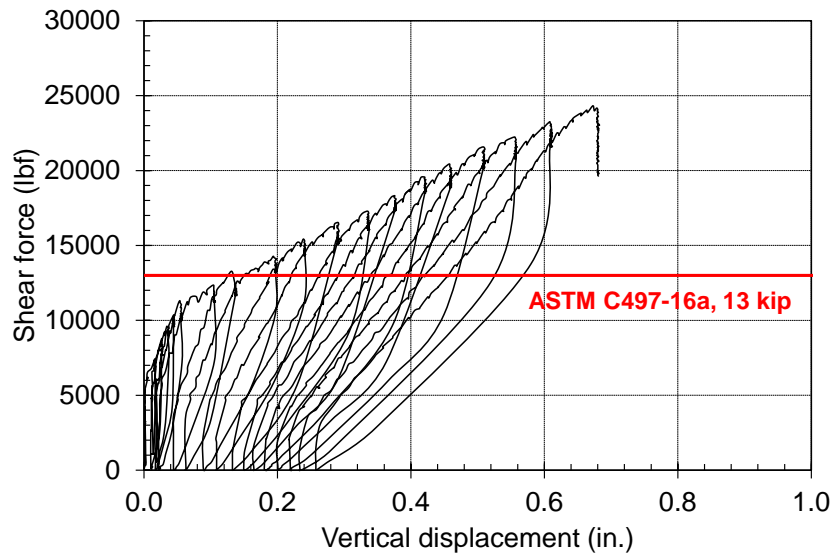


Figure 5-10: Load deflection plot of TW36-3W-24H

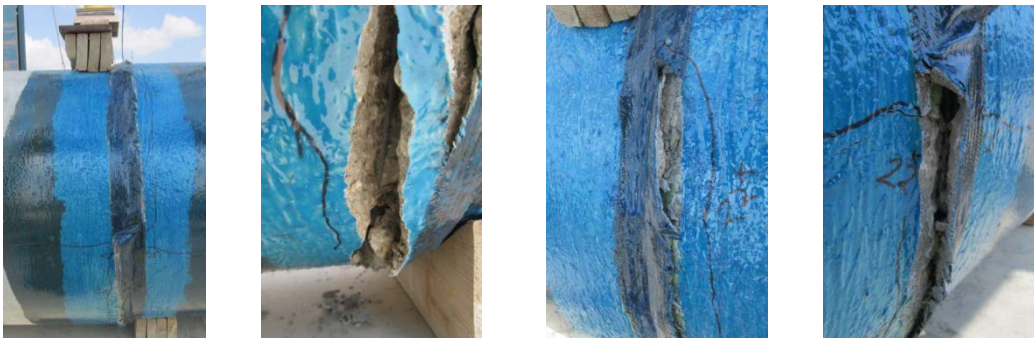


Figure 5-11: Flaking concrete of TW36-3W-24H

TW-36-3W-24H exposure in environment

As shown in Figure 5-12, the maximum shear strength reached 18kips with surface flaking concrete (Mode I) at both spring lines of assembled regions. At maximum loading, deflection of considered pipe crown was 0.65inch. 9kips load made an initial crack on considered concrete invert. Crack on crown of concrete pipe appeared at 9kips load. When crown crack occurred, crack at both spring lines of concrete also was observed at 10kips.

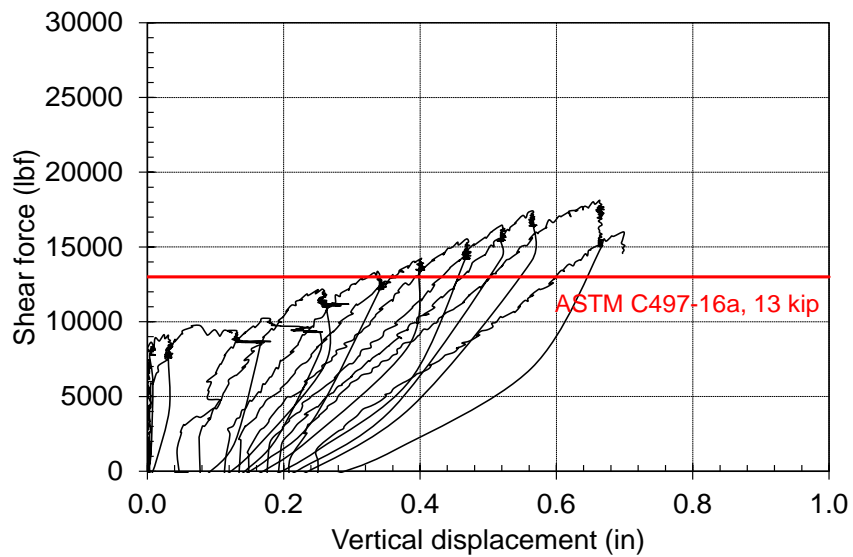


Figure 5-12: Load deflection plot of TW36-3W-24H-D



Figure 5-13: Flaking concrete of TW36-3W-24H with Dirty

TW-36-6W-24H

As shown in Figure 5-14, the maximum shear strength was 17kips with surface flaking concrete (Mode I) at both spring lines of assembled portion. When loading is 17kips, deflection of crown considered pipe is 0.67 inch. 8kips load made an initial crack on invert of loaded pipe. Crack on crown of concrete pipe appeared at 7kips load. When crown crack occurred, crack at both spring lines of concrete also was observed at 8kips and 10kips.

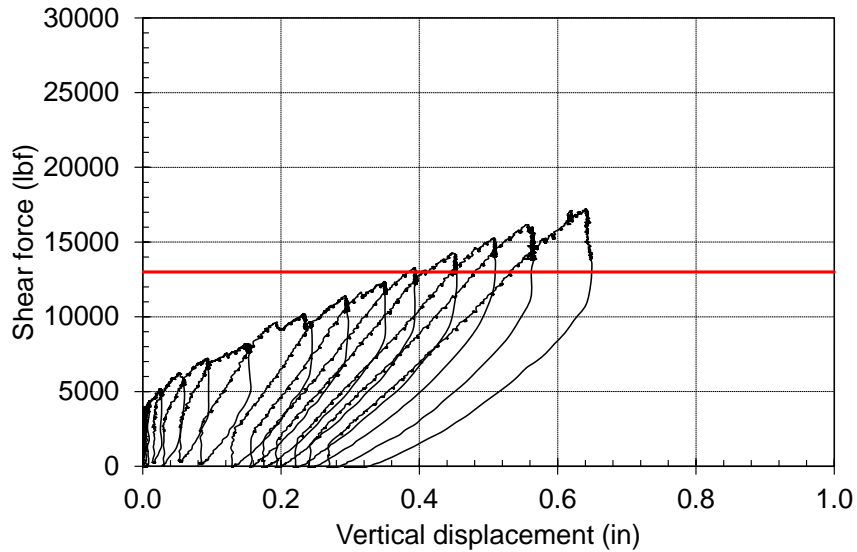


Figure 5-14: Load deflection of TW36-6W-24H

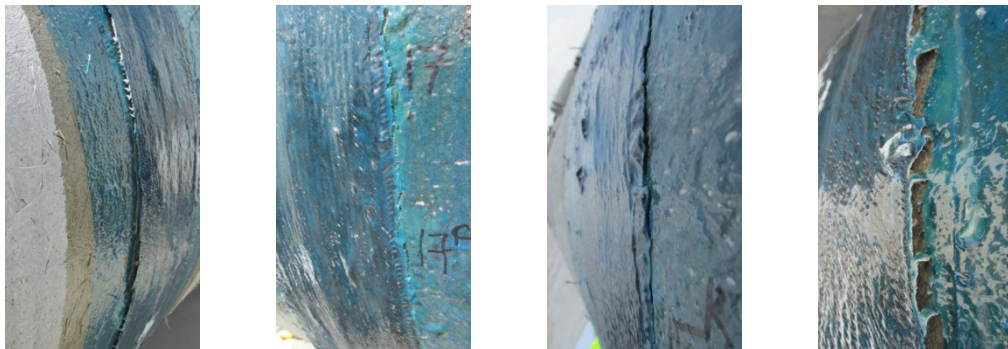


Figure 5-15: Flaking concrete of TW36-6W-24H

TW-60-12W-24H

As shown in Figure 5-16, the maximum shear strength reached 24kips with surface flaking concrete at crown of concrete. Differently from 36inch pipes tested, flaking or delamination of fabric with MBRACE epoxy matrix was not detected. Deflection of crown suspected at maximum load is 2.1inch. 9kips load made an initial crack on invert of suspected pipe. Crack on crown of concrete pipe appeared at 9kips load. When crown crack occurred, crack at both spring lines of concrete also was observed at 10kips.

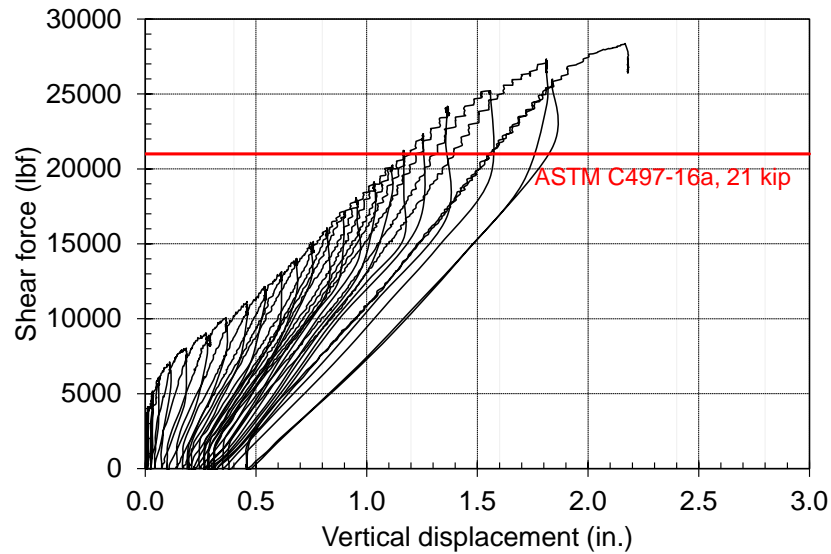


Figure 5-16: Load deflection of TW60-12W-24H



Figure 5-17: Concrete fracture of TW60-12W-24H

Compare TW36-3W-24H with Dirty and TW36-3W-24H without Dirty

Figure 5-18 shows 36inch pipes with 3inch CFRP fabric cured for 24 hours; one exposed on dirty environment and the other was not exposed on dirty environment. Concrete flaking occurred at 24kips. At the maximum load, the deflection of considered concrete pipe was 0.55 inch. In contract, thin-wall concrete pipe exposed on dirty environment, failure of concrete occurred at 17kips. Maximum deflection of considered pipe was 1.5 inch.

According to ASTM C497-16a, 36inch concrete pipes using 3inch fabric fiber satisfy the required shear load as 13kips.

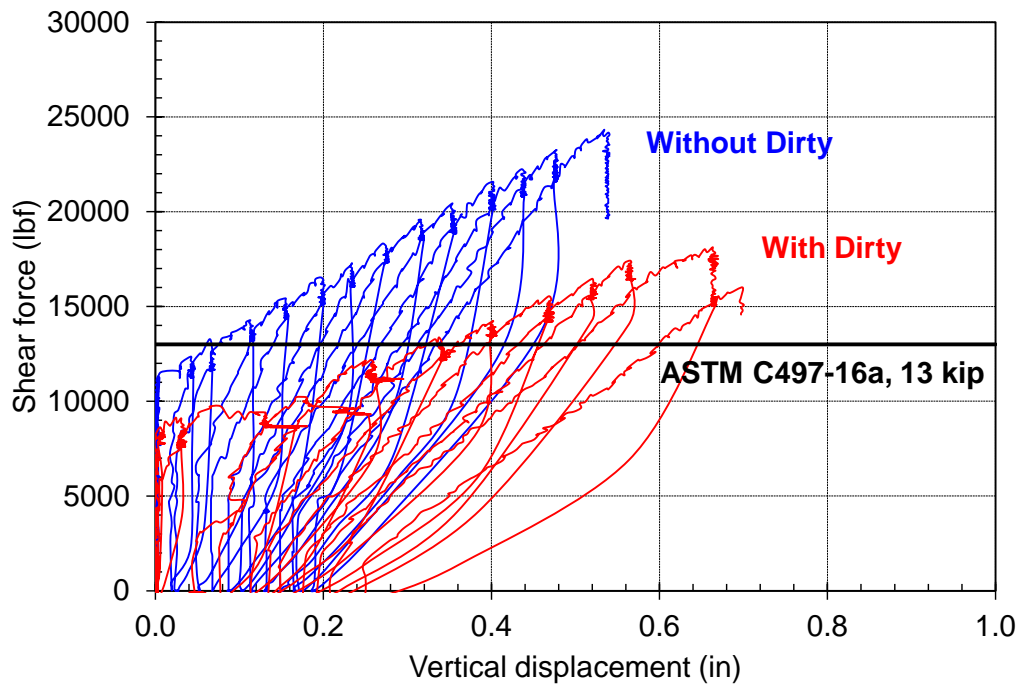


Figure 5-18: Comparison of specimens on dirty or clean environment

TW36-6W-1H

Figure 5-19 is curve of 36inch inside diameter thin-wall concrete pipe assembled with 6inch CFRP fabric fiber for 1hour curing time. As shown in Figure 5-19, shear strength of this specimen did not satisfy the requirement shear force from ASTM C497-16a. Furthermore, the test was interrupt because of CFRP fabric fiber slipped out from assembled connection. The main reason of failed test is insufficient curing time for hardening MBRACE epoxy.

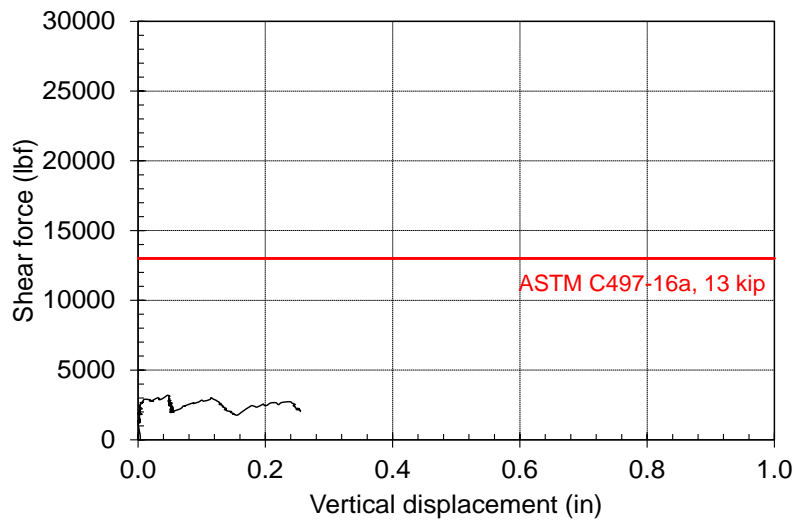


Figure 5-19: Load deflection plot of TW36-6W-1H



Figure 5-20: Slipped out CFRP fabric from assembled pipes on TW36-6W-1H

TW36-3W-2H

Similar as TW36-6W-1H, the 36inch inside diameter concrete pipe having two hours as curing time did not carry the required shear force from ASTM C497-16a. The CFRP fabric fiber was slipped out from assembled connection. Compared with TW36-6W-1H, the slipping occurred shortly since the use of narrow width of the CFRP fabric fiber.

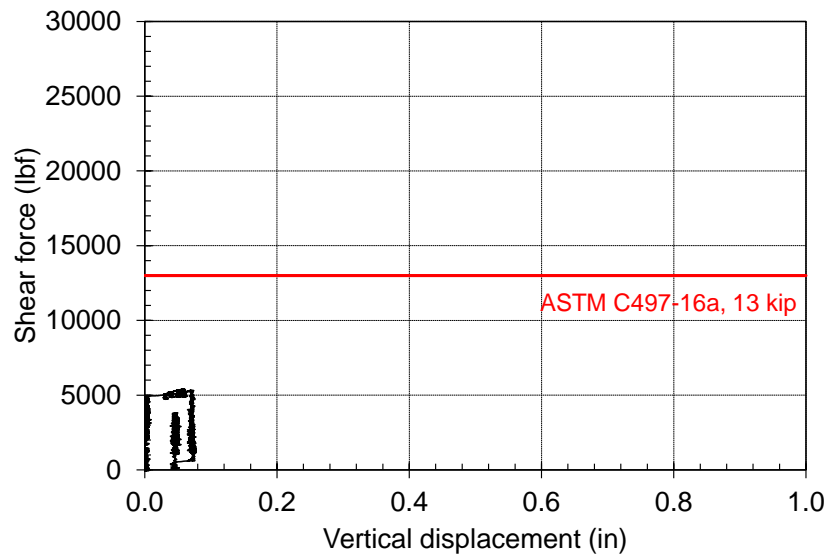


Figure 5-21: Load deflection of TW36-3W-2H



Figure 5-22: Slipped out CFRP fabric from assembled pipes on TW36-3W-2H

5.2.2 Internal CFRP coupler system

The internal coupler system, used as a connector for thin-walled concrete pipes, is designed of CFRP fabric sheets stacked in multiple layers, depending on the mid-thickness of the coupler system. The CFRP internal system is employed to assemble concrete pipes for the construction of pipelines, which are used as the drainage system for storm sewers and sewage water. Therefore, corrosion is an important issue in choosing a proper material for manufacturing the coupler system. The CFRP sheet was chosen for the development of a new joint system for concrete pipes with reduced wall thickness because of ease of installation, high strength to light weight ratio, and high resistance to corrosion (Erki et al., 1993; Seo et al., 1999; Tang et al., 1999; Meier et al., 1995; Al-Hammoud et al., 2010; and Zhou et al., 2003). The CFRP sheets consisted of two bidirectional fibers oriented at -45 and 45 degrees to vertical axes along the assembled surface. Saturant epoxy resin was employed to encapsulate the CFRP fabric layers. A 36-inch diameter Styrofoam cylinder was utilized to make the first layer of the CFRP fabric sheet shell shaped, as shown in Figs. 5-23 and 5-24.

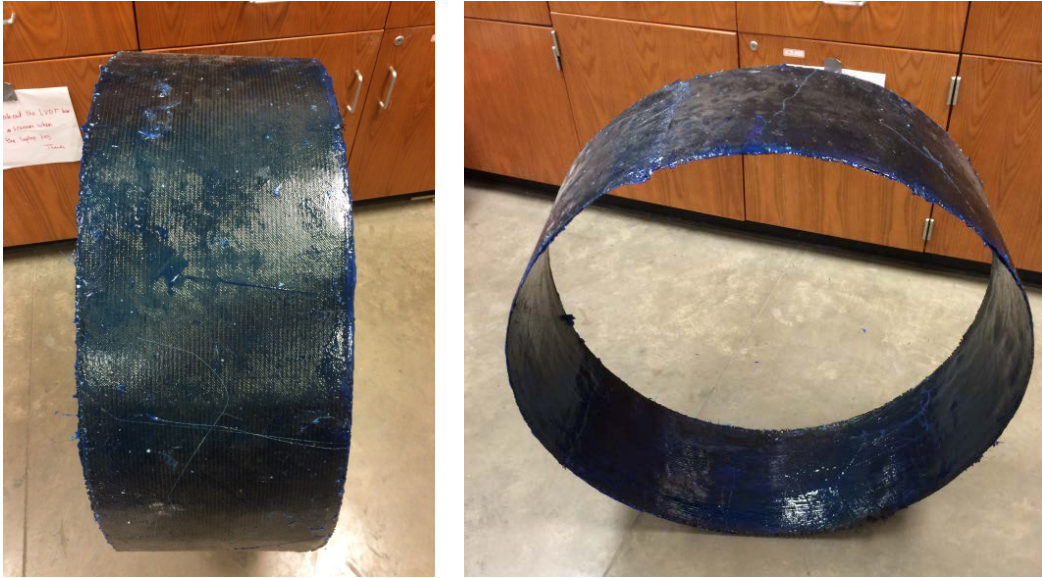


Figure 5-23 - Configuration of internal joint system



Figure 5-24 - 36-inch Styrofoam wrapped by the CFRP fabric sheet

The CFRP internal coupler was made by following the sequence shown below.

Manufacturing process of the CFRP coupler:

1. A film was wrapped around the Styrofoam to facilitate demolding after the epoxy resin hardened.
 2. The MasterBrace Saturant resin epoxy was applied to a film thickness of 5 mils, using a nap roller.
 3. The desired MasterBrace fabric was applied onto the saturant.
 4. After the first CFRP fabric sheet had hardened, the Styrofoam was pulled out of the CFRP sheet.
 5. A second layer of MasterBrace Saturant resin was applied inside the CFRP fabric, using a nap roller.
 6. A second layer of the CFRP sheet was applied onto the second layer of saturant resin epoxy.
 7. A third layer of MasterBrace saturant resin was applied inside the CFRP fabric, using a painting knife to force it down to encapsulate the saturant resin.
 8. A third layer of saturant resin was applied over the last CFRP fabric.
 9. The CFRP coupler was cured at ambient room temperature for 24 hours.
- Details of the manufacturing process are shown in the appendix.

5.2.2.1 Experimental Joint Shear Test

A joint shear test is a proof-of-design test used to evaluate the CFRP coupler's structural capability to support a shear force applied at the joints of pipes. The joint shear tests were performed in accordance with ASTM C497-16a (ASTM, 2016), with full-scale, different-sized thin-walled concrete pipes, ranging from 36 inches through 84 inches. All of the experimental joint shear tests were conducted at the Forterra Pipe and Precast plant in Grand Prairie, Texas. The CFRP internal coupler systems, with thicknesses ranging from 0.0625 inch through 0.375 inch, depending on the pipe diameter size, were used to assemble the concrete pipes. All of the joint shear tests were controlled by the shear force applied by a hydraulic cylinder and pump. The applied shear forces were compared to the shear strength requirement of the ASTM C497-16a specification. Geometrical details for all of the tested specimens are given in Table 5-2.



Figure 5-25 - Experimental joint shear test setup for CFRP internal coupler

5.2.2.2 Geometry and mechanical properties of specimens

The pipes used in this study were 48 inches long, with various inside diameters and corresponding wall thicknesses. ASTM C76 "*Standard Specification for Reinforced Concrete Culvert, Storm Drain, and Sewer Pipe*" prescribes design tables in terms of the diameter, wall thickness, compressive strength of the concrete, and the area of the circumferential reinforcement for Classes I to V. The diameters of concrete pipes range from 12 inches through 144 inches, and the thickness of the pipes is classified as Wall A, Wall B, or Wall C. The thickness of Wall A is equal to the inside diameter of pipe in inches, divided by 12. Wall B is 1 inch thicker than Wall A, and Wall C is $1\frac{3}{4}$ inches thicker than Wall A. In this study, Wall C concrete pipes were used. The wall thickness of the thin-walled concrete pipes was reduced as much as the reduced area of steel reinforcement. For example, the regular wall concrete pipe, which has a 36-inch inside diameter, has $4\frac{3}{4}$ inches of wall thickness according to ASTM C76. However, for thin-walled concrete pipes, the wall thickness is 56% of that, reduced by $2\frac{1}{4}$ inches. ASTM C76-14 limits the wall thickness to a minimum of $2\frac{1}{2}$ inches, because the circumferential reinforcement should be placed in protective concrete cover greater than 1 inch (ASTM, 2014). In addition, depending on the inside diameter of the pipe, either single or double circumferential steel reinforcements are embedded to resist flexural bending stress subjected to soil pressure on the concrete pipe.

Table 5-4 - Thin-walled concrete pipe design specifications

Inside diameter (in.)	Wall thickness (in.)	Area of steel reinforcement (in ² /linear ft.)	Length of pipe (in.)	Fiber dosage (lbs./yd ³)
36	2.25	0.17	48	8
48	2.50	0.24	48	8
54	2.75	0.29	48	8
72	4.50	0.49	48	8
84	4.875	0.64	48	8

5.2.2.3 Experimental setup and instrumentation

Figure 5-26 shows the experimental setup two concrete pipes on four cradles.

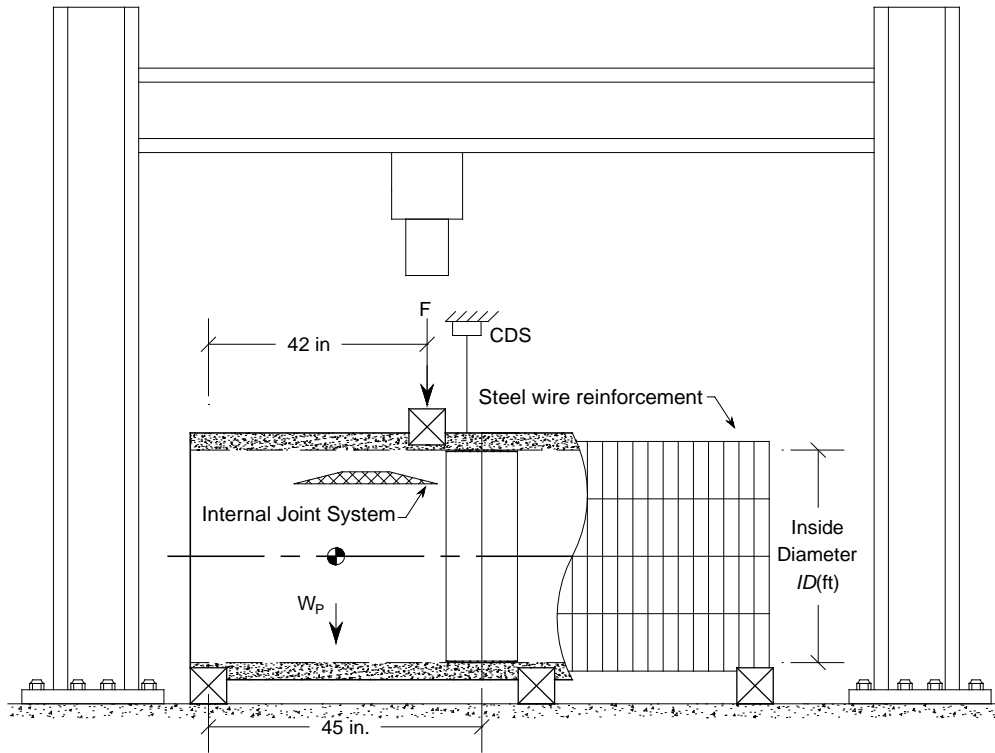


Figure 5-26 - Configuration of joint shear test on TW concrete pipe with the CFRP coupler

Two thin-walled concrete pipes were assembled by using the internal joint system. One pipe was fully supported by two timber cradles, which were placed 6 inches from the surface of the assembled concrete pipes. Another was supported by one timber cradle at the end of the pipe, suspended, and subjected to applied shear force. To apply shear force, a hydraulic cylinder was mounted on a $\frac{3}{4}$ inch steel plate, which was placed between the hydraulic cylinder and the wooden cradles. In addition, to acquire the applied shear force, a 50 kips load cell was placed between the hydraulic cylinder and the steel plate.

Two cable displacement sensors (CDS) were employed to measure the relative vertical displacement of the two concrete pipes. Additional four Linear Variable Differential Transformers (LVDTs) were used to measure horizontal movement of the TW concrete pipes at both ends of the pipes. All of the sensors were connected to a Data Acquisition (DAQ) system to collect data at a rate of one data point per second. Smartstrain, a commercial data acquisition software, was connected to the DAQ system and used to check the test status and data in real time.

Figure 5-27 shows a sequence of assembling concrete pipes with the CFRP internal coupler system.

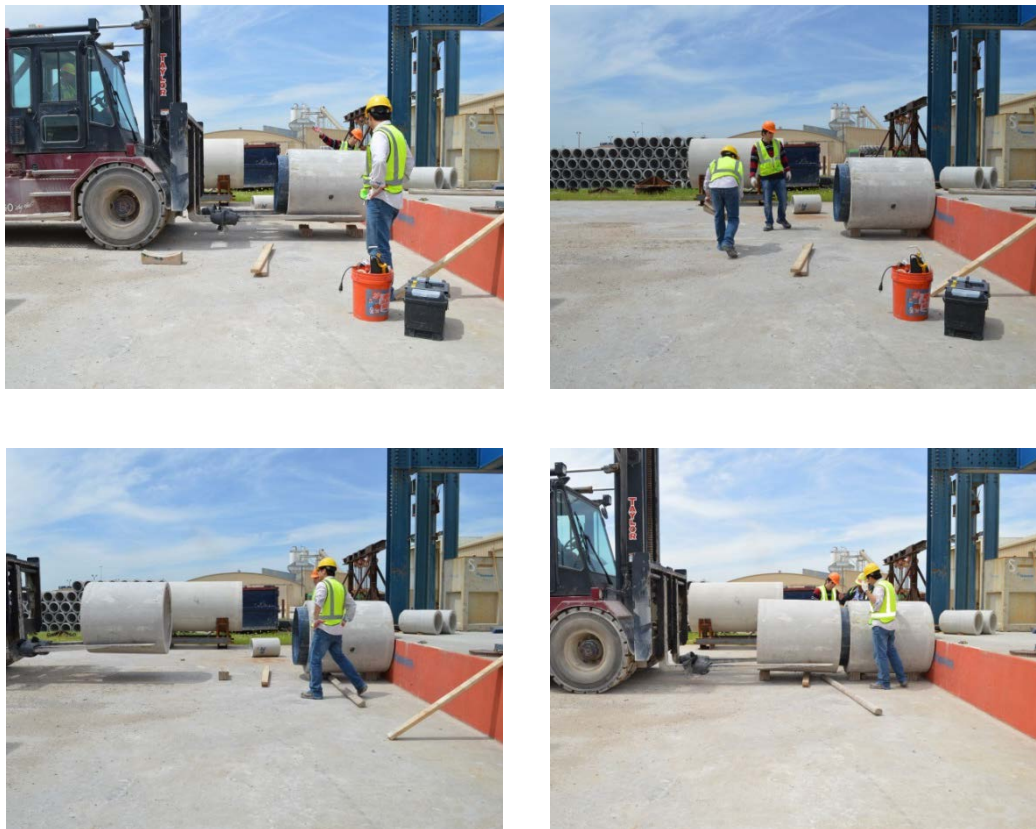


Figure 5-27 - Assembling concrete pipes with the CFRP coupler

Three strain gauges were installed along the circumferential center line, and three strain gauges were attached in two transverse directions on top of the CFRP couplers on pipes with inside diameters of from 48 inches to 84 inches, to measure the strain values of the coupler system, up to failure, as shown in Fig 5-18.

5.2.2.4 Experimental results of CFRP internal coupler

A comparison of the shear strength required by ASTM C497-16a and the ultimate peak load determined by the experimental test shows that the pre-fabricated CFRP internal coupler systems are suitable as an alternative joint system for the TW concrete pipes.

Depending on the thickness of the coupler, failure mode should be expected on either the CFRP coupler or the concrete pipe. From the full-scale joint shear tests, idealized mid-thicknesses of CFRP couplers show an average of 26.72% higher shear strength than that required by ASTM C497-16a. The idealized mid-thicknesses on different diameter concrete pipes (36, 48, 54, 72, and 84 inches) are 0.125, 0.1875, 0.25, 0.375, and 0.375 inch. All of the tested TW concrete pipes were 12 inches wide.

The CFRP coupler failures occurred in couplers with thicknesses of 0.0625 through 0.375 inch, as shown in Figs. 5-29 (a) to 5-35 (a). The joint system of the those couplers transferred fully-shear force onto the thin walled concrete pipe.

The required shear force on different inside diameters of TW concrete pipes are given in Table. 5-5 and were derived by employing Eq. 5.1 from ASTM C497-16a.

Table 5-5 - Required shear force computed by ASTM C497-16a

Inside diameter (in.)	Required shear force (lbf)
36	13,000
48	17,500
54	20,000
72	26,000
84	31,000

All of the test results are given in Table 5-6. Specimen names were followed as in Table 5-6. The first character of “RCP” represents the type of concrete pipe, and the second and third digits of “36-0.0625” represent the inside diameter of the concrete pipe and the thickness of the CFRP coupler in US units.

Table 5-6 - Summary of joint shear test results

Specimen	P_{ult} (kips)	$P_{req'd}$ (kips)	Difference (%)	Failed/ Passed
RCP-36-0.25	30.0	13.0	130.77	Passed
TW-36-0.0625	7.1	13.0	-45.38	Failed
TW-36-0.125	16.8	13.0	29.23	Passed
TW-36-0.25	20.1	13.0	54.62	Passed
TW-48-0.125	12.6	17.0	-25.88	Failed
TW-48-0.1875	21.5	17.0	26.47	Passed
TW-54-0.1875	20.9	20.0	4.50	Passed
TW-54-0.25	25.3	20.0	26.50	Passed
TW-72-0.25	27.6	26.0	6.15	Passed
TW72-0.375	34.5	26.0	32.69	Passed
TW-84-0.375	36.8	31.0	18.71	Passed

Internal joint systems of 36-inch TW concrete pipes with 0.0625, 0.125, and 0.25 inch coupler thickness failed at 7.1, 16.8, and 20.2 kips, respectively. The RCP pipe had 30.0 kips of the ultimate shear force for 0.25 inch thickness of coupler, compared to the required shear strength by ASTM C497.

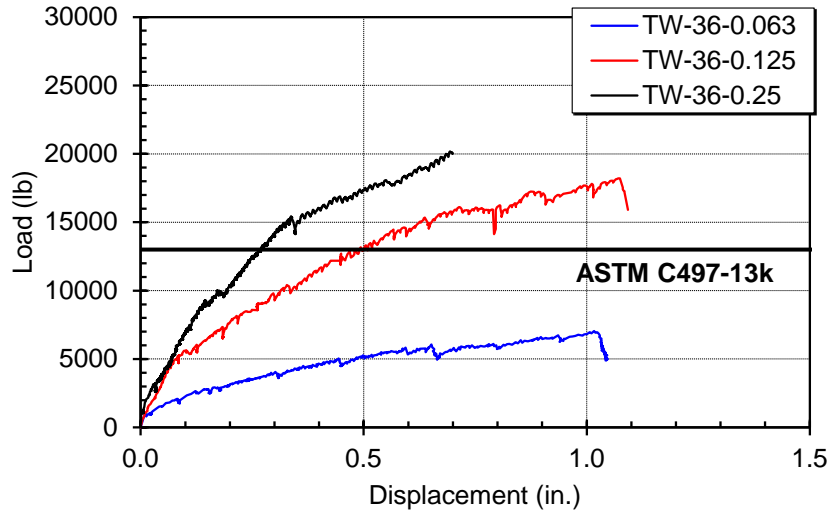


Figure 5-28 - Joint shear test results on 36-inch inside diameter of TW pipes

The ultimate shear forces were 29.23% and 54.62% higher than the required shear strength for 0.125 and 0.25 inch thick couplers, which means that the specimens of the internal joint systems with the CFRP coupler satisfied the ASTM C497-16a requirement for the pipe joint. Furthermore, in case of the 36-inch RCP pipe, the ultimate shear force showed more than twice the required shear force. For the mid-thickness of the 0.0625 inch CFRP coupler system, the ultimate shear force reached 7.1 kips, which is 45.38% less than the required shear strength of the ASTM C497-16a specification. At the ultimate shear force of 7.1 kips, a sudden collapse of the CFRP internal coupler was observed at the crown as a three-hinge collapse failure mode, as shown in Fig. 5-29 (a). Cracks more than 0.01 inch wide were observed on the RCP and TW concrete pipes

assembled with the mid-thickness of 0.25 inch CFRP coupler, as shown in Fig. 5-29 (b). A crack width of 0.01 inch on the surface of the concrete pipe is service limitation. At the ultimate shear force of 20.1 and 30.0 kips on TW pipes and RCPs, crack development at the invert of suspended concrete pipes exceeded 0.01 inch. Due to this service limitation, the joint shear tests were terminated.

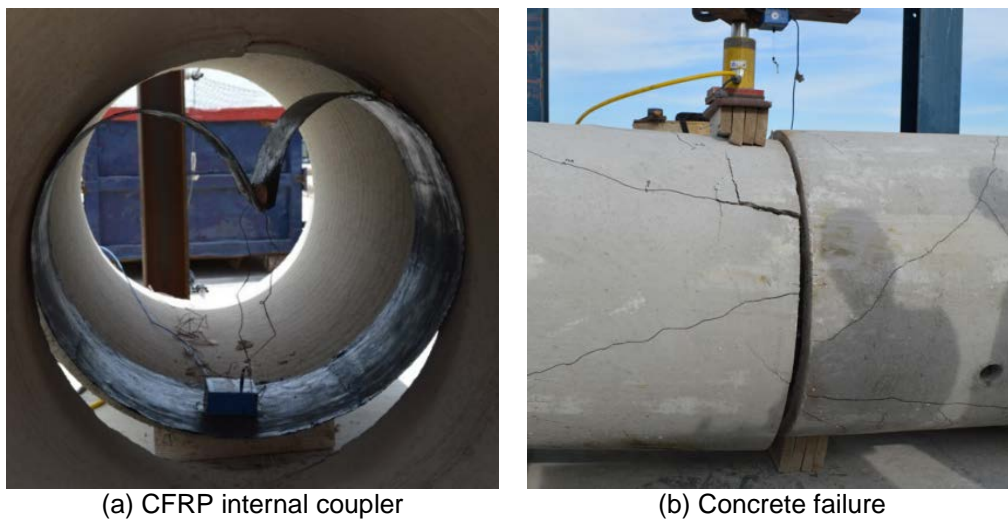


Figure 5-29 - Failure mode of joint shear test

During the test, initial cracks were shown on the invert and crown-supported end side. The cracks were wider at the invert and crown, causing the mid-height exterior substrate to develop cracks. More cracks occurred around the major cracks on the crown, invert, and at both springlines.

A similar crack pattern was observed on RCP pipes. The initial cracks started at the invert and crown simultaneously, then propagated up to the assembled joint surface. Cracks were shown on both sides of the springlines, as shown in Fig. 5-33 (b).



Figure 5-30 - Propagated crack pattern on springline of pipes at 24 kips for 36-inch RCP

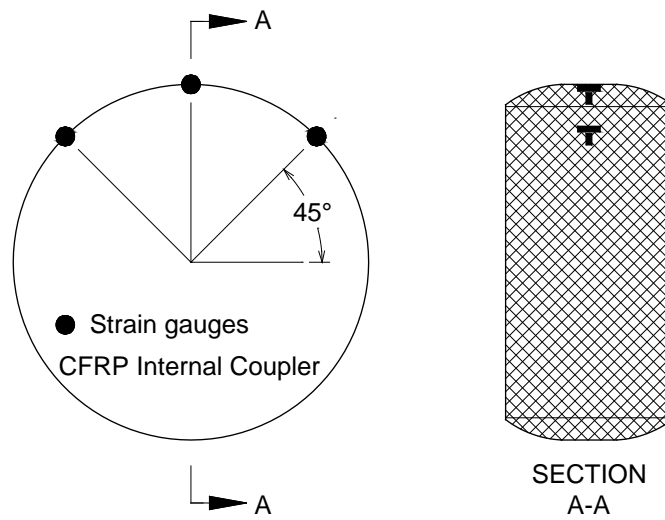


Figure 5-31 - Strain gauge installation of the CFRP internal coupler

RCP-36-0.25

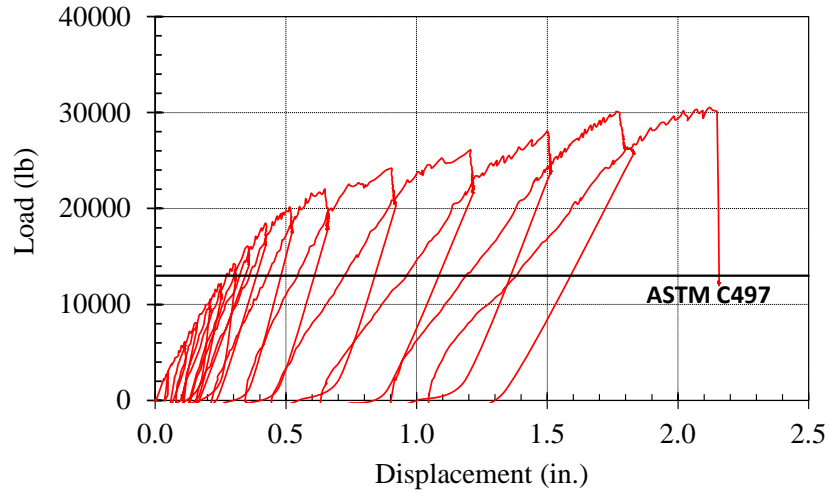


Figure 5-32 - Load vs. displacement curve of RCP-36-0.25

Figure 5-32 shows the worst case scenario for load vs. vertical deflection response under pseudo-static loading. The pseudo-static loading was applied with 2 kips of the incremental loading. After 18 kips, stiffness degradation occurred. As shown in Fig. 5-33 (b), the cracking failure was observed on the springline. The local buckling was shown on the CFRP coupler due to the changed geometry of the CFRP coupler at the ultimate shear force of 30.0 kips, as shown in Fig. 5-33 (a).



Figure 5-33 - Local buckling of CFRP coupler and crack pattern on springline

TW-36-0.0625

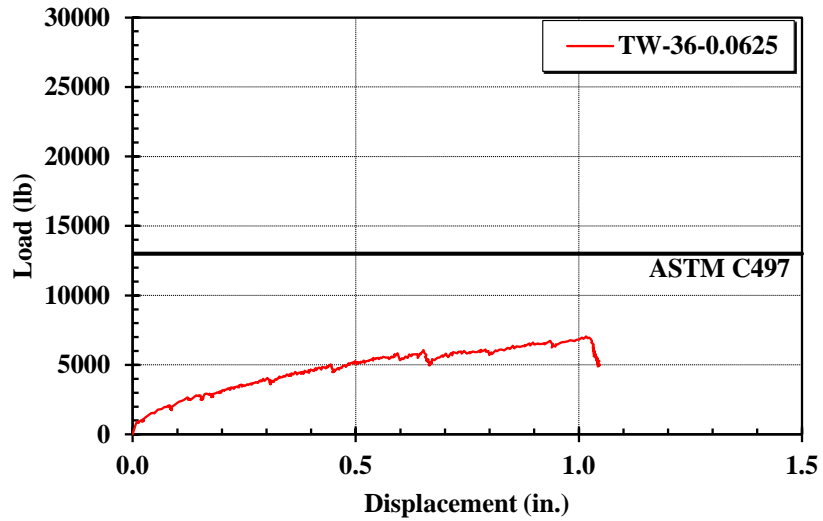


Figure 5-34 - Shear force vs. vertical deflection response of TW-36-0.0625

As shown in Figs. 5-34 and 5-35 (a), the coupler thickness of 0.0625-inch was not sufficient for use as the joint system. The CFRP coupler failure was observed at the top before reaching the shear strength required by ASTM C497-16a. When the CFRP coupler failed, no damage (crack) was visible on either the outside or the inside of the concrete pipes, as shown in Fig. 5-35 (b).



Figure 5-35 - CFRP coupler of 0.0625 inch failed; no visible damage on concrete pipe

TW-36-0.125

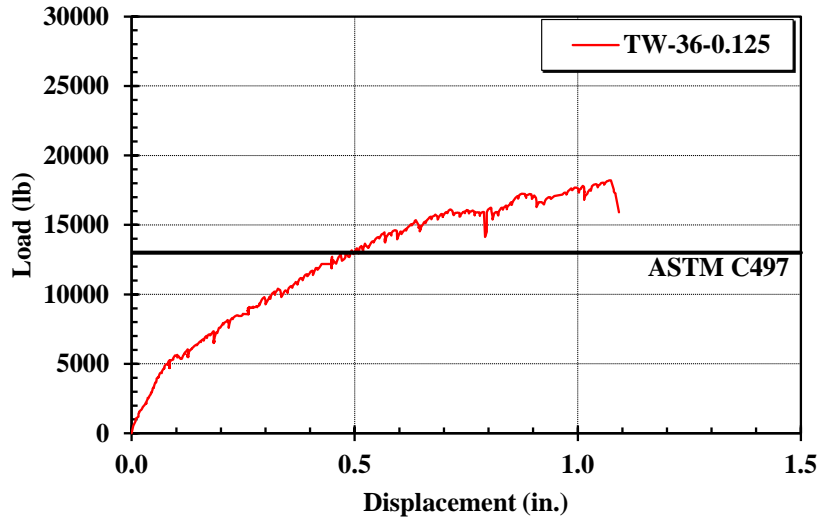


Figure 5-36 - Shear force vs. vertical deflection response of TW-36-0.125

Figure 5-36 shows shear force and vertical deflection response of the TW-36-0.125 specimen. The ultimate shear force was 17.5 kips, compared to the required shear strength of 13.0 kip for a 36-inch TW concrete pipe. At 16 kips, local buckling was observed along the CFRP coupler at the top of the CFRP coupler, and was propagated to the CFRP coupler failure at the ultimate shear force of 17.2 kips. Governed failure of this system occurred at the top of the CFRP coupler, as shown in Fig. 5-37 (a).



Figure 5-37 - Internal joint system failed for TW-36-0.125

TW-48-0.125

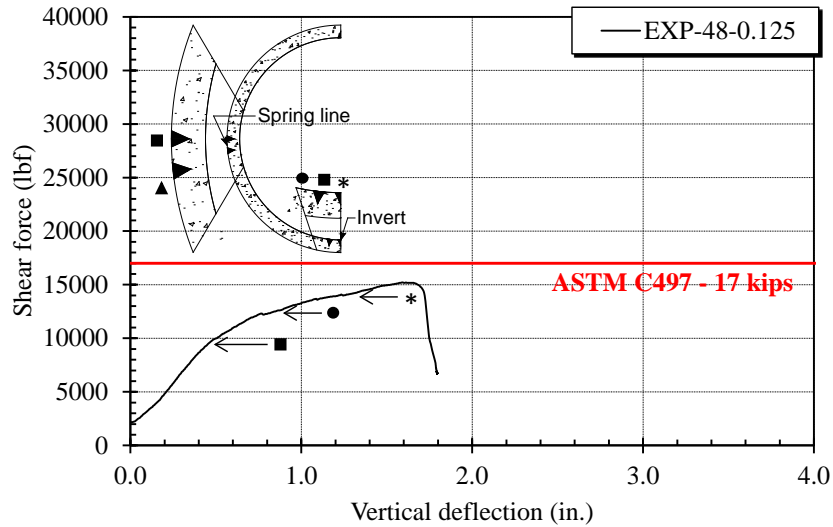


Figure 5-38 - Shear force vs. vertical deflection response of TW-48-0.125

Figure 5-38 shows shear force vs. vertical deflection response obtained by the joint shear test. The CFRP internal coupler with a mid-thickness of 0.125 inch showed 18% less shear strength than the 17 kips required by the ASTM C497-16a specification.

The initial cracks were observed on the invert and crown at 8.5 kips, on the inside of the TW concrete pipes subjected to shear force, as shown in a rectangular shape of the crack configuration in Fig. 5-38. Simultaneously, hairline cracks were on the springlines on the outside of TW concrete pipe at 12.6 kips, as shown by the filled circular shape in Fig. 5-38. Those cracks propagated up to the assemblage region. The final buckling failure occurred at the bottom of the CFRP internal coupler, at the ultimate shear force of 15 kips, as shown in Fig. 5-39 (a). The ultimate shear force was 12% less than the required shear strength, which resulted in a mid-thickness greater than the 0.125 inch required for the 48-inch concrete pipes.



Figure 5-39 - Compressive failure on concrete pipe for TW-36-0.25

TW-48-0.1875

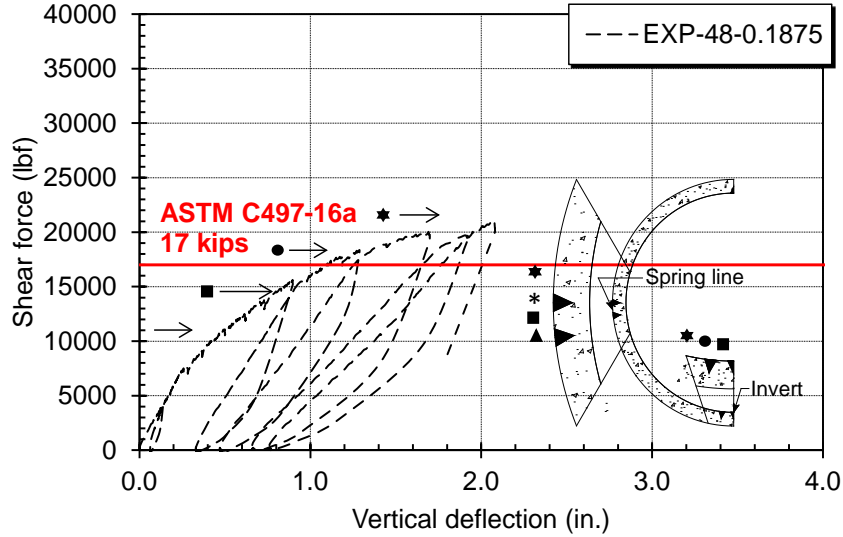


Figure 5-40 - Shear force vs. vertical deflection response of TW-48-0.1875

As shown in Fig. 5-40, the ultimate shear force for a 0.1875 inch of the mid-thickness CFRP coupler exceeded 17 kips of the required shear strength recommended by ASTM C497-16a. As shown in Fig. 5-43 (a), the collapse at the crown of the CFRP internal coupler occurred at the ultimate shear force of 21 kips. From these results, it can be concluded that the 0.1875 inch coupler thickness fully transmitted the shear force applied to the joint system on the 48-inch TW concrete pipes. As shown in the crack configuration in Fig. 5-43, at 11 kips, initial hairline cracks were observed at the invert and crown on the inside of the TW concrete pipes, as shown in a star-shaped marker in Fig. 5-43. The observed cracks propagated to the assemblage of the concrete pipes. At the ultimate shear force of 21 kips, minor hairline cracks were observed surrounding the four major cracks, as depicted by the 7-point star shaped marker.

TW-54-0.1875

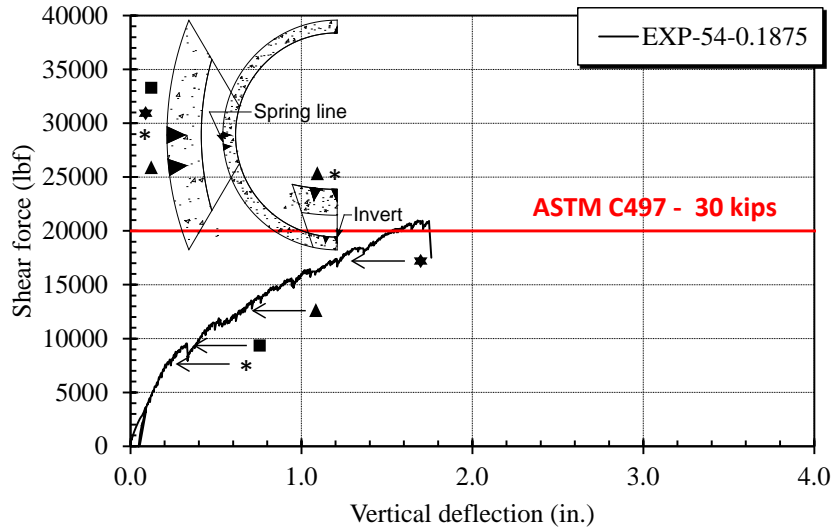


Figure 5-41 - Shear force vs. vertical displacement response of TW-54-0.1875

As shown in Fig. 5-41, the ultimate shear force for the 0.1875-inch-thick coupler slightly exceeded the 20 kips required by ASTM C497-16a, and was 5% higher than the shear strength. As shown in Fig. 5-44 (a), the collapse at the crown of the CFRP internal coupler occurred at the ultimate shear force of 20 kips. The coupler thickness of 0.1875 inch was not sufficient to transmit shear force on a 54-inch TW pipe. Figure 5-41 shows the crack developments on the corresponding shear forces of 7 kip, 9 kip, 12.3 kip, 17.6 kip, and ultimate shear force of 21 kips, respectively. The initial hairline cracks were observed at the invert and crown on the inside of the TW concrete pipes, as shown in a star-shaped marker in Fig. 5-41. The propagated crack development in the invert and crown, the minor hairline cracks were observed surrounding the four major cracks, as depicted by the triangle and 7-point star shaped markers in Fig. 5-41.

TW-54-0.25

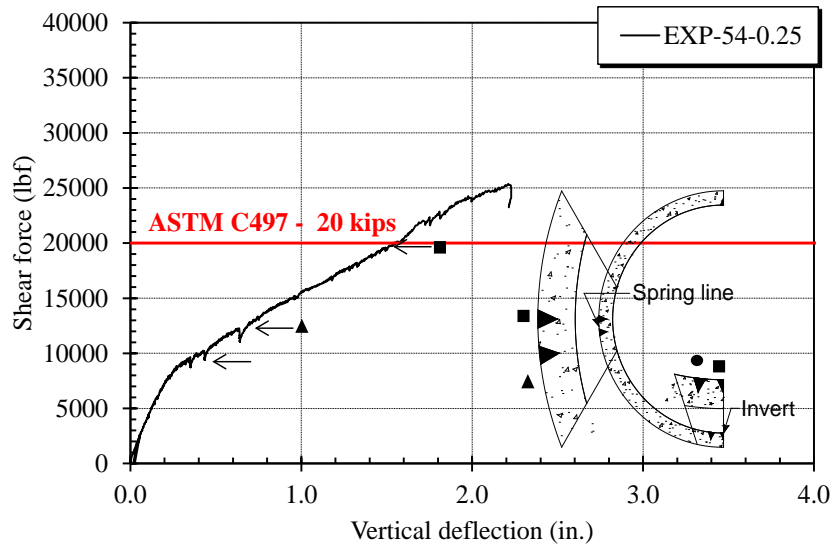


Figure 5-42 - Shear force vs. vertical displacement response of TW-54-0.25

As shown in Fig. 5-42, the ultimate shear force of the 0.25 inch thick CFRP coupler exceeded the required shear strength recommended by ASTM C497-16a of 20 kips by 25%. As shown in Fig. 5-45, the collapse at the crown of the CFRP internal coupler occurred at the ultimate shear force of 21 kips. From these results, it can be concluded that a coupler thickness of 0.25 inch transmits shear force applied to the joint system of the 54-inch TW concrete pipe. The crack developments on the 54-inch TW concrete pipe were shown in similar patterns on the 48-inch concrete pipes. The first cracks were observed at the invert and crown of the inside TW concrete pipes, as shown in Fig. 5-45 (b), with the first cracks wider. The second cracks were shown on the outside of the TW concrete pipes.



Figure 5-43 - Collapse of the CFRP internal coupler for TW-48-0.1875 specimen



Figure 5-44 - Collapse of the CFRP internal coupler for TW-54-0.1875 specimen



Figure 5-45 - Collapse of the CFRP internal coupler for TW-54-0.25 specimen

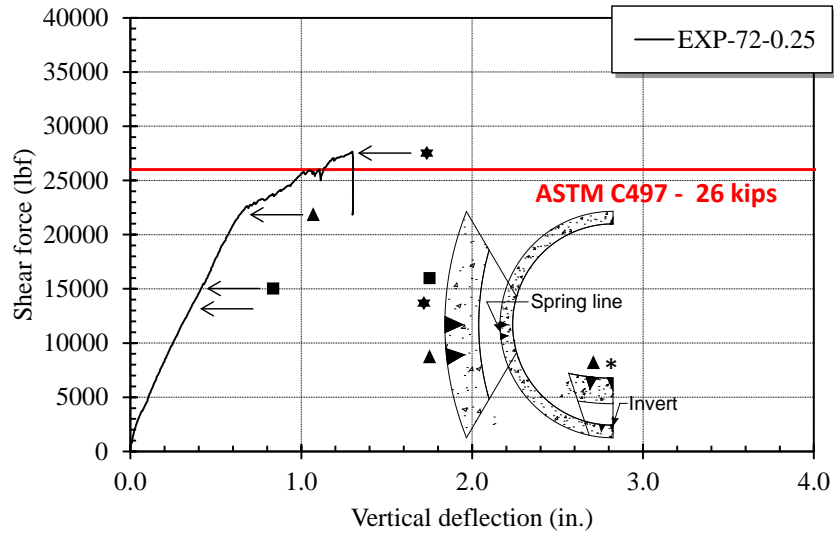


Figure 5-46 - Shear force vs. vertical displacement response of TW-72-0.25

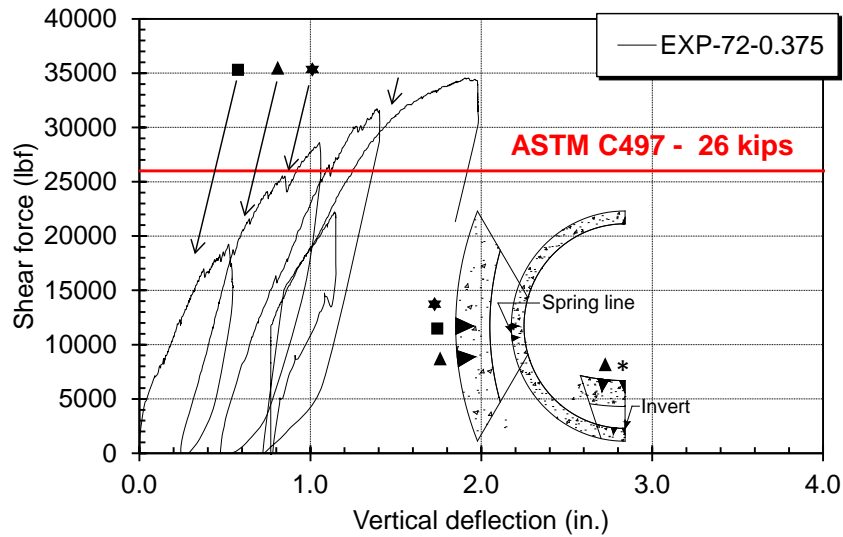


Figure 5-47 - Shear force vs. vertical displacement response of TW-72-0.375

Figures 5-46 and 5-47 show the global behavior responses of the shear force and corresponding vertical deflections on TW-72-0.25 and TW-72-0.375 joint shear test specimens. In the both specimens, the CFRP couplers failed at the ultimate shear forces of 27.5 kips and 34.7 kips, respectively, compared to the shear strength of 26 kips.

The mid-thickness CFRP couplers of 0.25 and 0.375 inches showed 10% and 32.6% higher shear force, respectively, than the shear strength required by ASTM C497-16a. In addition to the global behavior of the shear force plots against the corresponding vertical deflections, crack patterns observed on the 48 and 54-inch concrete pipes were also shown on the 72-inch TW concrete pipes.

TW-84-0.375

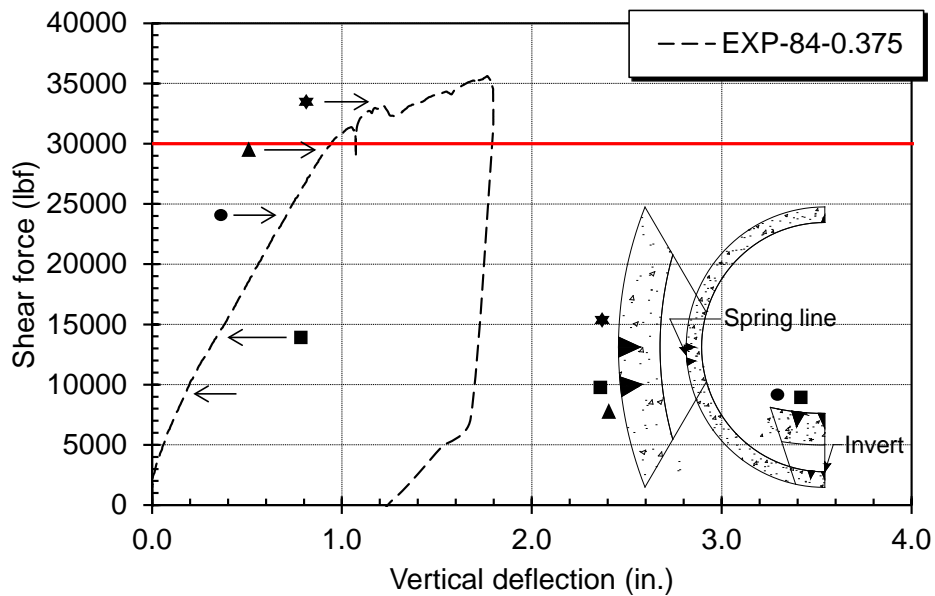


Figure 5-48 - Shear force vs. vertical displacement response of TW-84-0.375

Figure 5-48 depicts the shear force plot against the corresponding vertical deflection at the CFRP internal coupler. It shows an ultimate shear force of 35.5 kips, compared to the required shear strength of 30 kips. The mid-thickness of 0.375 inch CFRP internal coupler can transmit 16.7% higher shear force than the required shear strength. At the ultimate shear force, the diagonal crack widths at the springline exceeded a service crack width limitation of 0.01 from ASTM C76-16, as shown in Fig. 5-49 (b).



Figure 5-49 - Collapse of the CFRP internal coupler for TW-72-0.25 specimen



Figure 5-50 - Collapse of the CFRP internal coupler for TW-72-0.375 specimen



Figure 5-51 - Collapse of the CFRP internal coupler for TW-84-0.375 specimen

Shear force plots against the strain values on 48, 54, 72, and 84-inch concrete pipes.

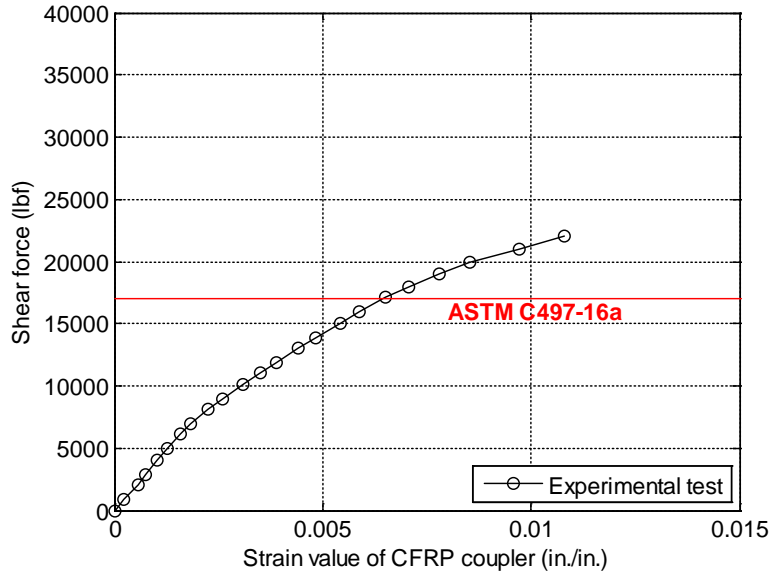


Figure 5-52 - Strain value versus shear force on the TW-48-0.25 specimen

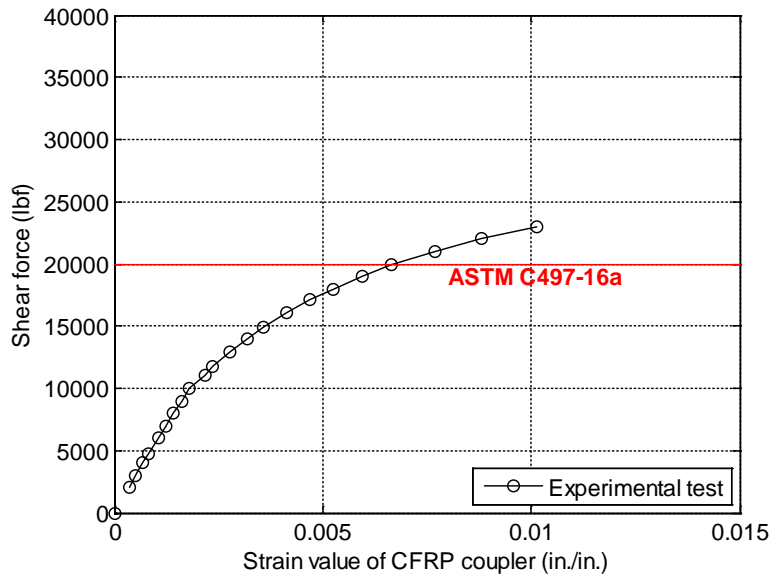


Figure 5-53 - Strain value versus shear force on the TW-54-0.25 specimen

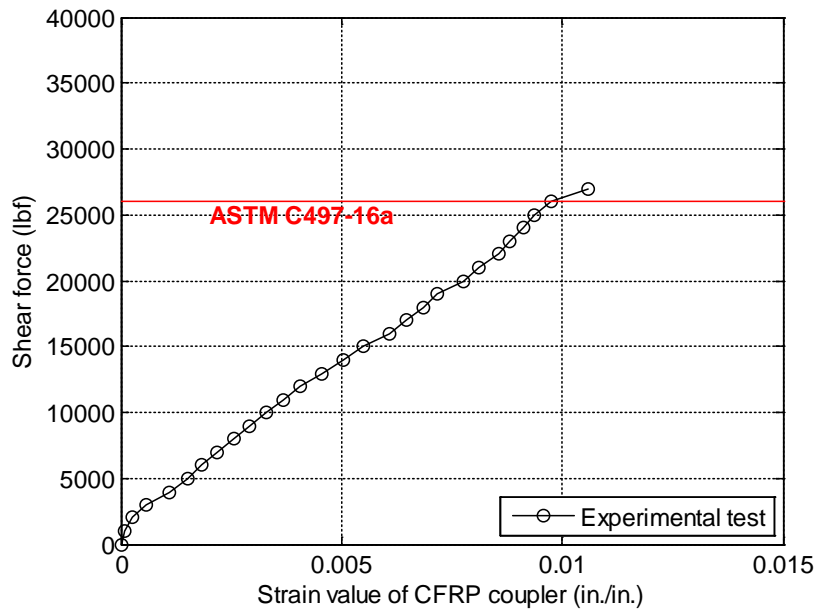


Figure 5-54 - Strain value versus shear force on the TW-72-0.25 specimen

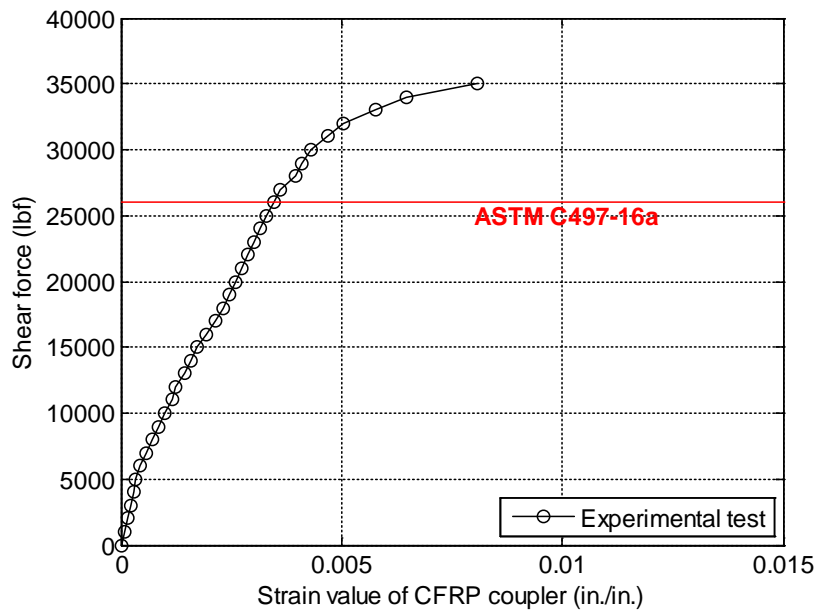


Figure 5-55 - Strain value versus shear force on the TW-72-0.375 specimen

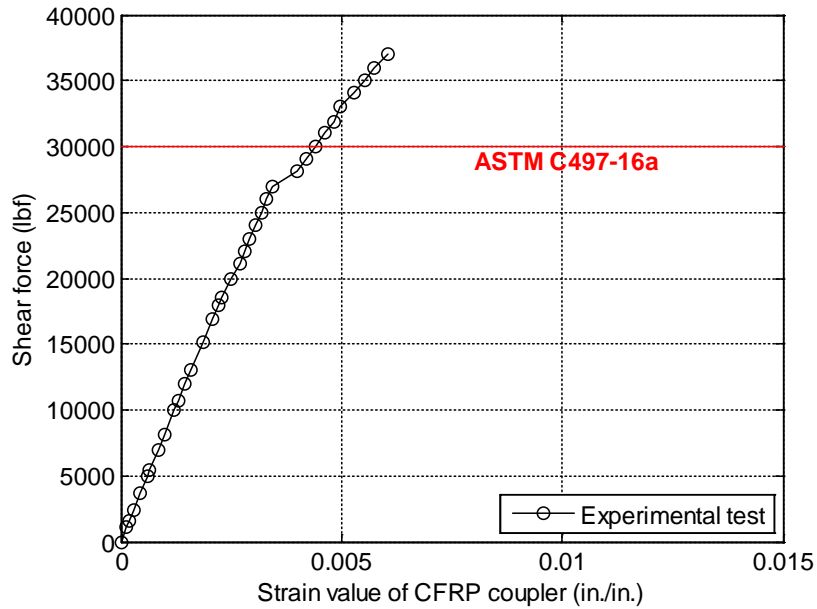


Figure 5-56 - Strain value versus shear force on the TW-84-0.375 specimen

Figures 5-52 through 5-56 indicate the ultimate shear force vs. strain values at the CFRP internal couplers on pipes with inside diameters of 48, 54, and 72 inches. As seen in Figs 5.52 through 5-56, the strain values at the ultimate shear forces reached the ultimate strain value of 0.01 in./in. At the 0.01 in./in. strain value, rupture of the inside CFRP internal couplers (48-0.125, 54-0.25, and 72-0.25 specimens) occurred at the crown (top), but no rupture or buckling failure mode was observed on the 72-0.375 and 84-0.375 specimens.

The strain values at the ultimate shear force of the 72-inch and 84-inch inside diameter of concrete pipes with 0.375 inch thicknesses were equal to 0.008 in./in. and 0.062 in./in., respectively. Their strain values were less than 0.01 in. /in. of the failure strain value.

5.2.3 Hydrostatic test of CFRP coupler system for concrete pipe



Figure 5-57 - Hydrostatic test setup

A hydrostatic pressure test was performed in accordance with ASTM C497-16a, Section 8. The assembled concrete pipes were filled with water to exclude air. A standardized pressure gage and pressure transducer sensor were installed to acquire time-based pressure data, as shown in Fig. 5-57. The joint assembly was subjected to the required hydrostatic pressure of 13 psi for 20 minutes, without leakage. Two steel plates blocked the assembled concrete pipe with axial force to create the internal water pressure.

5.2.3.1 Hydrostatic test setup

For a 36-inch inside diameter concrete pipe, as for any other RCP assembly, a rubber gasket was installed between the inside concrete pipe and the CFRP coupler to prevent leakage at the joint. However, when the pipes were filled with water, leakage was observed at the joint, as shown in Fig. 5-60. The geometric specifications of the used concrete pipes are described below. The schematic of the hydrostatic water pressure test, employed to investigate the leakage at the CFRP internal coupler, is shown in Fig. 5-58.

- 36inch concrete pipe with 8 ft. length
- 0.125 inch CFRP coupler joint system
- 12 inch CFRP internal coupler width

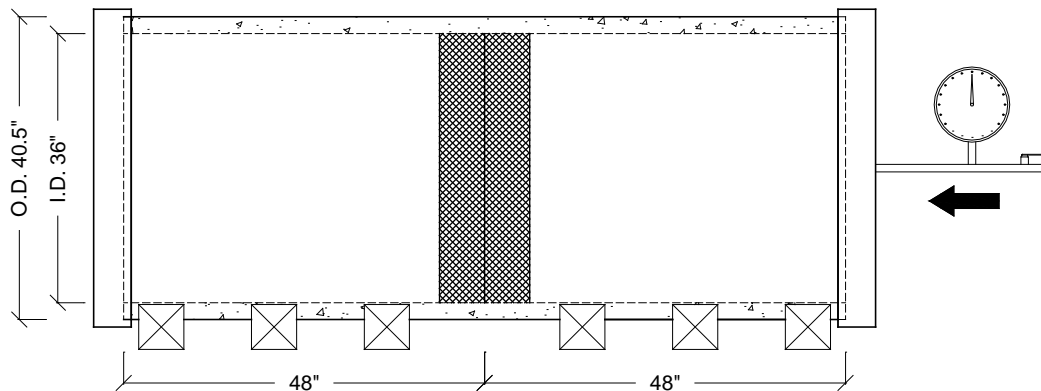


Figure 5-58 - Hydrostatic test setup configuration



Figure 5-59 - Pressure gage and sensor

Table 5-7 - Summary of trials to prevent leakages

Num.	Treatment	Pass/Fail	Reason
1	Rubber gasket	Failed	Leakage at joint
2	Rubber gasket + sealant foam at end of coupler	Failed	Leakage at joint
3	Rubber gasket + sealant foam + caulking	Failed	Leakage from end of pipes
4	Rubber gasket + sealant foam + caulking + rubber pads	Passed	

Because the fitting between the inside of the concrete pipe and the coupler was not perfect, in the second trial, as depicted in Table 5-7, expanding sealant foam was used to fill in the area between the coupler and the inside of the concrete pipe, shown in Fig. 5-61 (a). It was expected that this would make the joint watertight; however, when the pipes were more than half-filled with water, leakages occurred at the joint and wall of the concrete pipe, as shown in Fig. 5-61 (b). During the third trial, urethane caulking was used to provide additional sealant on ends of the sealant foams.



(a) The 1st trial (failed) (b) The 2nd trial (failed) (c) The 3rd trial (Success)

Figure 5-60 - Leakage at the assembled joint



(a) The 2nd trial

(b) The 3rd trial

Figure 5-61 - Assembled CFRP coupler with sealant

5.2.3.2 Hydrostatic test result

As shown in Fig. 5-62, water pressure was maintained at 13 psi for 20 minutes, which met the requirement of ASTM C497-16a. However, leakages were observed, as shown in Figs. 5-63 through 5-65. The first leakage occurred on the wall, on the left side of the concrete pipe, at water pressure of 12 psi, as shown in Fig. 5-63. Water pressure was maintained at 13 psi until the second leakage was observed, shown in Fig. 5-64. The pressure dropped slightly, but recovered to 13 psi. No leakage was observed at the CFRP internal coupler during the 20-minute hydrostatic test.

The observed leakages along the wall of the concrete pipe, shown in Fig. 5-65, were attributed to the synthetic fibers not being thoroughly mixed into the concrete used for the pipes, revealing that permeability needs to be considered in the construction of synthetic-fiber-reinforced concrete pipes.

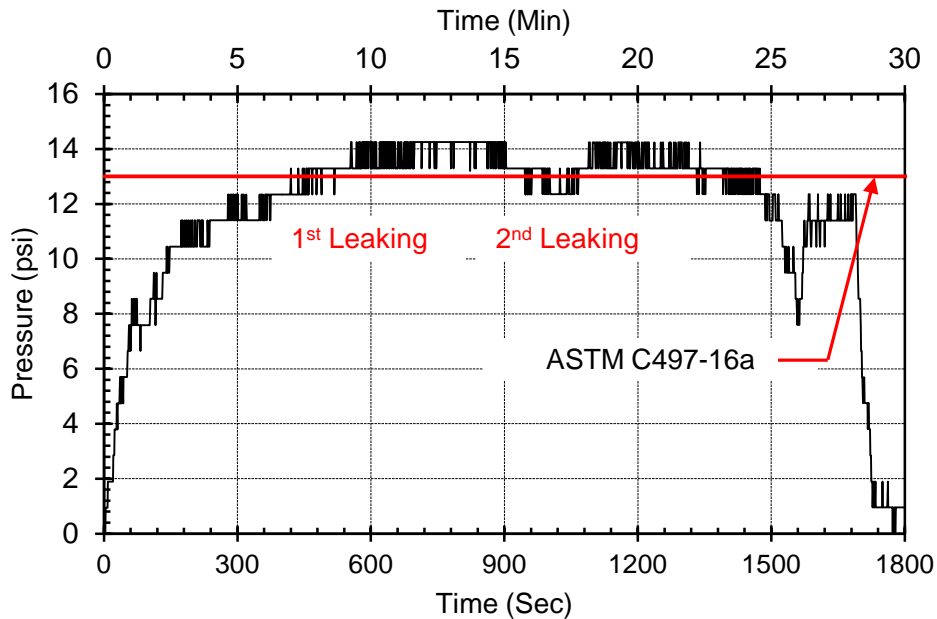


Figure 5-62 - Pressure vs. time curve for 20 minutes



Figure 5-63 - The 1st leakage on the concrete pipe wall



Figure 5-64 - The 2nd leakage on the mid-wall of the concrete pipe



Figure 5-65 - Leakage on wall of the left concrete pipe

5.3 Conclusion

Joint shear tests on externally bonded CFRP sheets and CFRP internal couplers were conducted in accordance with the ASTM C497-16a Sec. 13 to investigate the structural capacity of the joint systems developed utilizing carbon-fiber-reinforced-polymer (CFRP) fabric sheets.

The externally-bonded CFRP fabric sheet was the first proposed system for assembling two concrete pipes. Based on the results from the joint shear tests, it is an adequate alternative to the bell and spigot with rubber gasket for semi-rigid concrete pipes. The joint shear tests on the 36-inch inside diameter concrete pipes revealed final failure mode at the interface between the concrete substrate and the CFRP sheets. On the two concrete pipes assembled by the externally-bonded CFRP sheet, Initial flexural cracks appeared on the crown and inverts of the concrete pipe subjected to shear force, and propagated along the length of the concrete pipe up to the assembled line of the two concrete pipes. All of the external-wrapping joint systems on pipe specimens (36-inch and 60-inch) exceeded the shear strength of 13 kips and 21 kips, respectively, required by ASTM C497-16a. The CFRP sheets with widths of 3 inches to 6 inches resulted in 27.7% higher initial stiffness and 10.2% increased ultimate load than the displacement curves for joint systems of 36-inch pipes. Curing time of a saturant chemical epoxy was investigated to enhance serviceability in ambient temperature ranging 75 Fahrenheit degree to 100 Fahrenheit degree. By reducing curing time from 24 hours to 3 hours, cure behaviors of the saturant epoxy were checked. As results of the curing behavior, the saturant epoxy was not hardened, which indicates that the saturant epoxy chemical requires at least 3 hours to harden.

The CFRP internal coupler was the second system developed, and consisted of stacking multiple layers of CFRP sheets in balanced and symmetric sequences. A total of 12 full-scale joint shear tests were performed on concrete pipes with 36-inch through 84-inch inside diameters and with CFRP internal couplers with different mid-thicknesses. From the joint shear tests, the ultimate shear forces on 36 in., 48 in., 72 in., and 84-inch concrete pipes with corresponding CFRP internal coupler thicknesses of 0.125 in, 0.1875 in, 0.375 in, and 0.375 inch showed an average of 20.5 % higher shear strength than required by the ASTM C497-16a specification. Crack patterns similar to those of the external CFRP wrapping system were shown on the concrete pipes. At the ultimate shear forces, three-hinge plastic collapse failure modes were observed on the CFRP coupler, with corresponding strain values of 0.01 in. /in at positive and negative 45 degrees to y-axis of the top. The water tightness test, administered in accordance with ASTM C497 16a, showed no leakage on the assembled concrete pipe or CFRP coupler under 13 psi of water pressure for 20 minutes.

Chapter 6 Parameter Study

Based on the developed 3-D finite element models in Chapter 5, a parametric study was conducted to investigate the sensitivity of the solution to the parameters, and to establish a design equation for the internal CFRP coupler system with the variables shown in Fig. 6-1.

Figure 6-1 is a flow chart of the parametric study in terms of three parameters: (1) The CFRP coupler width; (2) the CFRP coupler mid-thickness; and (3) the pipe diameter.

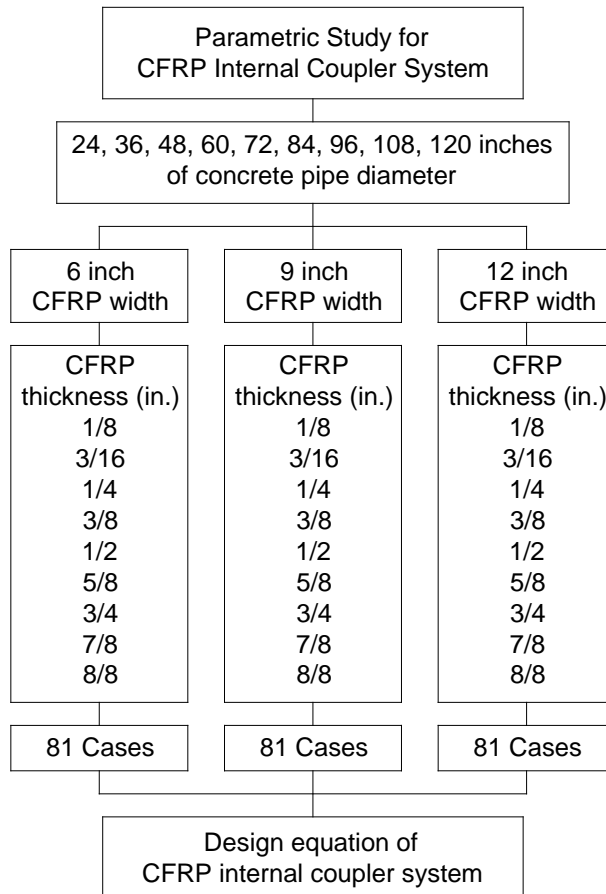


Figure 6-1 - Flow chart of parametric cases for CFRP coupler

The parametric study was conducted by following several steps, as shown in Fig. 6 -2. This chapter has three parts: (1) pre-process, (2) analytical solution, and (3) post-process.

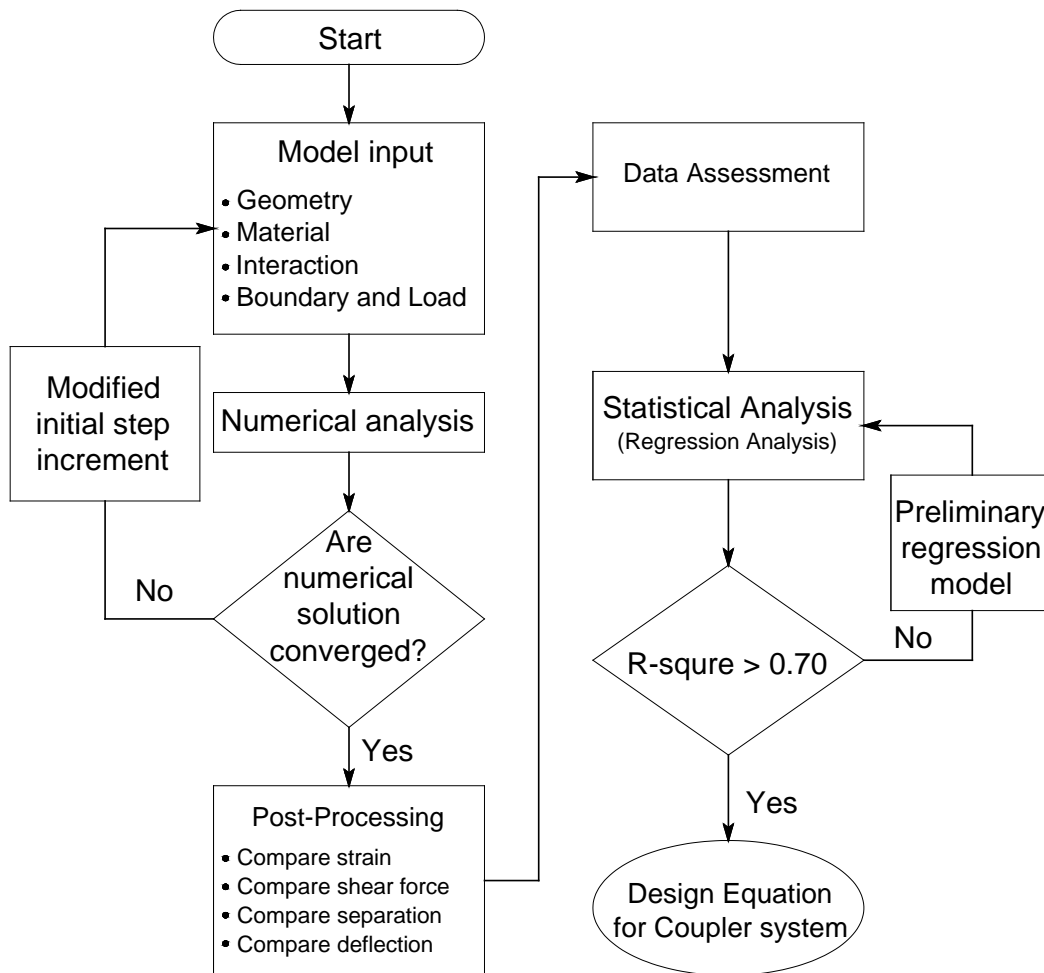


Figure 6-2 - Parameter study flow chart

6.1 Pre-processor

The pre-processing step involves building 3D finite element models based on analysis-type procedures, element types, material behaviors, loading conditions, and boundary conditions. At the final step of the pre-processing stage, the numerical model is complete, which creates an input file.

This pre-processing stages were defined by MATLAB, a multi-paradigm numerical computing environment and fourth-generation programming language developed by MathWorks, Corp. Input variables are summarized in Table 6-1. Building the numerical model manually requires several steps, which are time consuming. However, utilizing the pre-processing steps saves time and reduces computational resources from the ram process rather than utilizing Graphic User Interface (GUI) from the ABAQUS commercial numerical analysis program.

Table 6-1 - Input variables for building models

No.	Input variable	Description
1	ID	Inside diameter of concrete pipe, in.
2	t_{pipe}	Pipe wall thickness, in.
3	w_{coupler}	Width of CFRP coupler system, in.
4	t_{coupler}	Mid-thickness of CFRP coupler system, in.

The input files in python format were generated as an output of the pre-processing step. The pre-processing script was written in sequences of the following modules:

1. Part module: Each instant part was sketched in a three-dimensional profile.
2. Property: Material constitutive laws of all different parts and sectional properties were pre-assigned.
3. Assembly: All instant parts assigned material and sectional properties were assembled, and surfaces and sets were pre-defined to be used to extract specific stress, strain values, and deflections.
4. Step: Newton-Rapson's analysis was assigned. Output requests were pre-defined for post-analysis.
5. Interaction: Mechanical interactions between regions of a model or its surroundings, analysis constraints between regions of a model, and connectors between two parts of a model or ground were defined.
6. Load module: Included definitions of loads, boundary conditions, predefined fields, and load cases.
7. Mesh module: Contained generating meshes on parts and assemblies by assigning mesh attributes such as seeds, mesh techniques, mesh algorithm, and element types.
8. Job module: After completing all of the tasks above to create the model, such as defining the geometry of the model, assigning section properties, and defining interaction contact properties, the model was analyzed in this job module.
9. Visualization module: Provided graphical display of the analyzed models and results from the current model databases or output database.

6.2 Post-processing

The post-process step involved the extraction of data from 243 finite element models. The post-process step also wrote python scripts to extract required data for post-analysis by employing MATLAB, language programming software. The post-process step contained results data listed below:

1. In-plane maximum principal strain values of CFRP coupler with relative orientations of 0 degree, 30 degrees, 45 degrees, 90 degrees, and 180 degrees of the y-axis CFRP coupler
2. Vertical deflection of the CFRP coupler at the crown (inside upper) to invert (inside bottom)
3. Relative separation length at the bottom of the assembled concrete pipes
4. Moment and shear forces obtained from the top of loading cradle
5. A hoop stress of the CFRP coupler.

After extracting all of the data results, a regression analysis was conducted to derive a design equation to predict the CFRP coupler's structural performance and global behavior under shear forces, such as the vertical deflection of the CFRP coupler, the relative separation at bottom of two assembled concrete pipes, and crack patterns on concrete pipes. Considered independent variables are described below:

- Inside diameter of concrete pipe 24 inches through 120 inches
- Thickness of concrete pipe
- Thickness of the CFRP coupler, which ranged from 1/8 inch through 1.0 inch
- Width of the CFRP coupler: 6 in., 9 in., or 12 inches

A dependent variable is defined as the shear force of analyzed model. The correlation between variables was investigated by conducting the multiple linear regression analysis.

6.3 Development of CFRP coupler design equation

Multiple linear regression (MLR) analysis is one of the most widely used statistical methods for modeling the relationship between one or more independent variables and a dependent variable. It is employed to establish a design equation for the CFRP internal coupler system. To build the multiple regression model, four independent variables were considered: (1) concrete pipe diameter; (2) thickness of the concrete pipe; (3) thickness of CFRP coupler; and (4) width of CFRP coupler. The ultimate shear force, critical strain values, relative separation length, and vertical deflections were considered as dependent variables. The predictable variable from the linear regression model functions of one or more independent variables as shown in Eq. 6.1.

$$y = \beta_0 + \sum_{i=1}^n \beta_i X_i \quad (6.1)$$

where β_0 is an intercept of the linear regression model

β_i is an estimated coefficient in i independent variable

X_i is the i independent variable

The design equations of each dependent variable were built by following the steps shown below.

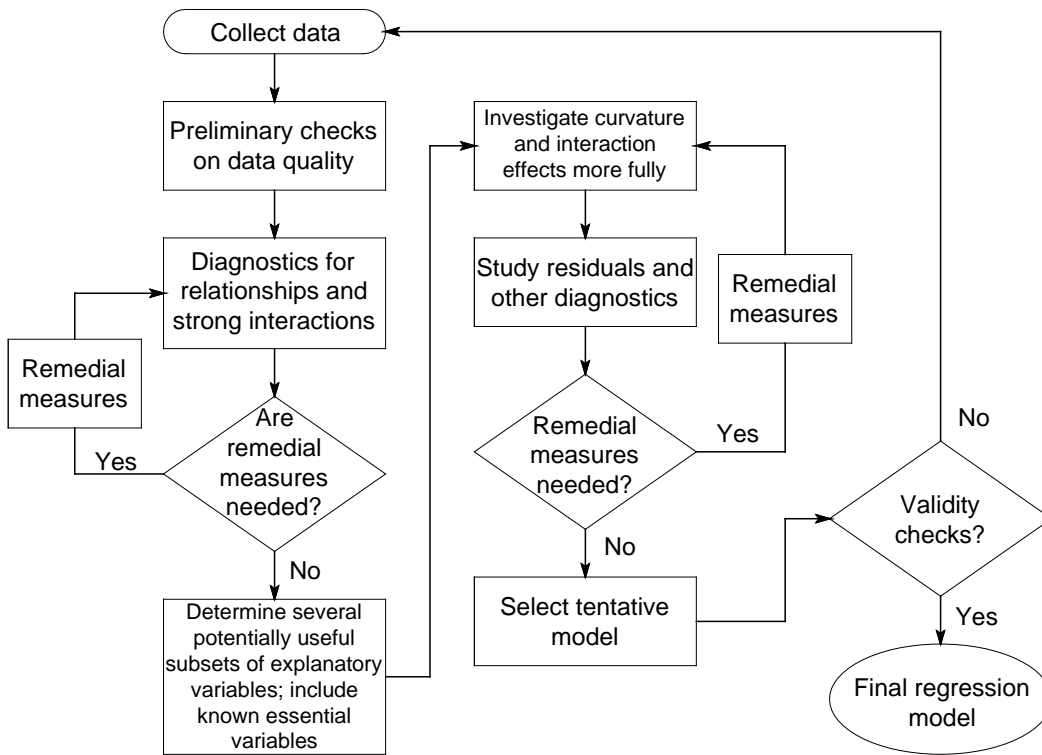


Figure 6-3 - Strategy for building a regression model
(Applied Linear Statistical Models, 5th Ed., 2004)

6.3.1 Preliminary model investigation

This preliminary model investigation included a method for detecting improper functional forms of explanatory variables, outliers, influential observations, and multicollinearity. The relationship between explanatory variables and dependent variables was determined by using scatter plots and residual plots.

The diagnostic model investigation was based on assumptions below:

1. The current multiple linear statistical model form was to be reasonable
2. The residuals were to have constant variance
3. The residuals were to be normally distributed
4. The residuals were to be uncorrelated
5. No outliers
6. The predictors were not to be highly correlated with each other

6.3.1.1 Correlation analysis

The Pearson correlation matrix scatter plot was useful for checking for linear trends, curvatures, or outliers. The matrix scatter plot, as shown in Fig. 6-4, presents correlation coefficients between one variable and other variables, and is used to investigate interdependence of multiple variables. By analyzing correlations between multiple variables, a correlation matrix shows correlation between variables in values ranging from 0.0 to 1.0, and is symmetric with the main diagonal values of 1s because the correlated coefficient of identified variables is equal to 1.0.

Table 6.2 represents the correlation coefficients of explanatory variables: shear force, pipe diameter in inches, pipe wall thickness in inches, thickness of CFRP coupler in inches, and width of CFRP coupler in inches.

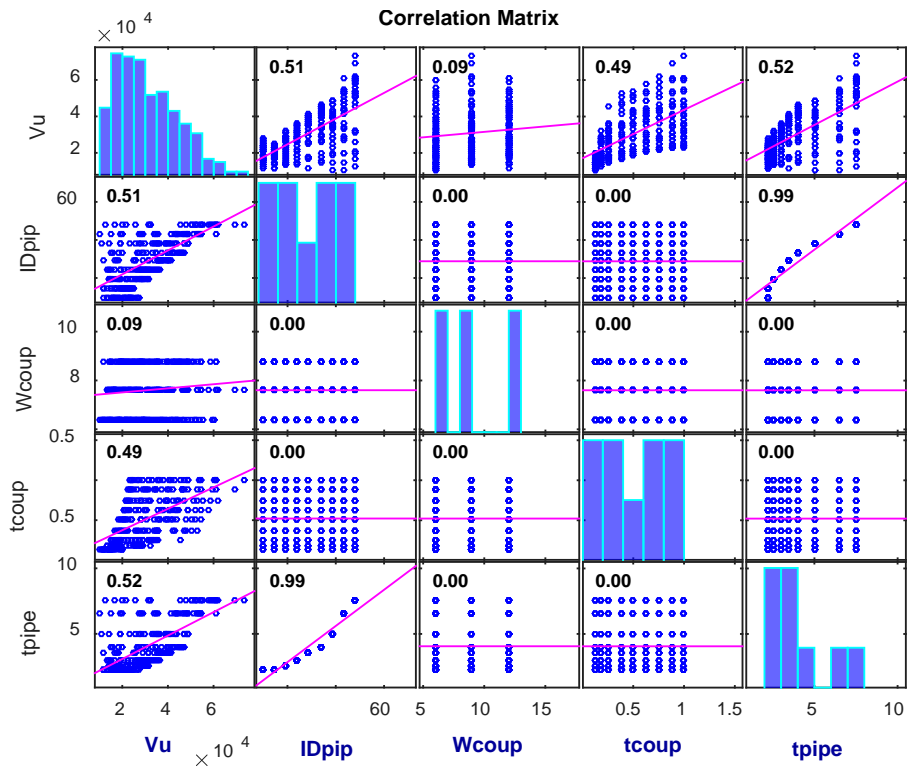


Figure 6-4 - Pearson correlation matrix scatter plot

Table 6-2 - Correlation coefficient matrix of shear force and independent variables

	Shear Force	ID _{pipe}	Width _{Coupler}	t _{coupler}	t _{pipe}
Shear Force	1.0	0.514	0.086	0.492	0.522
ID _{pipe}	0.514	1.0	0.0	0.0	0.985
Width _{Coupler}	0.086	0.0	1.0	0.0	0.0
t _{coupler}	0.492	0.0	0.0	1.0	0.0
t _{pipe}	0.522	0.985	0.0	0.0	1.0

Coefficients higher than 0.7 are described as highly correlated variables. In Table 6.2, the ultimate shear force is positively correlated with the inside diameter and thickness of the concrete pipe, which is equal to 0.512 and 0.522. Those values are less than 0.7, which indicates strong correlation between variables. However, the pipe diameter is highly correlated with the thickness of the concrete pipe, as shown by the correlation coefficient of 0.985.

6.3.1.2 Residual analysis

A residual analysis was used to detect outlying y values and check linear regression assumptions by examining the residuals of a fitted linear regression model. The residuals were plotted against four predictor variables; (1) the inside diameter of the concrete pipe, (2) the thickness of the concrete pipe, (3) the width of the CFRP internal coupler, and (4) the mid-thickness of the CFRP internal coupler, as shown in below Figs. 6-5 through 6-8. From those residual plots, curvature effects were checked. No curvature was presented in other residual plots. A variety of transformations were investigated, as well as the curvature shape of the residual plot. No funnel shape was presented on the residual plots, as shown in Figs. 6-5 through 6-8.

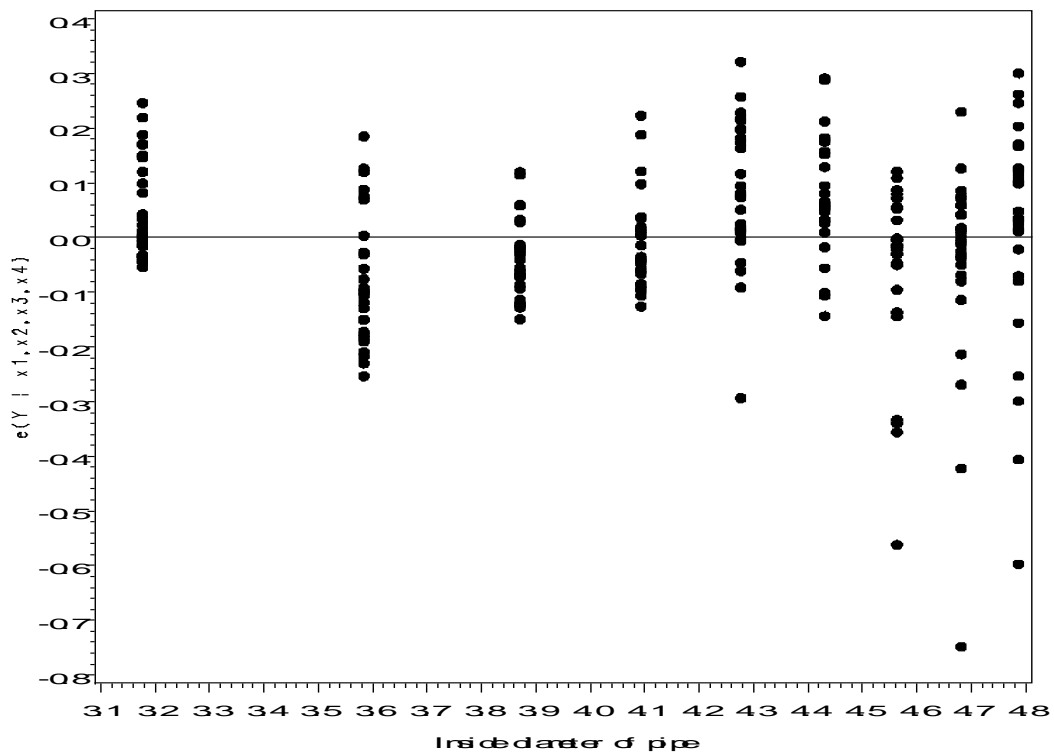


Figure 6-5 - Residual plot on inside diameter of concrete pipe

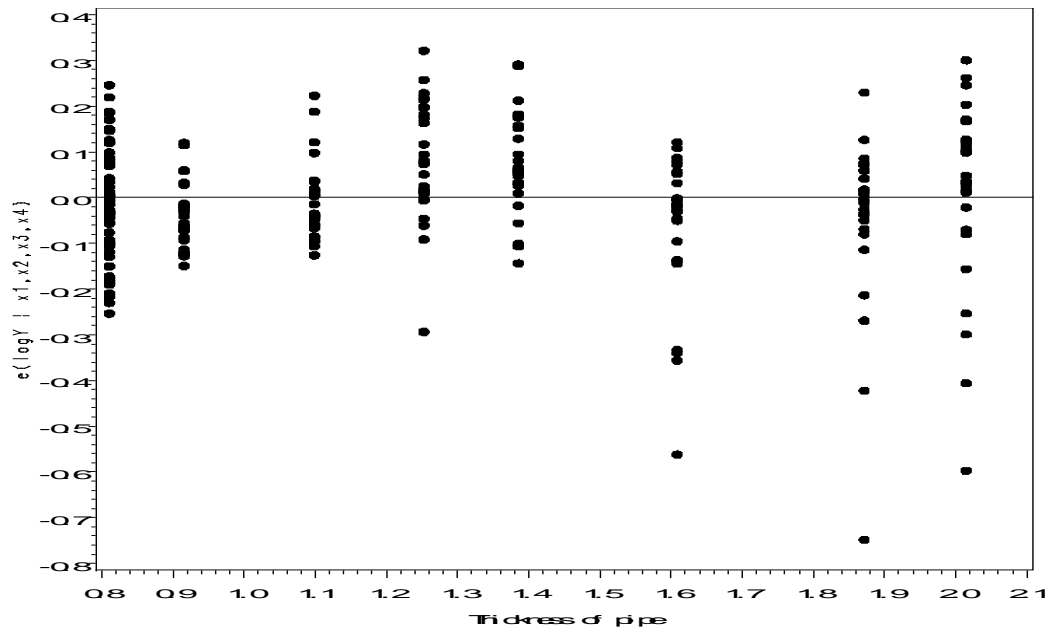


Figure 6-6 - Residual plot on thickness of concrete pipe

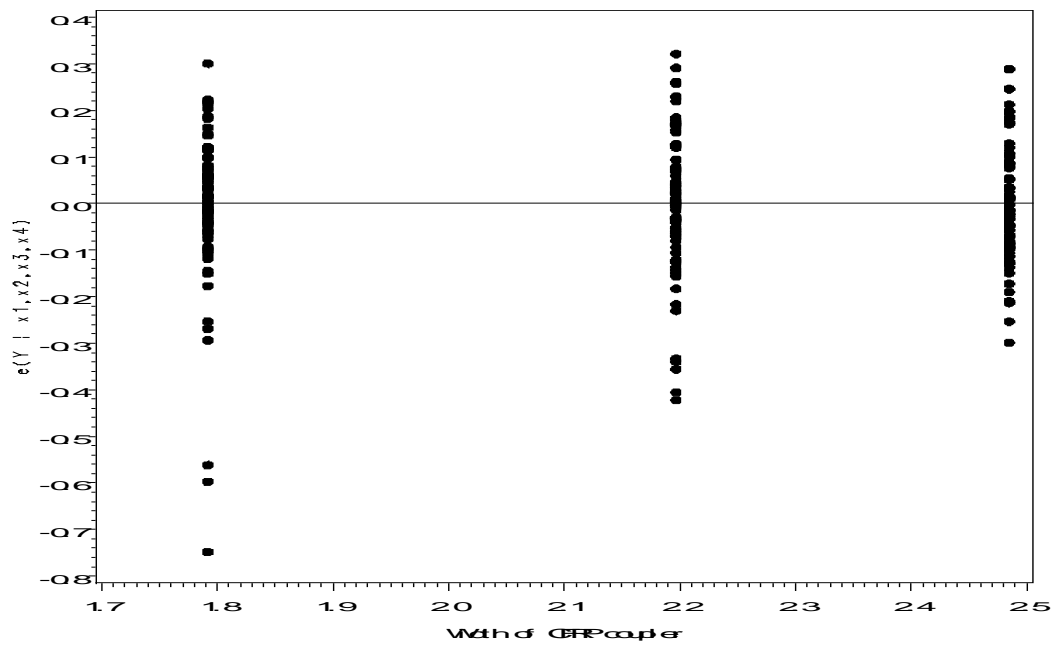


Figure 6-7 - Residual plot on width of CFRP internal coupler variable

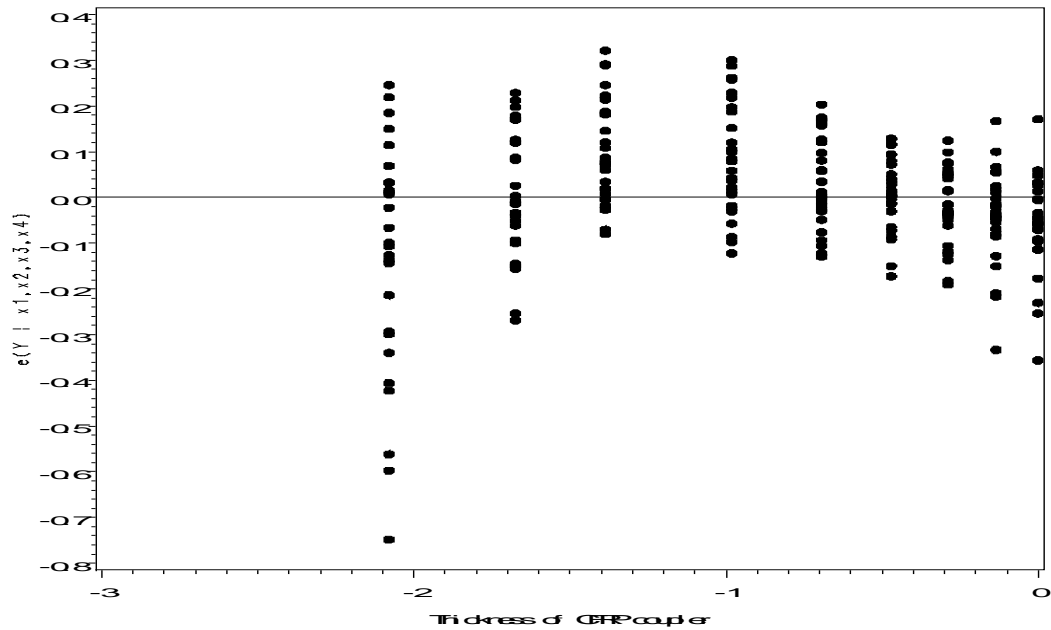


Figure 6-8 - Residual plot on mid-thickness of CFRP internal coupler

6.3.2 Best-fitted model selection

The best potential models for a given response and predictor variables can be defined by using two methods: (1) best subsets selection and (2) stepwise regression method. In the best-fitted model selection, four additive parameters account for the contribution of the ultimate shear force, vertical deflection, and relative separation in length. Interaction parameters are employed to explain the dependent variables. In this dissertation, interaction parameters higher than the 3rd were ignored. The total of additive parameters and interaction parameters was equal to 28, which can be used for best fitted model selection.

6.3.2.1 Best subsets selection

The best subsets selection method was performed with all possible regression subsets, with initial and the interaction terms. Every possible subset was used to explain the most proper regression model. Based on higher R^2 and adjusted R^2 values and low SSE (Error Sum of Squares) and MSE (Mean Square of Errors) values, the best model was identified.. Furthermore, Mallows' C_p generated as a criterion on each model was used to evaluate the best model. While searching for a proper regression model, adjusted R^2 values and C_p are the most influentially considered. A potential good regression model will have number of parameters almost close to Mallows' C_p . It should be pointed out that the initial full model's C_p is equal to the number of the parameters; for this reason, C_p should not be a criterion for selecting the full model as a potential "best" one. As well as the AIC, and the SBC are used to determine the potentially best models.

Table 6-3 - Results of best subset regression method

# in Mode	R_a^2	R^2	C(p)	AIC	SBC	Variables
1	0.4785	0.4807	823.37	-561.91	-554.93	$t_{coupler}$
1	0.3701	0.3727	1044.2	-516.02	-509.03	t_{pipe}
2	0.8522	0.8534	62.894	-867.27	-856.79	$t_{coupler}$ t_{pipe}
2	0.8474	0.8487	72.531	-859.58	-849.10	ID_{pipe} $t_{coupler}$
3	0.8695	0.8711	28.74	-896.49	-882.51	$W_{coupler}$ $t_{coupler}$ t_{pipe}
3	0.8647	0.8664	38.38	-887.76	-873.79	ID_{pipe} $W_{coupler}$ $t_{coupler}$
4	0.8817	0.8837	5.0	-919.44	-901.97	ID_{pipe} $W_{coupler}$ $t_{coupler}$ t_{pipe}
4	0.8817	0.8837	5.0	-919.44	-907.97	ID_{pipe} $W_{coupler}$ $t_{coupler}$ t_{pipe}
3	0.8695	0.8711	28.74	-896.49	-882.51	$W_{coupler}$ $t_{coupler}$ t_{pipe}

In comparing the R-square and adjusted R-square, the best subset variables are four additive variables: the thickness and inside diameter of the concrete pipe, and the width and mid-thickness of the CFRP internal coupler. Furthermore, when using four variables, C_p value of 5.0 is the closest to the number of the variables of 4.

6.3.2.2 Stepwise regression method

The stepwise regression method is composed of two parts: (1) forward selection method and (2) backward elimination method. In both methods, each predictor is added or eliminated, depending on how the predictor explains the regression model. This is determined by conducting a statistical analysis, using those specified predictors. The stepwise regression method is the most widely used, and was developed to make computational efforts more economical.

6.3.2.2.1 Forward selection regression method

The forward selection regression method is conducted in terms of the t^* statistics and their associated p-values for the regression models with explanatory variables. The t^* statistic to test the slope is zero or is obtained by Eq. 6.2, shown below.

$$t_k^* = \frac{b_k}{s\{b_k\}} \quad (6.2)$$

The forward stepwise regression method selects the explanatory variables with the largest t^* value as a candidate for the first addition. If the t^* value is greater than a predetermined level of a significance level, or if the corresponding p-value is less than the significance level, the explanatory X variable is added to the forward regression model. However, the forward stepwise method is not economical with regard to computational efforts.

Table 6-4 - Initial step of the stepwise model selection method

Stepwise Selection: Step 1					
Variable Thickness of CFRP Entered: R-Square = 0.4807 and C(p) = 823.3712					
Analysis of Variance					
Source	DF	Squares	Square	F Value	P _r >F
Model	1	21.9084	21.9084	223.07	<.0001
Error	241	23.6698	0.09822		
Corrected total	242	45.7582			
Parameter Standard					
Variable	Estimate	Error	Type II SS	F value	P _r >F
Intercept	10.62458	0.03220	10692	108863	<.0001
t _{CFRP}	0.43883	0.02938	21.90836	223.07	<.0001

Table 6-5 - Second step of stepwise variable selection

Stepwise Selection: Step 2					
Variable Thickness of pipe Entered: R-Square = 0.8534 and C(p) = 62.8938					
Analysis of Variance					
Source	DF	Squares	Square	F Value	P _r >F
Model	2	38.8965	19.4483	698.56	<.0001
Error	240	6.6817	0.02784		
Corrected total	242	45.5782			
Parameter Standard					
Variable	Estimate	Error	Type II SS	F value	P _r >F
Intercept	9.80664	0.03729	1925.756	69171.3	<.0001
t _{CFRP}	0.43883	0.01564	21.9084	786.93	<.0001
t _{pipe}	0.62553	0.02531	16.9881	610.20	<.0001

Table 6-6 - Third step of the stepwise model selection method

Stepwise Selection: Step 3					
Variable Width of CFRP Entered: R-Square = 0.8504 and C(p) = 189.0991					
Analysis of Variance					
Source	DF	Squares	Square	F Value	P _r >F
Model	3	39.7021	13.2340	539.27	<.0001
Error	239	5.8762	0.02459		
Corrected total	242	45.5782			
Parameter Standard					
Variable	Estimate	Error	Type II SS	F value	P _r >F
Intercept	9.36954	0.08402	305.7579	12436.1	<.0001
W _{CFRP}	0.20255	0.03539	0.80554	32.76	<.0001
t _{CFRP}	0.43883	0.01470	21.90836	891.08	<.0001
t _{pipe}	0.62553	0.02379	16.98815	690.96	<.0001

Table 6-7 - 4th step of the stepwise model selection method

Stepwise Selection: Step 4					
Variable Inside diameter of pipe Entered: R-Square = 0.9015 and C(p) = 46.1941					
Analysis of Variance					
Source	DF	Squares	Square	F Value	P _r >F
Model	4	40.2755	10.0688	451.92	<.0001
Error	238	5.3023	0.02228		
Corrected total	242	45.5782			
Parameter Standard					
Variable	Estimate	Error	Type II SS	F value	P _r >F
Intercept	8.69058	0.15591	69.2281	3107.16	<.0001
ID _{pipe}	0.24963	0.04920	0.57346	25.74	<.0001
W _{CFRP}	0.20255	0.03369	0.80554	36.16	<.0001
t _{CFRP}	0.43883	0.01399	21.9083	983.31	<.0001
t _{pipe}	0.34989	0.05883	0.78818	35.38	<.0001

Table 6-8 - Summary of Stepwise model selection method

Summary of Stepwise Selection method								
Step	Variable Entered	Variable Removed	Number Vars in	Partial R ²	Model R ²	C(p)	F-value	P _r > F
1	t _{CFRP}		1	0.4807	0.4807	823.37	223.07	<.0001
2	t _{pipe}		2	0.3727	0.8537	62.894	610.20	<.0001
3	W _{CFRP}		3	0.0177	0.8711	28.739	32.76	<.0001
4	ID _{pipe}		4	0.0126	0.8837	5.000	25.74	<.0001

As shown in Tables 6-4 through 6-8, in each step, the predictable variable was added based on the t-statistic value of variables' estimated coefficients up to no variables. This improved the fitted regression model significantly. According to the forward stepwise regression model method, the thickness and the width of the CFRP coupler, and the inside diameter of the concrete pipe are predictable variables. For the R² values, using the four additive variables, 90% of data is predictable, and the all of the additive variables are significant under the 0.1 level.

6.3.2.2.2 Backward elimination method

A backward elimination method is the opposite of the forward selection method. The backward elimination method starts with all potential explanatory variables, and identifies the one with the largest p-value as the candidate to be eliminated. From the t-test or F-test results, the most statistically insignificant deterioration of the model is deleted at each step, until no further variables can be eliminated without a significant loss of the regression model fit.

Table 6-9 - Backward elimination method, initial step

Dependent Variable: Vu					
Number of Observations Read: 243					
Number of Observations Used: 243					
Backward Elimination: Step 0					
All Variables Entered: R-Square = 0.8837 and C(p) = 5.0					
Analysis of Variance					
Source	DF	Squares	Square	F Value	P _r >F
Model	4	40.2755	10.0688	451.92	<.0001
Error	238	5.3023	0.02228		
Corrected total	242	45.5782			
Parameter Standard					
Variable	Estimate	Error	Type II SS	F value	P _r >F
Intercept	8.69058	0.15591	69.2281	3107.16	<.0001
ID	0.24963	0.04920	0.57346	25.74	<.0001
Width	0.20255	0.03369	0.80554	36.16	<.0001
THK	0.43883	0.01399	21.9083	983.31	<.0001
tpipe	0.34989	0.05883	0.78818	35.38	<.0001

As shown in Table 6-9, the initial backward step was processed with all four potential variables, which showed an R-square value of 0.8837. For the all explanatory variable regression models, the p-values were less than 0.1, which means all variables in this model were significant at the 0.1 confidence level. Therefore, the backward elimination method was performed because none of the p-values were greater than 0.1.

6.3.3 Fitted regression models

The three best predictable variable sets were decided by the preliminary steps for selecting the best regression models: (1) ultimate shear force, (2) vertical deflection at the CFRP internal coupler, and (3) relative separation length at bottom of assembled concrete pipes. Tables 6-11, 6-14, and 6-17 show how the selected explanatory variables are to each variable.

The equations were formed as functions of four variables:

$$V_{expected} = C_0 + C_1(ID_{pipe}) + C_2(t_{coupler}) + C_3(w_{coupler}) + C_3(t_{pipe}) \quad (6.3)$$

The multiple linear regression model function of the mentioned variables predicts the ultimate shear force with 0.6023 of R-square. However, 62% of data predicted from the regression model was not strong enough to explain the shear force. The multiple non-linear regression model was investigated as an alternative, and it was concluded that it shows more significant predictions when the independent variable set includes the complexity of the interaction.

The multiple non-linear regression was as shown below:

$$y = C_0 X_1^{C_1} X_2^{C_2} \dots X_n^{C_n} \quad (6.4)$$

Equation 6.4 can be expressed as Equation 6.5, by removing the logarithms on both sides.

$$\ln(y) = \ln(C_0) + C_1 \ln(X_1) + C_2 \ln(X_2) + \dots + C_n \ln(X_n) \quad (6.5)$$

Denoting the logarithms of the explanatory variables by the prime superscripts, Eq. 6.5 was rewritten as Eq. 6.6 to perform the non-linear multiple regression analysis and to obtain the best least-square-fit to data.

$$y' = C_0' + C_1 X_1' + C_2 X_2' + \dots + C_n X_n' \quad (6.5)$$

By conducting the regression analysis, the intercept of C_0' and coefficient parameters of C_1, C_2, \dots, C_n were determined.

6.3.4 Design equations

Three design equations were derived by conducting the multiple non-linear regression analyses: (1) the ultimate shear force, (2) vertical deflection at the CFRP coupler, and (3) the relative separation length at bottom of assembled concrete pipes. The models showed the coefficient of determination (R-square) as 0.8837, 0.9092, and 0.9405, respectively. Those values mean that all of the models predicted the dependent variables.

X-outliners and y-outliners were checked by investigating the leverage values, which is a measure of the distance an independent variable deviates from the regression model's mean, expressed as h_{ii} in the SAS program. The results were compared with the cut-off value, which was computed by the x-outliner guideline, as expressed in

$$h_{ii} < \frac{2p}{n} \quad (6.6)$$

A leverage value lower than the guideline value means that no x-outliner influences the estimate coefficient. In order to check the Y-outliner, the studentized deleted residuals were considered, compared with the cutoff, which is the Bonferoni outliner test based on Bonferoni simultaneous intervals. The studentized deleted residuals expressed in SAS were computed by Eq. 6.7.

$$t_i = \frac{d_i}{\sqrt{MSE_i(1 - h_{ii})}} \quad \text{or} \quad \sqrt{\frac{n - p - 1}{SSE(1 - h_{ii}) - e_i^2}} \quad (6.7)$$

The Bonferoni outliner test was computed by Eq. 6.8.

$$|t_i| > t\left(1 - \frac{\alpha}{2n}; n - p - 1\right) \quad (6.8)$$

6.3.4.1 Ultimate Shear Force Equation

The ultimate shear force equation is expressed as below:

$$V_{expected} = (e^{8.6909})(ID_{pipe})^{0.24963}(w_{coupler})^{0.20255}(t_{coupler})^{0.4388}(t_{pipe})^{0.3499} \quad (6.9)$$

Table 6-10 - ANOVA result of multiple linear regression for ultimate shear force equation

Source	DF	Sum of Squares	Mean Square	F value	P _r > F
Regression	4	40.27551	10.06888	451.92	<.0001
Residual	238	5.30268	0.02228		
Corr.otal	242	45.57819			
Root MSE		0.34064	R-square		0.8837
Dep. Mean		-0.79148	Adj. R-Square		0.8817
Coeff. Var		-43.03876			

Table 6-11 - The coefficient of the estimators on ultimate shear force equation

	Coefficients	Standard Error	t Stat	VIF	P-value
Intercept	8.69058	0.15591	55.74	0.000	<.0001
ID _{pipe}	0.24963	0.04920	5.07	6.7477	<.0001
w _{coupler}	0.20255	0.03369	6.01	1.0000	<.0001
t _{coupler}	0.43883	0.01399	31.36	1.0000	<.0001
t _{pipe}	0.34989	0.05883	5.95	6.7477	<.0001

The ANOVA table shown in Table 6-10 includes F-values and P-values to determine whether the shear force regression model is significant. A p-value less than 0.1 indicates that the regression model is significant. Table 6-11 shows the values for the coefficients of the ultimate shear force equation. All of the estimated variables are significant, based on the p-values in Table 6-11. Furthermore, the variance inflation factors (VIF) of all of the estimated variables were less than 7, which indicates that they were not multicollinear. The Pearson correlation coefficient is presented in Table 6-11.

Table 6-12 - Pearson correlation matrix of estimate variable on shear force equation

	Shear Force	ID _{pipe}	Width _{Coupler}	t _{coupler}	t _{pipe}
Shear Force	1	0.684	0.186	0.622	0.662
ID _{pipe}	0.684	1	0	0	0.925
Width _{Coupler}	0.186	0	1	0	0
t _{coupler}	0.623	0	0	1	0
t _{pipe}	0.662	0.925	0	0	1

The maximum coefficient value was 0.925 on two parameters; t_{pipe} and ID_{pipe}, which indicates that the thickness of the concrete pipe was very strongly correlated to the ID_{pipe} additive variable.

Figure 6-9 presents a comparison of observed and predicted ultimate shear force.

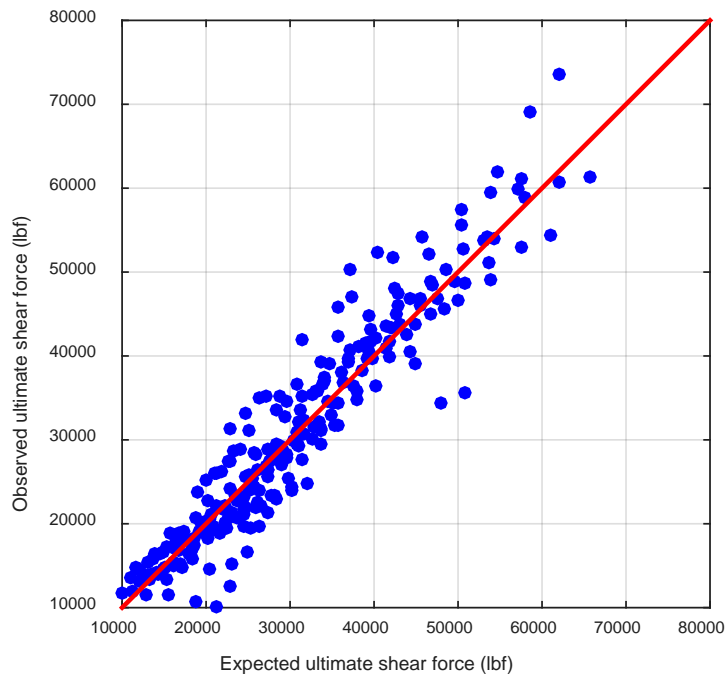


Figure 6-9 - Comparison of observed and predicted ultimate shear forces

6.3.4.2 Vertical Deflection at CFRP Internal Coupler

The vertical deflection equation is expressed as below:

$$\delta_{expected} = (e^{-11.966})(ID_{pipe})^{3.5597}(w_{coupler})^{-0.3648}(t_{coupler})^{-0.6858}(t_{pipe})^{-2.412} \quad (6.10)$$

Table 6-13 - ANOVA result of multiple linear regression for ultimate shear force equation

Source	DF	Sum of Squares	Mean Square	F value	P _r > F
Model	4	194.0403	48.51007	418.05	<.0001
Error	167	19.3784	0.11604		
Corr. Total	171	213.4187			
Root MSE		0.34064	R-square	0.9092	
Dep. Mean		-0.79148	Adj. R-Square	0.9070	
Coeff. Var		-43.03876			

Table 6-14 - The coefficient of the estimators on ultimate shear force equation

	Coefficients	Standard Error	t Stat	VIF	P-value
Intercept	-11.96588	0.37322	-32.06	0.00	<0.0001
ID _{pipe}	3.55973	0.11806	30.15	5.92511	<0.0001
w _{coupler}	-0.36477	0.09175	-3.98	1.02262	<0.0001
t _{coupler}	-0.68577	0.05527	-12.41	1.08035	<0.0001
t _{pipe}	-2.4119	0.15146	-15.92	5.78341	<0.0001

For the vertical deflection regression model, it can be concluded that according to F-values and p-values from the ANOVA table 6-13, there is no greater p-value than 0.1, which indicates that the vertical deflection model is significant at 0.1 level. Table 6-14 shows the values for the coefficient of the vertical deflection equation. All of the estimated variables are significant, based on the p-values in Table 6-14. Furthermore, the VIFs of all of the estimated variables were less than 7, which indicates that none of the estimated variables showed multicollinearity. The Pearson correlation coefficient for the vertical deflection regression model is presented in Table 6-14.

Table 6-15 - Pearson correlation matrix of estimate variable on deflection equation

	Shear Force	ID _{pipe}	Width _{Coupler}	t _{coupler}	t _{pipe}
Shear Force	1	0.8454	-0.0340	-0.0674	0.6283
ID _{pipe}	0.8454	1.0	0.00518	0.1847	0.9067
Width _{Coupler}	-0.0340	0.00518	1.0	-0.1320	-0.0125
t _{coupler}	-0.0674	0.18471	-0.13207	1.0	0.1066
t _{pipe}	0.6283	0.90696	-0.01251	0.1066	1.0

The vertical deflection equation is highly related to the inside diameter and thickness of the concrete pipe. The maximum coefficient value was 0.9067 on t_{pipe} and ID_{pipe}, which presents that the thickness of the concrete pipe was moderately correlated to the ID_{pipe} variable. Figure 6-10 presents a comparison of observed and predicted vertical deflection at the CFRP coupler.

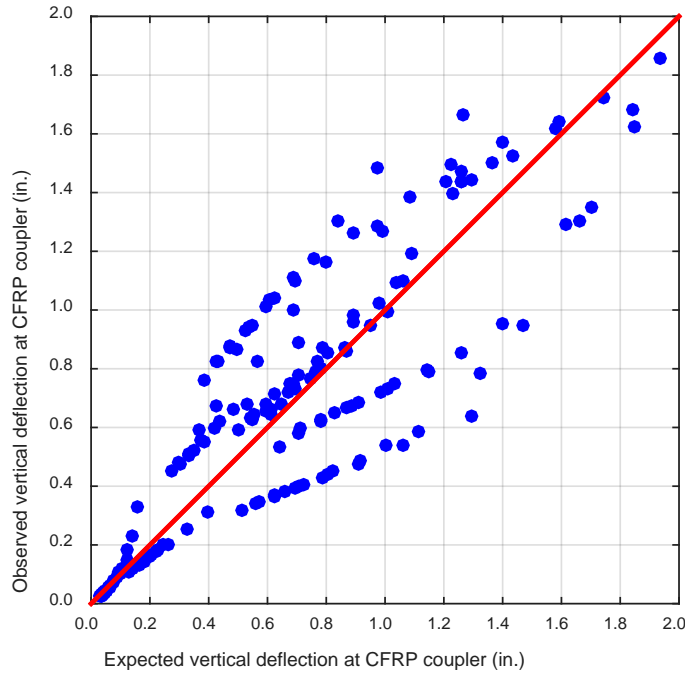


Figure 6-10 - Comparison of observed and predicted vertical deflection

6.3.4.3 Relative separation at bottom of assembled concrete pipes

The relative separation equation is expressed as below:

$$l_{expected} = (e^{-12.538})(ID_{pipe})^{3.6572}(w_{coupler})^{-0.5062}(t_{coupler})^{-0.83997}(t_{pipe})^{-2.2396} \quad (6.11)$$

Table 6-16 - ANOVA results of relative separation length equation

Source	DF	Sum of Squares	Mean Square	F value	P _r > F
Model	4	217.09728	54.27432	648.42	<.0001
Error	167	13.72726	0.08370		
Corr. Total	171	230.82454			
Root MSE		0.28931	R-square	0.9405	
Dep. Mean		-1.02472	Adj. R-Square	0.9391	
Coeff. Var		-28.23345			

Table 6-17 - The coefficient of the estimators on relative separation length equation

	Coefficients	Standard Error	t Stat	VIF	P-value
Intercept	-12.53832	0.33335	-37.61	0.00	<0.0001
ID _{pipe}	3.65715	0.10666	34.29	6.61898	<0.0001
w _{coupler}	-0.50621	0.07865	-6.44	1.01693	<0.0001
t _{coupler}	-0.83997	0.04754	-17.67	1.08287	<0.0001
t _{pipe}	-2.23961	0.13340	-16.79	6.45016	<0.0001

The ANOVA table shown in Table 6-16 includes f-values and p-values to determine whether the separation length regression model is significant. A p-value of less than 0.1 indicates that the regression model is significant. Table 6-17 shows the values of the coefficients of the relative separation length. The p-values of all estimated variables were less than 0.0001, which means that they are significant. The maximum VIF is equal to 6.61898, which indicates that none of the estimated variables were multicollinear. The Pearson correlation coefficient is shown in Table 6-17 for the relative separation length.

Table 6-18 - Pearson correlation matrix of estimate variable on deflection equation

	Separation	ID _{pipe}	Width _{Coupler}	t _{coupler}	ID-t _{pipe}
Separation	1.0	0.86581	-0.07068	-0.10163	0.68745
ID _{pipe}	0.86581	1.0	0.00117	0.19819	0.91689
Width _{Coupler}	-0.07068	0.00117	1.0	-0.11396	-0.01361
t _{coupler}	-0.10163	0.19819	-0.11396	1.0	0.12133
ID-t _{pipe}	0.68745	0.91689	-0.01361	0.12133	1.0

The maximum coefficient value was 0.9168 for two parameters, the inside diameter of the concrete pipe and the thickness of the concrete pipe, which indicates that the thickness of the concrete pipe was moderately correlated to the ID of the pipe variable. A coefficient value of 0.9167 is very high, but the VIF value was less than 7.0. Figure 6-11 presents a comparison of observed and predicted vertical deflections at the CFRP coupler system.

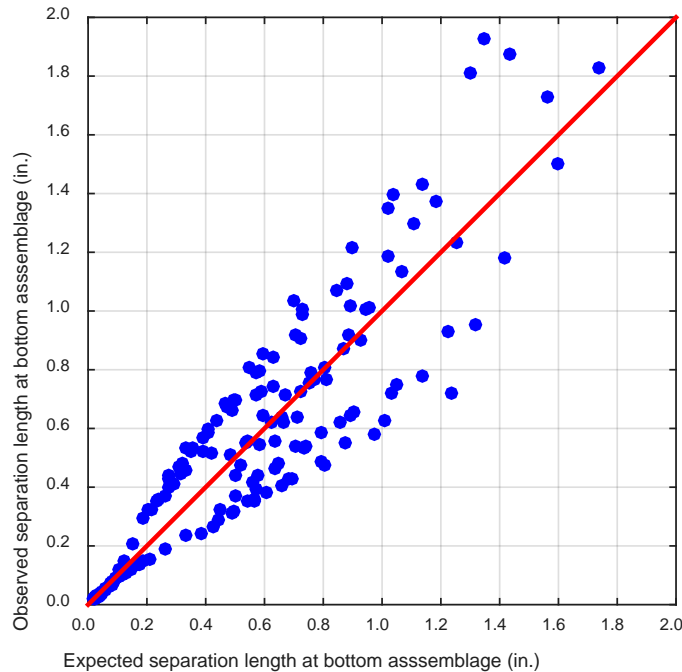


Figure 6-11 - Comparison of observed and predicted ultimate shear forces

6.3.5 Three-dimensional contour alignment chart

Figures 6-12 through 6-15 are contours of normalized shear forces of pipe diameters and the CFRP mid-thicknesses on 6-inch, 9-inch, and 12-inch wide CFRPs. For each pipe diameter, the normalized shear force was computed by Eq. 6.11.

$$\text{Normalized shear force} = \frac{V_{ui}}{V_{req'd}} \quad (6.11)$$

where V_{ui} is ultimate shear force of i case and $V_{req'd}$ is the shear strength required by ASTM C497-16a, and computed by Eq. 2.1 in terms of the pipe weight and the applied shear force. The X-axis represents the mid-thickness of the CFRP coupler, and the Y-axis represents the inside diameter of concrete pipe in US units. The normalized shear forces of Z-axis are plotted as constant Z slices, called contours, in a two-dimensional format.

A normalized shear force greater than 1.0 indicates that a CFRP coupler with specified geometric variables has sufficient structural capability, similar to the pipe joint system. The normalized shear forces ranged from 0.0 to 2.0, as shown in Figs. 6-12 through 6-15.

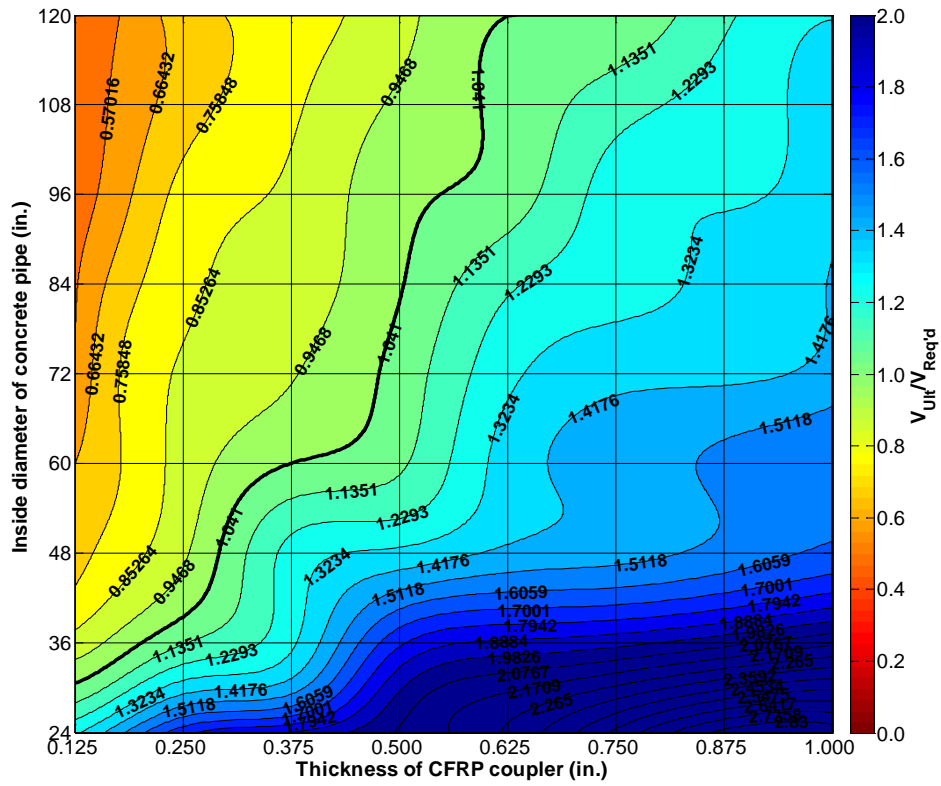


Figure 6-12 - Contours of normalized shear force as a function of pipe diameter and CFRP coupler thickness with 6-inch width of CFRP coupler

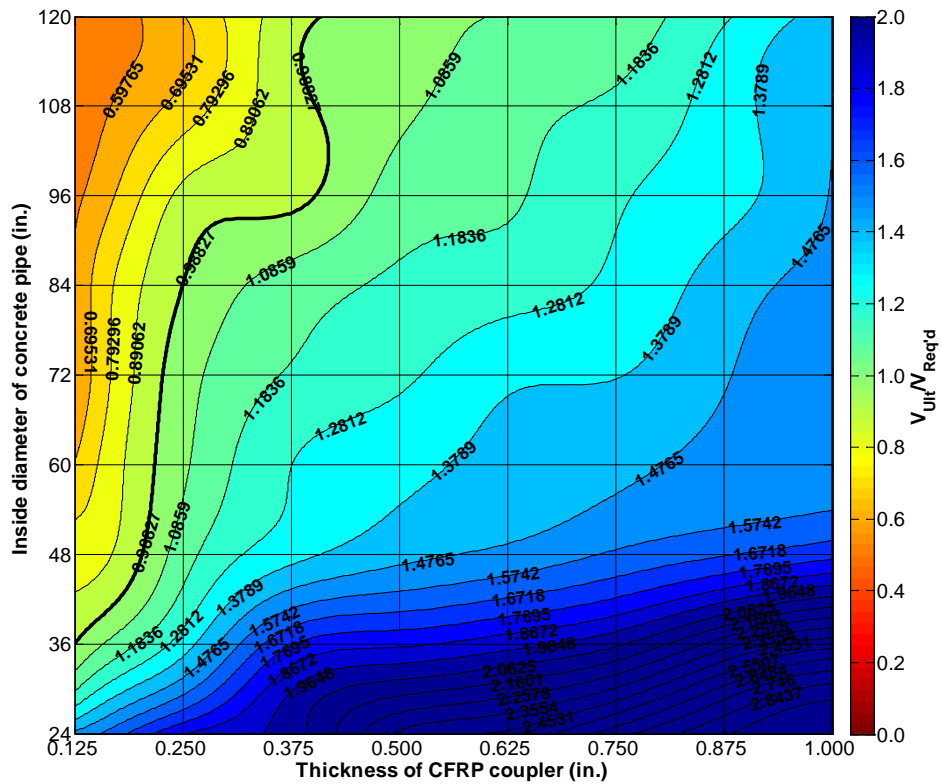


Figure 6-13 - Contours of normalized shear force as a function of pipe diameter and CFRP coupler thickness with 9-inch width of CFRP coupler

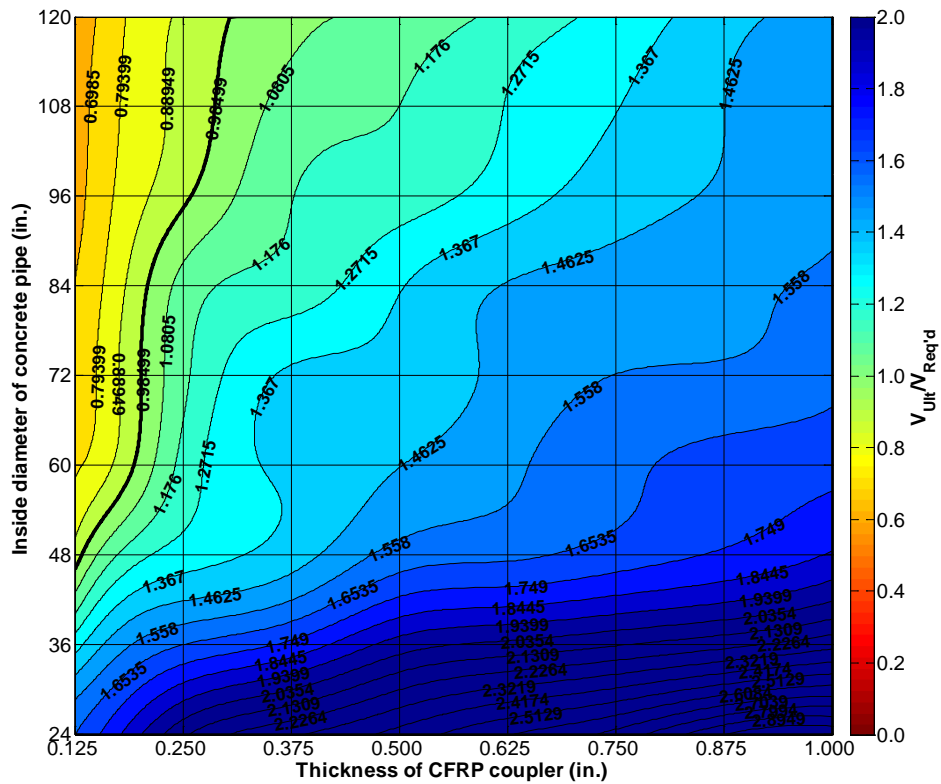


Figure 6-14 - Contours of normalized shear force as a function of pipe diameter and CFRP coupler thickness with 12-inch width of CFRP coupler

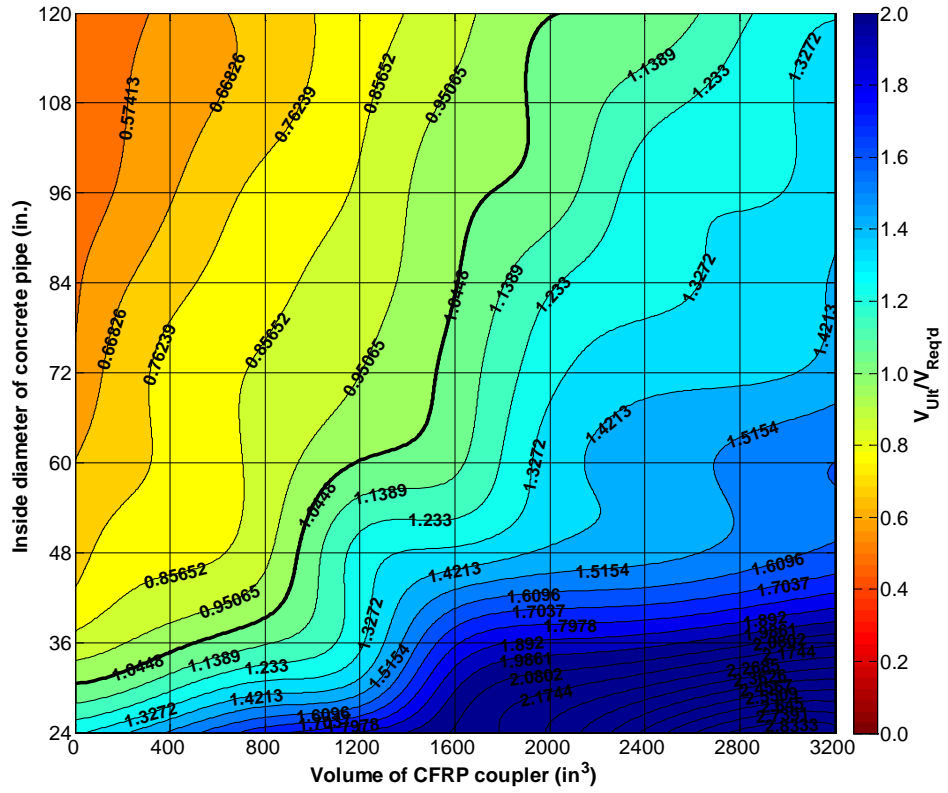


Figure 6-15 - Contours of normalized shear force as a function of pipe diameter and CFRP coupler volume

6.4 Conclusions of parametric study

A parametric study was performed with four independent additive variables, expressed as the thickness and inside diameter of the concrete pipe and the mid-thickness and width of the CFRP coupler, to develop design equations which could predict the behavior of the joint shear tests for the CFRP internal coupler system,.

A total of 243 cases were modeled by employing the MATLAB script-based language program for pre-processes and post-processes, and were analyzed by utilizing the ABAQUS numerical analysis program. For the best selection of the predictable variables and as the preliminary step in the regression analysis, best subset and stepwise regression methods were performed. With the best variables selected from the preliminary step, the multi-linear regression models were built up to predict the ultimate shear force, the vertical deflection of the CFRP internal coupler, and the relative separation length of assemblage of the concrete pipes. They were compared with the analyzed data from the parametric study. The multi-linear regression model, predicting the ultimate shear force on the CFRP internal coupler, showed a R-square value of 0.88, indicating that the built regression model shows a good fit with the model and represents 88% of the data from the parametric study. Randomly-distributed residuals were shown on the residual plot for the ultimate shear force regression model, indicating that the data from the parametric study was well prepared by the built regression model. In addition to the ultimate shear force equation, the vertical deflection and the relative separation length equations showed the R-square values of 0.90 and 0.94, respectively.

Furthermore, two-dimensional contour charts on widths of 6 inches, 9 inches, and 12 inches, and the volume of the CFRP internal coupler were plotted for a proper design of the CFRP internal coupler on specified concrete pipe wall thicknesses and inside diameters.

Chapter 7 Discussion of Results and Recommendations for Future Research

7.1 Discussion and Summary

A semi-rigid concrete pipe, with reduced wall thickness and an area of the circumferential steel reinforcement, was developed to provide more flexibility than the conventional rigid concrete pipe. However, due to the reduced wall thickness of the semi-rigid concrete pipe, the most often used method of joining pipes with a bell and spigot with rubber gasket could not be used. Therefore, a new joint system utilizing a CFRP multi-layer laminate, known as a CFRP internal coupler, was developed by employing a three-dimensional nonlinear finite element method to predict the global behavior at the joint region in various geometrical variables in terms of the CFRP internal coupler mid-thickness and width, and different thickness and inside diameter of the concrete pipe. In the finite element models, geometrical non-linearity, material non-linearity, contact non-linearity, and the time-dependent Newton-Rapson method were accounted for to compute stress and strain values at a specified region, such as the CFRP internal coupler. In addition to the numerical analyses, 12 full-scale joint shear tests were conducted on pipes with different diameters, 36 through 84 inches, to verify the developed finite element models. A comparison of results obtained by the experimental tests and the numerical analyses on the developed CFRP internal couplers' structural performance indicated that the numerical models predicted well the global behaviors of the CFRP internal joint system employed for the concrete pipes.

Based on the verified finite element model, a parametric study was conducted with four geometric variables; (1) the concrete pipe thickness, (2) the concrete pipe inside diameters ranging from 24 through 120 inches with 12-inch incremental diameters, (3) the width of the CFRP coupler, and (4) the mid-thickness of the CFRP coupler. A total of 243 numerical models were developed and analyzed. The parametric study was

composed of three steps: (1) the pre-processing, (2) the numerical analysis, and (3) the post-processing. Program scripts based on the MATLAB were developed and utilized in the pre-processing step. The developed MATLAB scripts, consisting of geometric nonlinearity, material nonlinearity, contact nonlinearity, and boundary conditions, generated the input files in a python format for the ABAQUS analysis program. Compared to manual modeling, generated input files reduce the computational load on the CPU process and save building length of time for model generation. The ABAQUS solver analyzed the input files in the python format by using the time-dependent Newton-Raphson method, and recorded all of the data in the data files.

The post-process was employed to extract shear force, corresponding vertical deflection of the CFRP coupler, and the relative separation length at the bottom of the assemblage pipes from analyzed numerical models. Those results were used to develop design equations by performing the multi-linear regression analysis. The design equations are expressed in terms of the mid-thickness and width of the CFRP coupler, and the thickness and inside diameter of the concrete pipes. To determine the best-fitted regression model, the best additive variable set to the regression model was investigated by conducting the best subset and stepwise regression methods. The multiple-regression models were used to make a design the CFRP internal coupler as a connector of concrete pipe, or different material pipes.

Based on the joint shear tests conducted in accordance with American Society for Testing and Materials (ASTM) C497-16a, the following conclusions are drawn:

1. The CFRP internal coupler system made by multiple-layup carbon fiber reinforced polymer (CFRP) sheets is a viable alternative for the bell and spigot with rubber gasket connection system for concrete pipes.
2. Ultimate shear forces of the joint shear tests on 36 in., 48 in., 72 in., and 84-inch concrete pipes with corresponding CFRP coupler thicknesses of 0.125 in., 0.1875 in., 0.375 in., and 0.375 in. average 20.5% higher than the shear strengths required by the ASTM C497-16a specification. With those thicknesses, governed failure mechanisms were three-hinge plastic collapses. At the instability of the CFRP coupler, the averaged strain value from the experimental tests was 0.01 in./in., with an angle of positive and negative 45 degrees to y-axis coming from the crown to the invert of the CFRP coupler.
3. Initial cracking patterns were observed on the top (known as crown) and bottom (known as invert) of the inside concrete pipe subjected to the applied shear force, and propagated up to a region where the concrete pipes were assembled by the CFRP internal coupler. Longitudinal cracking along the length of the TW concrete pipes, and diagonal cracking patterns were shown at mid-height of the outside the concrete pipes.
4. To verify that the CFRP internal coupler was able to prevent leaks, the assembled concrete pipes were subjected to hydrostatic water pressure of 13 psi for 20 minutes in accordance with ASTM C497-16a, Sec. 8. No leakage was observed.

The carbon fiber reinforced polymer (CFRP) laminate specimens were used to conduct the material tests to obtain the material constitutive model for the numerical analyses. Unidirectional material tests were performed in accordance with ASTM D3039 on -45/+45 and 0/90 stacking sequences in balanced and symmetric laminates. Both fiber direction laminates had 0.0625 in, 0.125 in, and 0.25 inch thicknesses.

1. To obtain the strain values and poisson's ratio, the longitudinal and transverse strain gauges along the length of the specimens were installed on the front and back of the CFRP laminate, at mid-length of the specimens.
2. Stacking sequences of -45/+45 in balanced and symmetric laminates showed non-linear stress and strain response, which was modeled as bilinear stress and strain response for more stable convergence during the numerical solution.
3. At around 0.015 in./in. of the strain values of the CFRP laminate specimens, fiber reorientation occurred simultaneously with a broken matrix, which changed the shape of the CFRP laminate specimens to that of a dumbbell.
4. Stress and strain responses of the 0/90 stacking sequence laminates were a linear, with 2% residual displacements of the total displacement.
5. To avoid the slippage at the end of the 0/90 degree CFRP laminate and the failure due to concentrated stress by the grip wedges, the aluminum tabs were attached by using the same saturant epoxy as was used to manufacture the CFRP laminates.
6. Sudden failure occurred on the mid-length of the CFRP laminate at the ultimate tensile force, with 0.015 in./in. of the corresponding strain value.

A three-dimensional finite element method was developed and adopted to simulate the joint shear tests on the CFRP internal coupler. The conclusions of the numerical analyses are represented below.

1. Comparisons of the results obtained by the numerical analyses and the full-scale experimental tests show a good agreement in the vertical deflection and corresponding shear force on the 36, 48, 54, 72, and 84-inch concrete pipes.
2. Strain values measured 45 degrees from the top of the CFRP coupler show are identical to the maximum principal strain value from the FEM models.
3. Parameters defined in the concrete damage plasticity material model for the synthetic-fiber-reinforced concrete mixture accurately predicted crack development by comparing actual crack patterns on the experimental tests and the numerical analyses.
4. Hard contact interaction with friction coefficients on contacted surface pairs between the outside concrete pipe and wooden cradles, between the assembled concrete wall sides, and between the CFRP coupler and the inside concrete pipe accurately predicted small sliding during the tests.

A parametric study was performed with various parameter variables. Parameter variables taken into consideration were the thickness and width of the CFRP coupler, and the various thicknesses and inside diameters of the concrete pipes. For the parametric studies on 243 cases, the conclusions are presented below.

1. To select the best explanatory variables, the preliminary analyses were adopted for building the multiple regression models which predict the ultimate shear force, vertical deflection, and relative separation length at the bottom of the concrete pipes. The best subset method was employed to investigate which combination of explanatory variables was a significant predictor, as well as to predict fitted regression models.
2. In the forward stepwise regression method, those independent variables aforementioned were modeled as the multiple non-linear equation, which shows R-square of 0.88, 0.90, and 0.94 for the ultimate shear force, vertical deflection at the CFRP coupler, and relative separation at the bottom of assembled concrete pipes, respectively.
3. The design equation predicting the ultimate shear force with four additive variables had an R-square value of 0.88 and the highest correlation coefficient of 0.925. The maximum VIF was equal to 6.747, which is less than 7.0. With those results, it can be concluded that the four independent variables were significant under 0.1 level.
4. The vertical deflection at the CFRP coupler with the thickness and inside diameter of the concrete pipe and the width and thickness of

the CFRP coupler predicted 90% of data, and all independent variables were significant under 0.1 level.

5. The highest correlation coefficient of $r = 0.925$ shows that the inside diameter of the concrete pipe is strongly correlated to the thickness of the concrete pipe. However, the VIF of 5.78 is less than 7.0, which concludes that the thickness of the concrete pipe is not removed.
6. The thickness and inside diameter of the concrete pipe and the width and mid-thickness of the CFRP internal coupler were used as the additive variables of the design equation for the relative separation length at the bottom of the concrete pipe assembly. Based on the R-square value of 0.94, the regression-fitted model accurately predicted the relative separation length with the four independent variables.
7. Even though the highest correlation coefficient of 0.9169 shows the highly correlated relationship between the thickness of the concrete pipe and the inside diameter of the concrete pipe, its VIF value of 6.45 is less than the significant level value of 7.0. It can be concluded that the thickness of the concrete pipe is not removed. With the results of the p-value and t-test, all of the independent variables were significant, with a level of 0.1.
8. Based on the design equations, three-dimensional surface contour plots on 6 inch, 9 inch, and 12 inch wide CFRP couplers were drawn, which is the easiest method for selecting the proper mid-thickness of the CFRP coupler.

7.2 Main Conclusions

1. External wrapping joints using the Carbon Fiber Reinforced Polymer (CFRP) sheet showed 45.5% higher shear strength in average when compared with the requirements of ASTM C497. To provide adequate bond strength between the CFRP sheet and concrete pipe, at least 3 hours was required for epoxy curing time, which is not suitable for current pipeline construction practices.
2. Structural performance and water-resistance of a pre-fabricated CFRP internal coupler were evaluated by ASTM C497. Based on the joint shear tests, the CFRP internal coupler showed, on average, 20.5% higher shear strengths when compared to the strengths required by the ASTM C497.
3. The FEM model analyses accurately mimicked the experimental test results with high degree of reliability.
4. The CFRP coupler can be used for both regular and thin-wall concrete pipes.
5. The CFRP internal coupler satisfied water-tightness requirement of ASTM C497.
6. The CFRP internal coupler had the higher ductility in elastic region, which resulted in the internal coupler returning to its original shape after unloading.

7. Design contour guidelines and design equations were developed based on detailed parametric study of 243 different test case.
 - a. For 36 inch inside diameters (or smaller), the minimum required CFRP internal coupler thickness is 0.125 in.
 - b. For 48 in. through 60 in. inside diameters, the minimum required internal coupler thickness is 0.25 in.
 - c. For 72 in. inside diameters (and larger), the required thickness of CFRP internal coupler thickness is 0.375 in.
8. The CFRP internal coupler is a revolutionary solution for pipe connection which would eliminate joint failures.

7.3 Recommended Future Works

On a basis of this research, future research is recommended below.

1. Conducting joint shear tests under axially-restrained pipe movements to simulate and better understand joint systems of pipelines, which consist of thousands of pipe segments.
2. Investigation of the structural performance of the CFRP coupler itself, without concrete pipe, to compare its performance to the numerical analytical solution based on the FRP theoretical equation.
3. Joint shear tests for two different types of pipes. The CFRP internal coupler system is applicable to all types of pipes because it is designed primarily according to the inside diameter of the pipe.
4. Accelerated aging of the CFRP coupler exposed to chemicals and/or UV to investigate how they affect the CFRP coupler's structural performance.
5. Unidirectional compressive material test on the CFRP laminate to obtain orthotropic material property, and to be modeled as the CFRP coupler system.
6. Narrower range of the mid-thickness of the CFRP coupler to make more detailed guidelines for the CFRP coupler design.
7. Various FRP materials are suggested to expand usability as a connector for pipes and to reduce manufacturing cost. A pipeline subjected to external low pressure requires a coupler system made of low material properties.

Appendix A

Results of uni- and bi- directional material tests

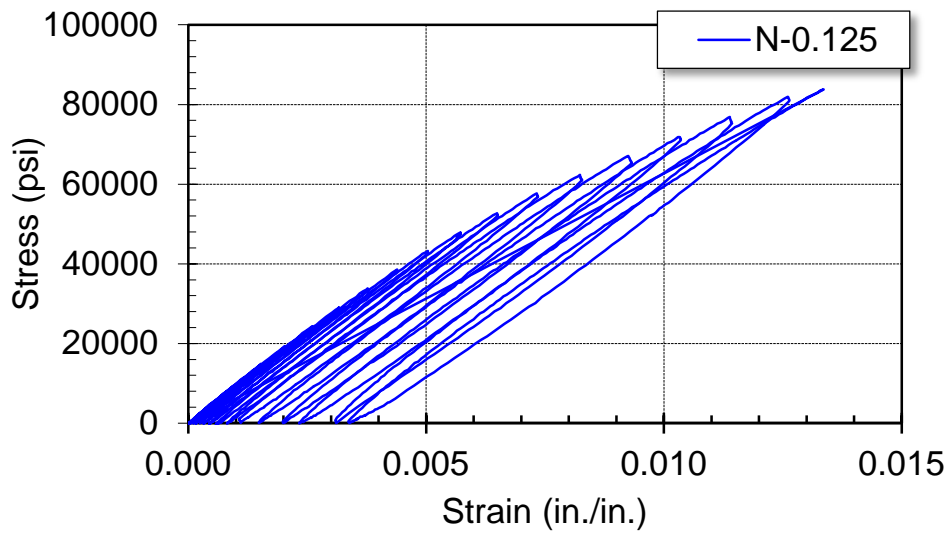
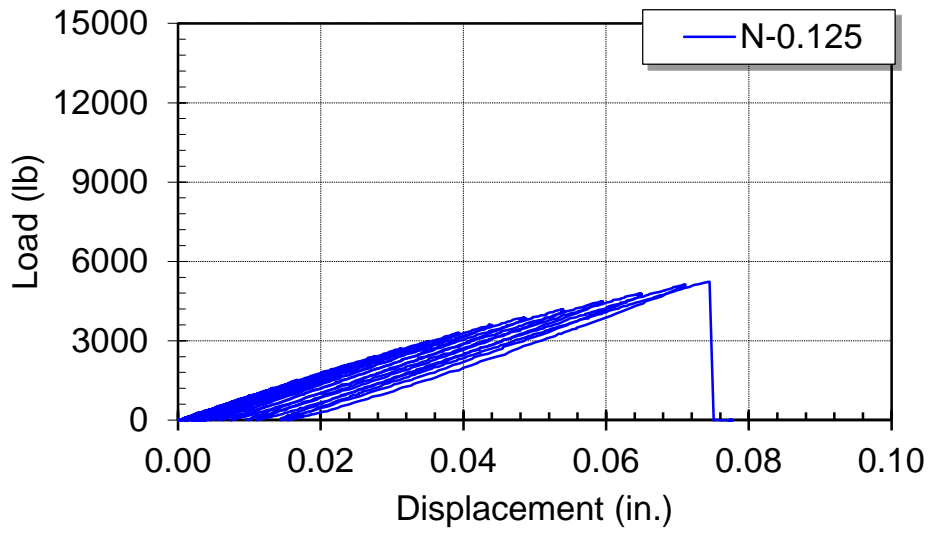


Figure A-1. Load vs. displacement and stress vs. strain responses of 0.125 inch thickness coupon specimen of uni-directional fiber

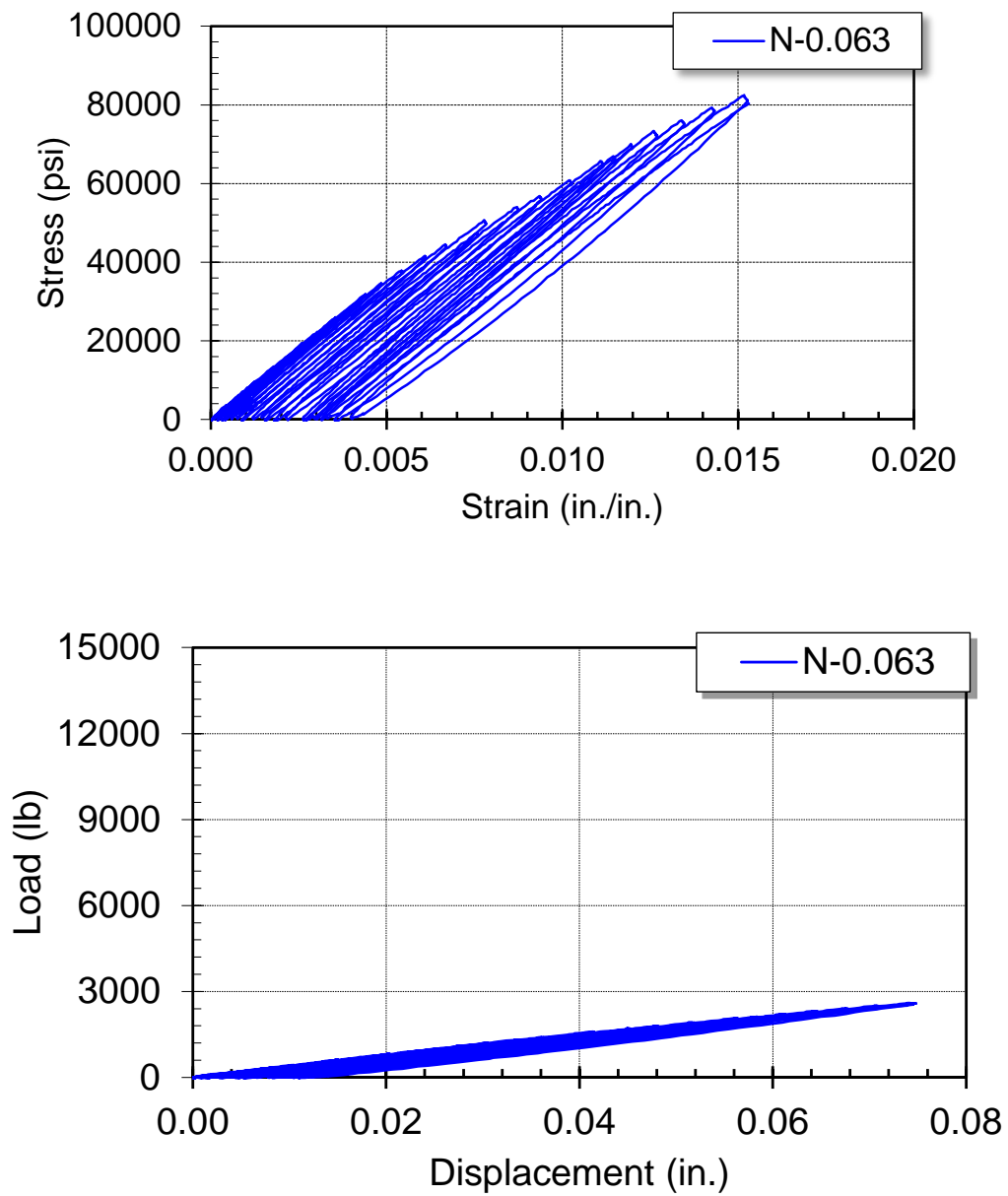


Figure A-2. Load vs. displacement and stress vs. strain responses of 0.063 inch thickness coupon specimen of uni-directional fiber

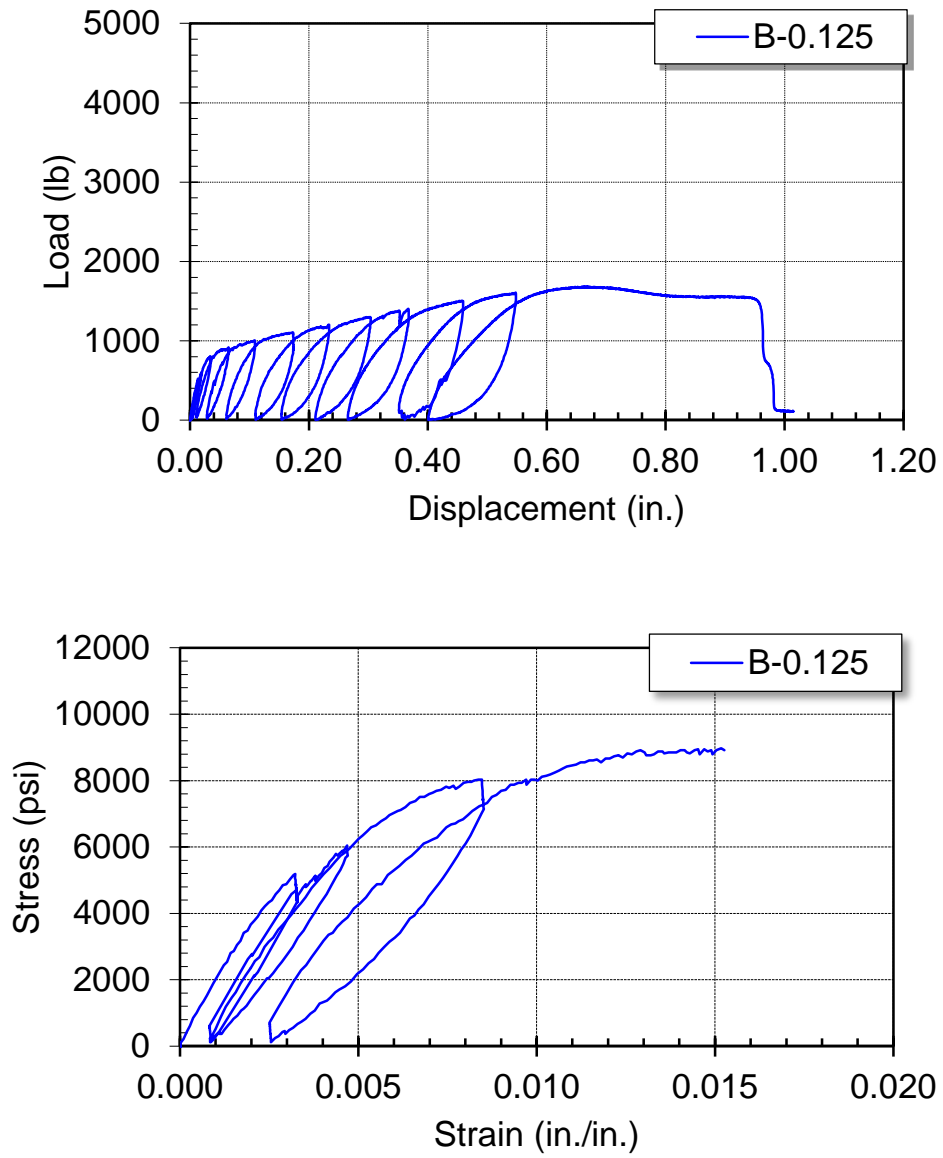


Figure A-3. Load vs. displacement and stress vs. strain responses of 0.125 inch thickness coupon specimen of bi-directional fiber

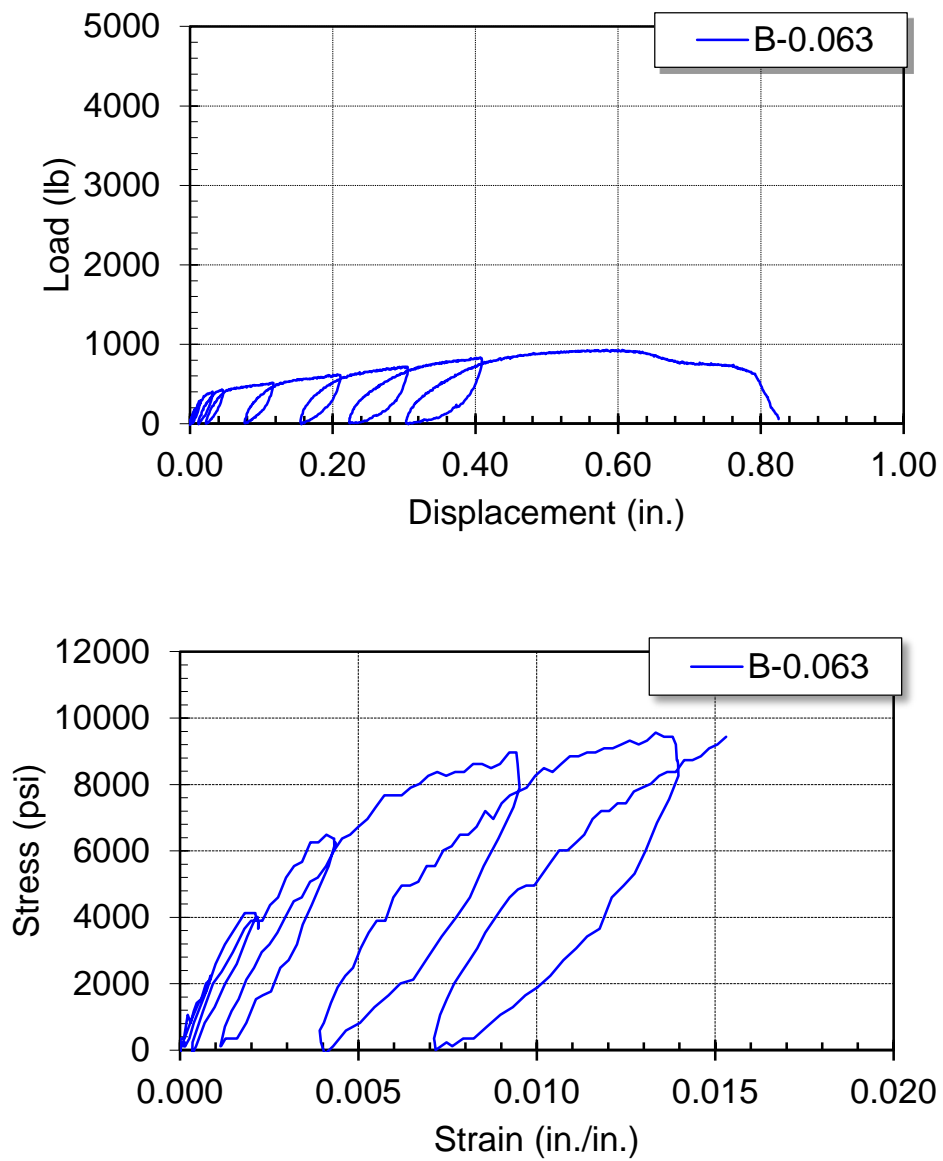
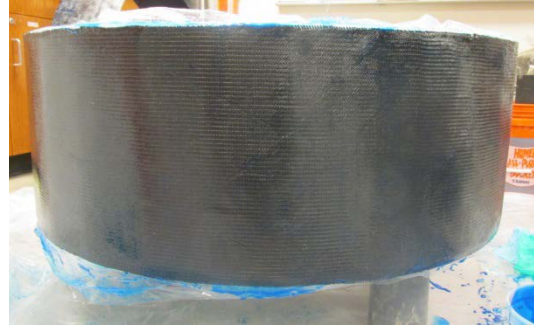


Figure A-4. Load vs. displacement and stress vs. strain responses of 0.125 inch thickness coupon specimen of bi-directional fiber



Filmed Styrofoam



1st CFRP sheet on filmed Styrofoam



Multiple layerup CFRP sheet



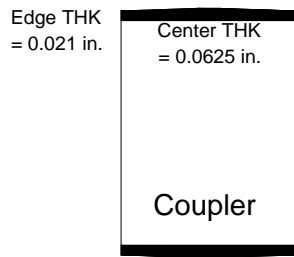
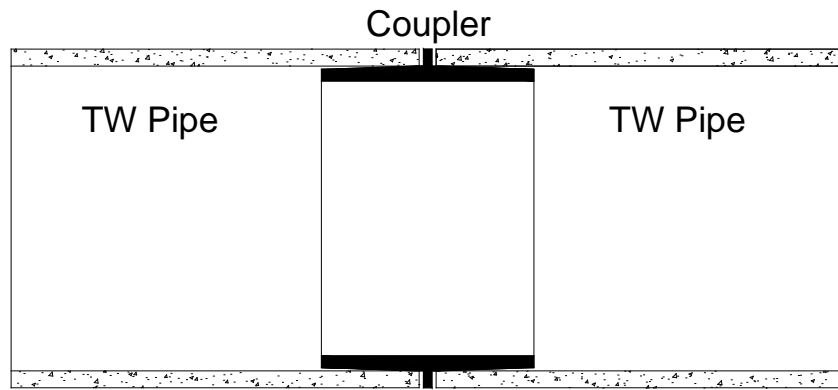
Completed of fabrication



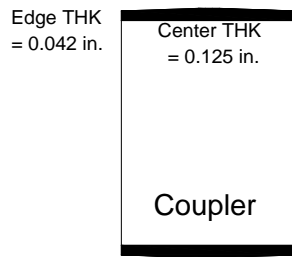
Curing CFRP coupler in ambient temperature



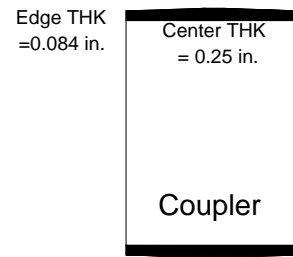
Figure A-5. CFRP coupler fabrication procedure



(a) Case-1 : 0.0625 in.



(b) Case-1 : 0.125 in.



(c) Case-1 : 0.25 in.

Figure A-6. Coupler Thickness on layers

Appendix B

Results of Finite Element Analyses

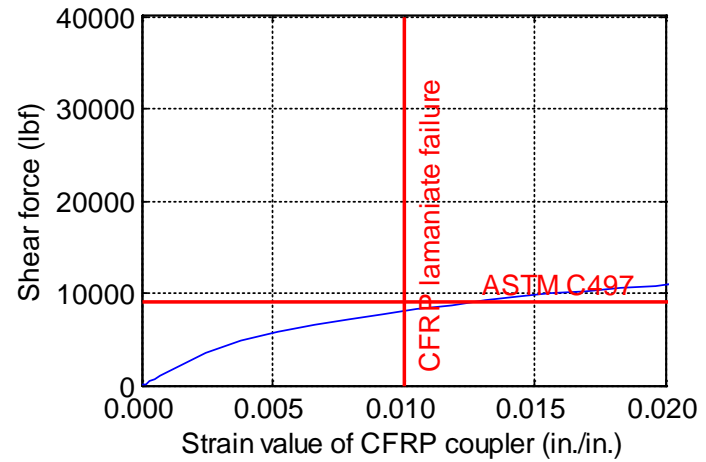
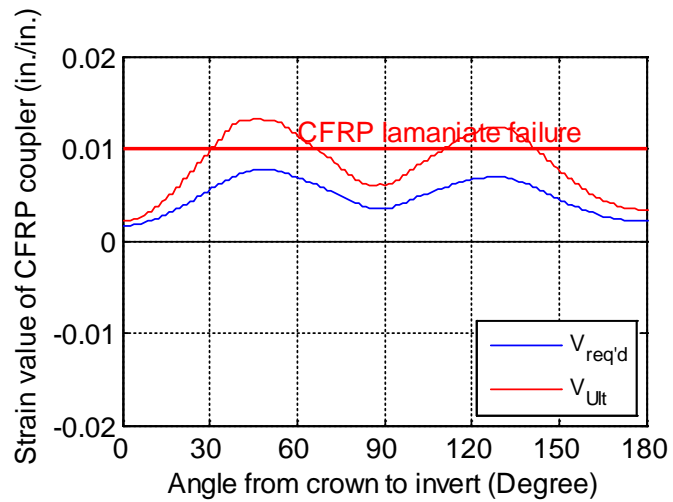
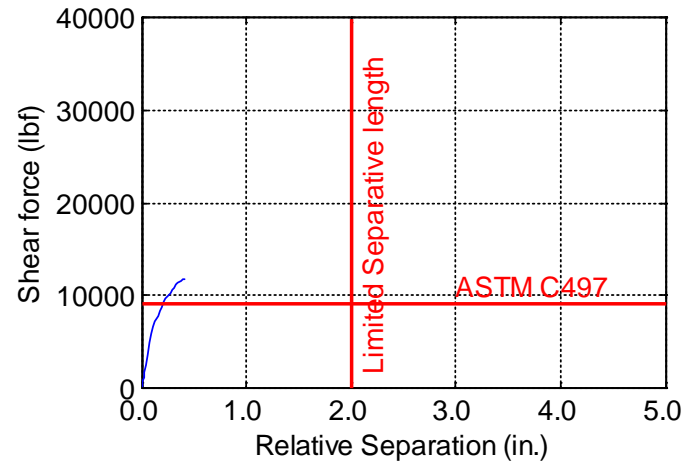
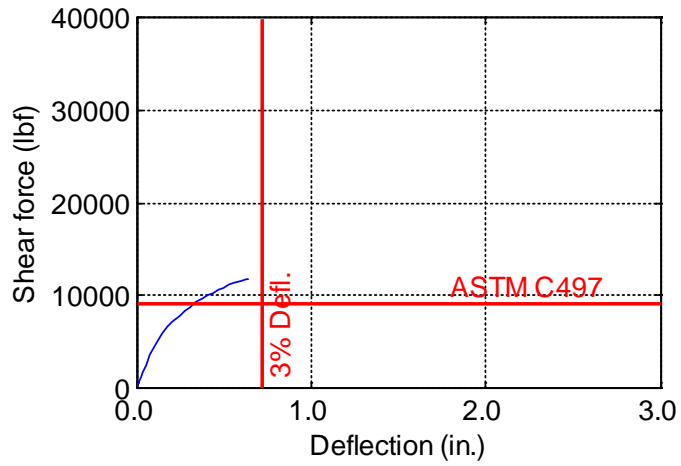


Figure B-1. TW-024-06-0.125

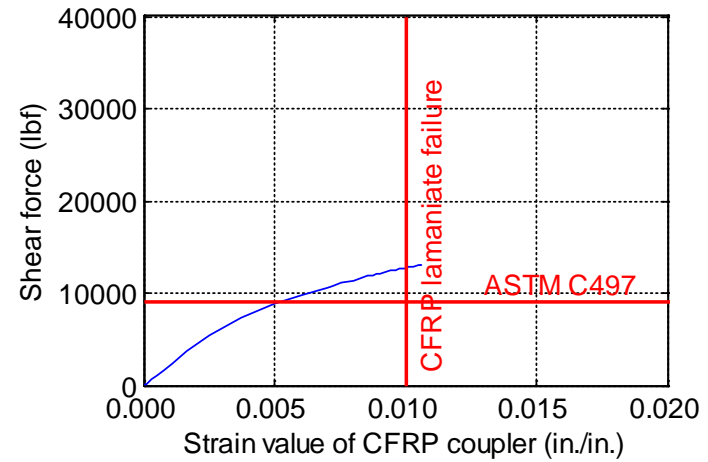
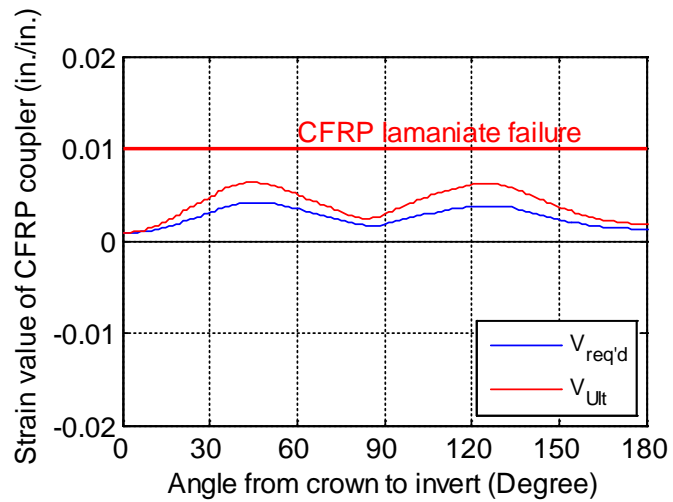
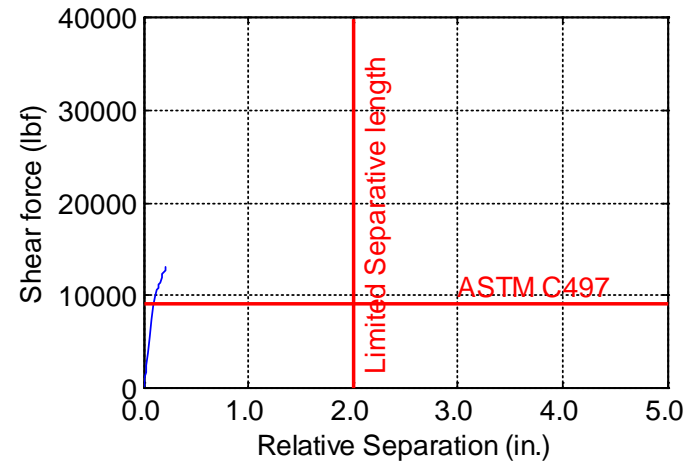
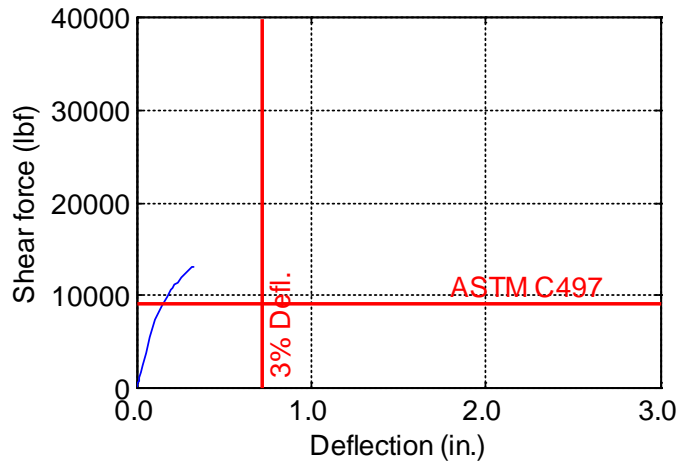


Figure B-2. TW-024-06-0.1875

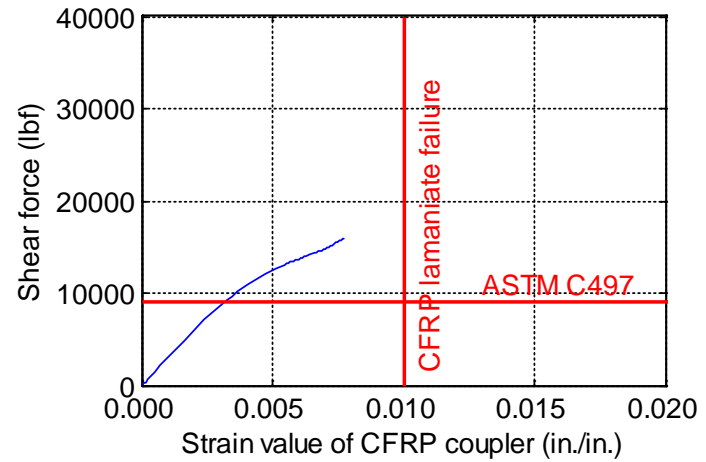
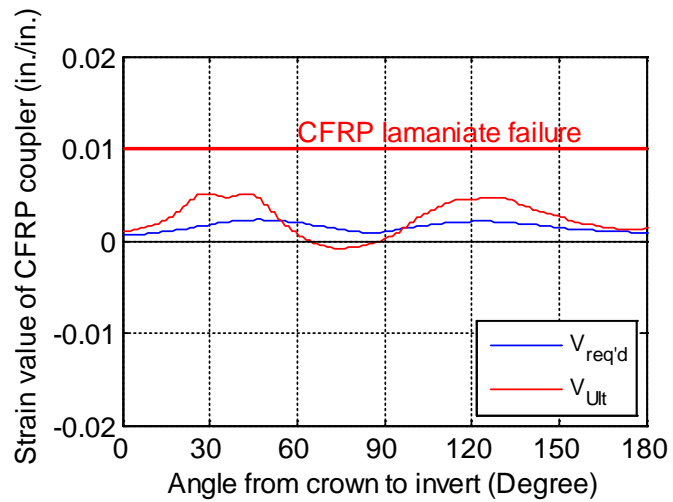
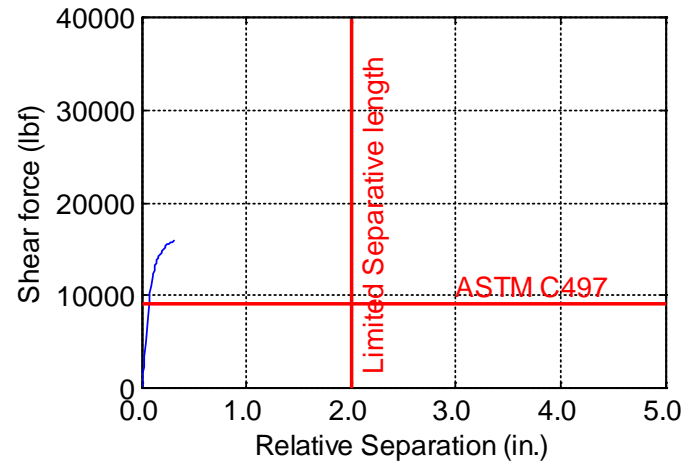
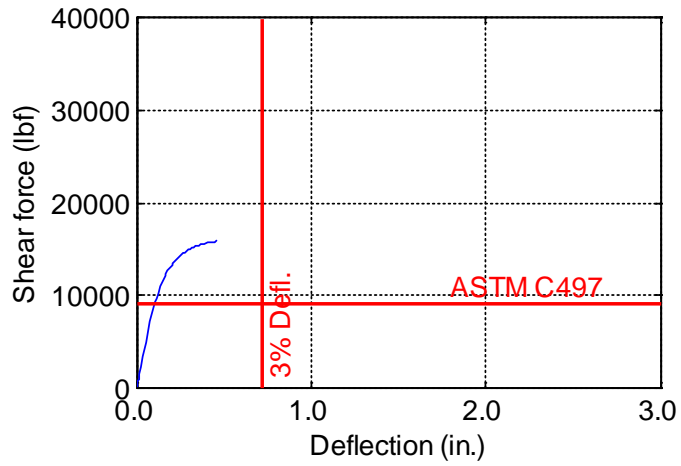


Figure B-3. TW-024-06-0.25

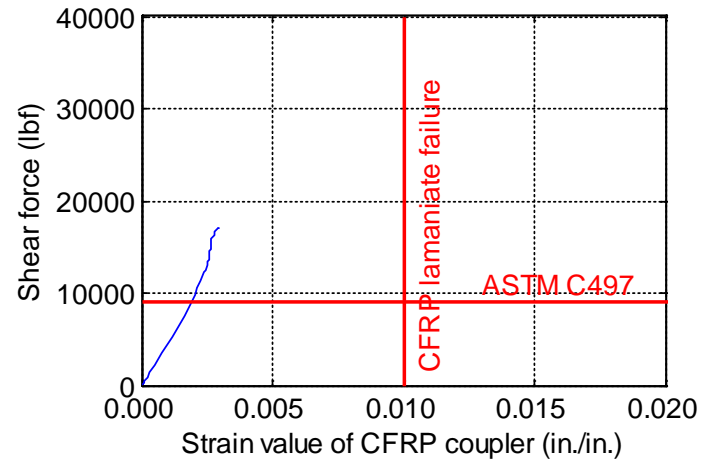
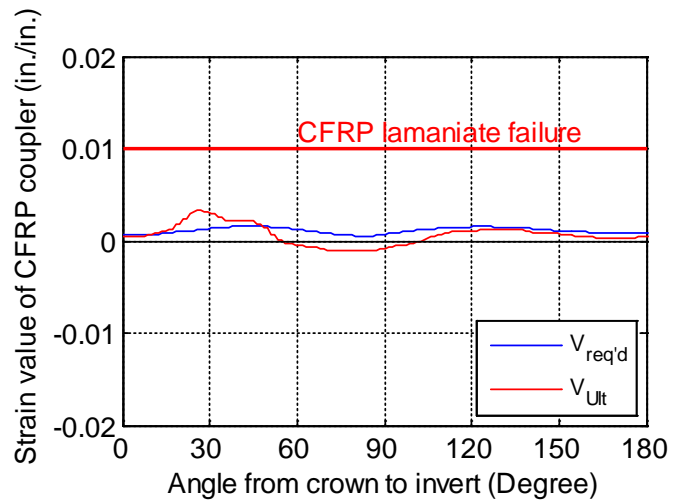
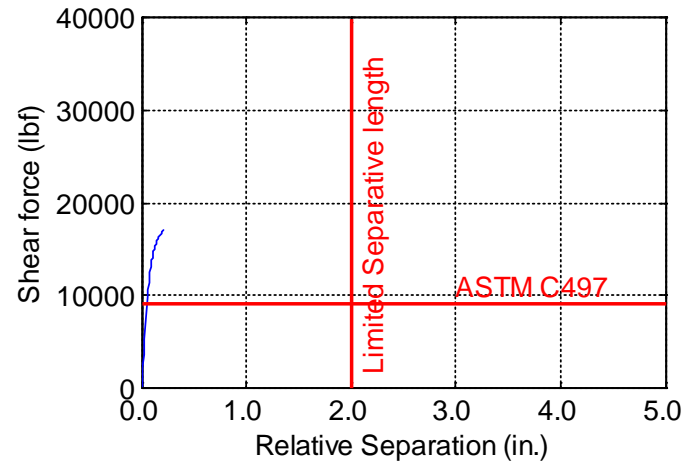
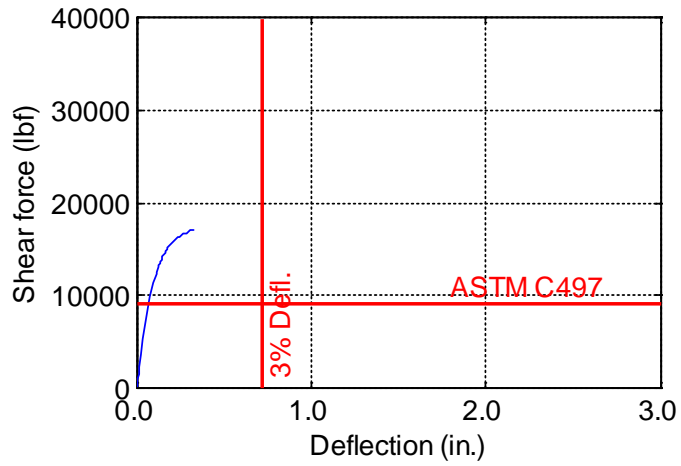


Figure B-4. TW-024-06-0.375

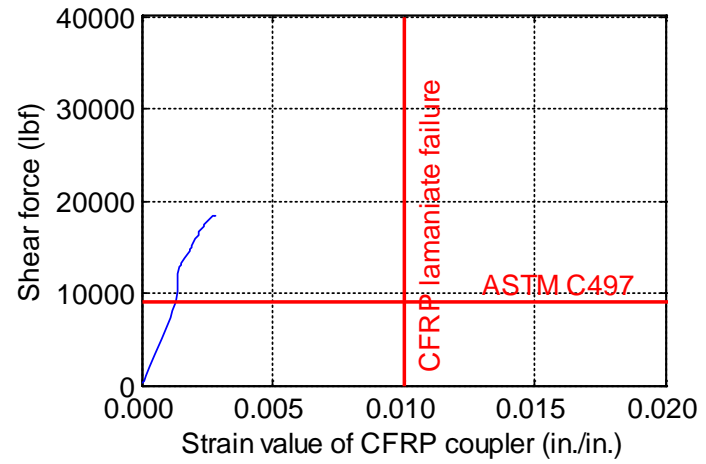
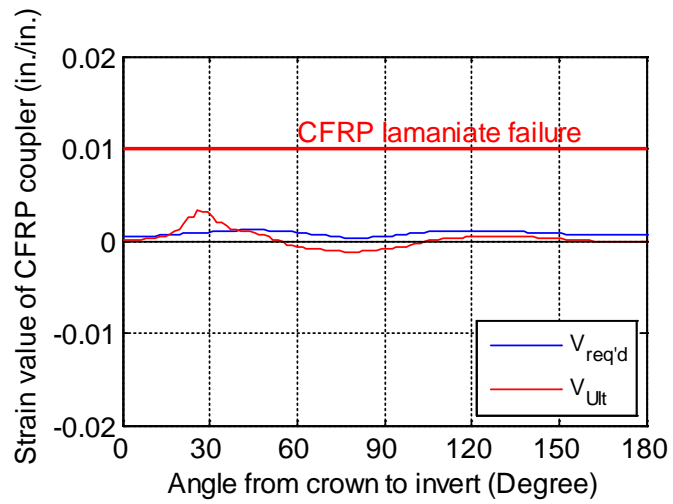
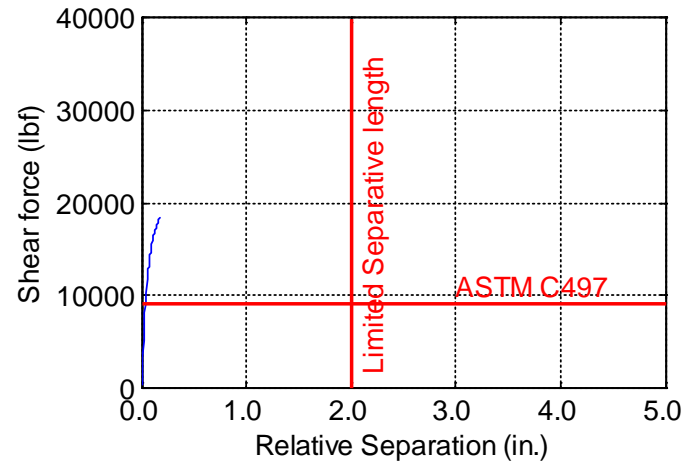
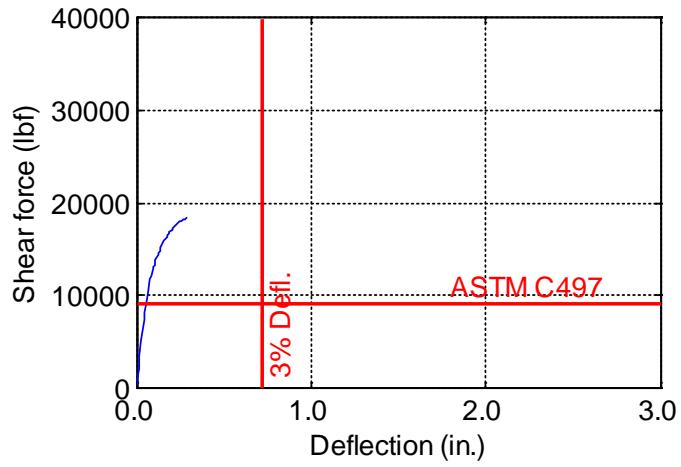


Figure B-5. TW-024-06-0.5

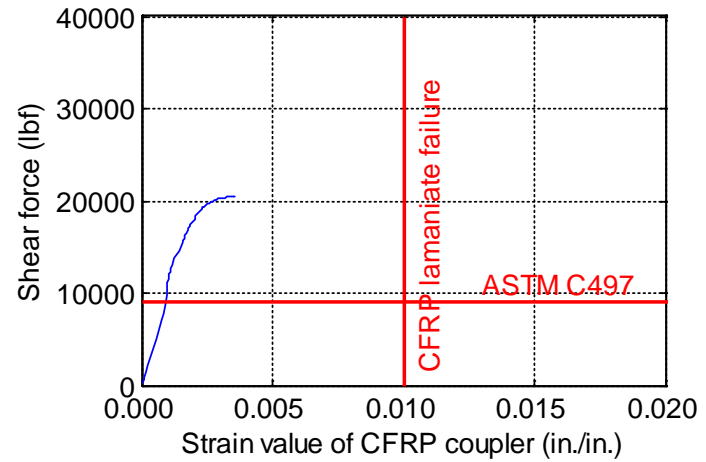
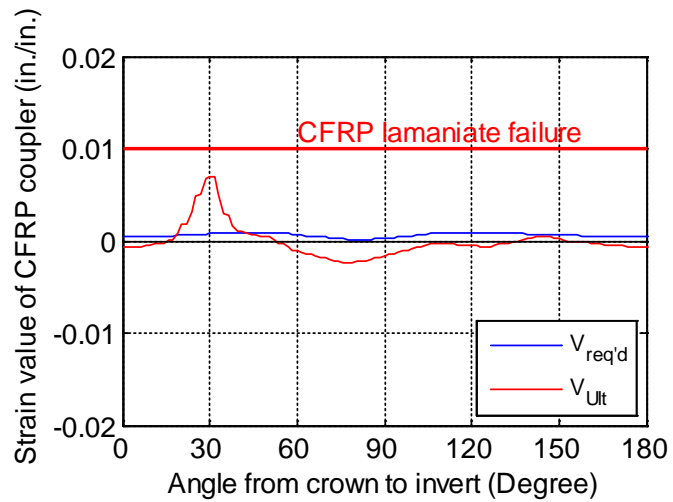
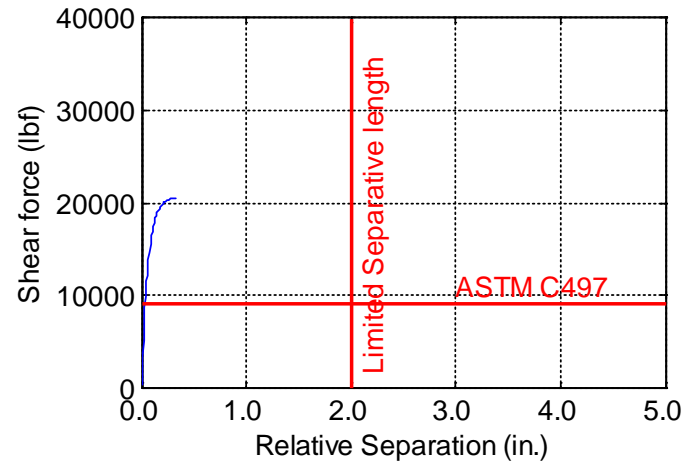
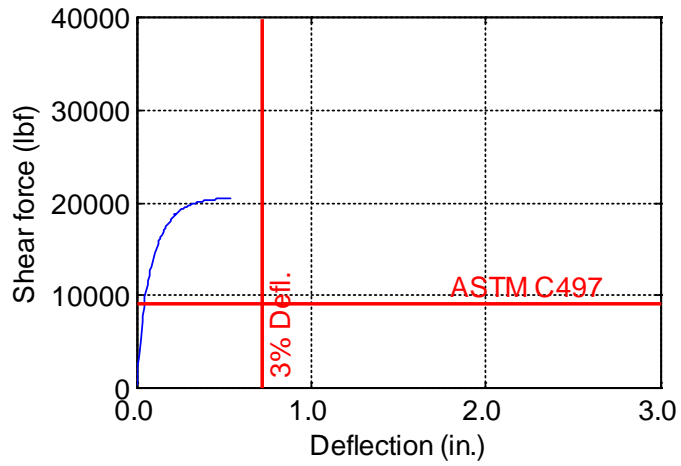


Figure B-6. TW-024-06-0.625

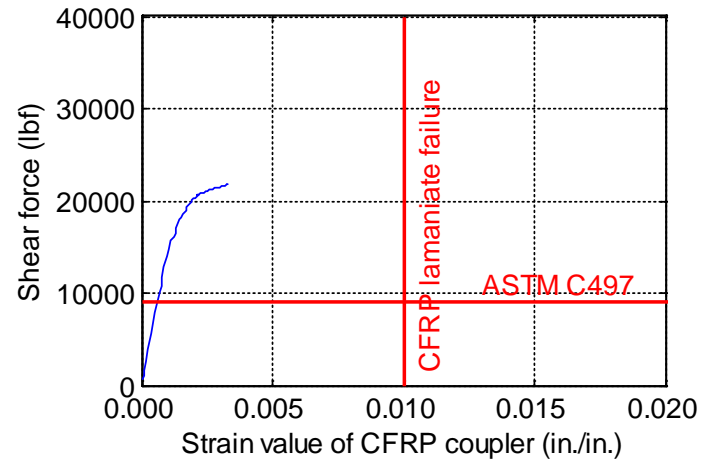
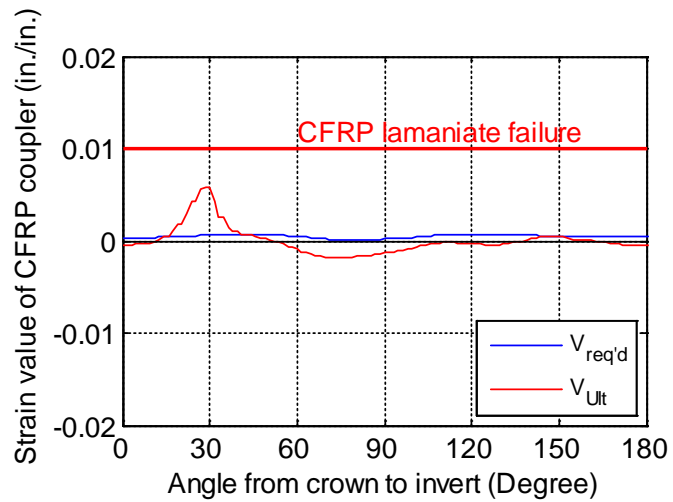
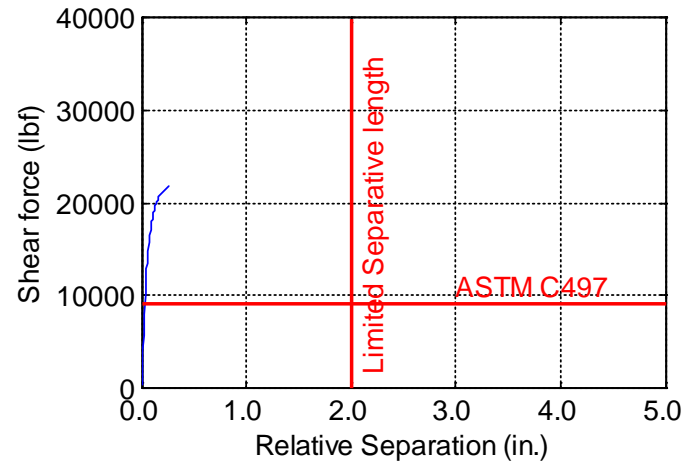
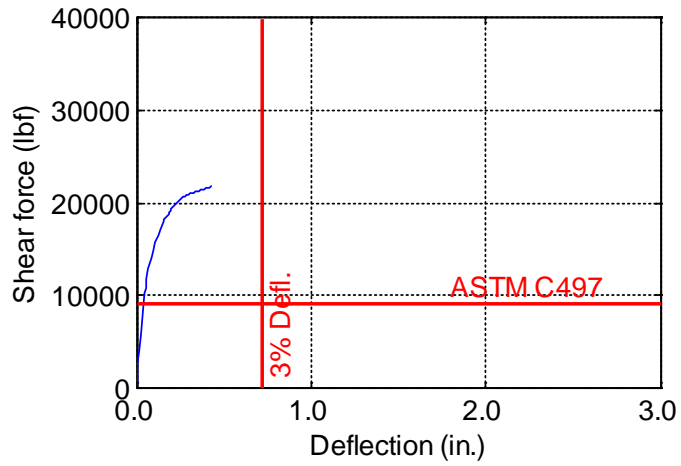


Figure B-7. TW-024-06-0.75

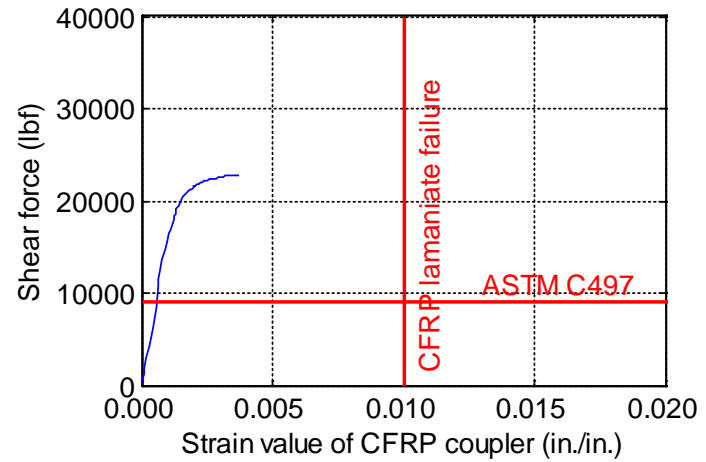
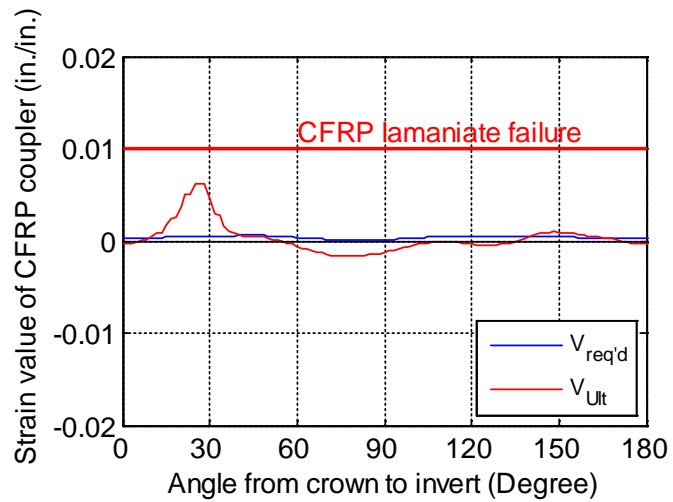
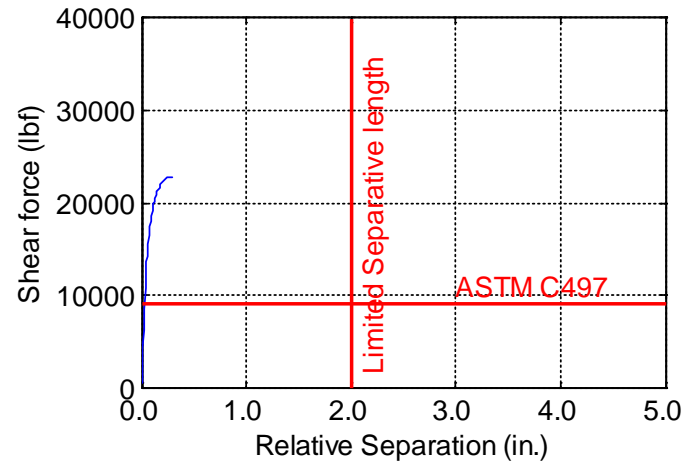
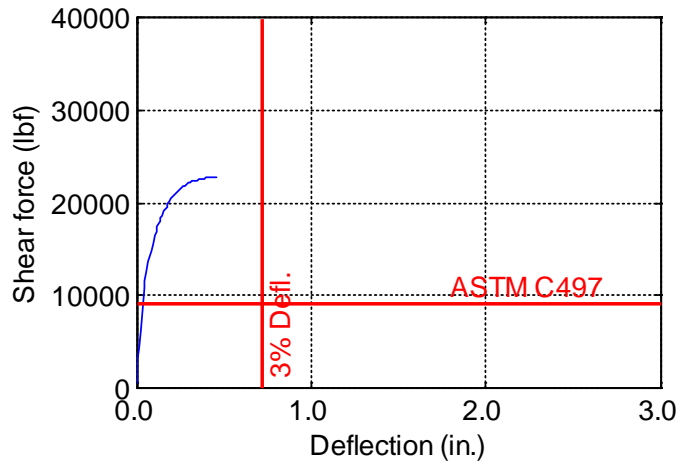


Figure B-8. TW-024-06-0.875

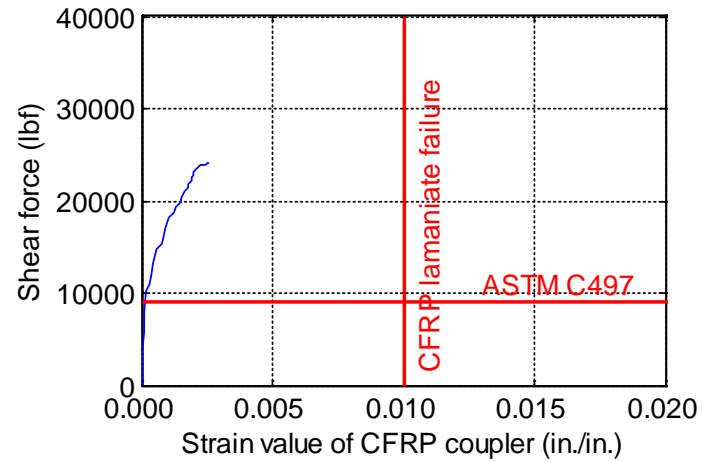
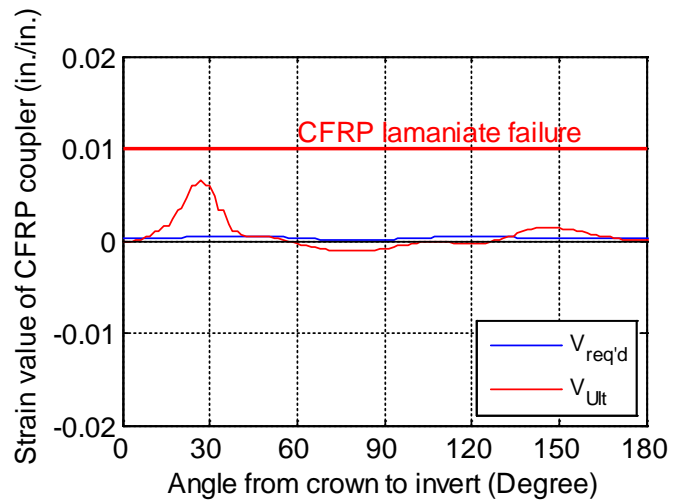
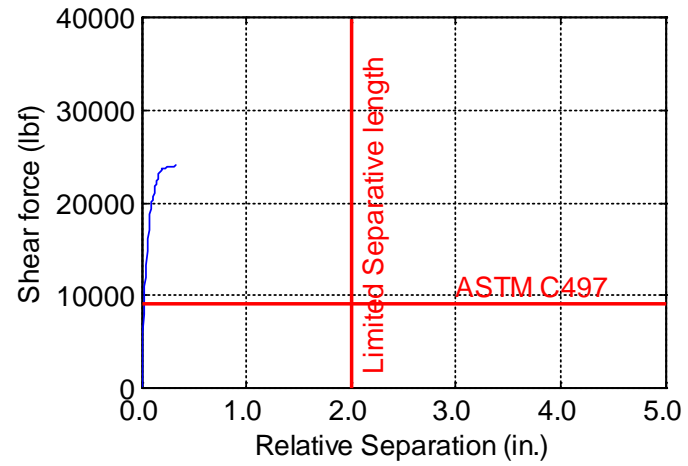
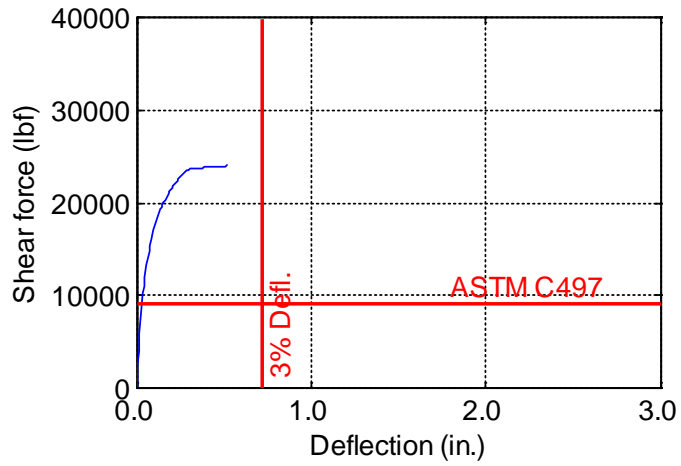


Figure B-9. TW-024-06-1.0

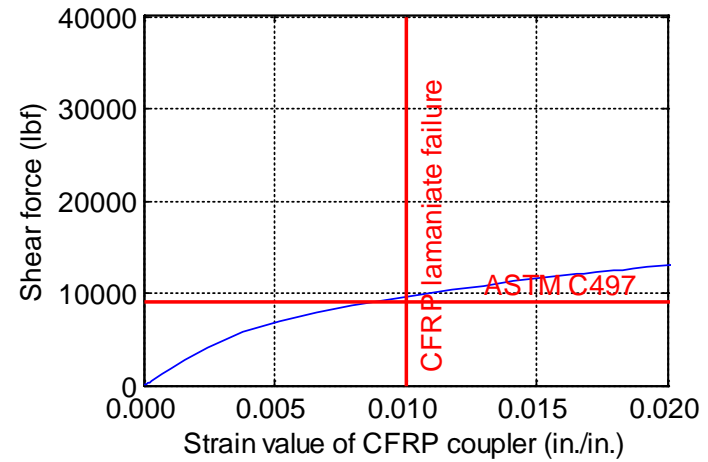
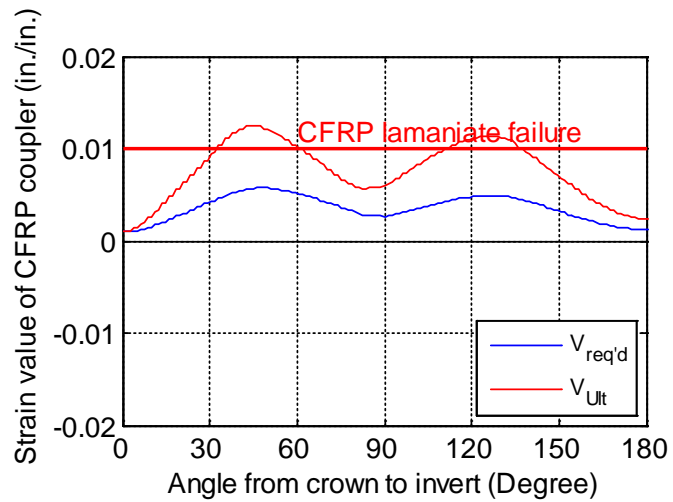
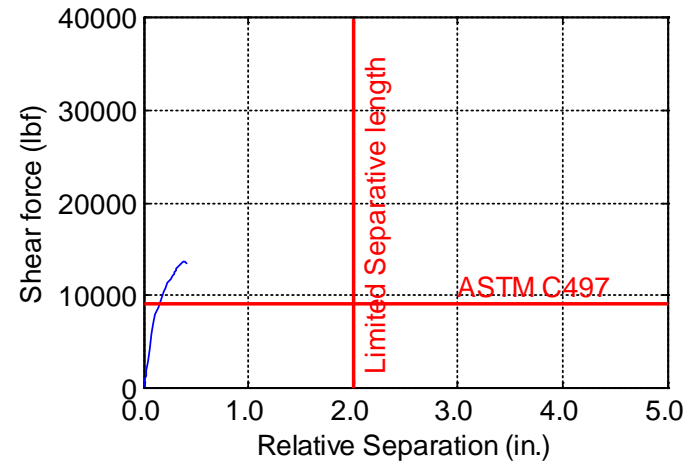
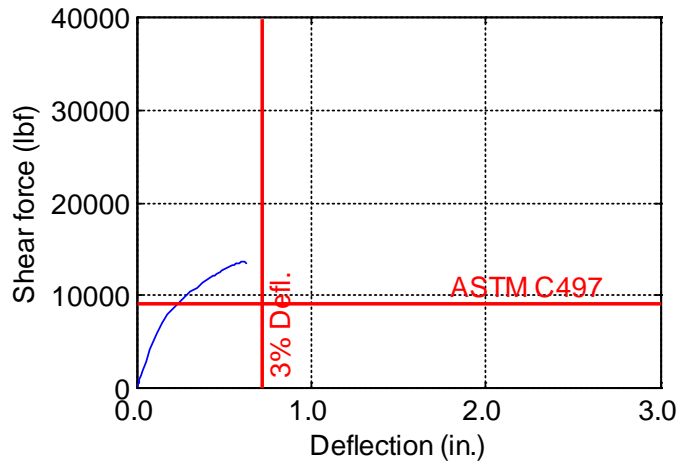


Figure B-10. TW-024-09-0.125

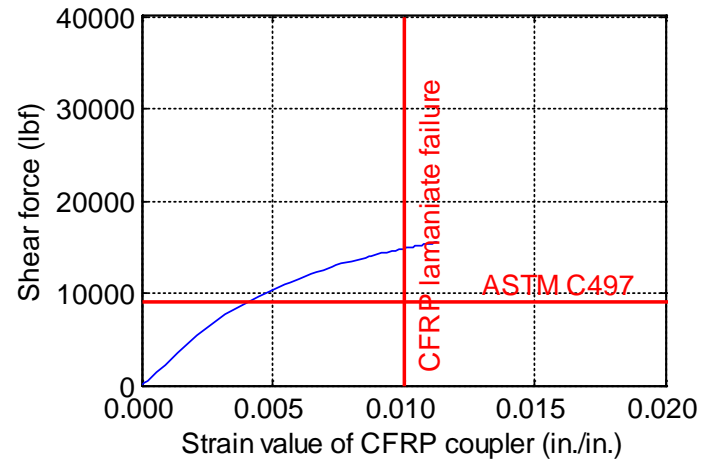
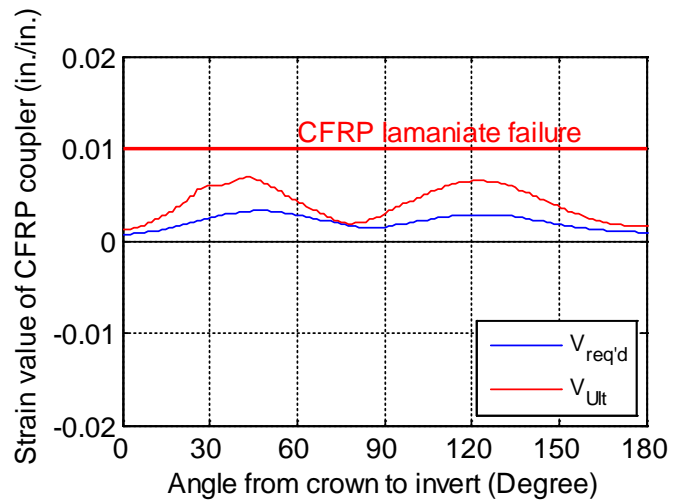
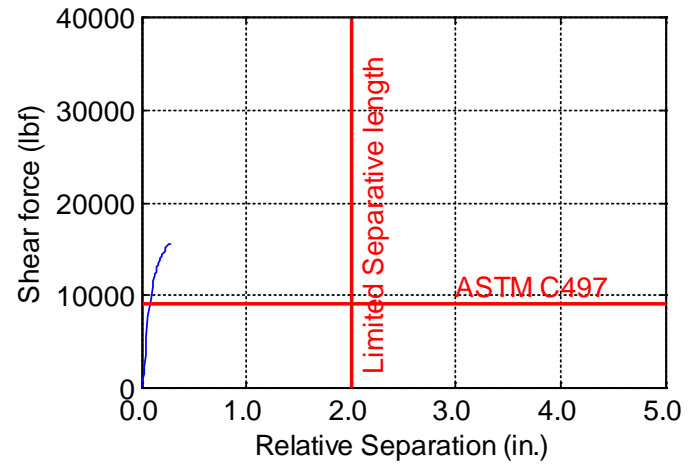
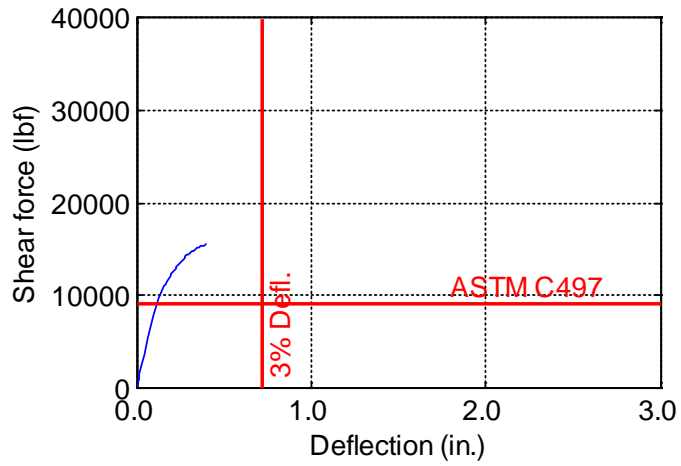


Figure B-11. TW-024-09-0.1875

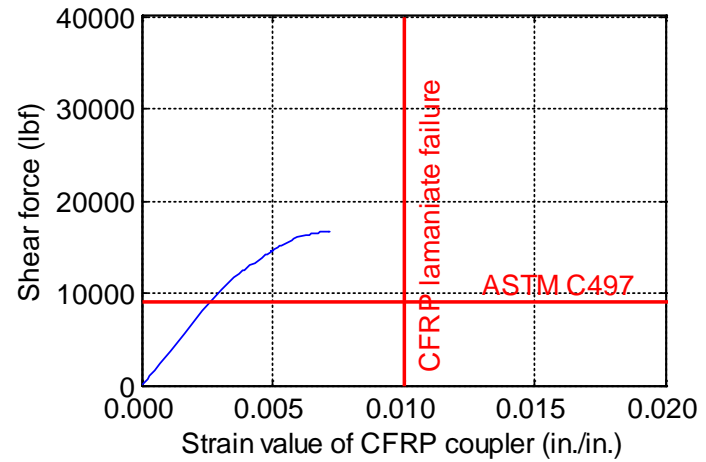
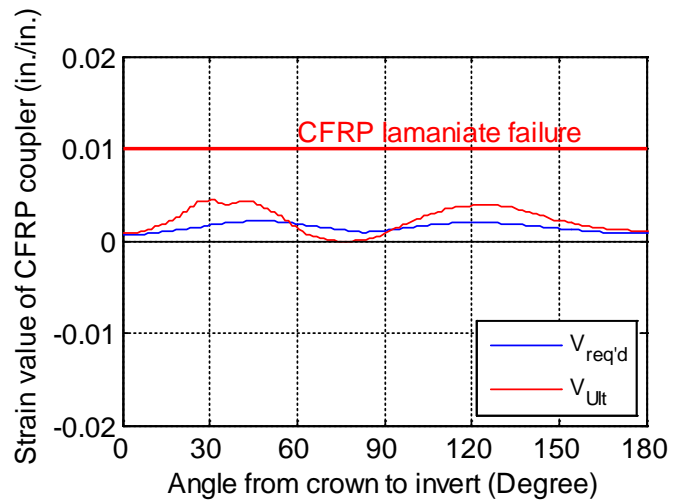
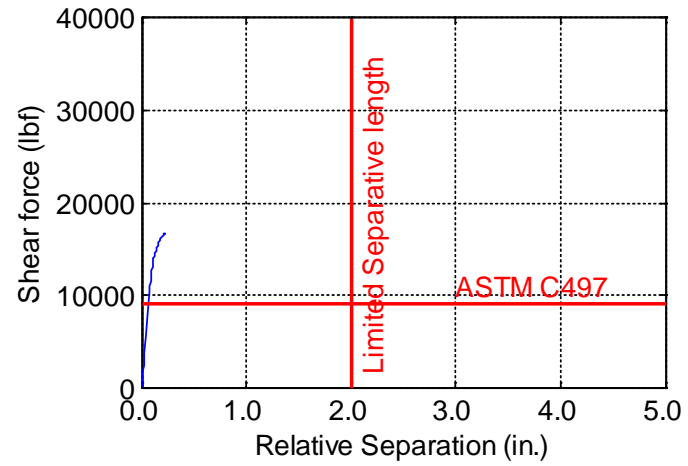
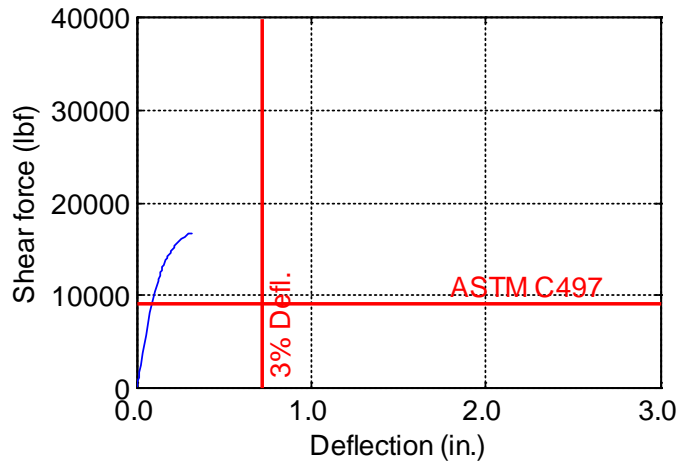


Figure B-12. TW-024-09-0.25

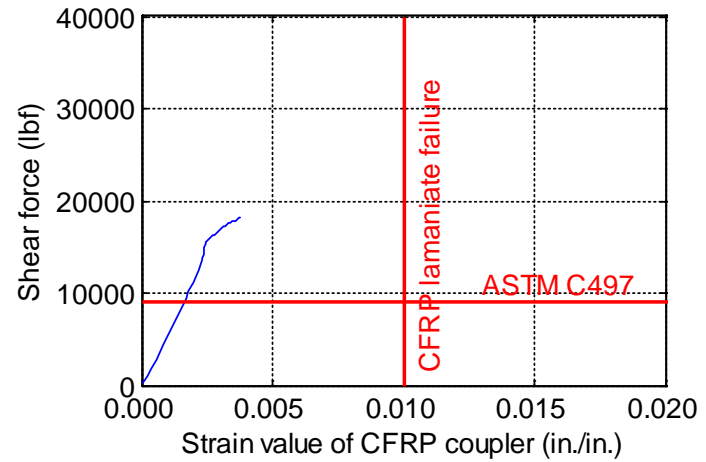
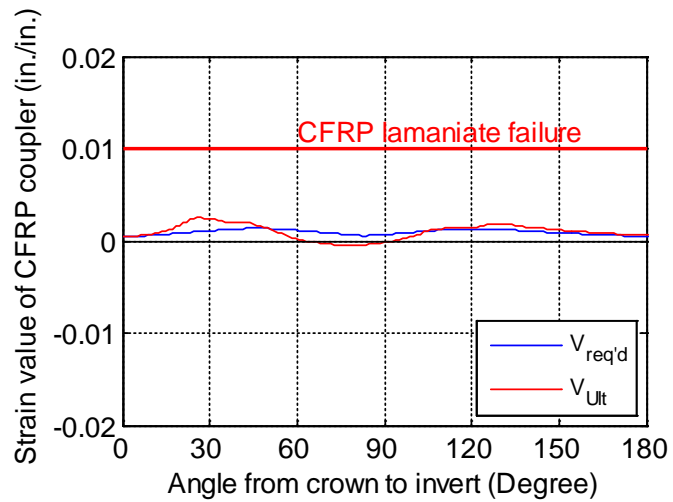
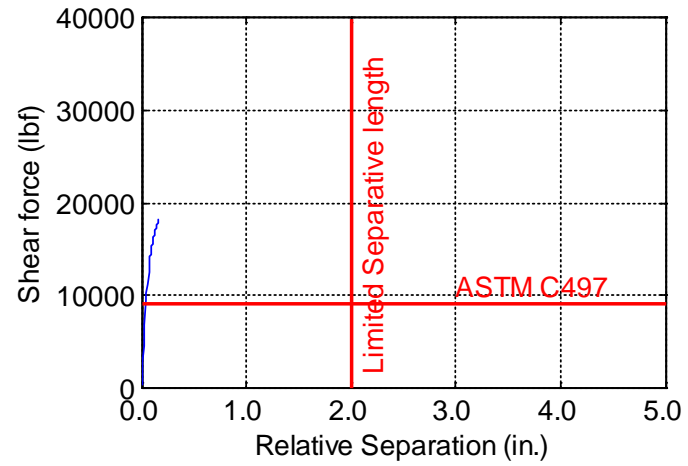
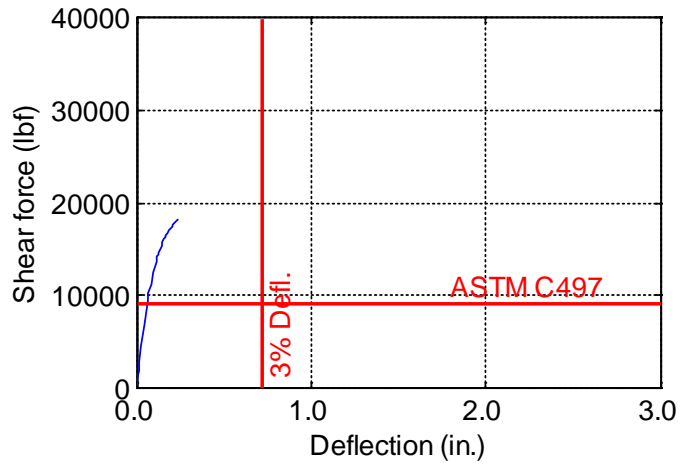


Figure B-13. TW-024-09-0.375

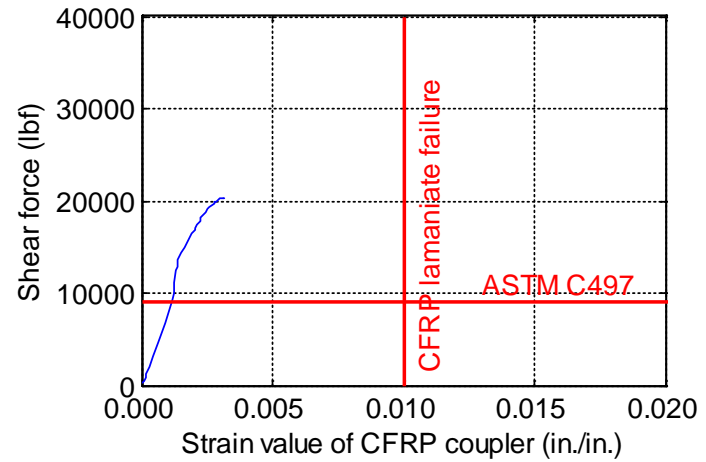
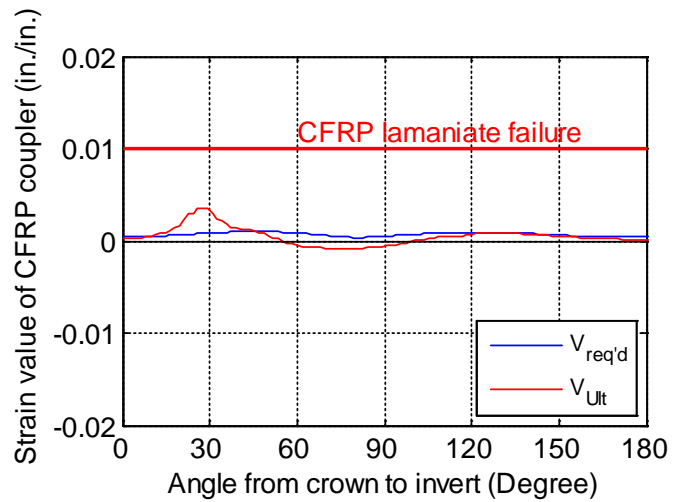
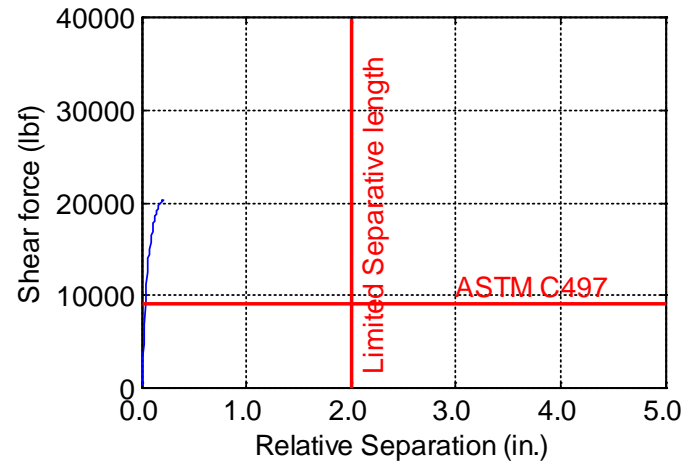
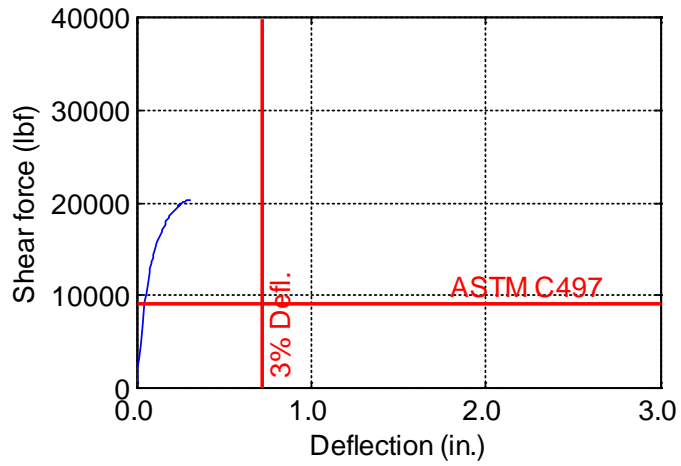


Figure B-14. TW-024-09-0.5

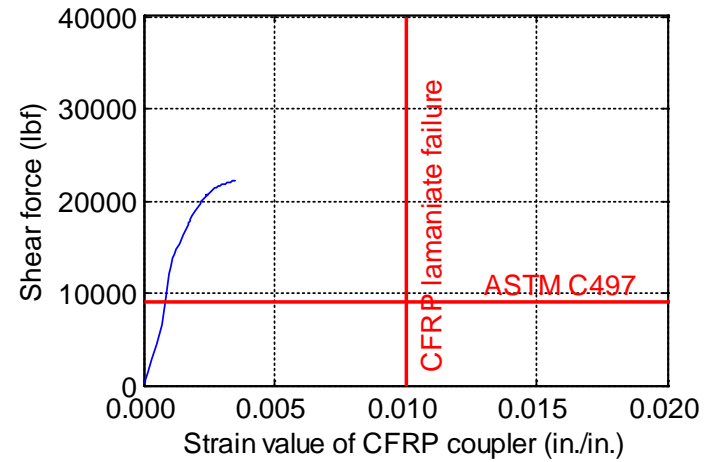
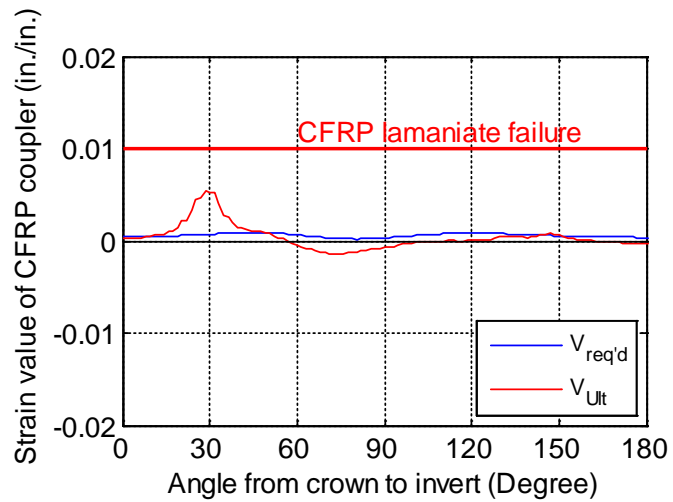
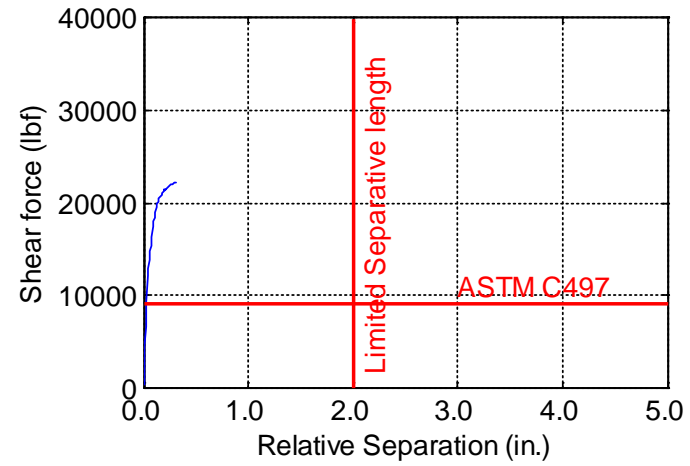
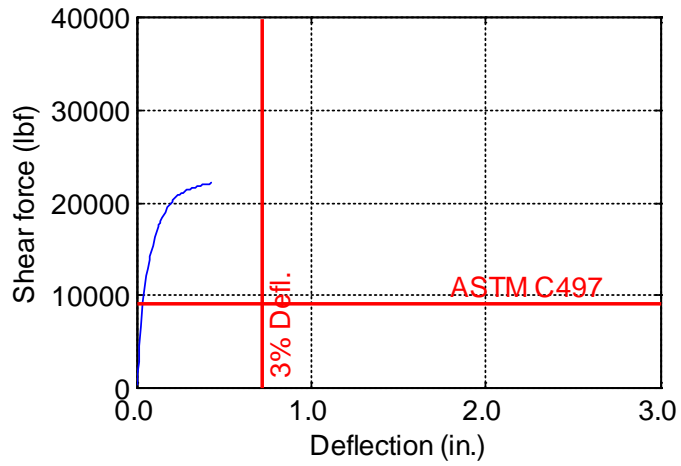


Figure B-15. TW-024-09-0.625

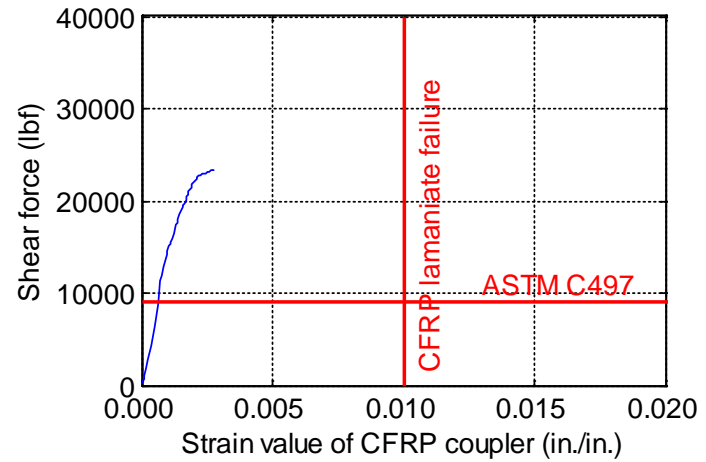
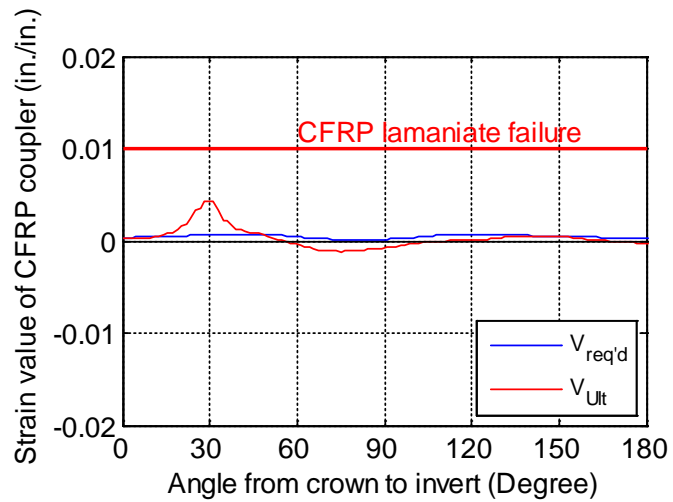
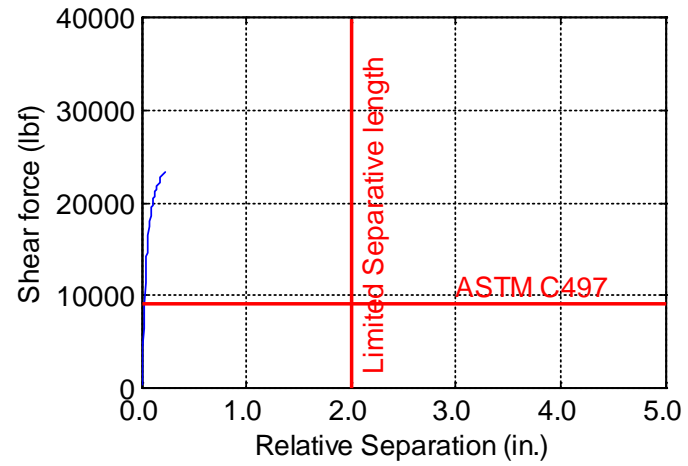
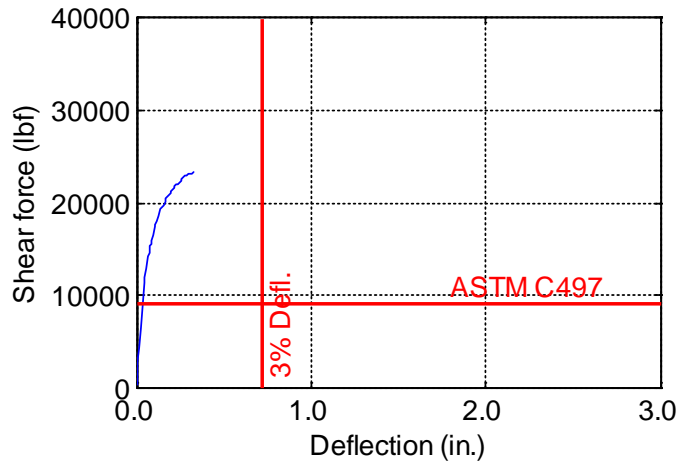


Figure B-16. TW-024-09-0.75

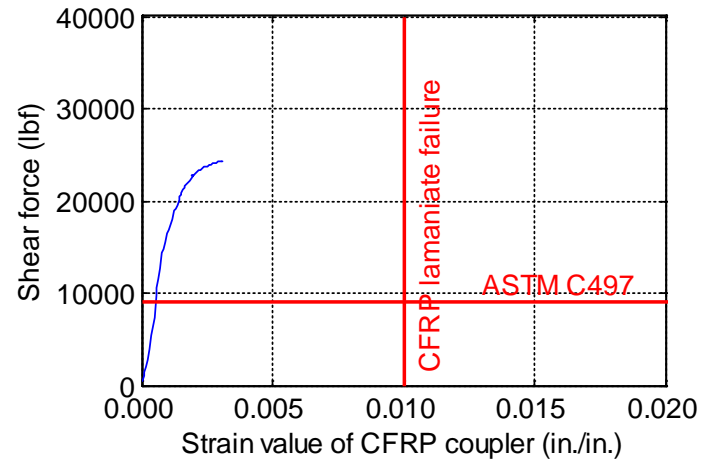
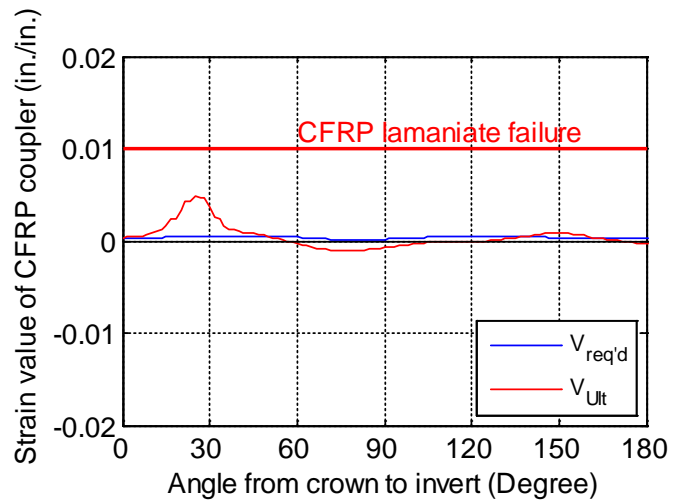
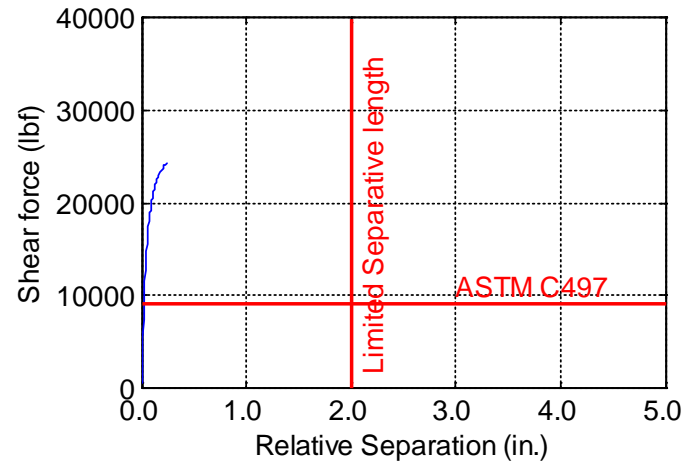
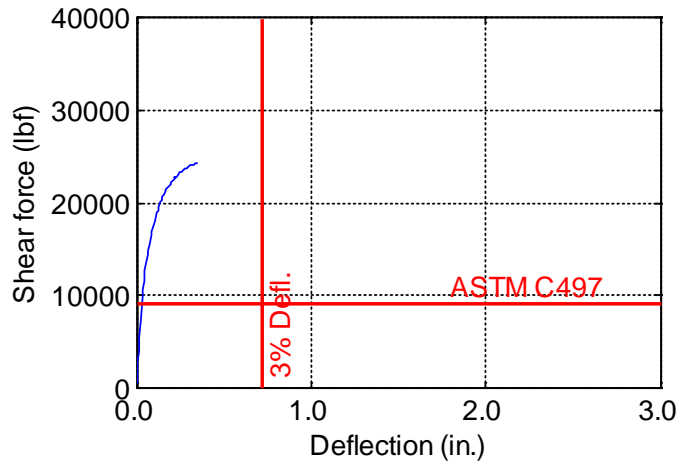


Figure B-17. TW-024-09-0.875

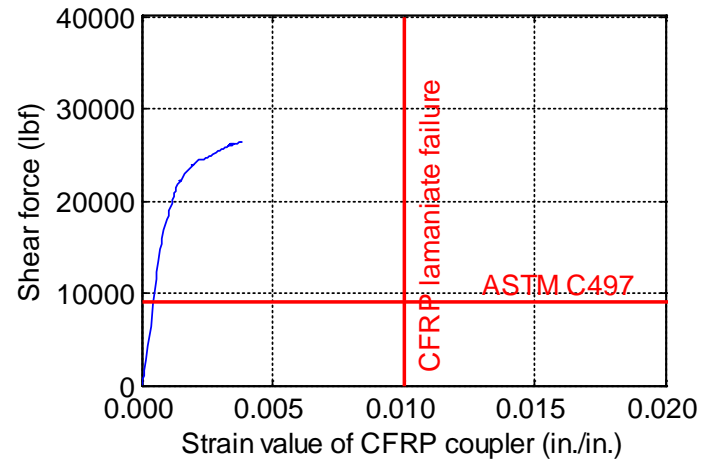
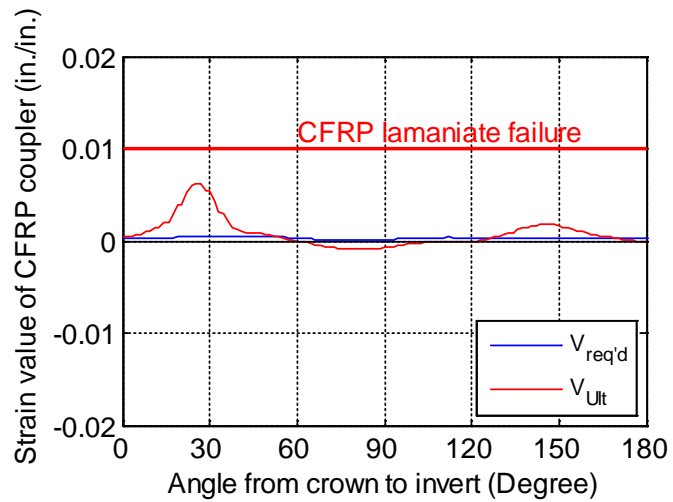
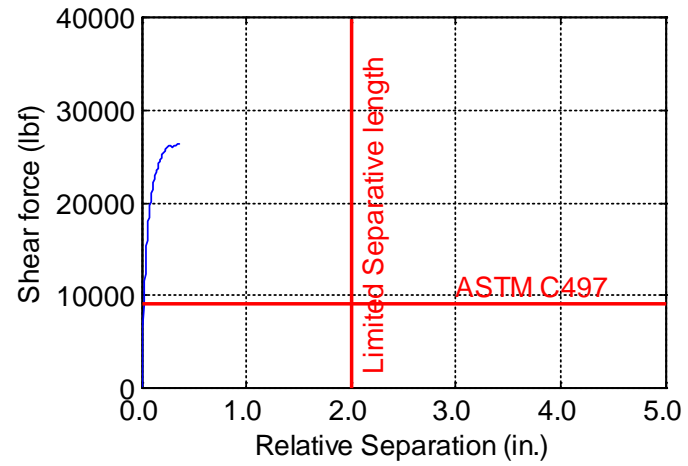
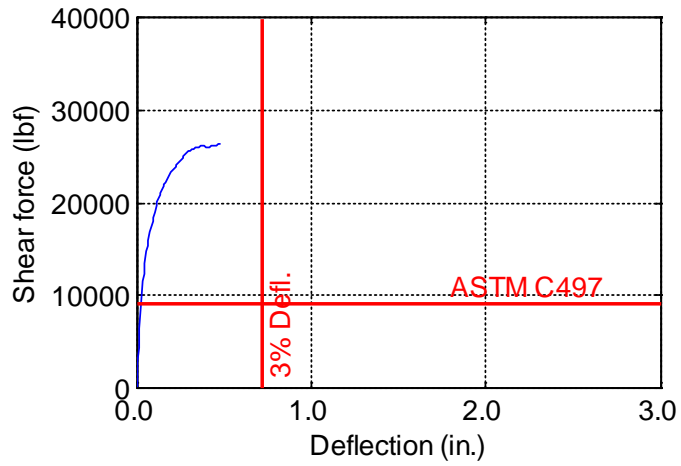


Figure B-18. TW-024-09-1.0

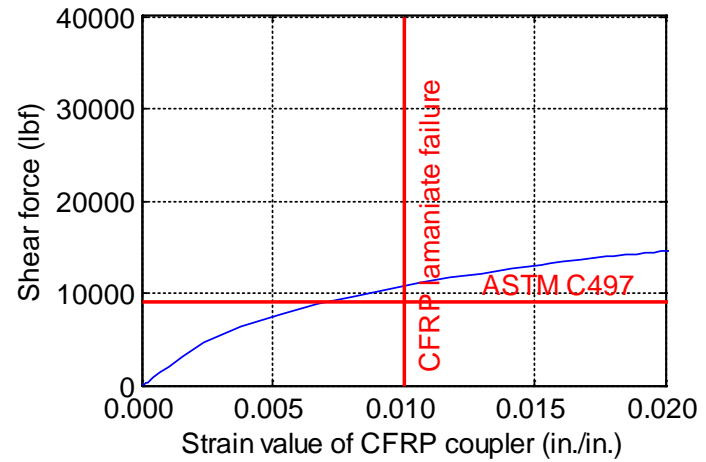
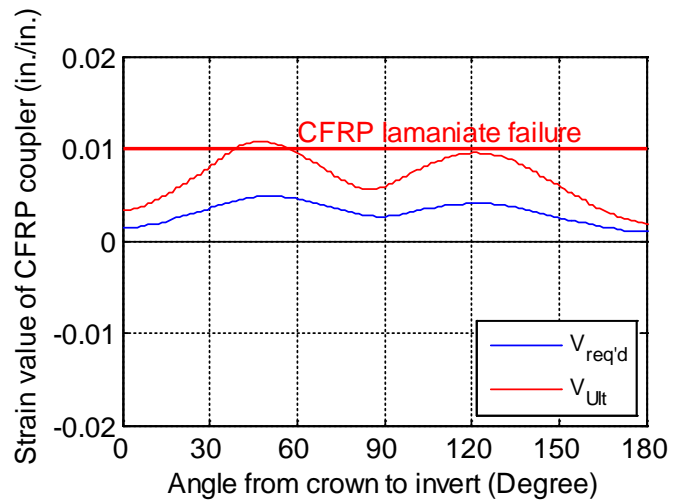
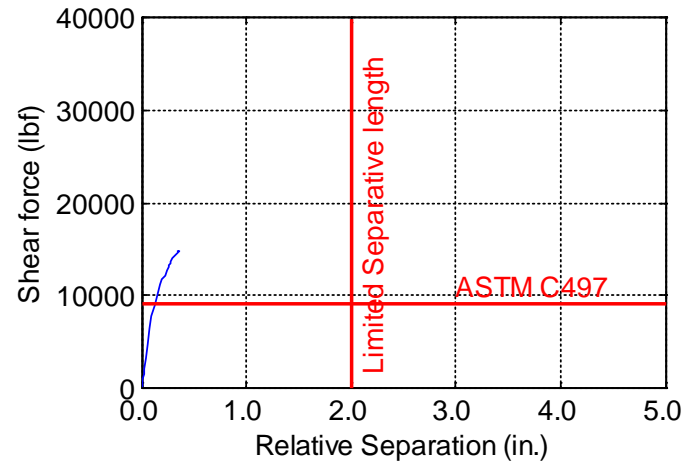
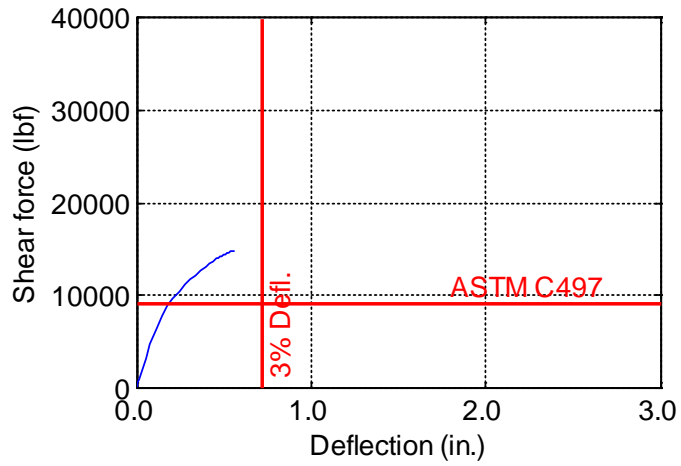


Figure B-19. TW-024-12-0.125

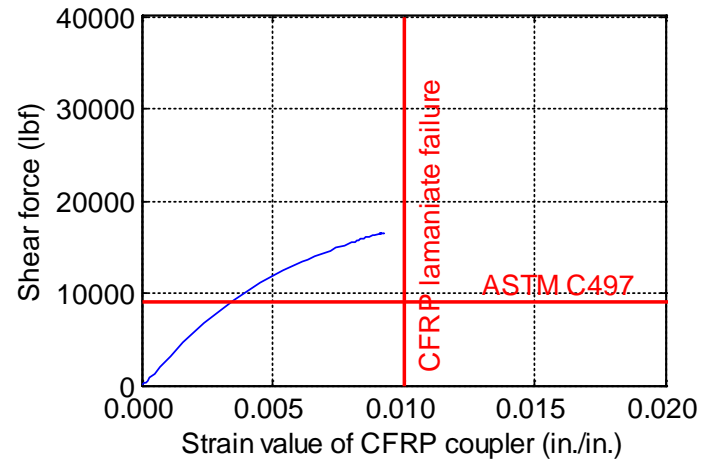
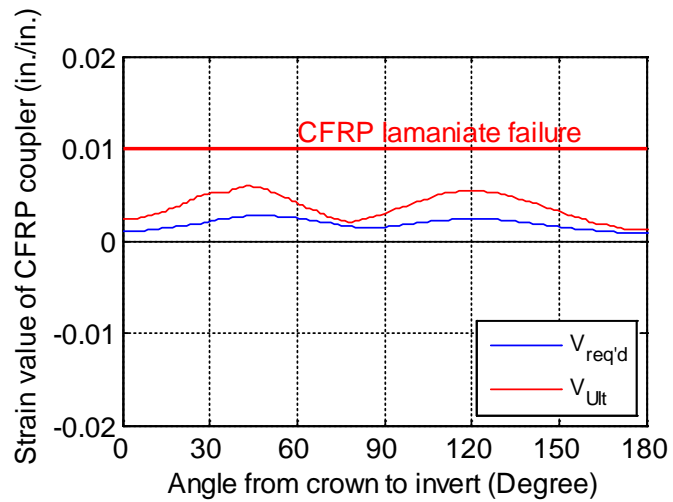
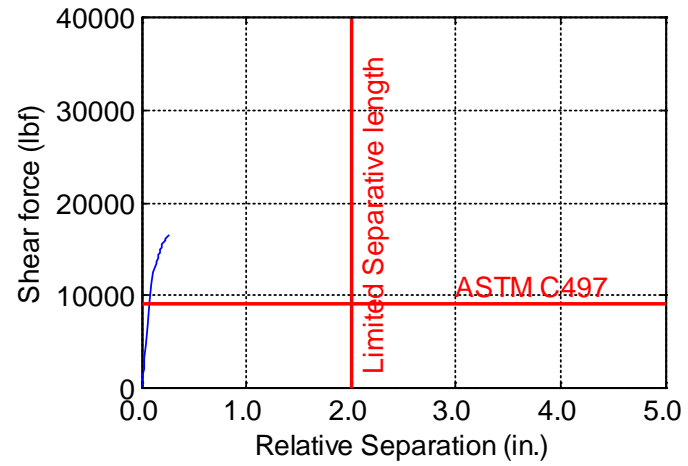
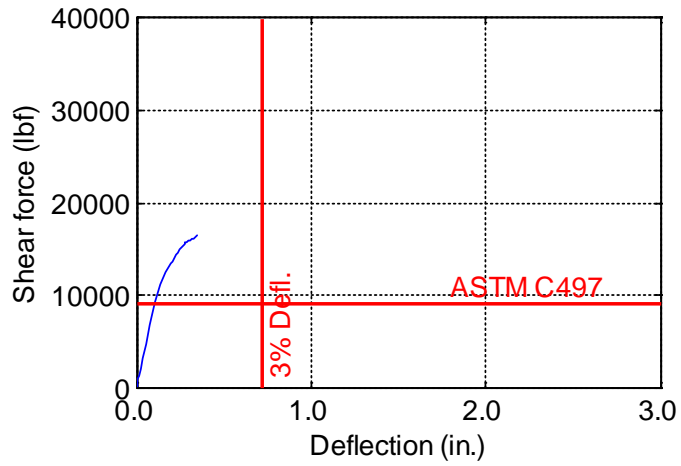


Figure B-20. TW-024-12-0.1875

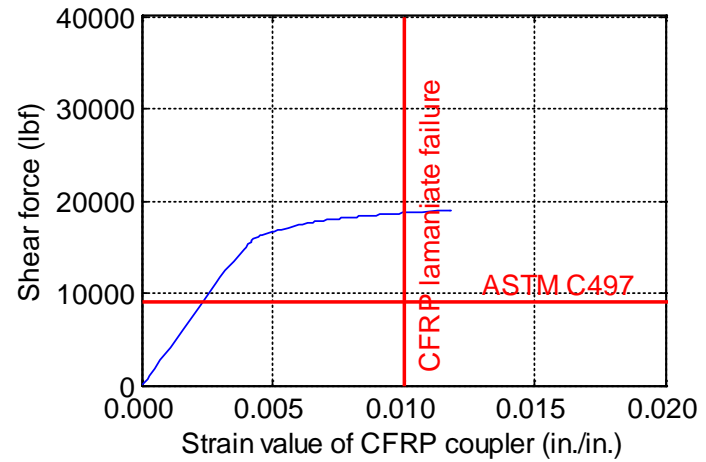
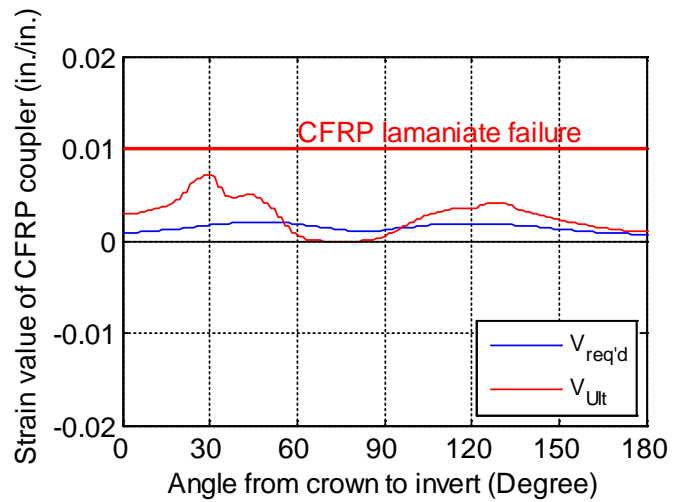
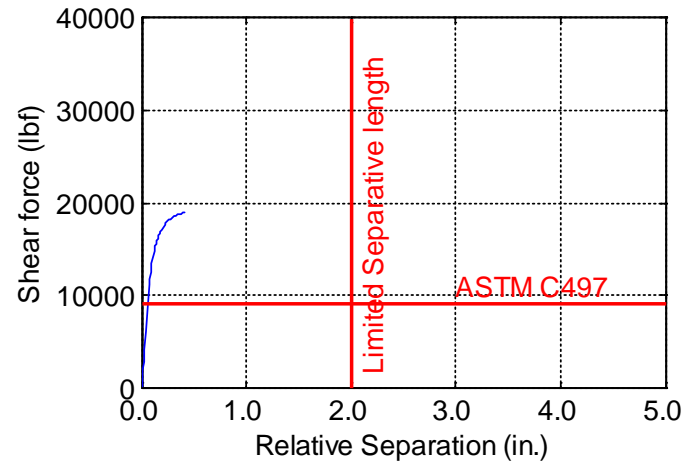
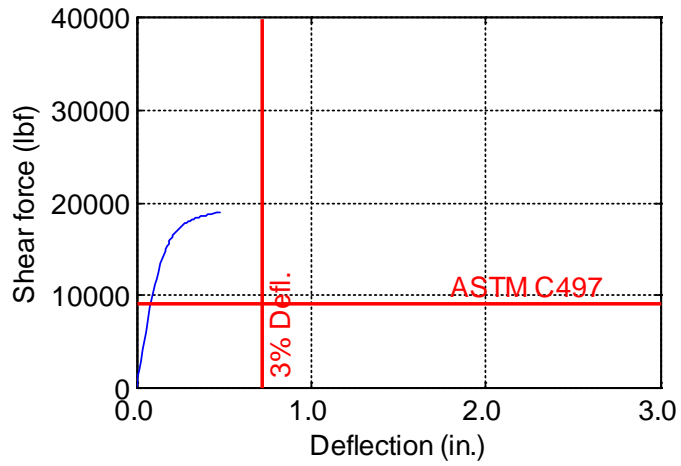


Figure B-21. TW-024-12-0.25

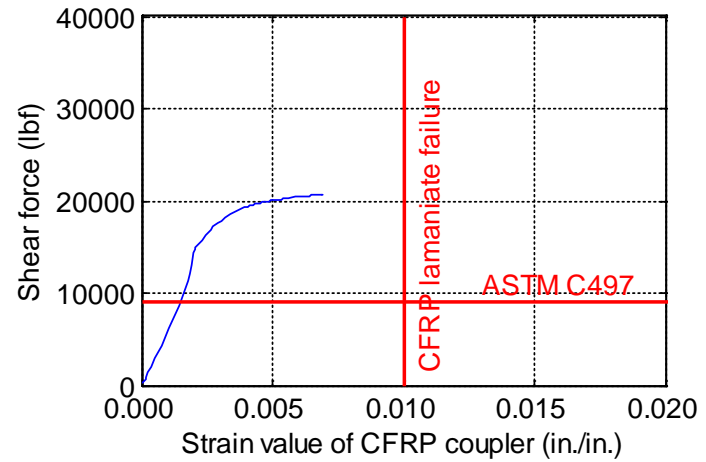
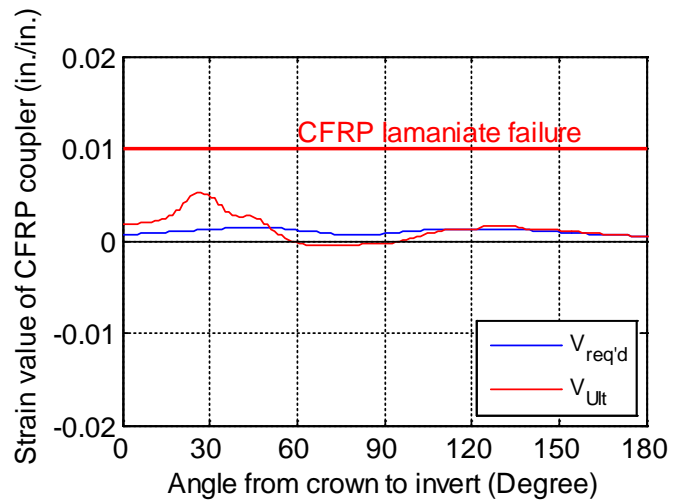
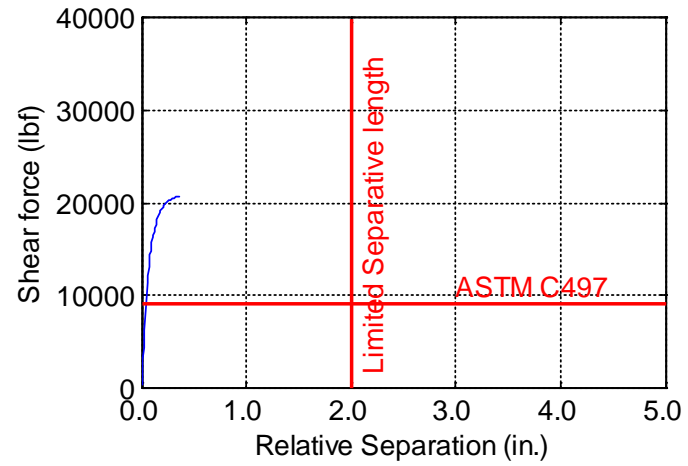
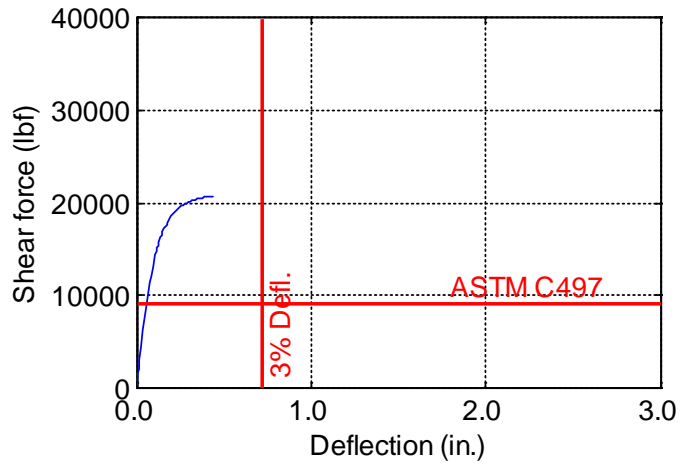


Figure B-22. TW-024-12-0.375

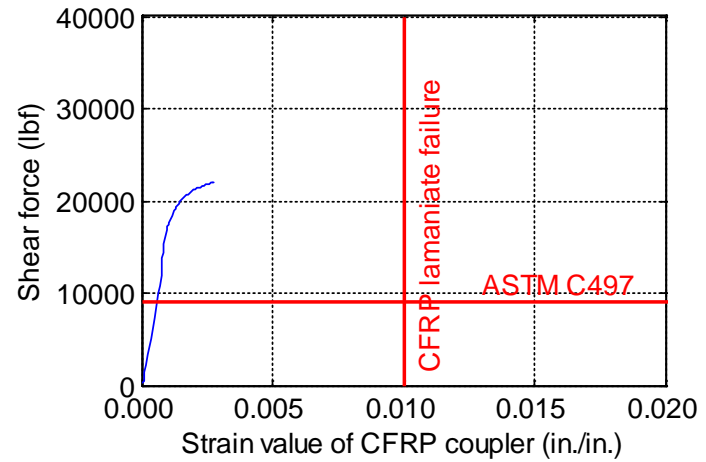
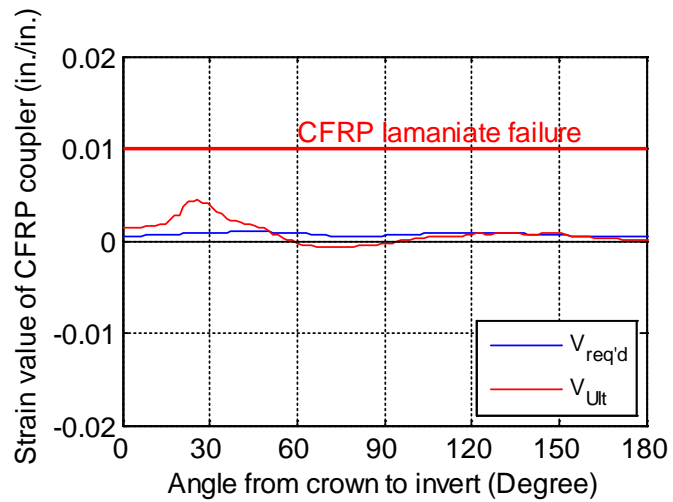
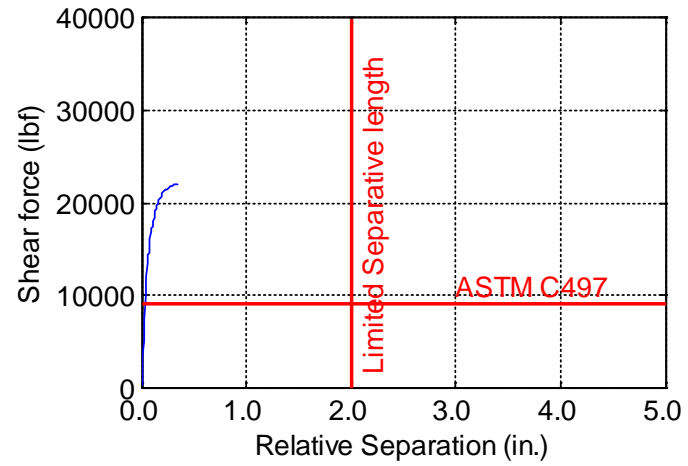
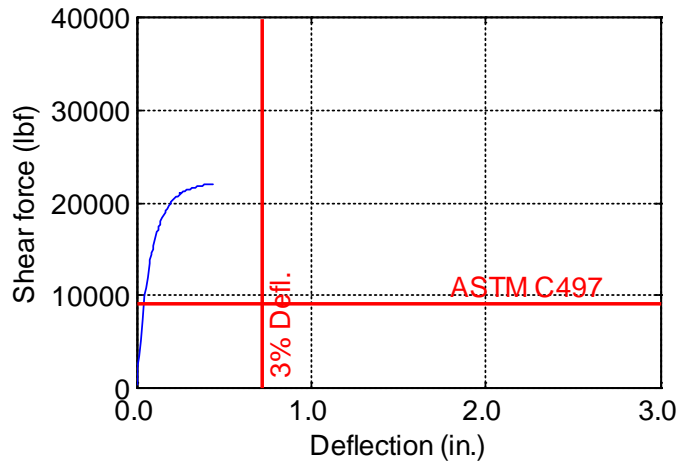


Figure B-23. TW-024-12-0.5

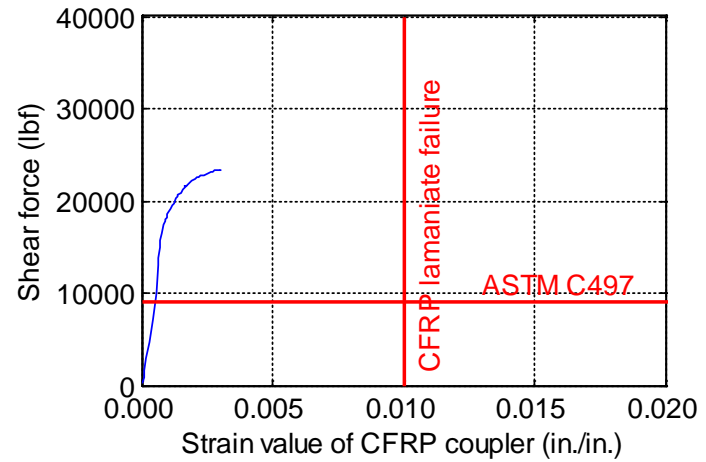
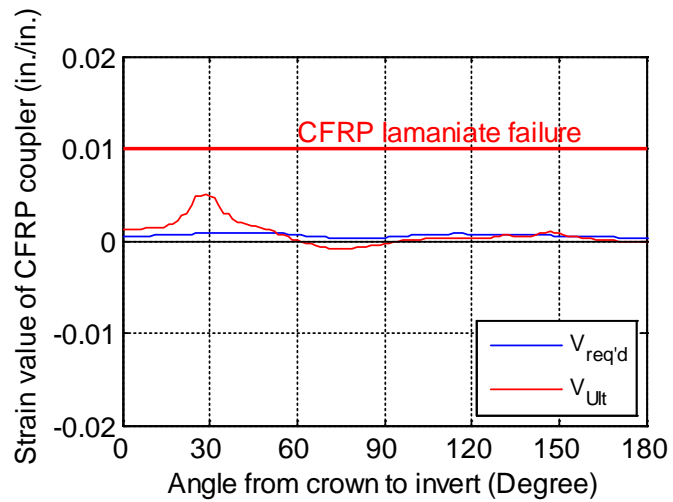
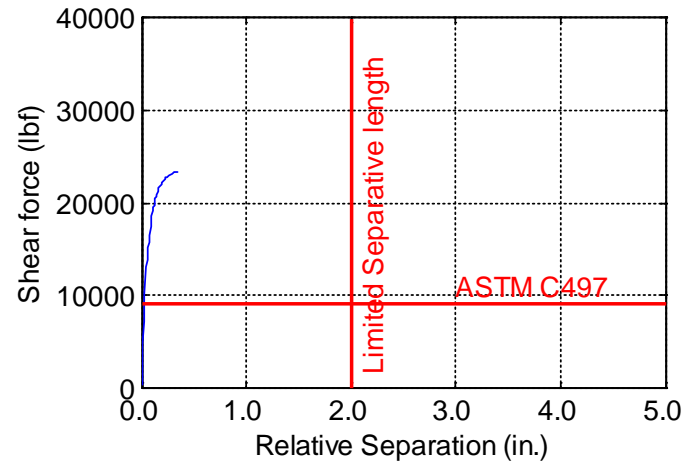
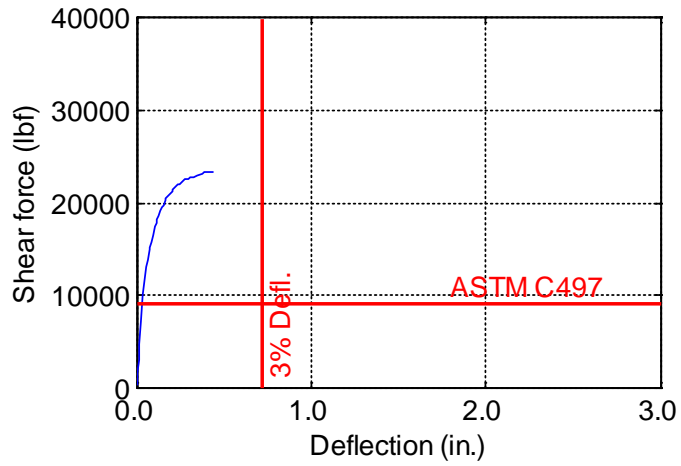


Figure B-24. TW-024-12-0.625

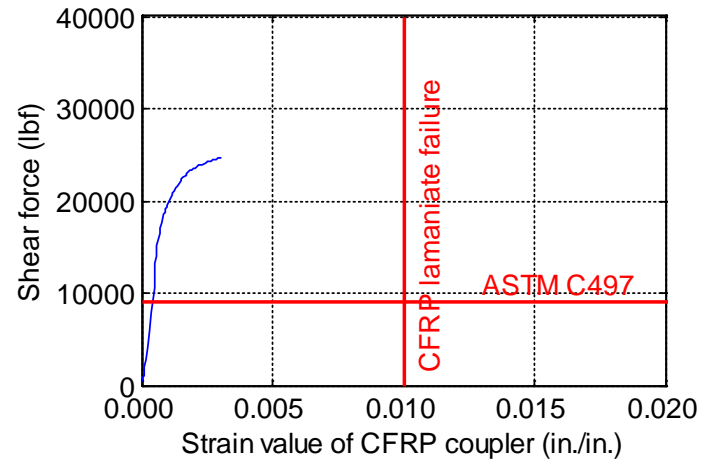
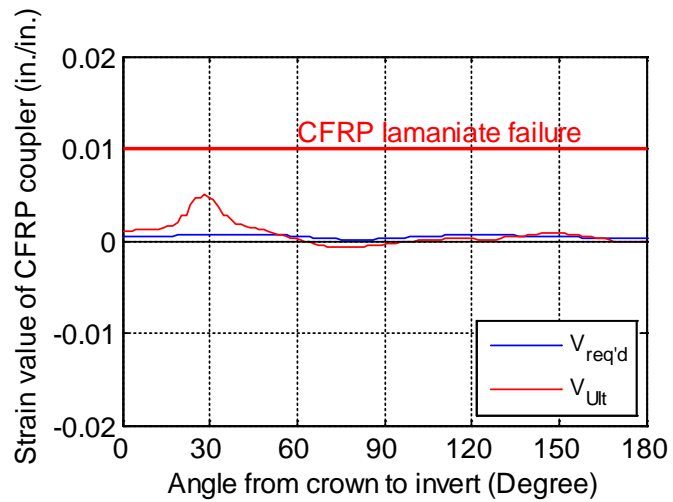
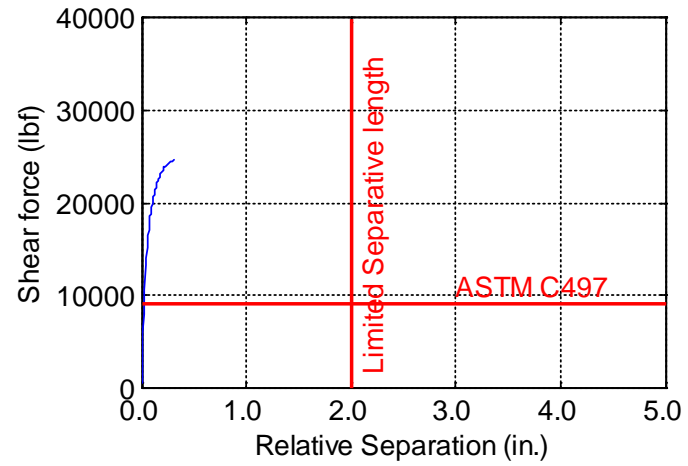
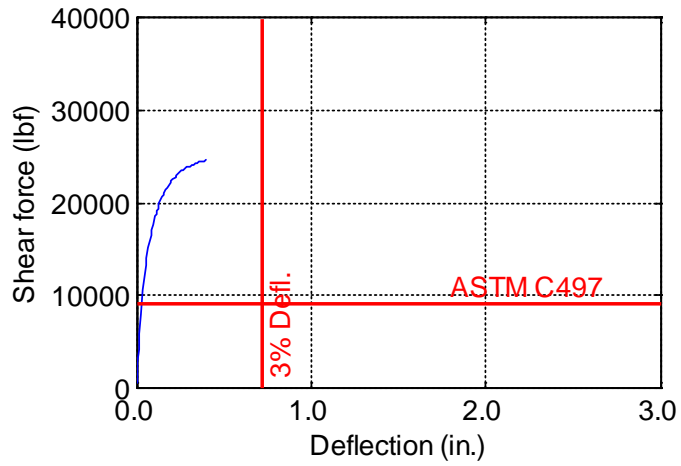


Figure B-25. TW-024-12-0.75

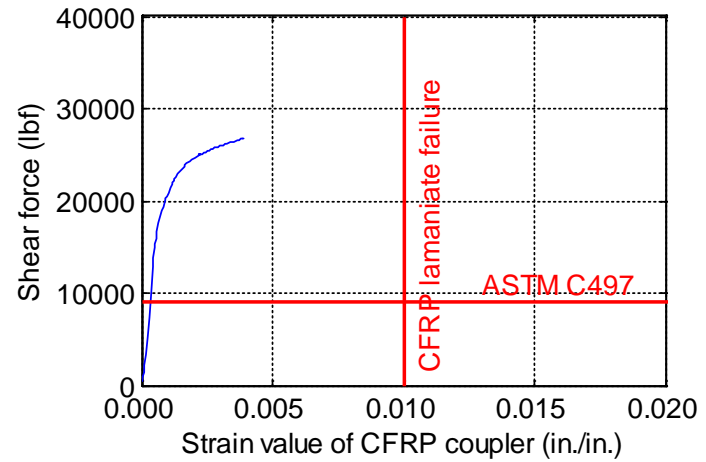
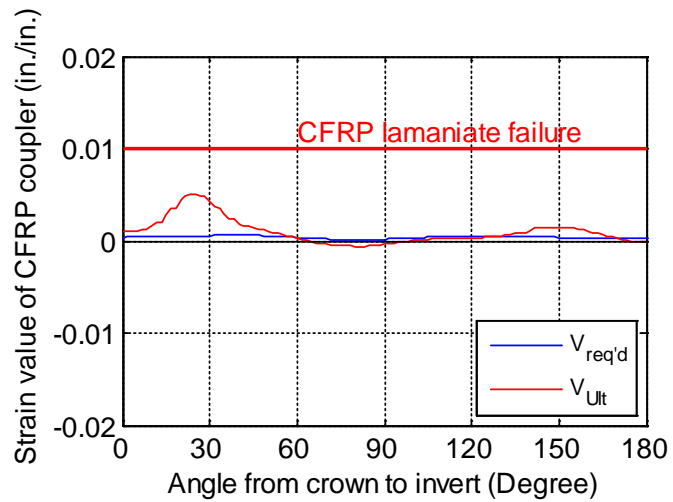
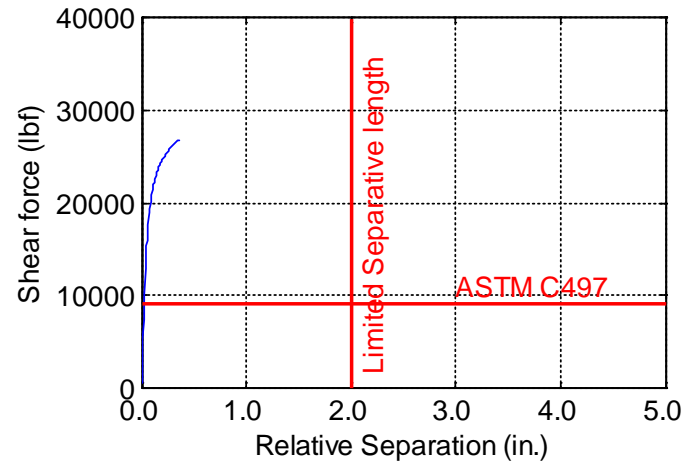
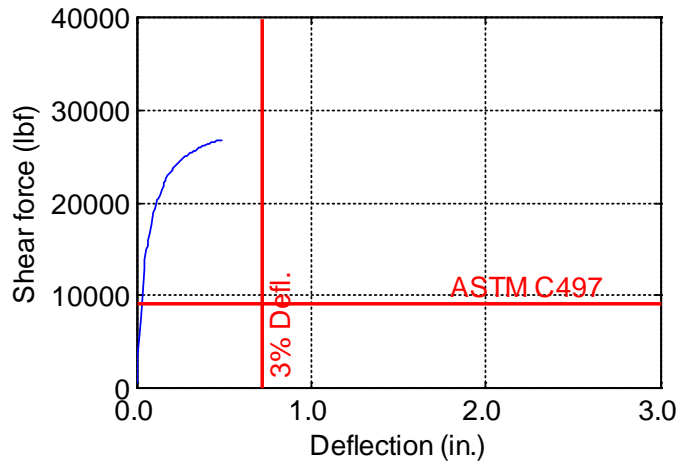


Figure B-26. TW-024-12-0.875

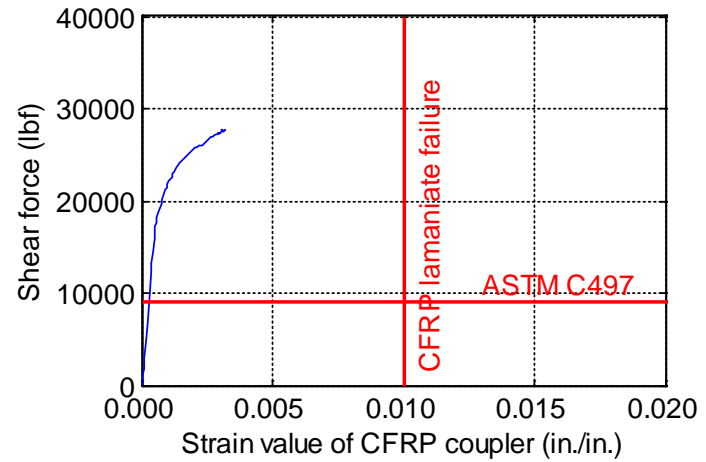
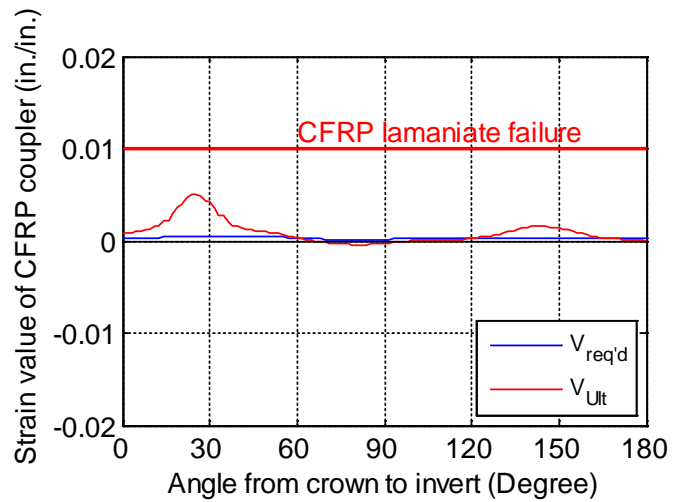
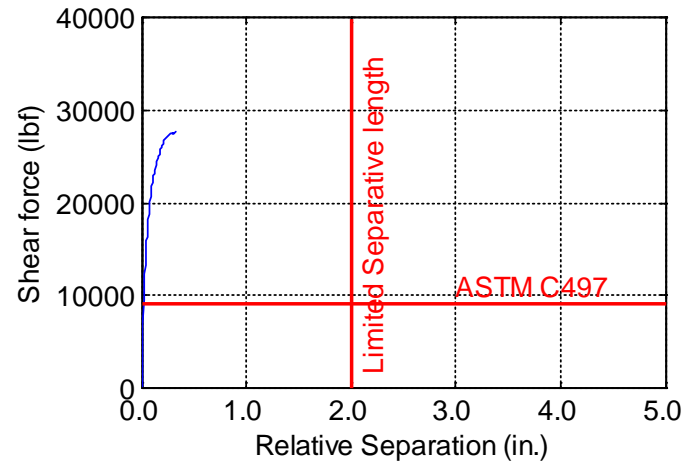
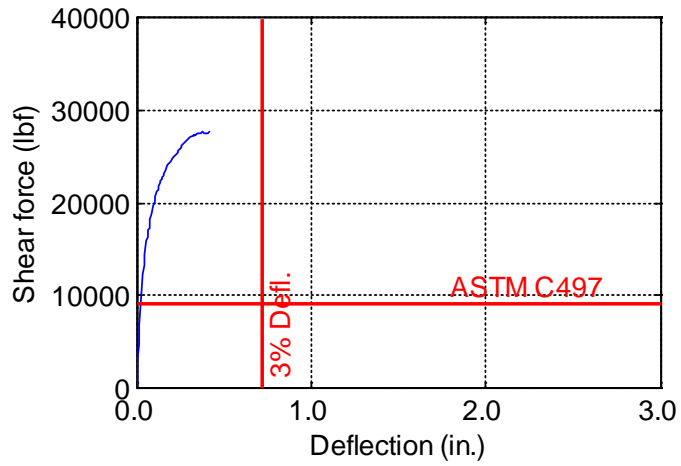


Figure B-27. TW-024-12-1.0

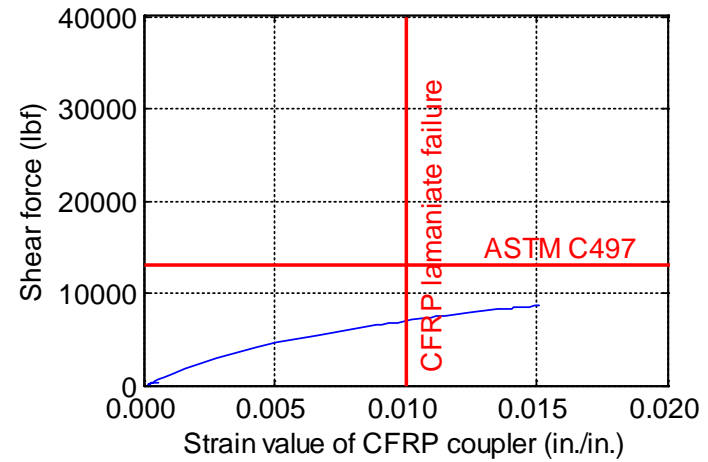
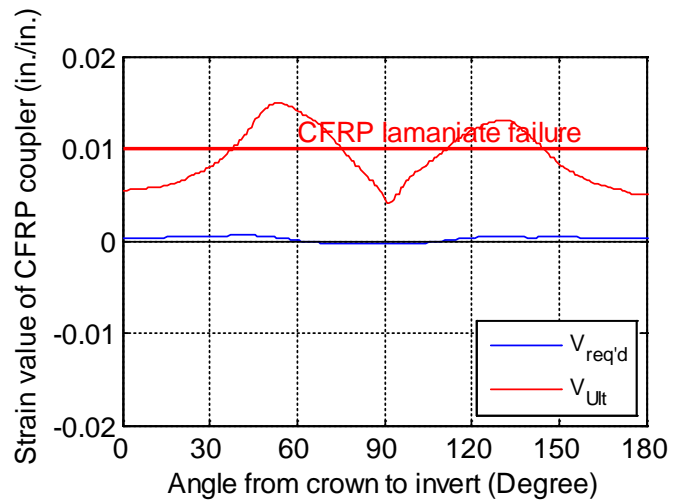
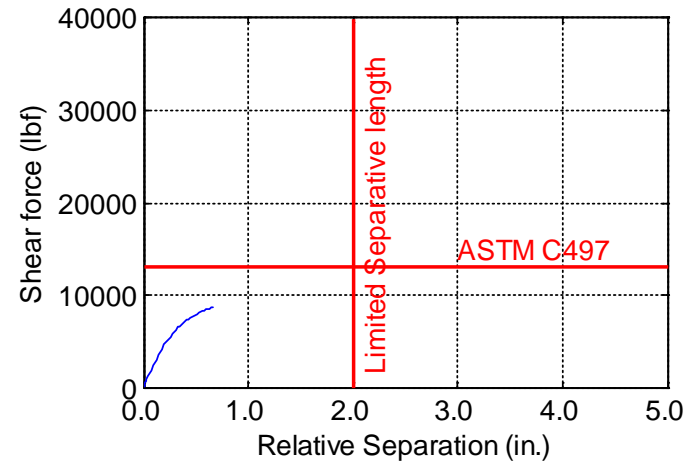
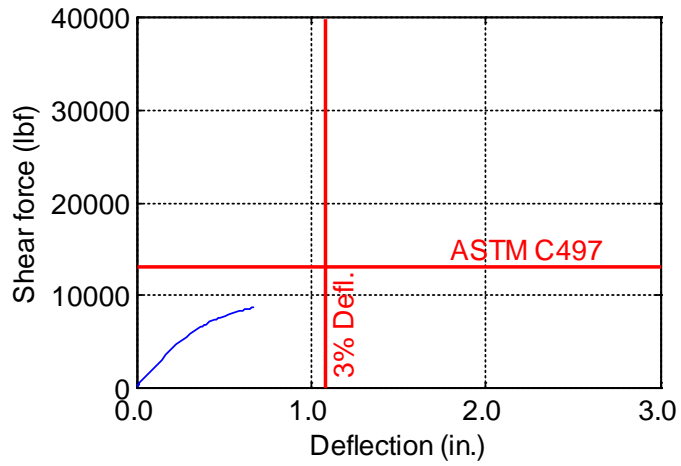


Figure B-28. TW-036-06-0.125

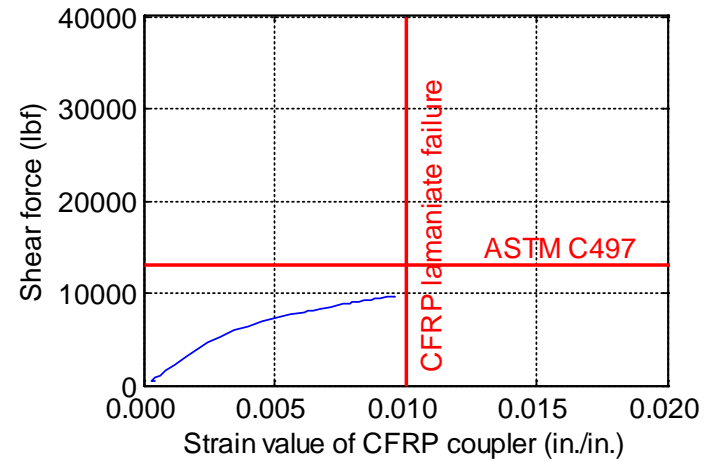
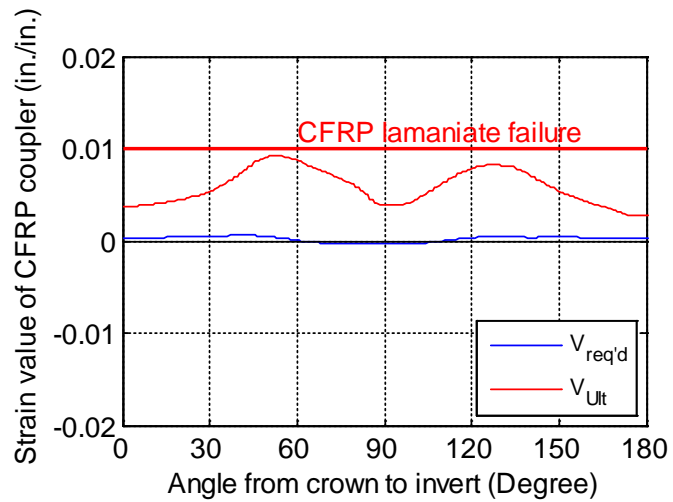
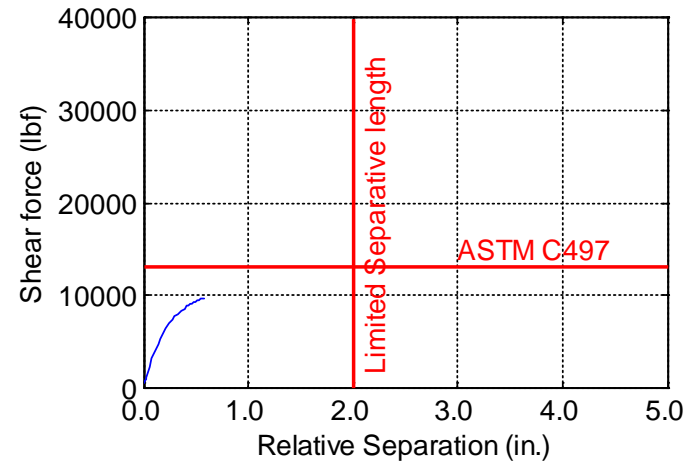
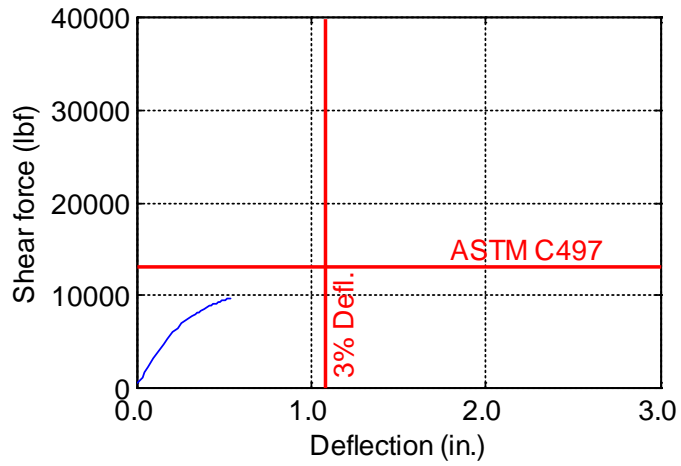


Figure B-29. TW-036-06-0.1875

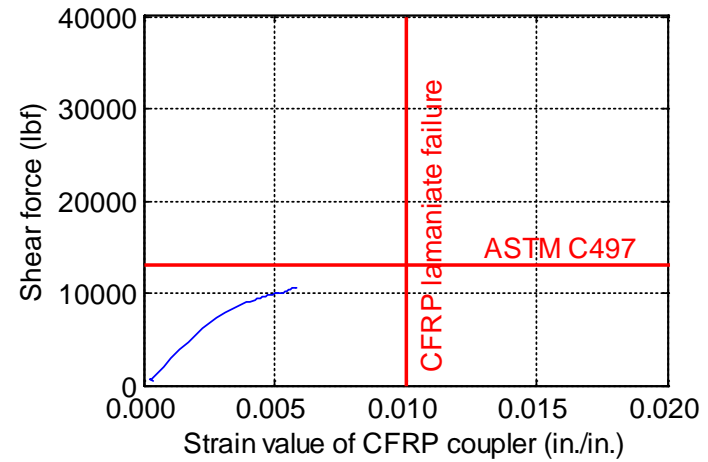
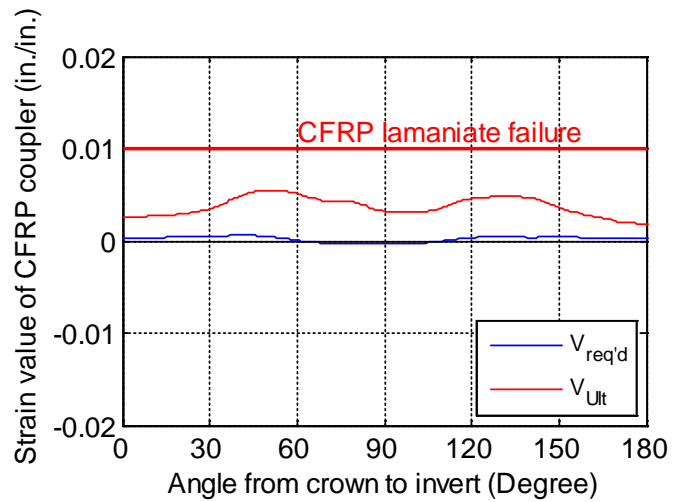
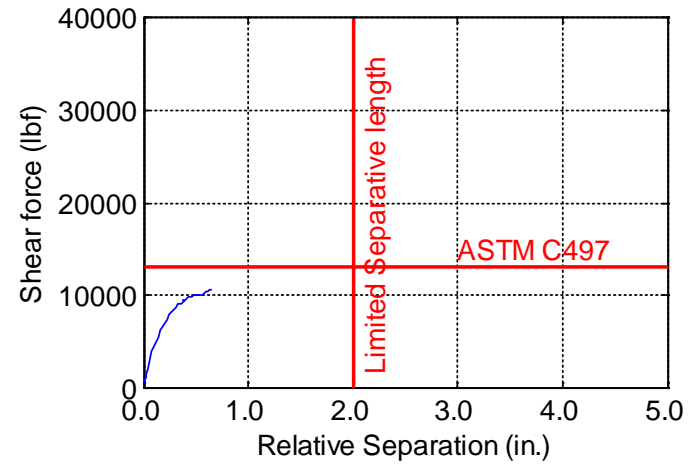
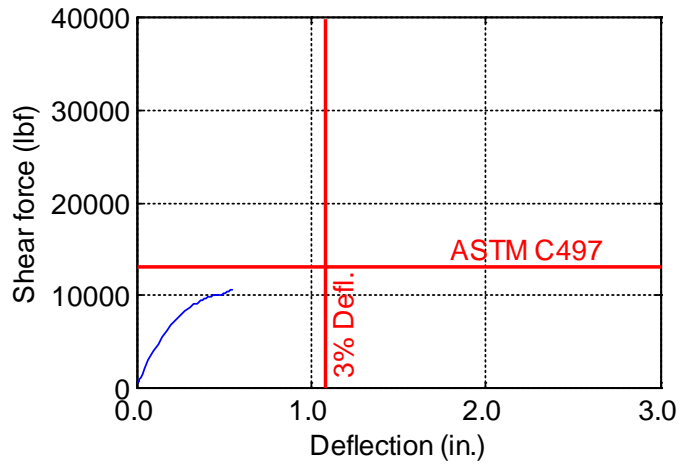


Figure B-30. TW-036-06-0.25

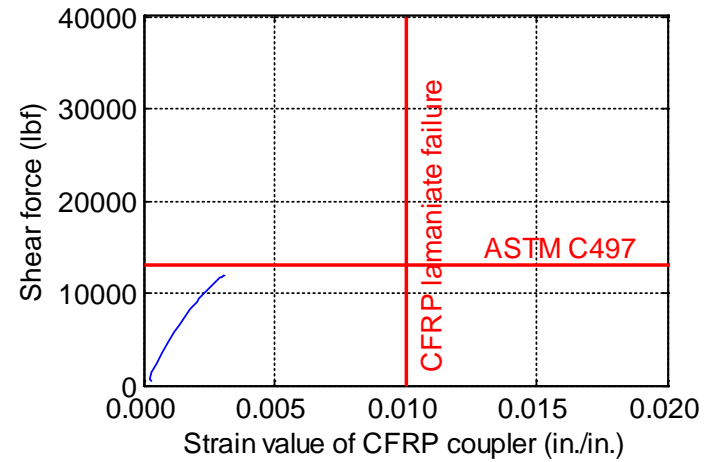
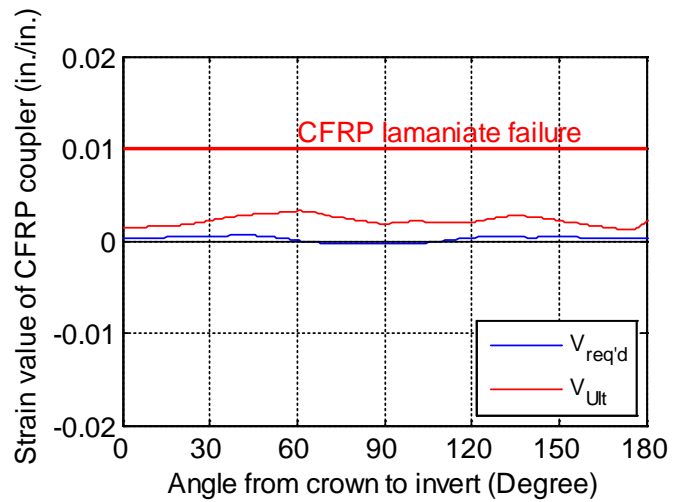
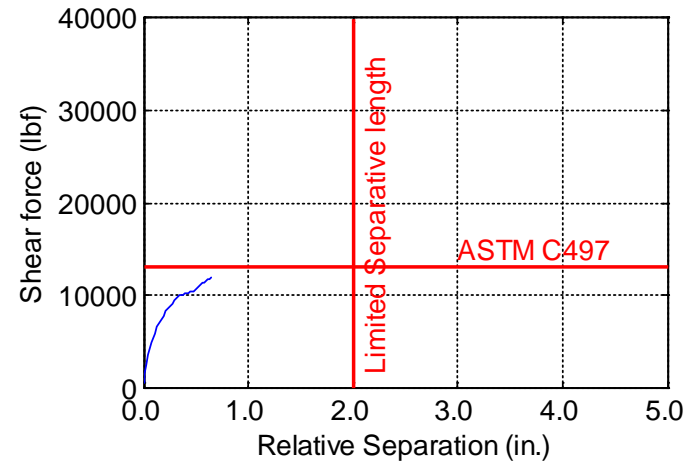
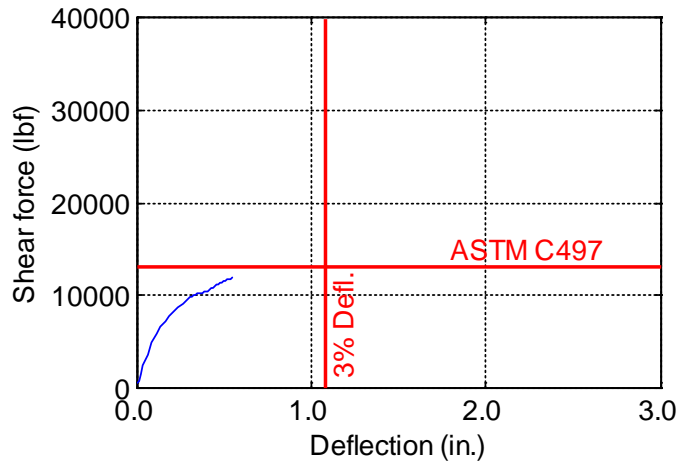


Figure B-31. TW-036-06-0.375

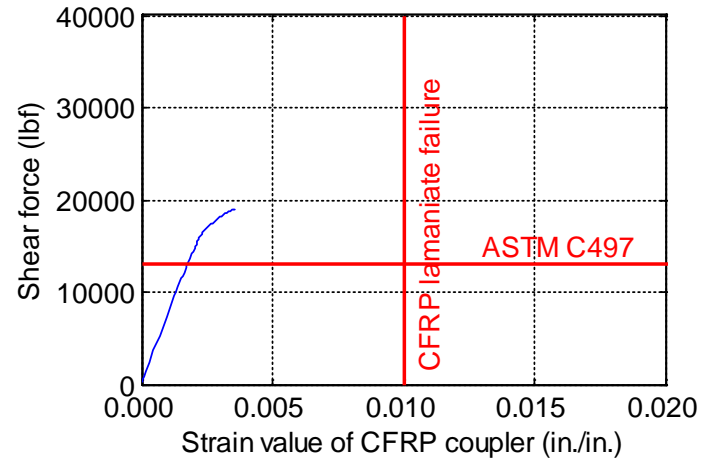
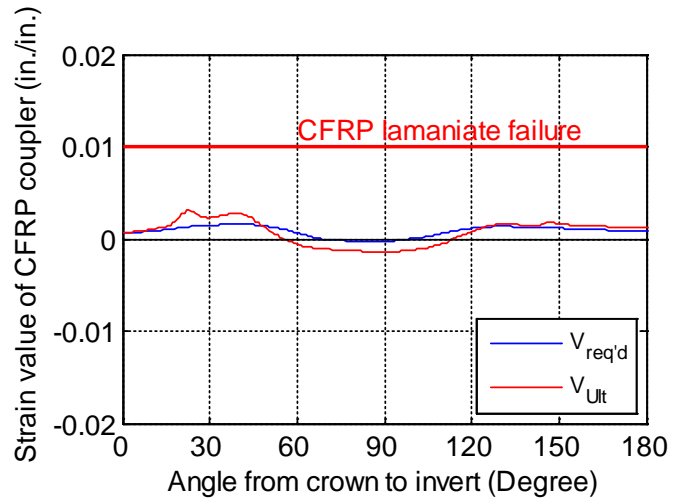
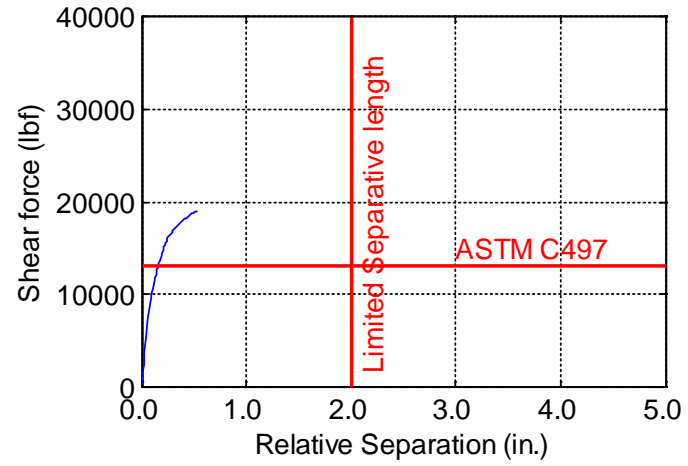
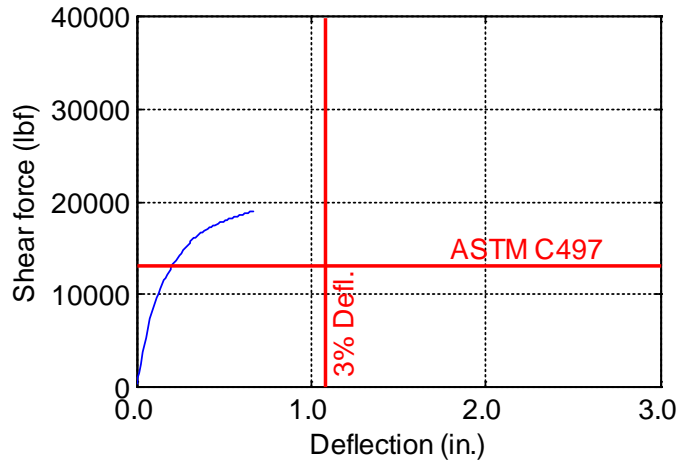


Figure B-32. TW-036-06-0.5

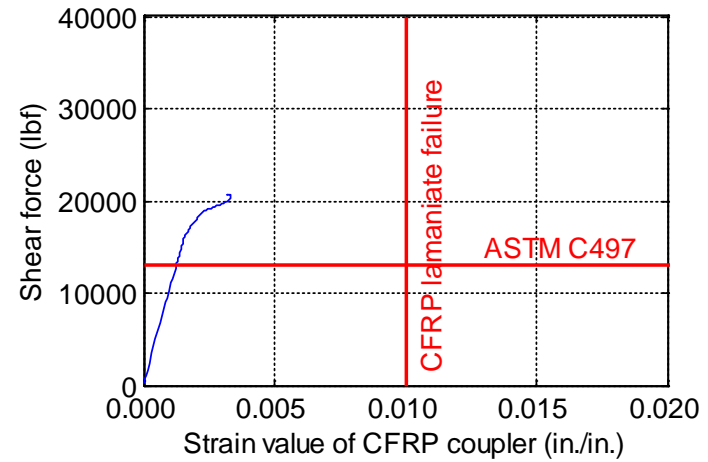
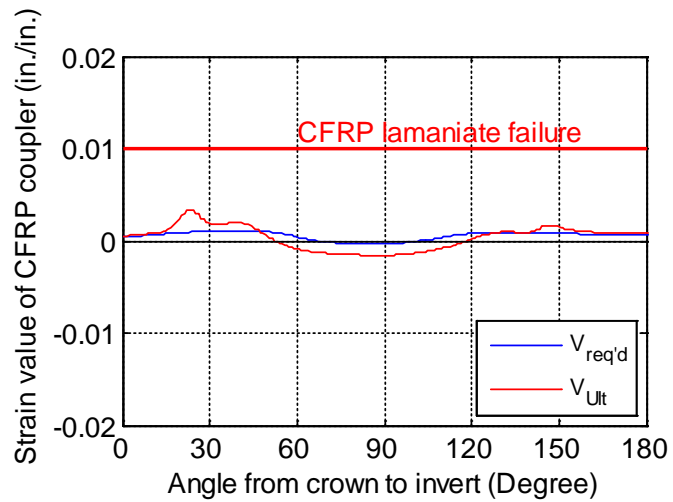
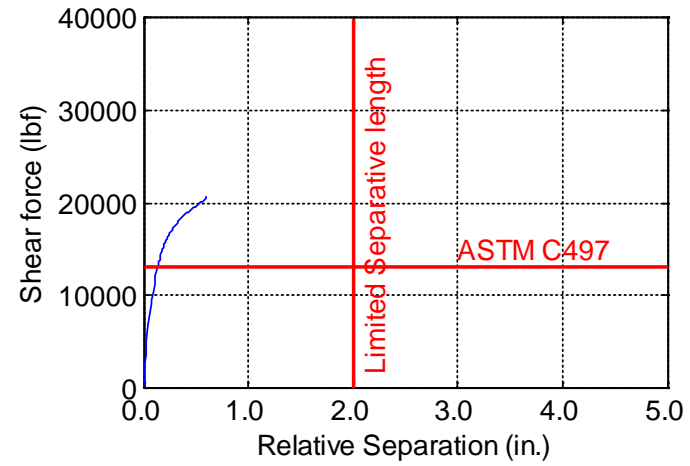
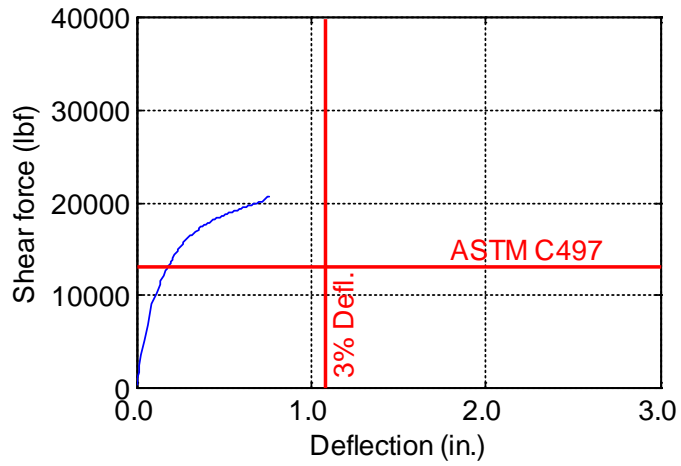


Figure B-33. TW-036-06-0.625

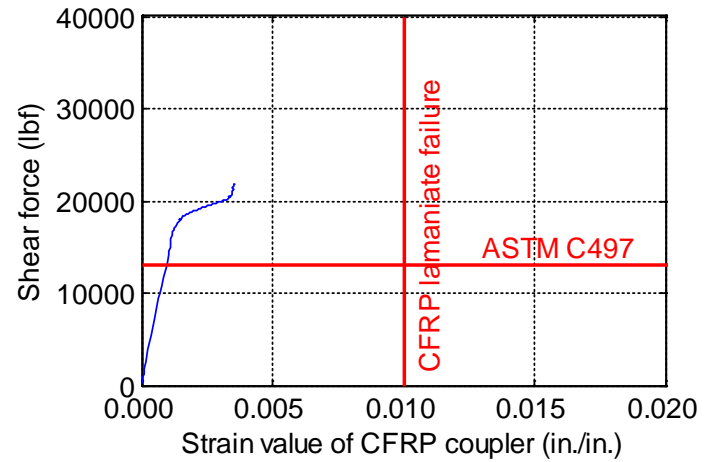
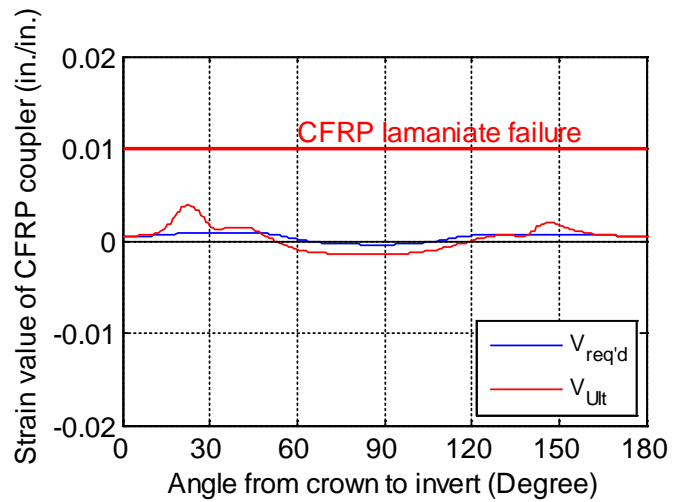
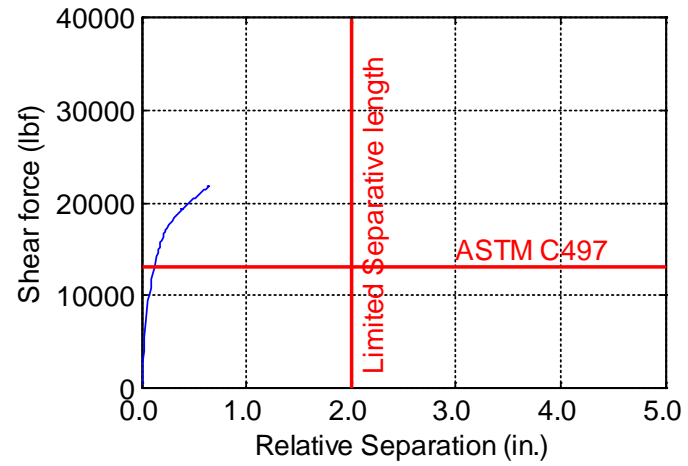
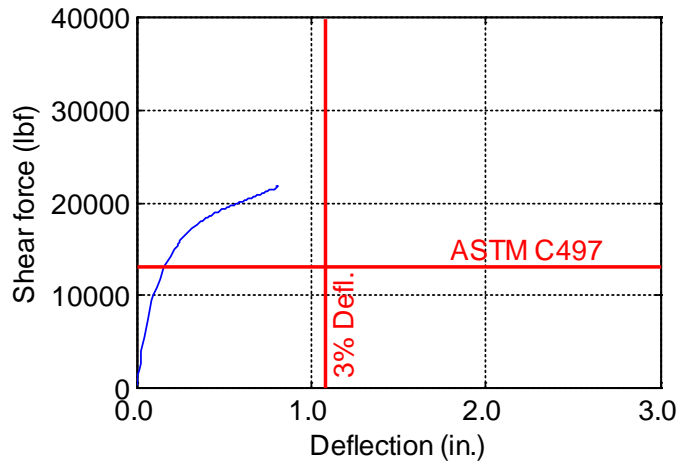


Figure B-34. TW-036-06-0.75

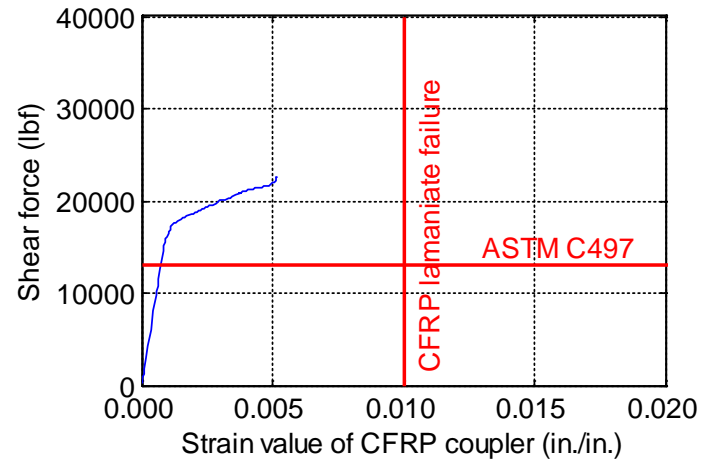
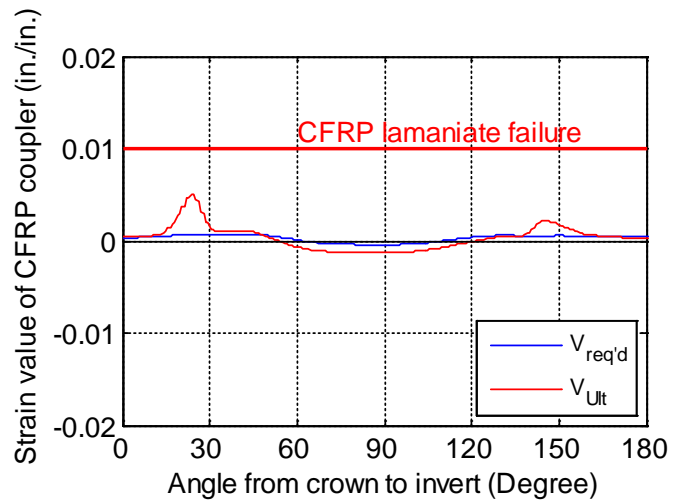
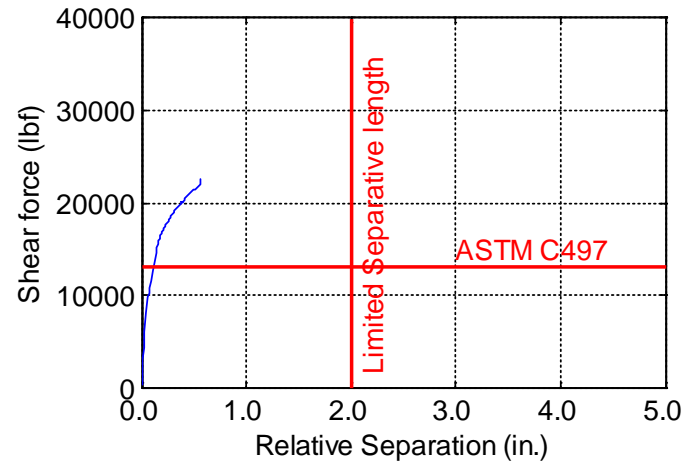
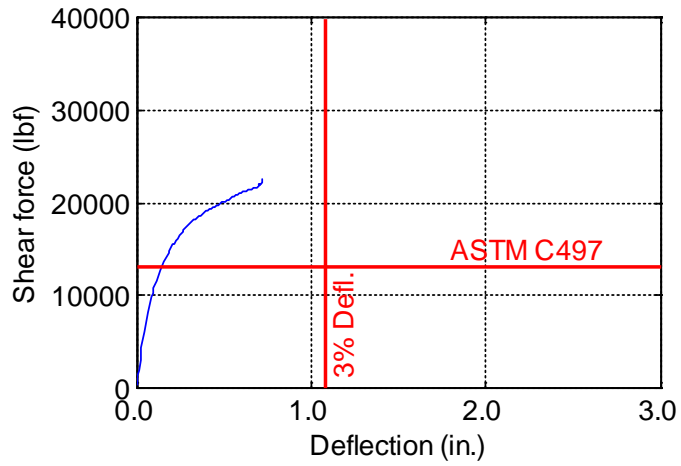


Figure B-35. TW-036-06-0.875

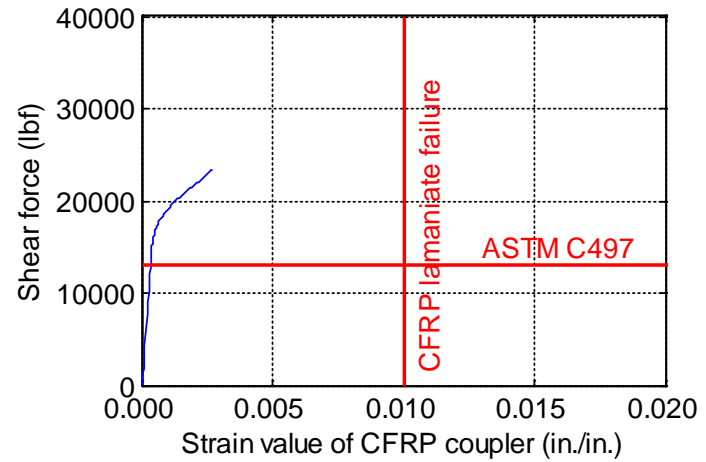
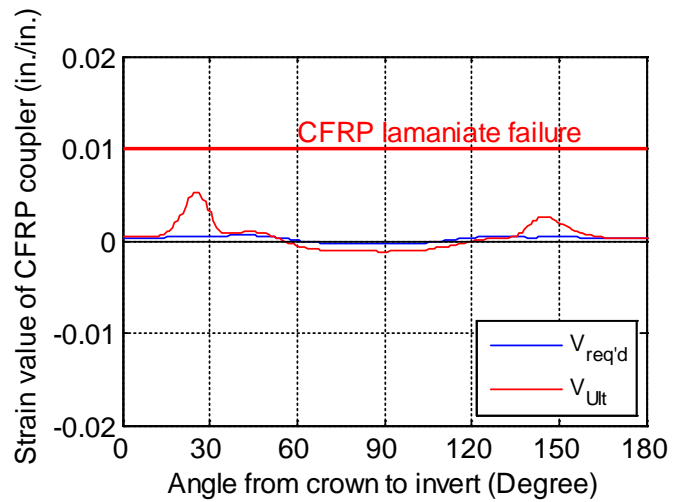
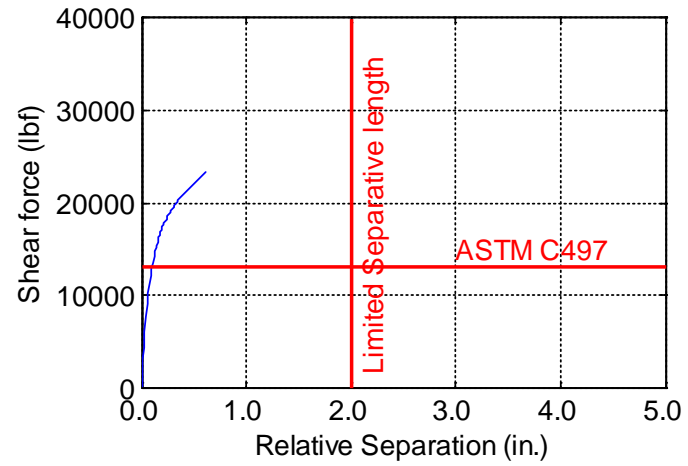
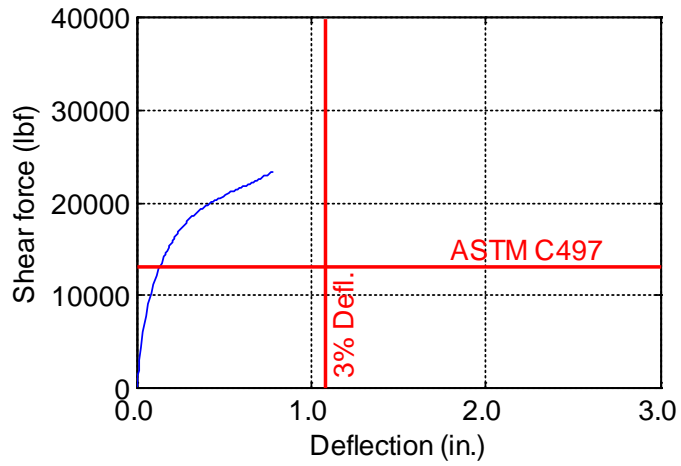


Figure B-36. TW-036-06-1.0

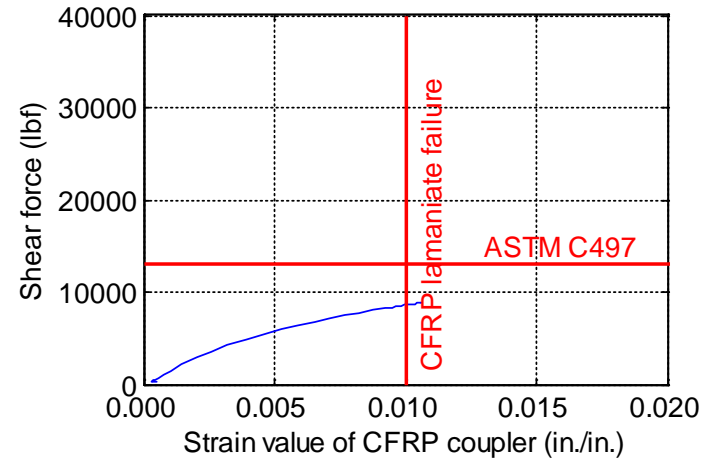
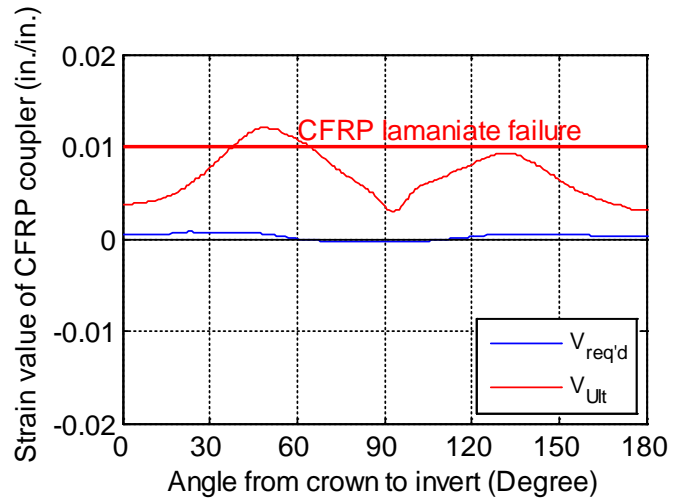
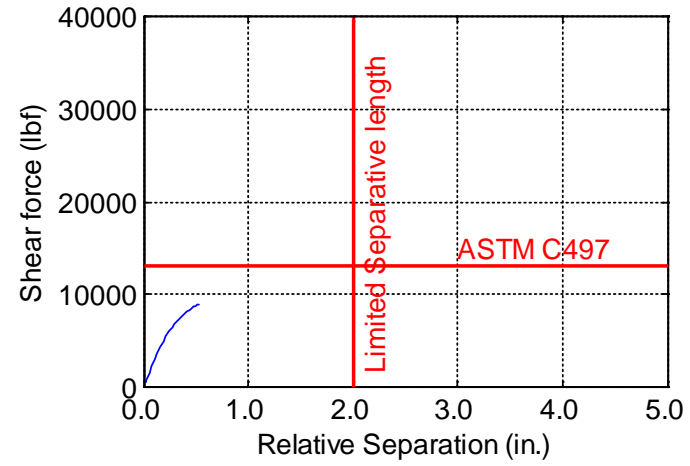
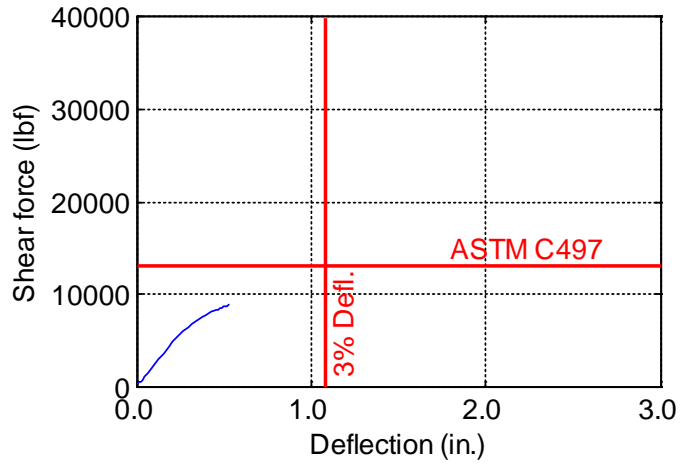


Figure B-37. TW-036-09-0.125

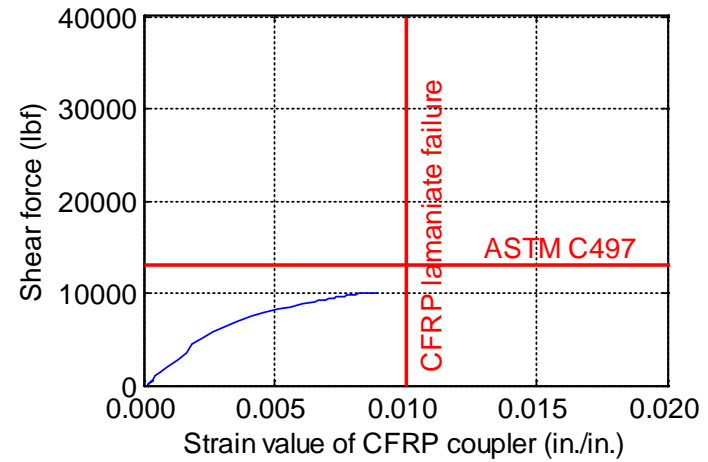
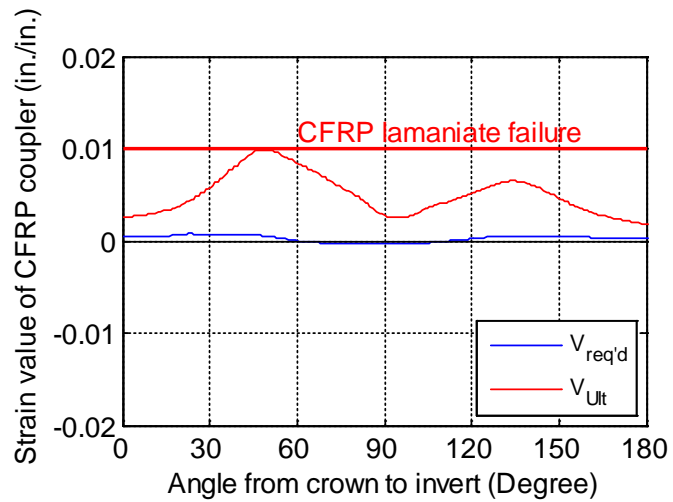
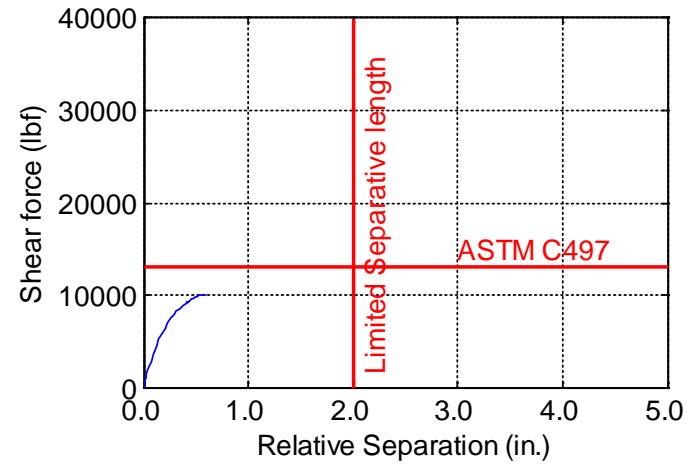
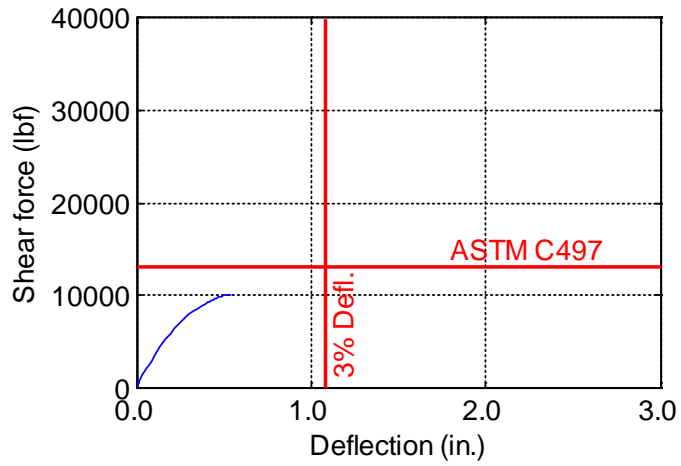


Figure B-38. TW-036-09-0.1875

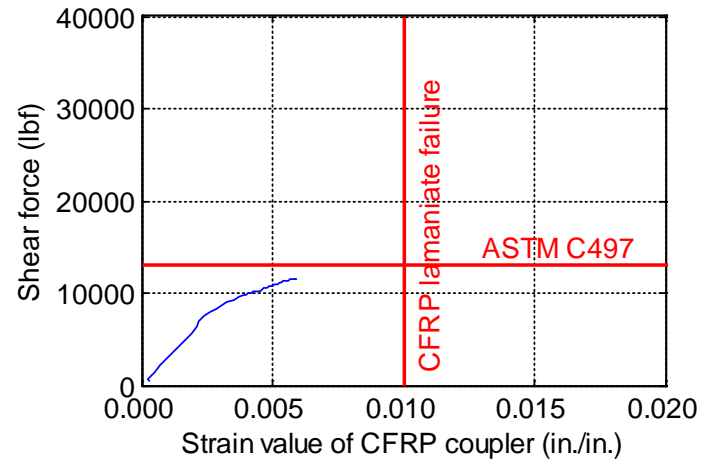
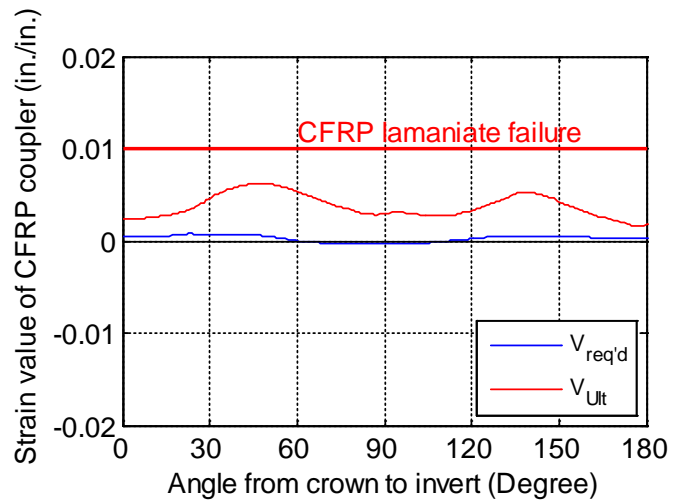
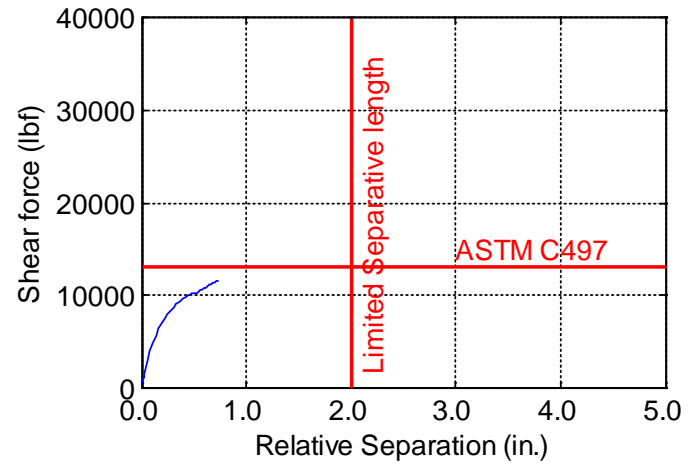
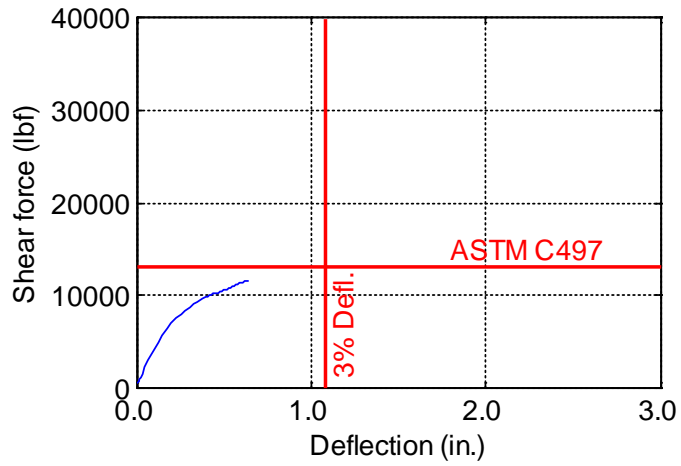


Figure B-39. TW-036-09-0.25

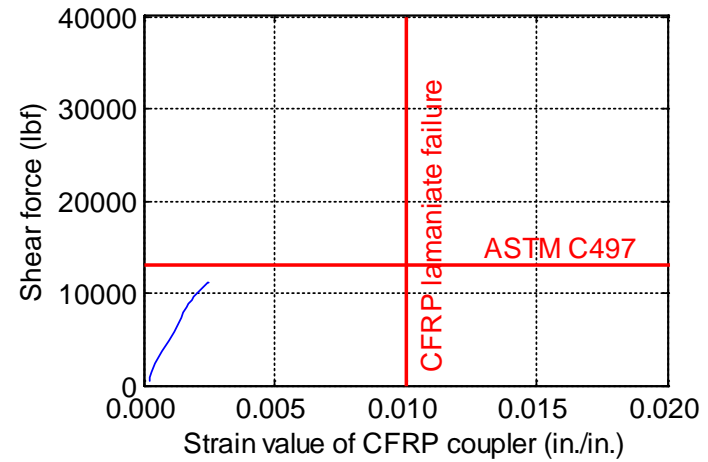
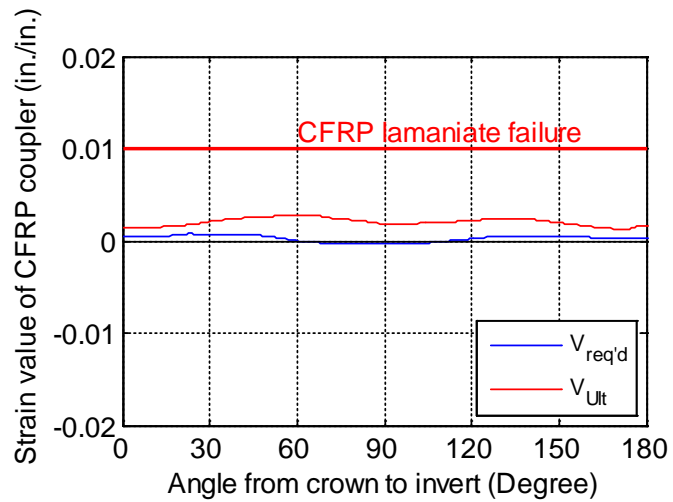
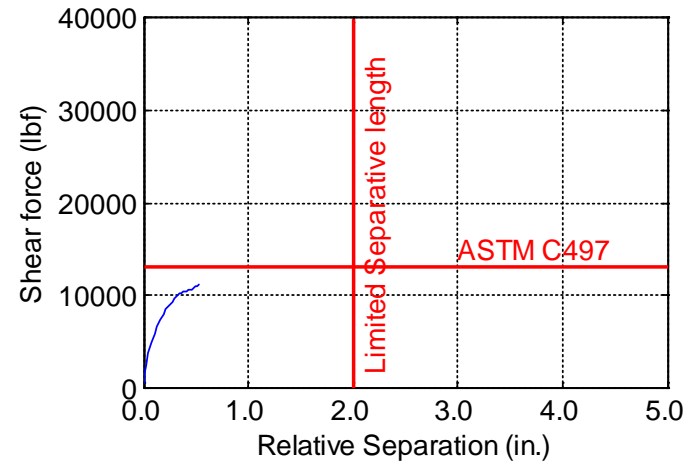
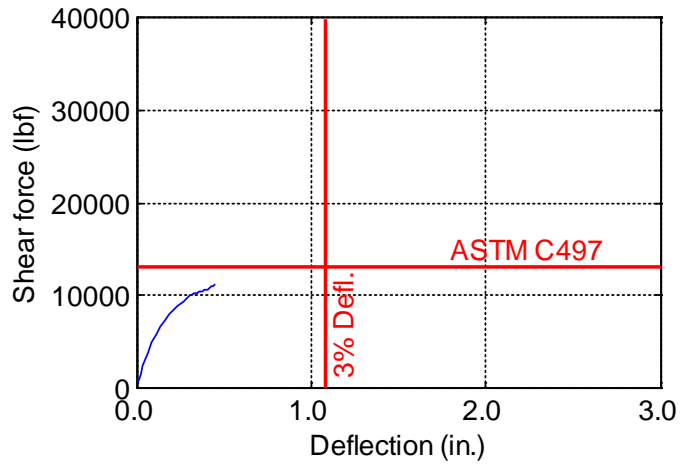


Figure B-40. TW-036-09-0.375

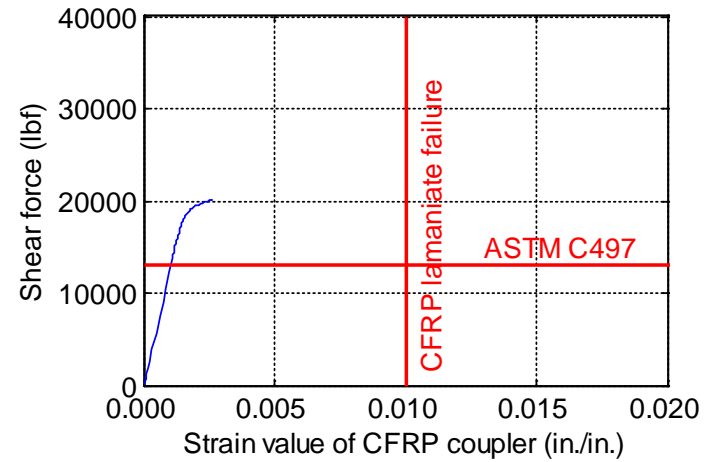
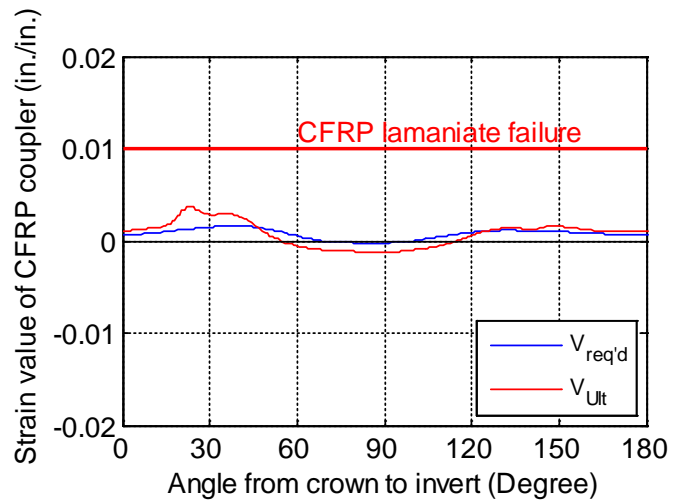
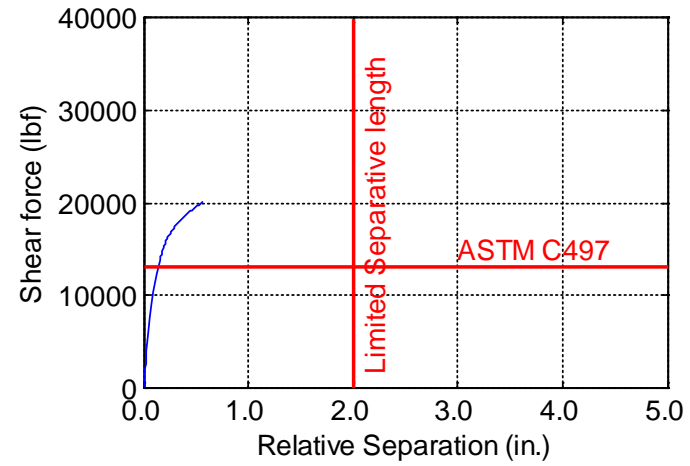
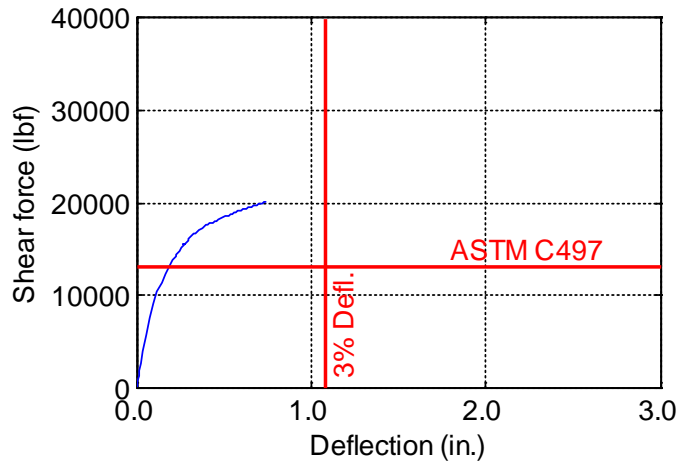


Figure B-41. TW-036-09-0.5

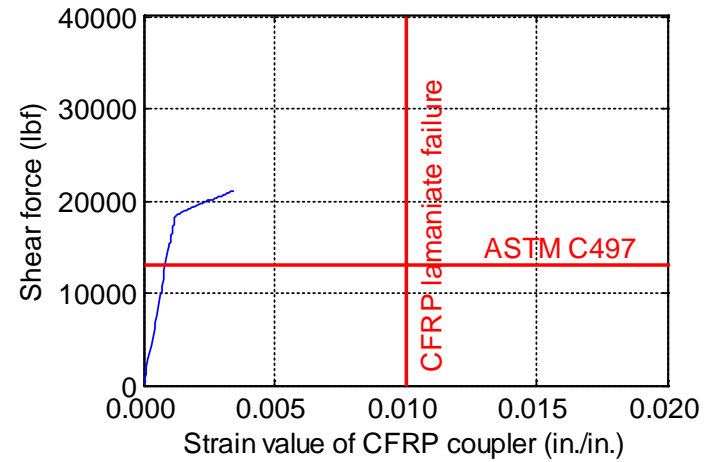
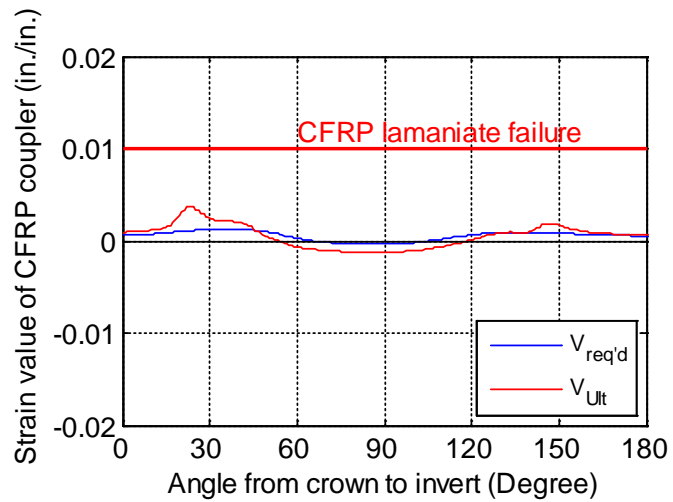
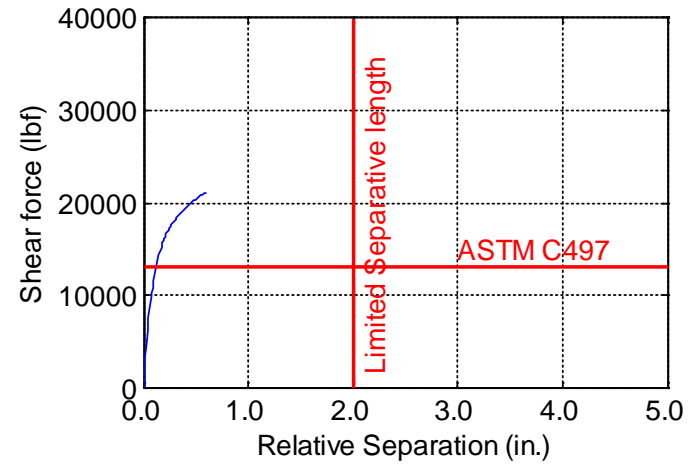
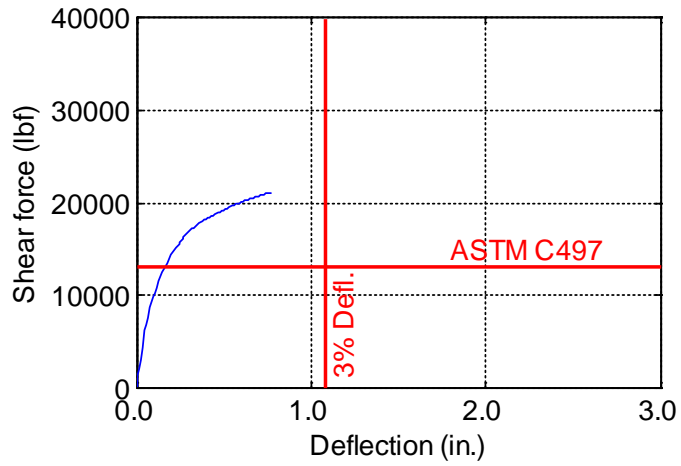


Figure B-42. TW-036-09-0.625

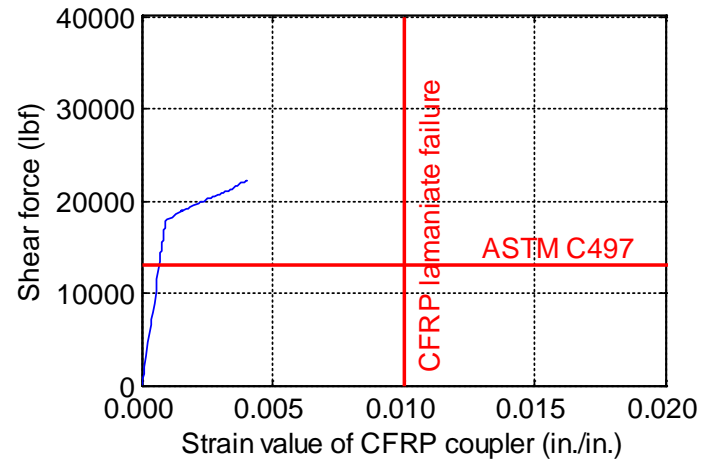
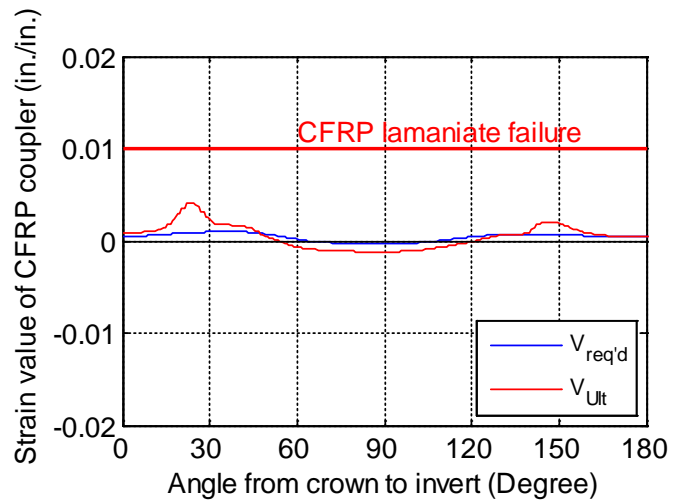
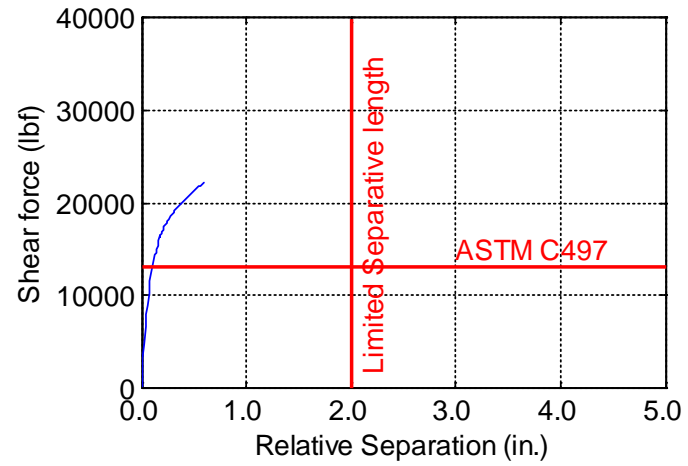
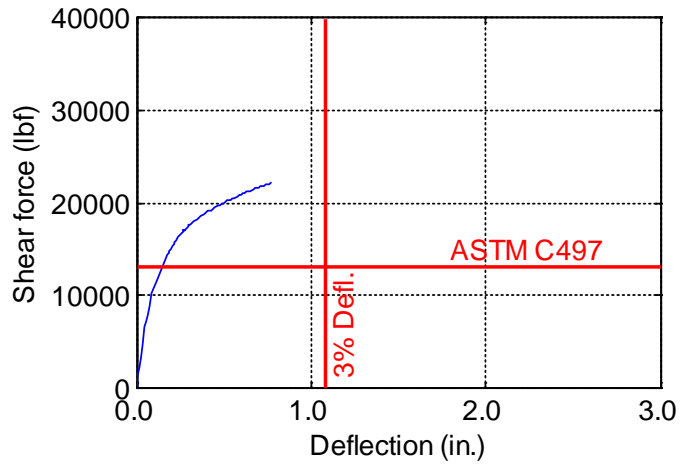


Figure B-43. TW-036-09-0.75

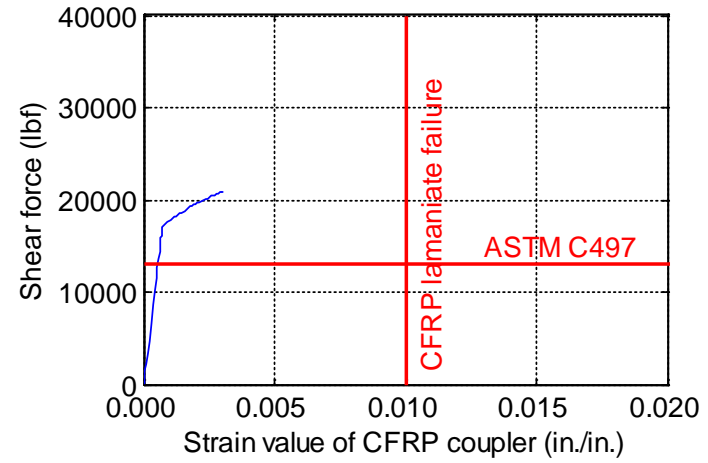
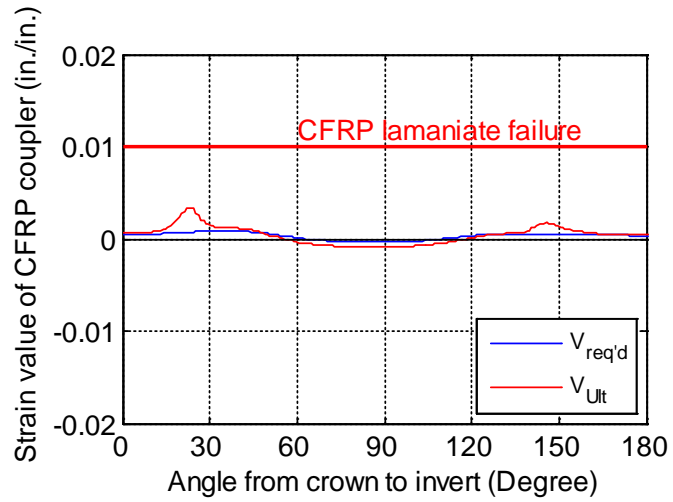
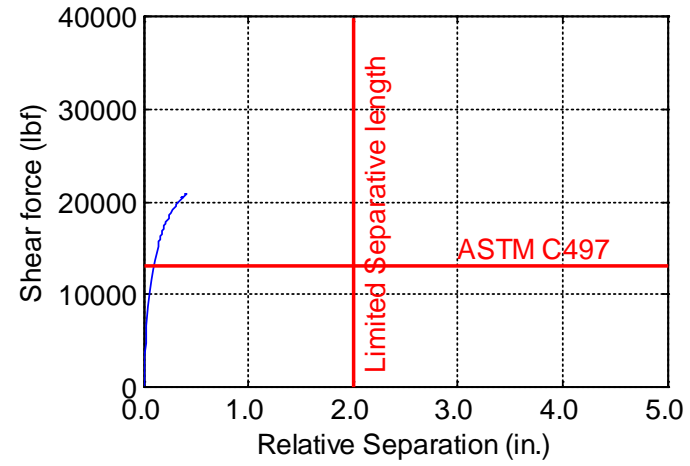
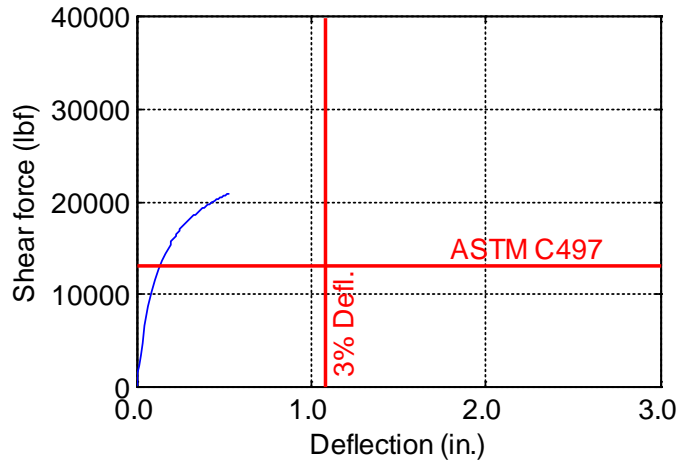


Figure B-44. TW-036-09-0.875

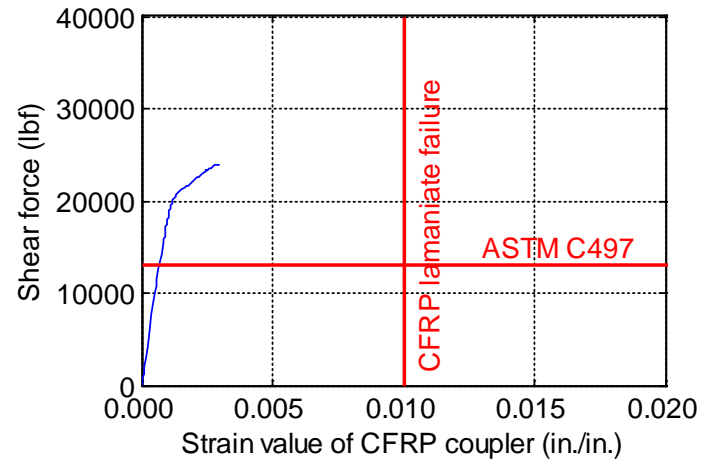
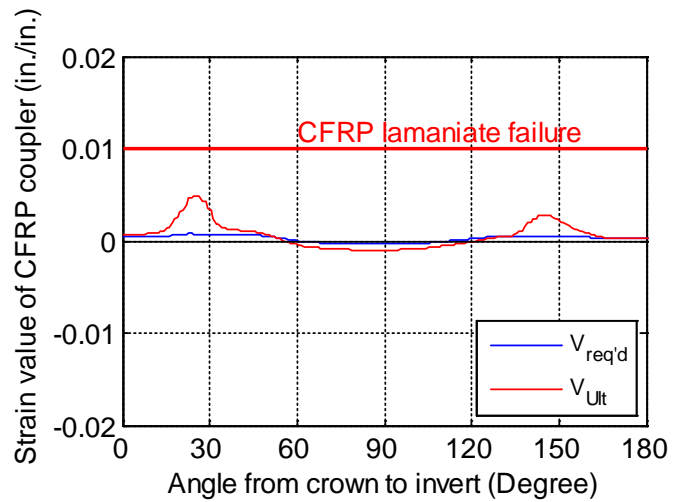
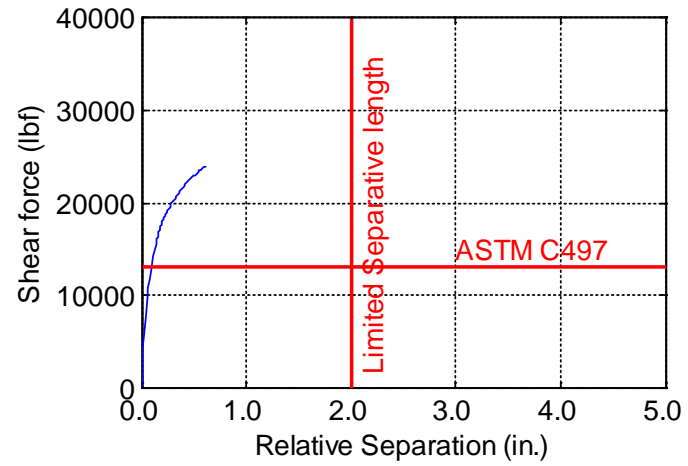
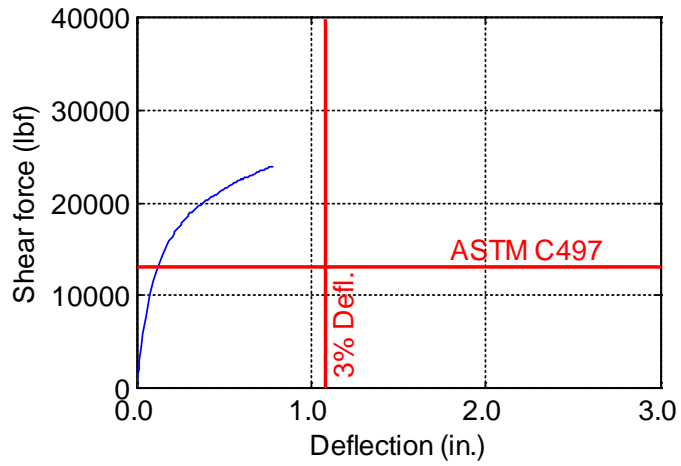


Figure B-45. TW-036-09-1.0

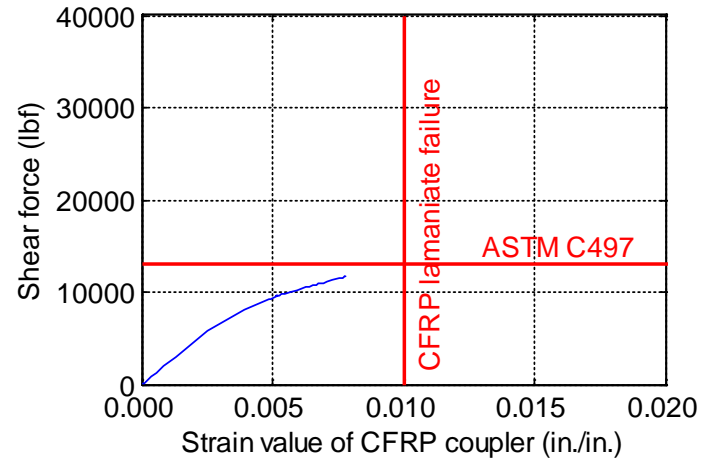
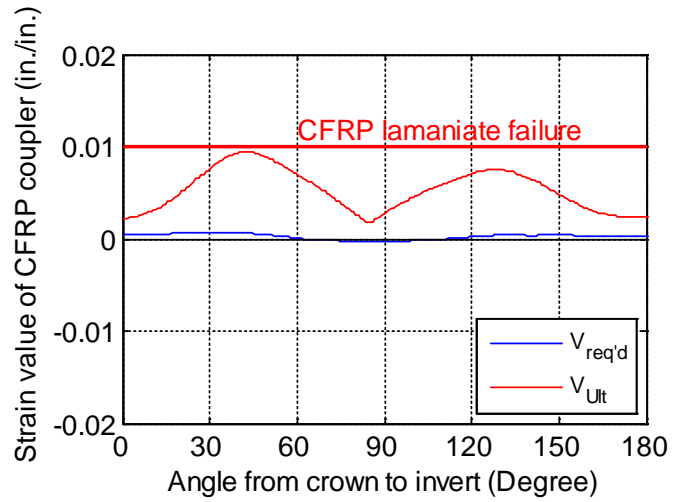
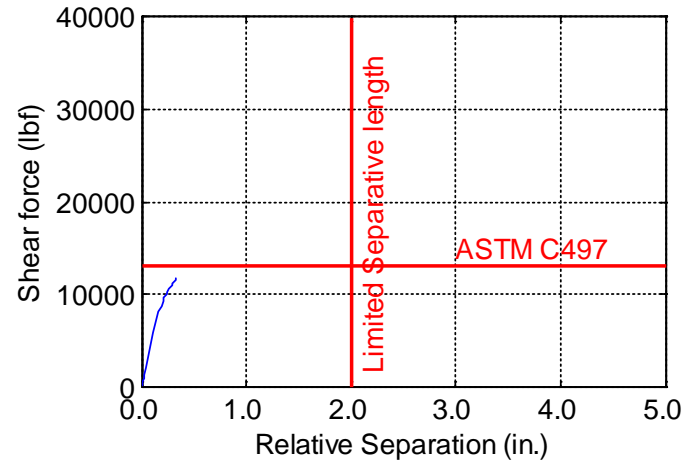
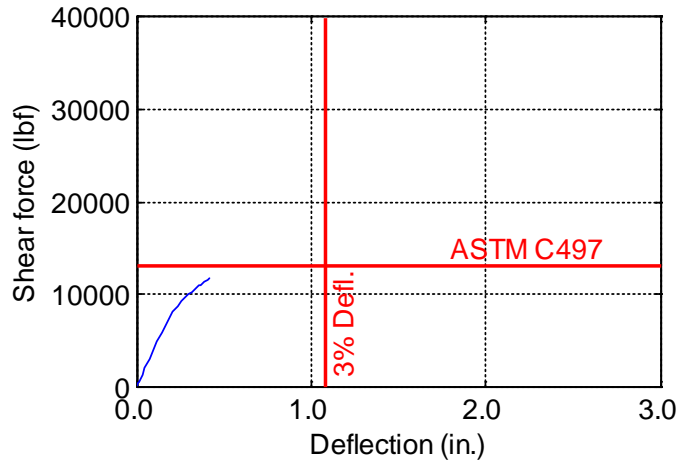


Figure B-46. TW-036-12-0.125

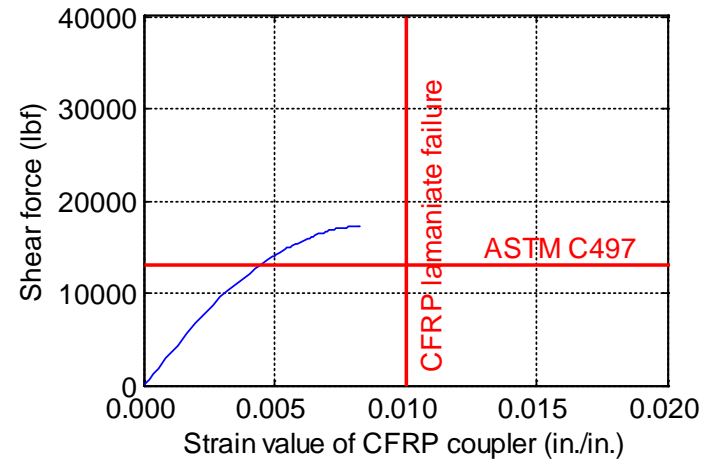
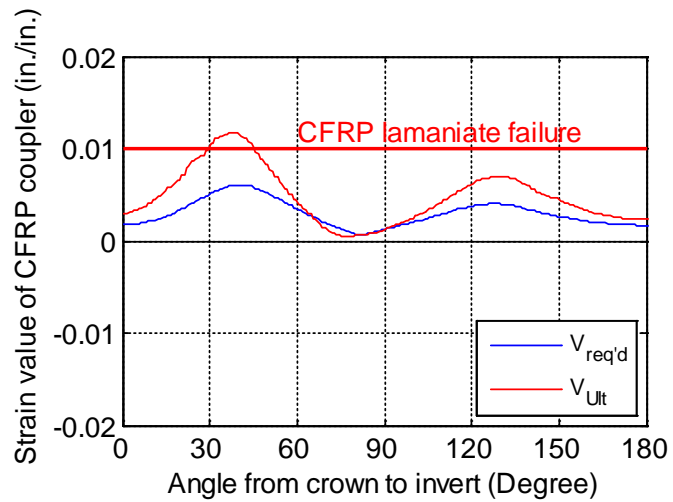
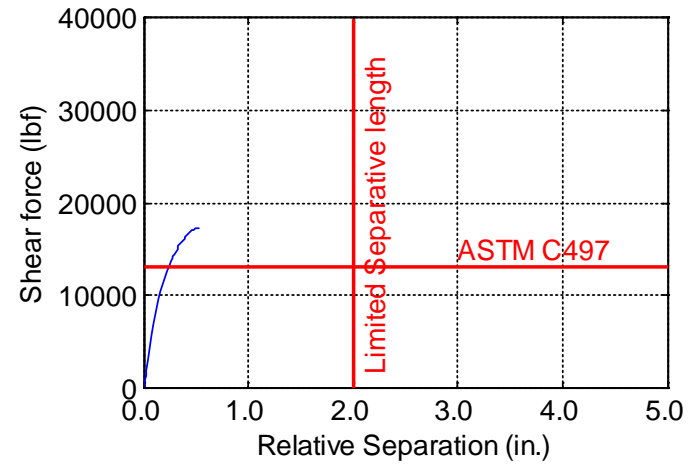
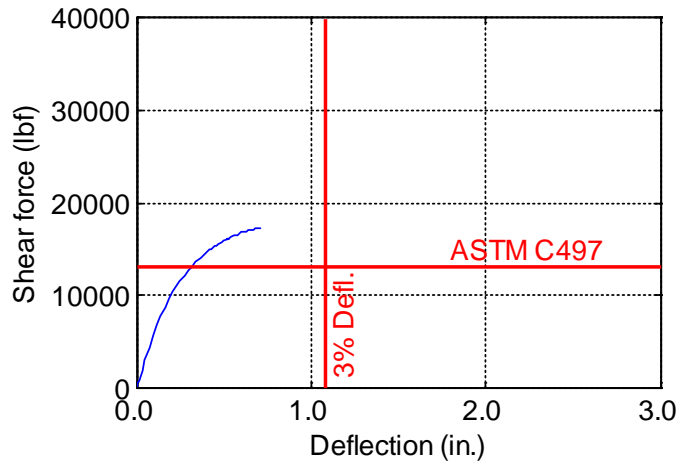


Figure B-47. TW-036-12-0.1875

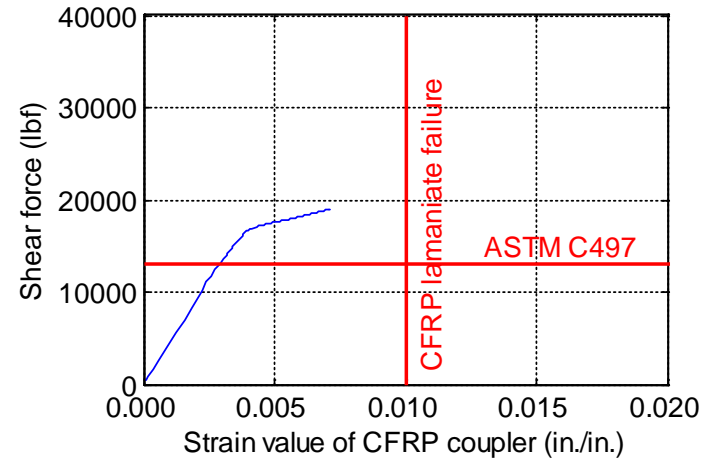
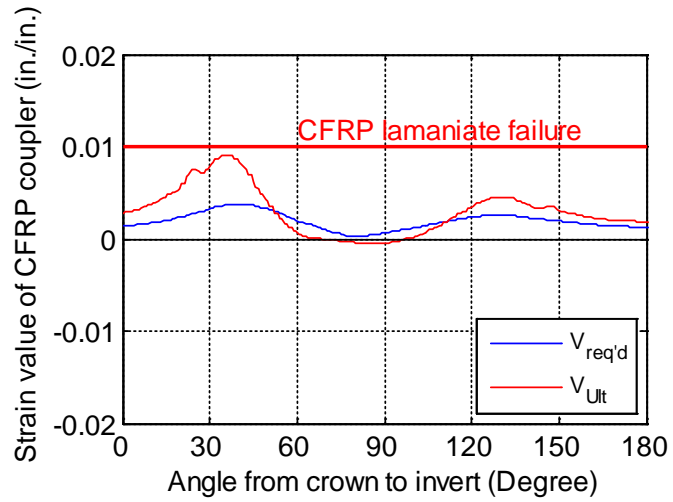
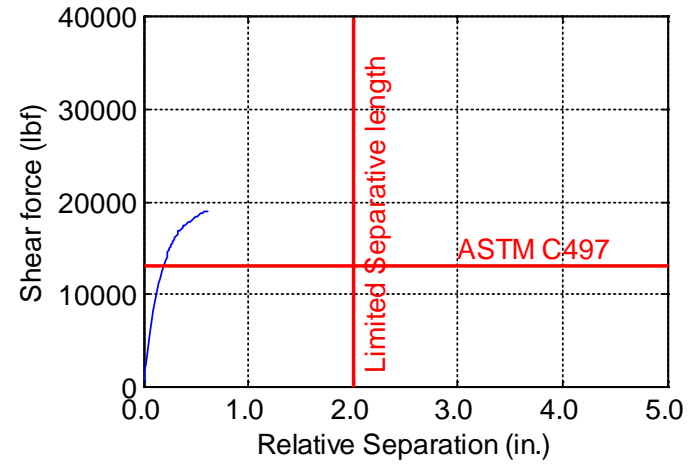
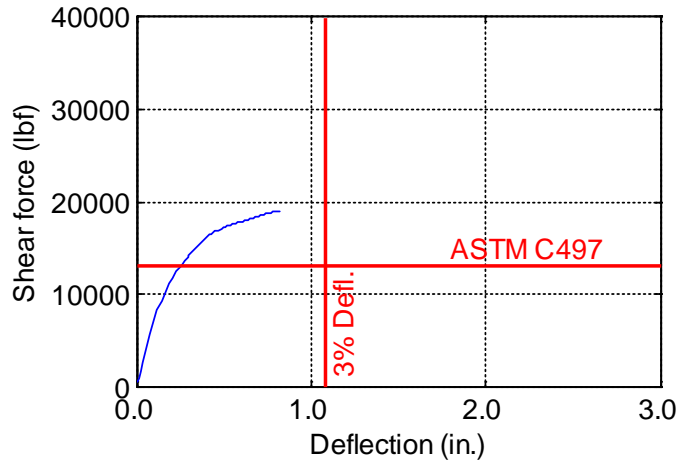


Figure B-48. TW-036-12-0.25

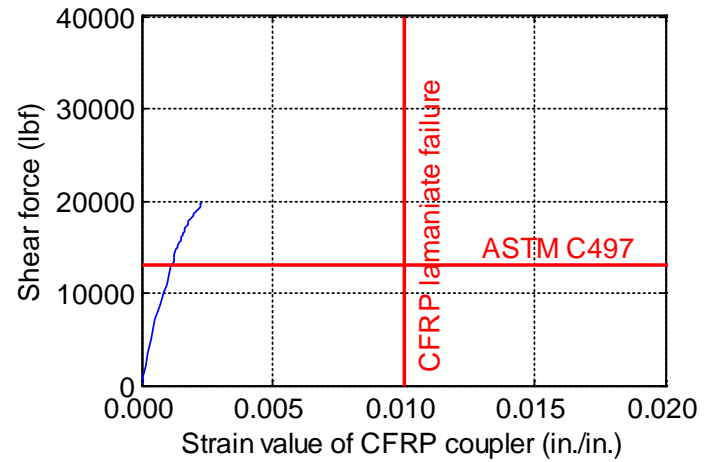
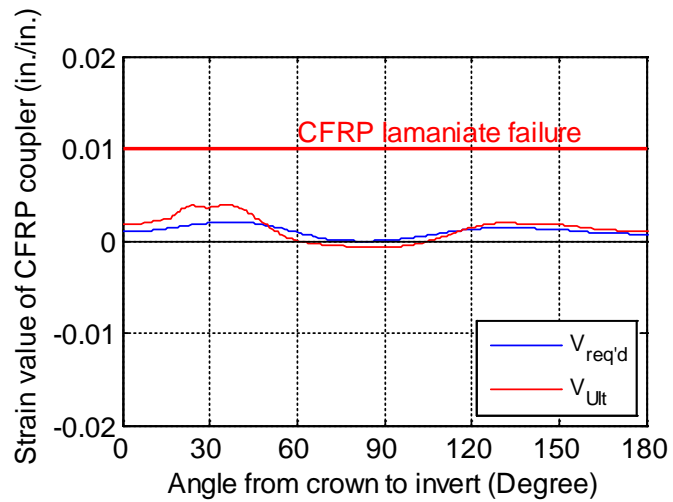
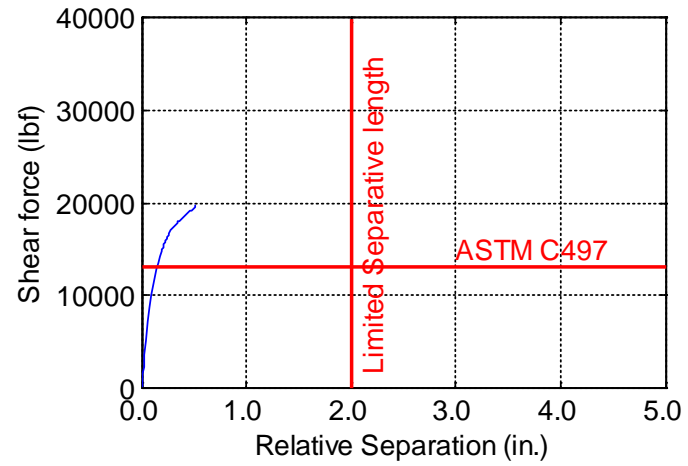
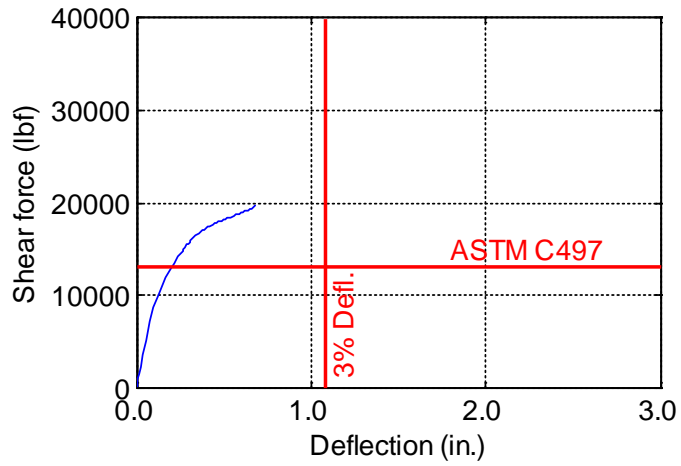


Figure B-49. TW-036-12-0.375

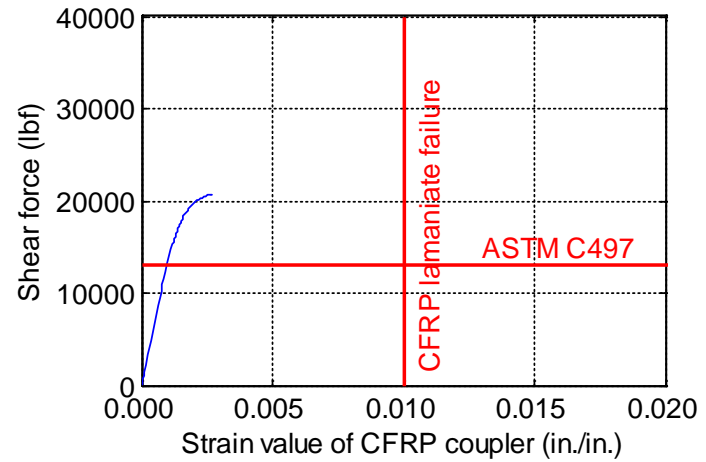
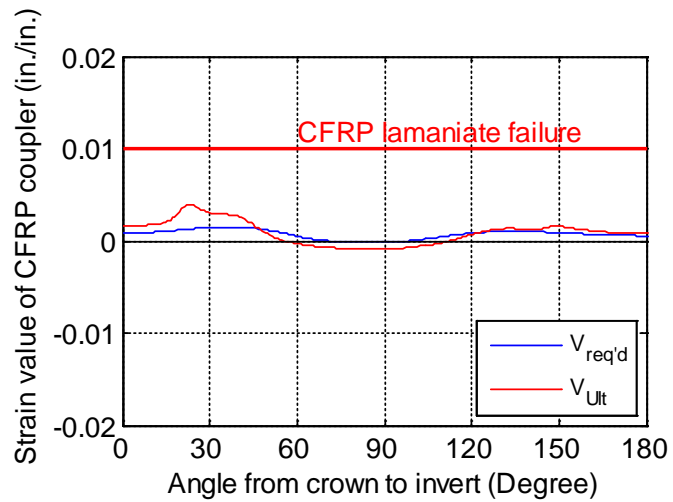
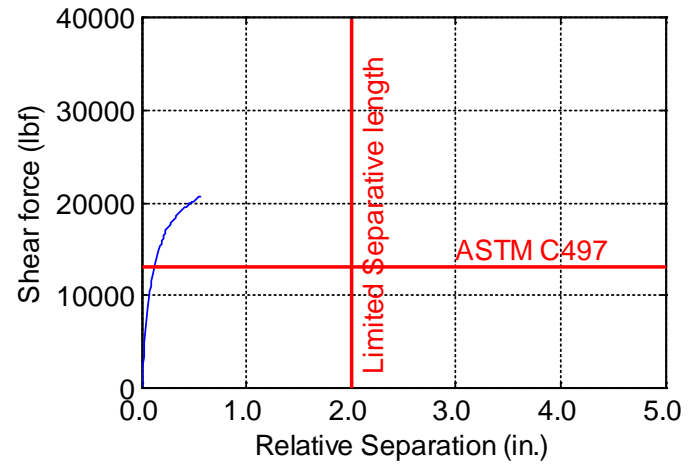
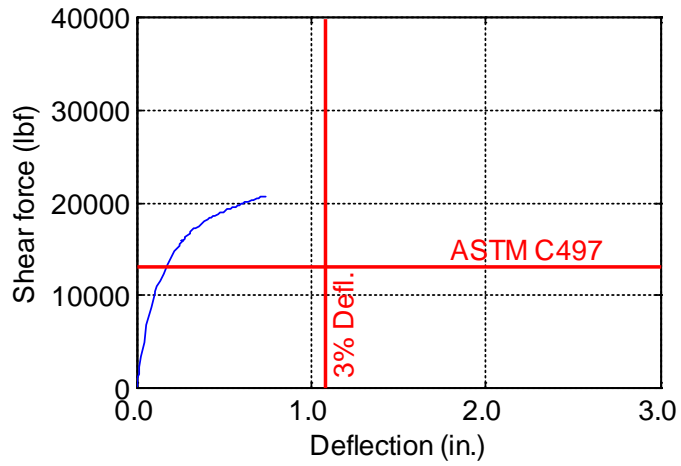


Figure B-50. TW-036-12-0.5

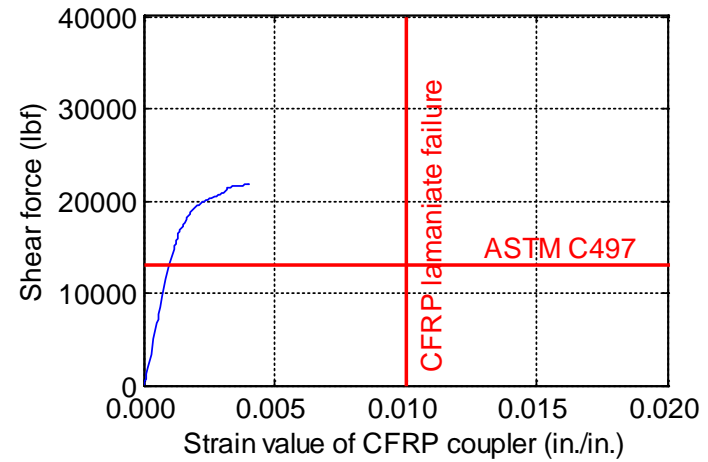
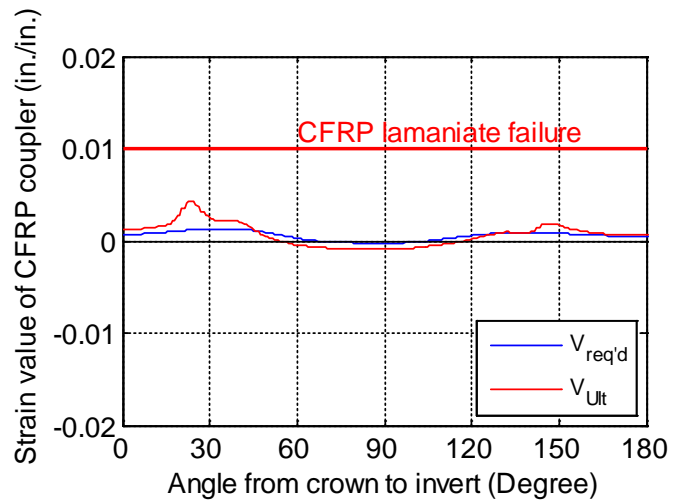
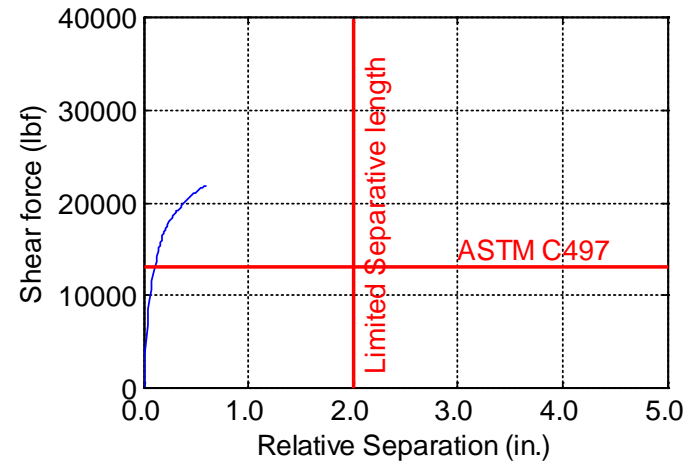
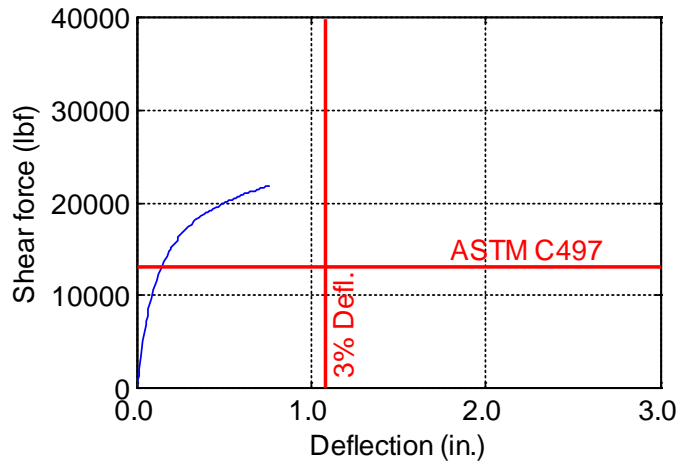


Figure B-51. TW-036-12-0.625

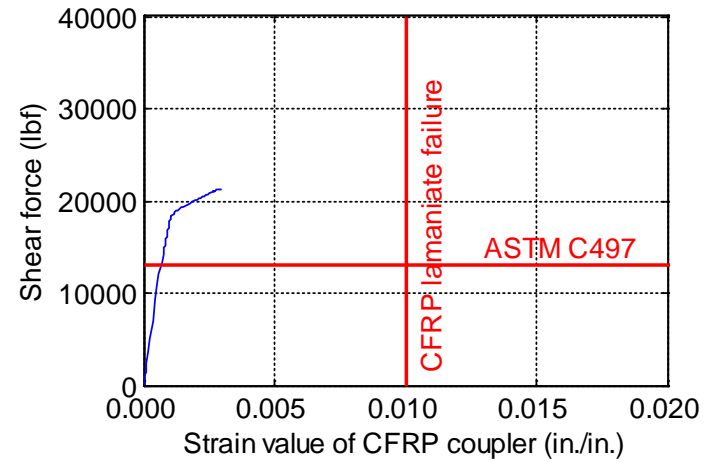
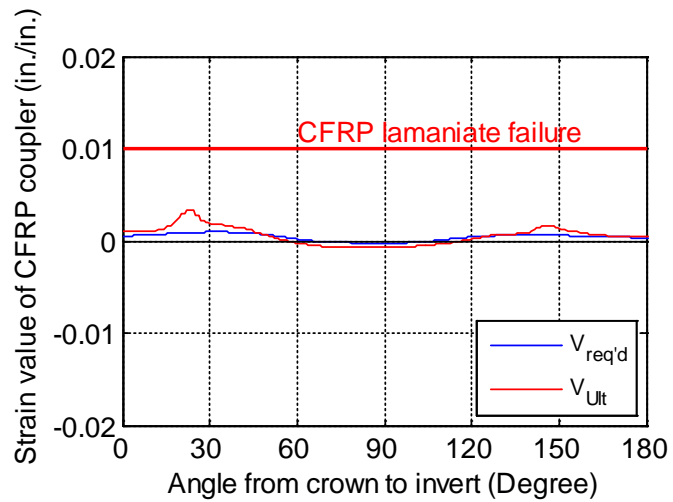
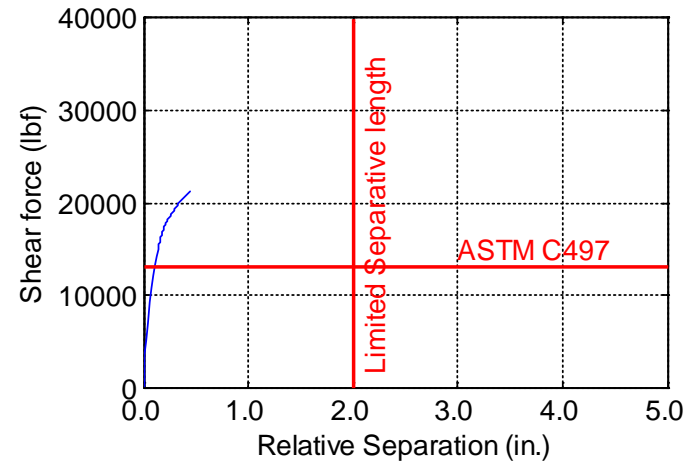
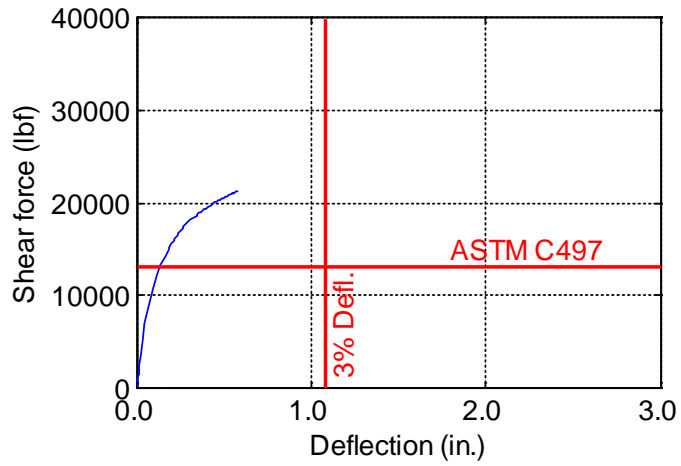


Figure B-52. TW-036-12-0.75

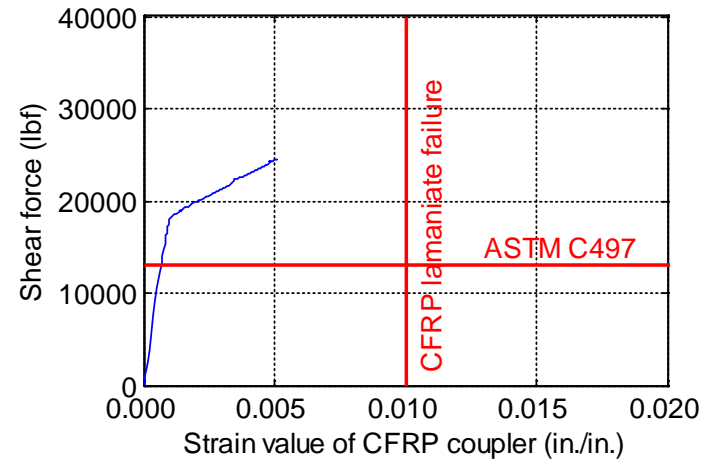
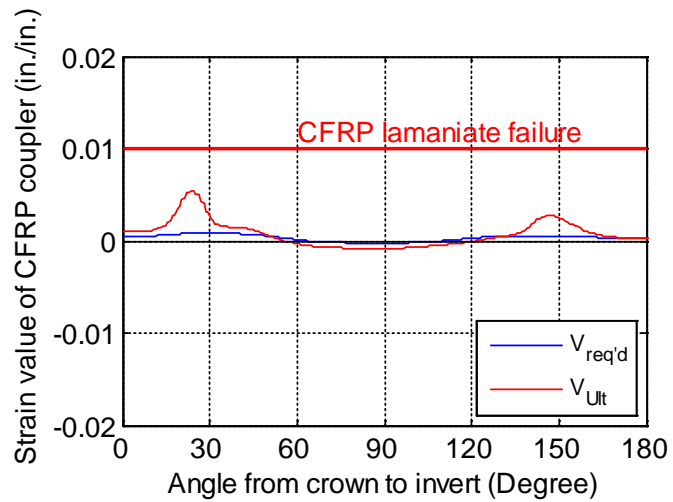
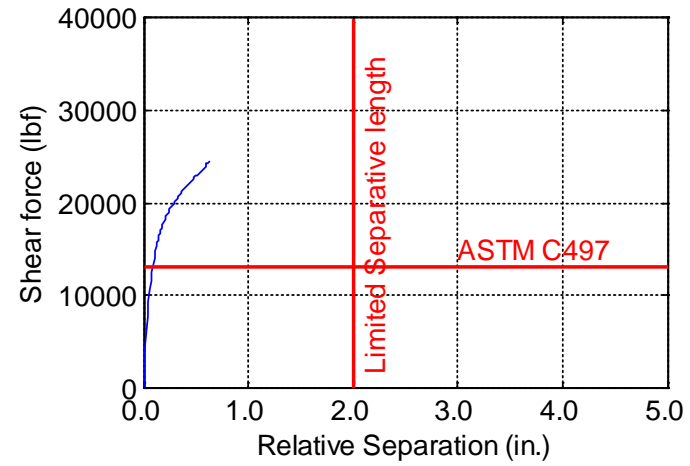
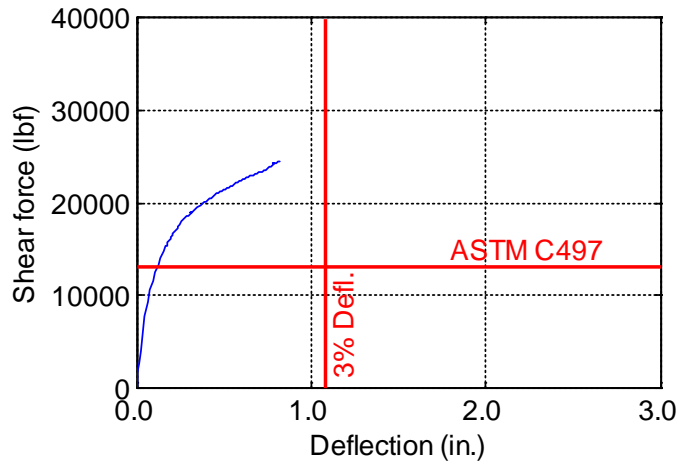


Figure B-53. TW-036-12-0.875

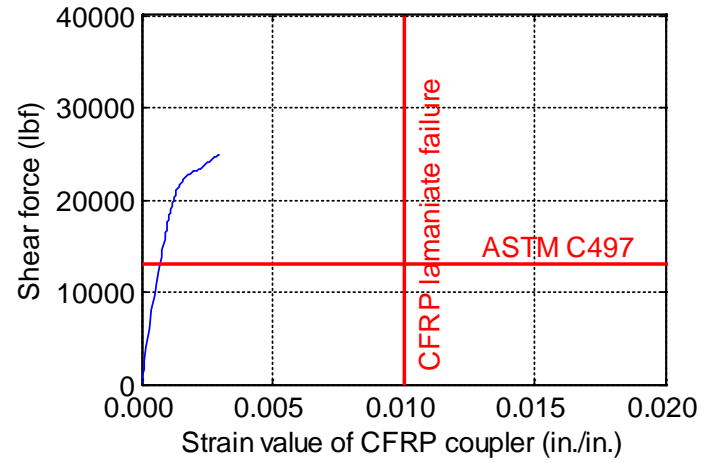
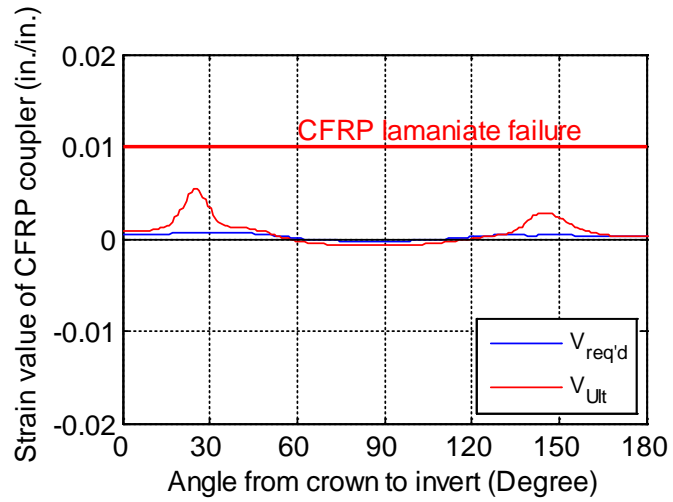
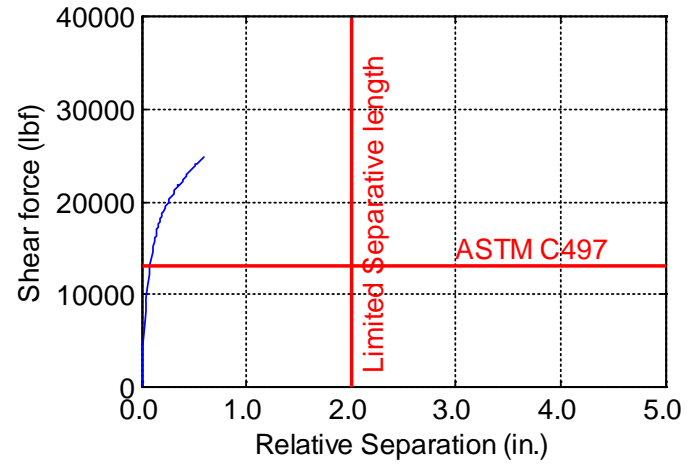
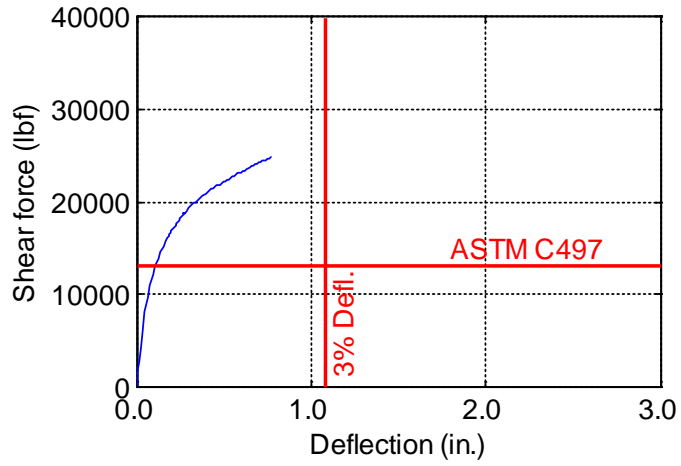


Figure B-54. TW-036-12-1.0

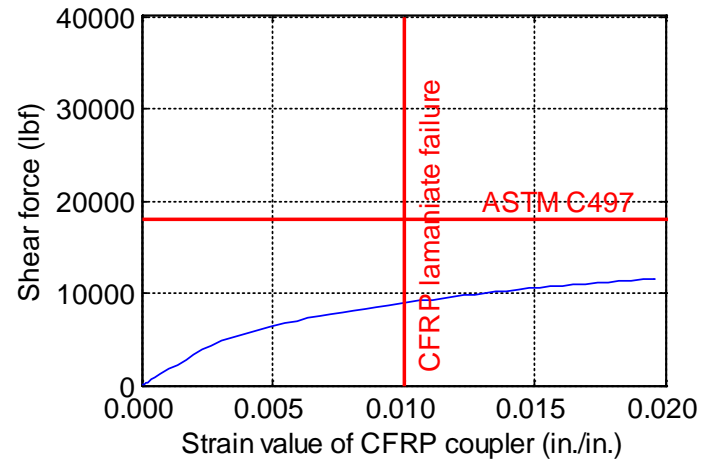
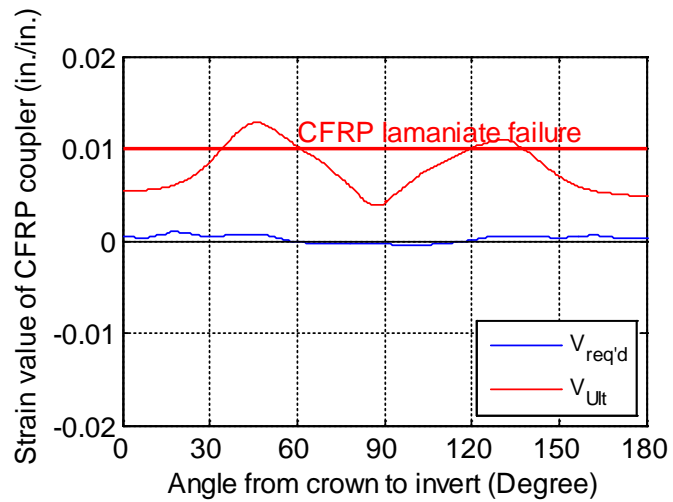
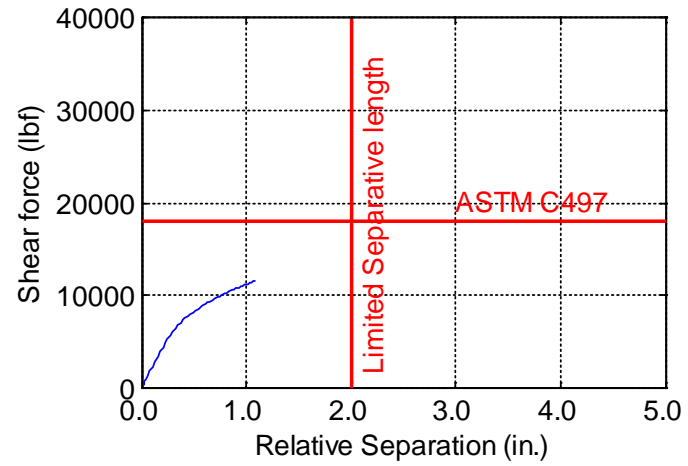
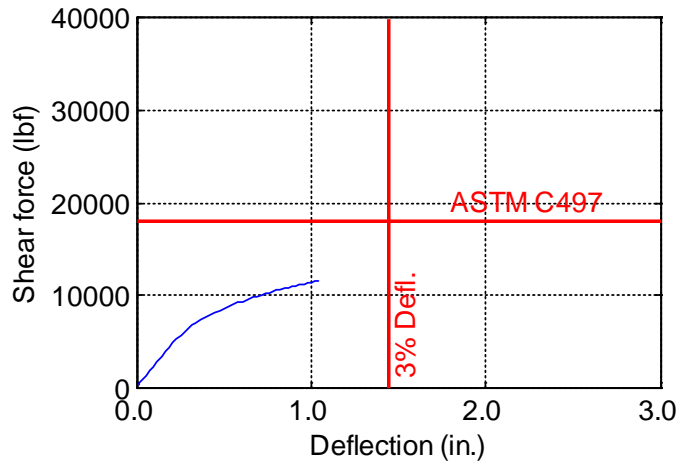


Figure B-55. TW-048-06-0.125

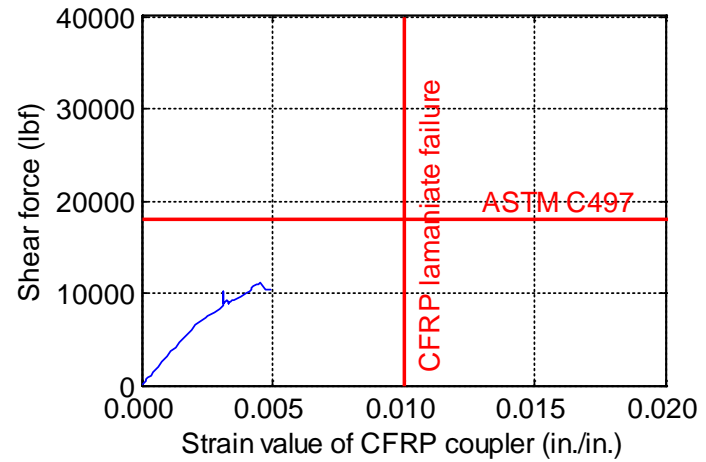
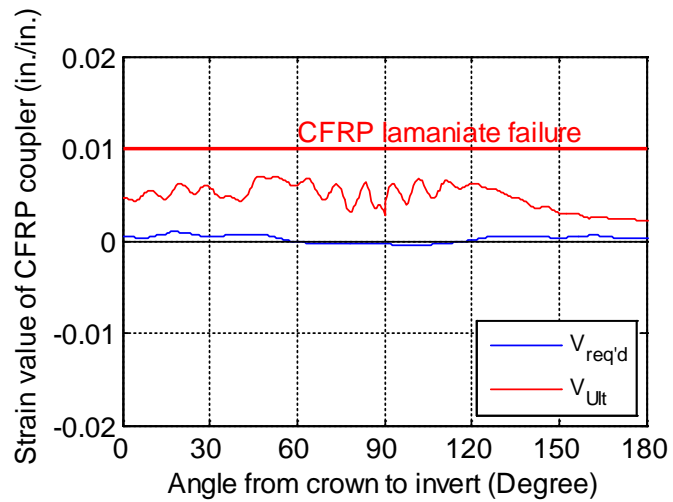
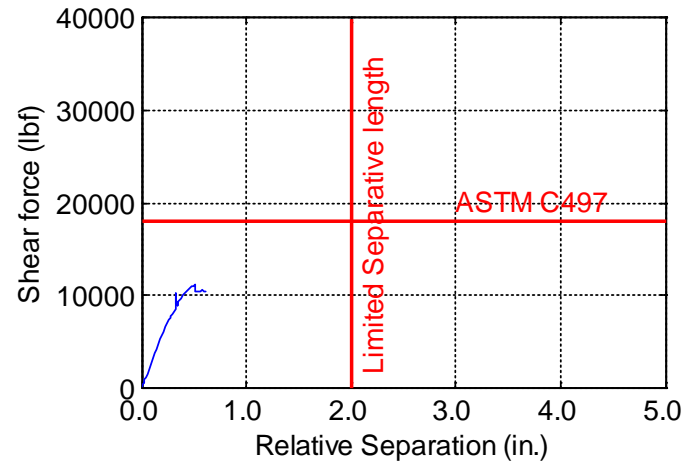
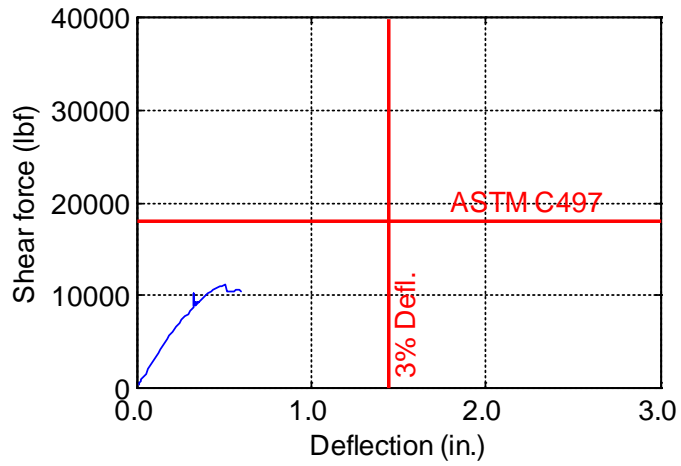


Figure B-56. TW-048-06-0.1875

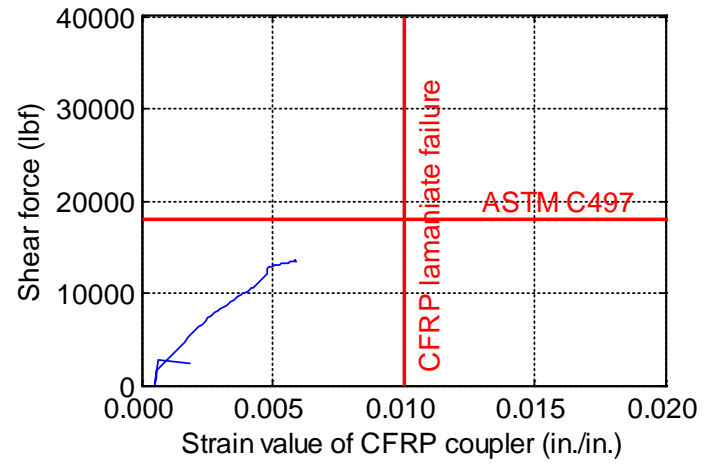
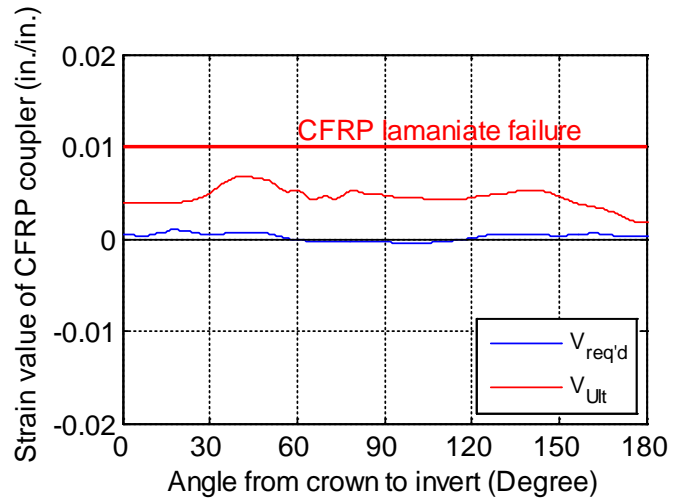
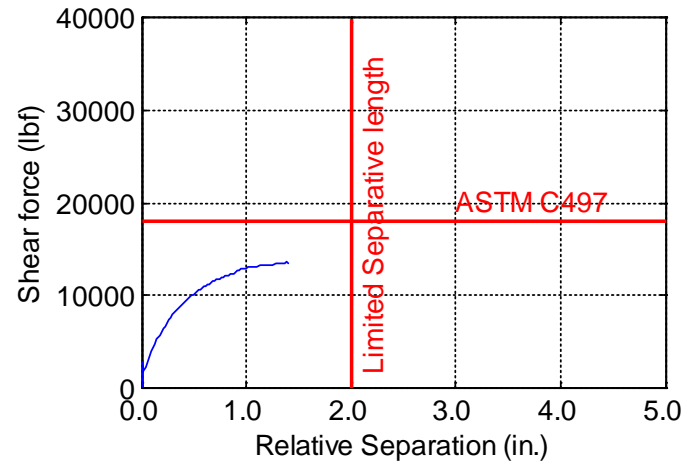
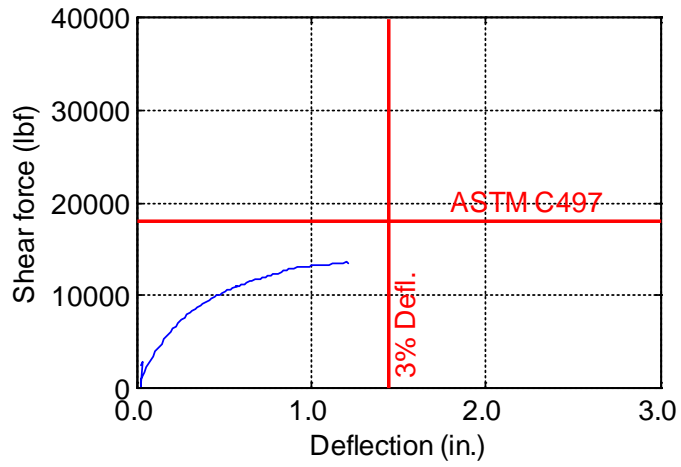


Figure B-57. TW-048-06-0.25

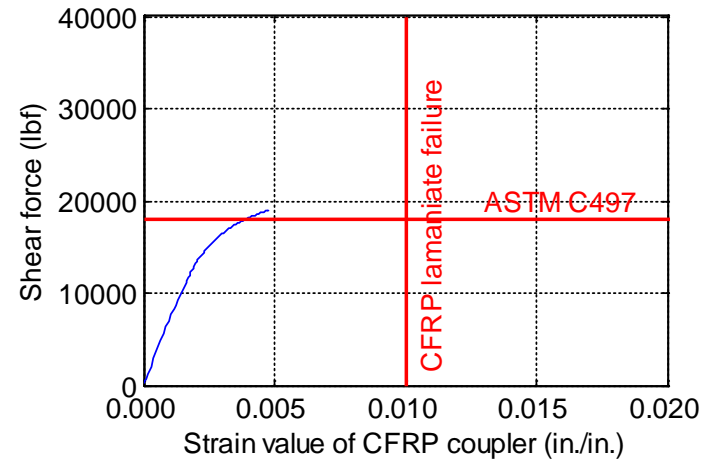
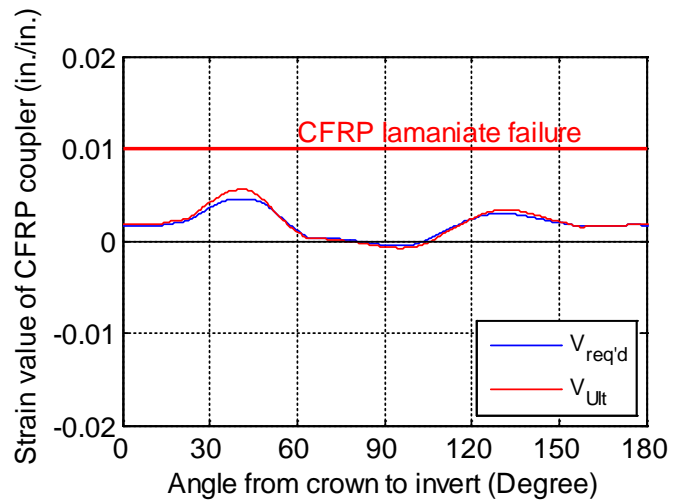
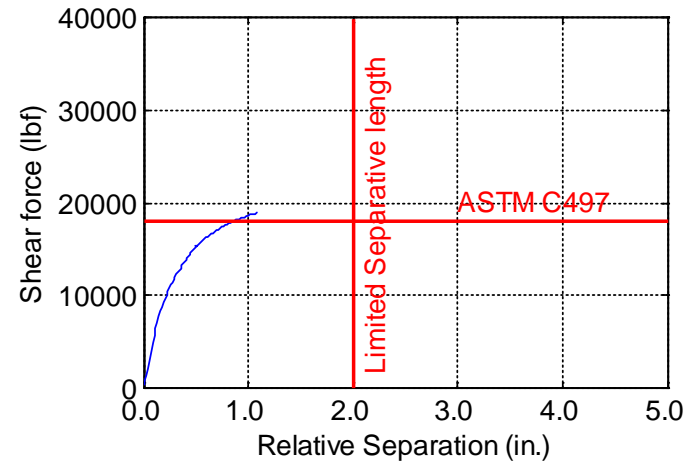
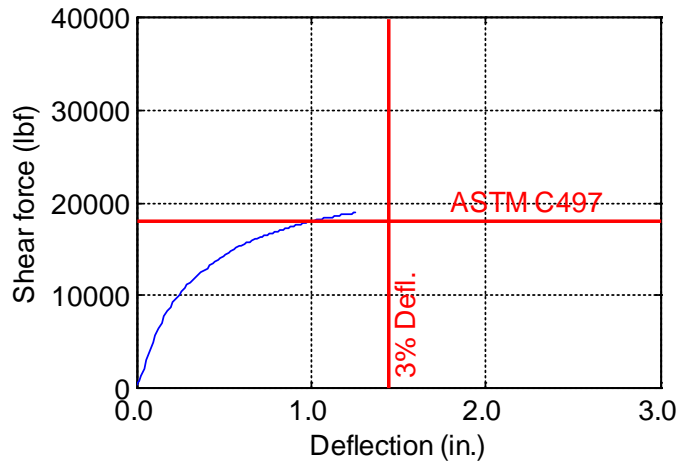


Figure B-58. TW-048-06-0.375

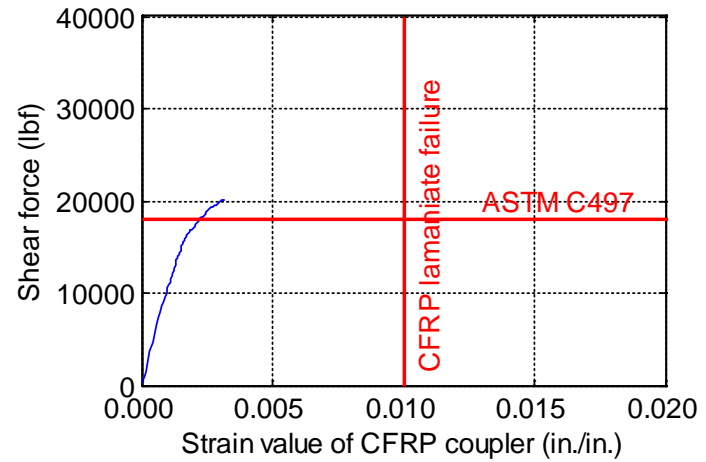
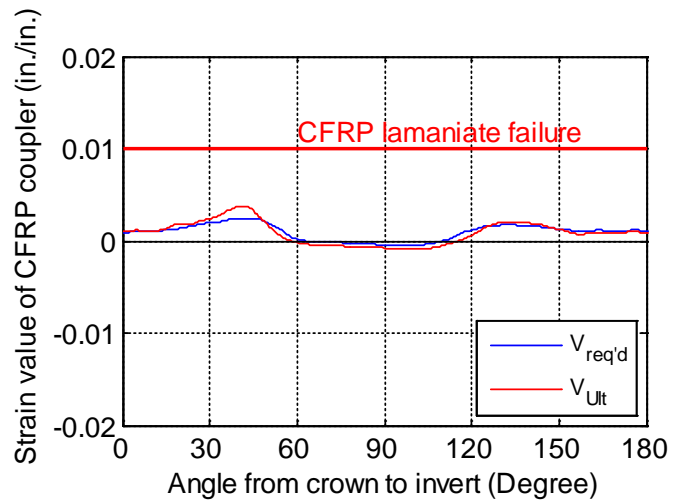
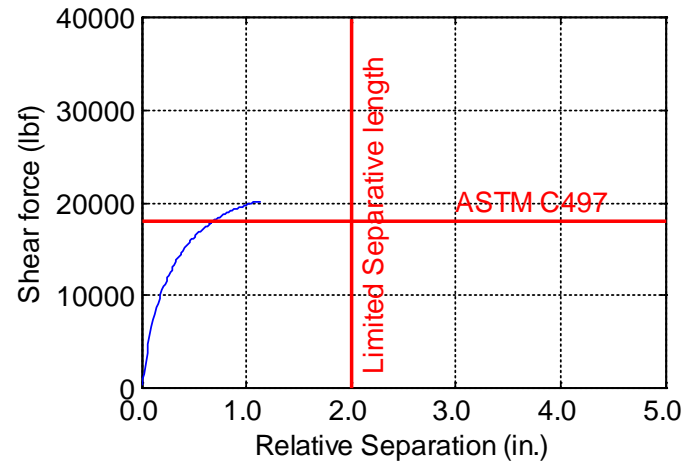
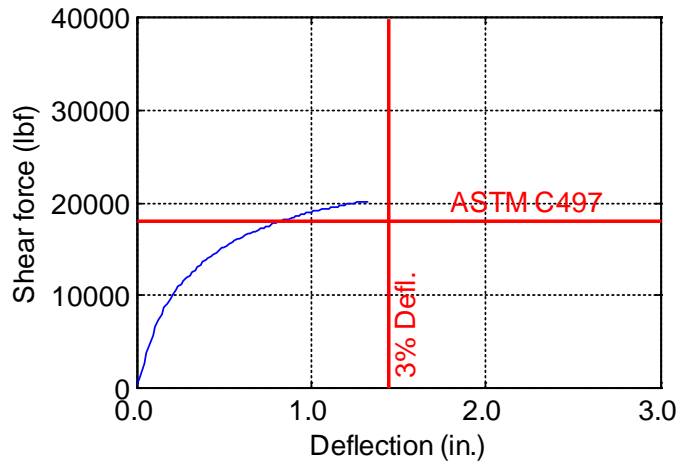


Figure B-59. TW-048-06-0.5

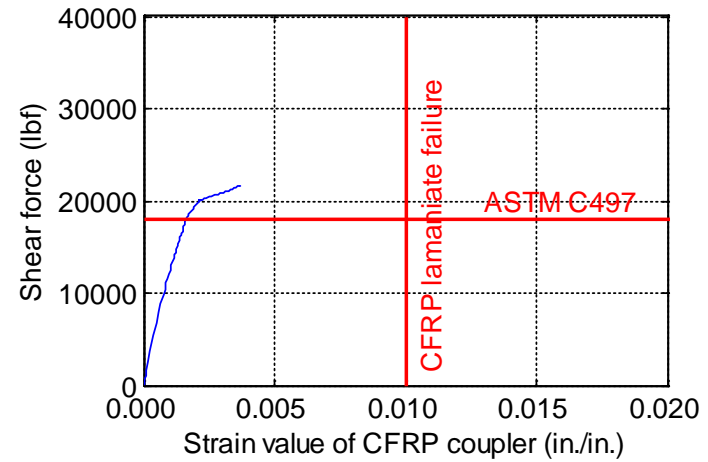
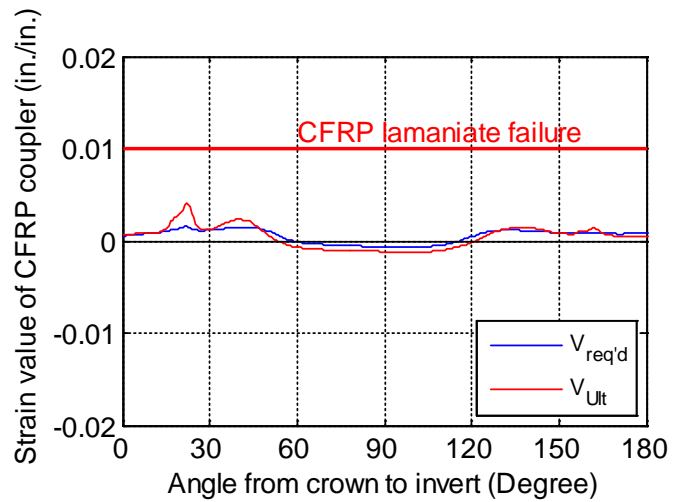
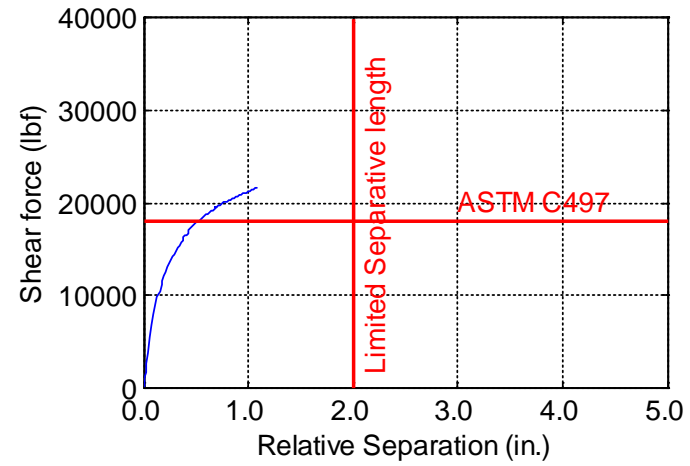
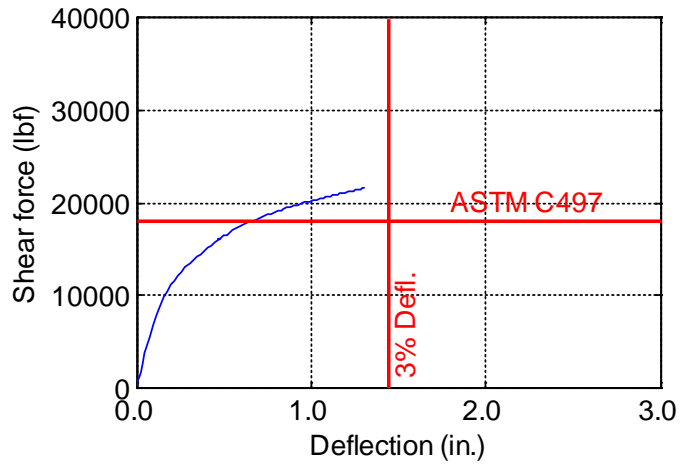


Figure B-60. TW-048-06-0.625

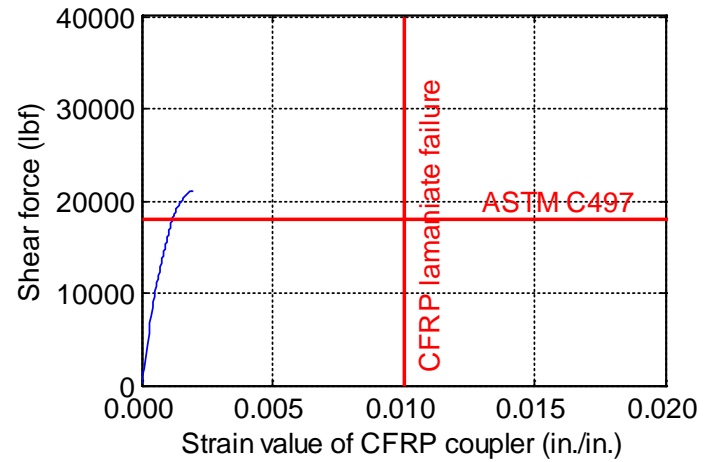
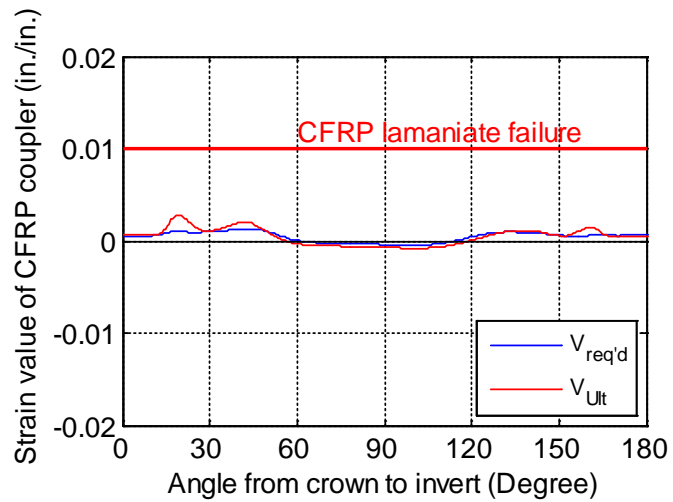
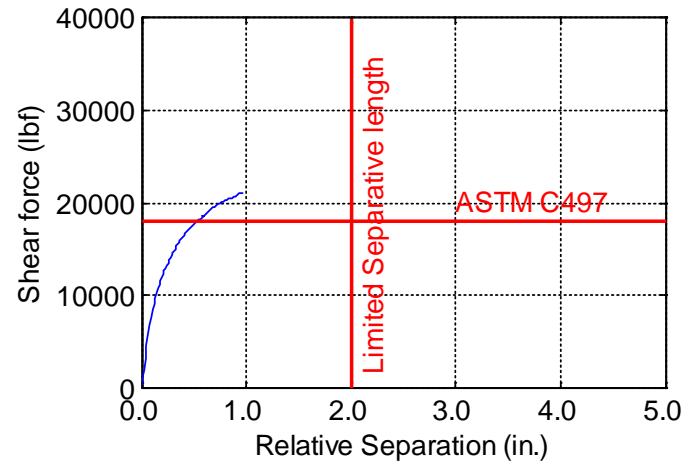
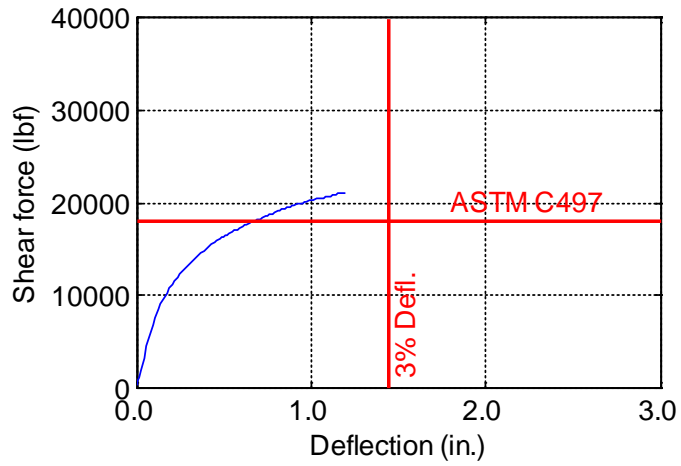


Figure B-61. TW-048-06-0.75

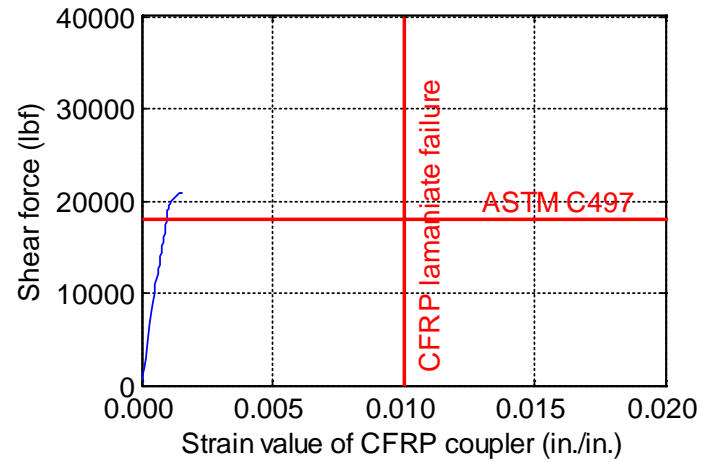
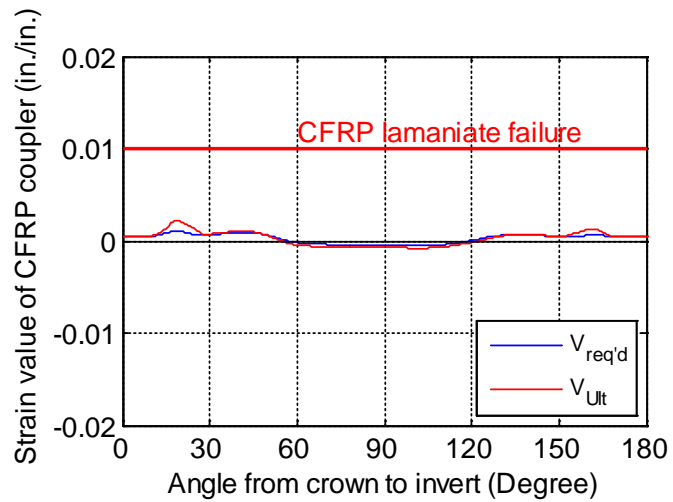
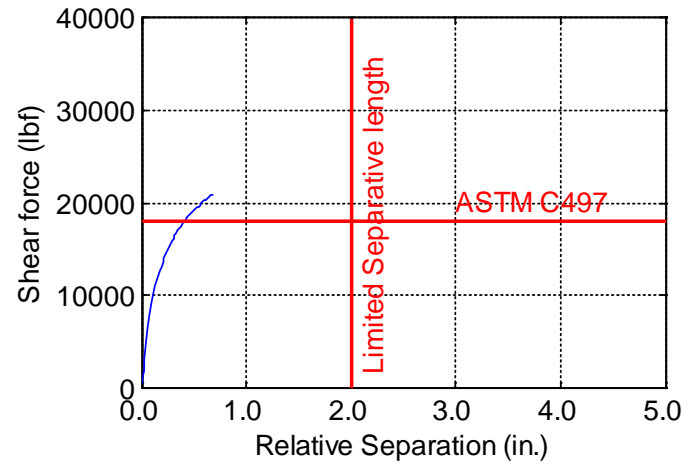
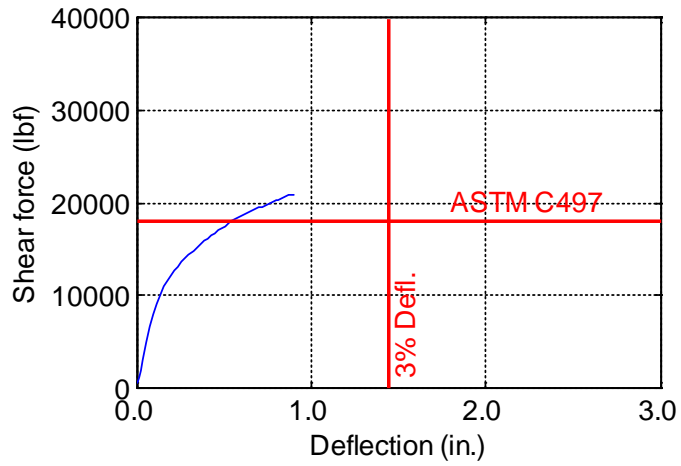


Figure B-62. TW-048-06-0.875

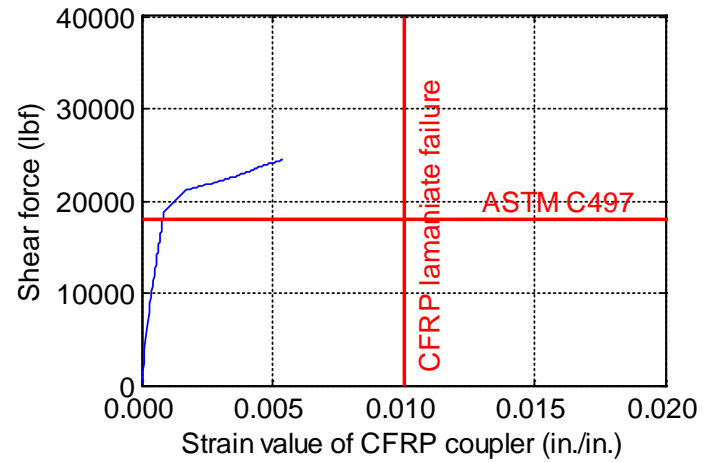
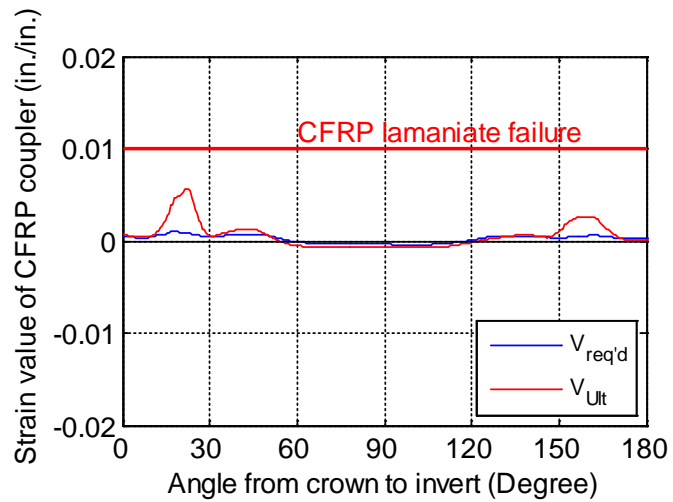
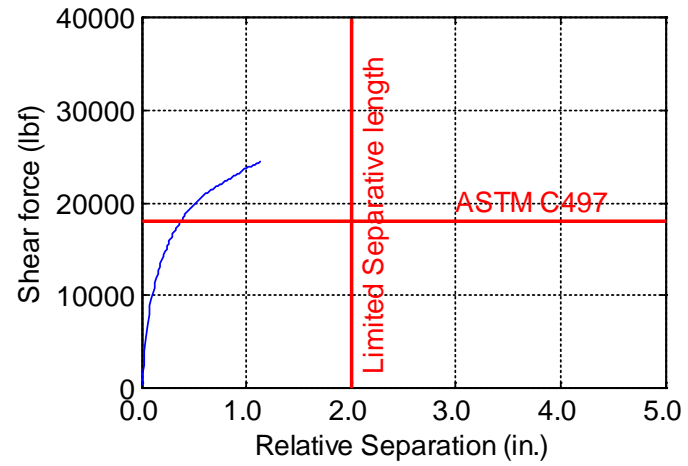
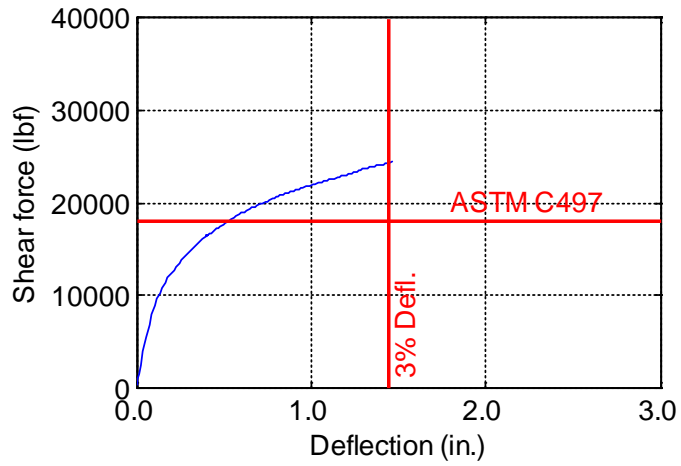


Figure B-63. TW-048-06-1.0

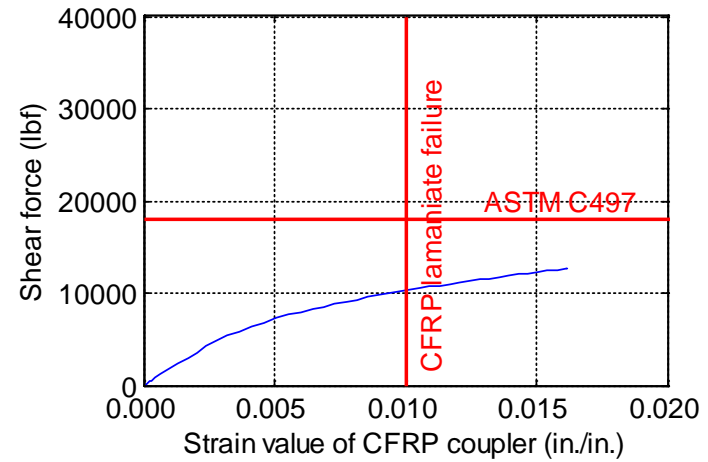
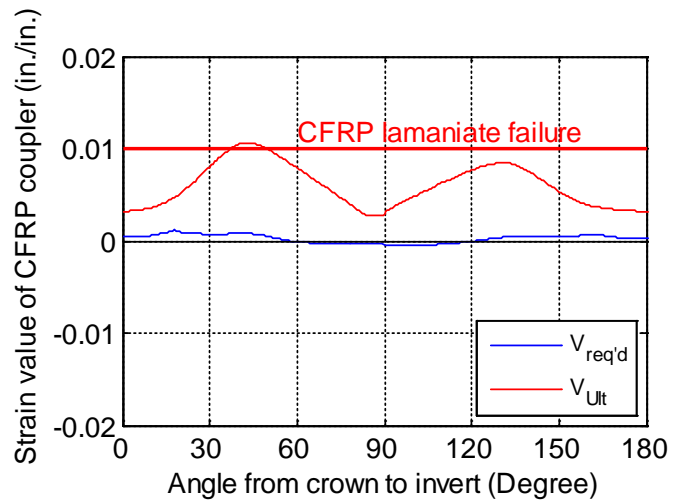
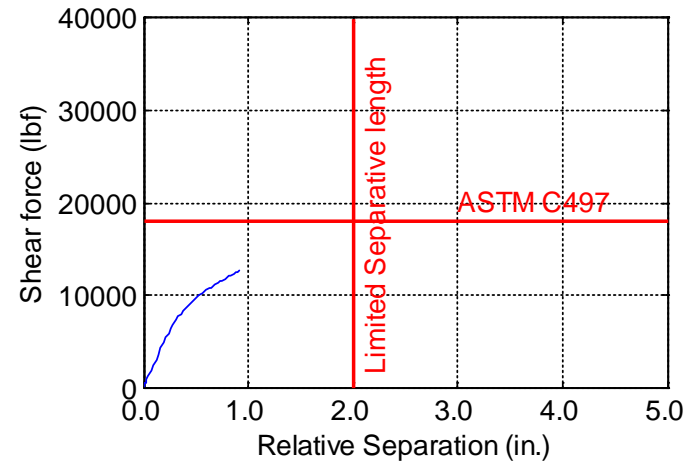
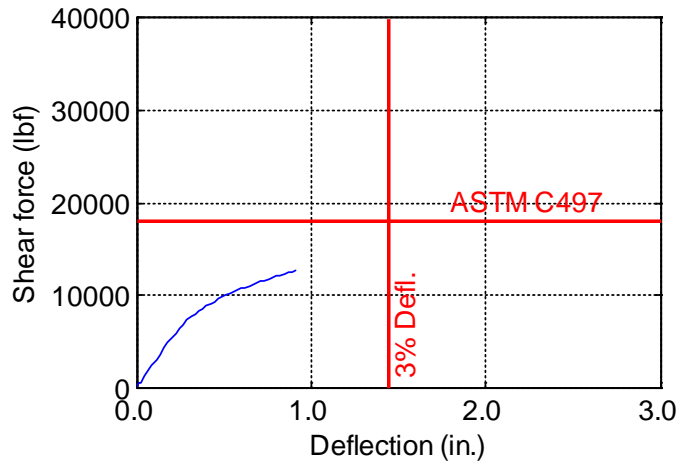


Figure B-64. TW-048-09-0.125

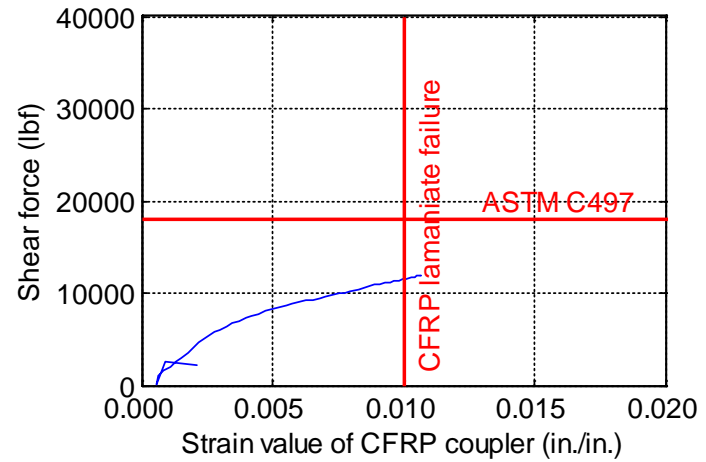
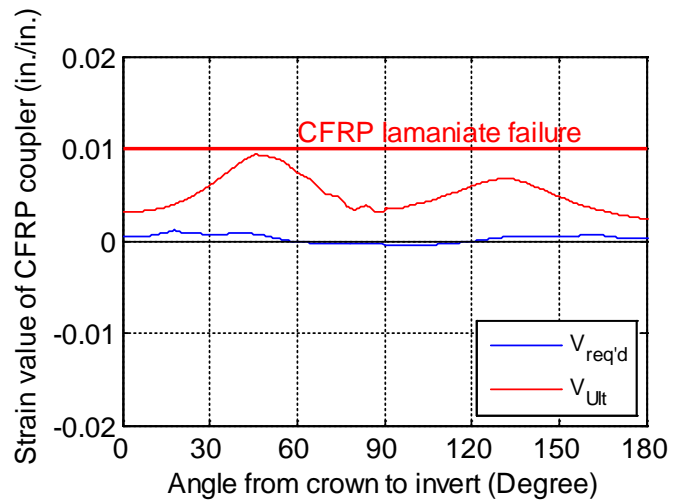
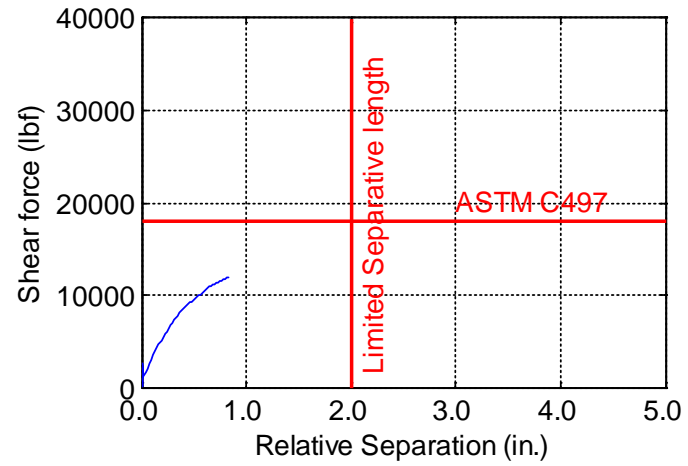
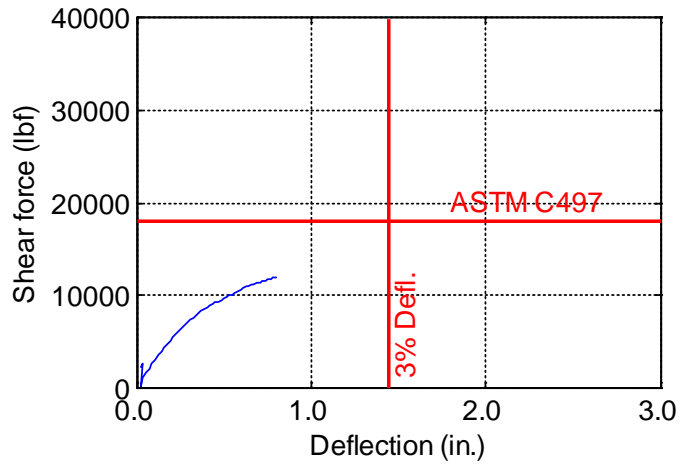


Figure B-65. TW-048-09-0.1875

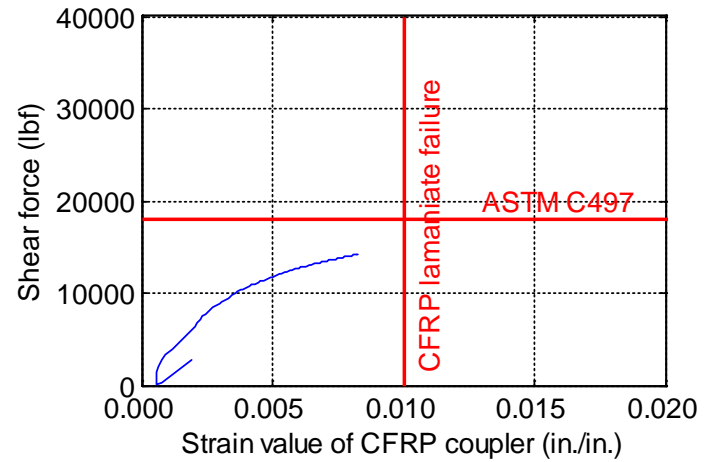
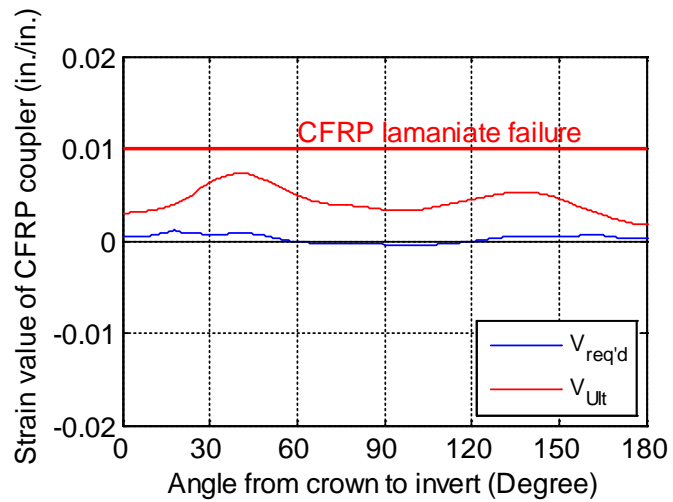
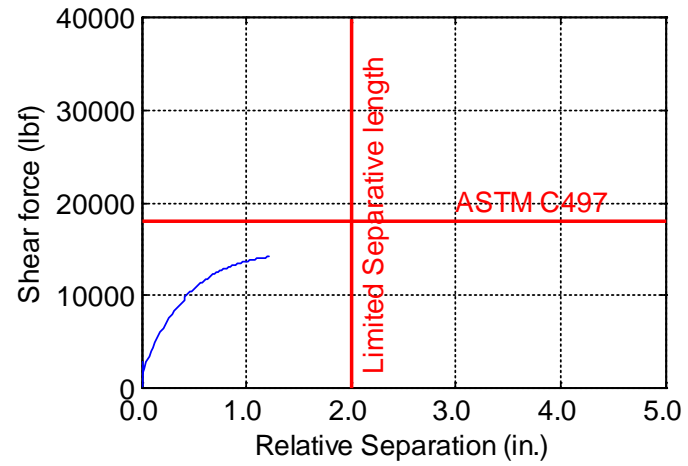
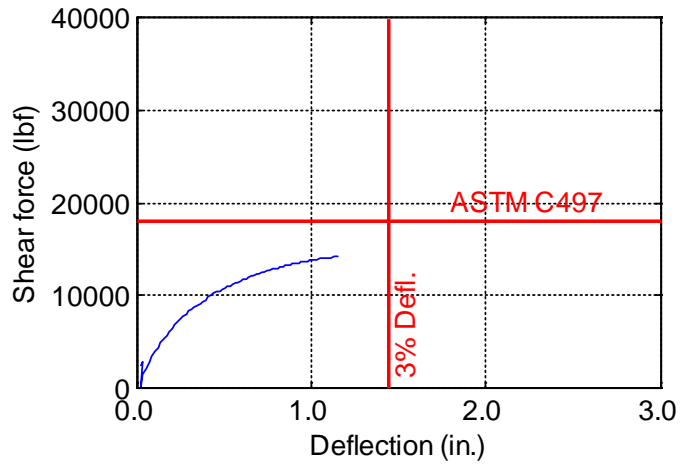


Figure B-66. TW-048-09-0.25

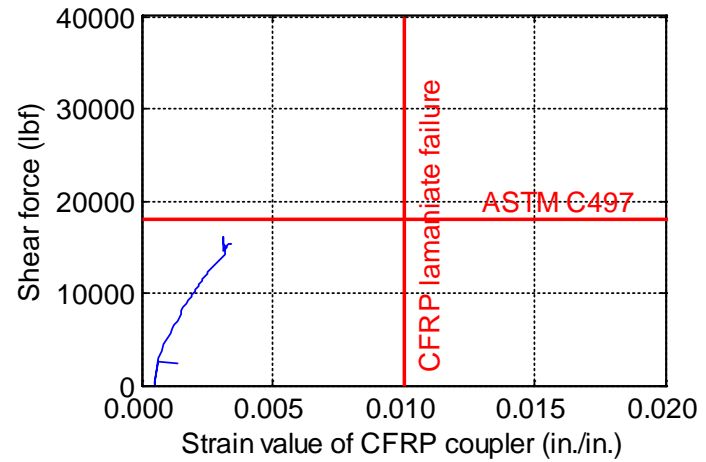
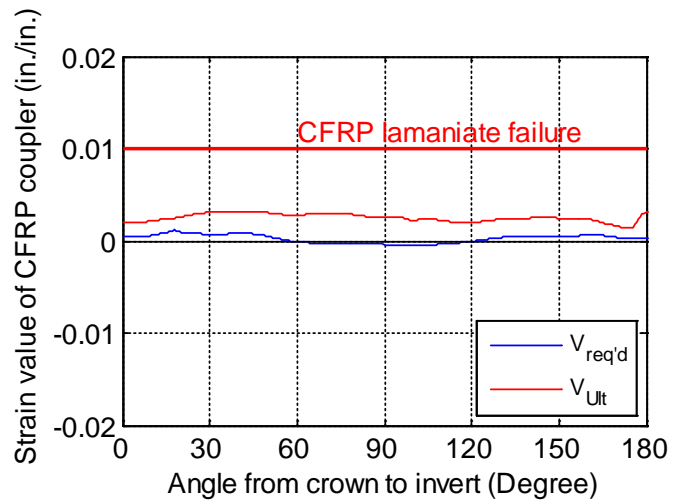
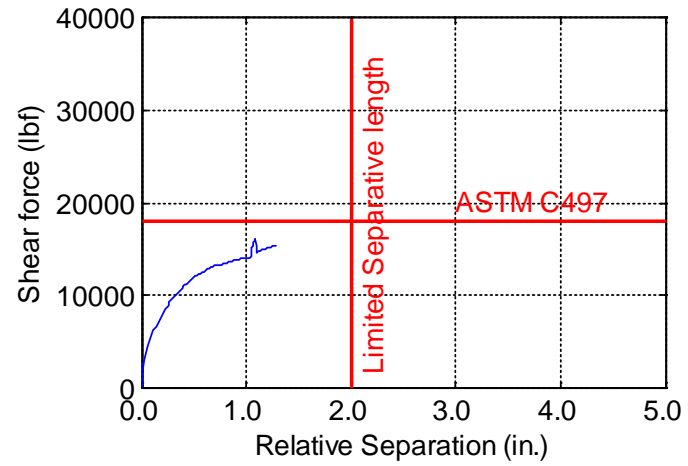
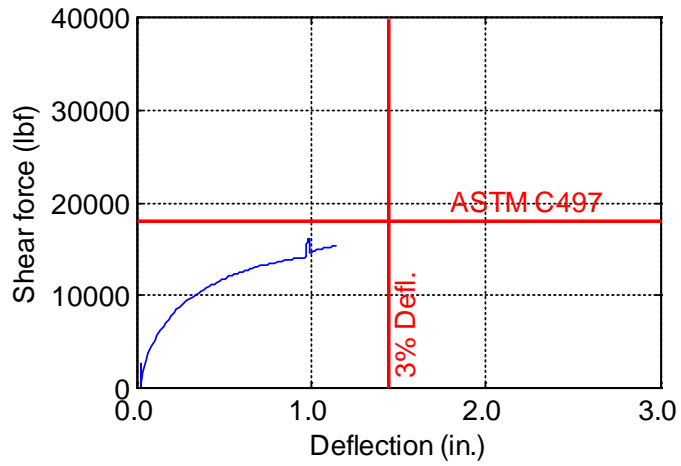


Figure B-67. TW-048-09-0.375

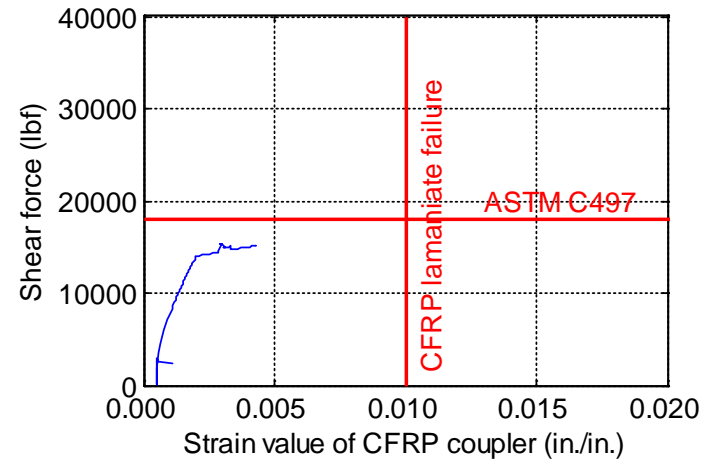
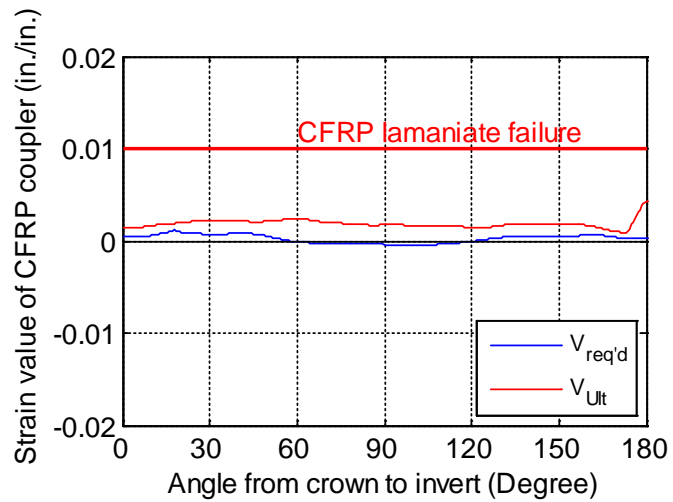
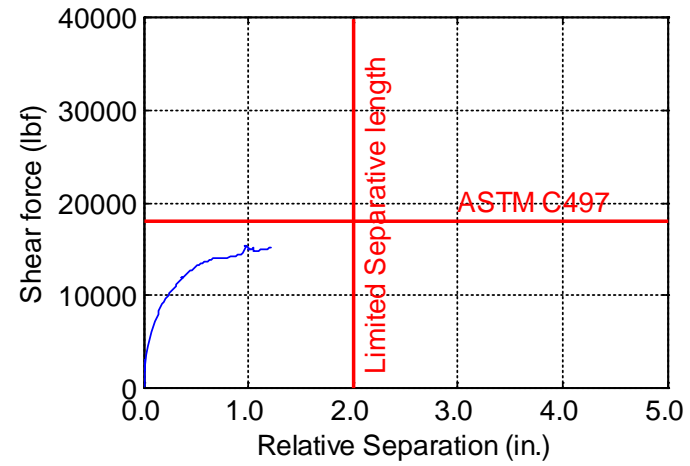
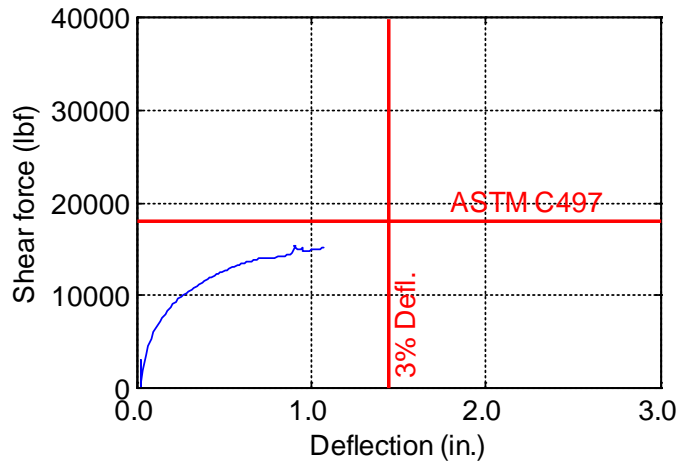


Figure B-68. TW-048-09-0.5

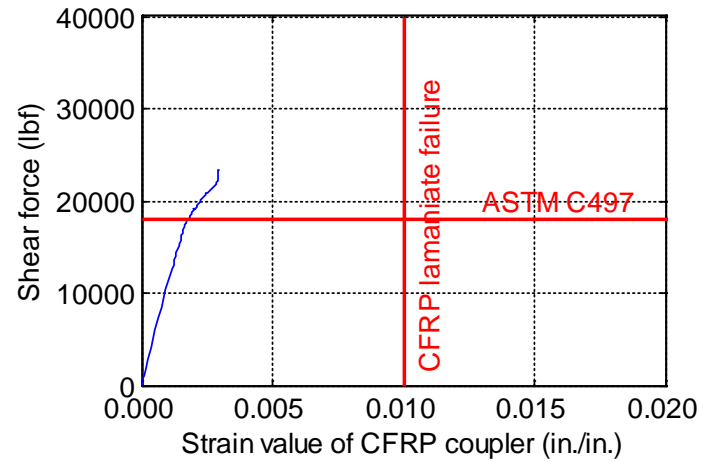
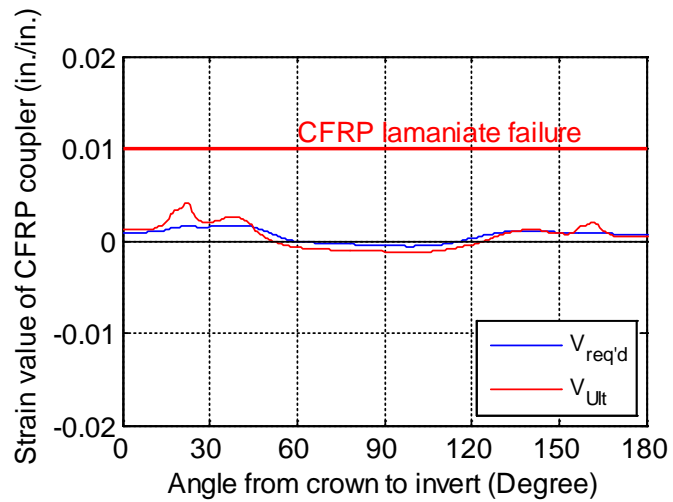
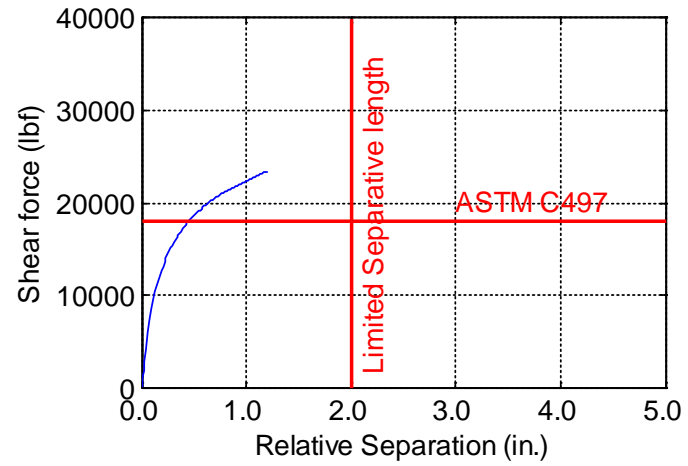
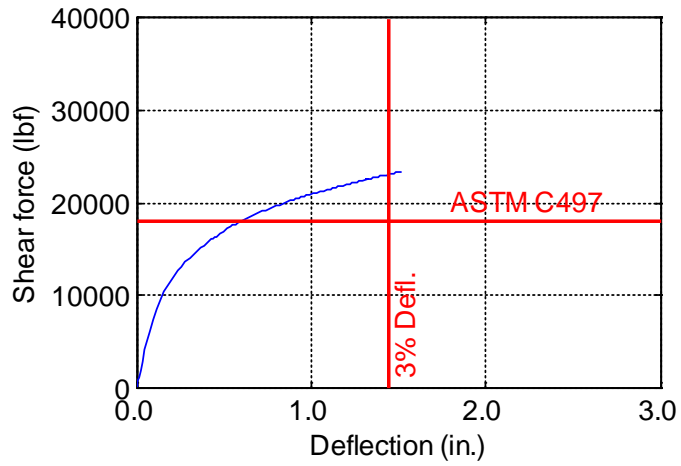


Figure B-69. TW-048-09-0.625

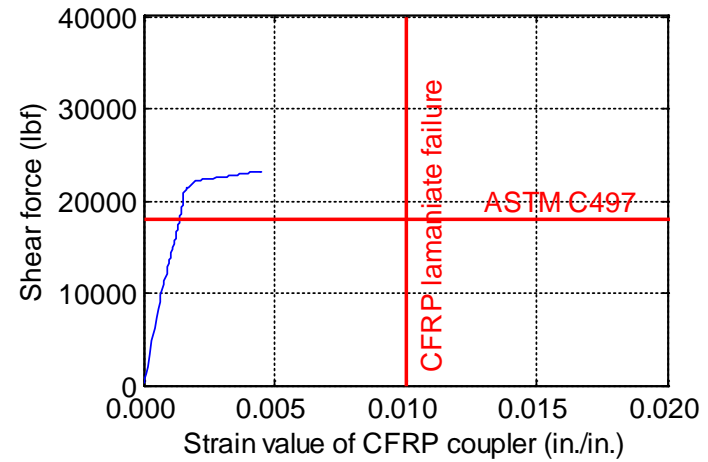
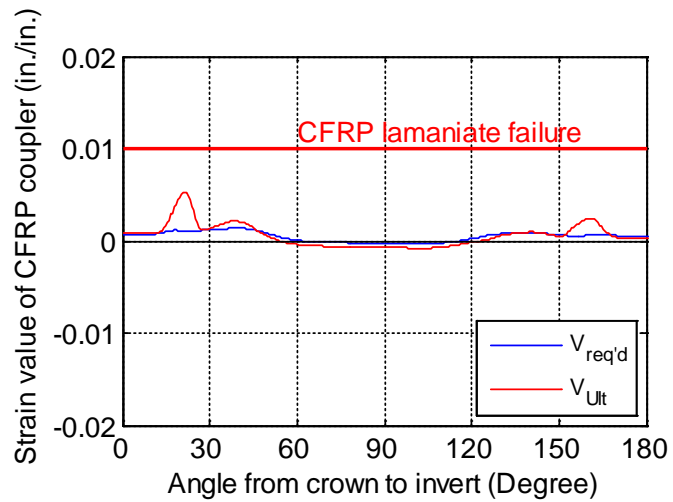
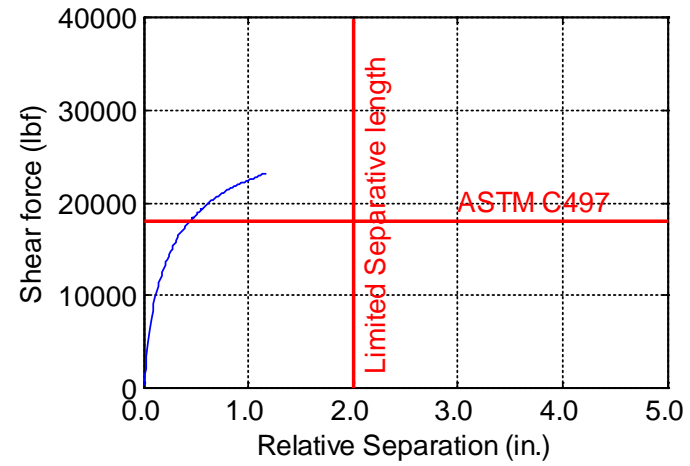
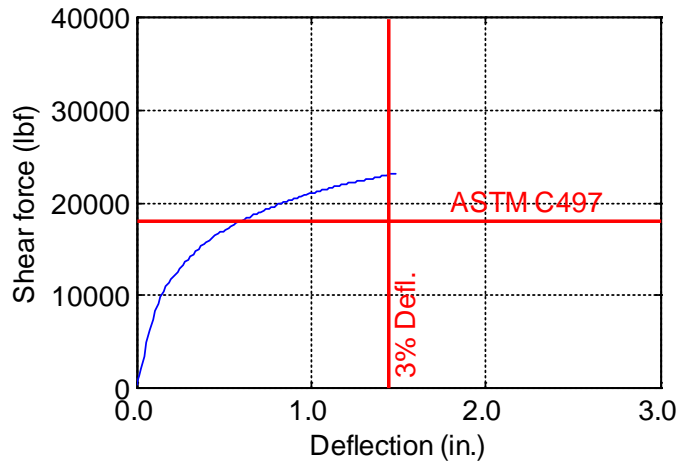


Figure B-70. TW-048-09-0.75

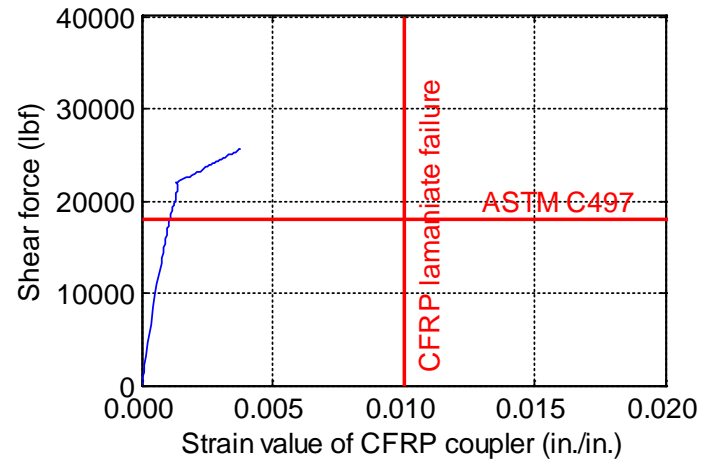
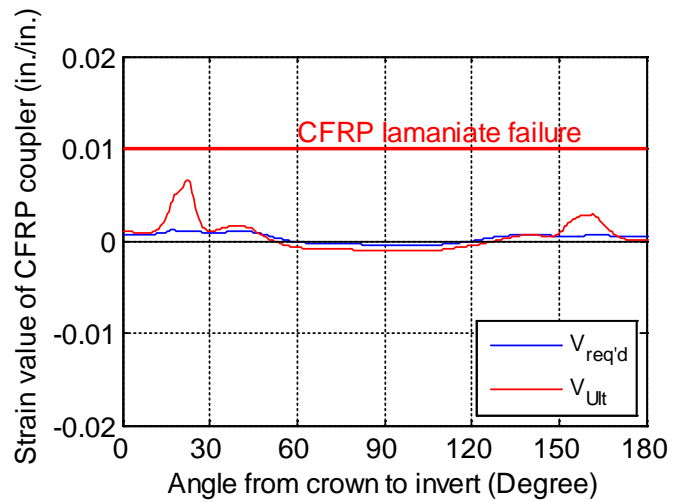
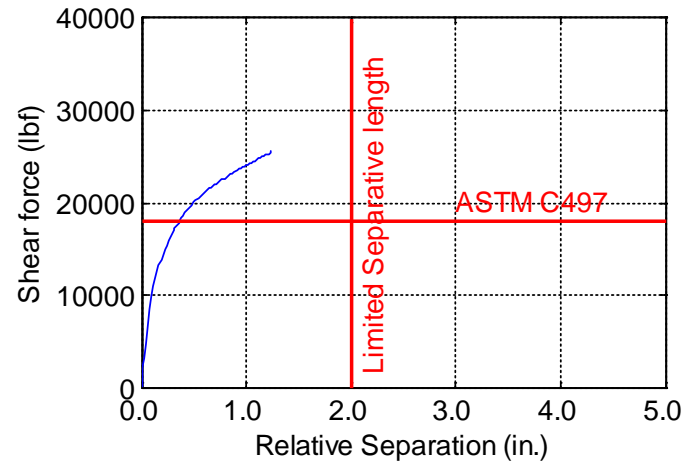
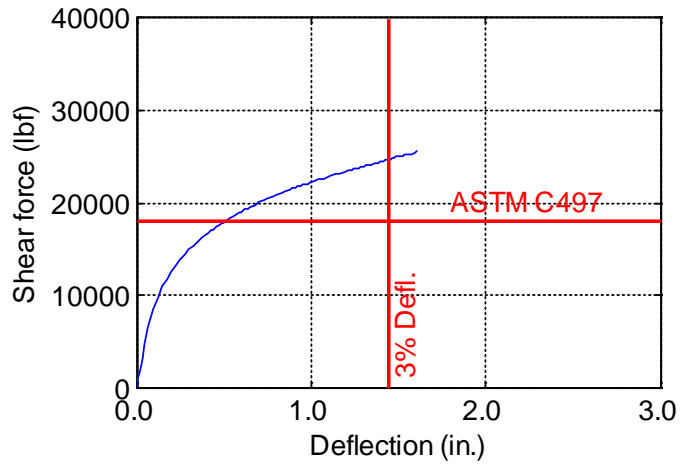


Figure B-71. TW-048-09-0.875

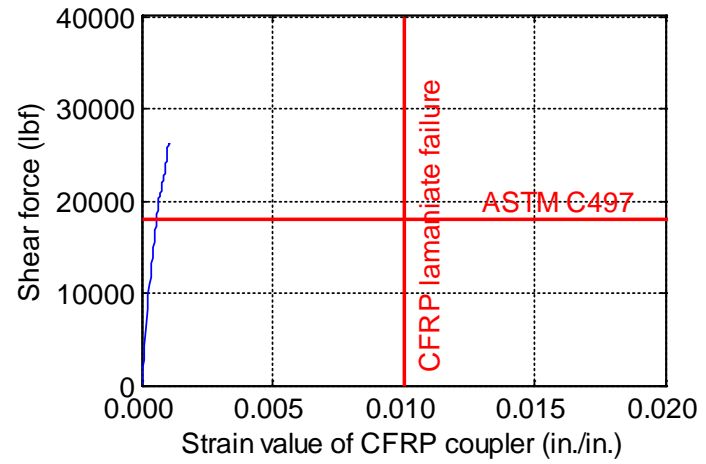
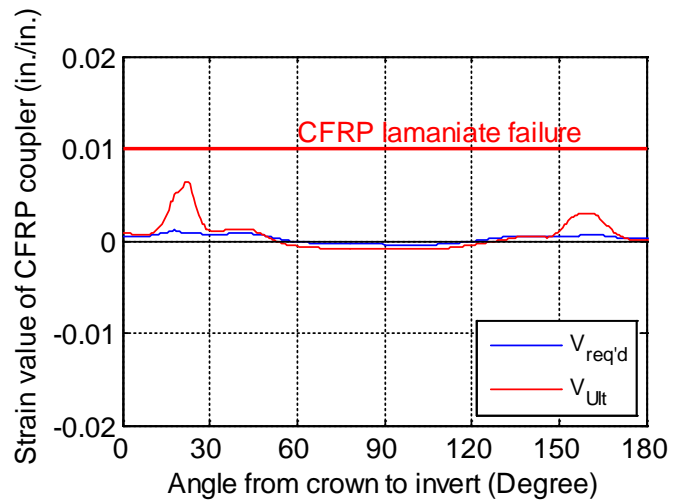
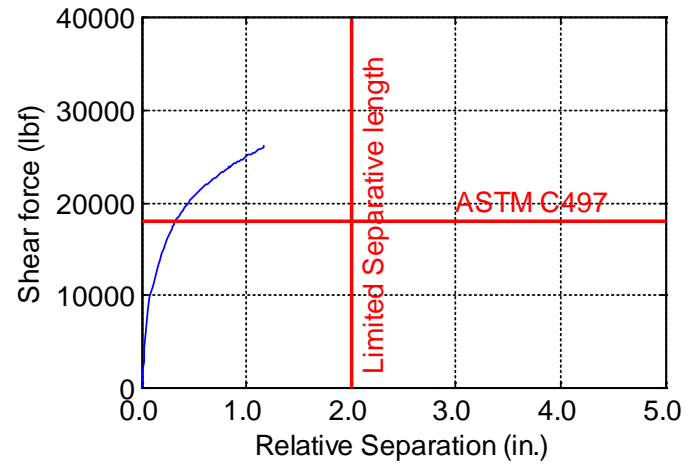
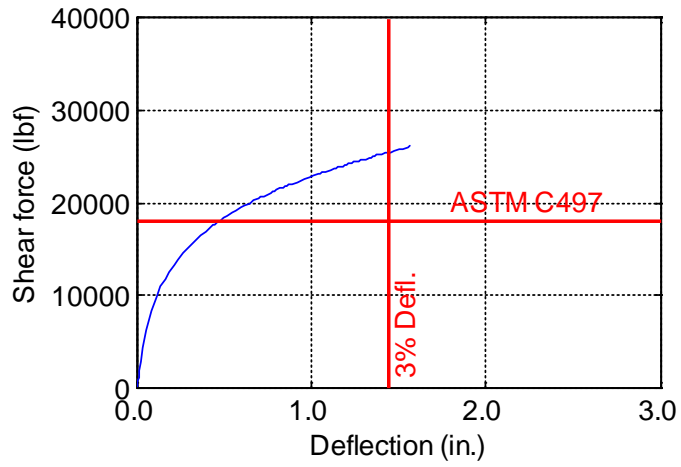


Figure B-72. TW-048-09-1.0

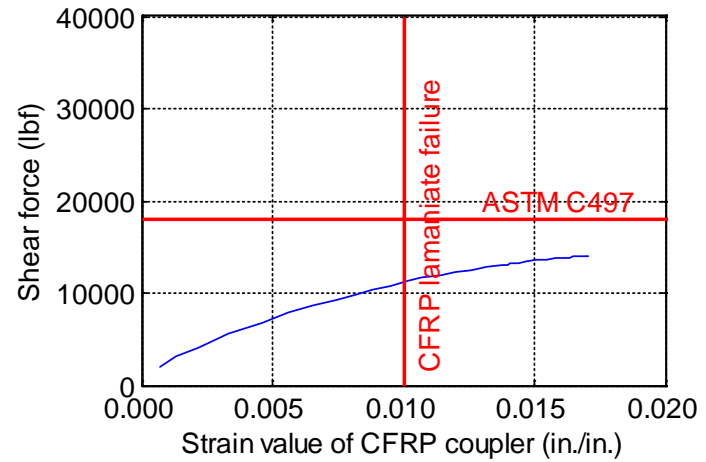
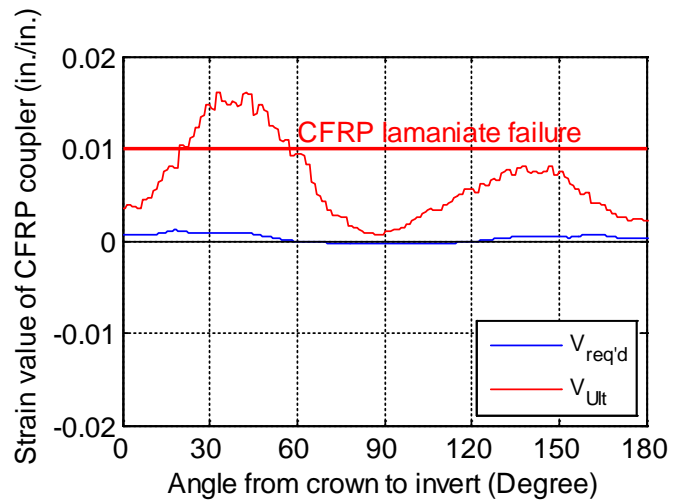
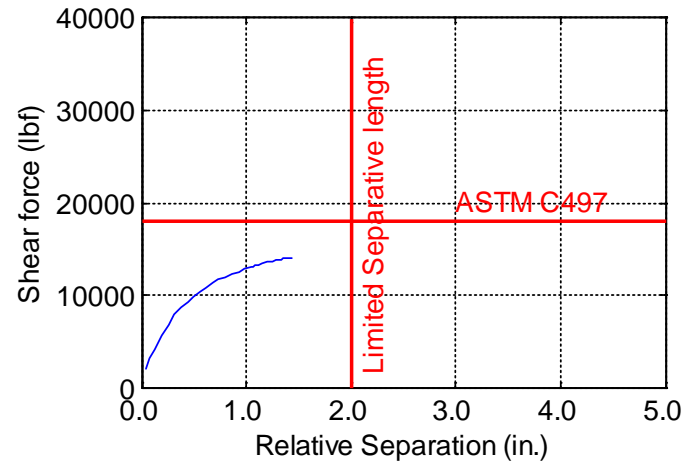
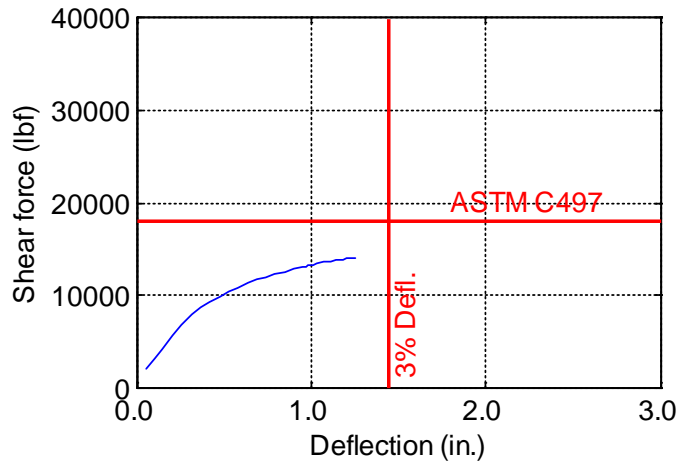


Figure B-73. TW-048-12-0.125

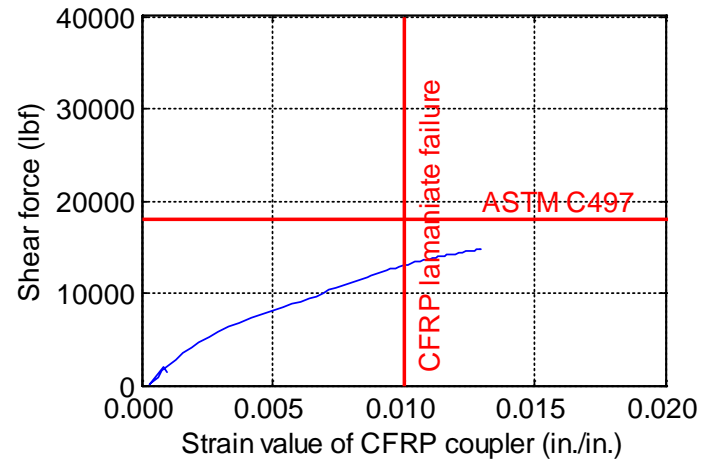
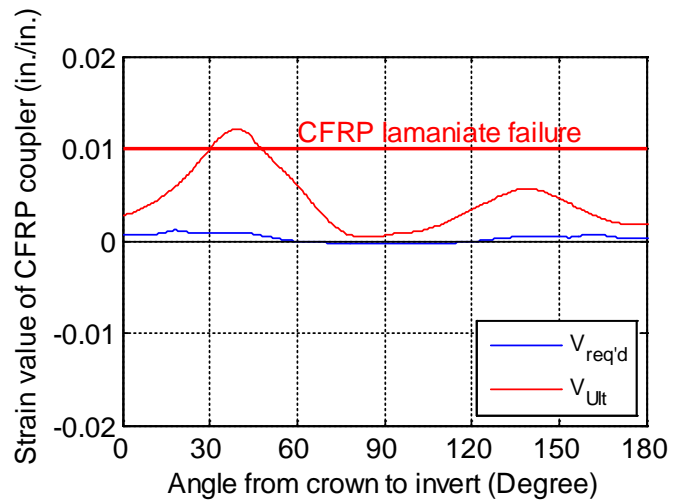
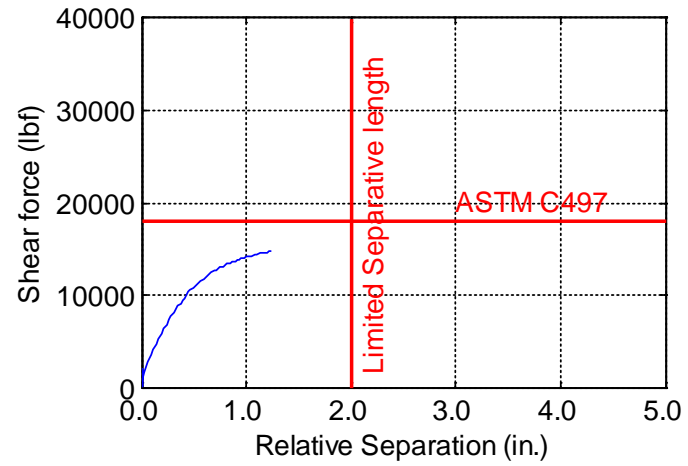
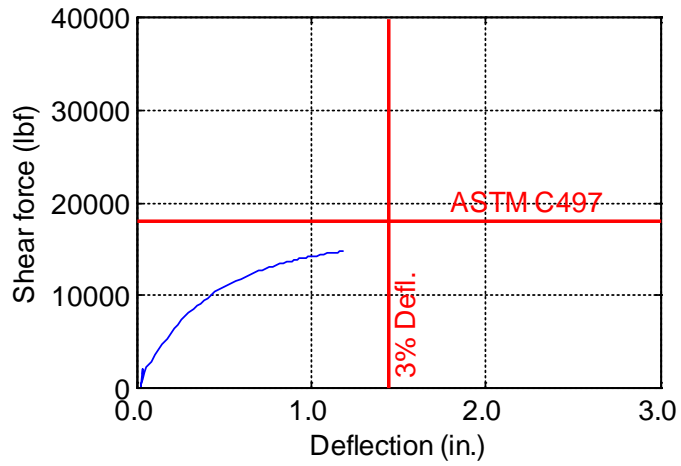


Figure B-74. TW-048-12-0.1875

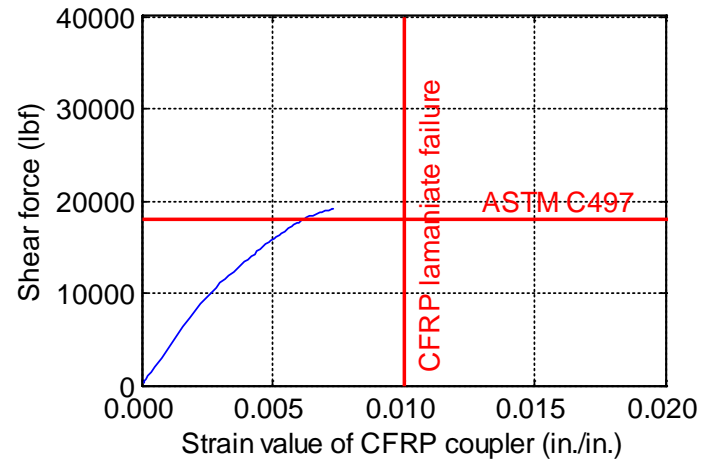
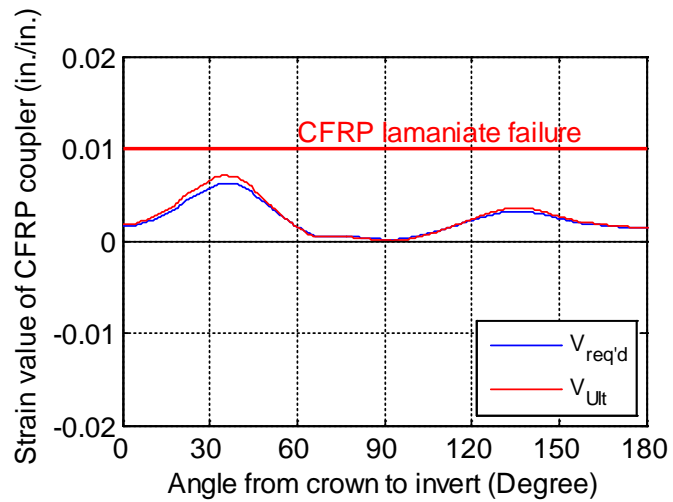
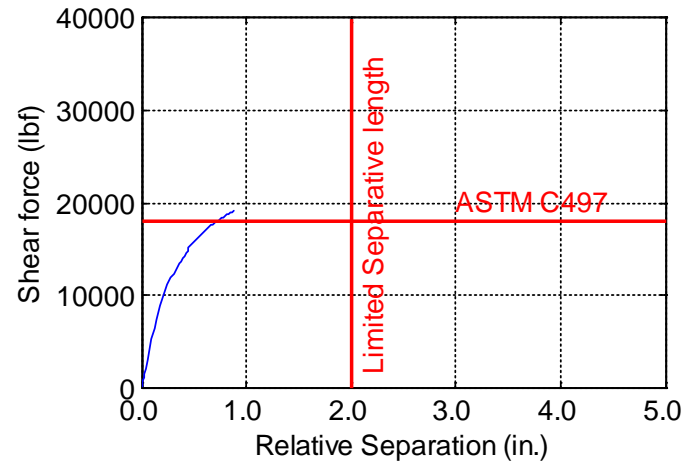
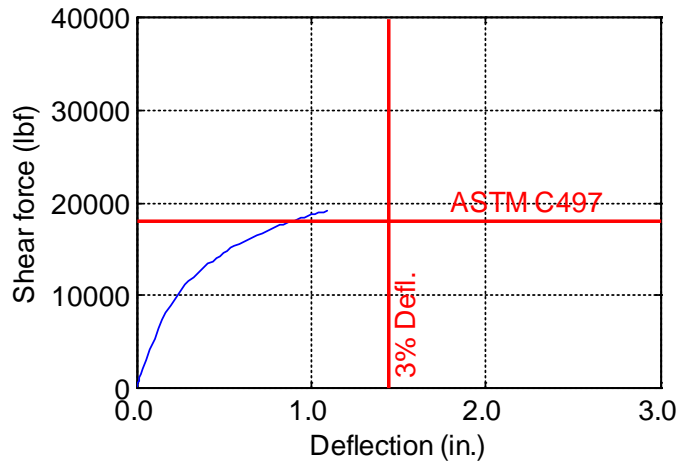


Figure B-75. TW-048-12-0.25

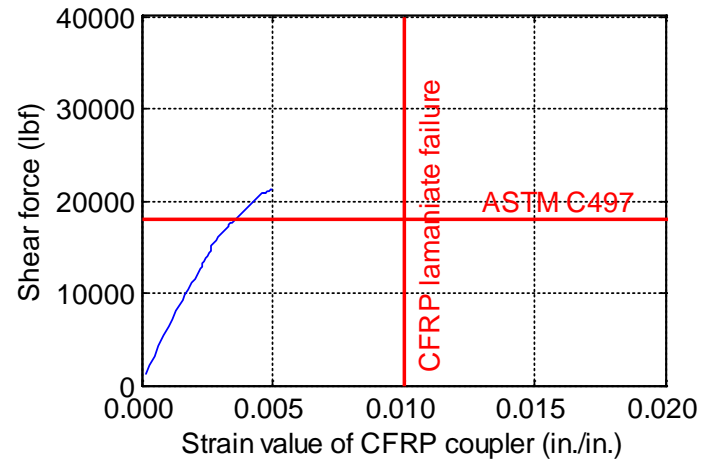
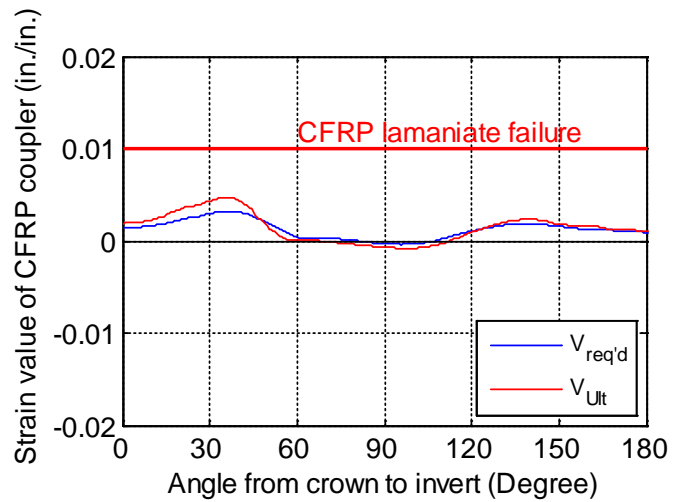
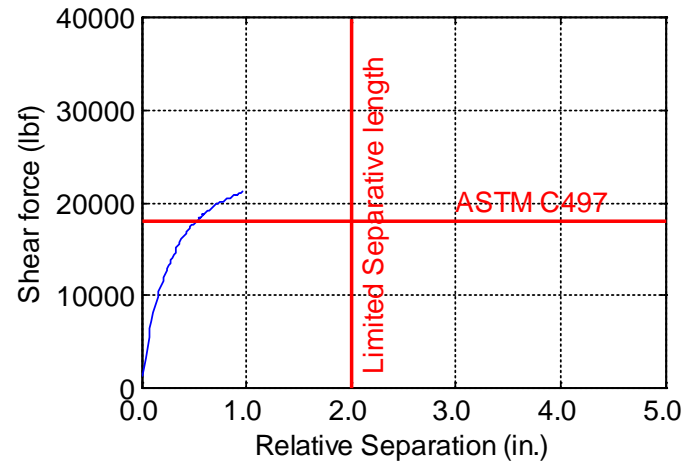
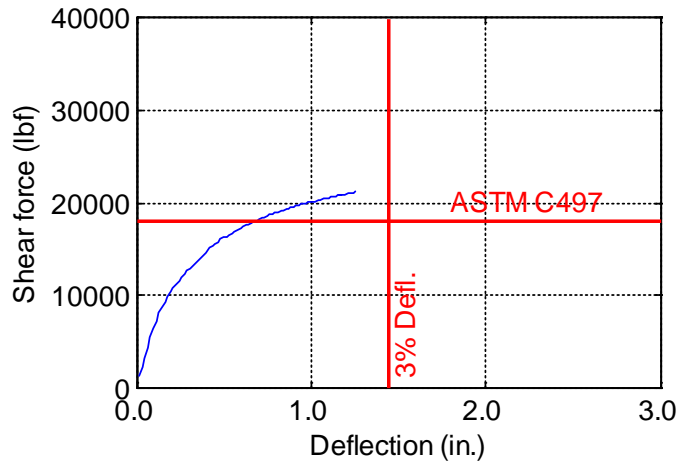


Figure B-76. TW-048-12-0.375

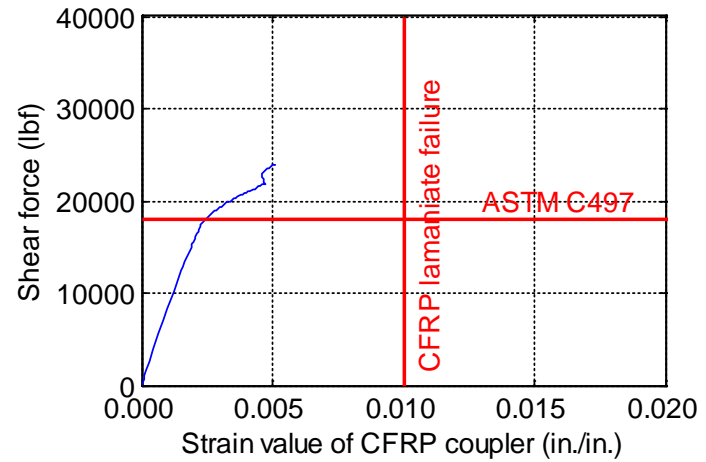
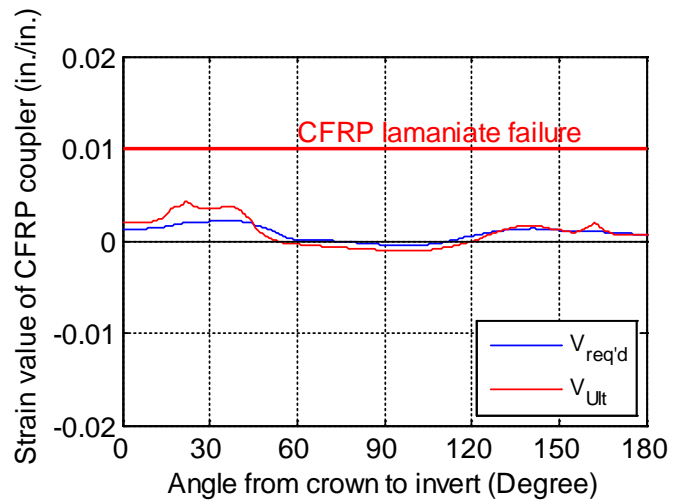
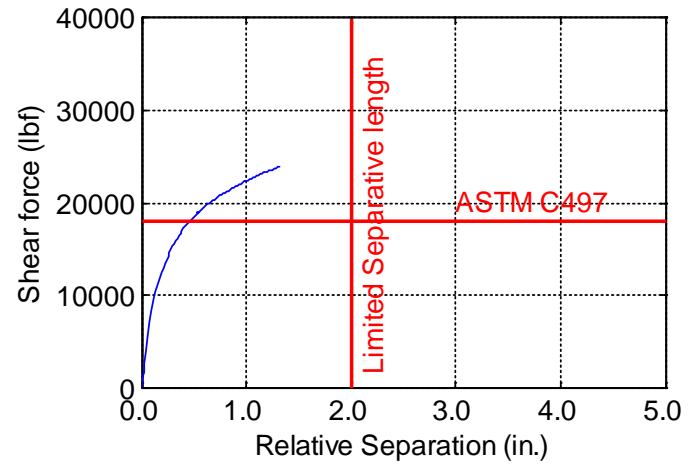
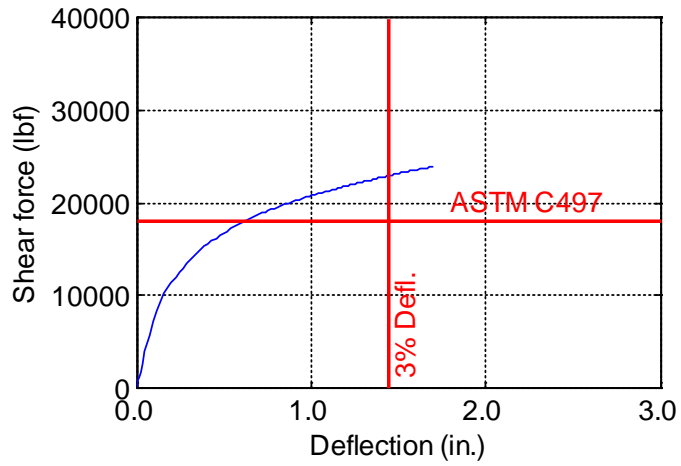


Figure B-77. TW-048-12-0.5

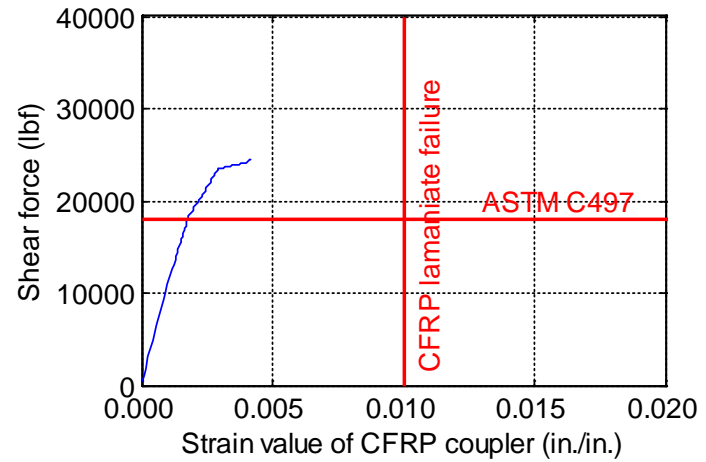
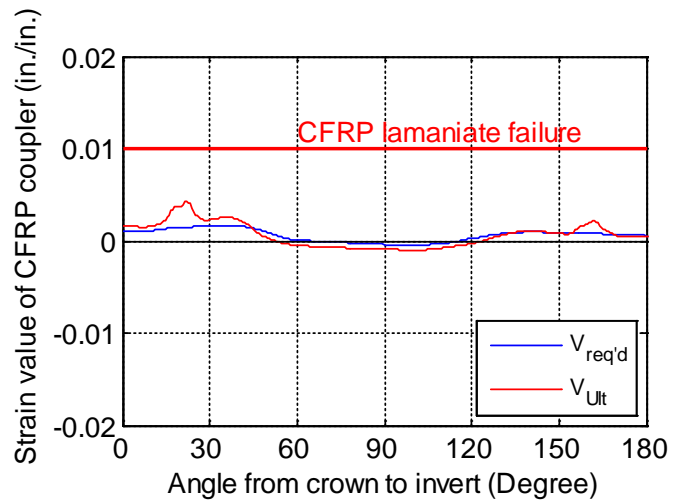
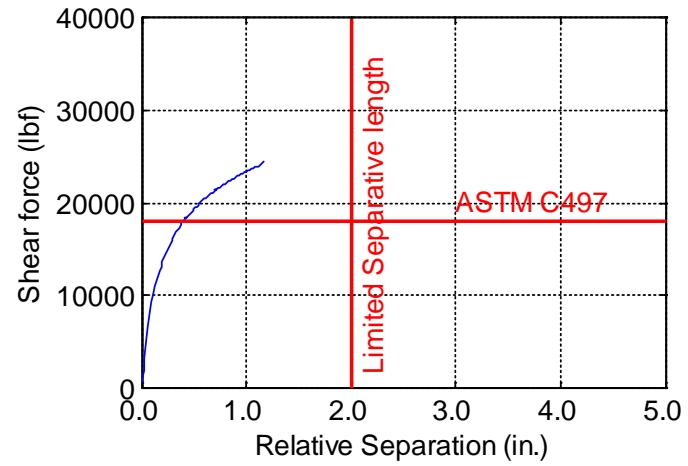
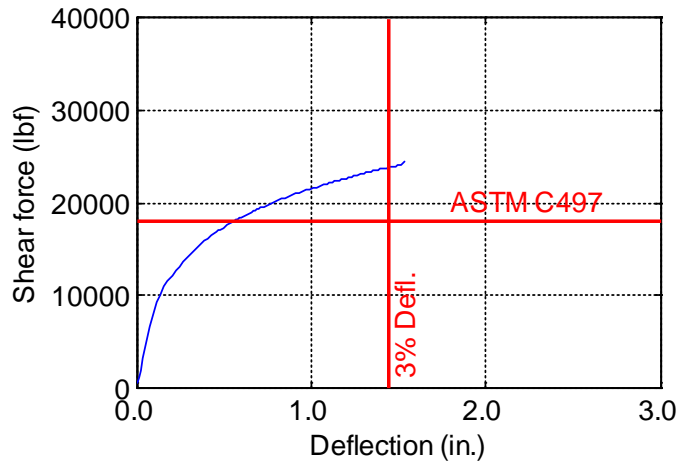


Figure B-78. TW-048-12-0.625

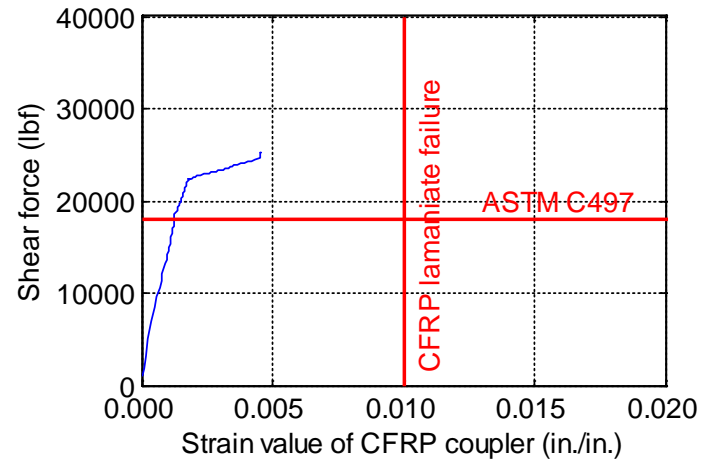
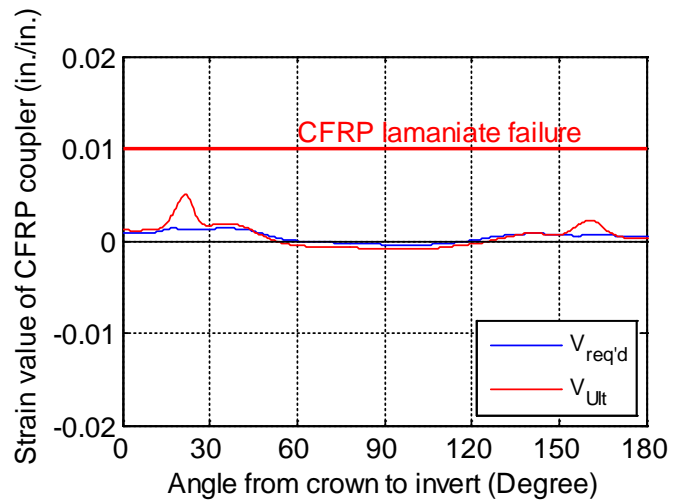
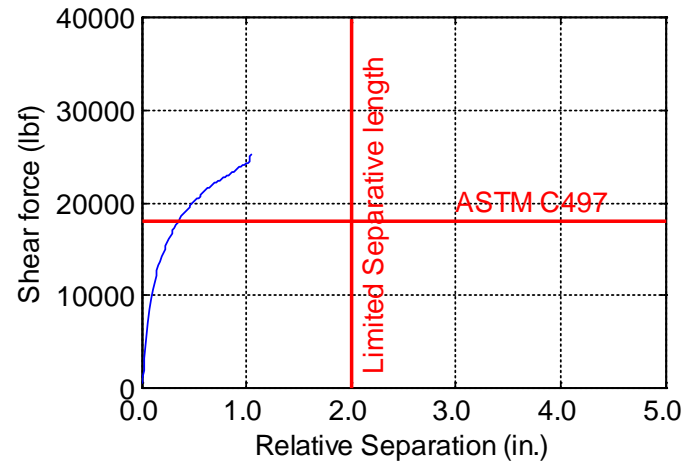
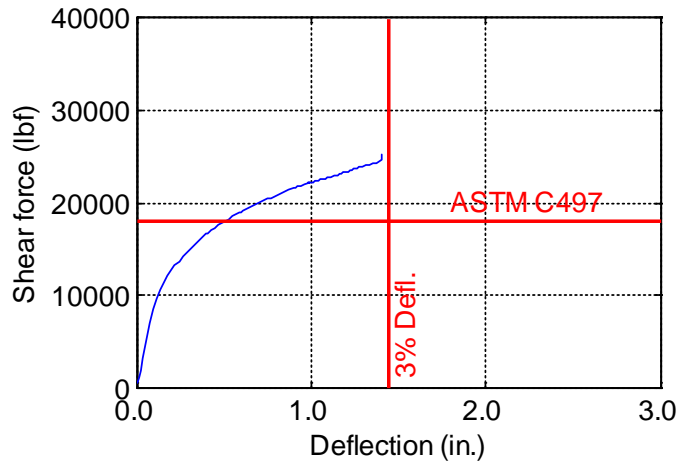


Figure B-79. TW-048-12-0.75

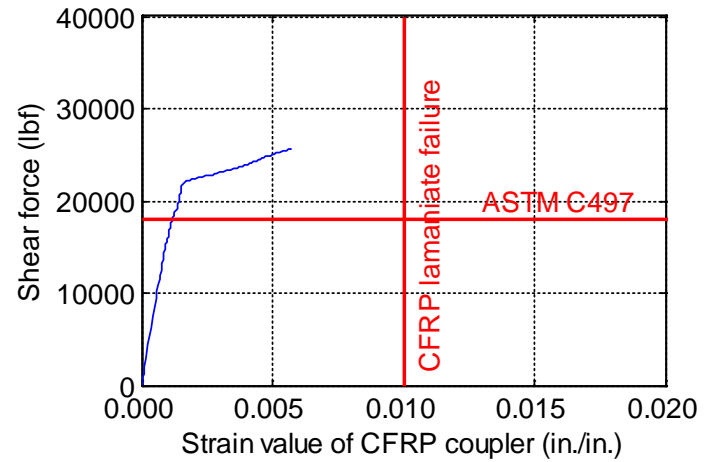
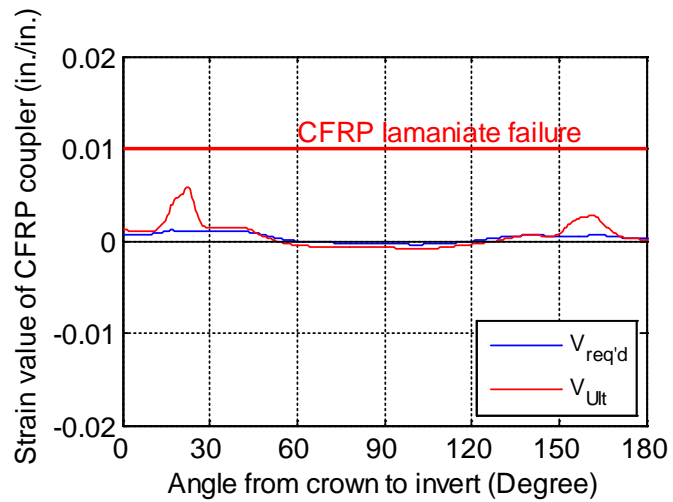
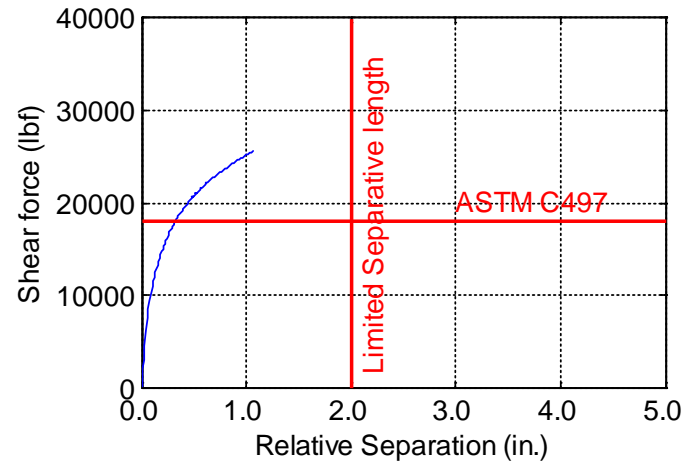
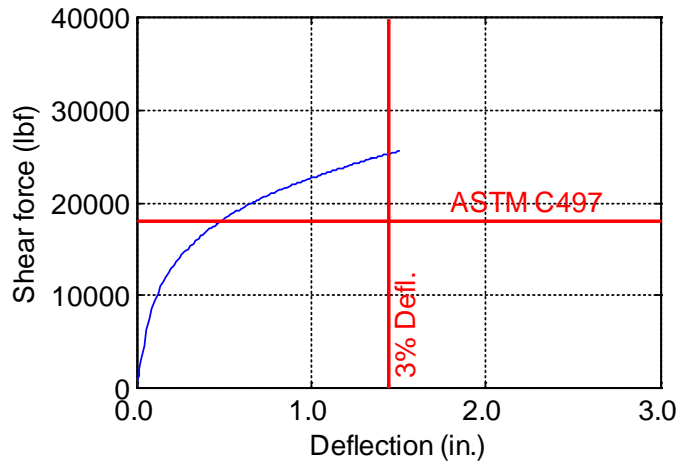


Figure B-80. TW-048-12-0.875

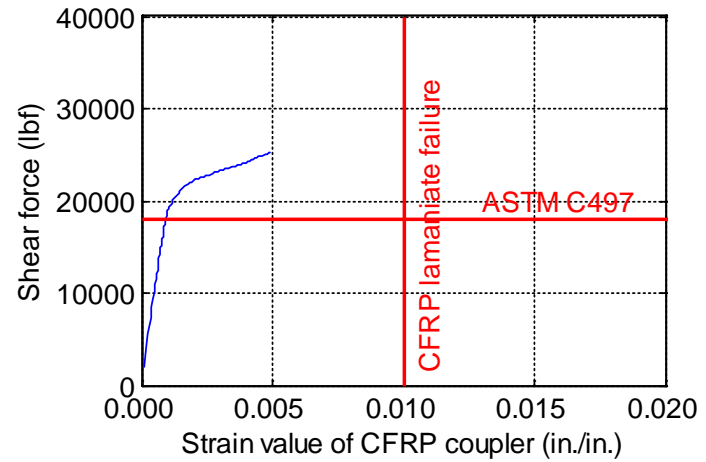
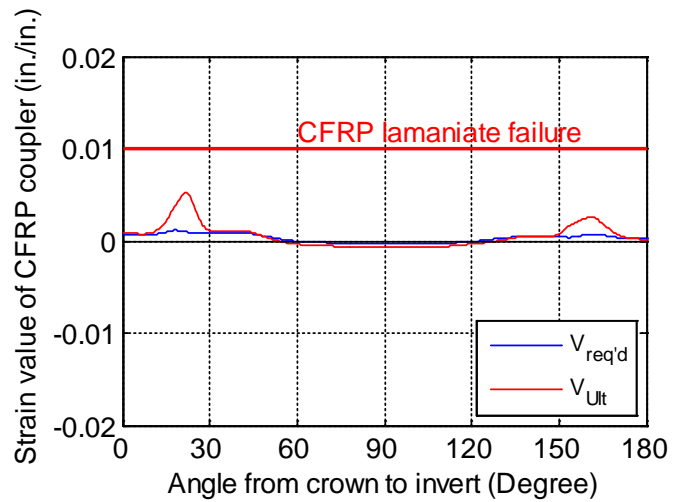
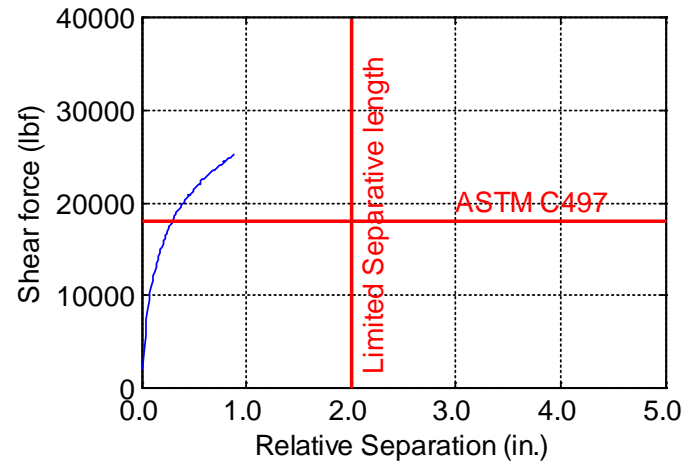
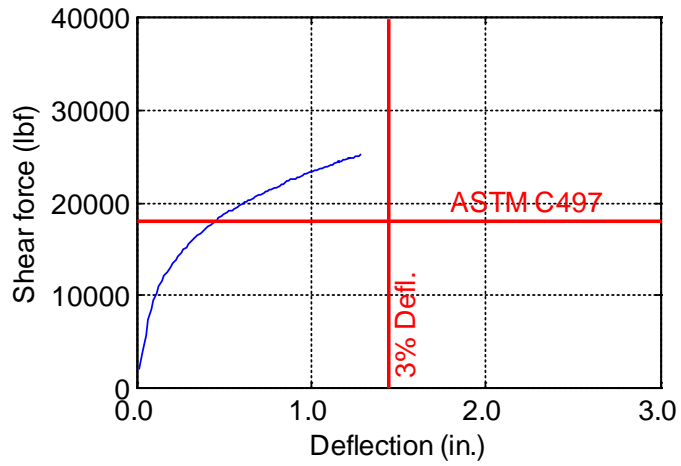


Figure B-81. TW-048-12-1.0

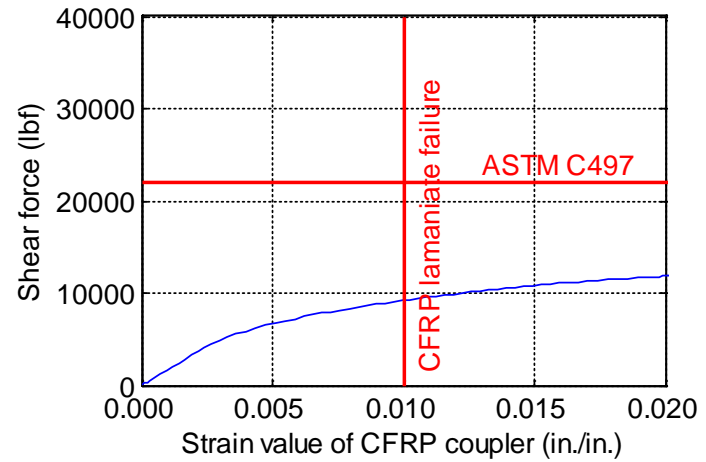
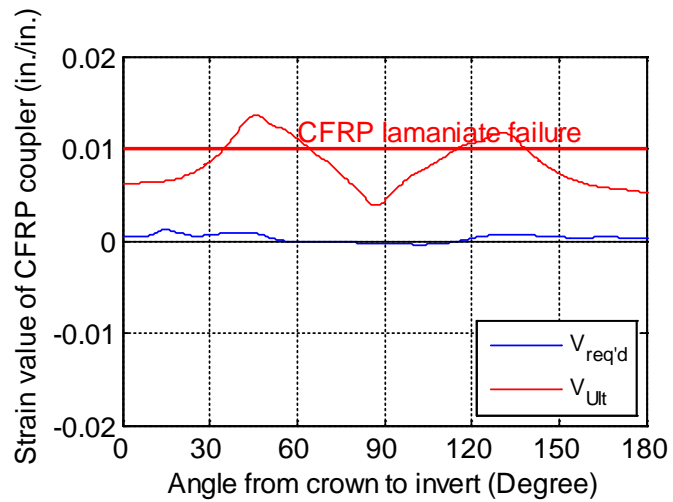
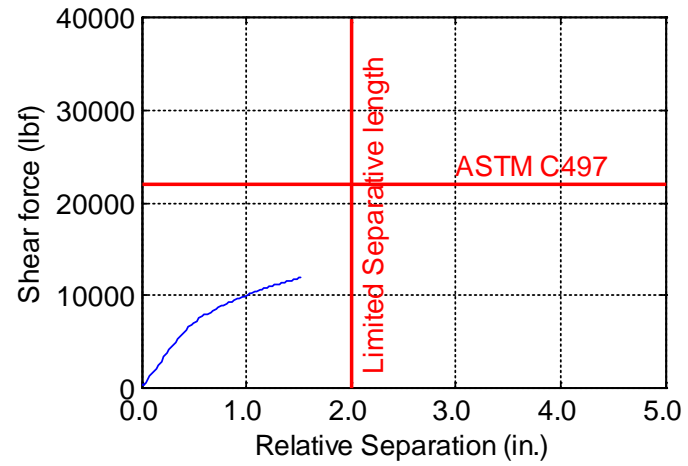
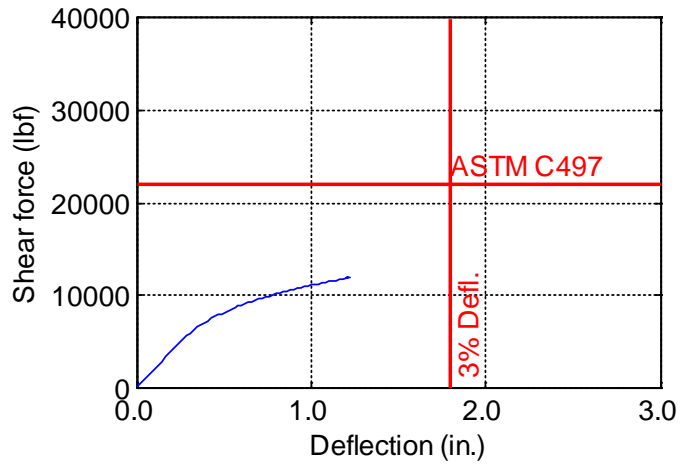


Figure B-82. TW-060-06-0.125

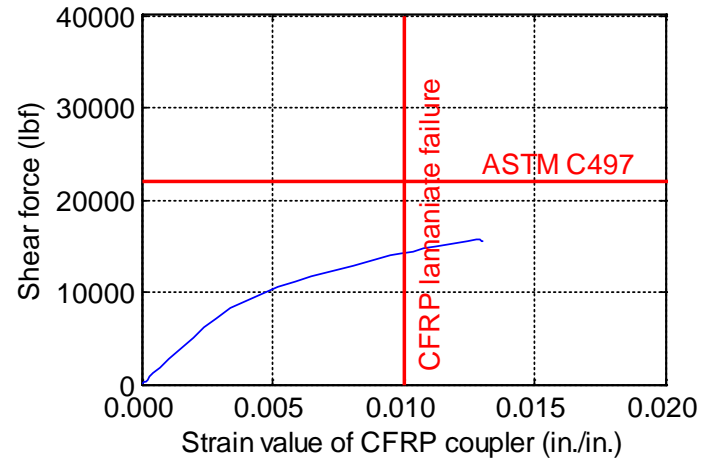
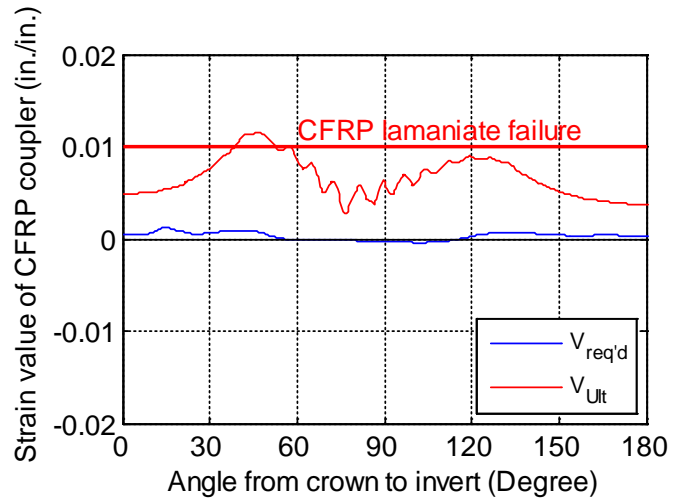
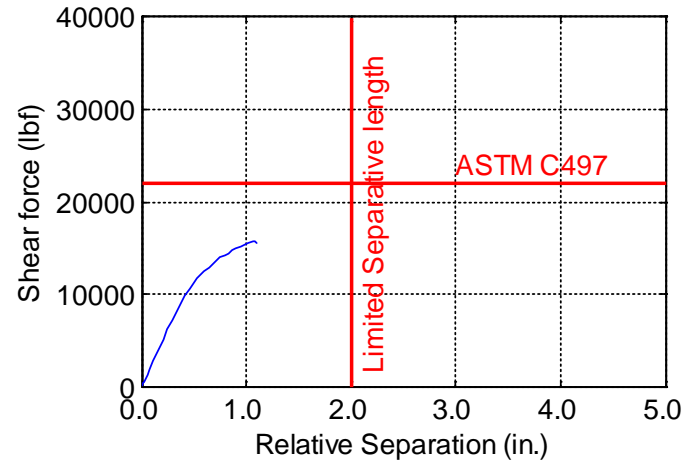
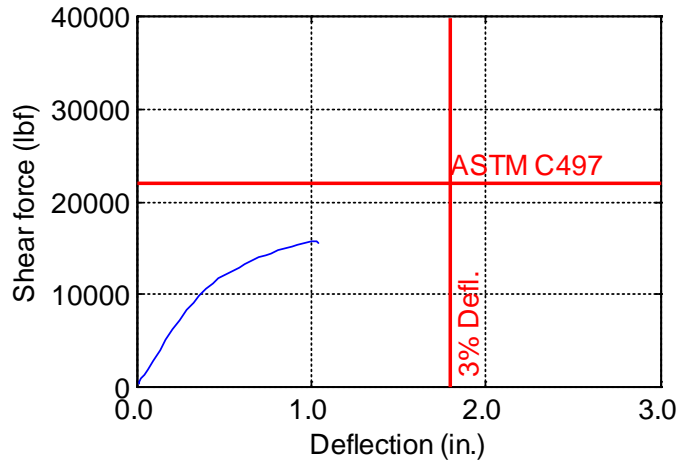


Figure B-83. TW-060-06-0.1875

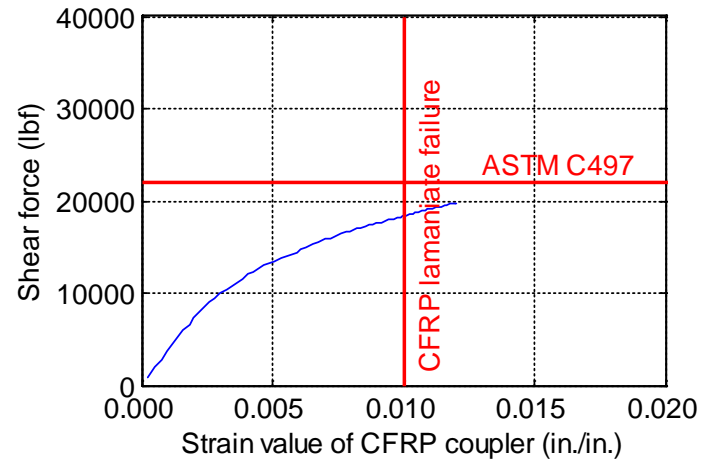
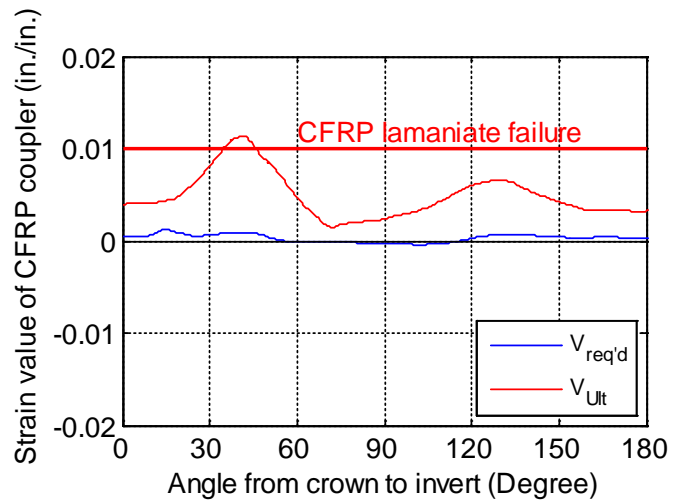
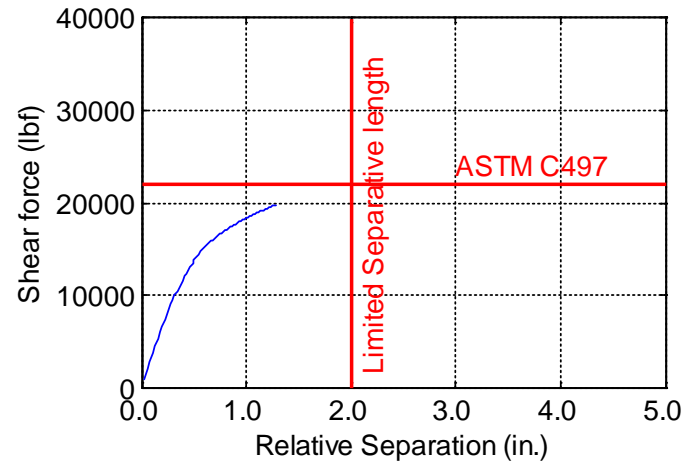
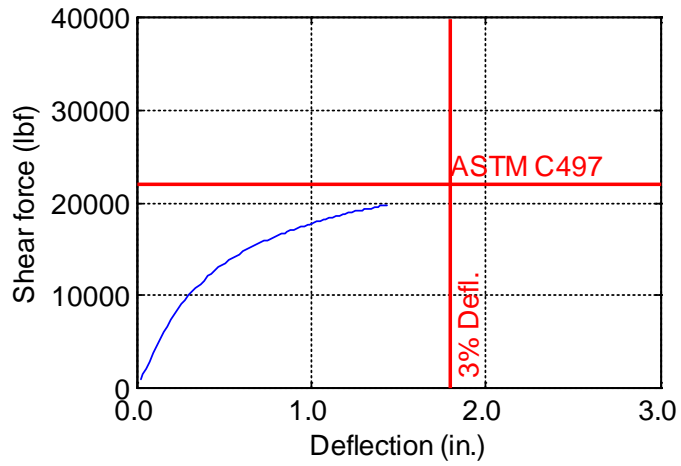


Figure B-84. TW-060-06-0.25

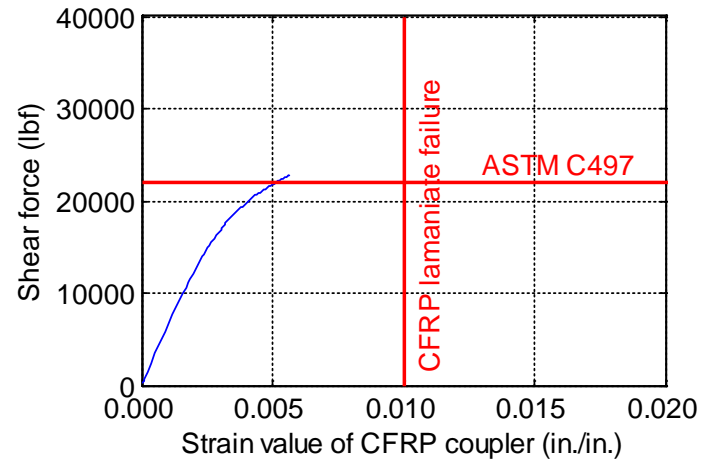
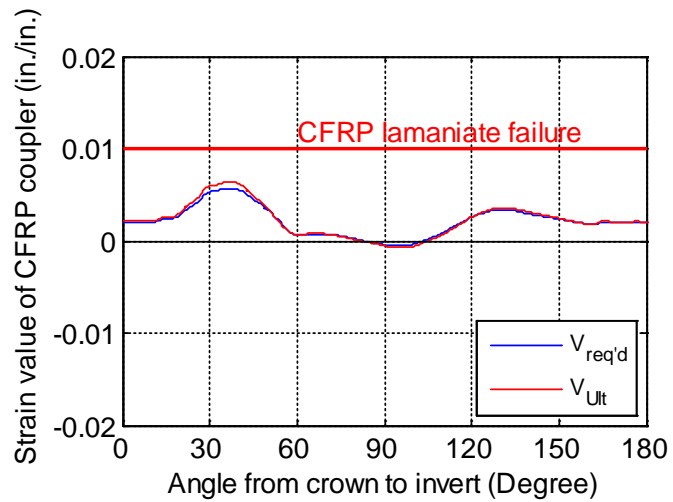
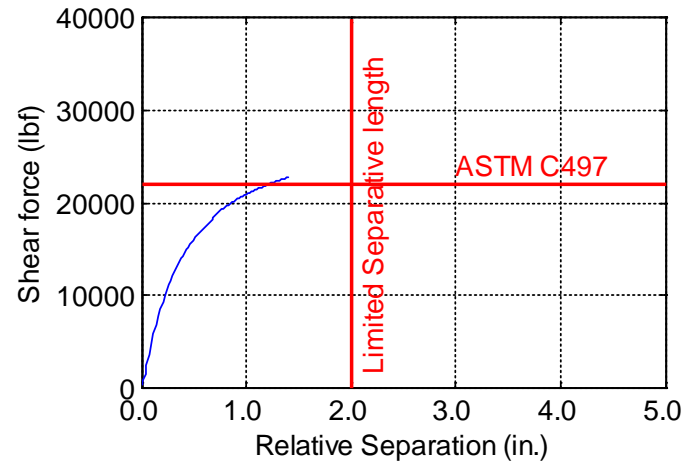
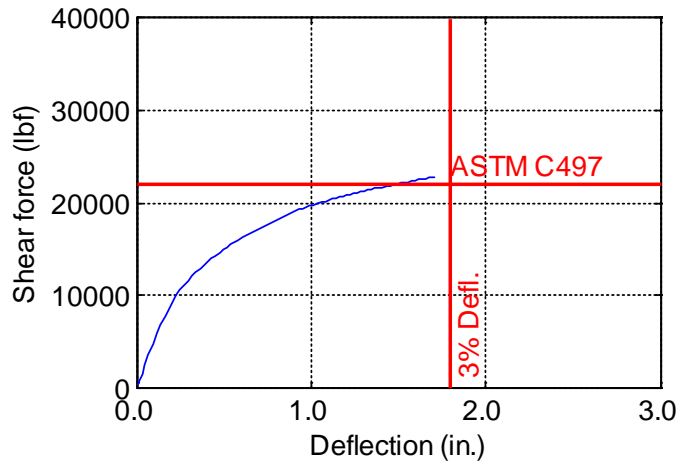


Figure B-85. TW-060-06-0.375

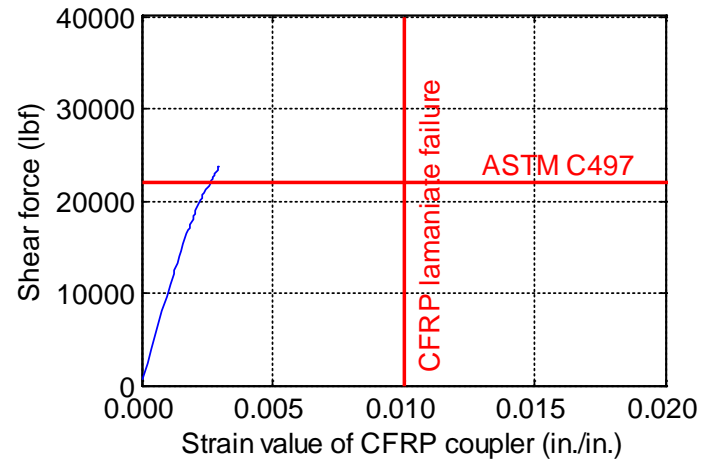
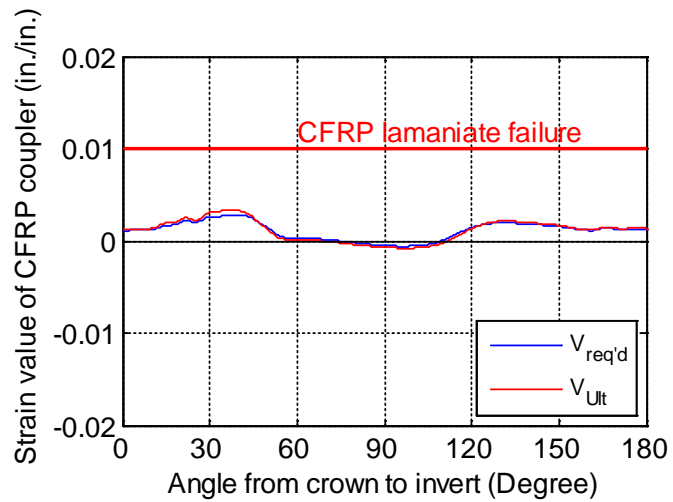
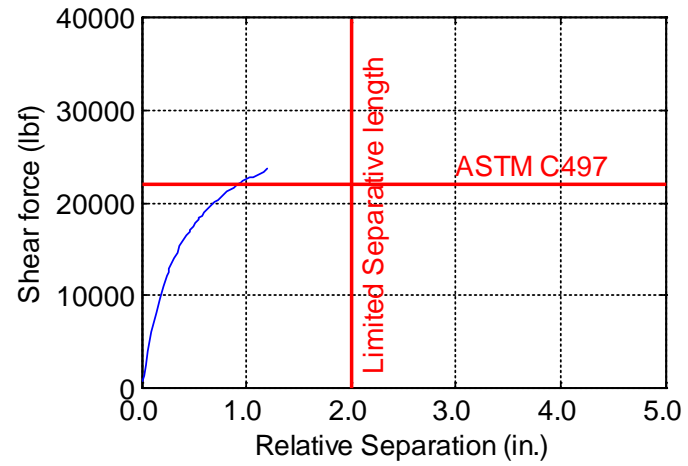
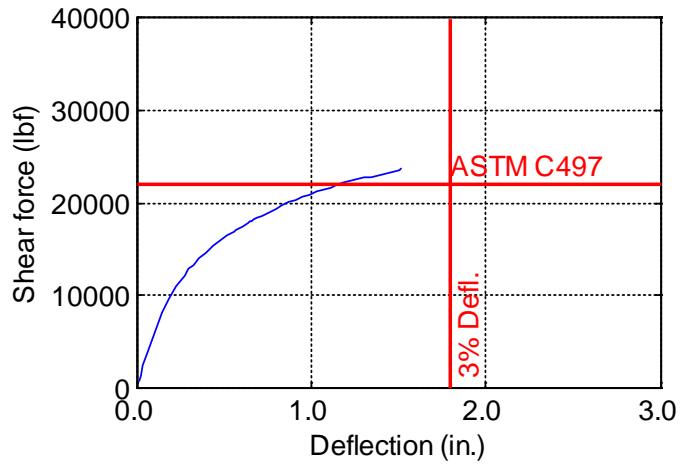


Figure B-86. TW-060-06-0.5

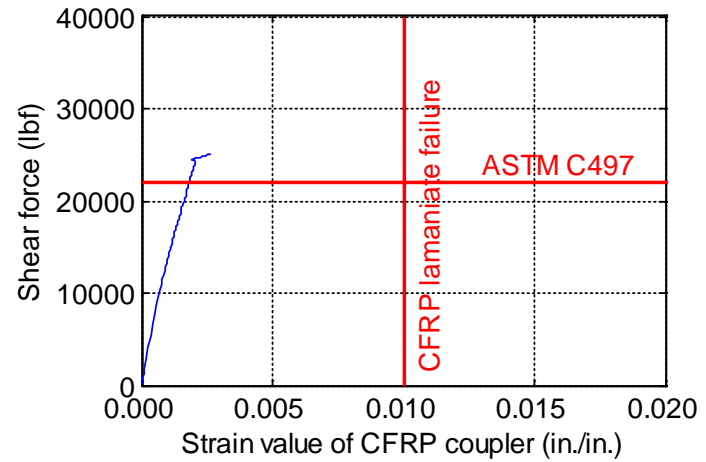
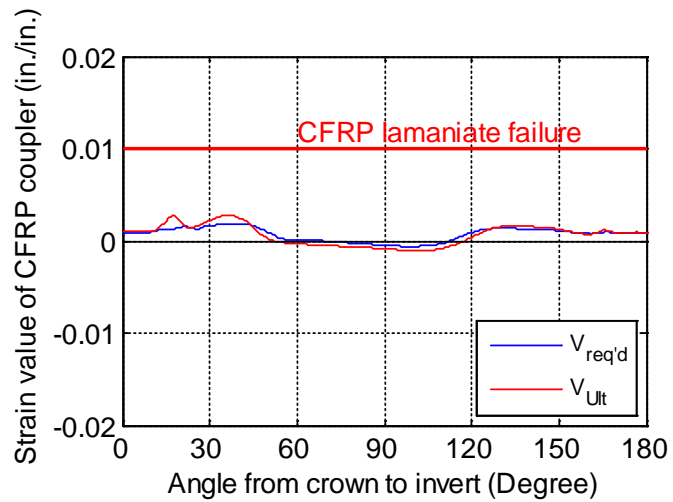
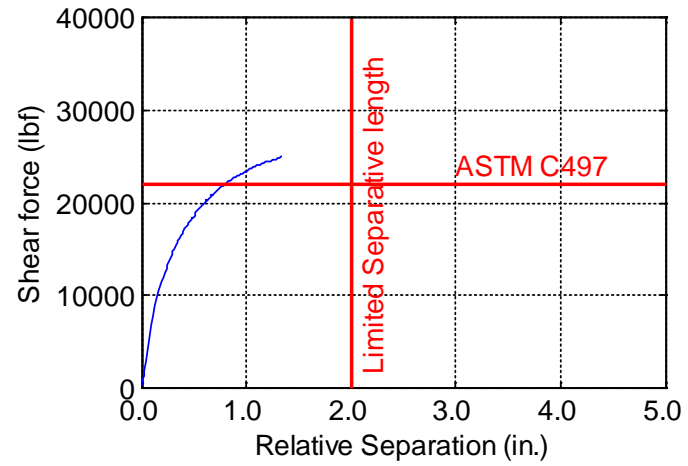
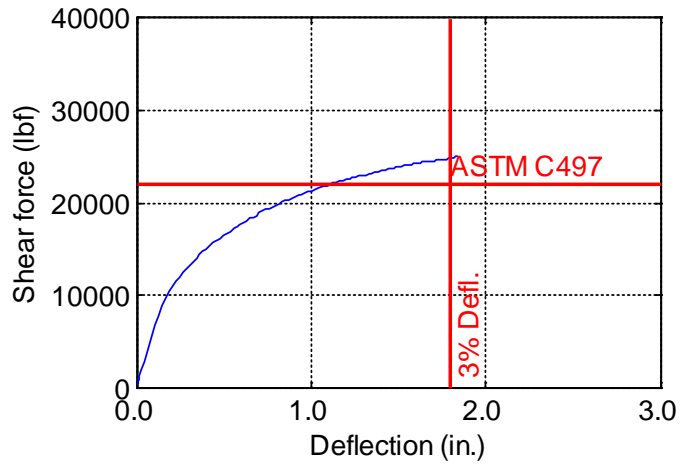


Figure B-87. TW-060-06-0.625

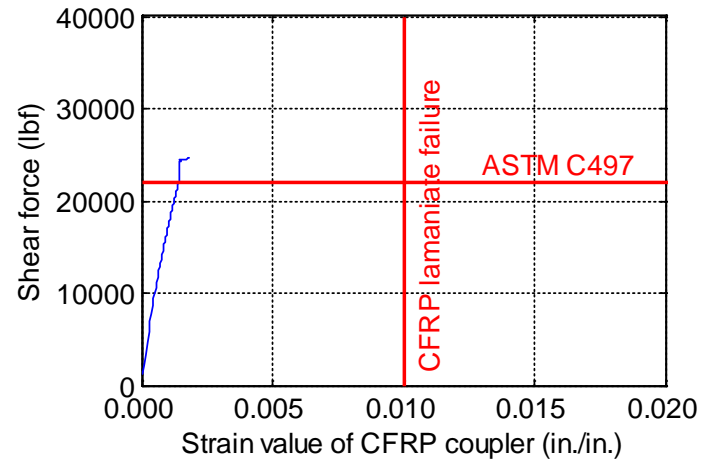
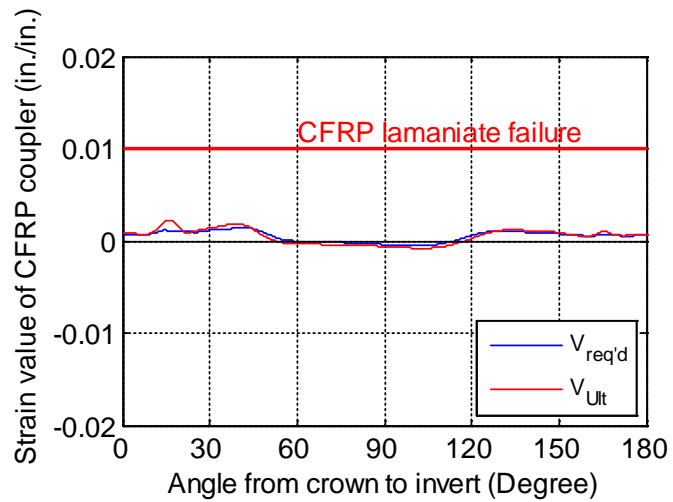
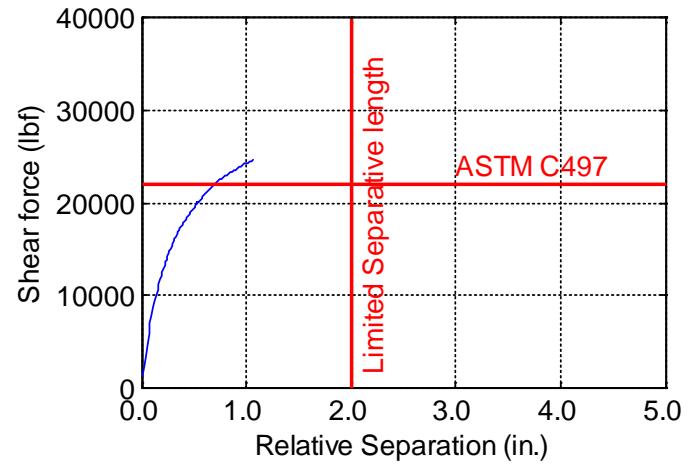
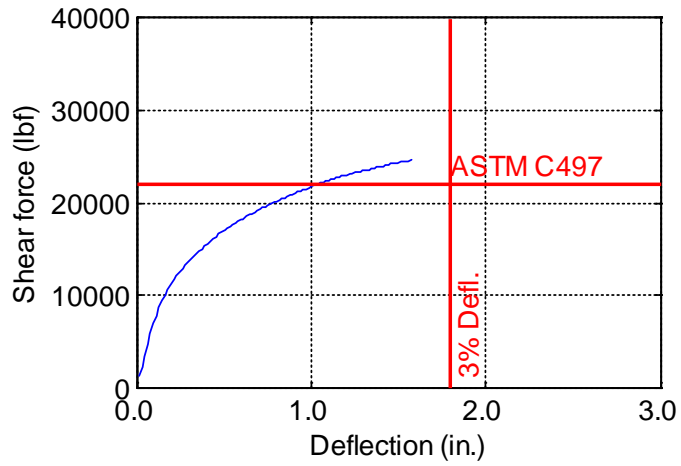


Figure B-88. TW-060-06-0.75

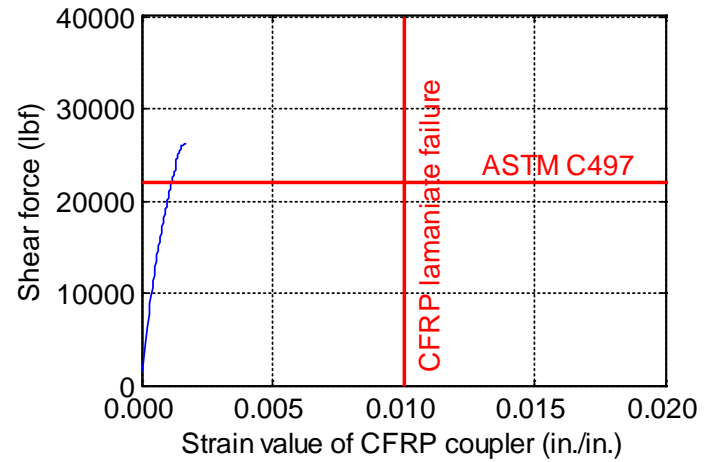
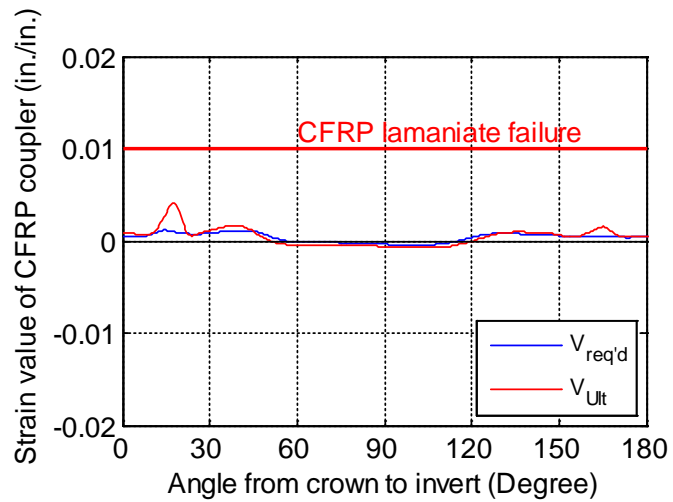
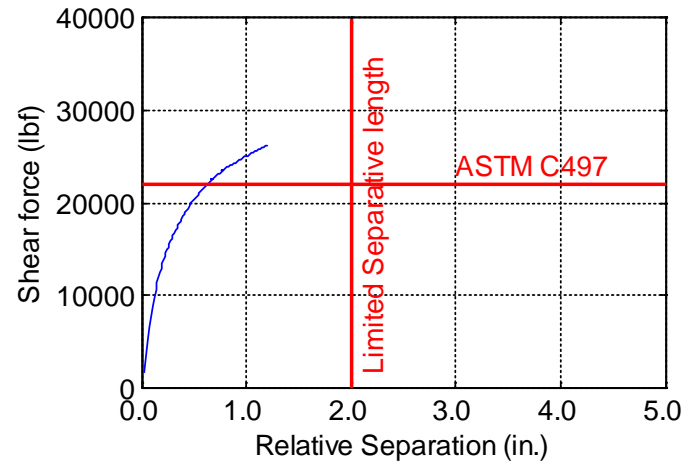
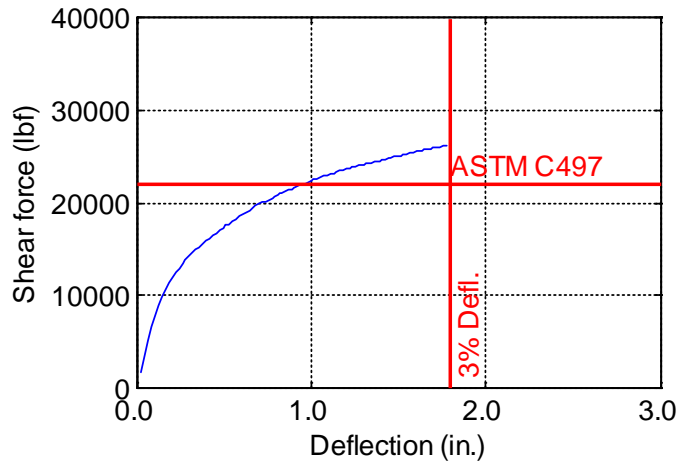


Figure B-89. TW-060-06-0.875

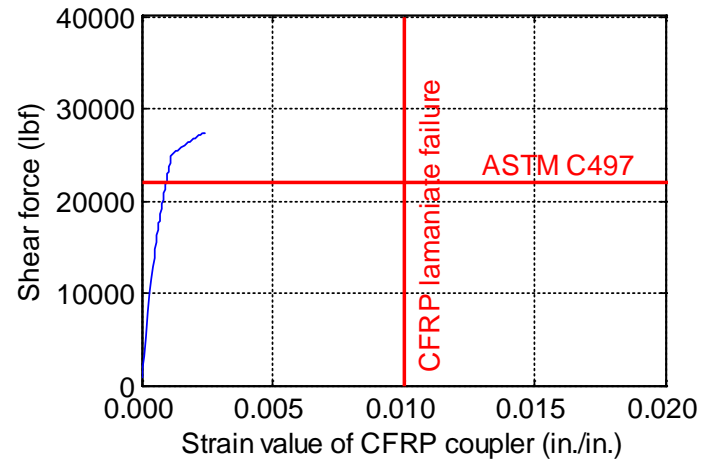
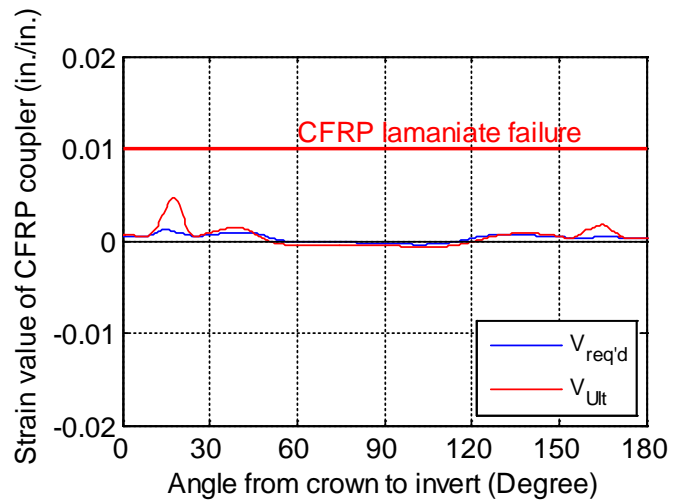
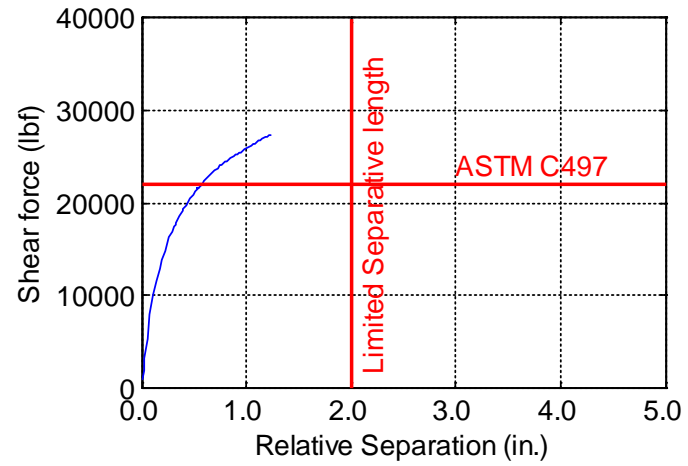
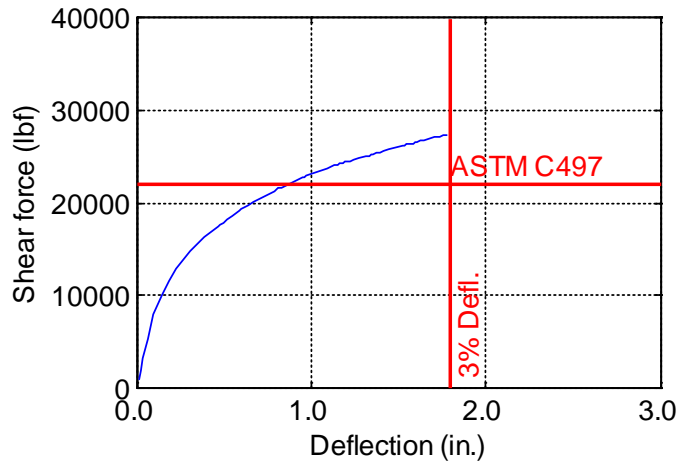


Figure B-90. TW-060-06-1.0

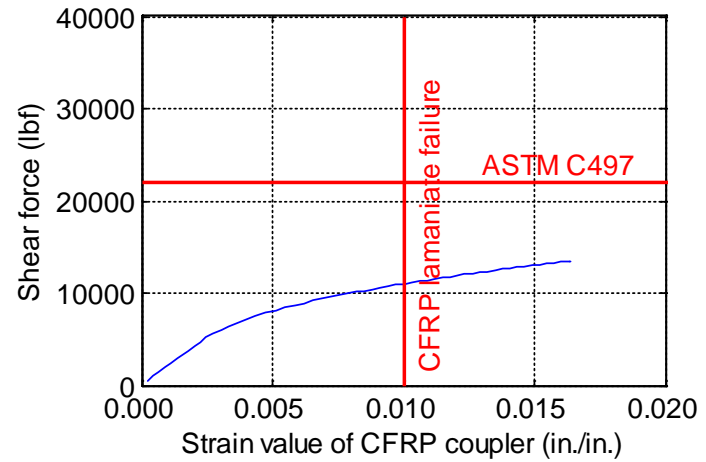
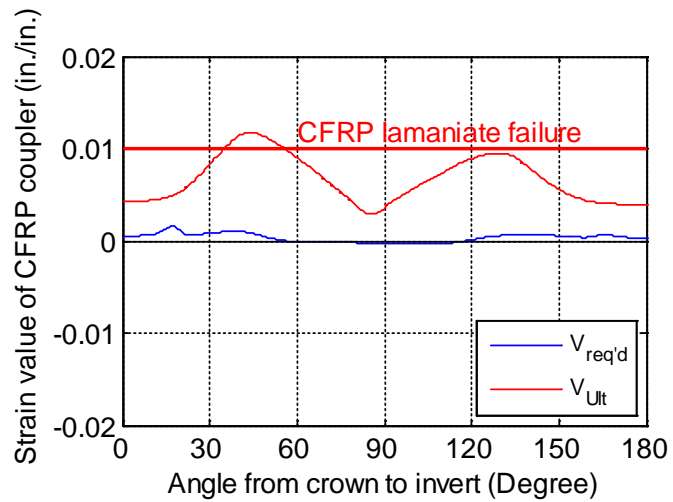
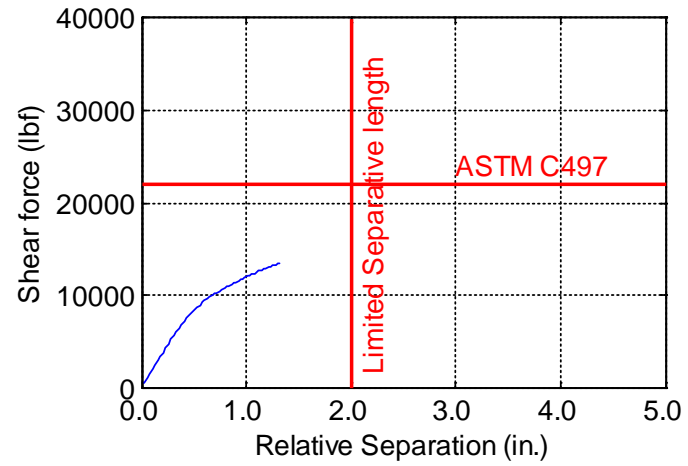
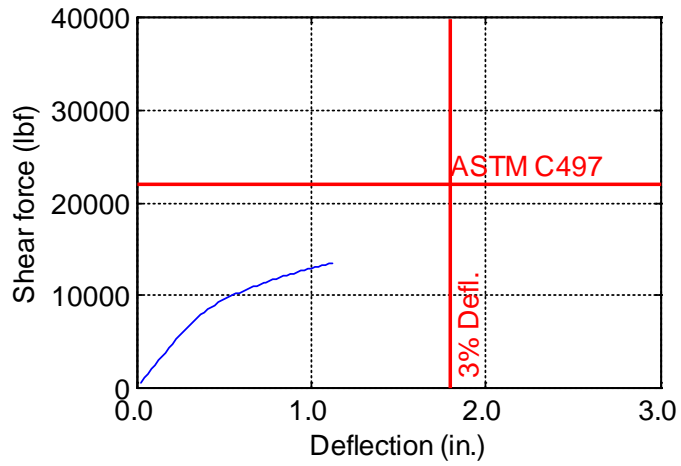


Figure B-91. TW-060-09-0.125

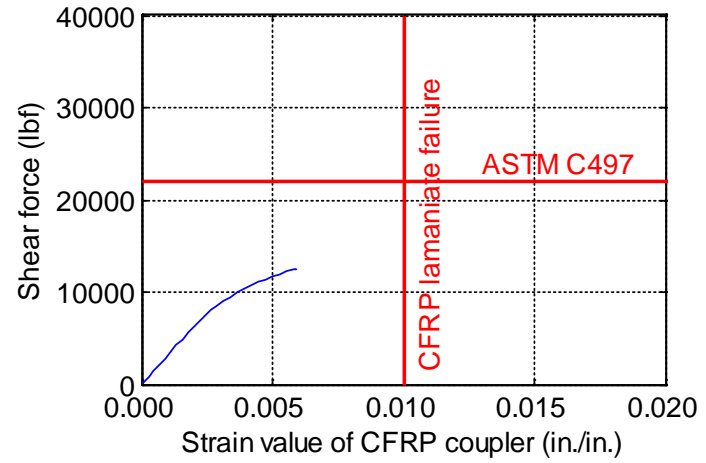
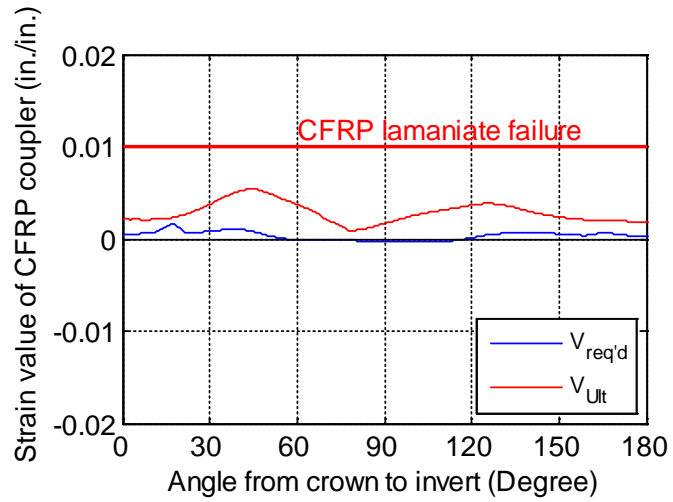
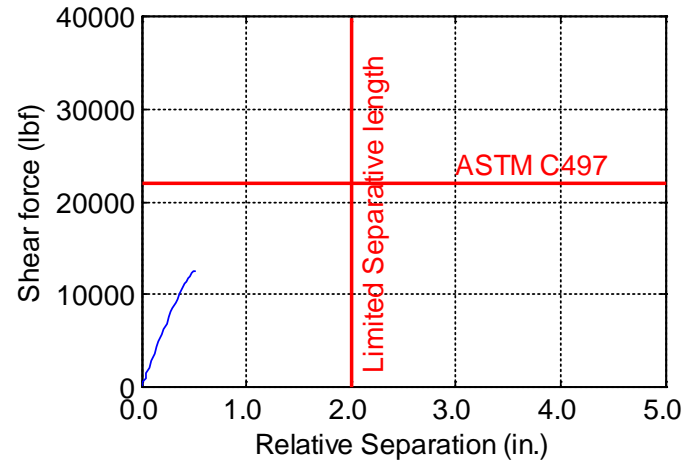
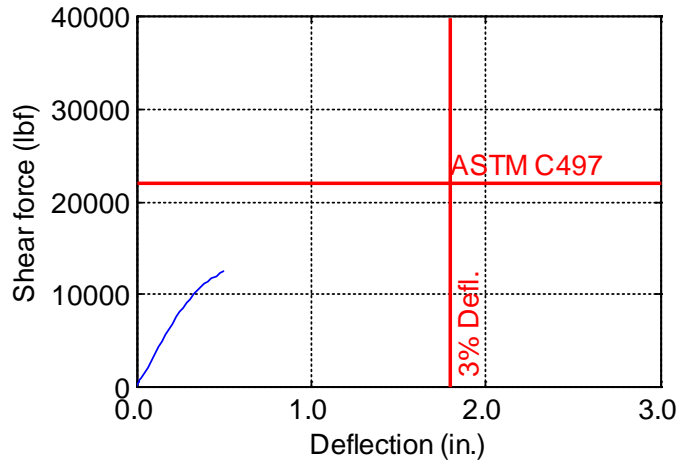


Figure B-92. TW-060-09-0.1875

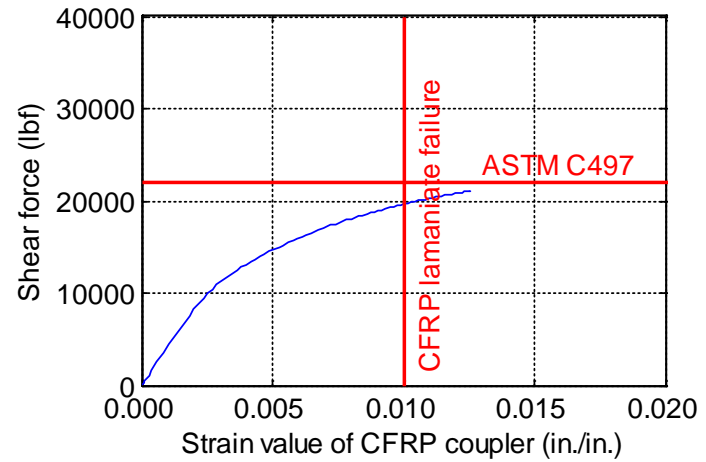
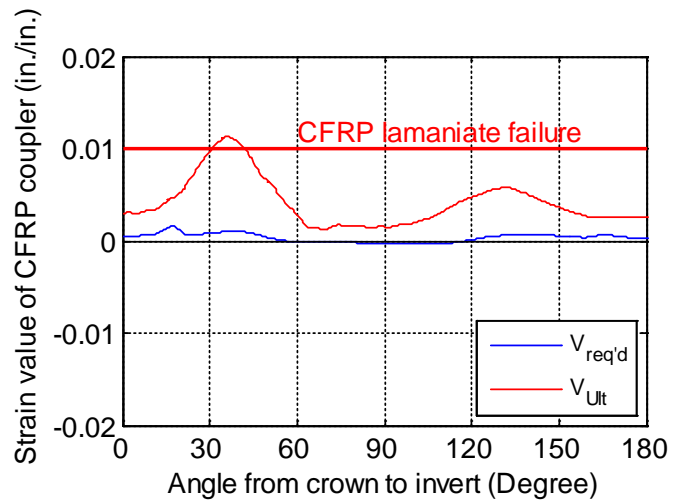
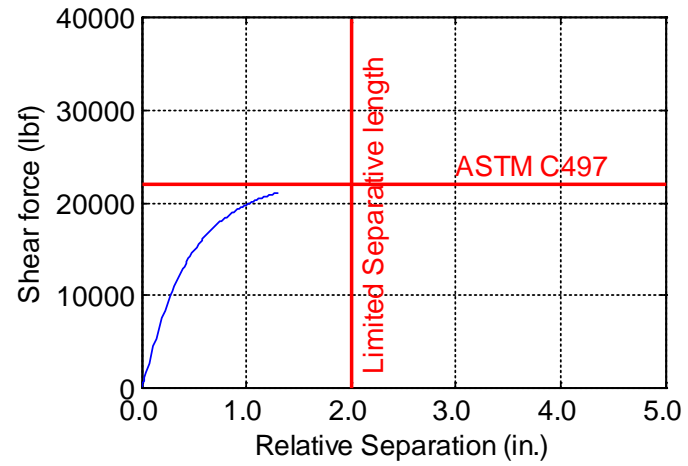
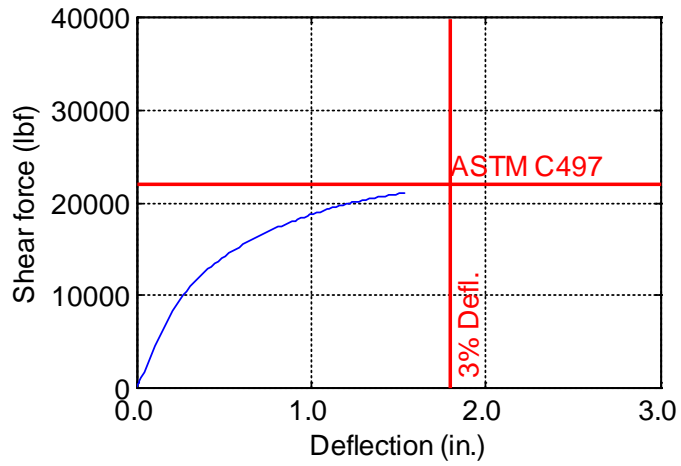


Figure B-93. TW-060-09-0.25

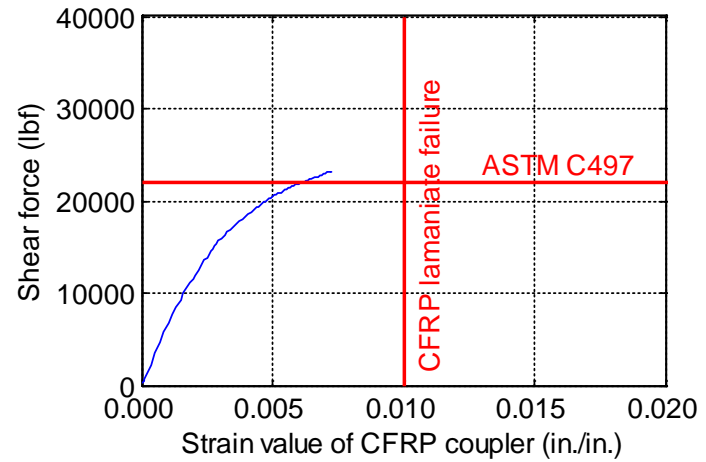
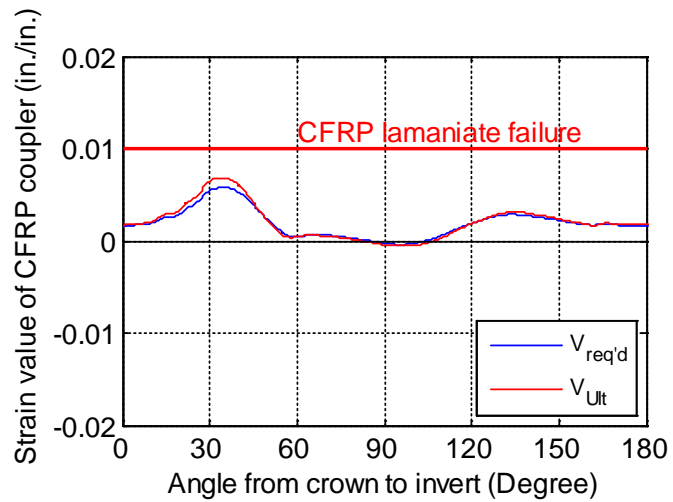
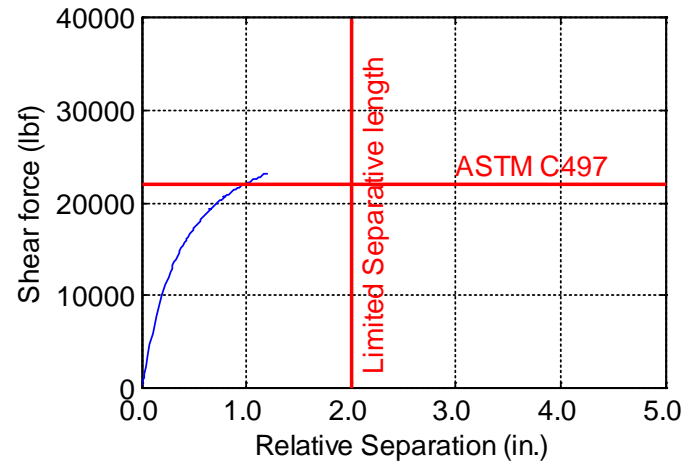
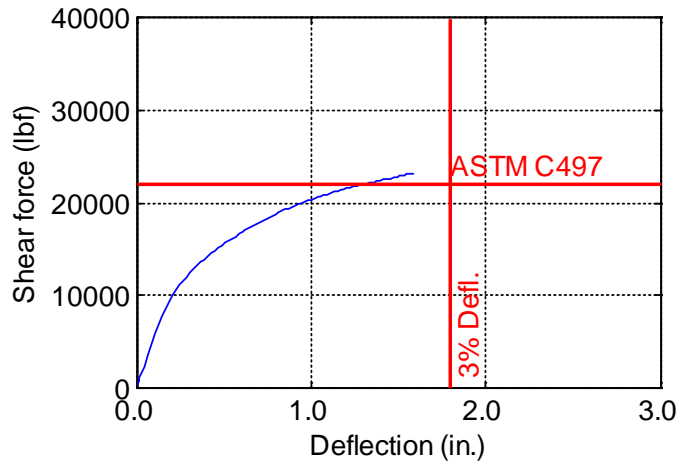


Figure B-94. TW-060-09-0.375

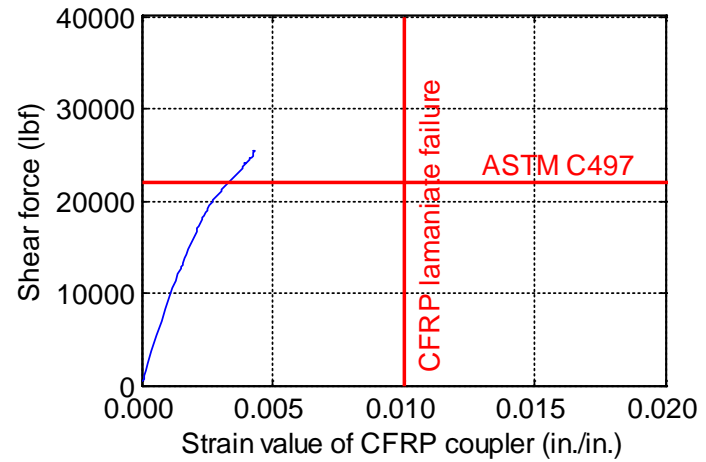
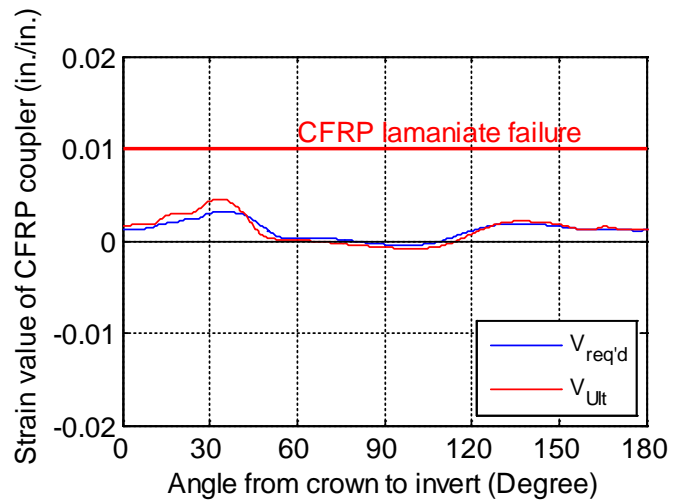
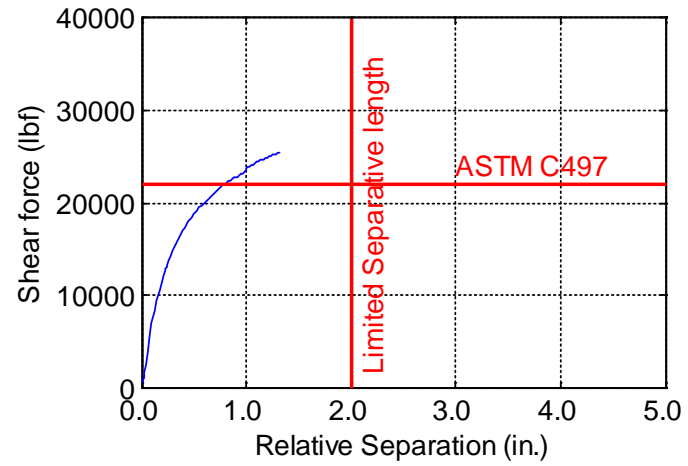
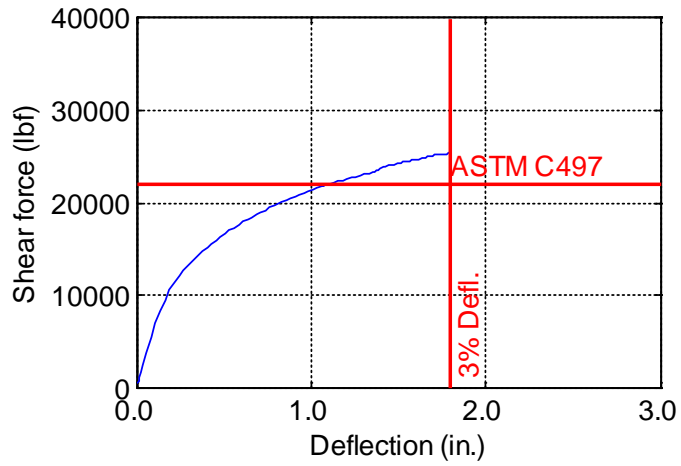


Figure B-95. TW-060-09-0.5

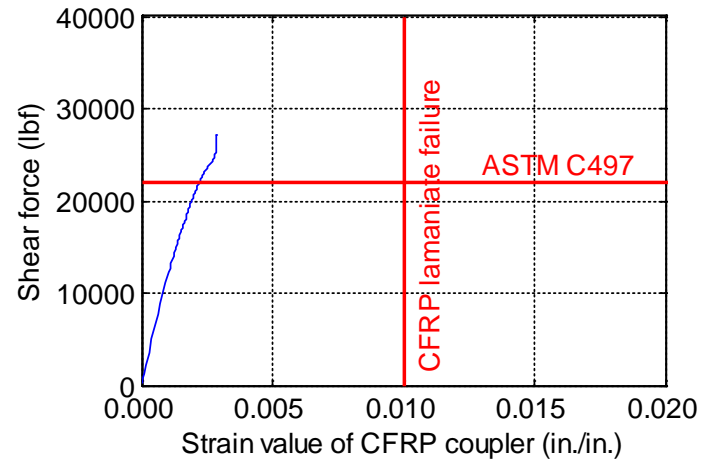
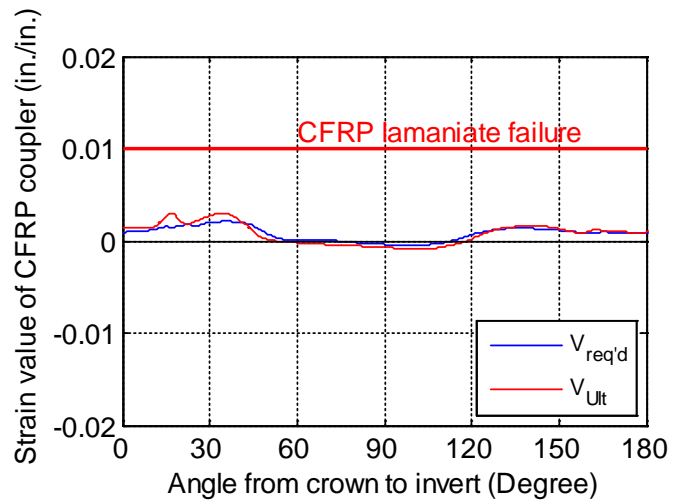
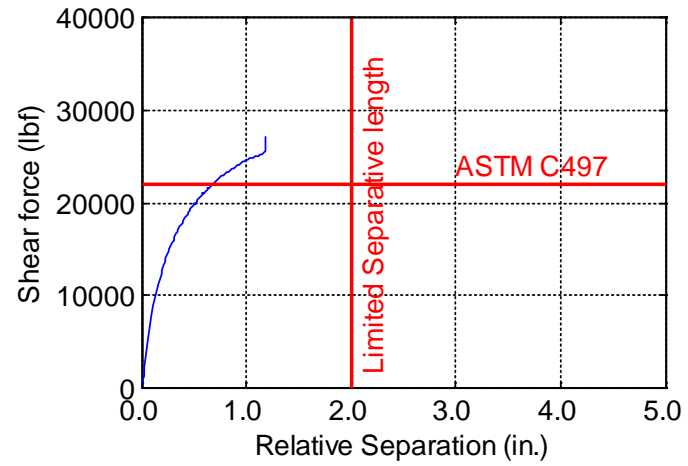
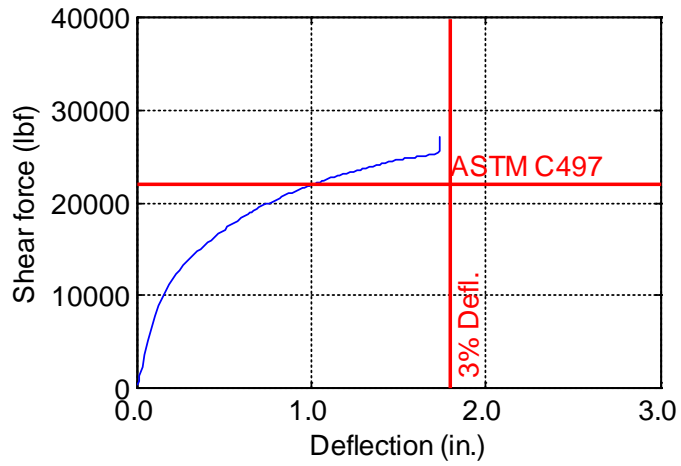


Figure B-96. TW-060-09-0.625

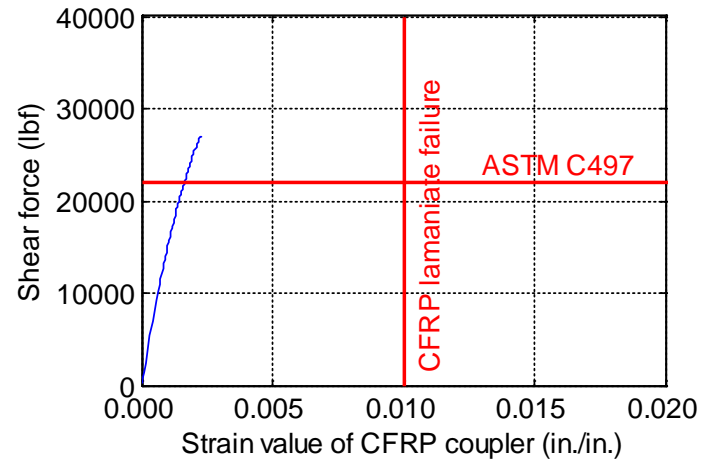
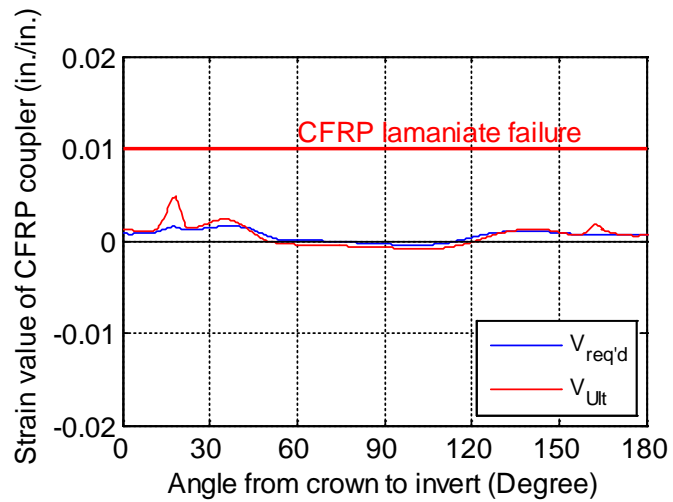
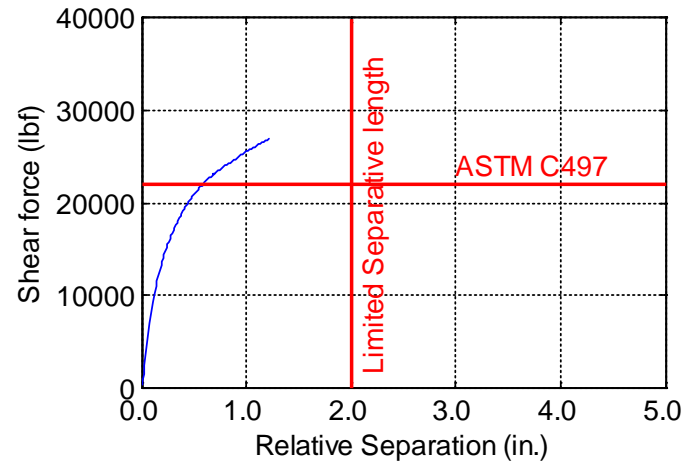
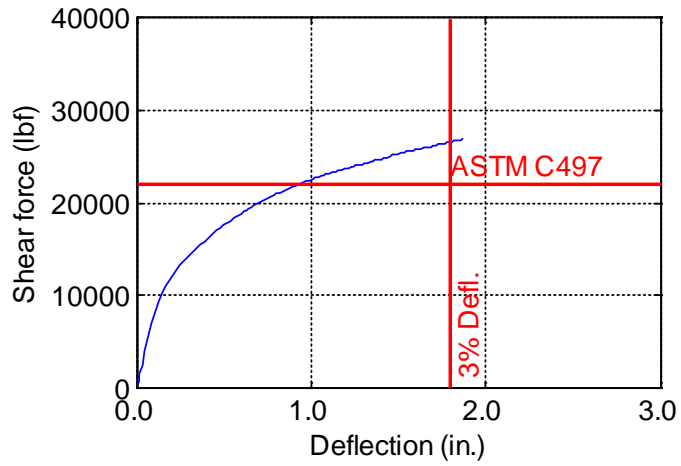


Figure B-97. TW-060-09-0.75

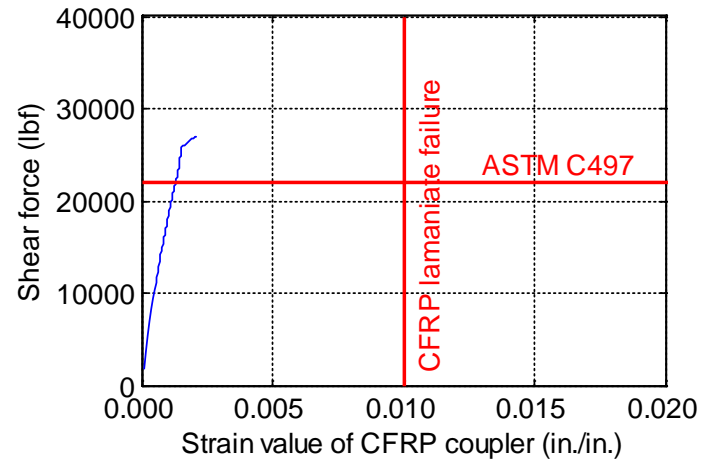
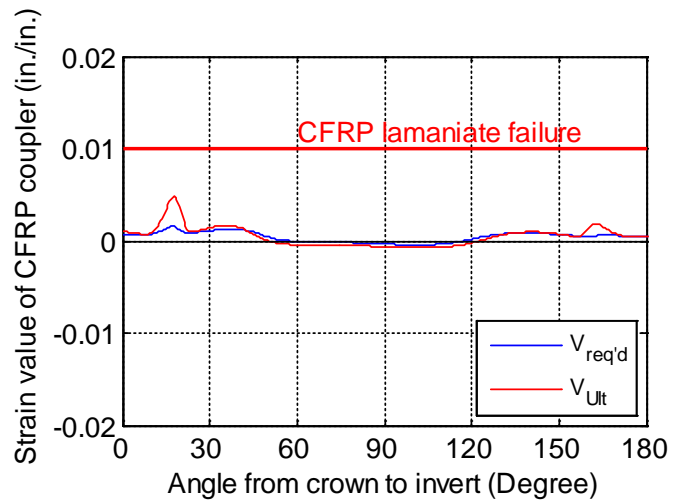
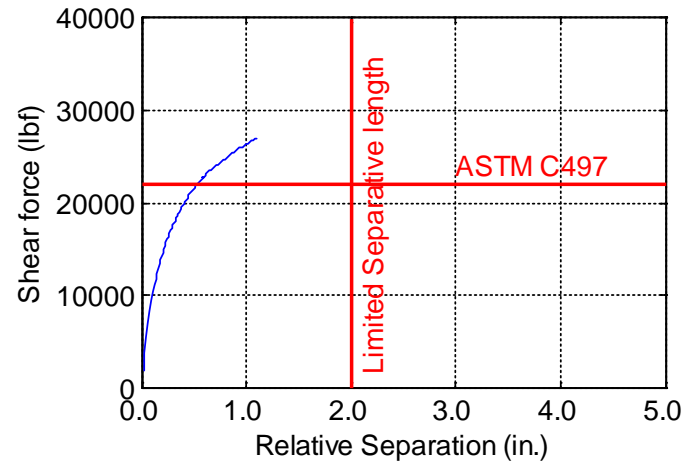
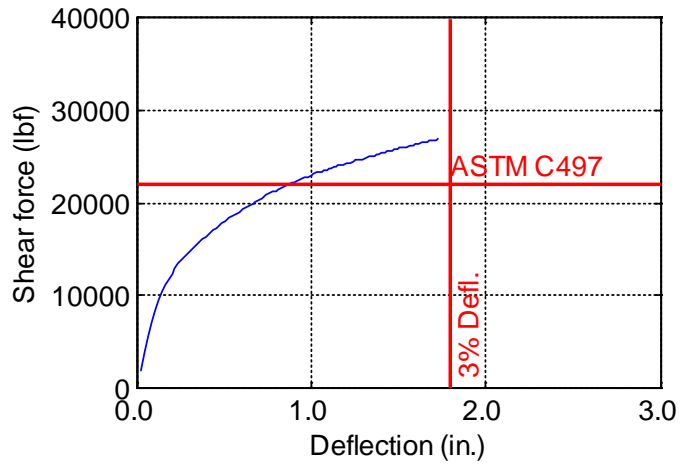


Figure B-98. TW-060-09-0.875

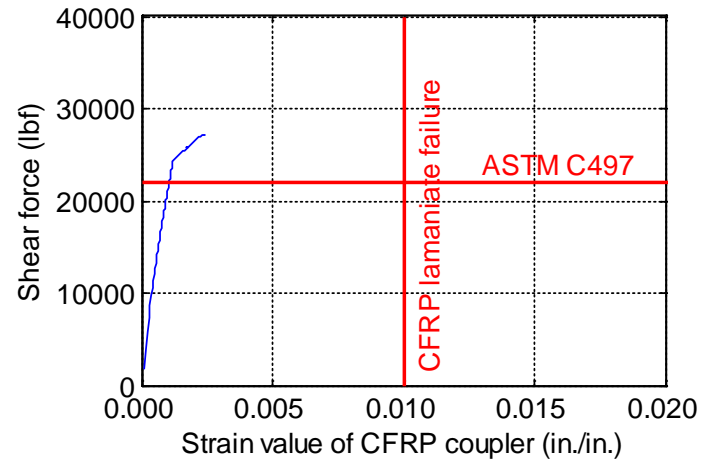
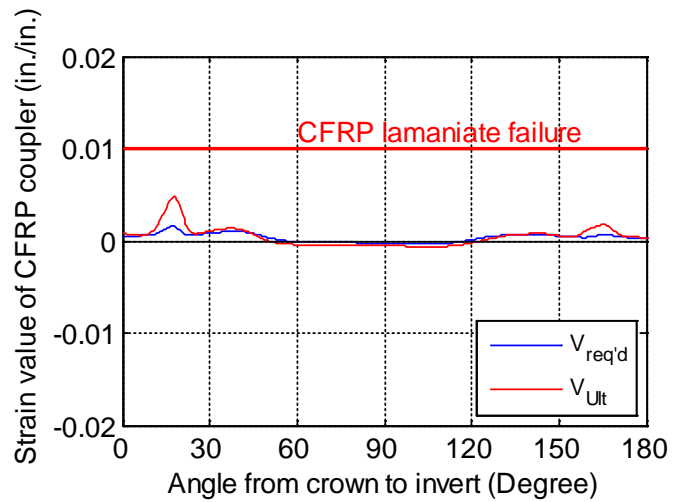
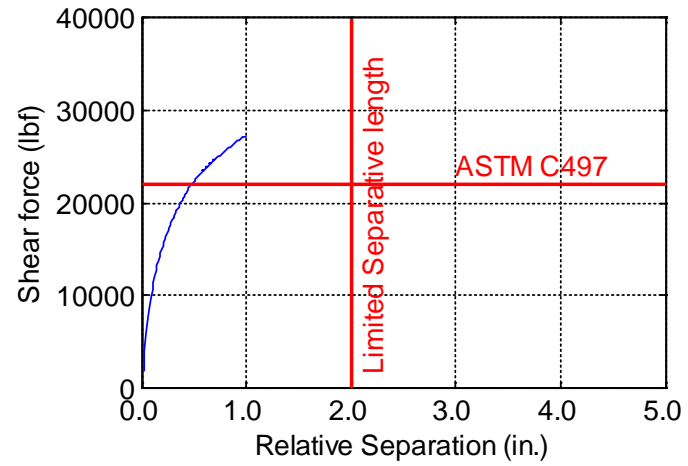
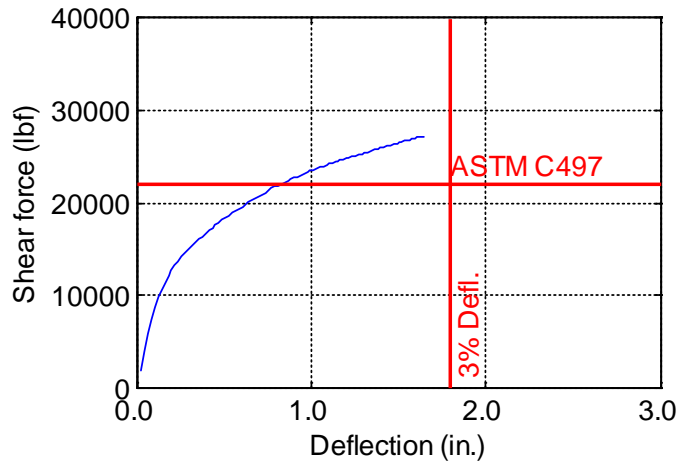


Figure B-99. TW-060-09-1.0

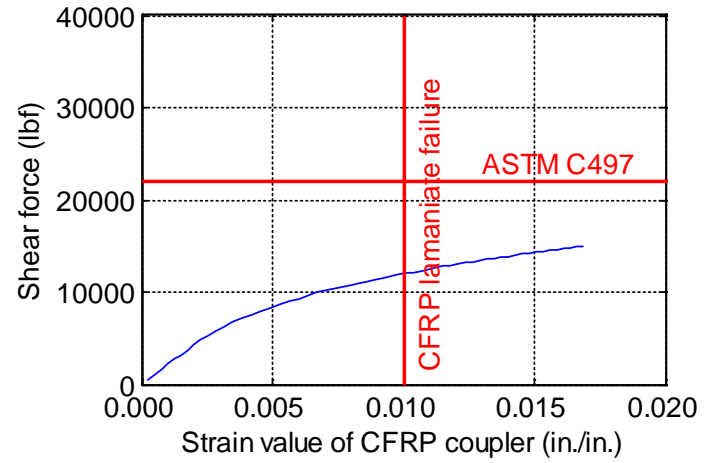
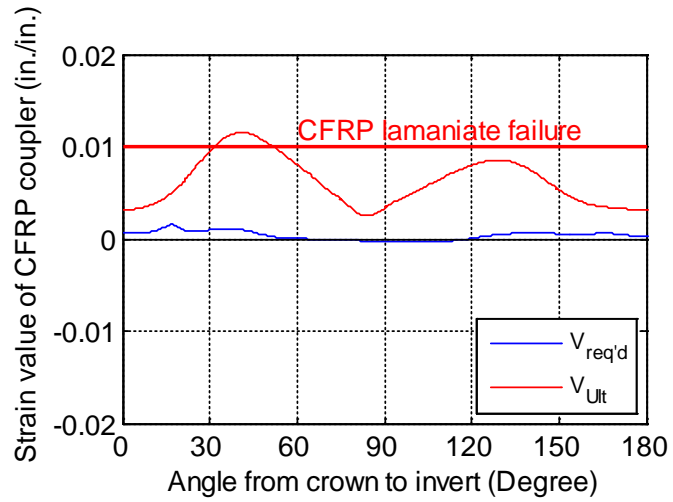
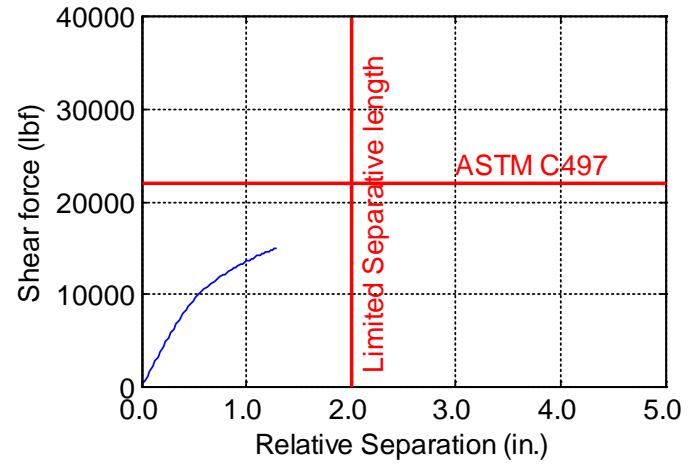
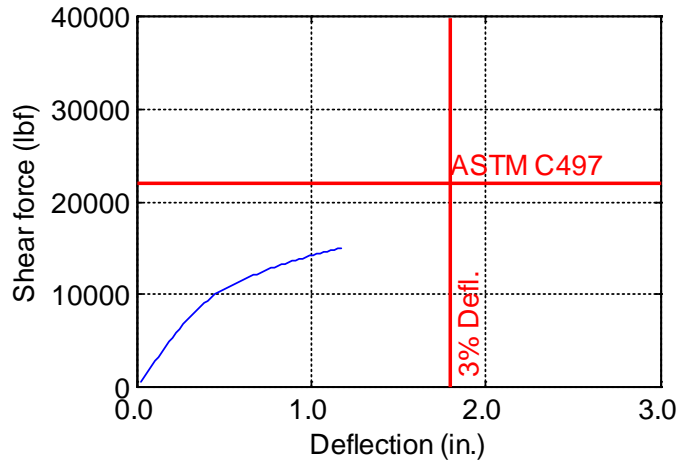


Figure B-100. TW-060-12-0.125

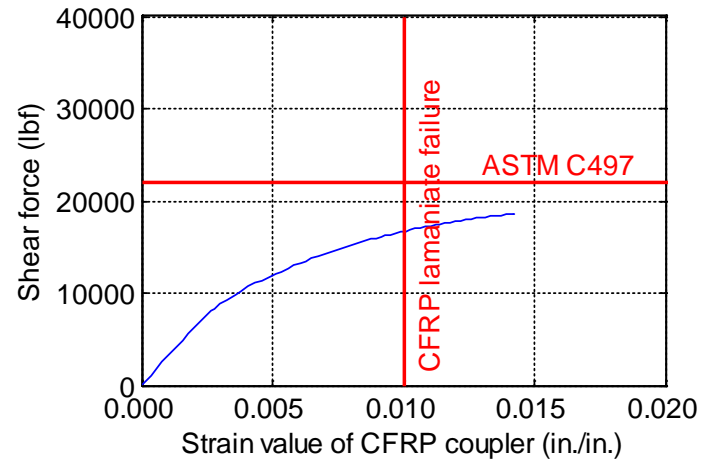
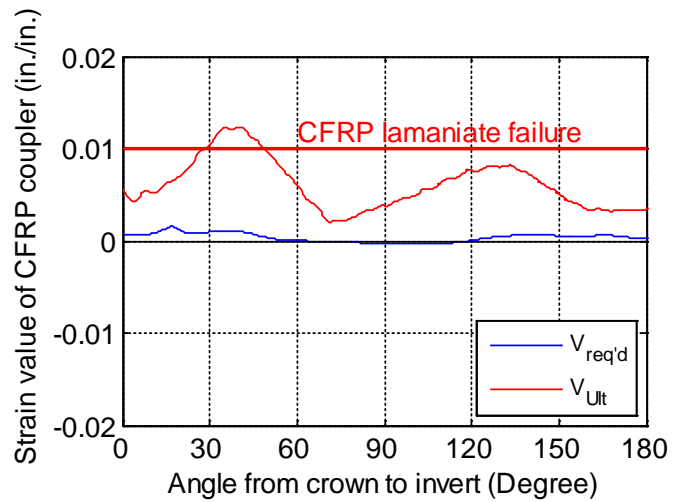
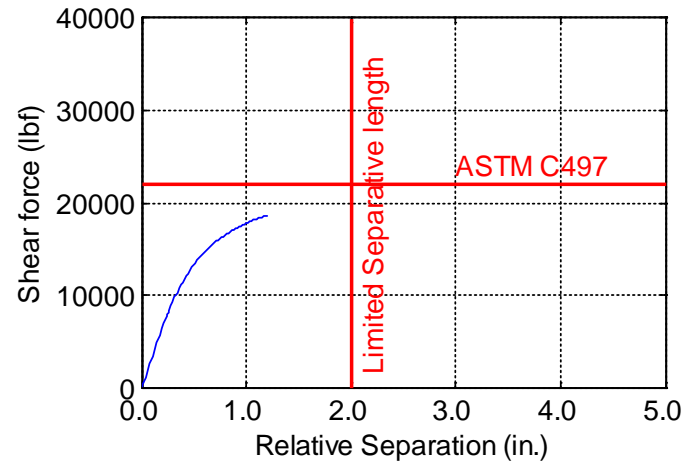
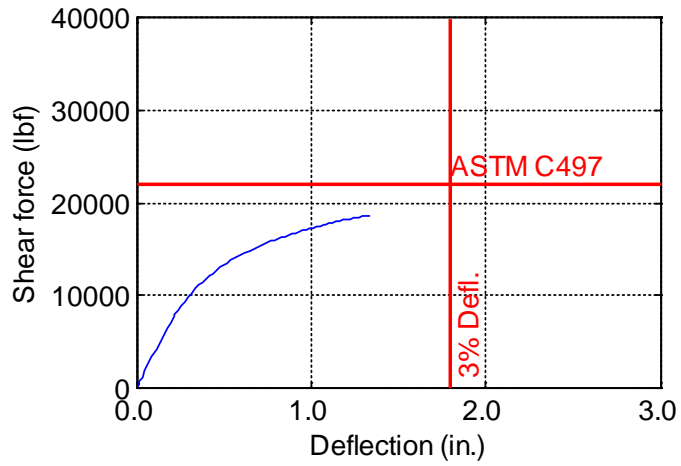


Figure B-101. TW-060-12-0.1875

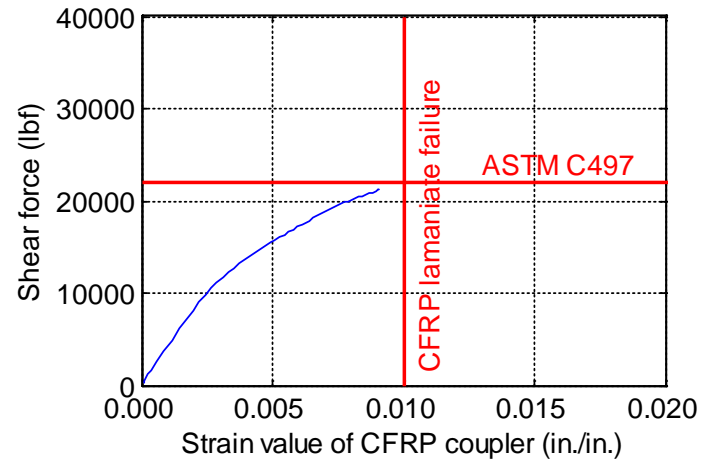
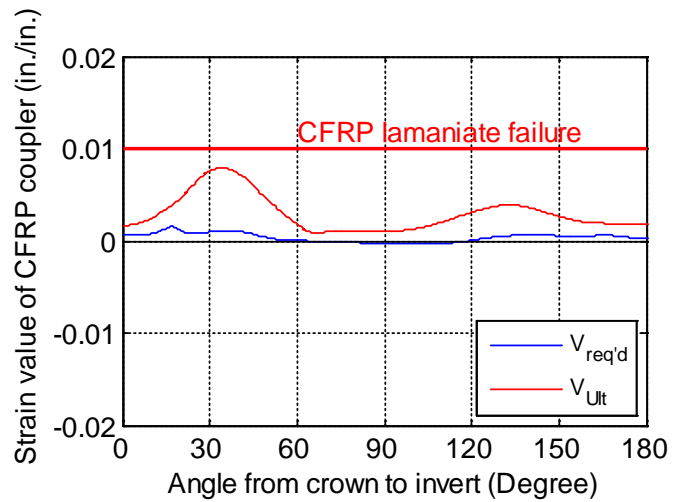
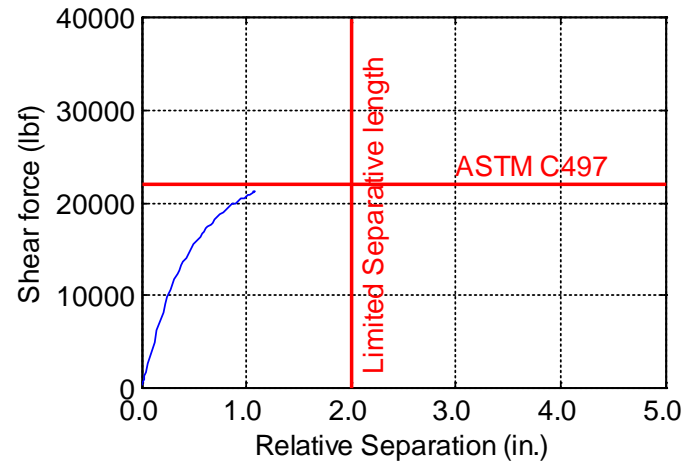
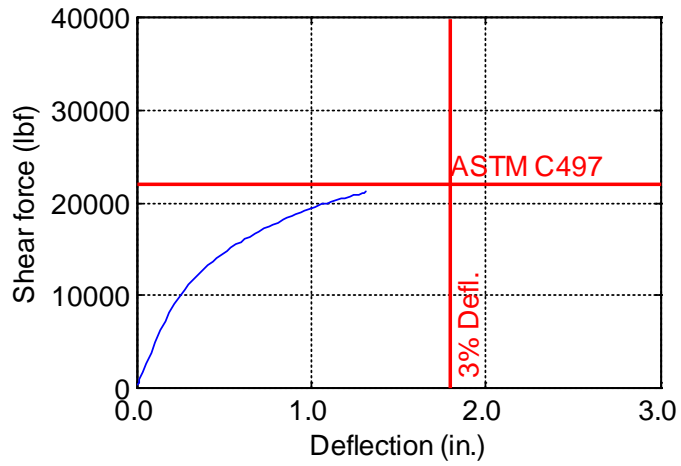


Figure B-102. TW-060-12-0.25

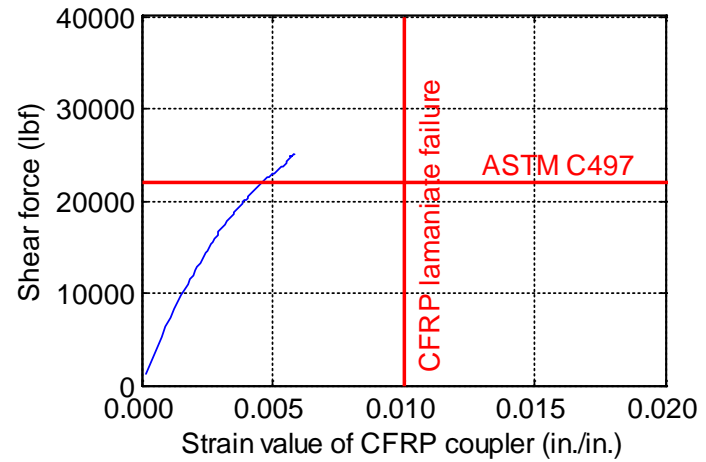
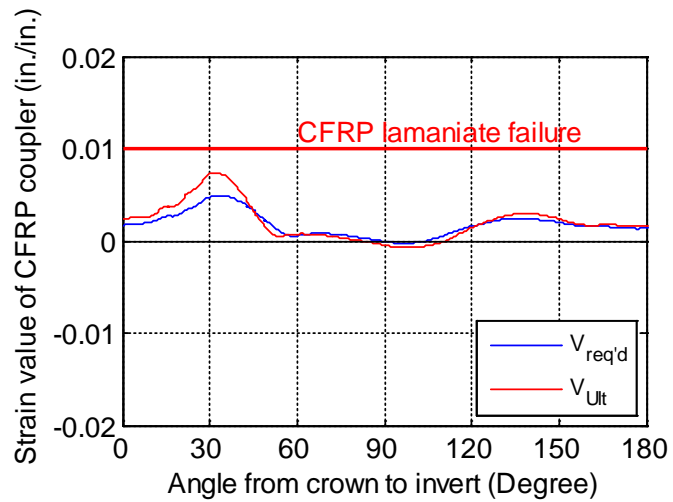
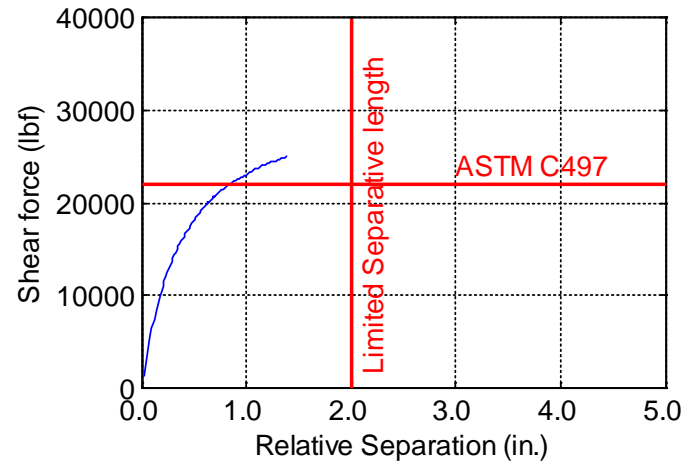
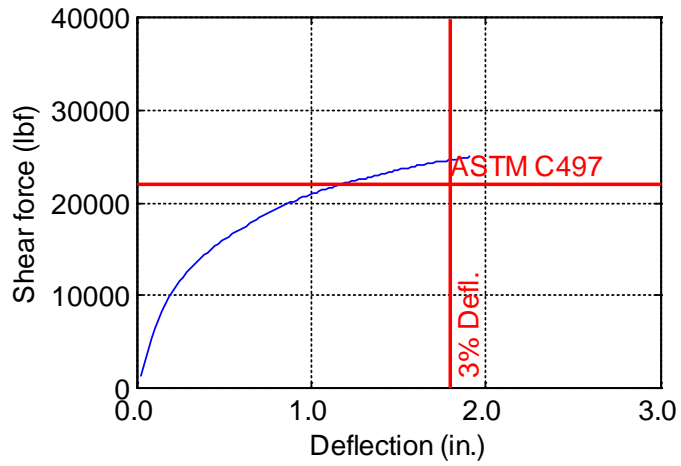


Figure B-103. TW-060-12-0.375

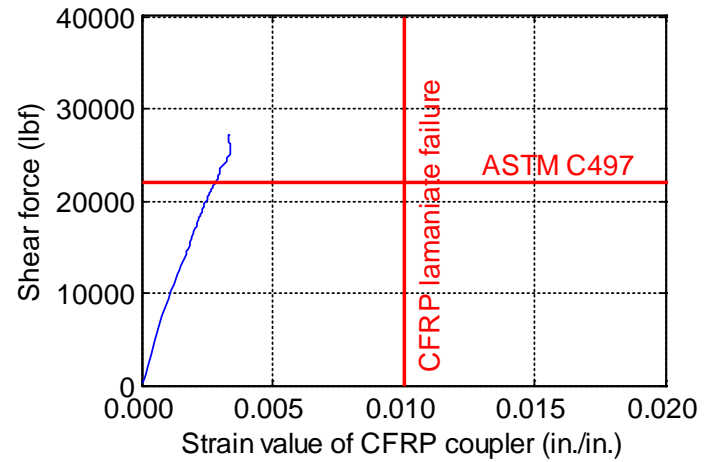
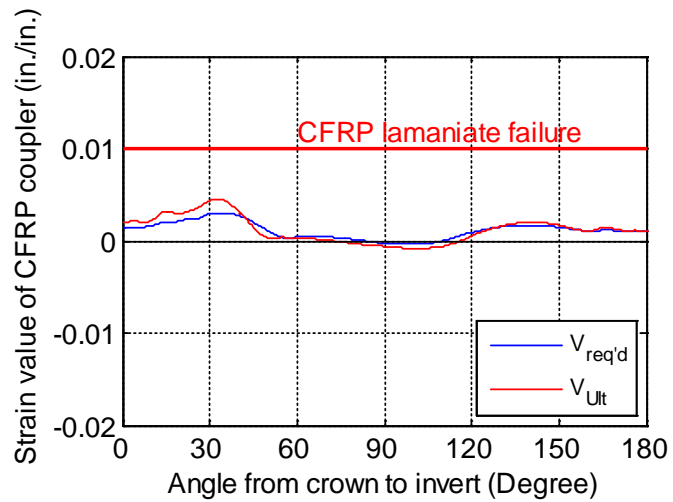
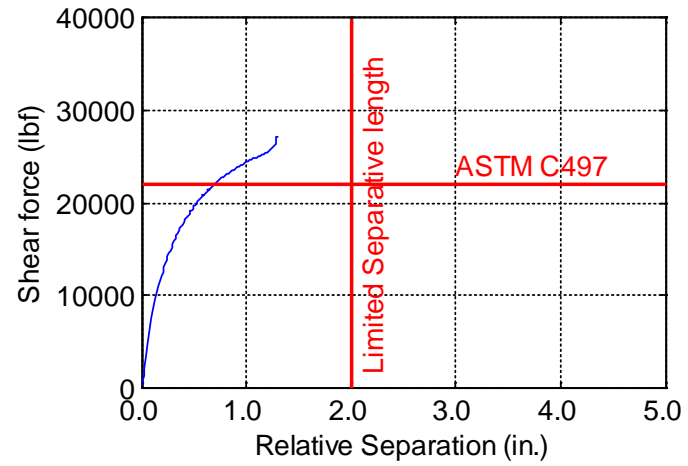
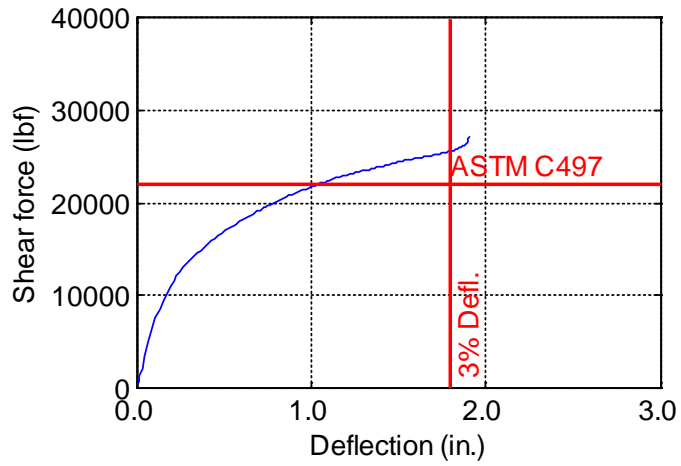


Figure B-104. TW-060-12-0.5

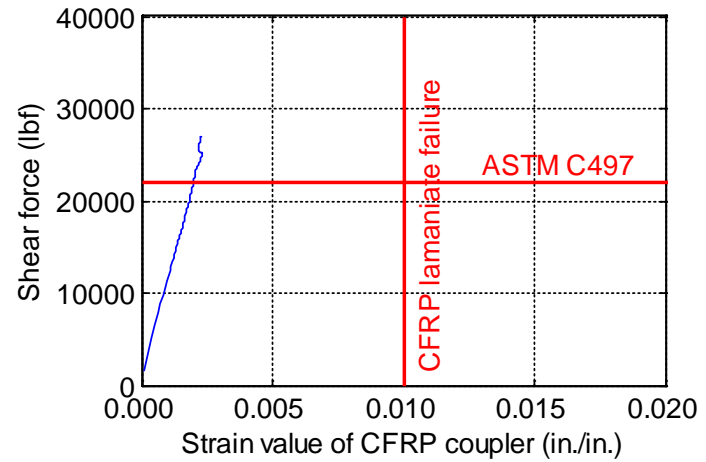
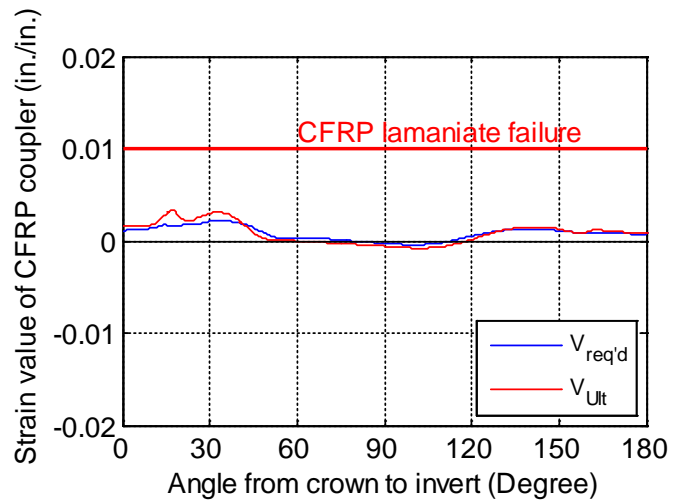
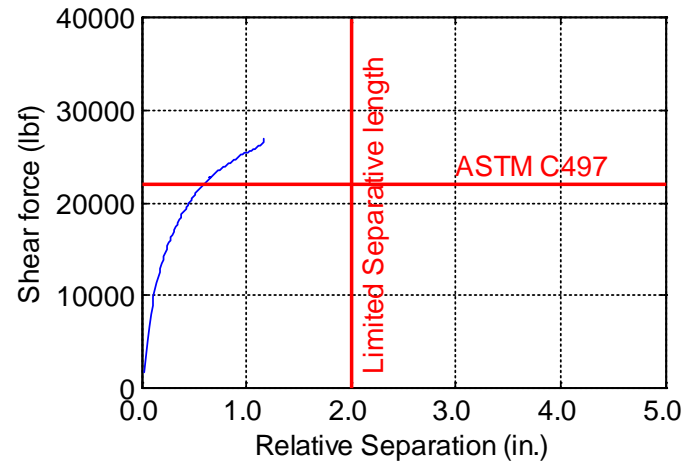
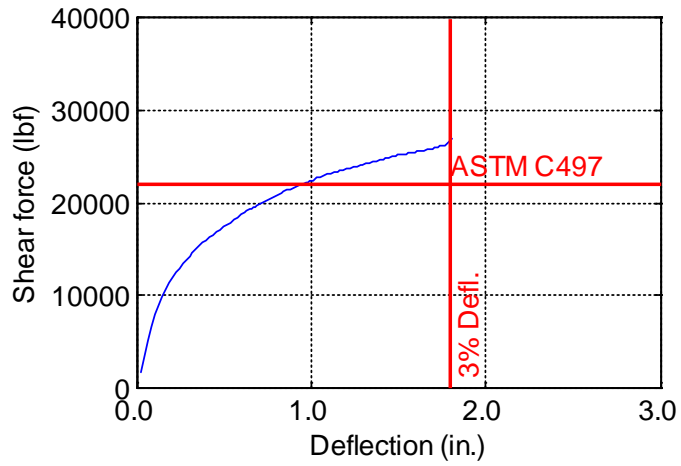


Figure B-105. TW-060-12-0.625

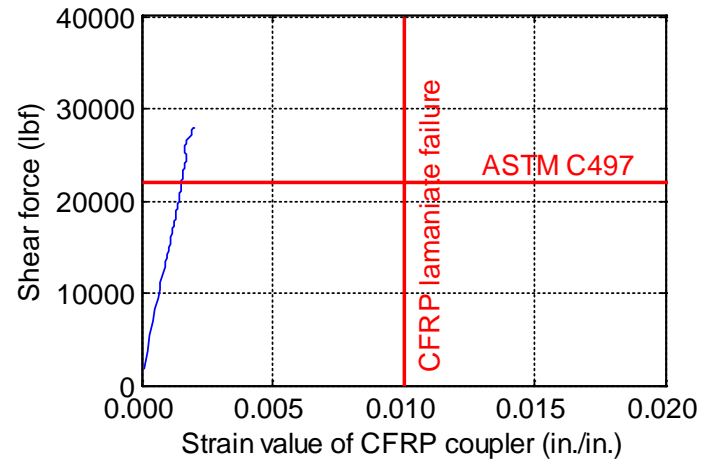
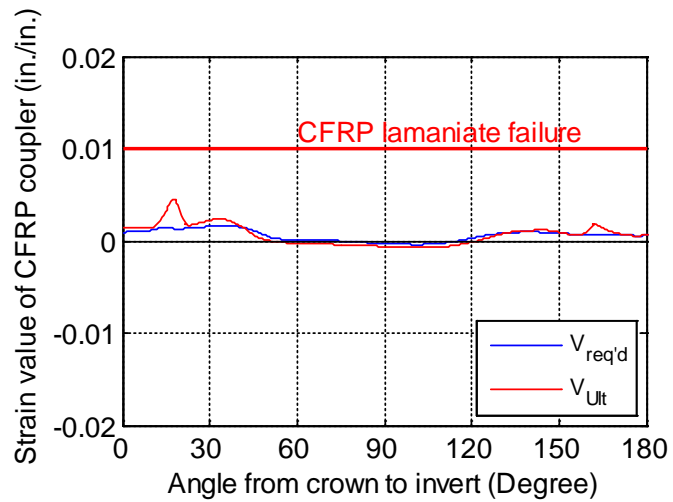
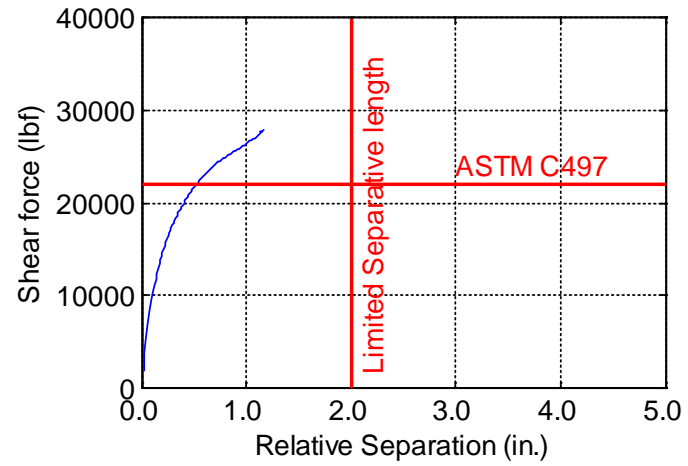
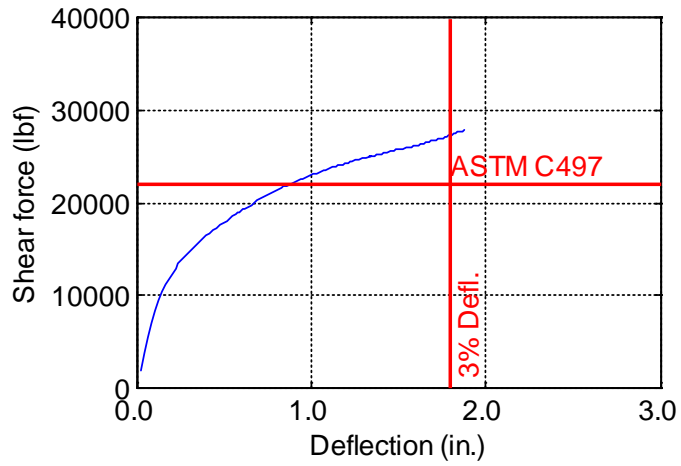


Figure B-106. TW-060-12-0.75

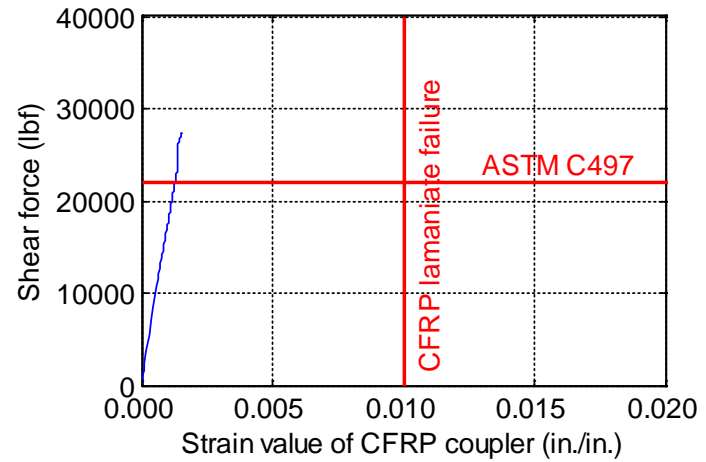
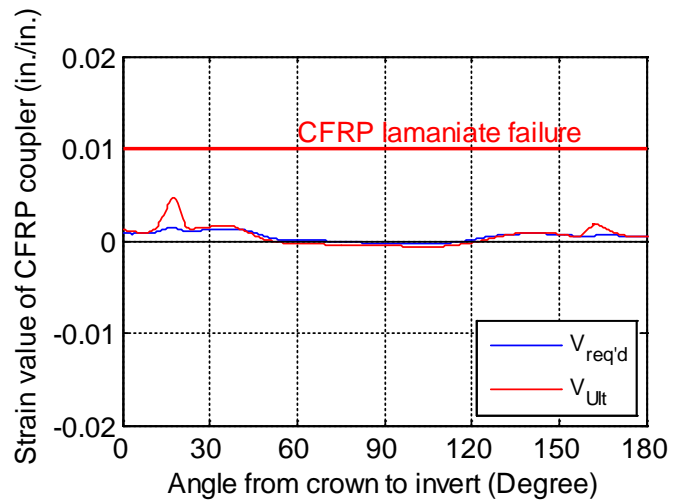
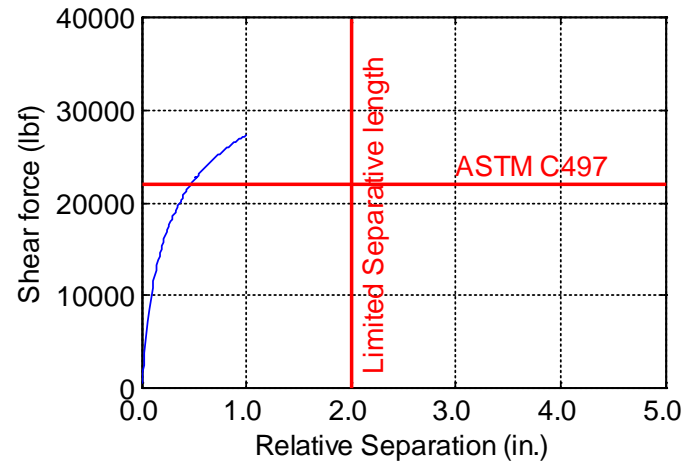
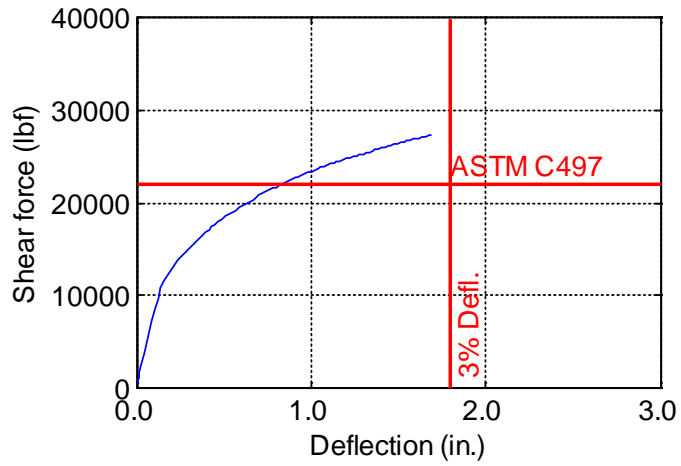


Figure B-107. TW-060-12-0.875

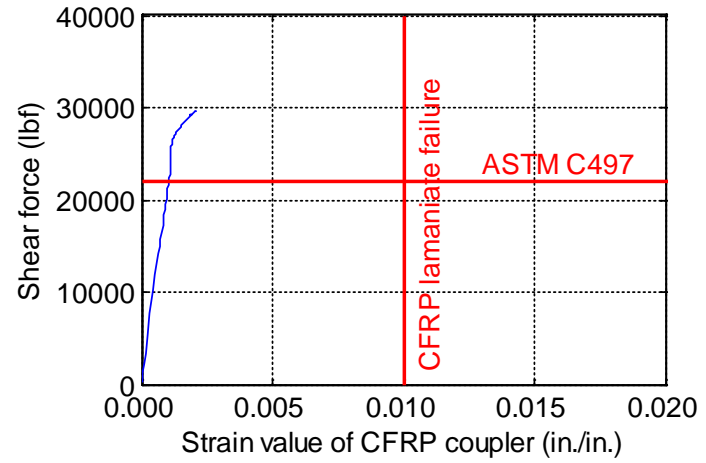
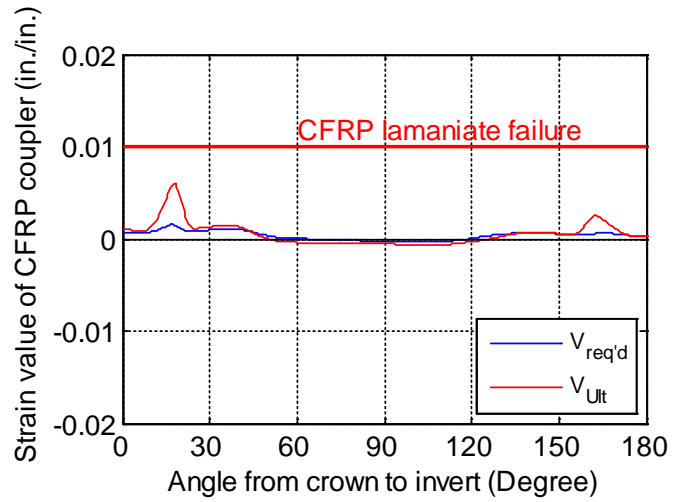
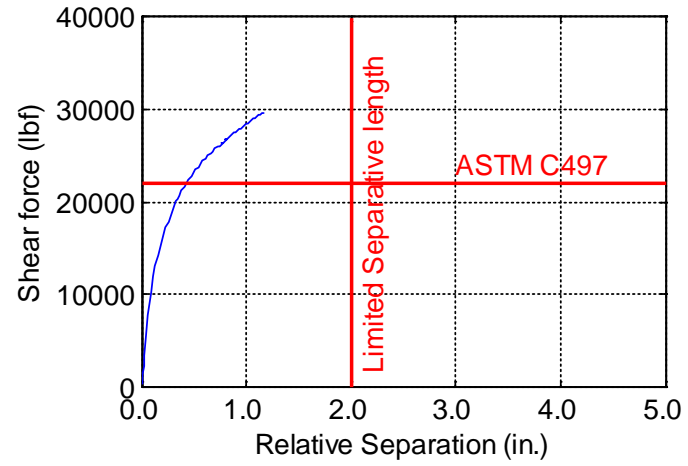
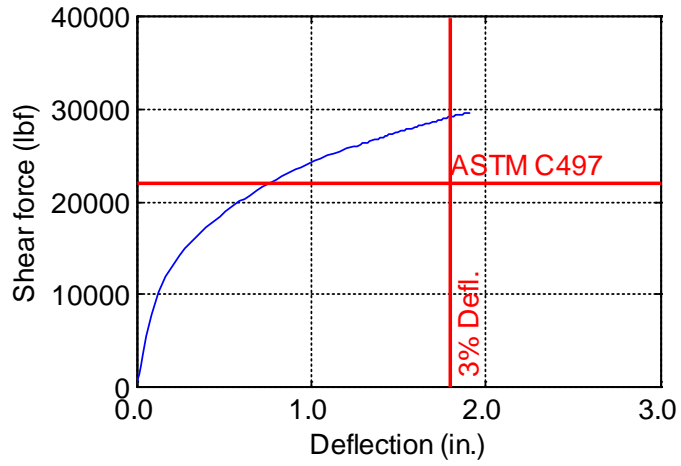


Figure B-108. TW-060-12-1.0

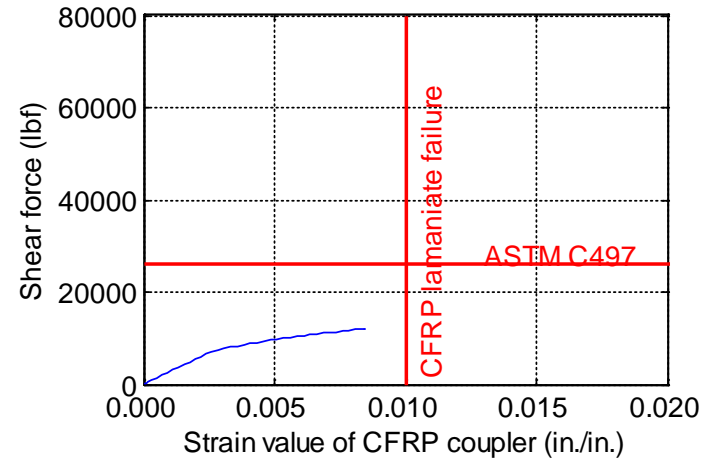
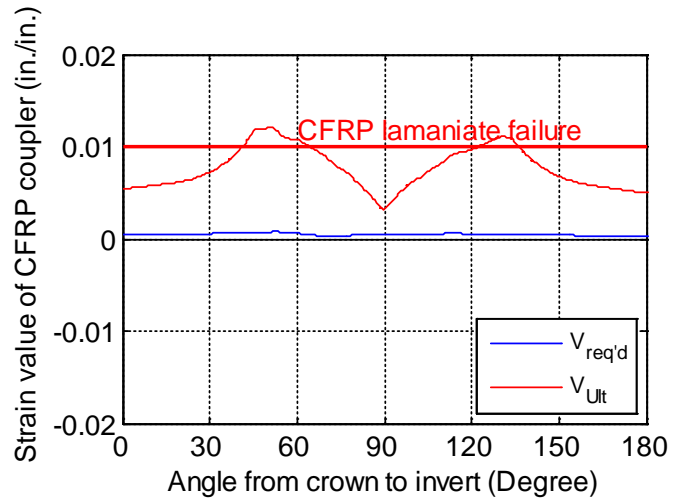
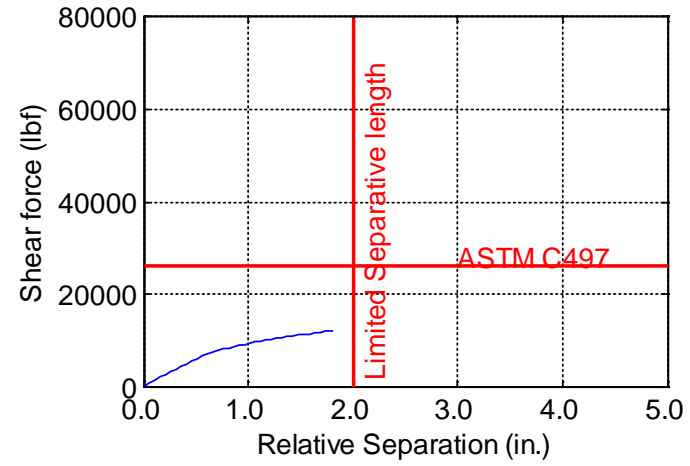
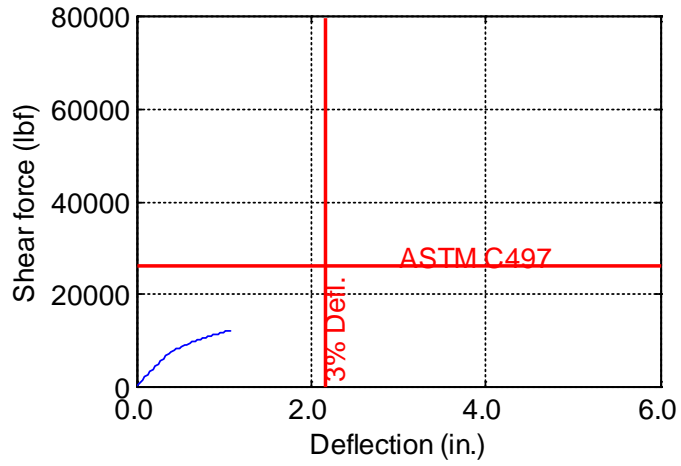


Figure B-109. TW-072-06-0.125

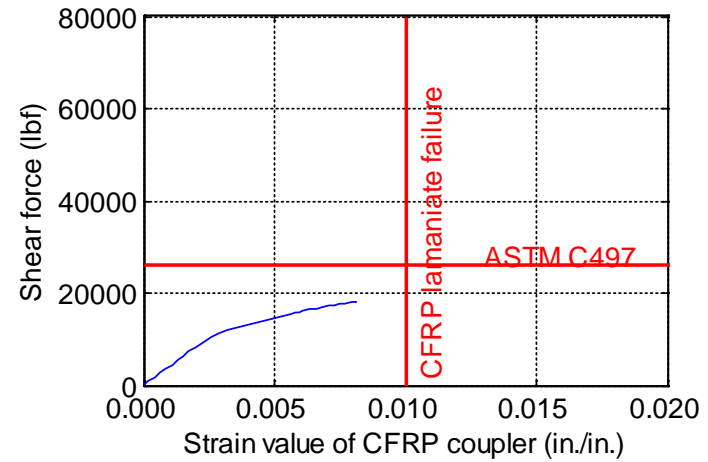
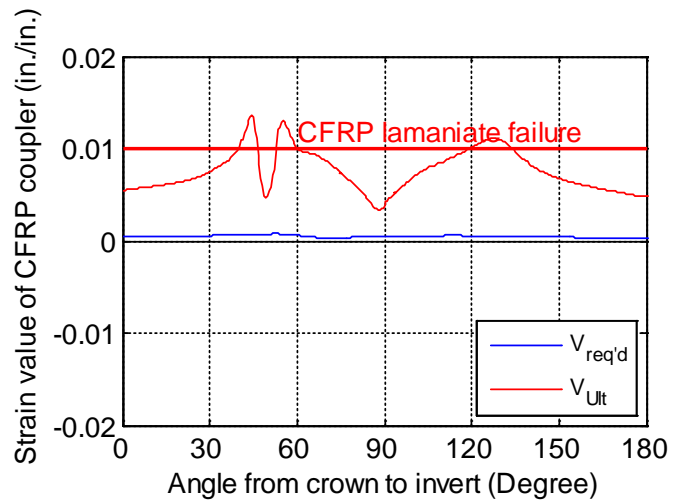
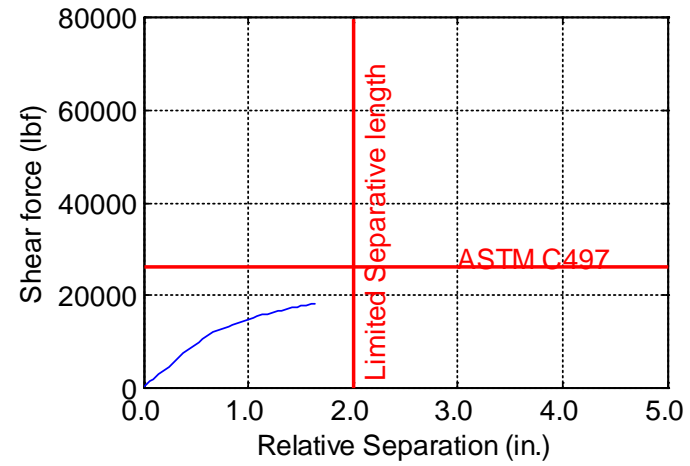
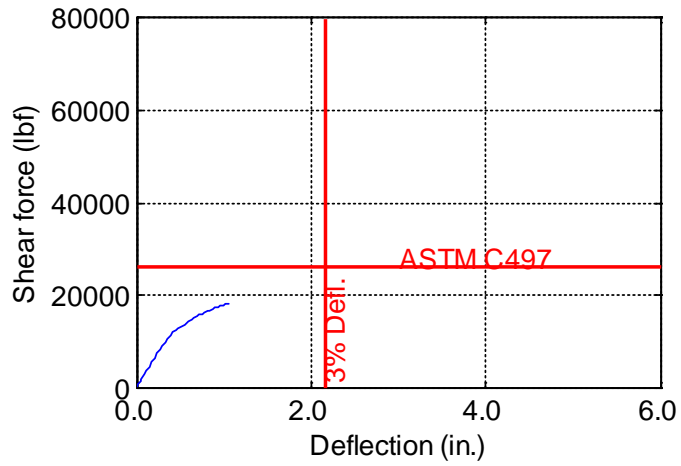


Figure B-110. TW-072-06-0.1875

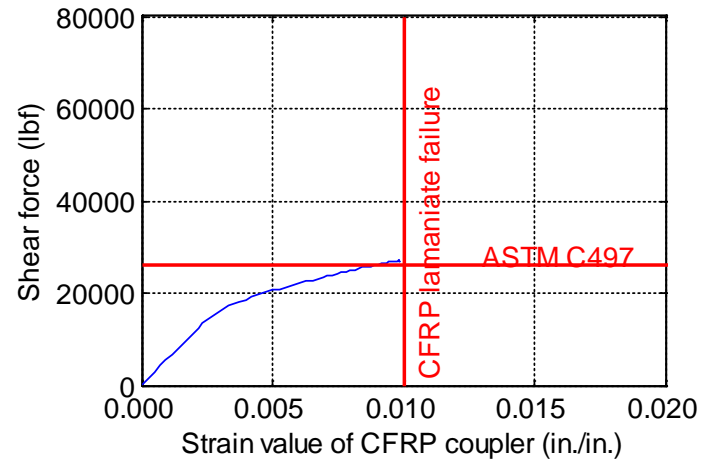
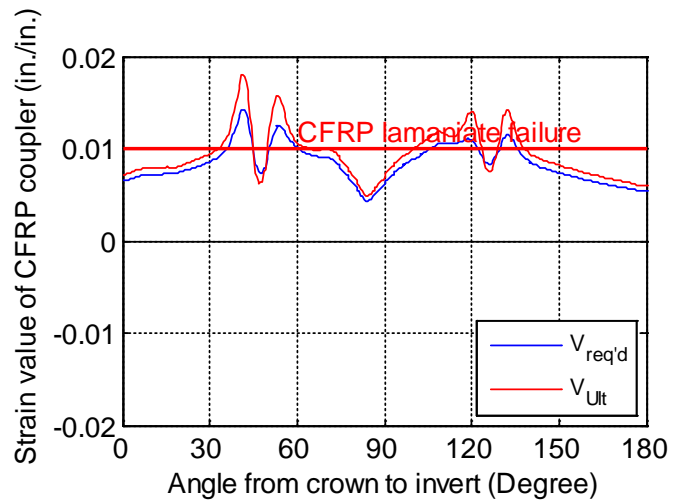
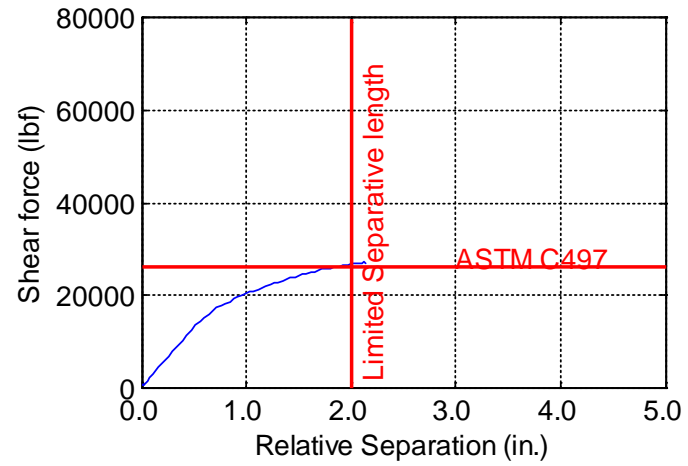
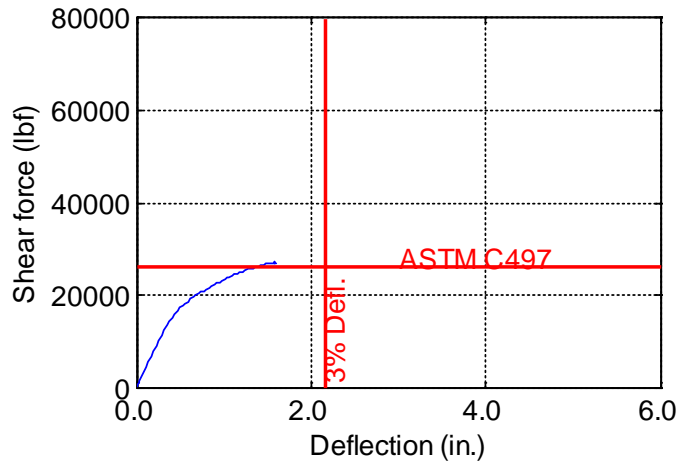


Figure B-111. TW-072-06-0.25

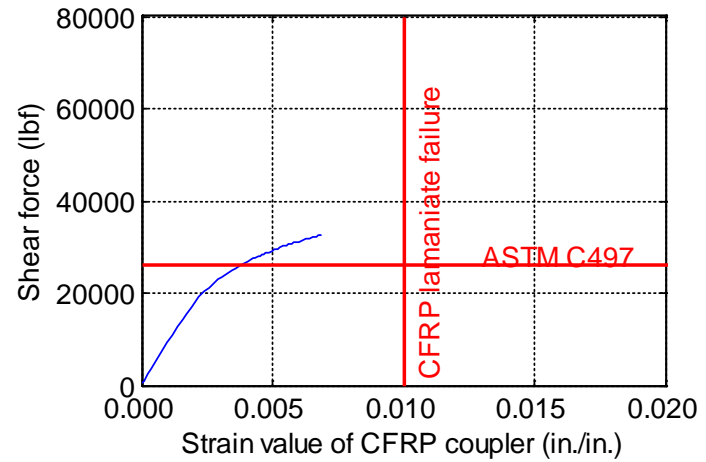
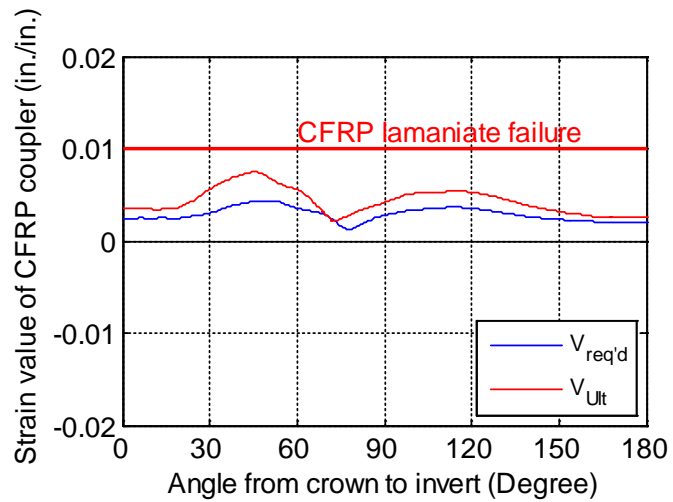
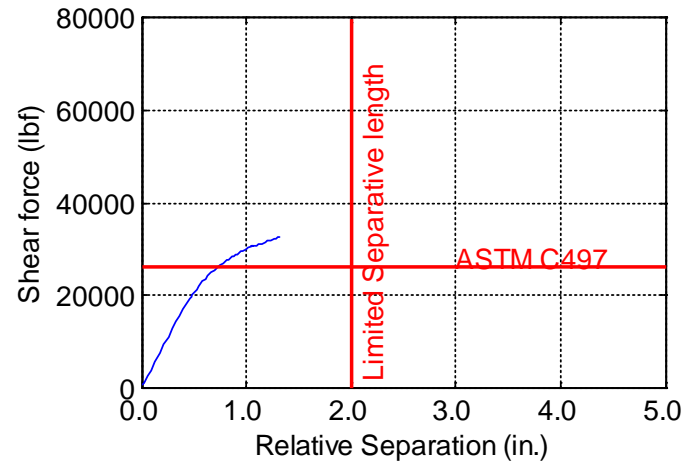
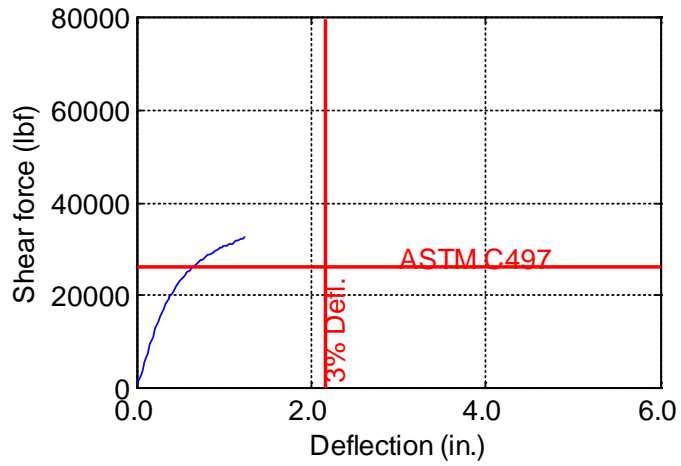


Figure B-112. TW-072-06-0.375

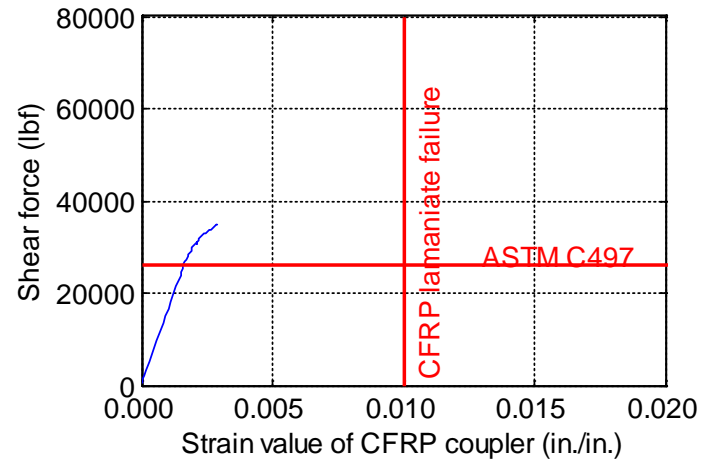
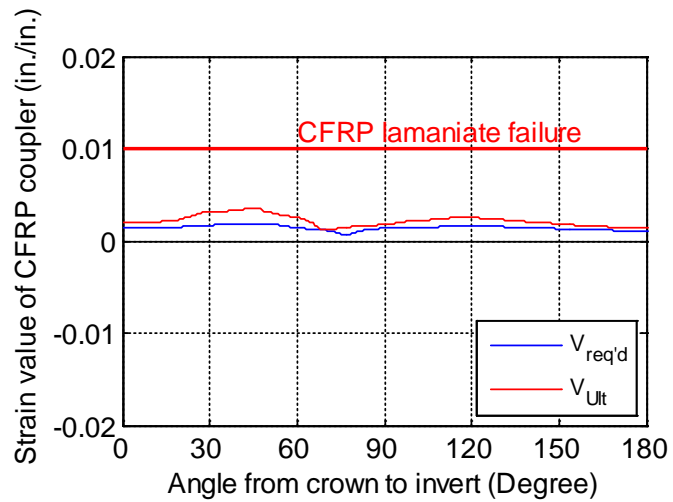
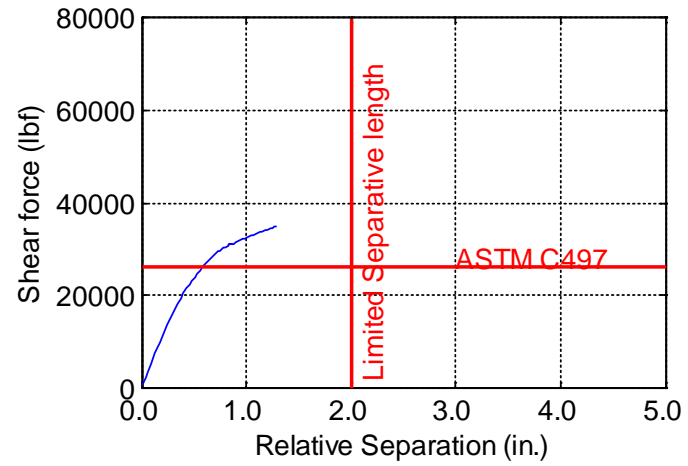
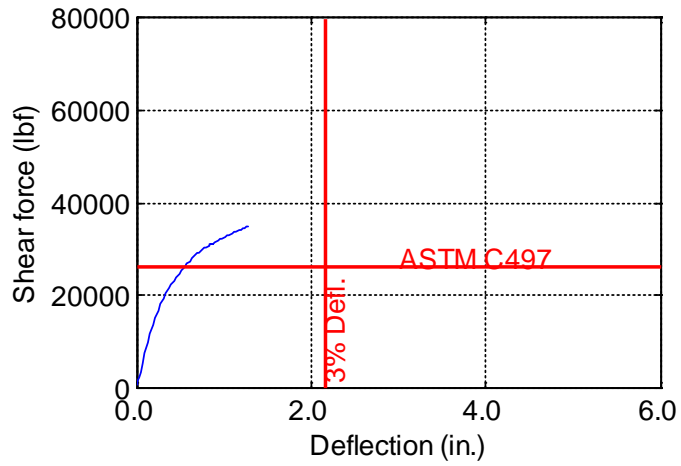


Figure B-113. TW-072-06-0.5

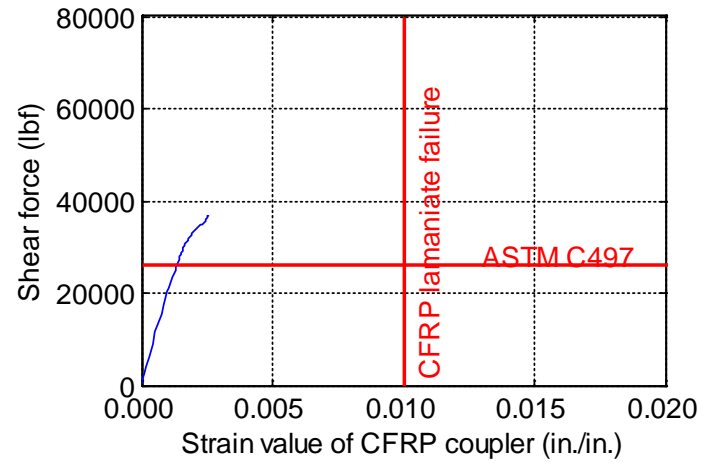
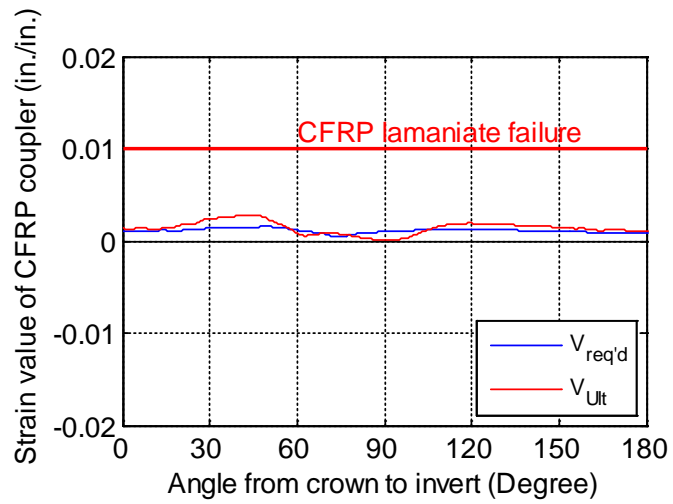
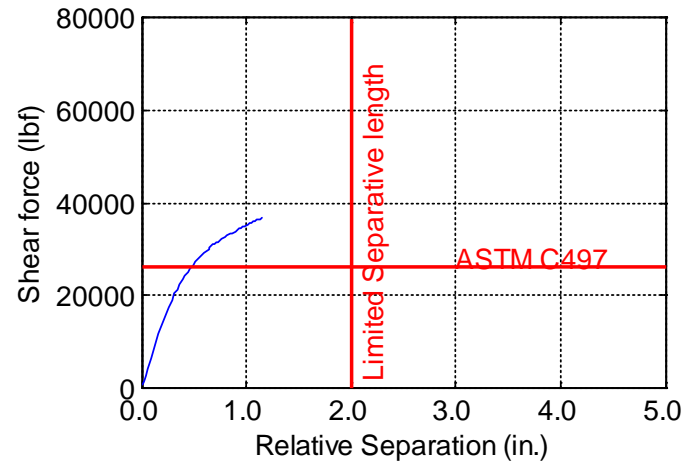
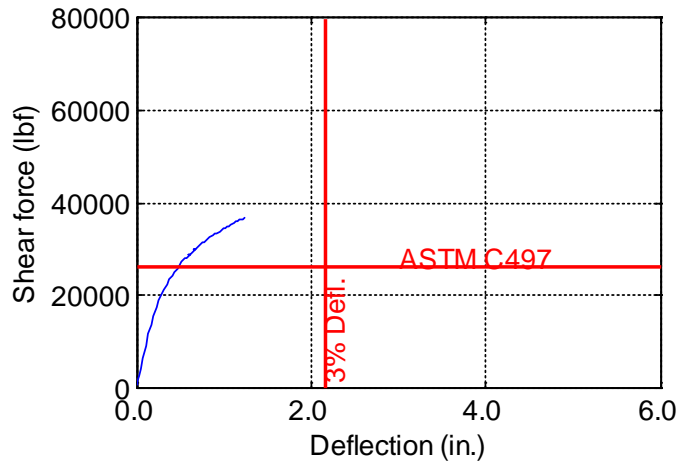


Figure B-114. TW-072-06-0.625

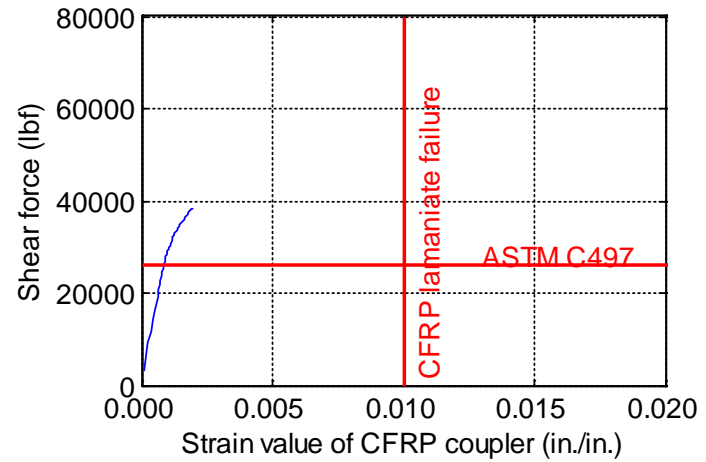
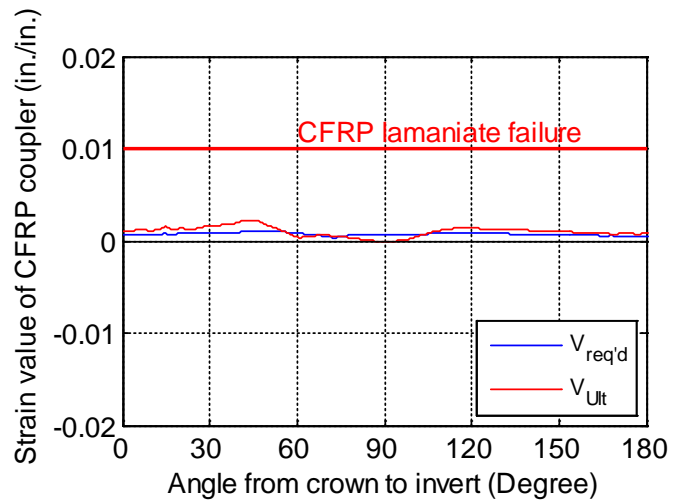
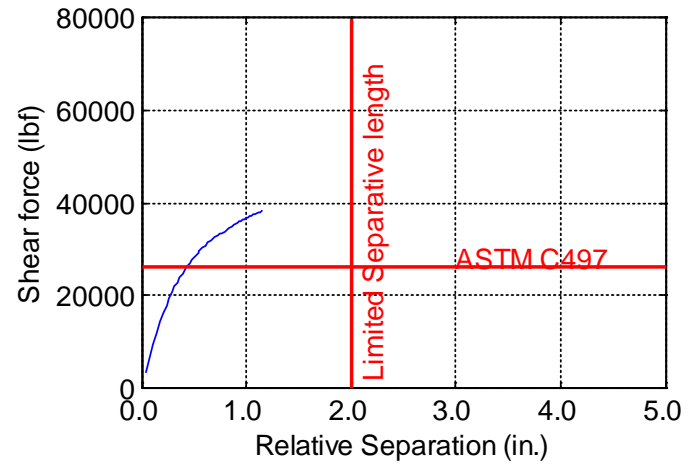
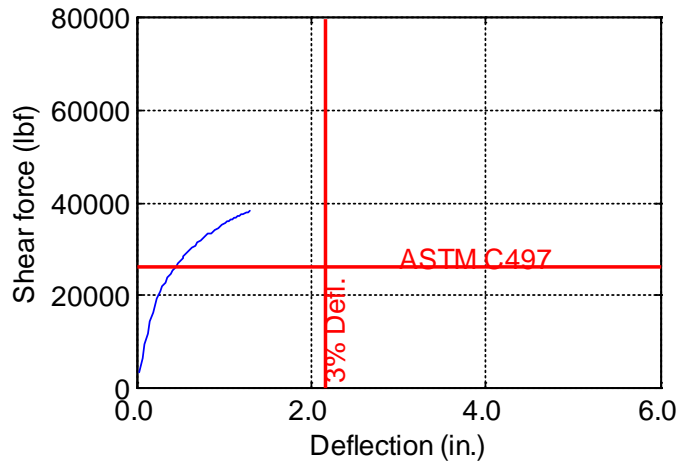


Figure B-115. TW-072-06-0.75

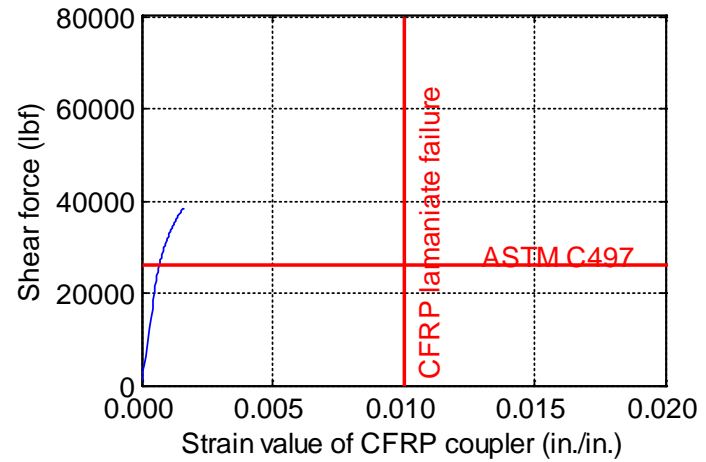
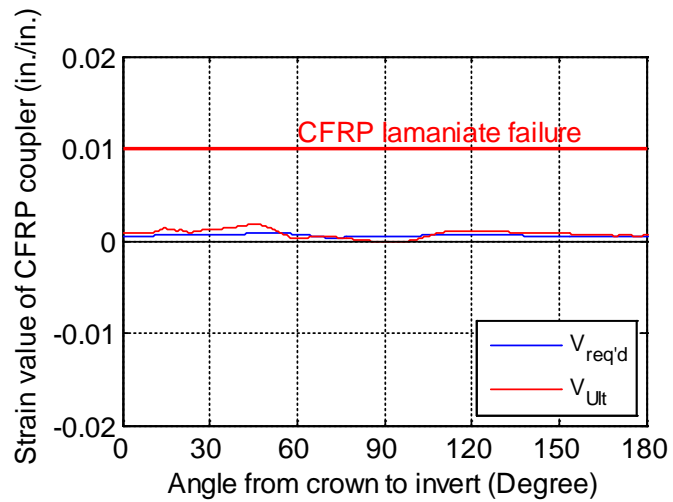
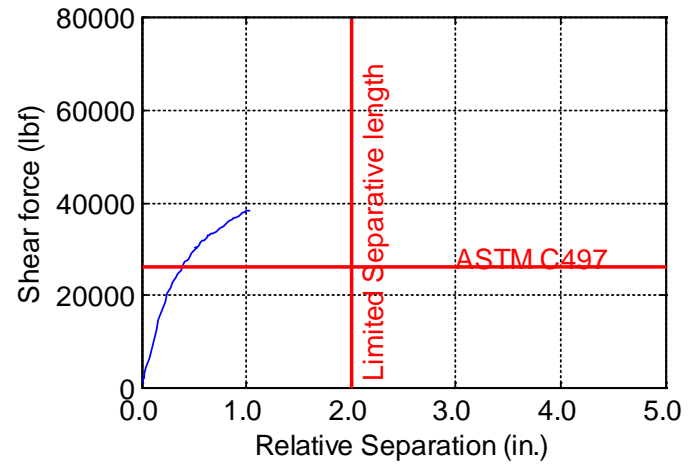
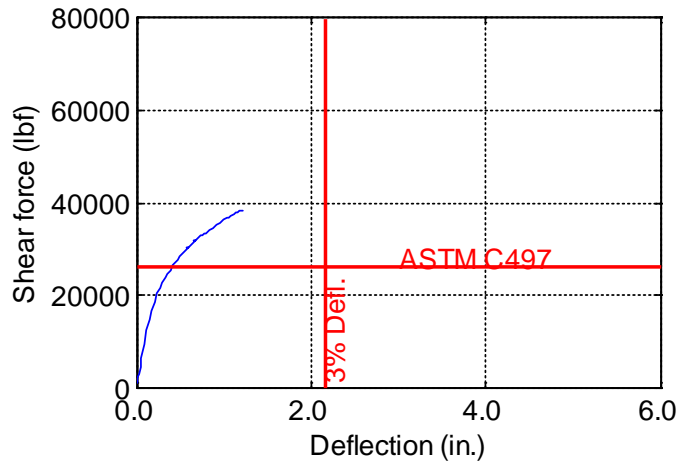


Figure B-116. TW-072-06-0.875

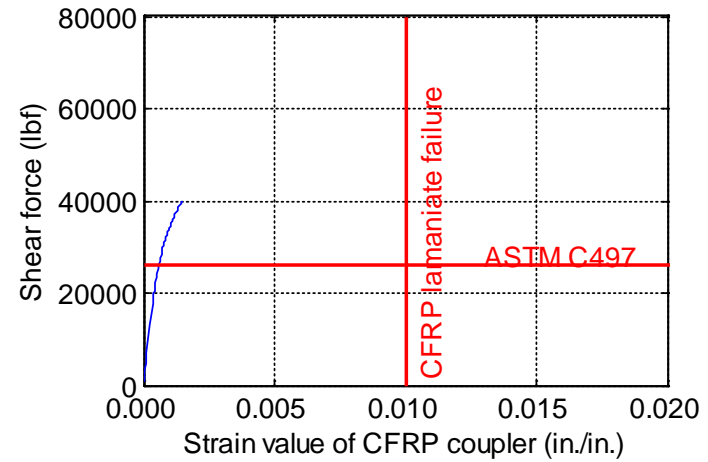
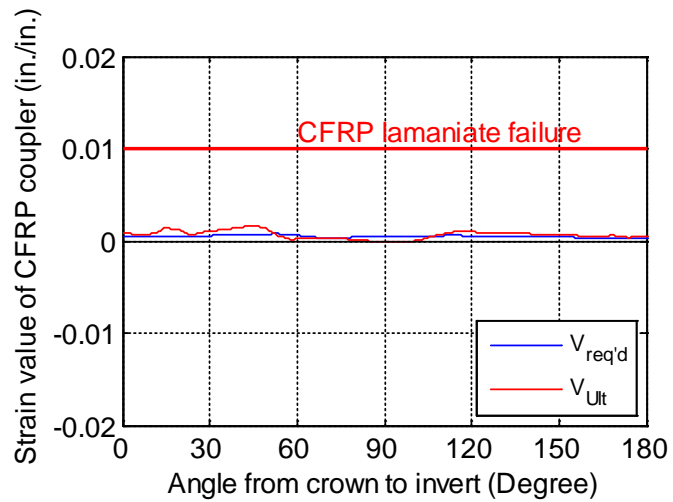
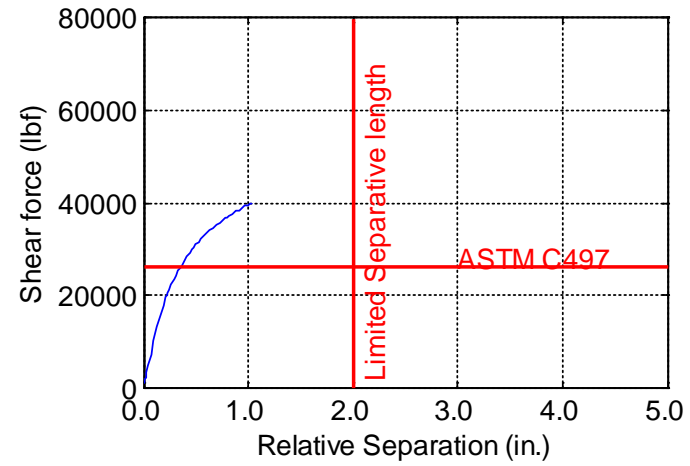
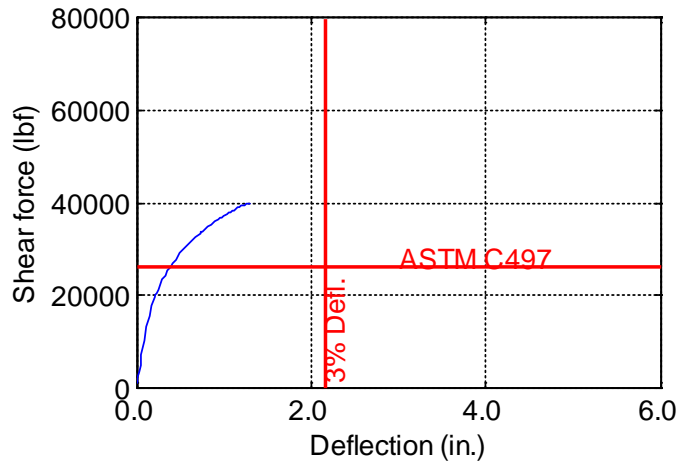


Figure B-117. TW-072-06-1.0

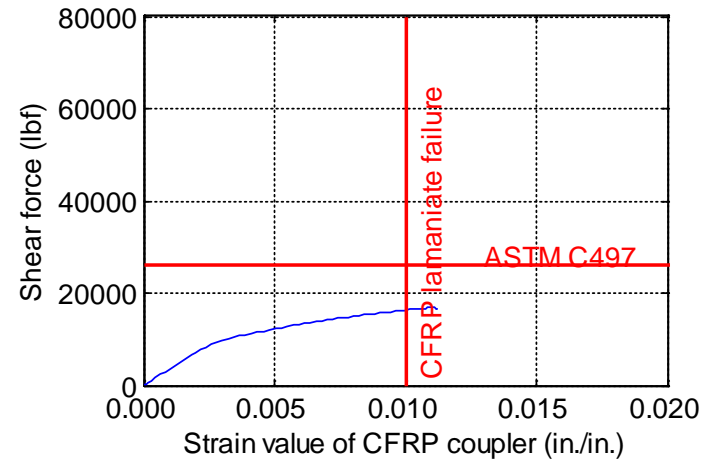
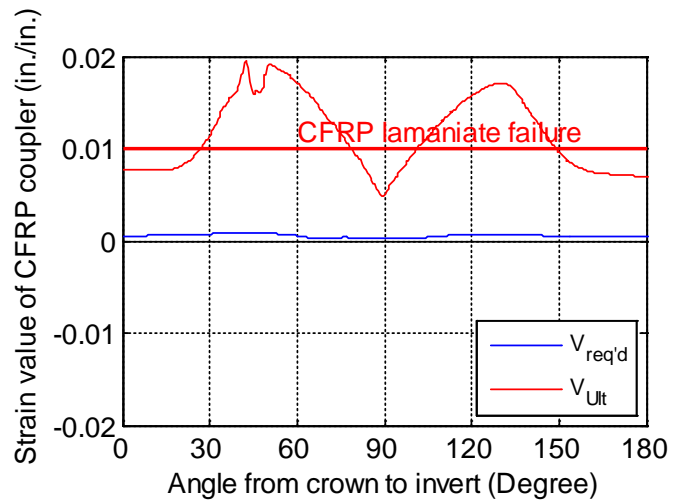
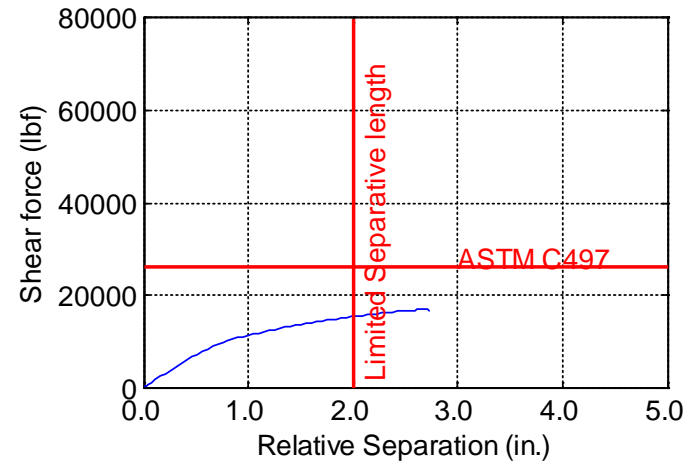
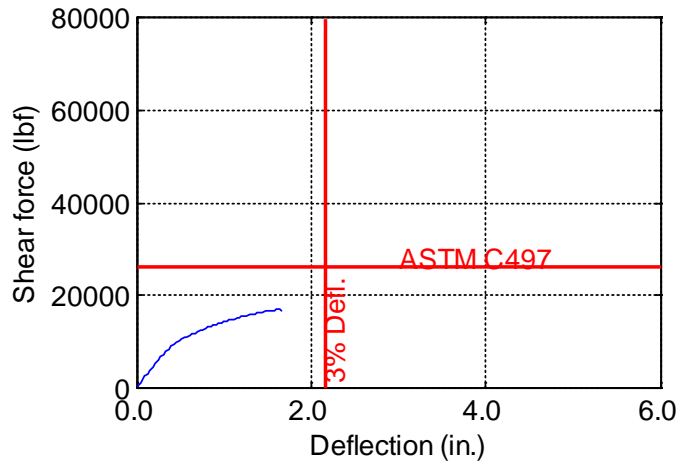


Figure B-118. TW-072-09-0.125

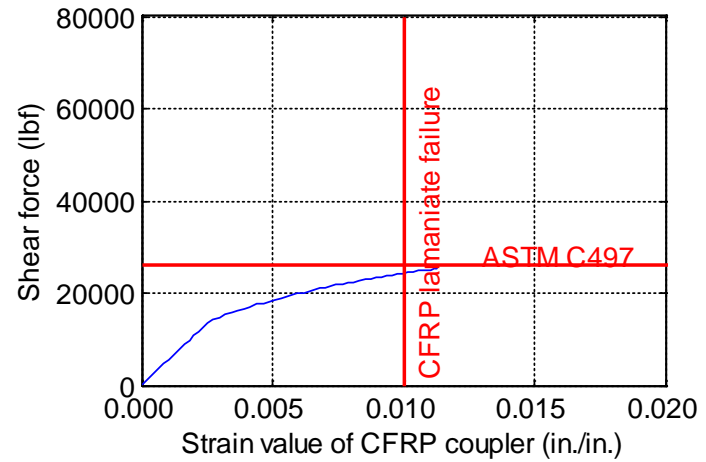
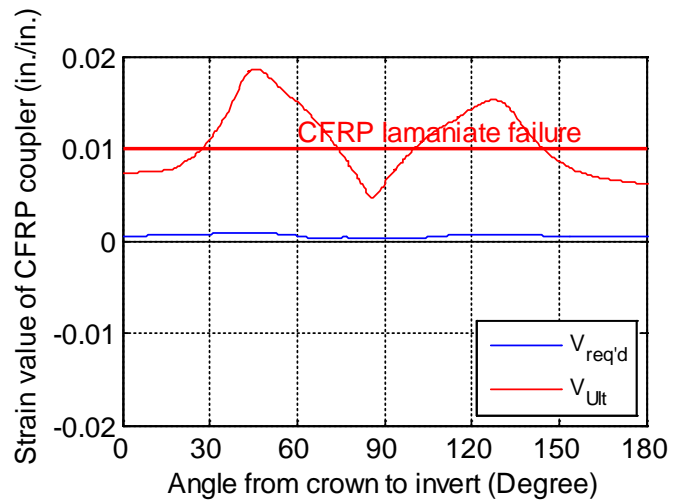
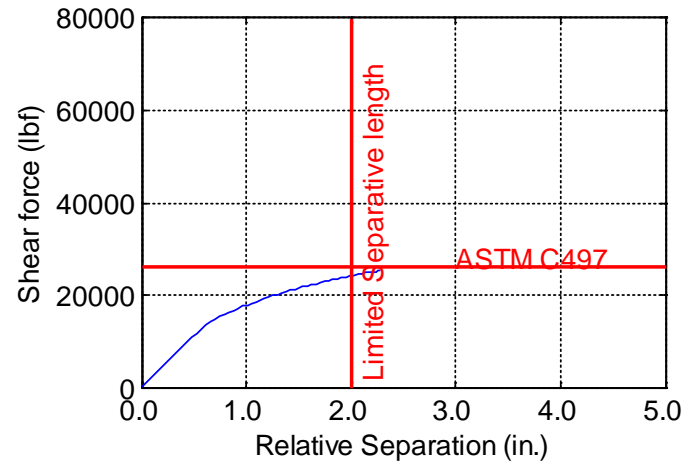
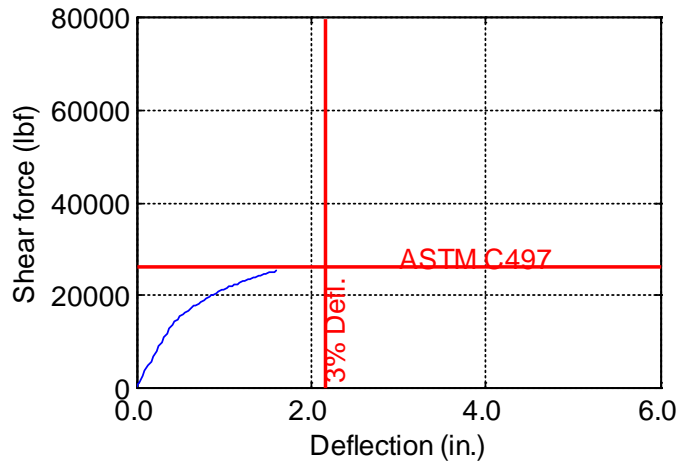


Figure B-119. TW-072-09-0.1875

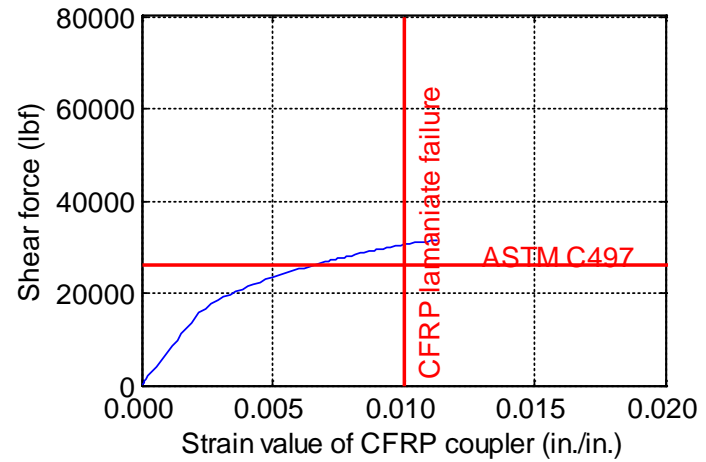
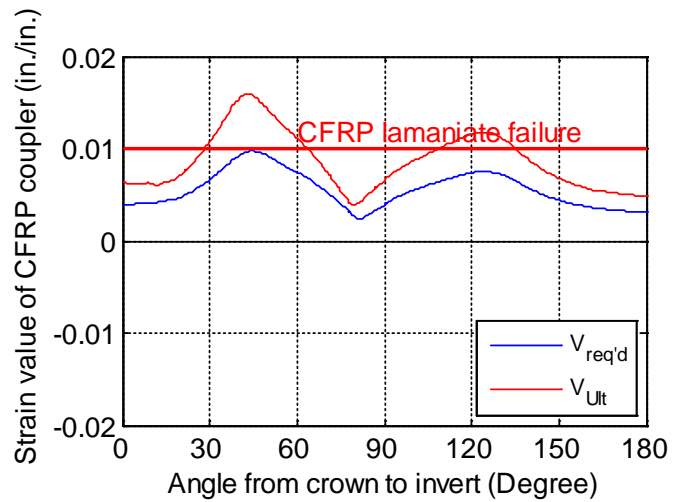
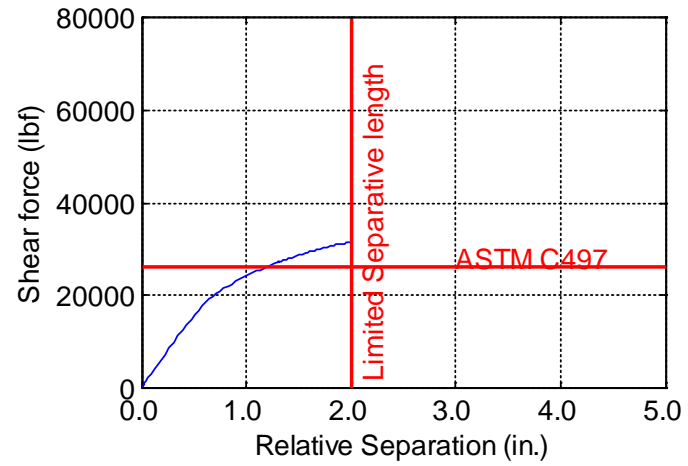
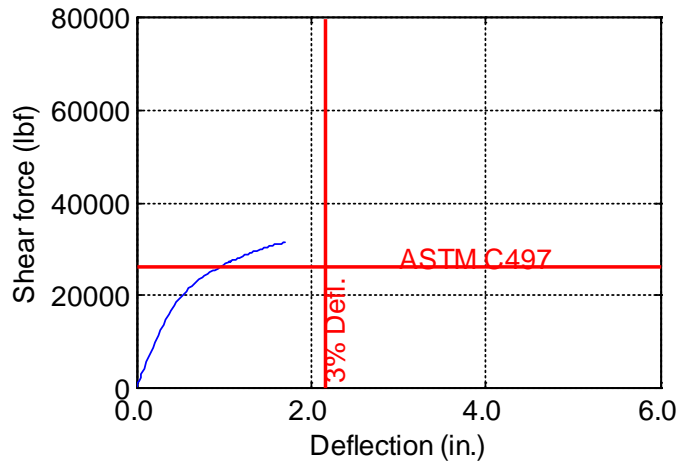


Figure B-120. TW-072-09-0.25

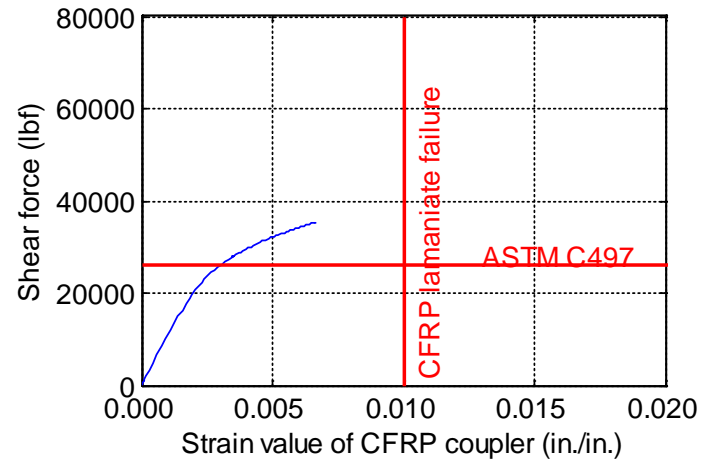
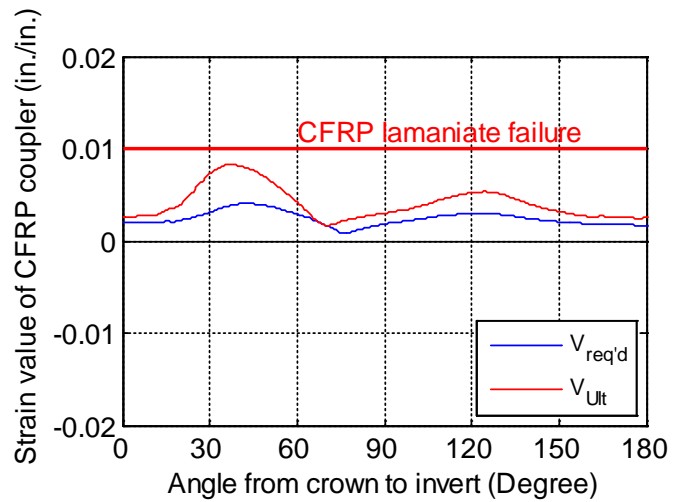
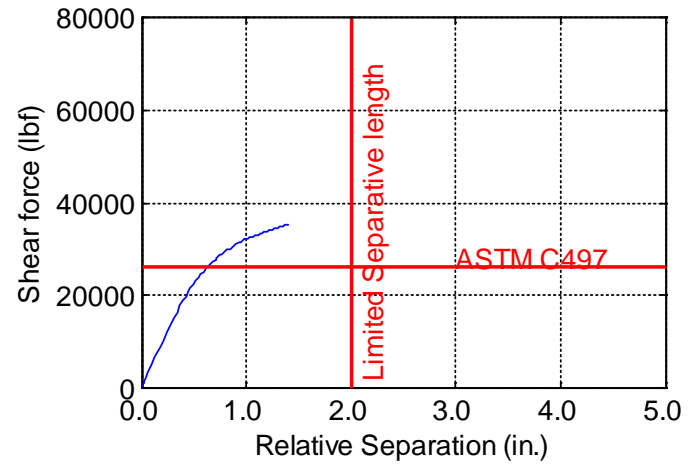
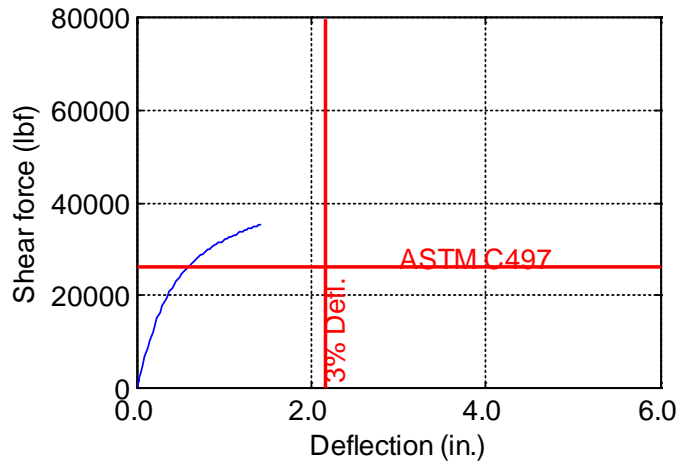


Figure B-121. TW-072-09-0.375

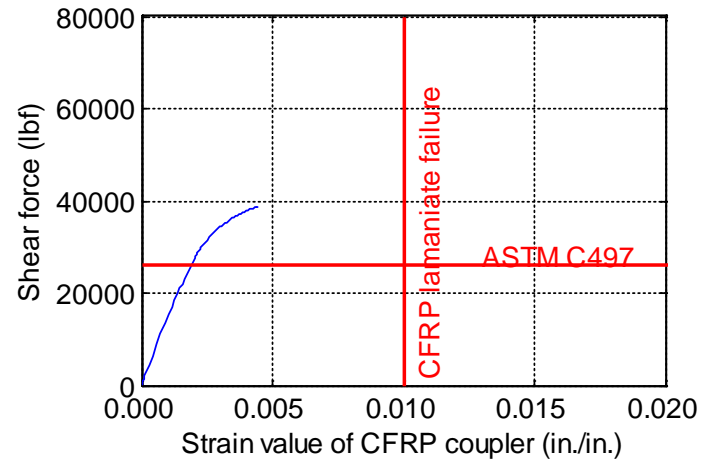
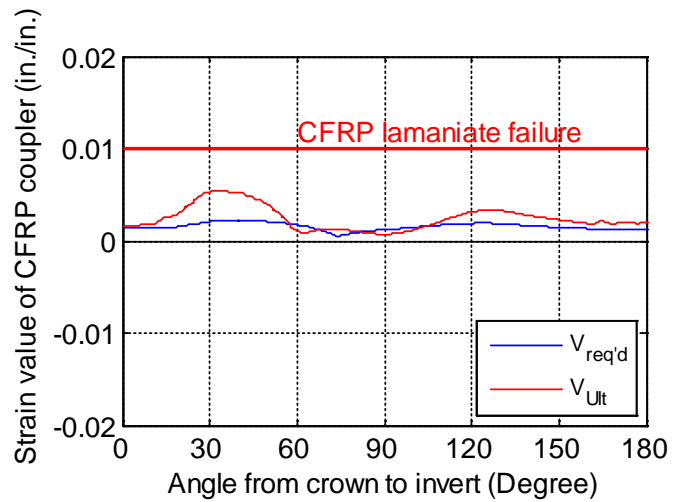
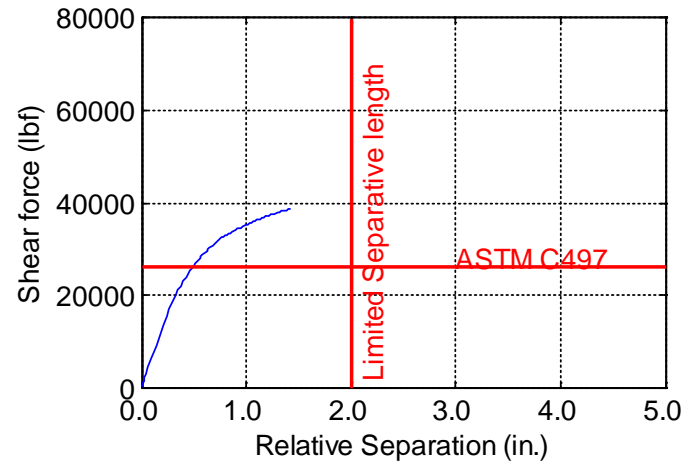
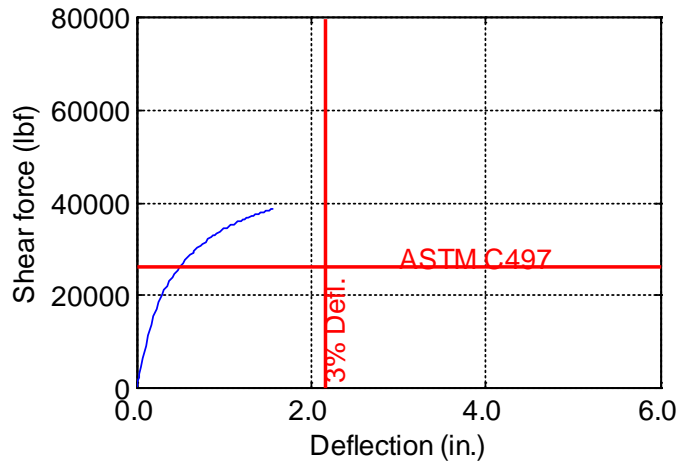


Figure B-122. TW-072-09-0.5

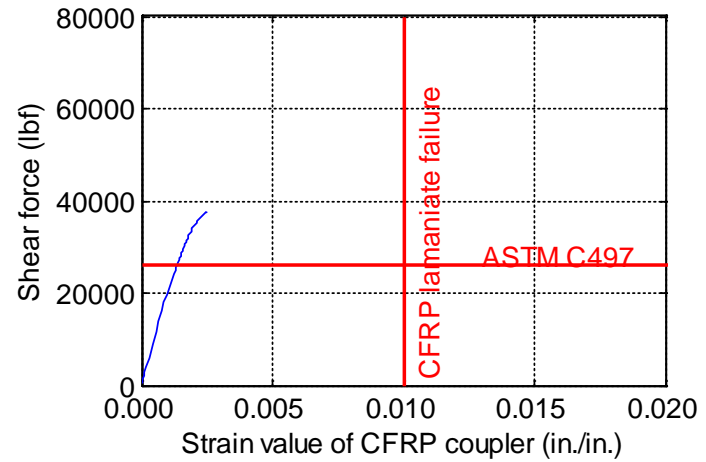
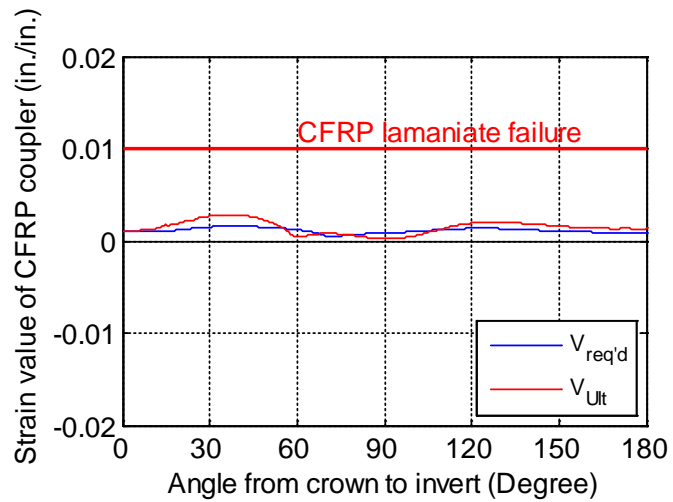
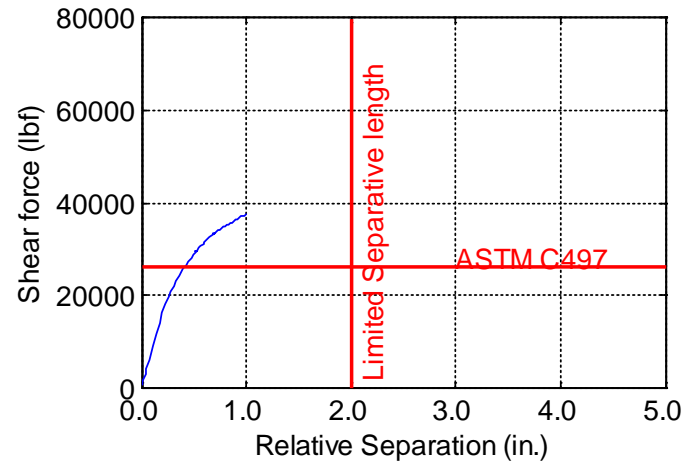
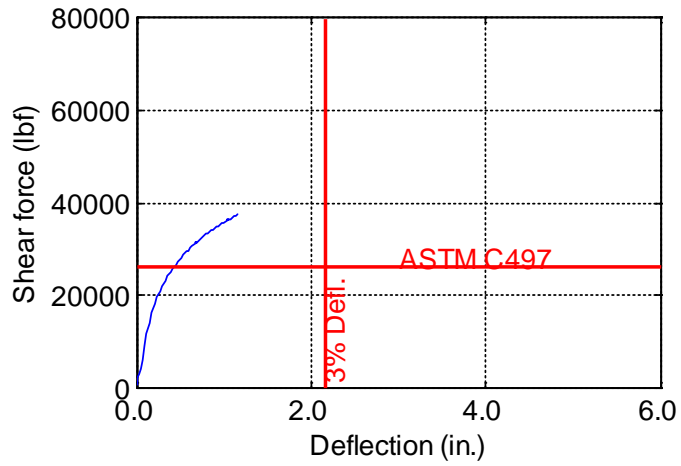


Figure B-123. TW-072-09-0.625

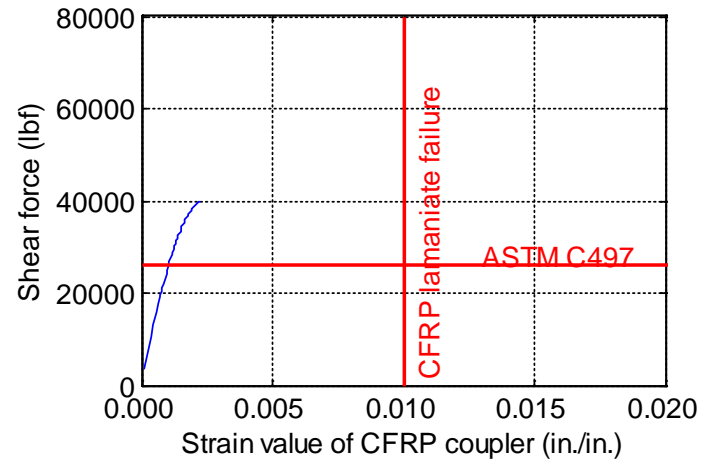
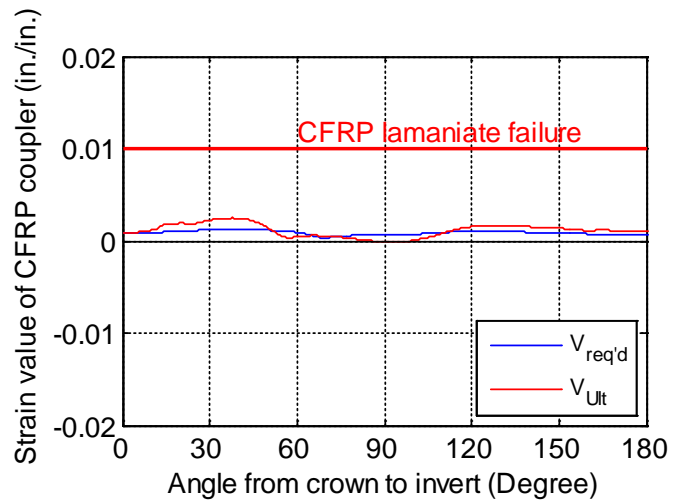
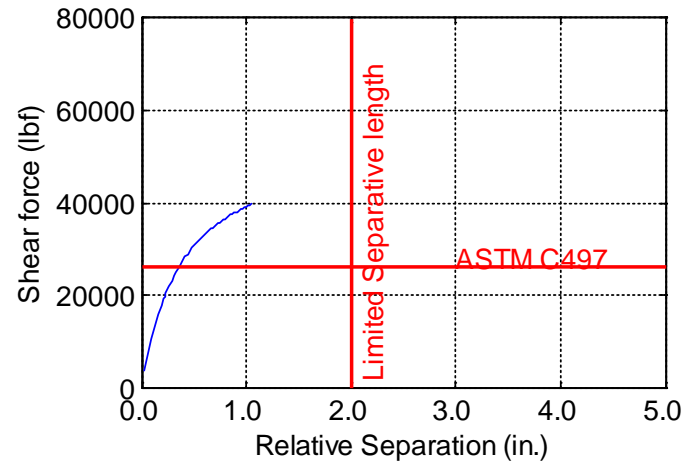
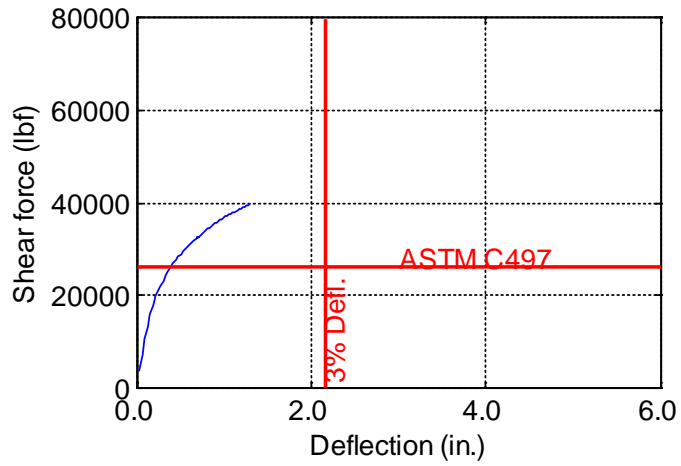


Figure B-124. TW-072-09-0.75

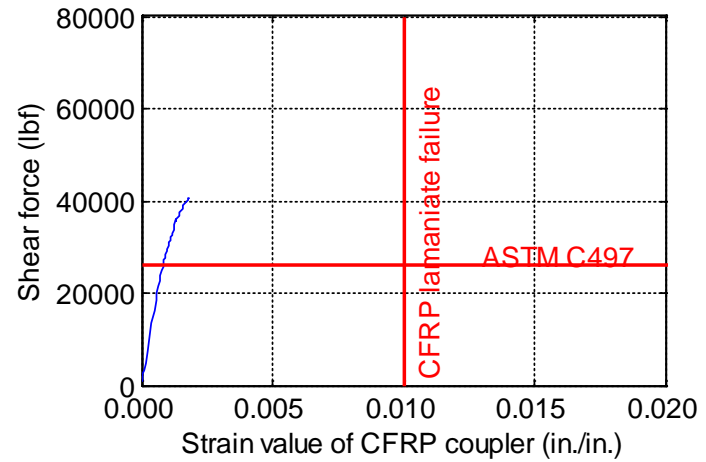
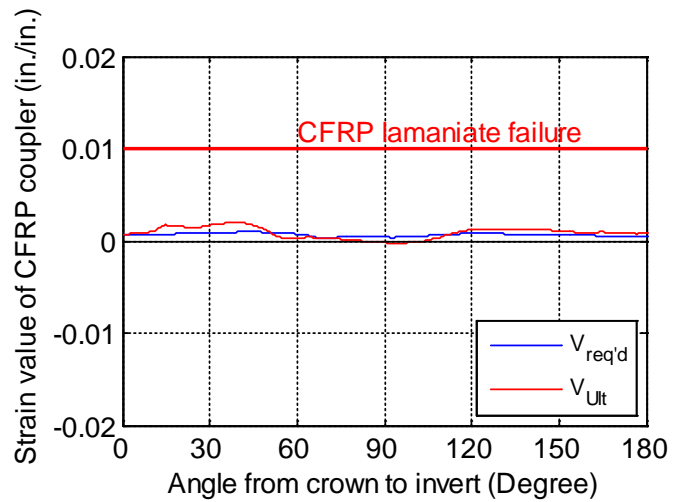
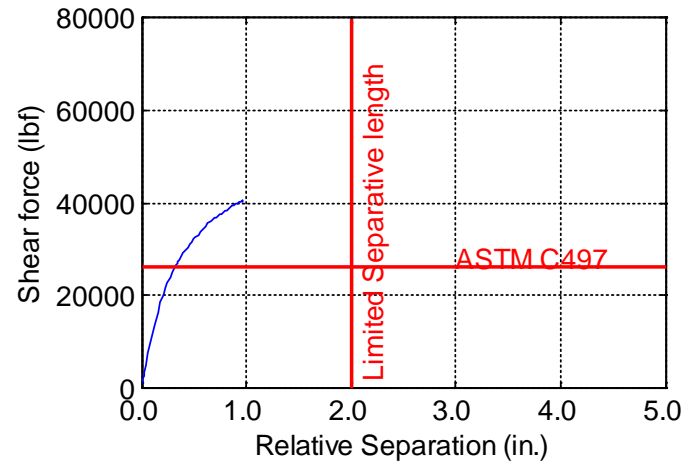
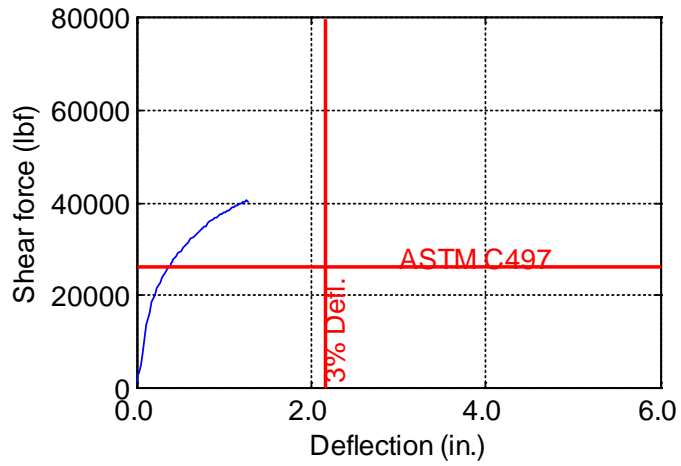


Figure B-125. TW-072-09-0.875

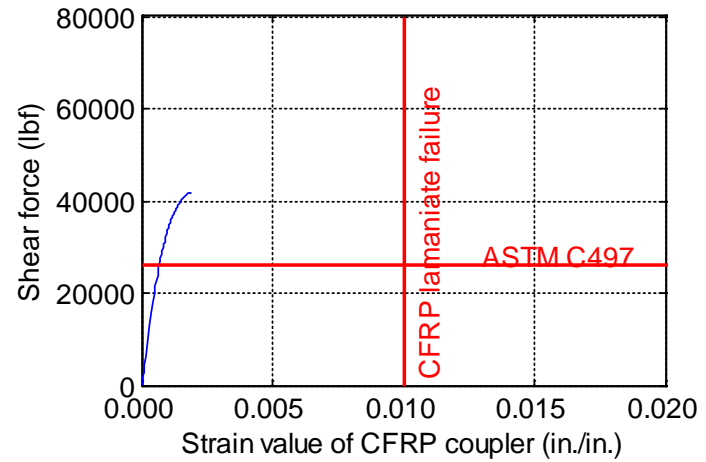
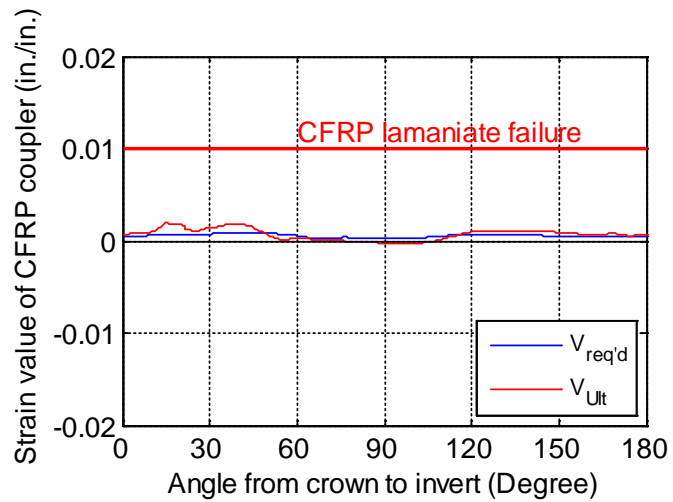
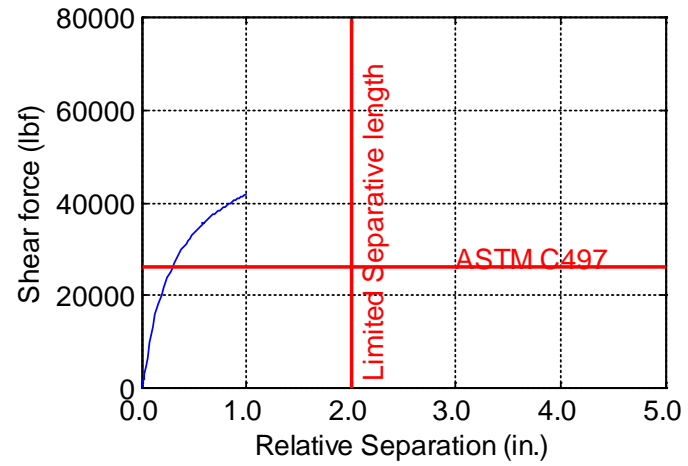
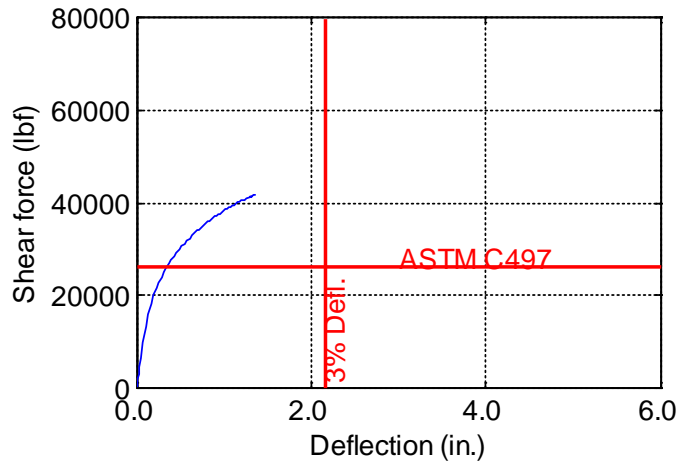


Figure B-126. TW-072-09-1.0

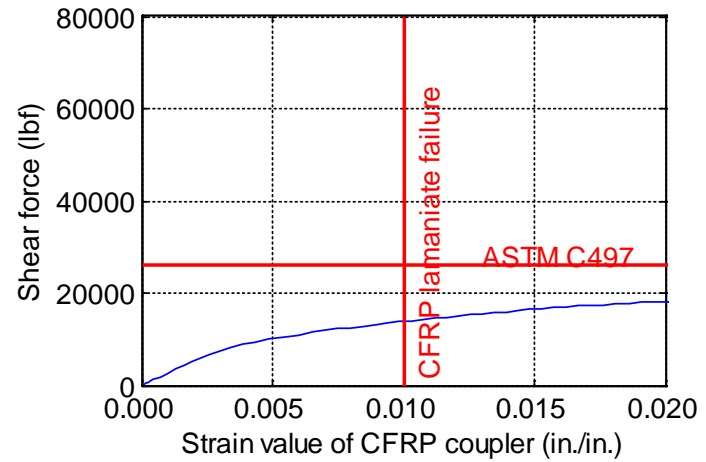
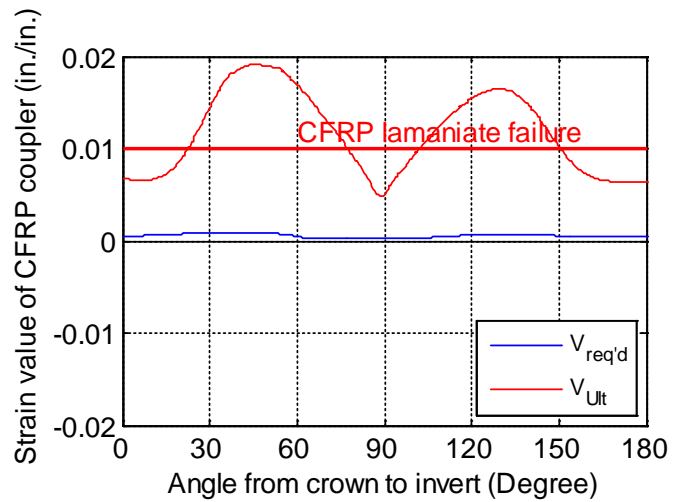
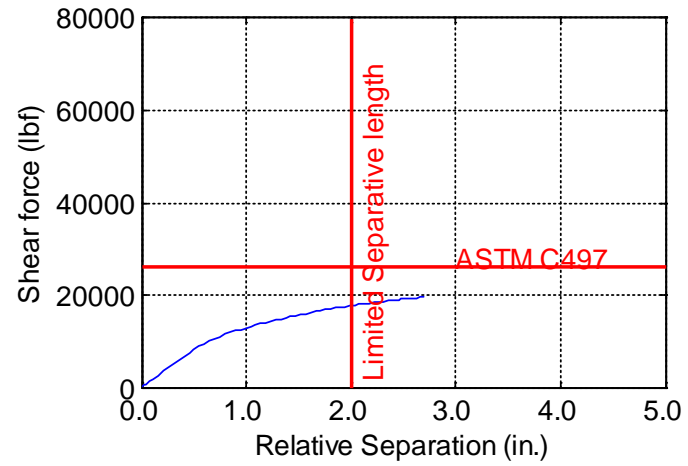
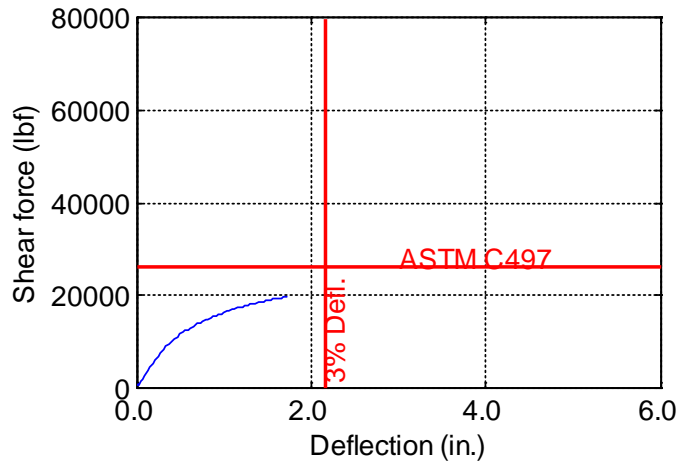


Figure B-127. TW-072-12-0.125

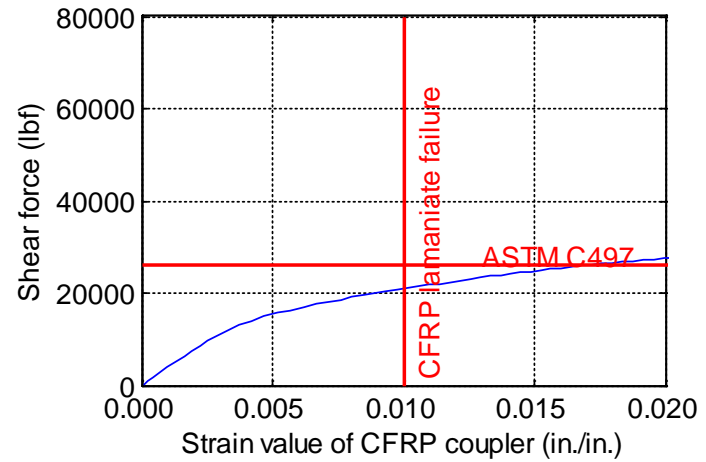
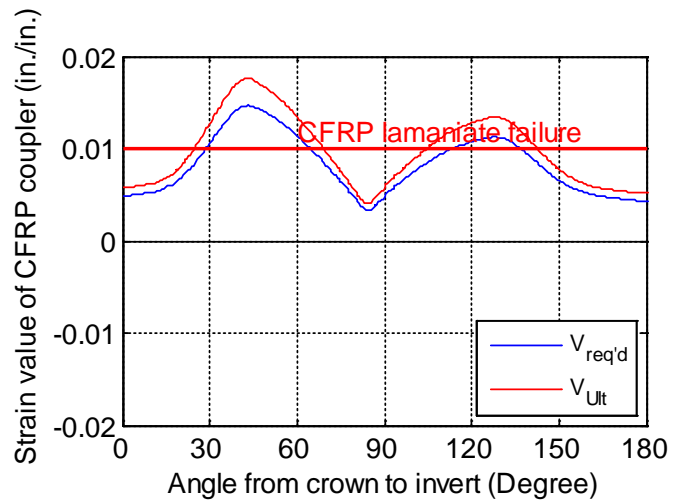
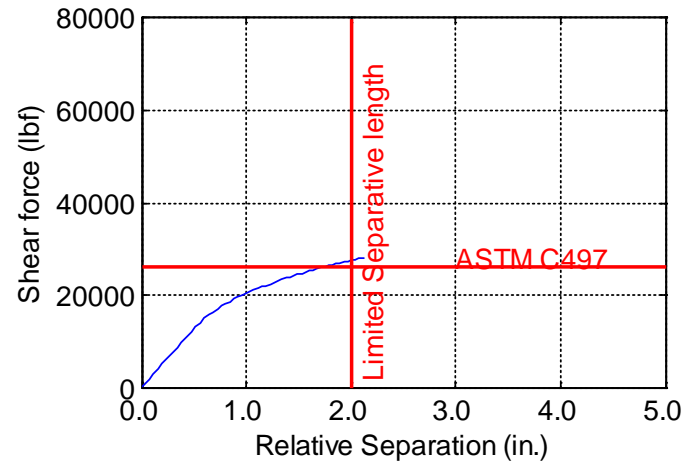
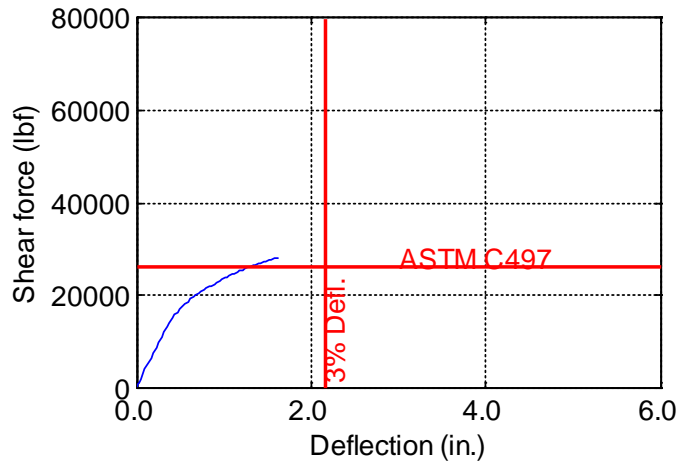


Figure B-128. TW-072-12-0.1875

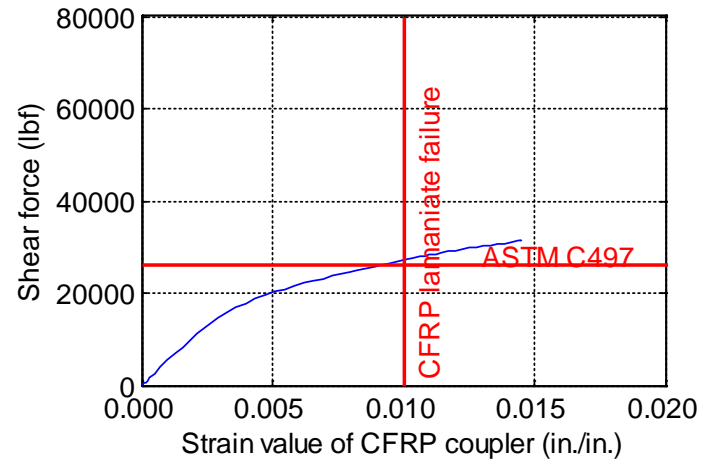
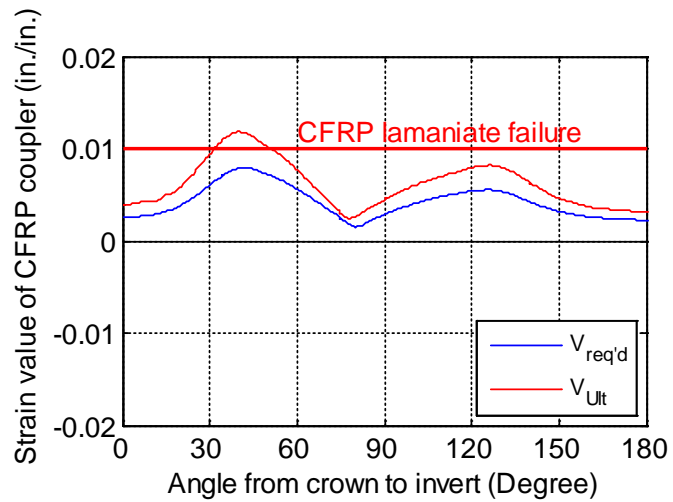
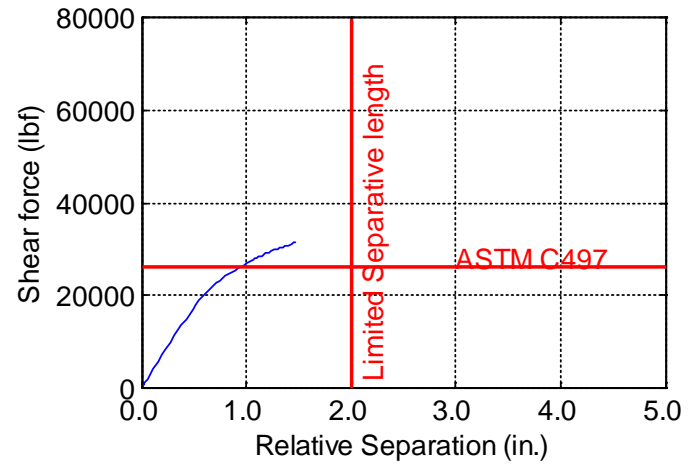
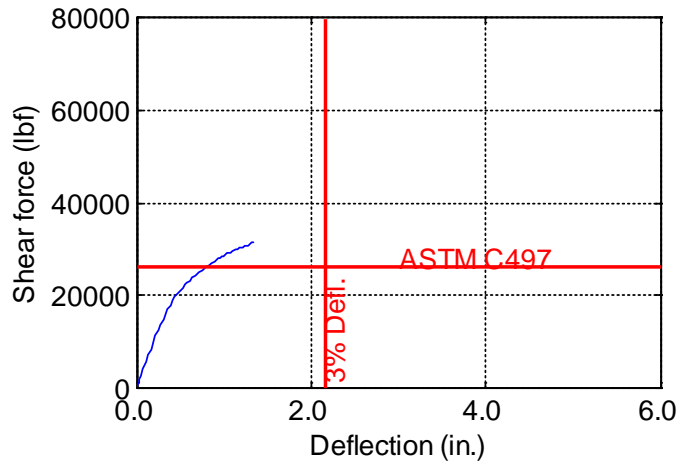


Figure B-129. TW-072-12-0.25

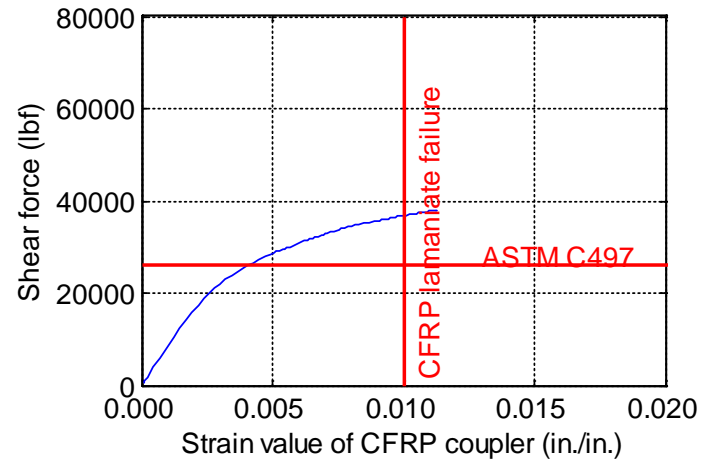
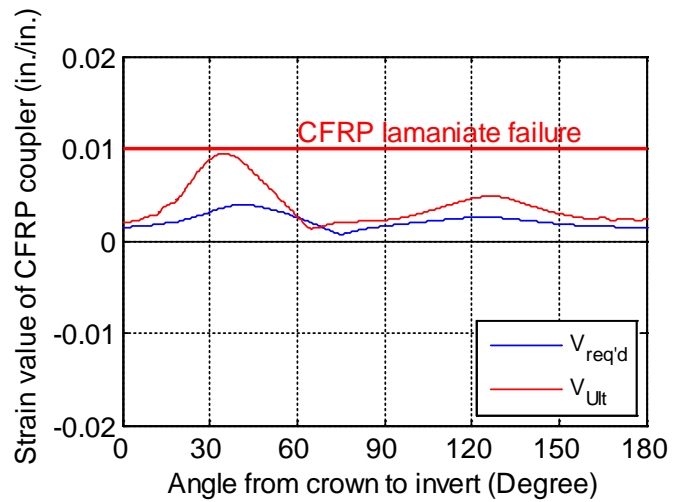
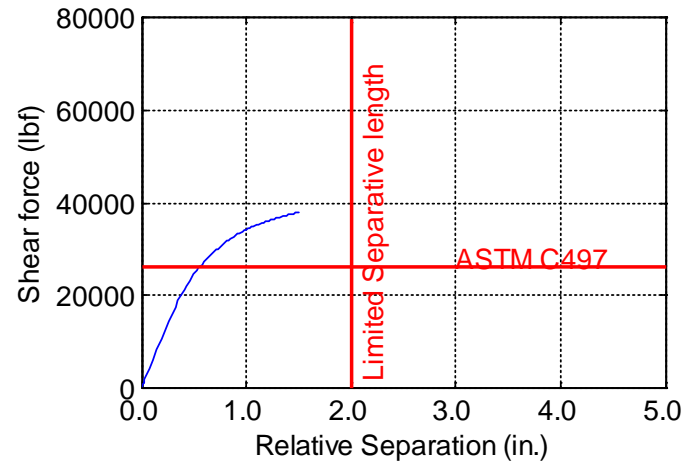
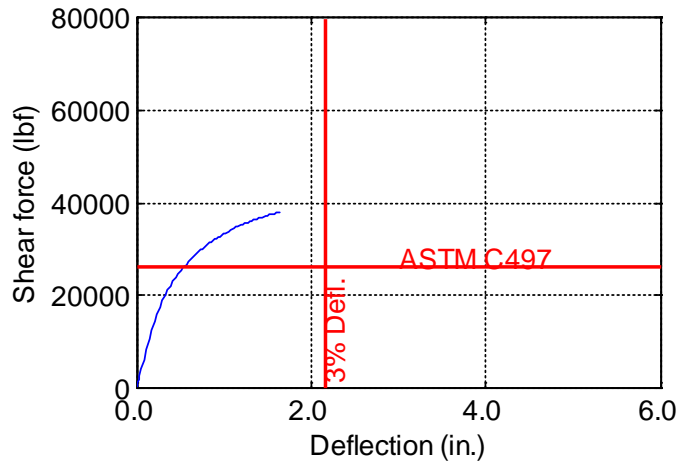


Figure B-130. TW-072-12-0.375

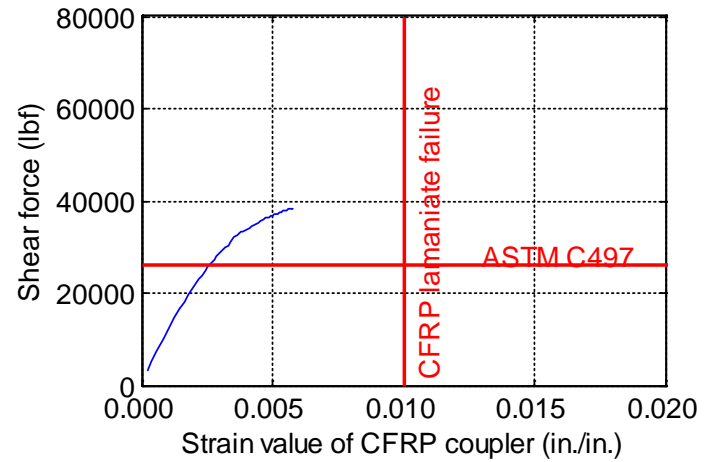
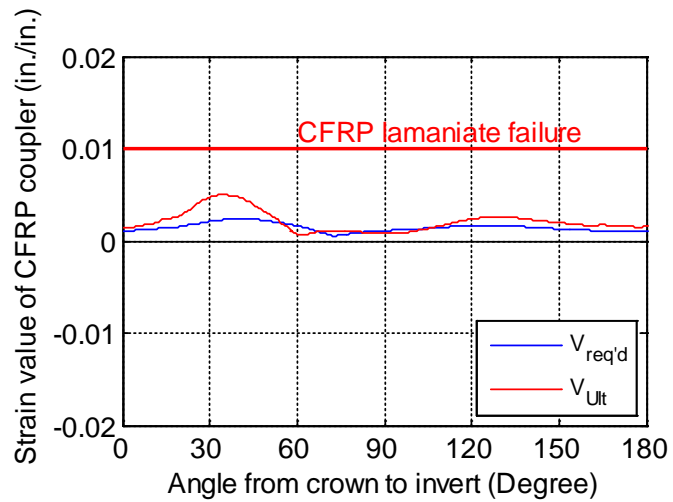
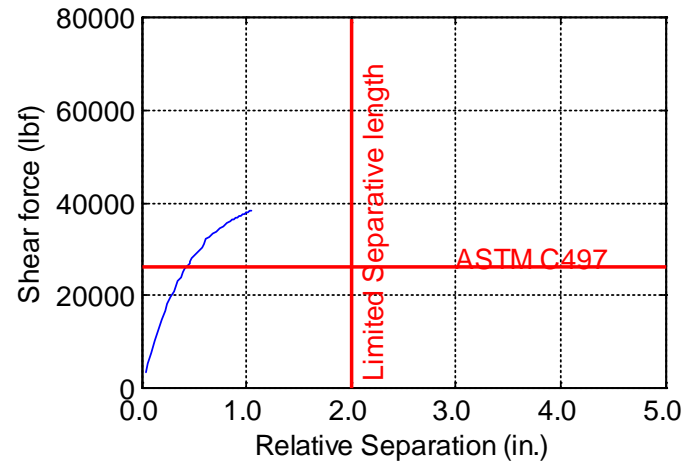
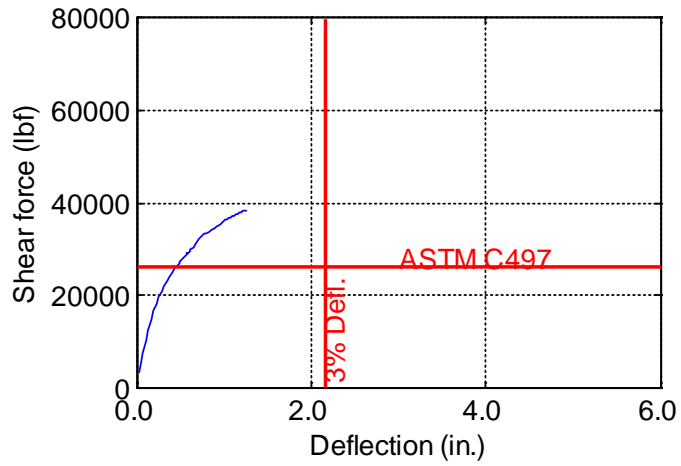


Figure B-131. TW-072-12-0.5

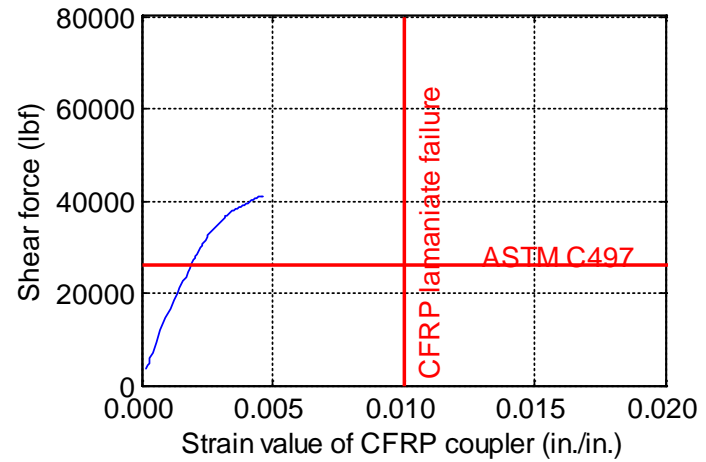
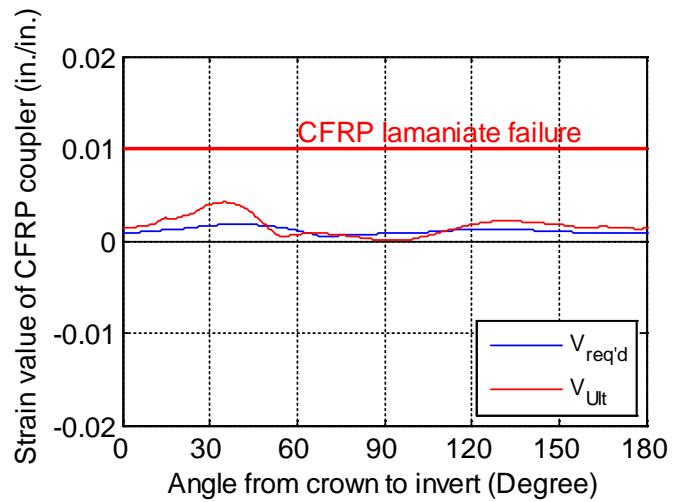
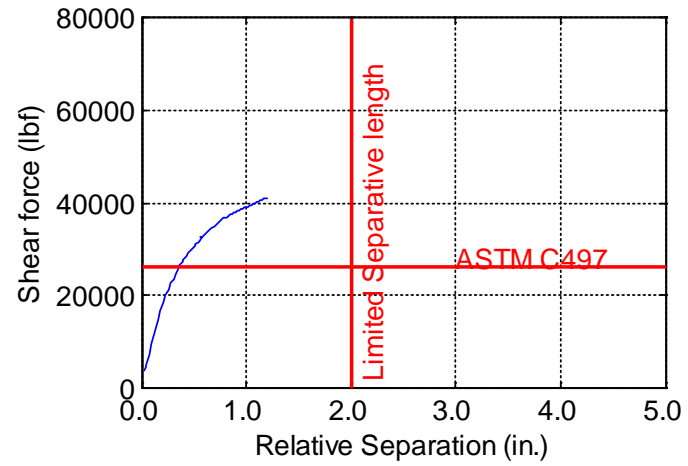
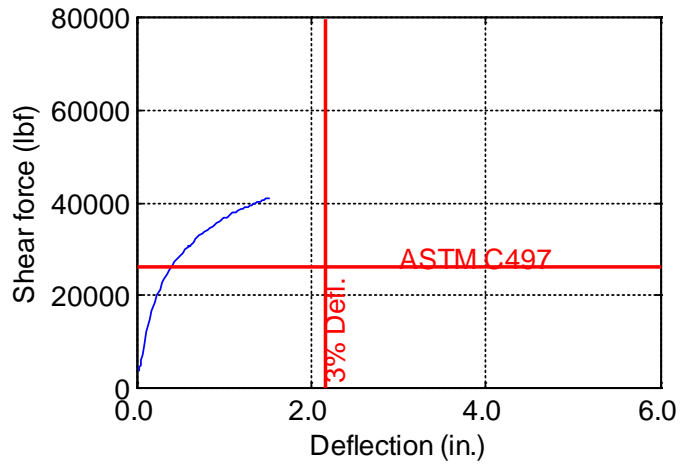


Figure B-132. TW-072-12-0.625

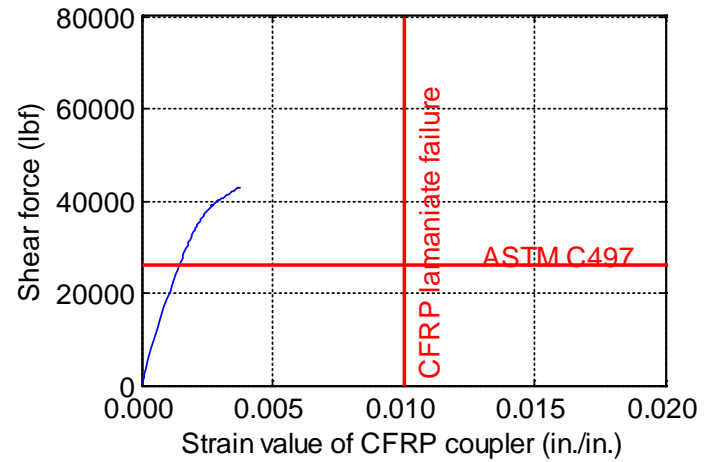
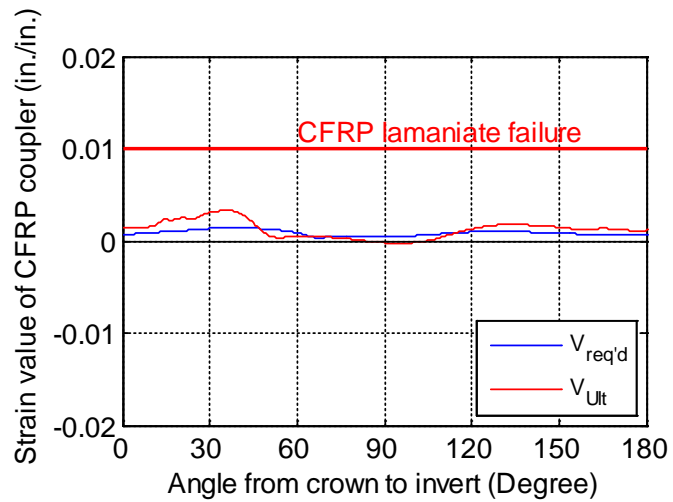
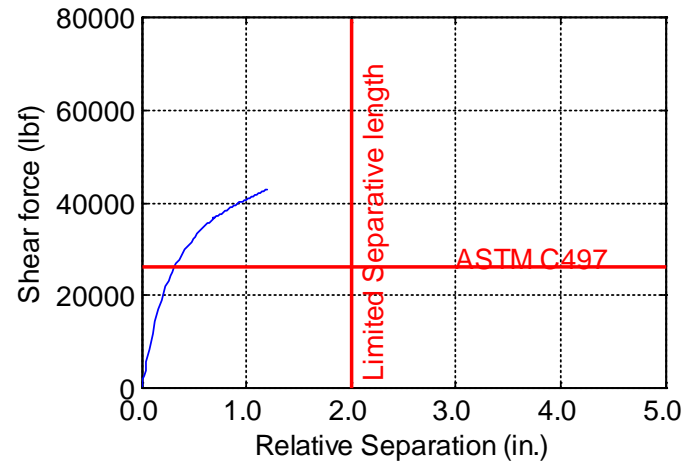
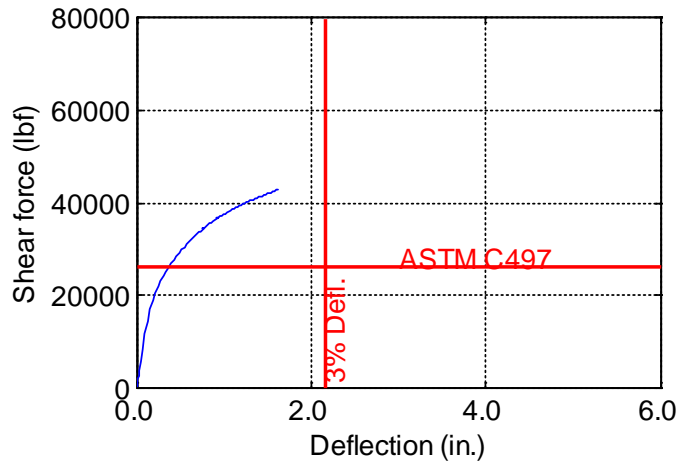


Figure B-133. TW-072-12-0.75

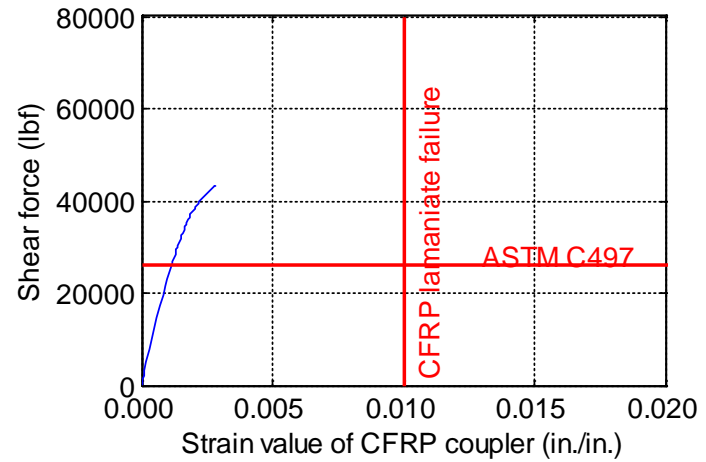
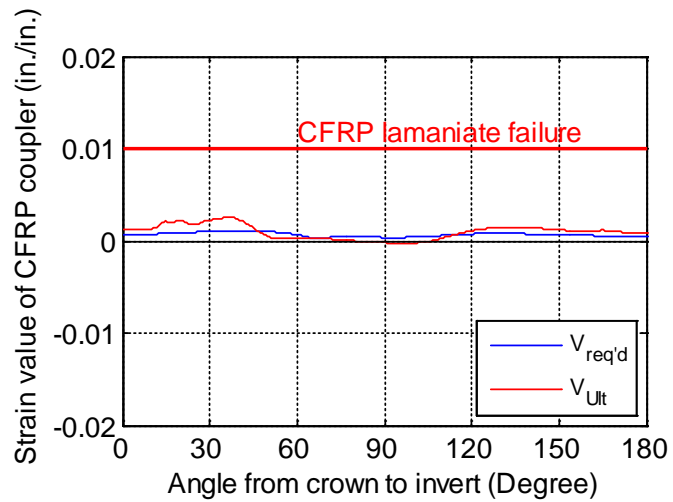
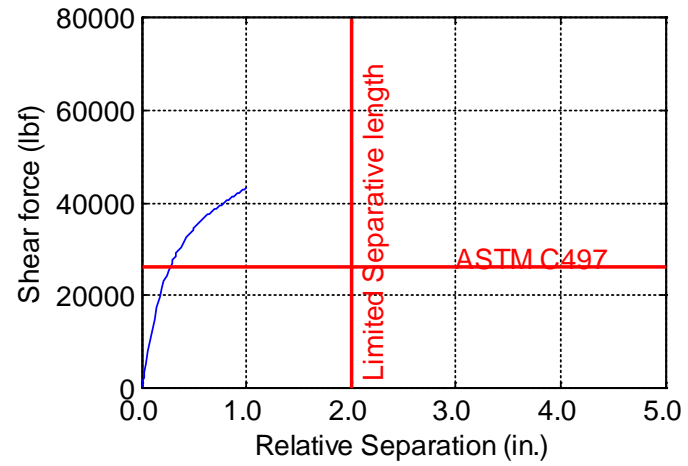
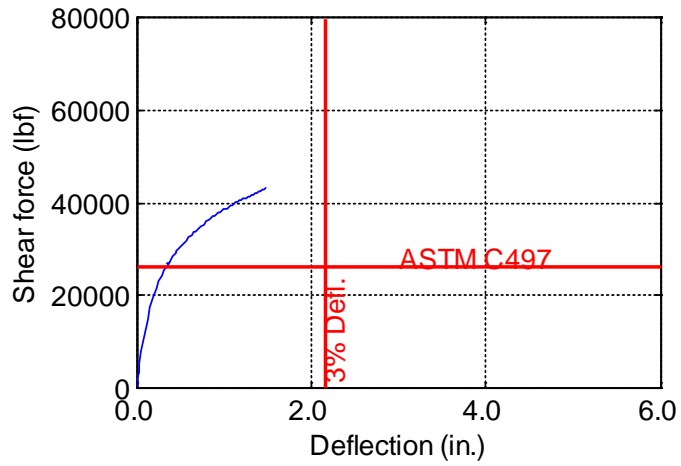


Figure B-134. TW-072-12-0.875

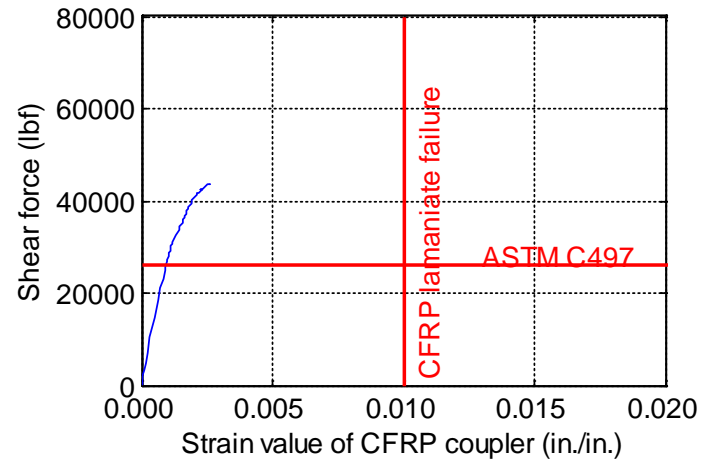
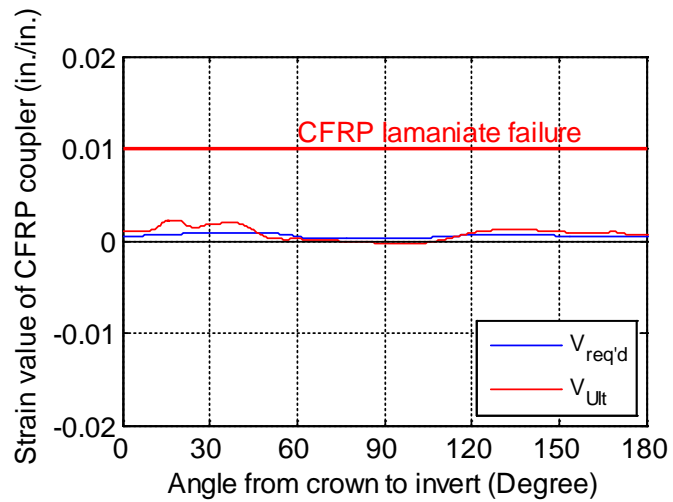
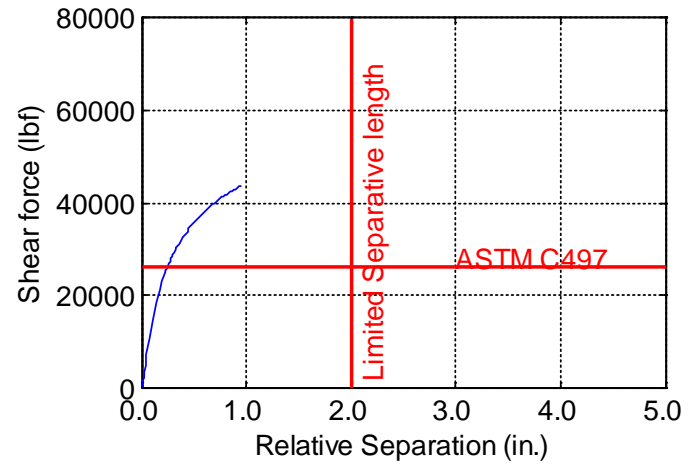
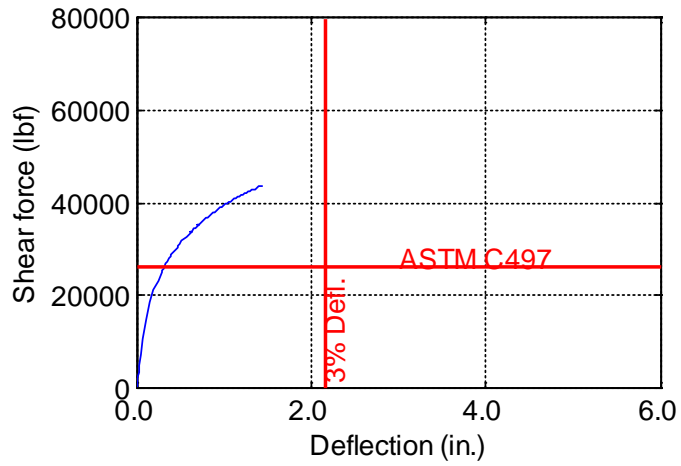


Figure B-135. TW-072-12-1.0

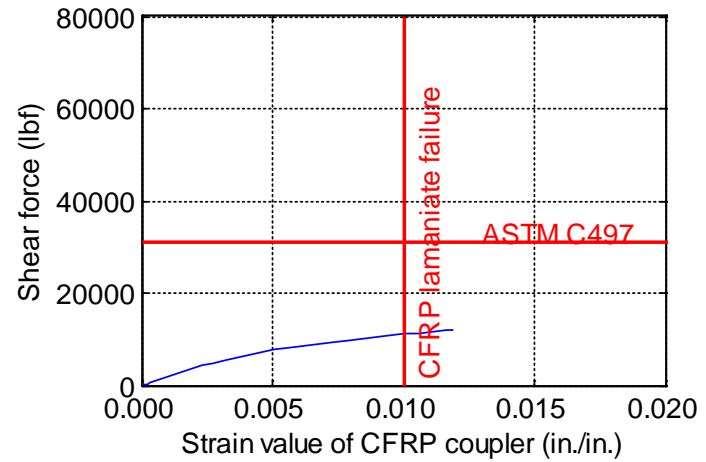
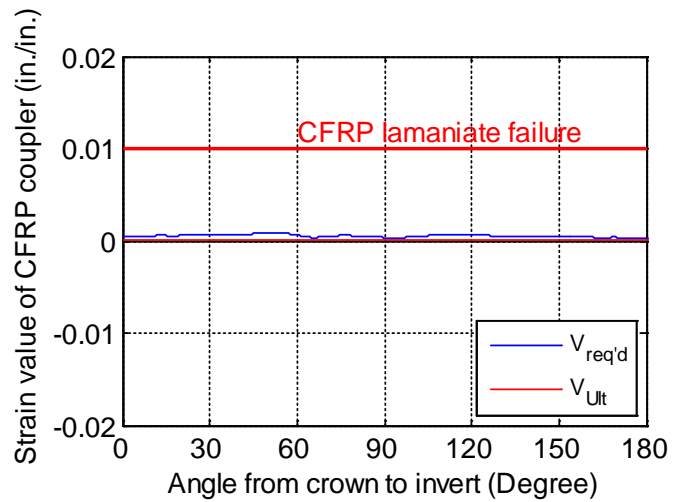
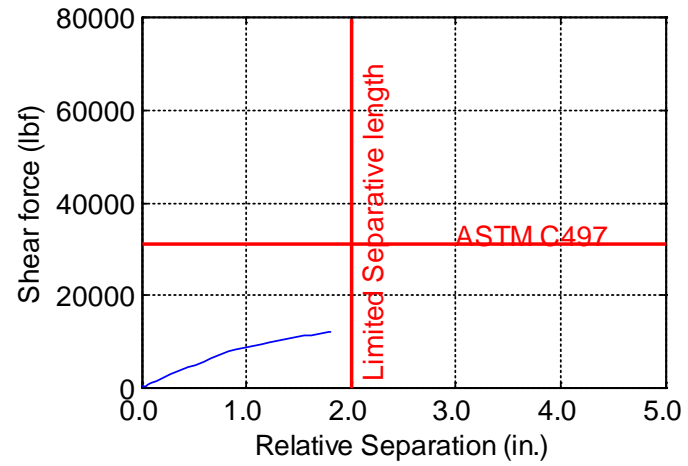
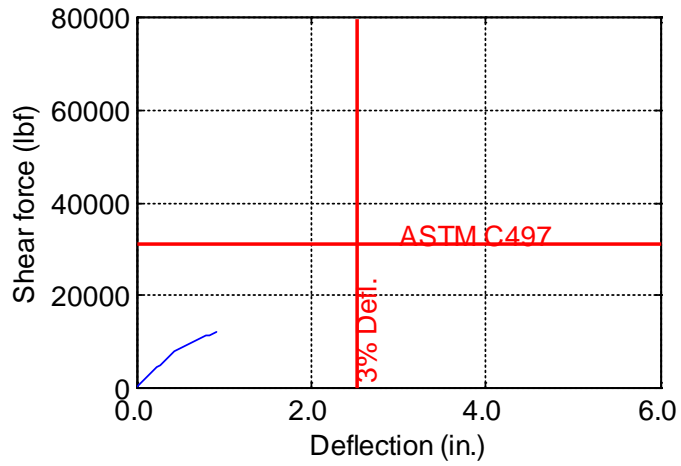


Figure B-136. TW-084-06-0.125

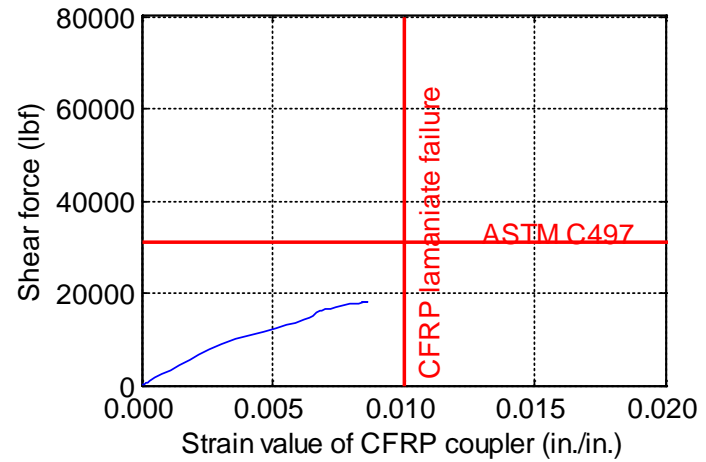
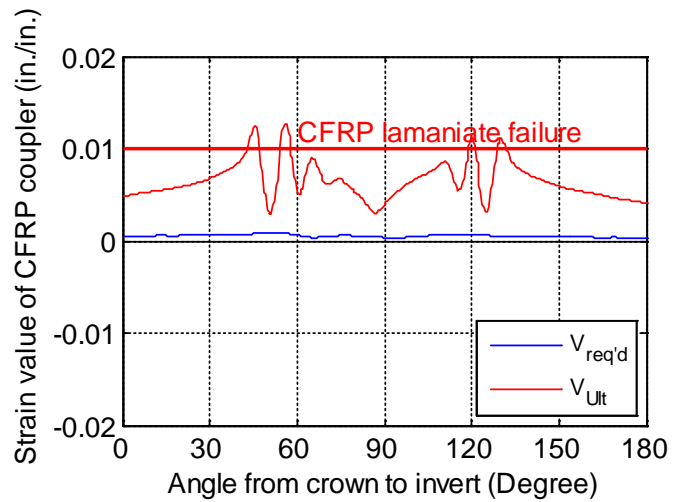
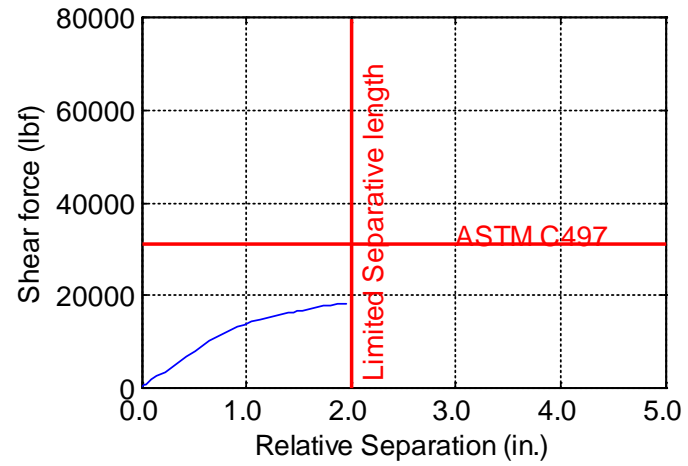
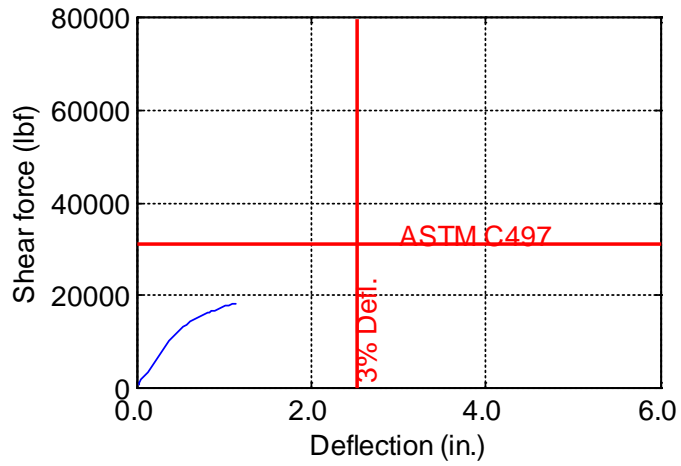


Figure B-137. TW-084-06-0.1875

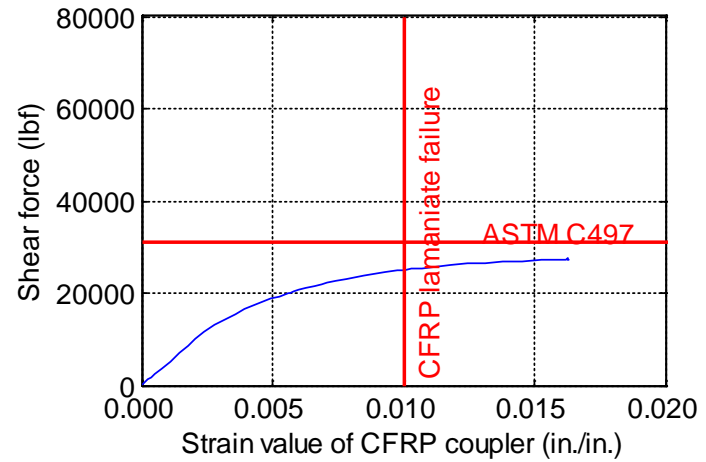
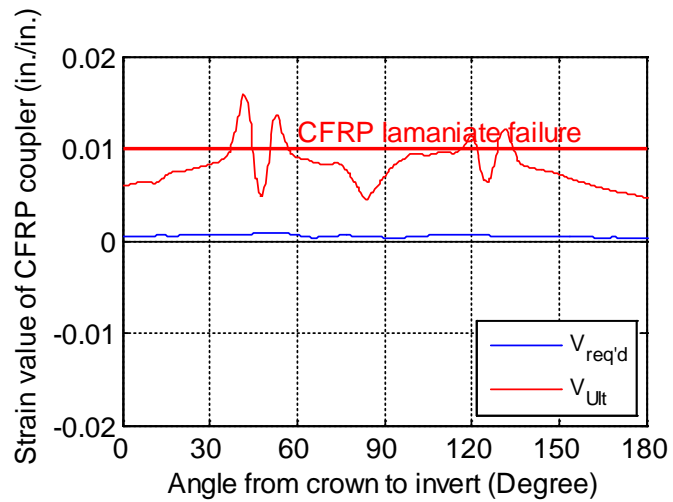
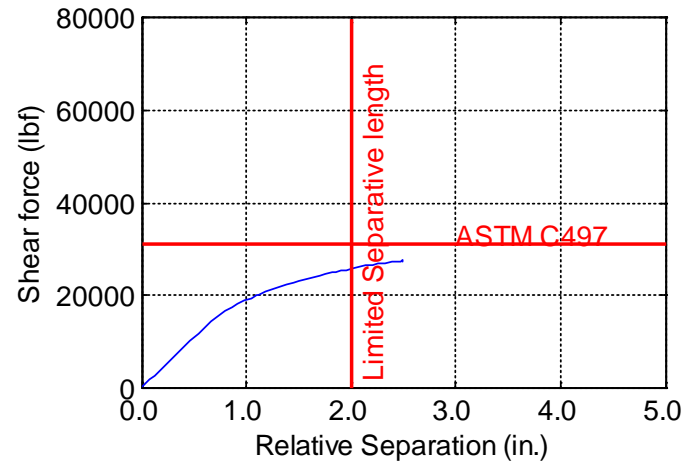
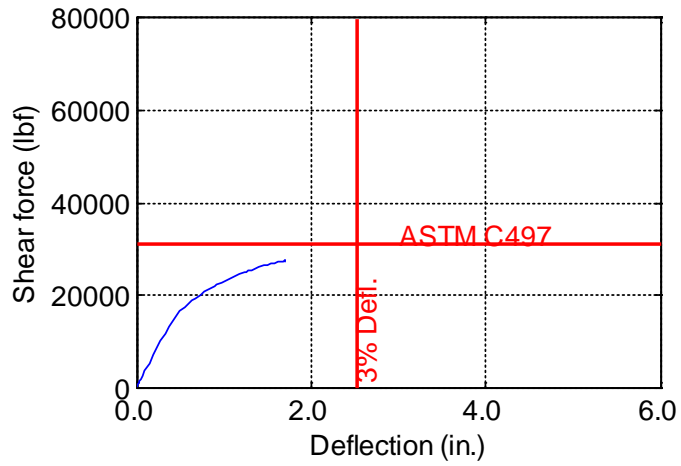


Figure B-138. TW-084-06-0.25

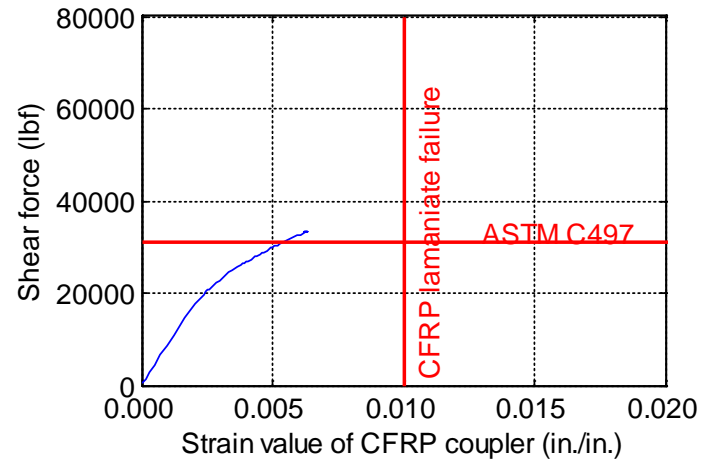
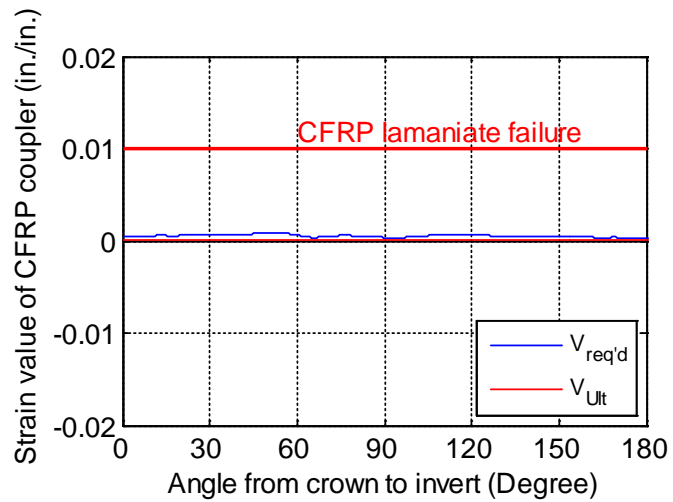
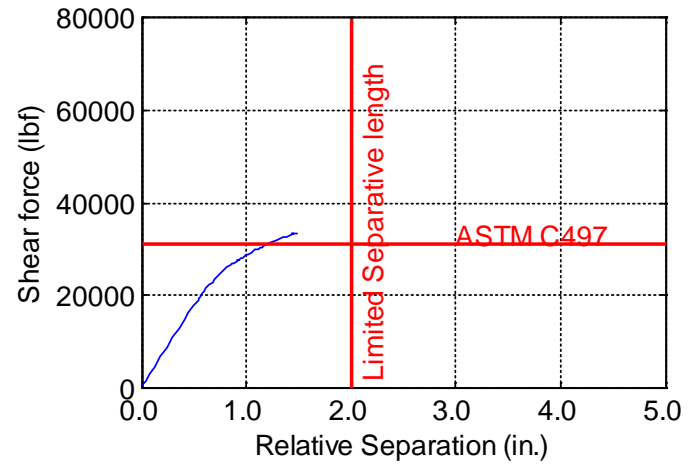
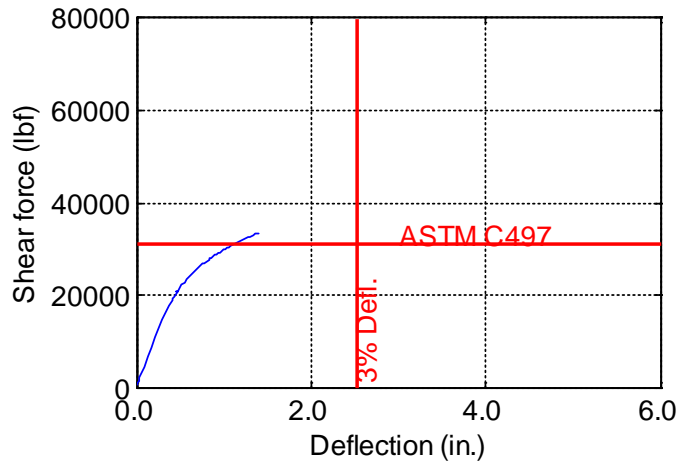


Figure B-139. TW-084-06-0.375

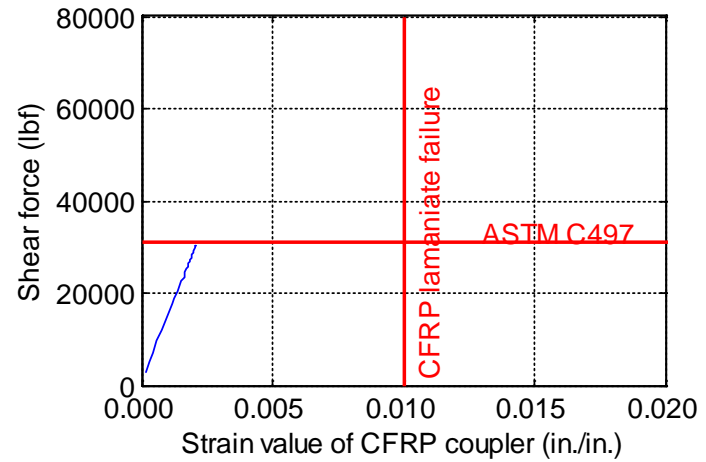
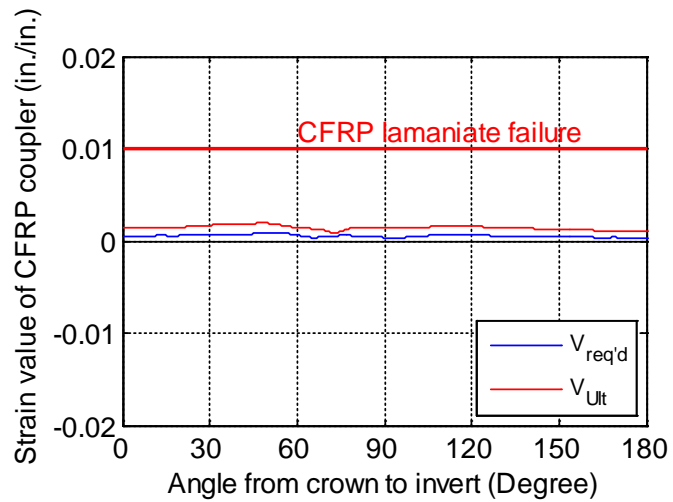
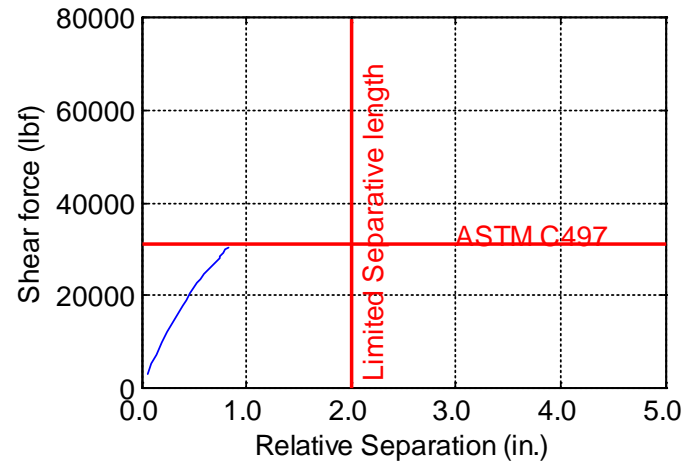
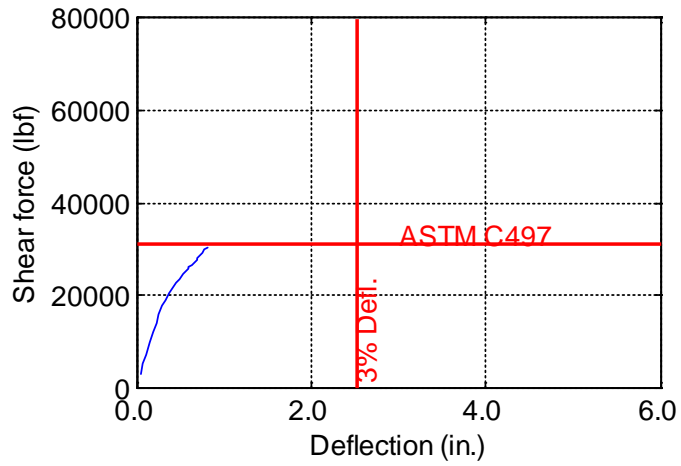


Figure B-140. TW-084-06-0.5

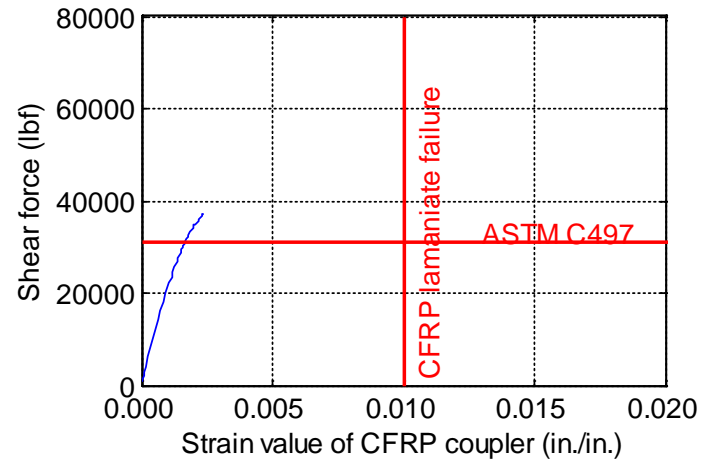
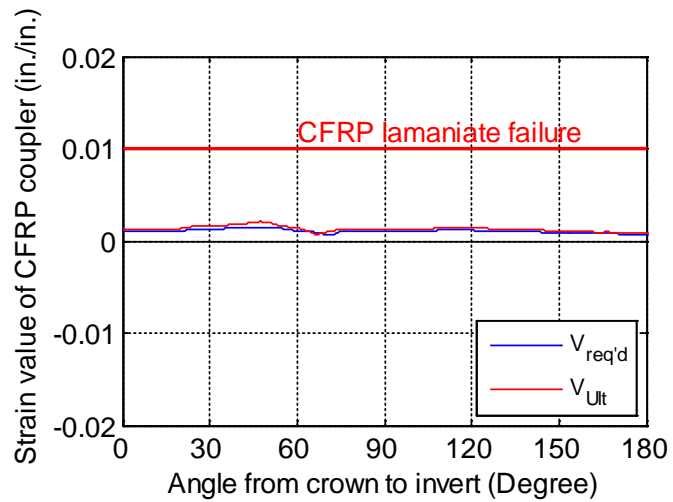
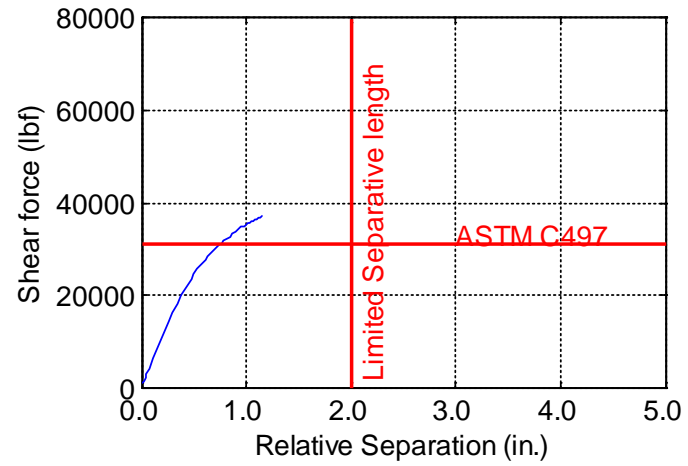
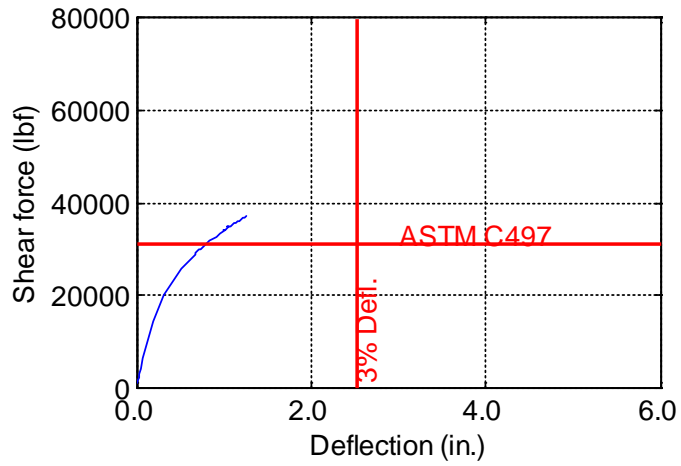


Figure B-141. TW-084-06-0.625

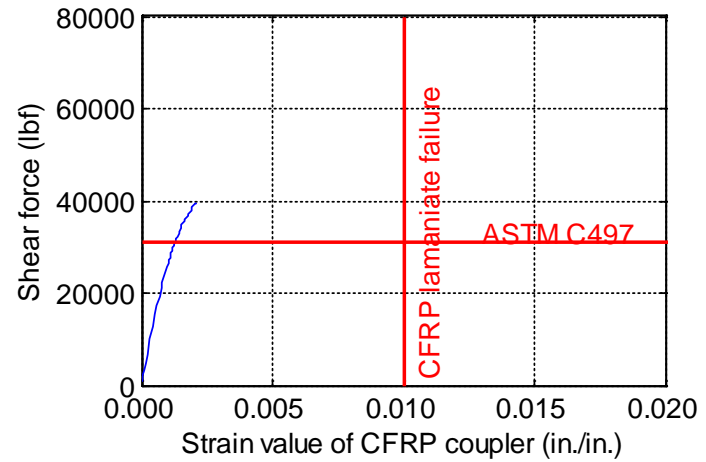
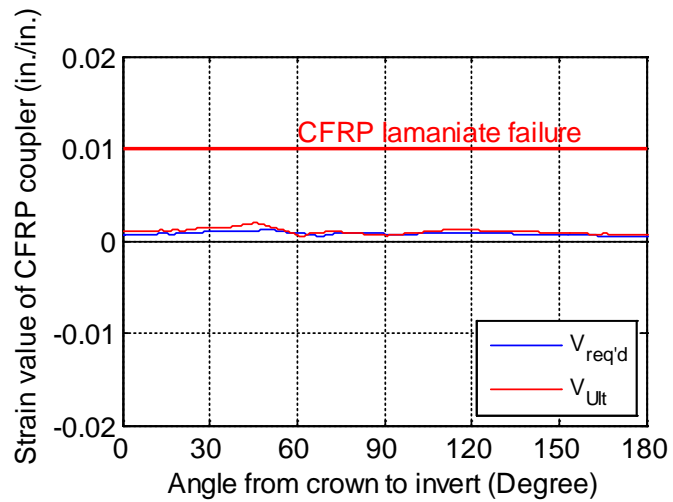
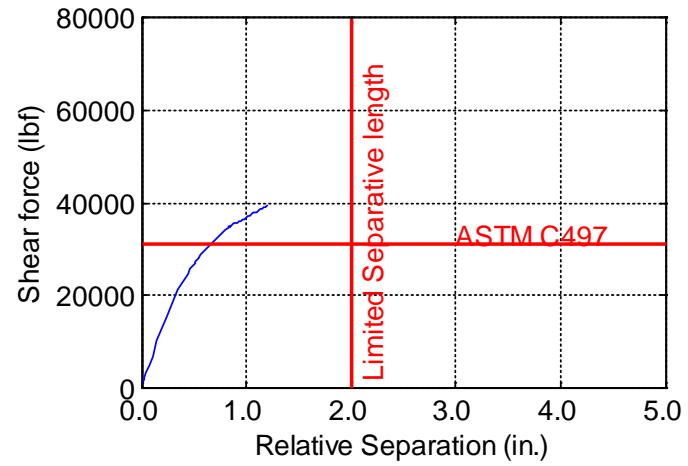
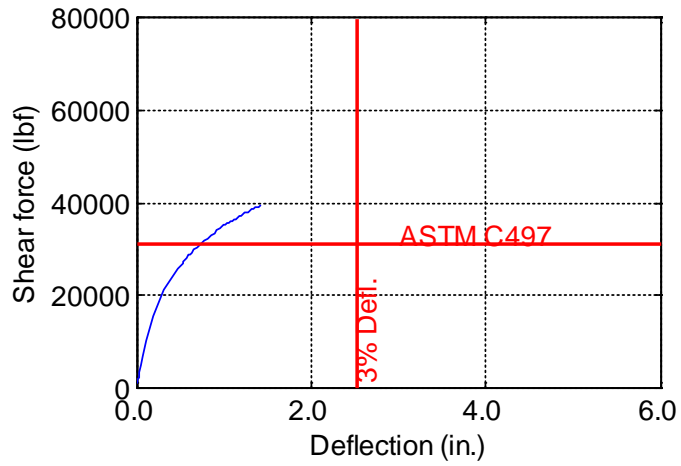


Figure B-142. TW-084-06-0.75

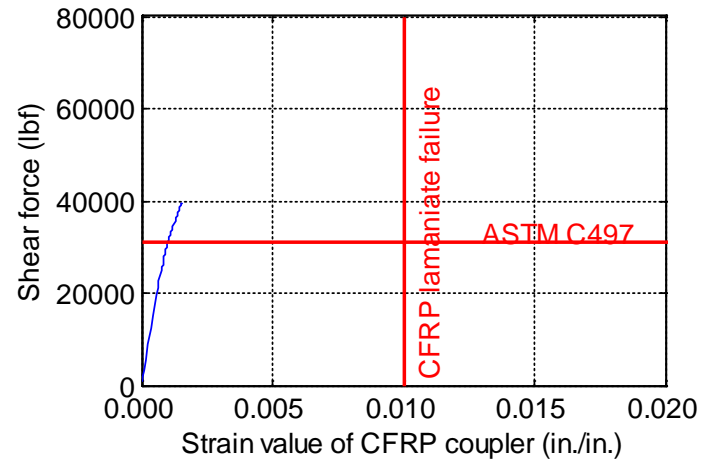
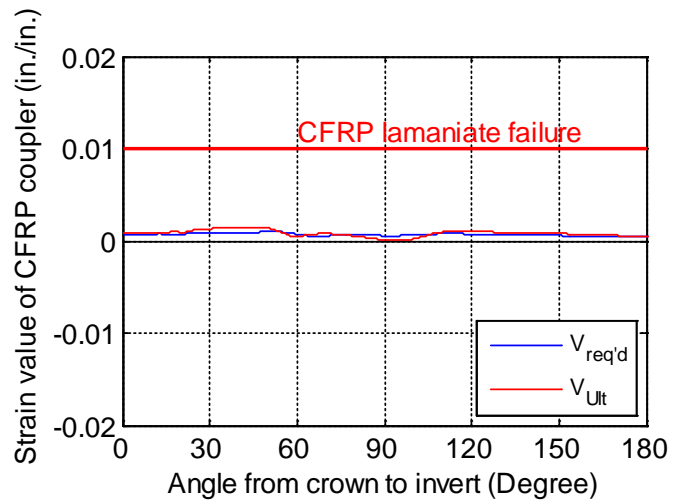
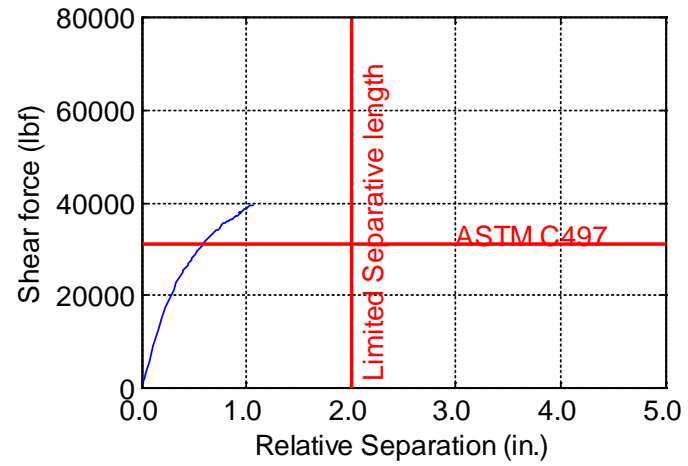
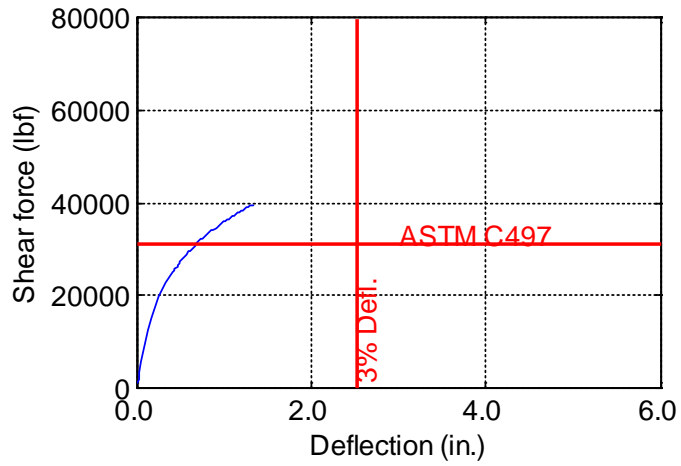


Figure B-143. TW-084-06-0.875

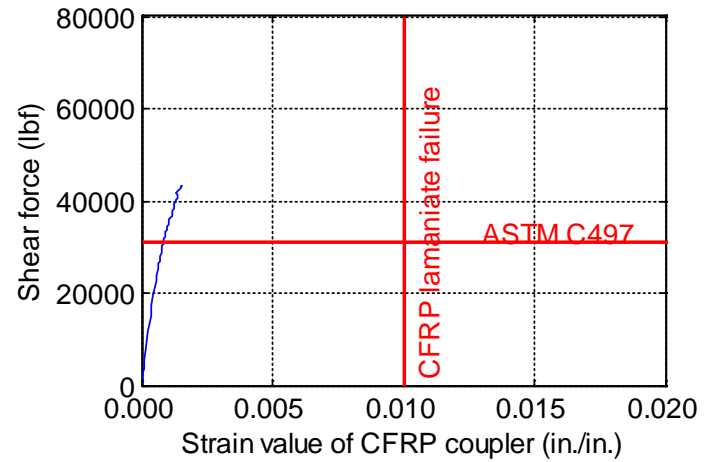
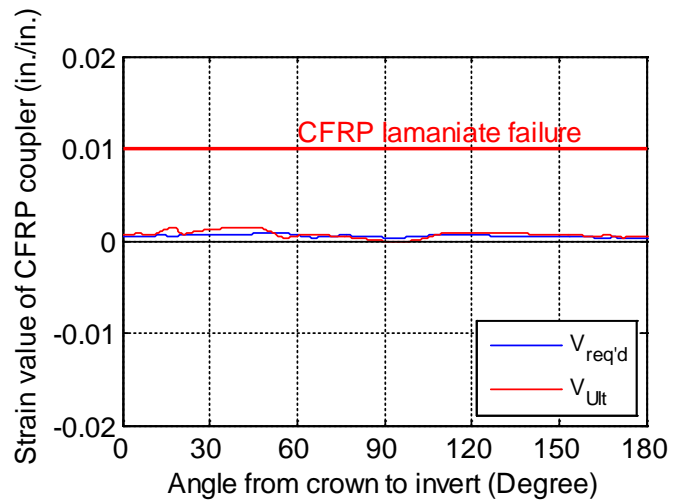
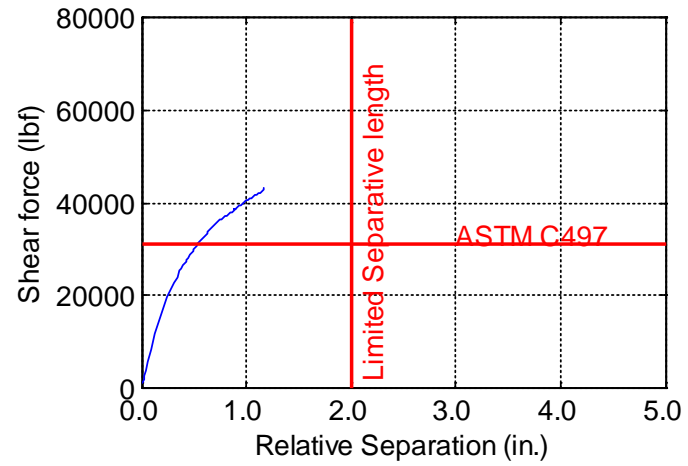
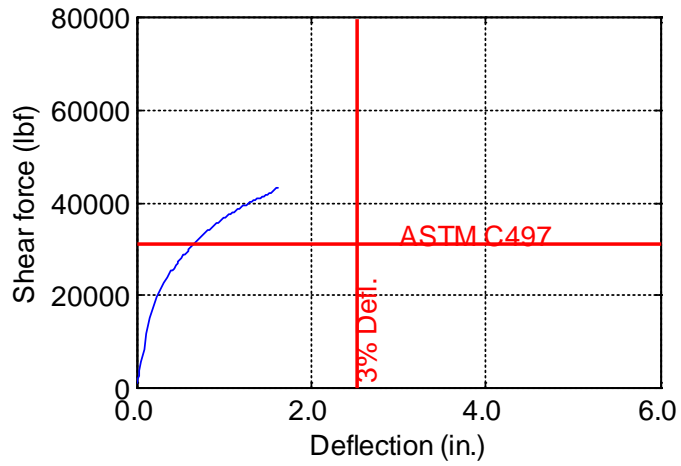


Figure B-144. TW-084-06-1.0

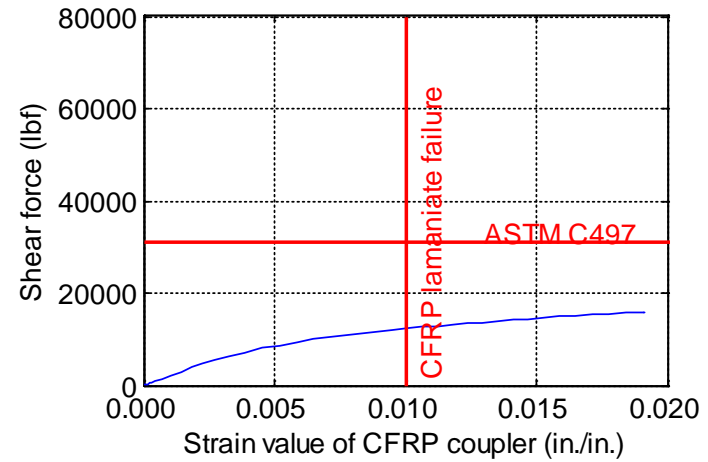
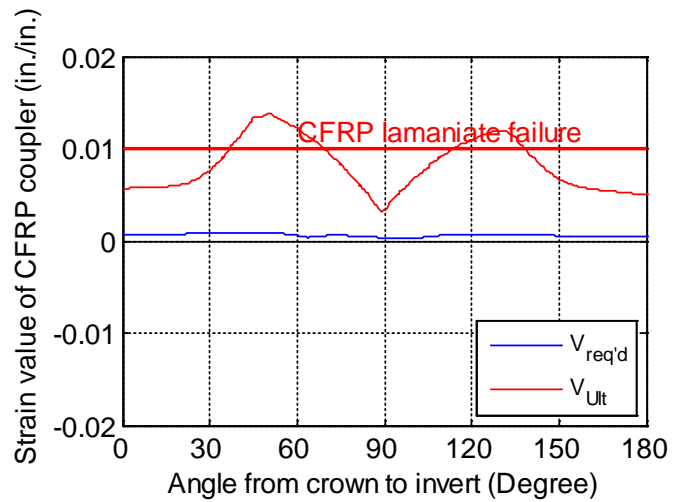
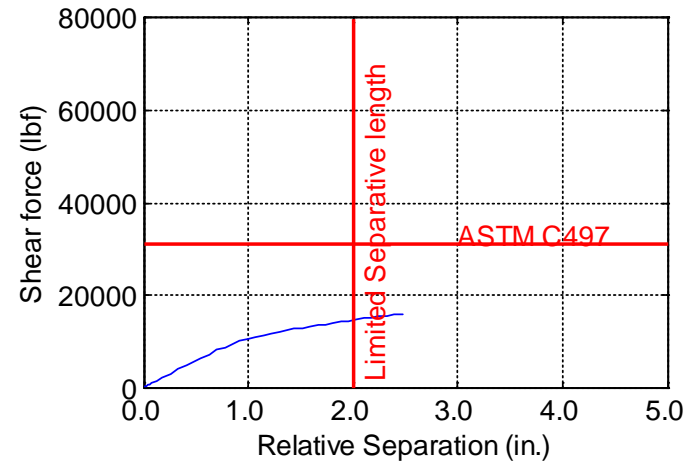
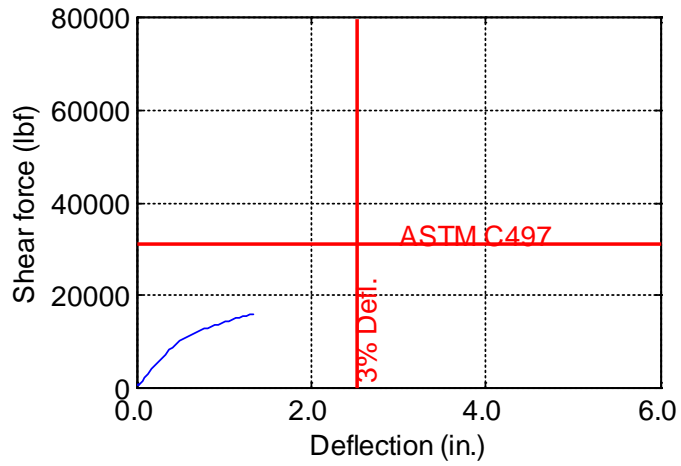


Figure B-145. TW-084-09-0.125

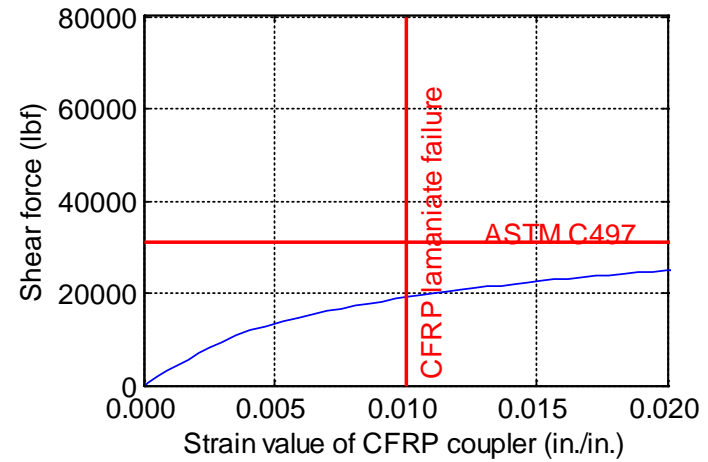
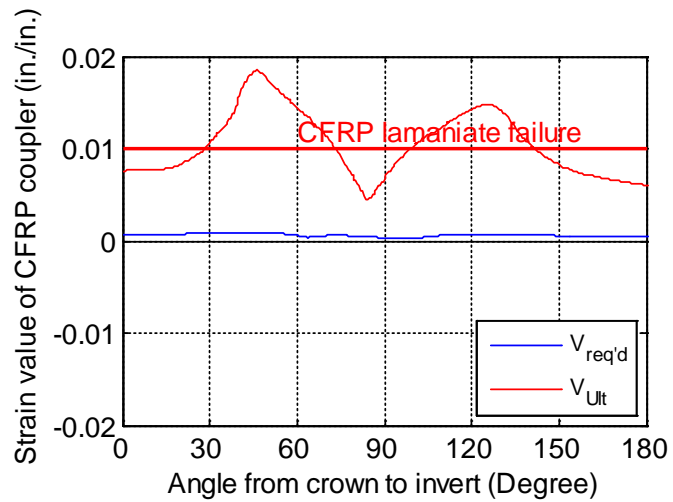
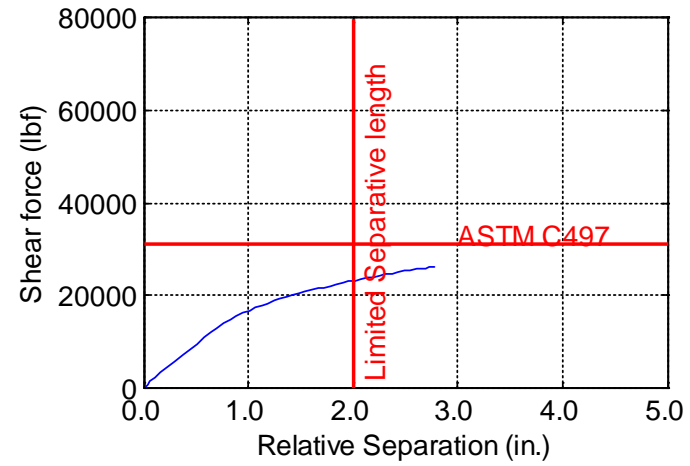
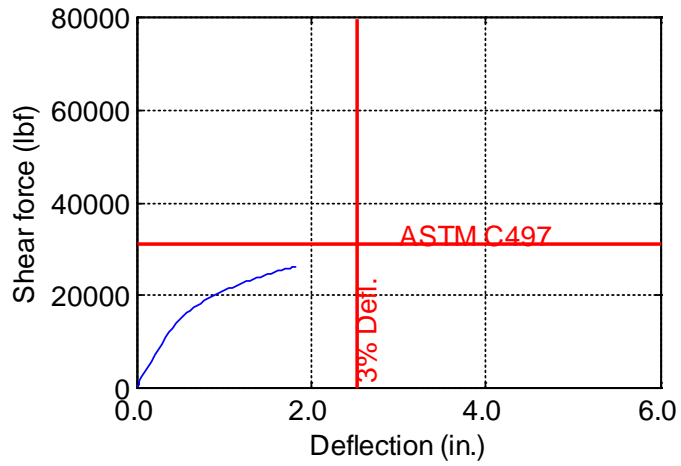


Figure B-146. TW-084-09-0.1875

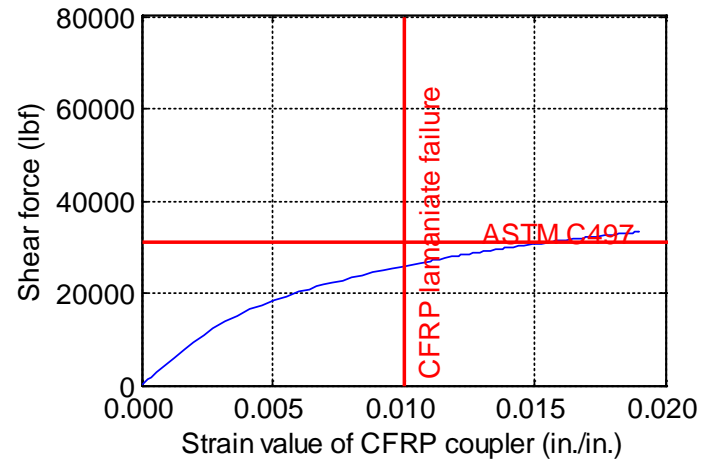
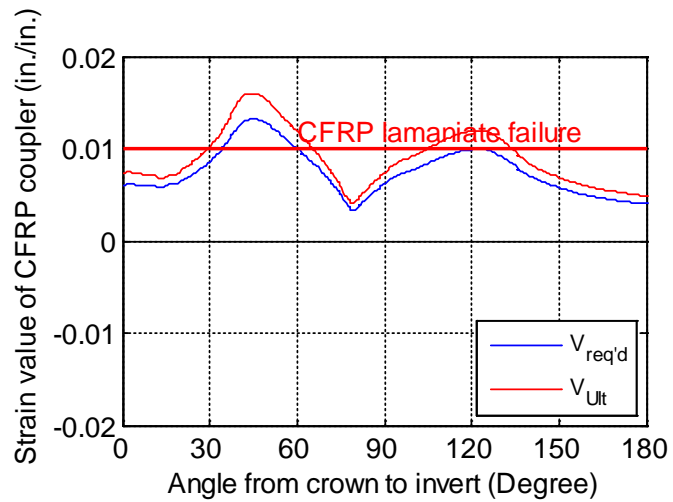
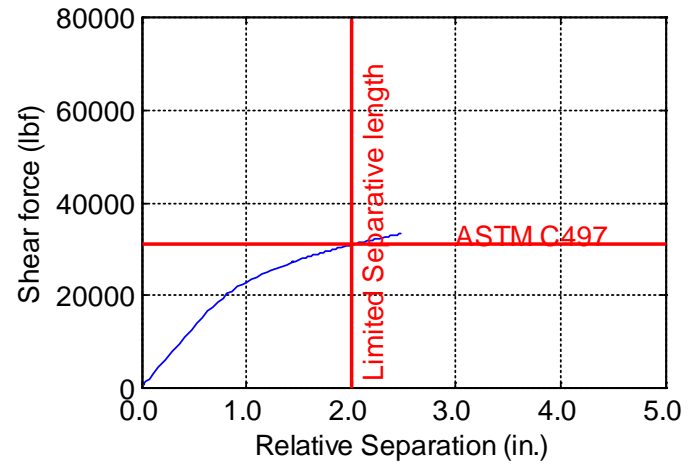
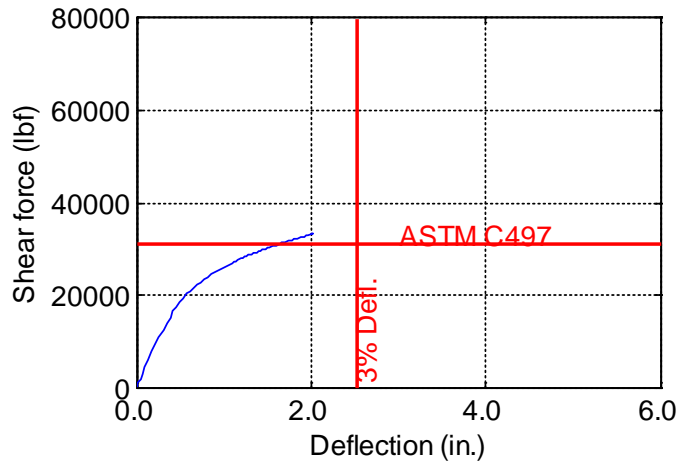


Figure B-147. TW-084-09-0.25

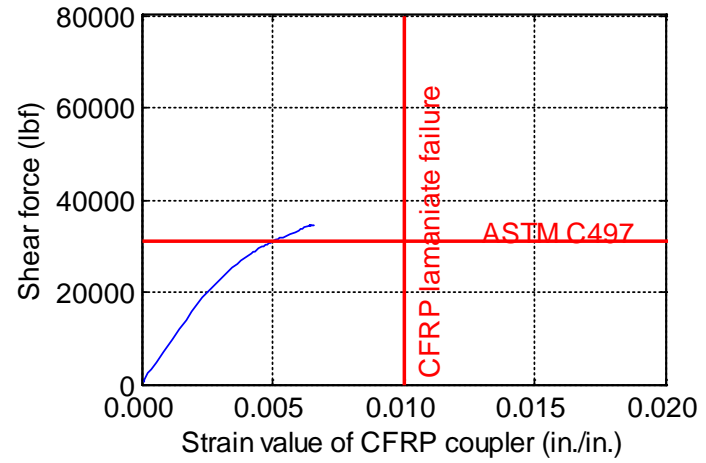
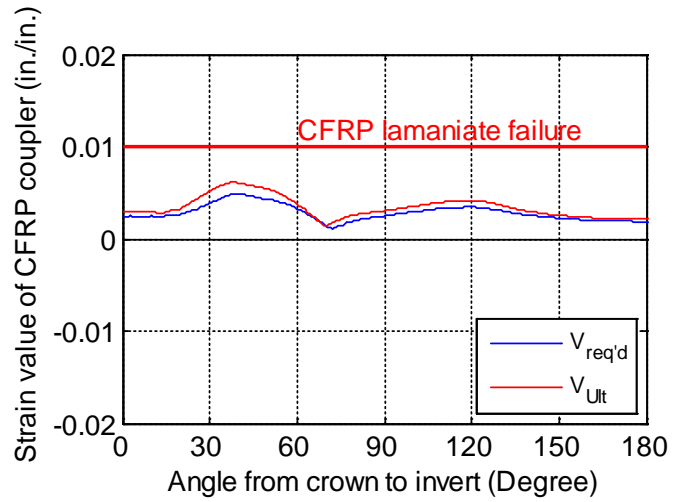
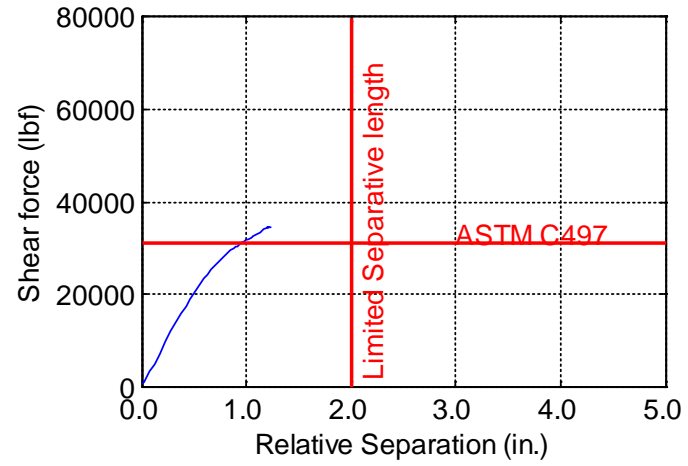
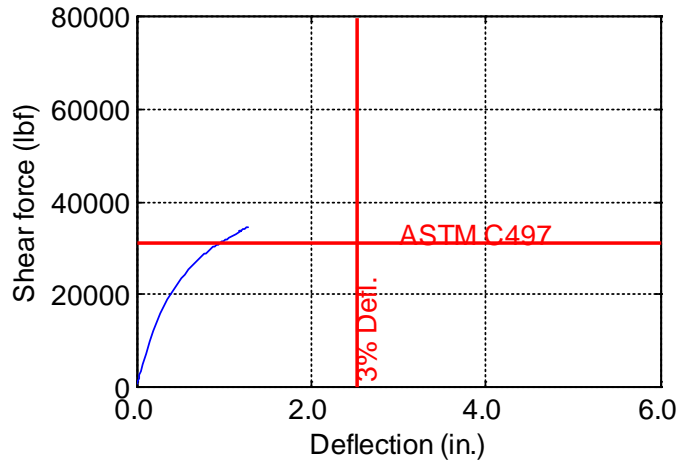


Figure B-148. TW-084-09-0.375

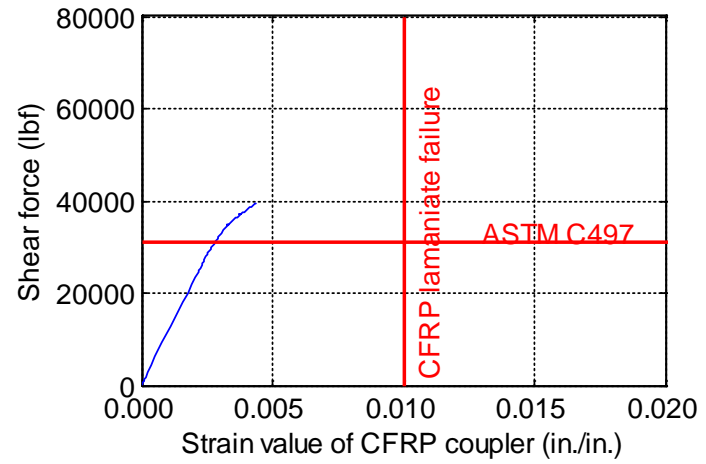
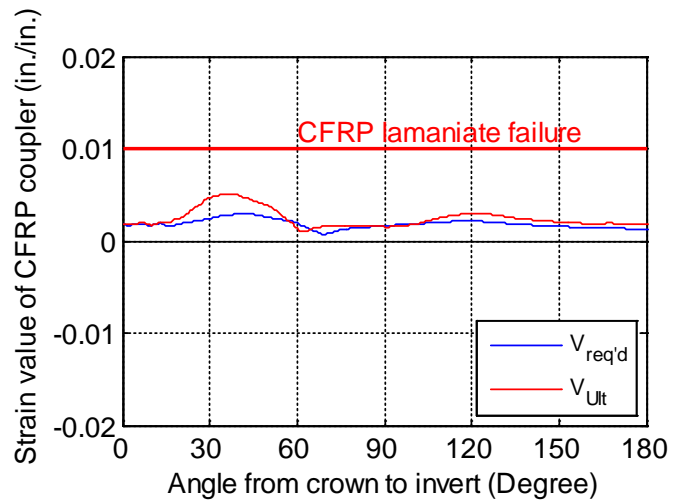
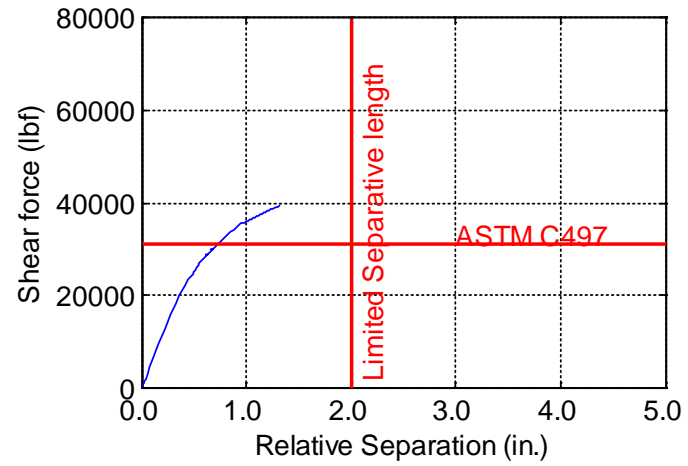
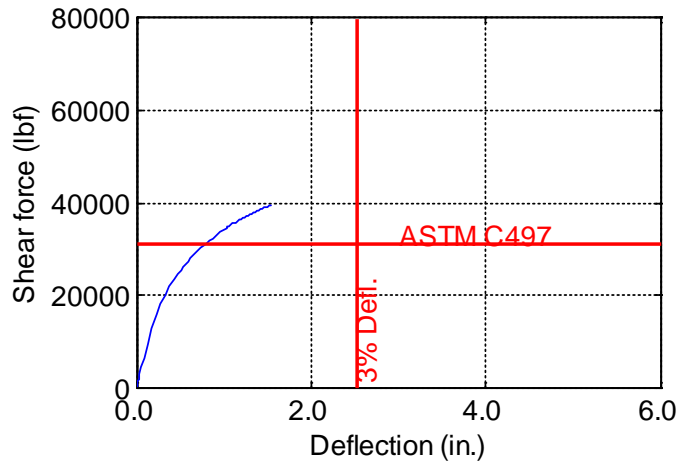


Figure B-149. TW-084-09-0.5

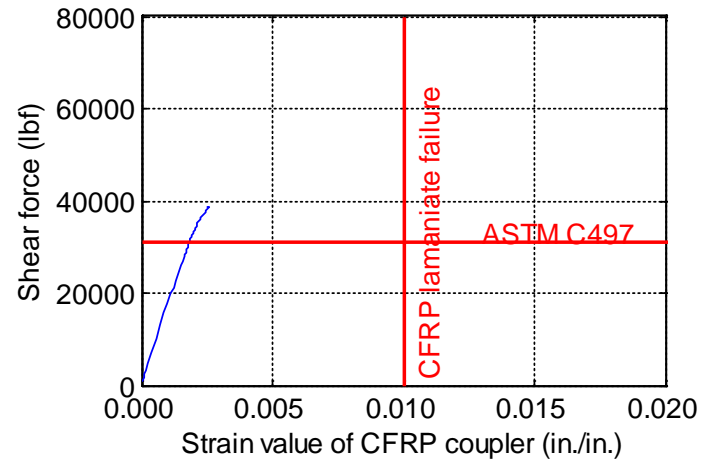
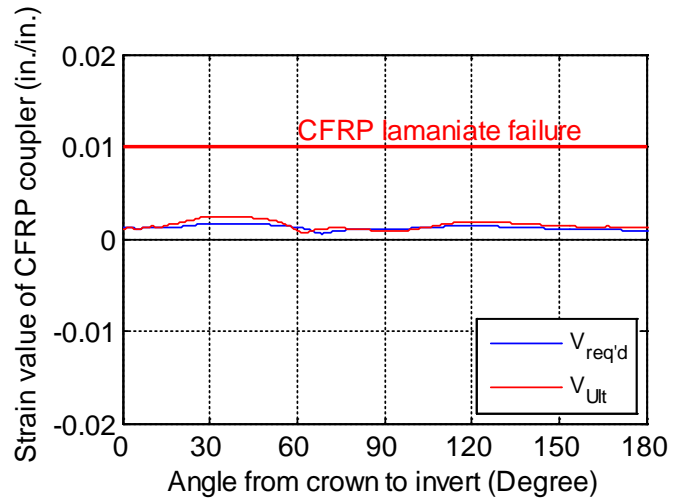
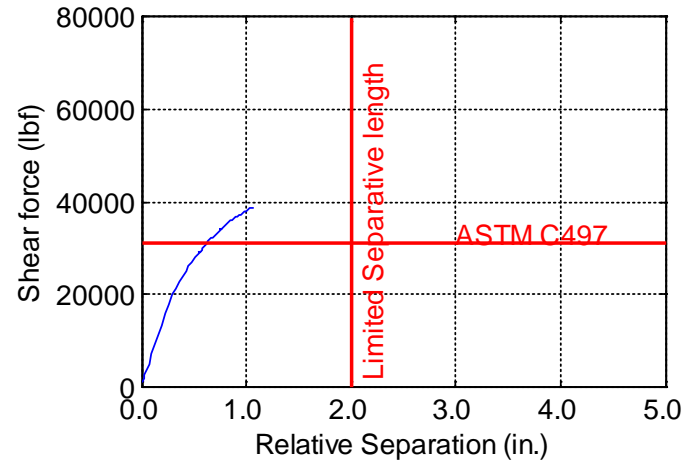
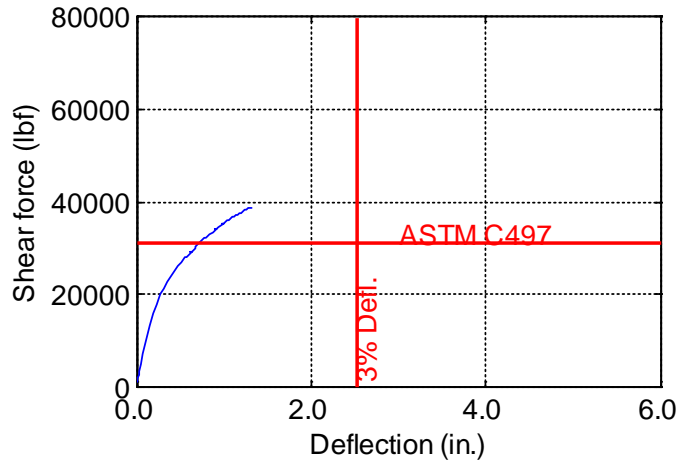


Figure B-150. TW-084-09-0.625

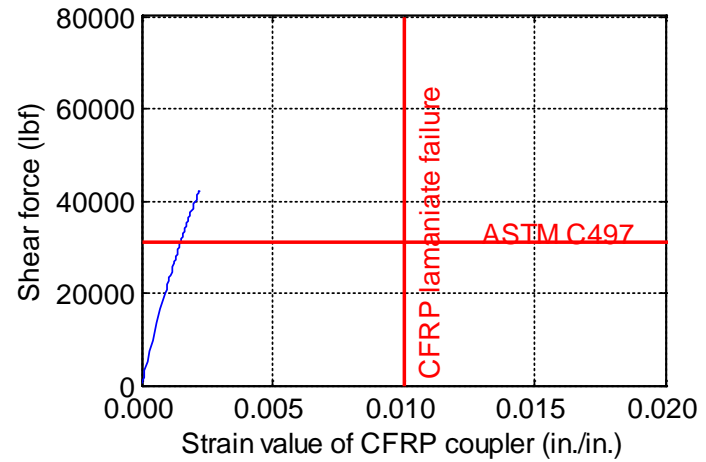
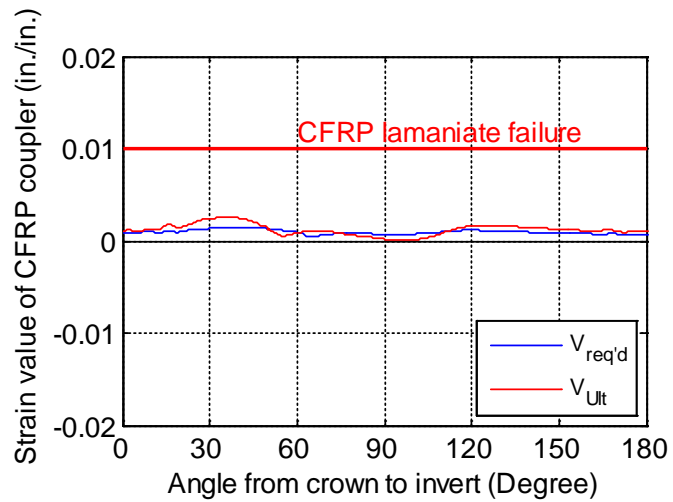
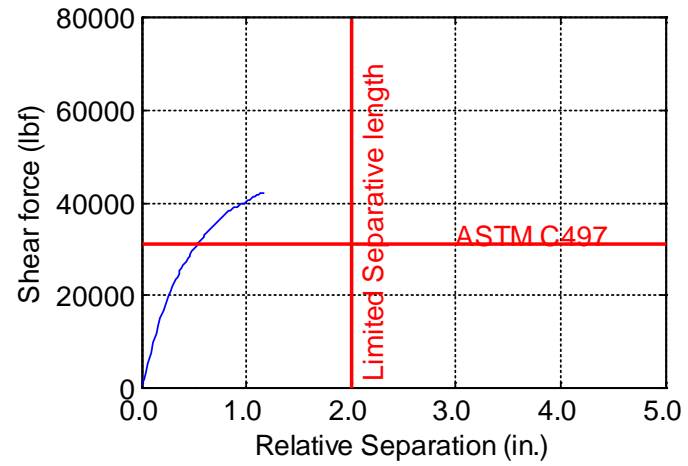
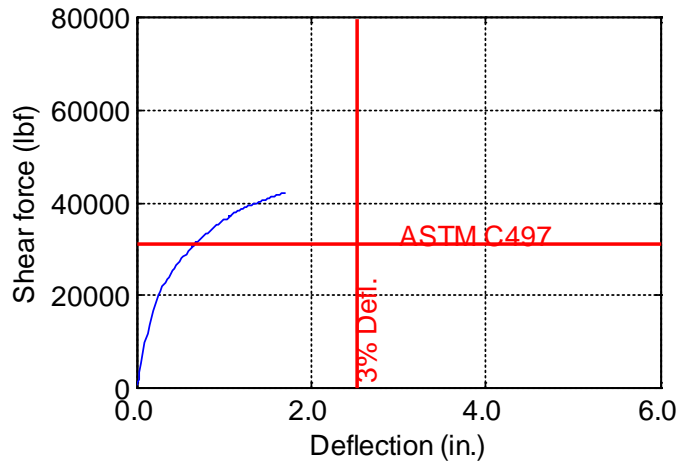


Figure B-151. TW-084-09-0.75

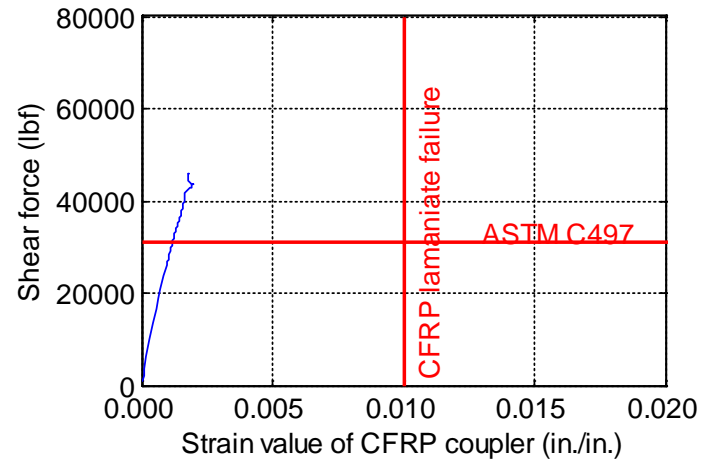
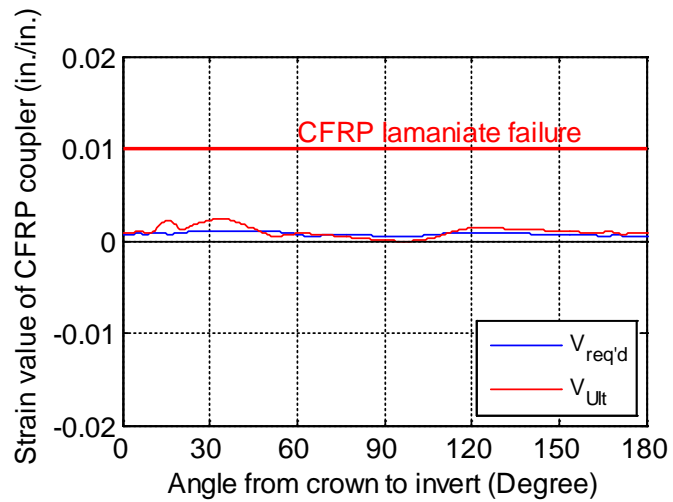
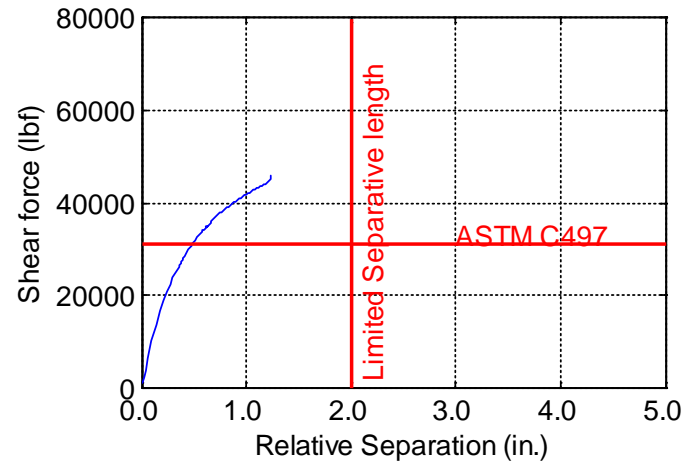
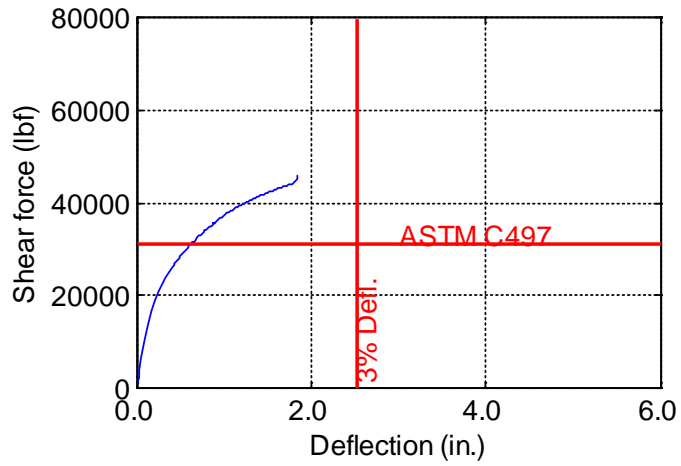


Figure B-152. TW-084-09-0.875

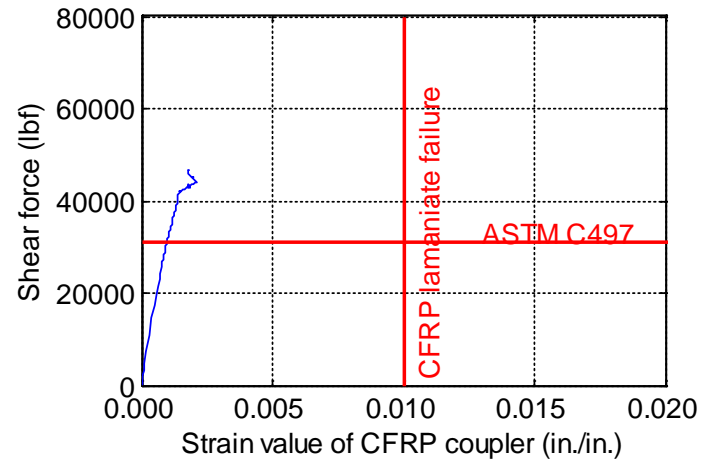
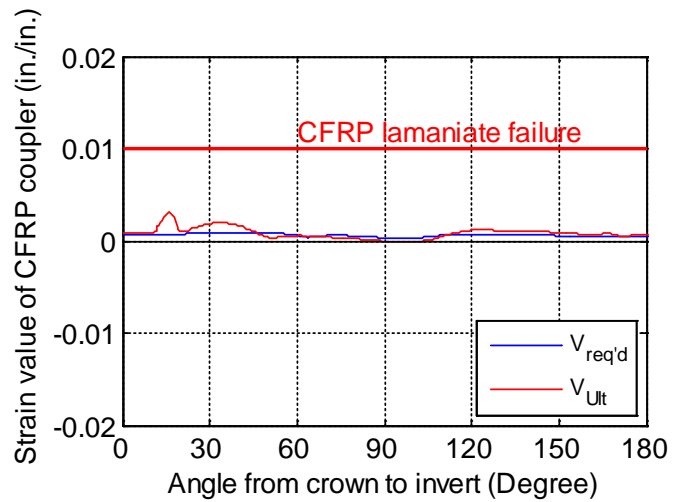
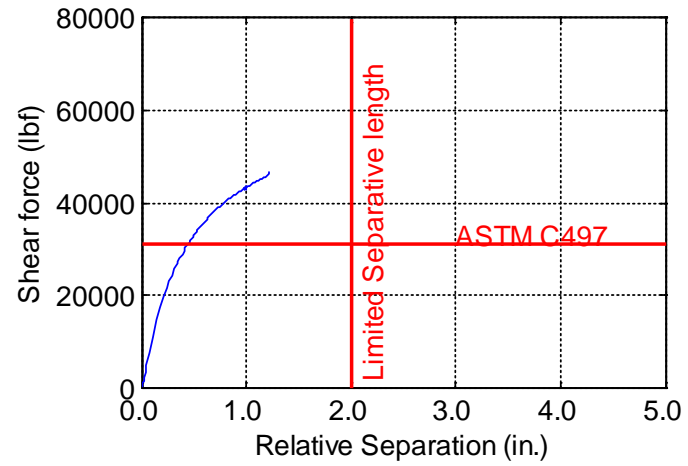
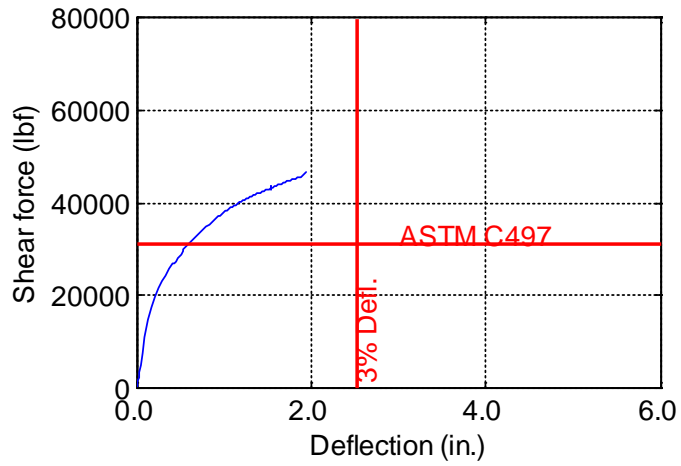


Figure B-153. TW-084-09-1.0

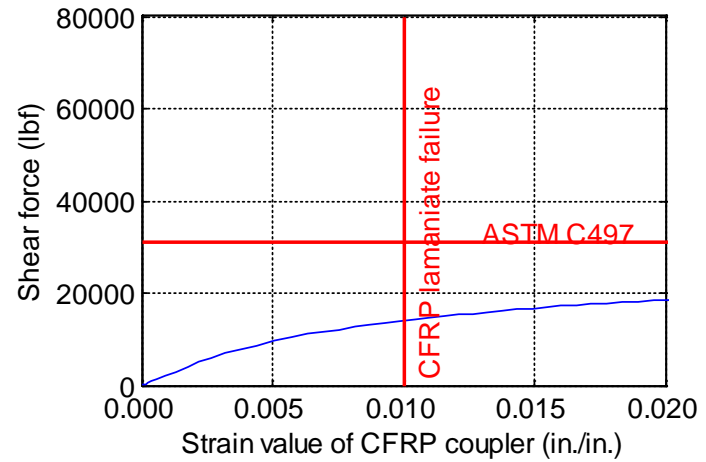
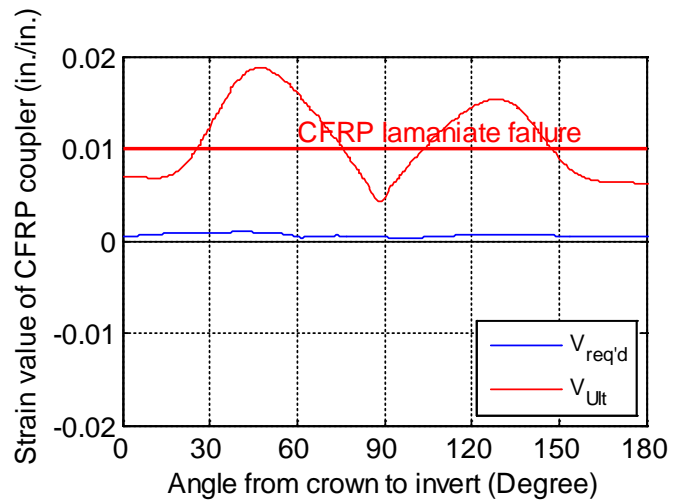
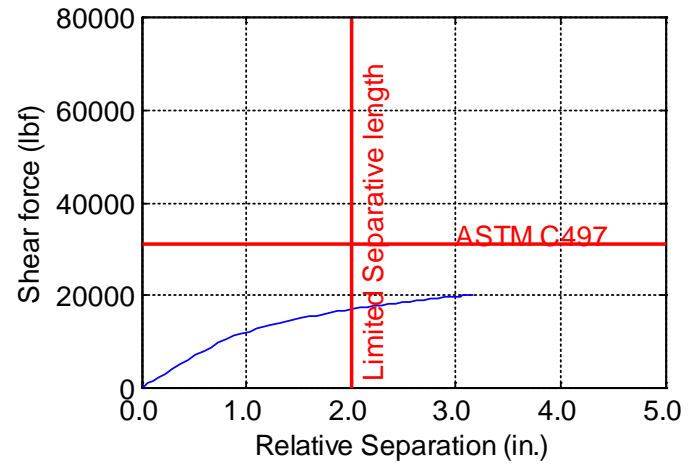
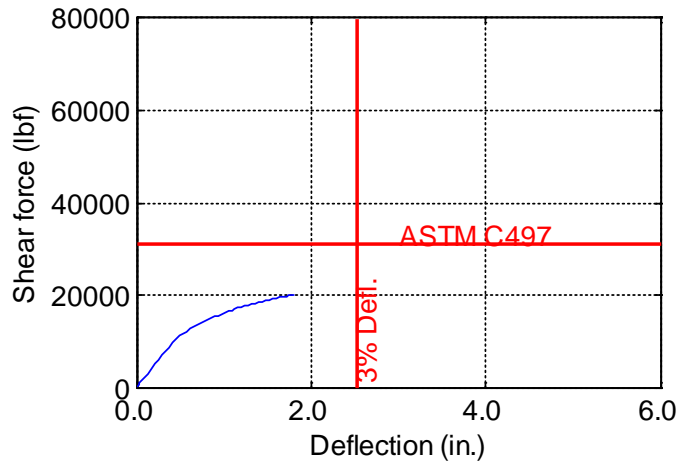


Figure B-154. TW-084-12-0.125

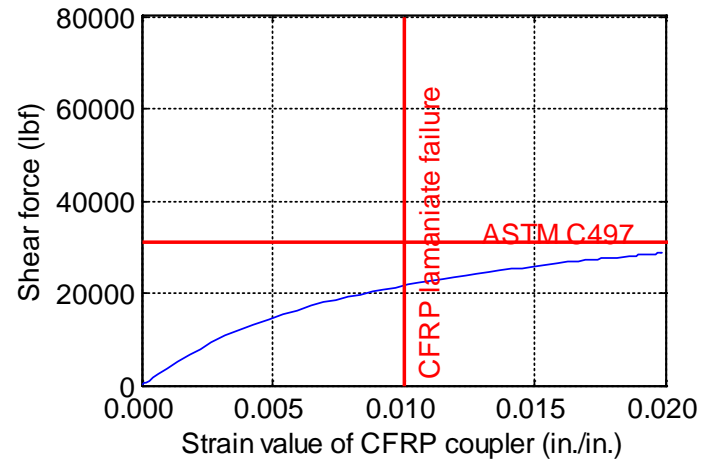
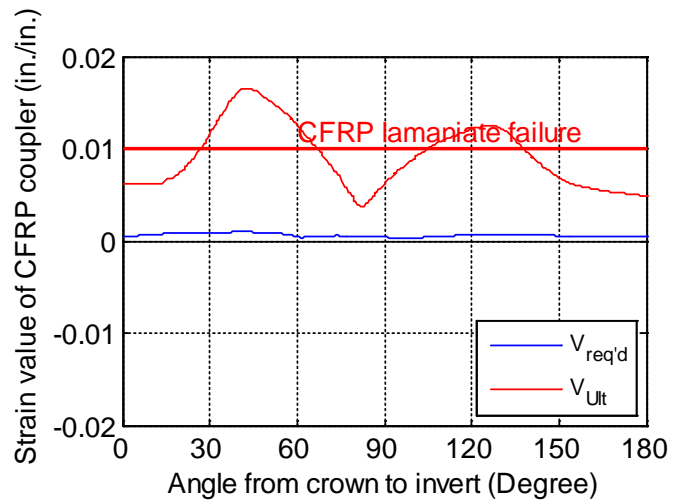
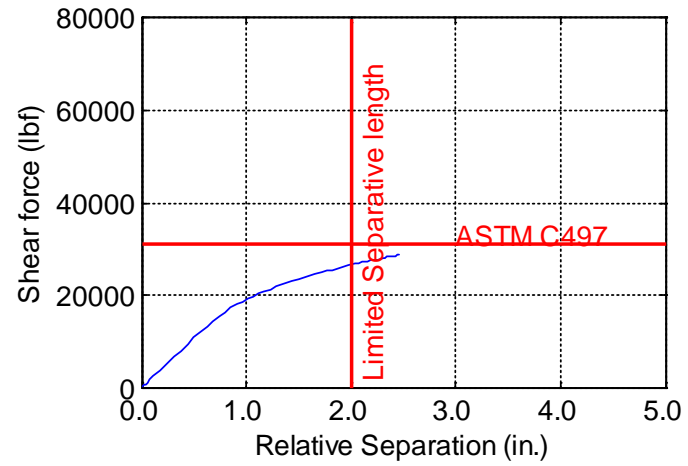
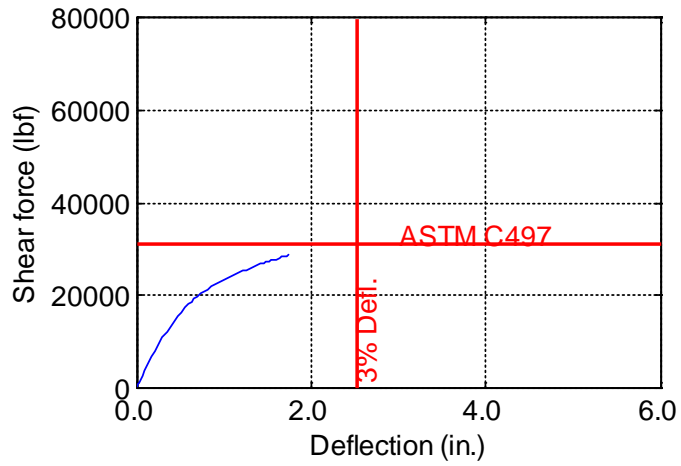


Figure B-155. TW-084-12-0.1875

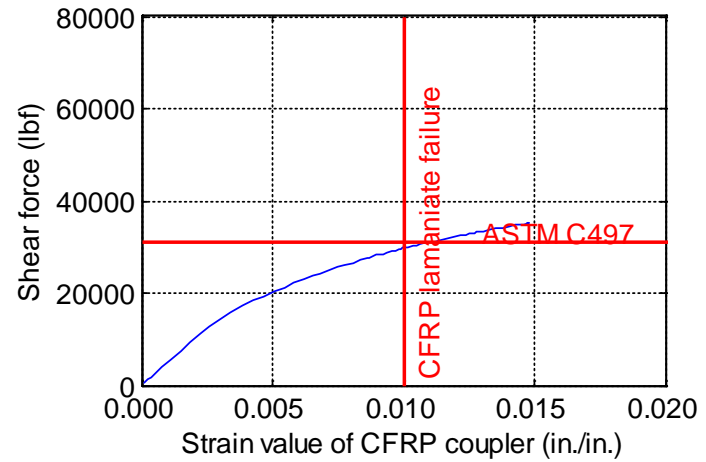
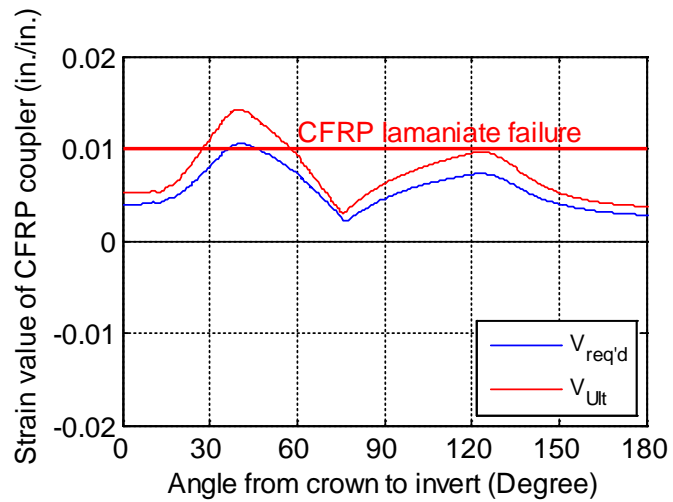
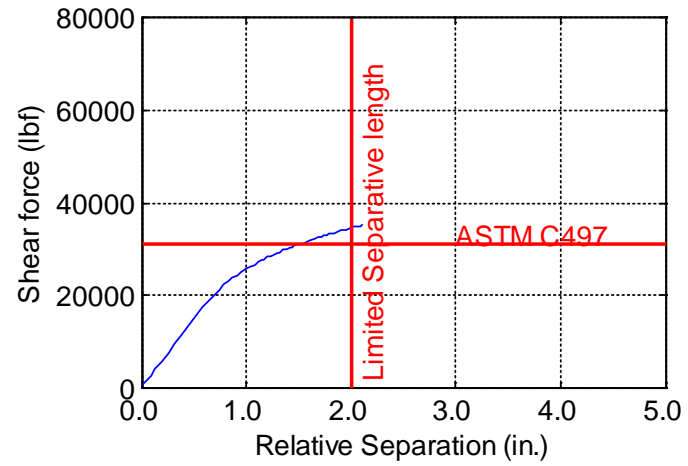
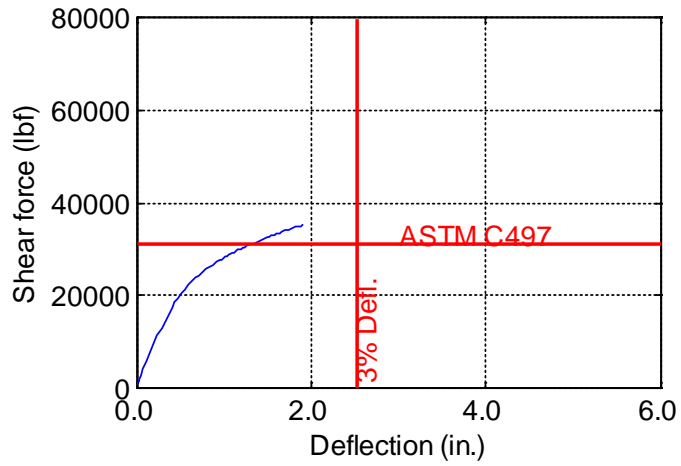


Figure B-156. TW-084-12-0.25

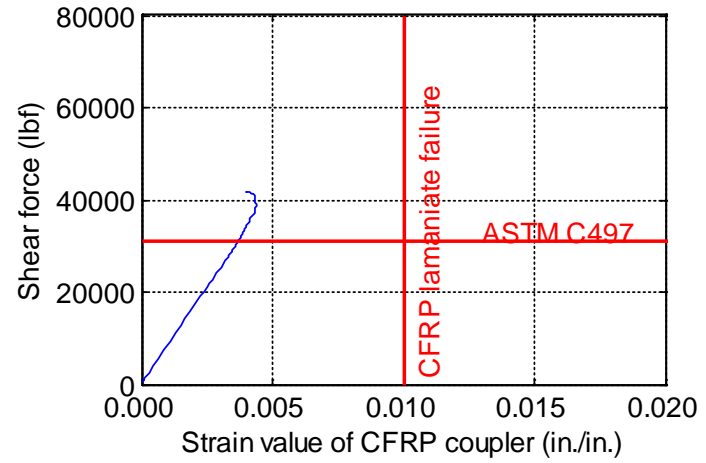
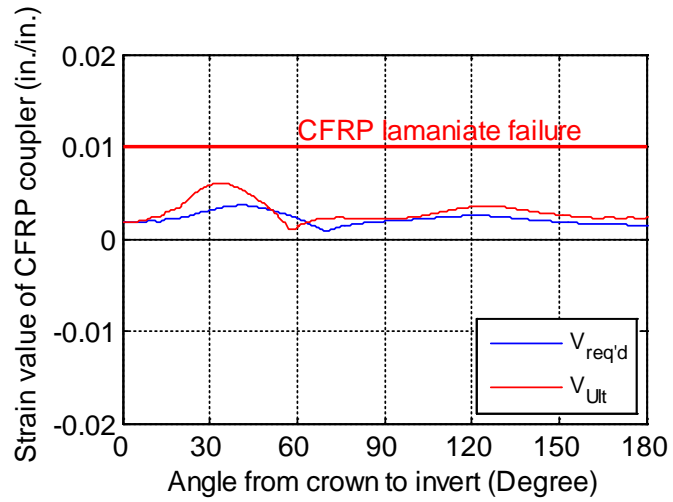
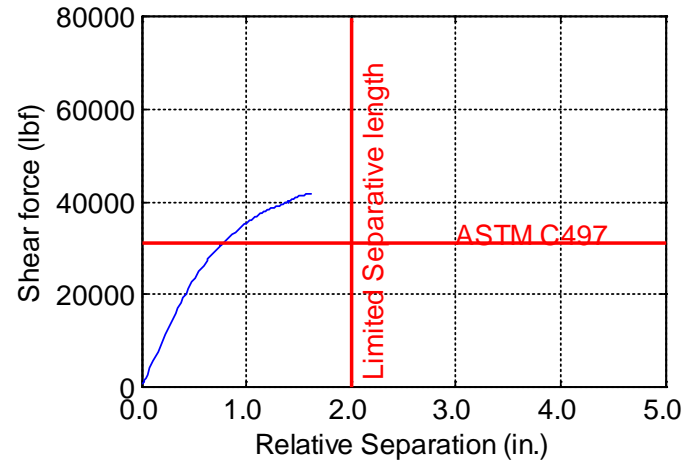
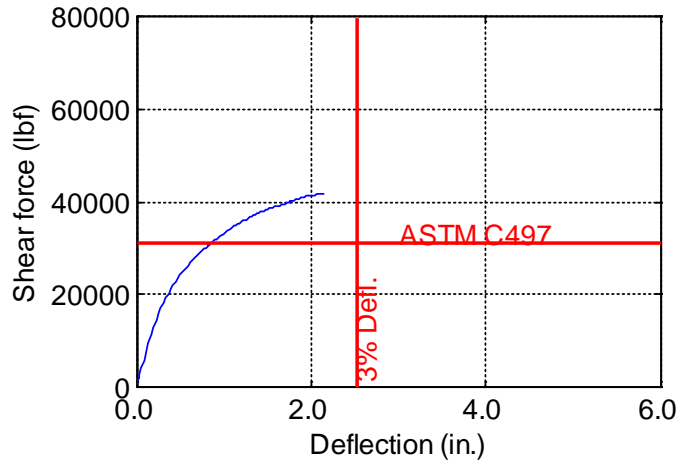


Figure B-157. TW-084-12-0.375

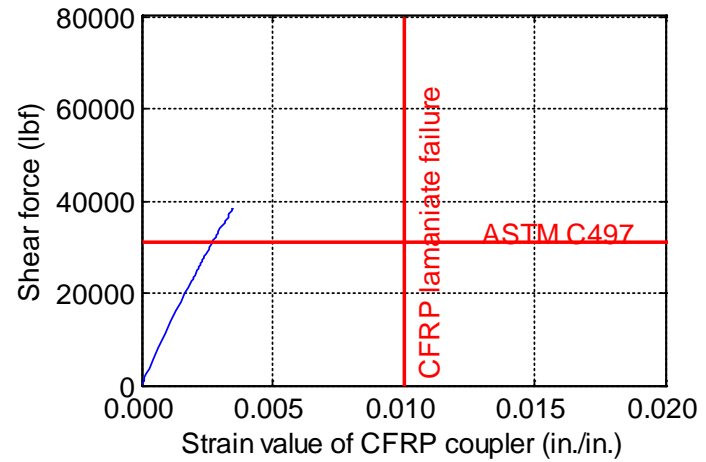
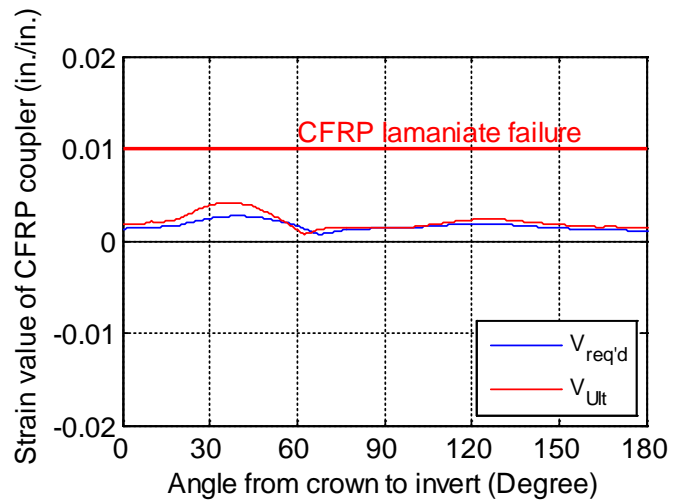
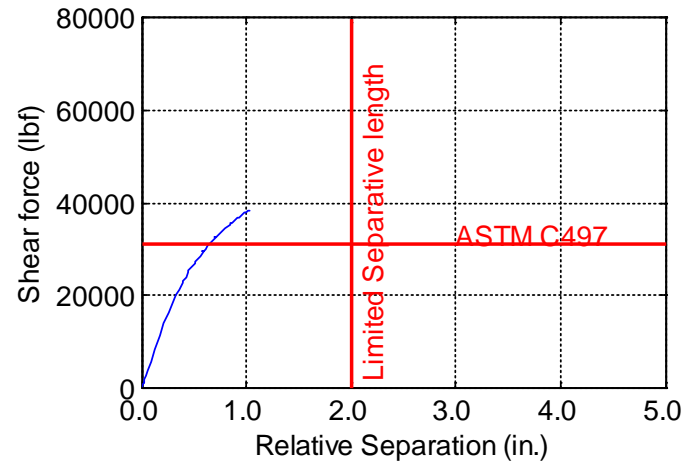
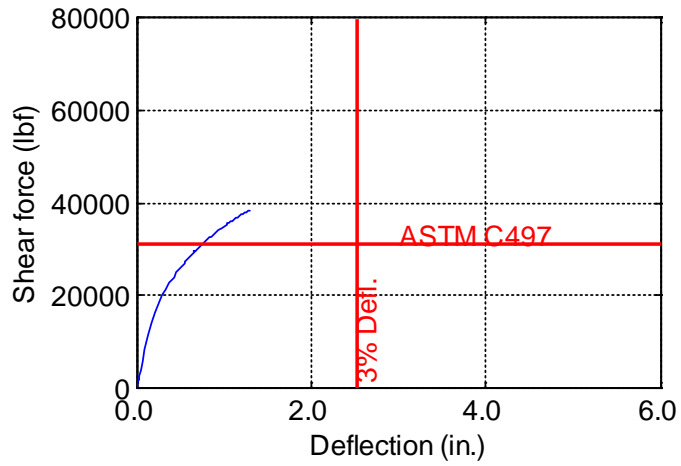


Figure B-158. TW-084-12-0.5

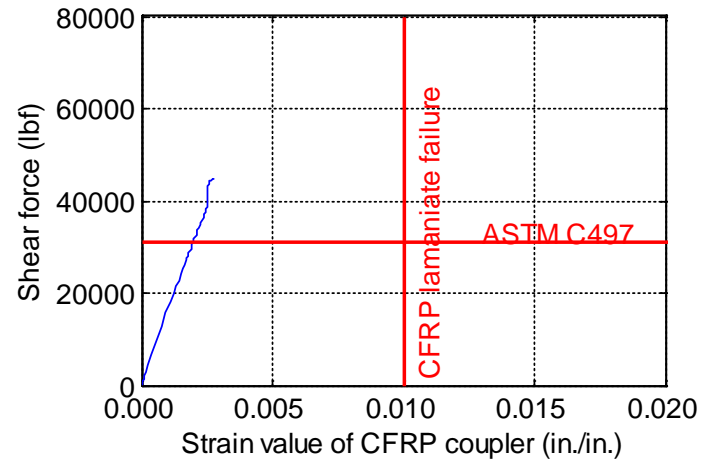
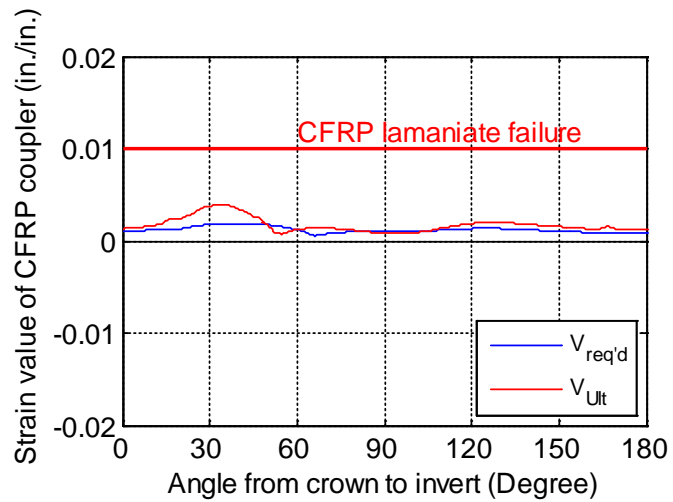
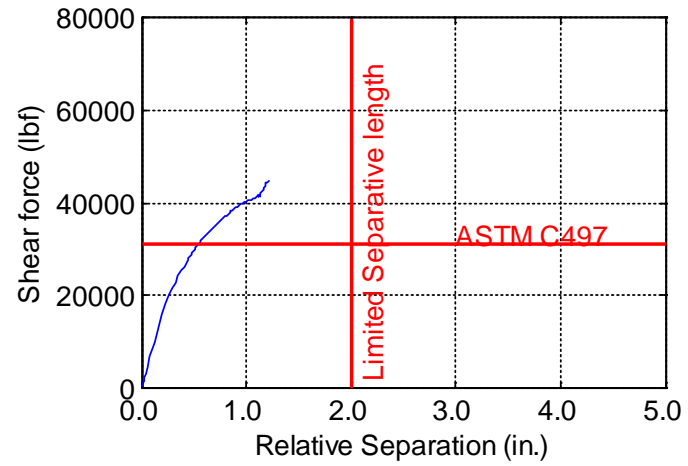
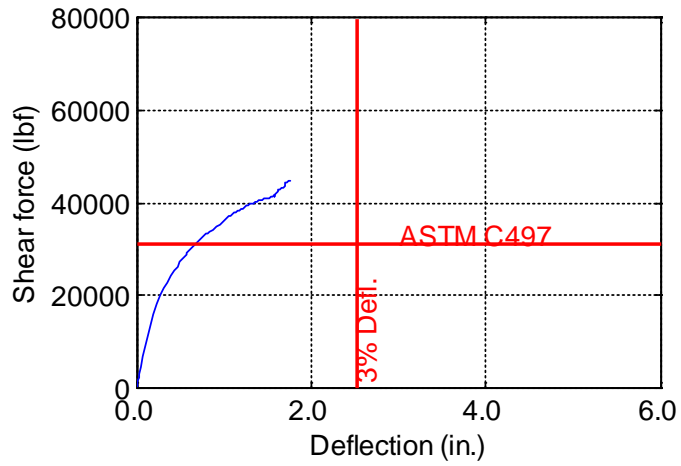


Figure B-159. TW-084-12-0.625

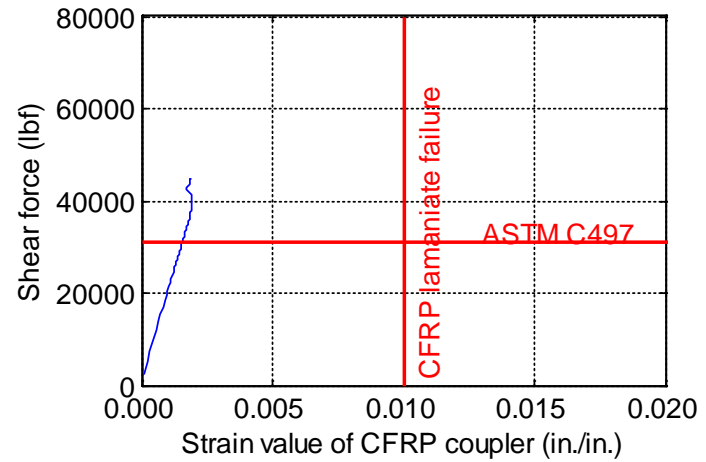
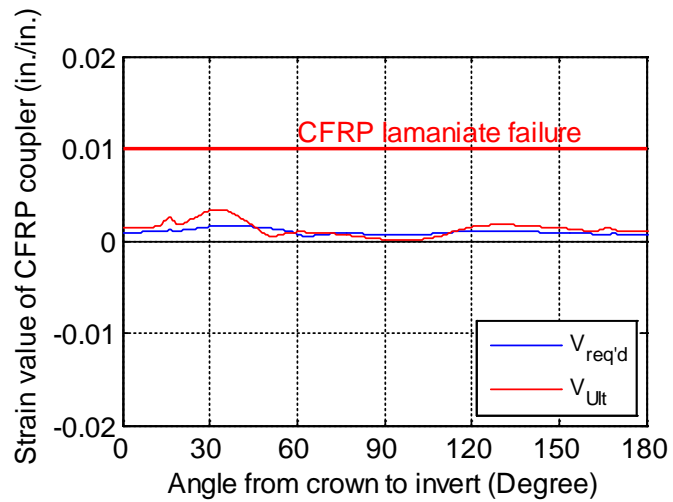
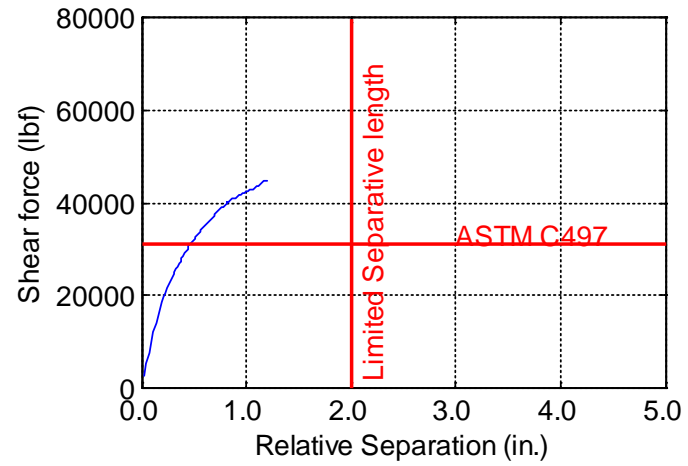
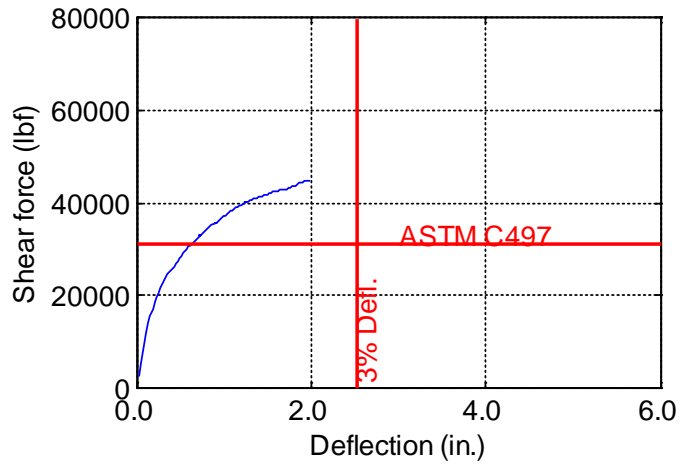


Figure B-160. TW-084-12-0.75

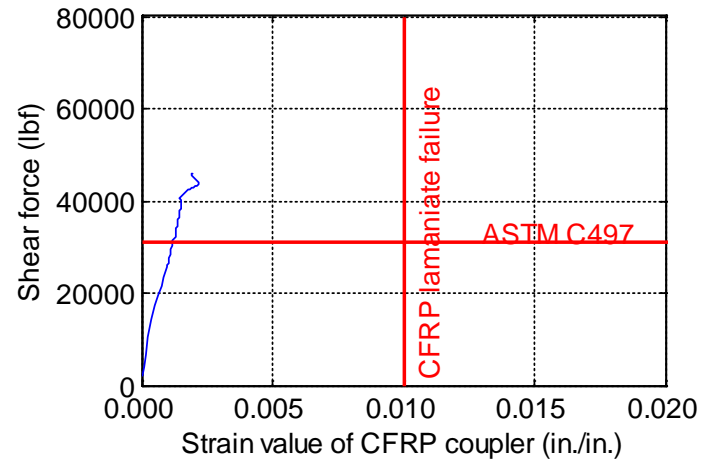
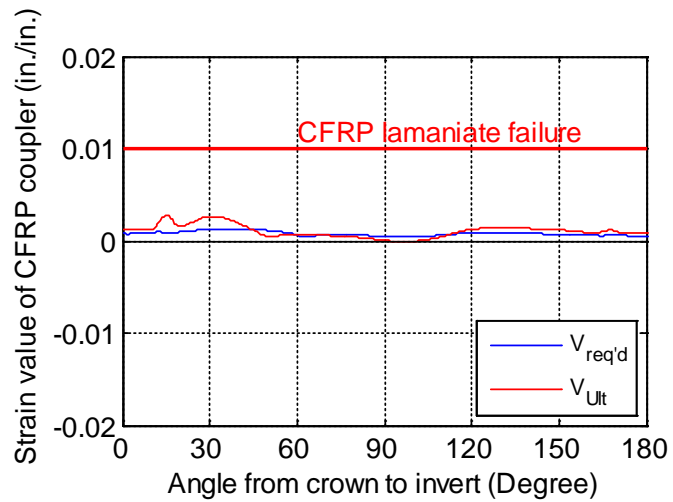
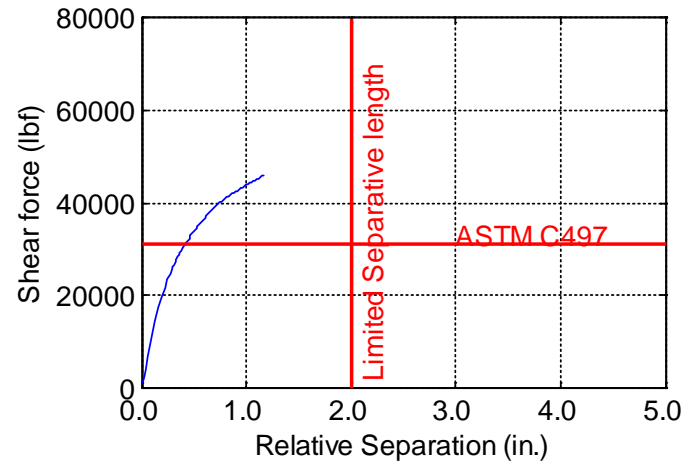
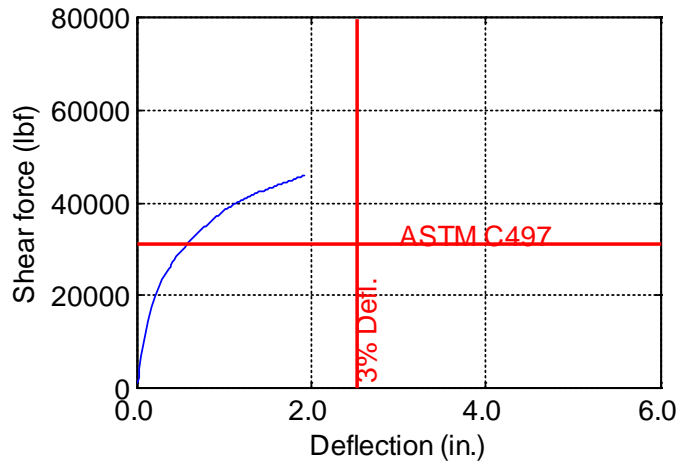


Figure B-161. TW-084-12-0.875

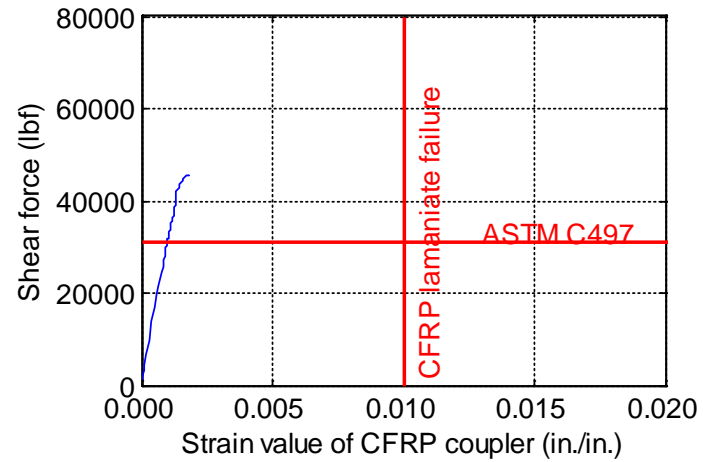
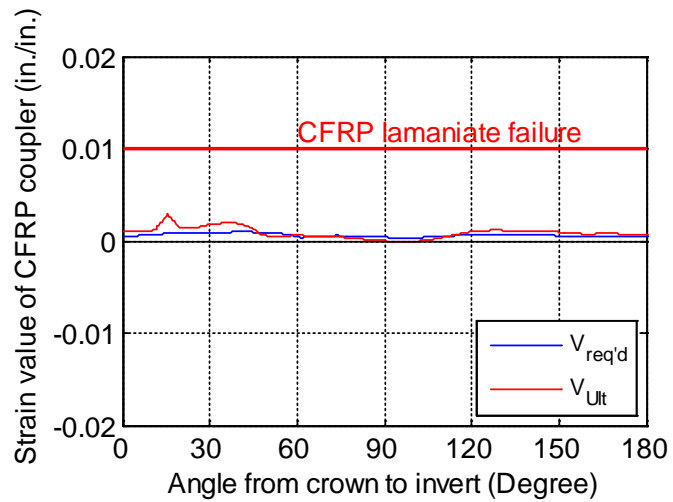
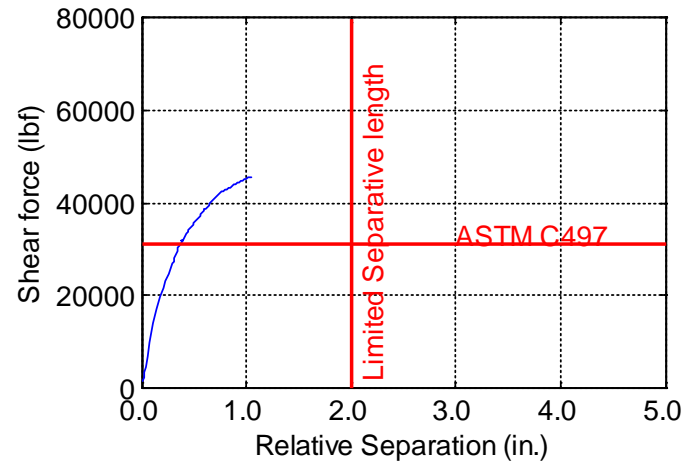
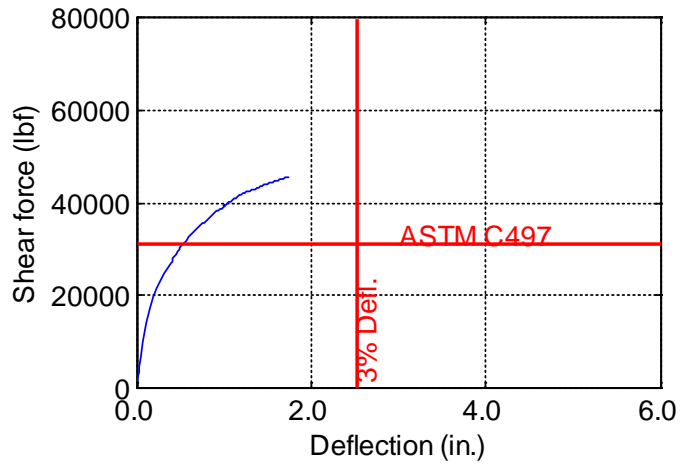


Figure B-162. TW-084-12-1.0

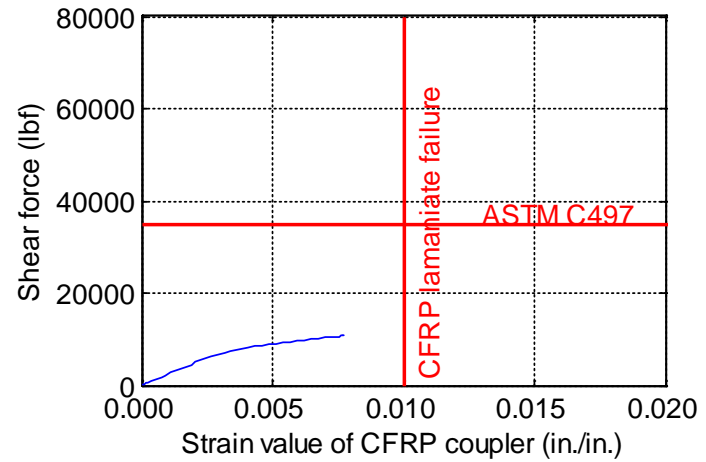
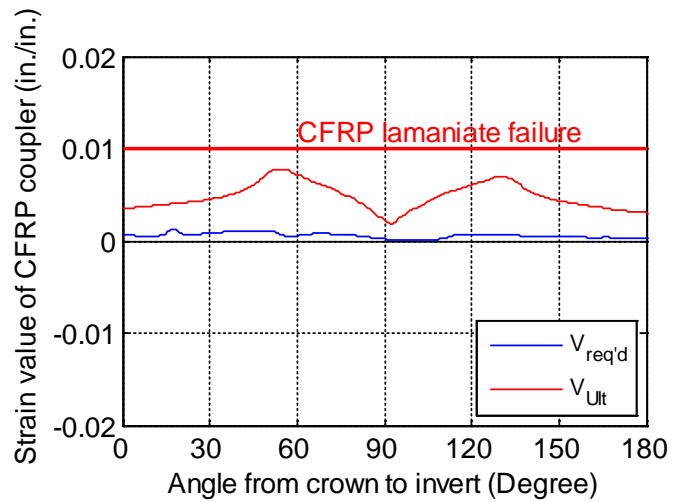
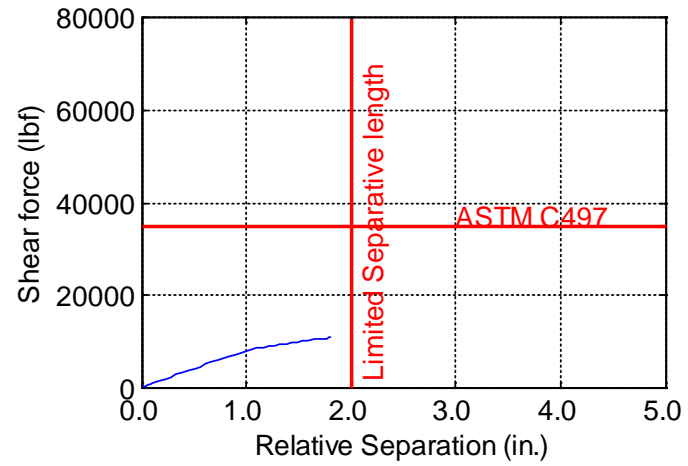
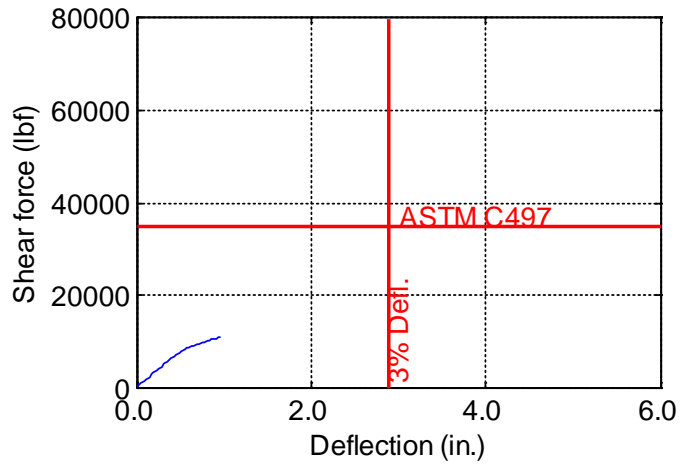


Figure B-163. TW-096-06-0.125

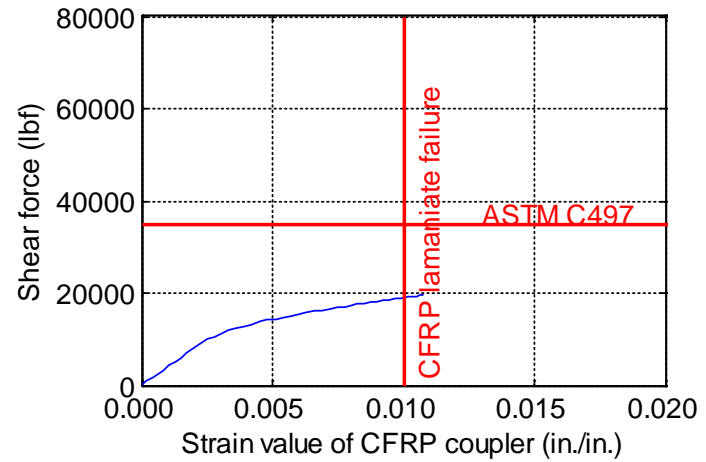
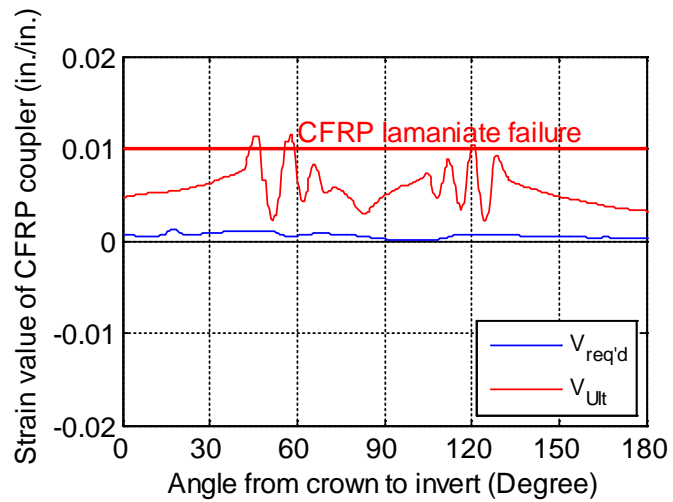
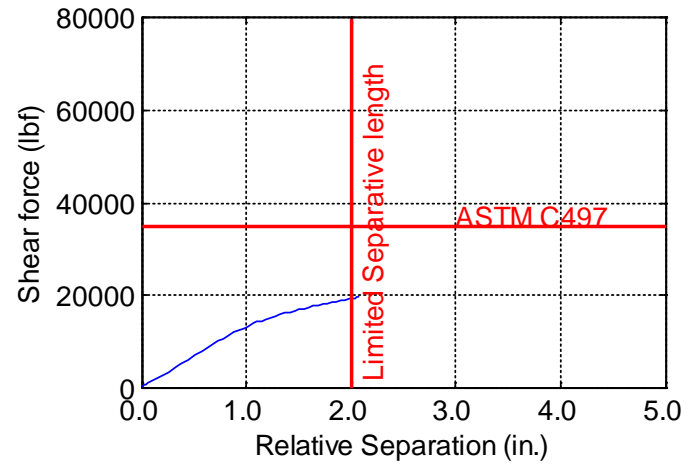
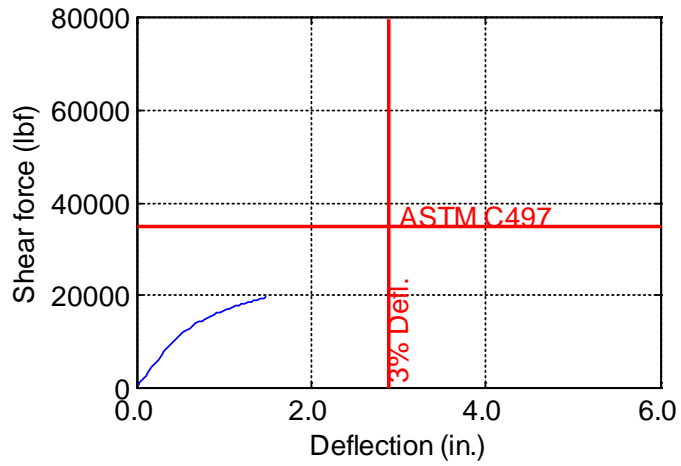


Figure B-164. TW-096-06-0.1875

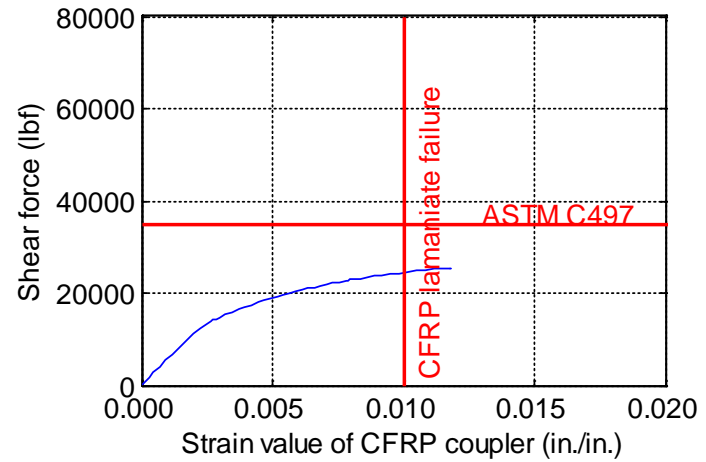
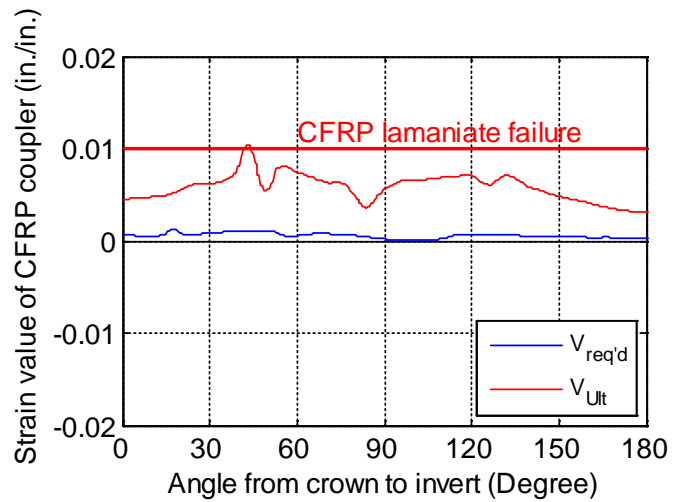
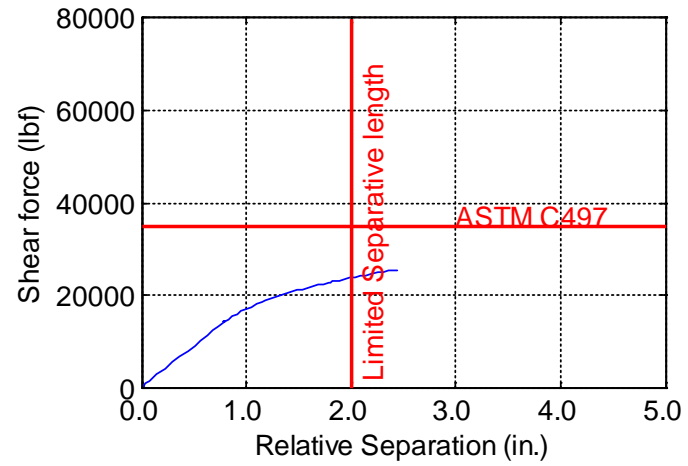
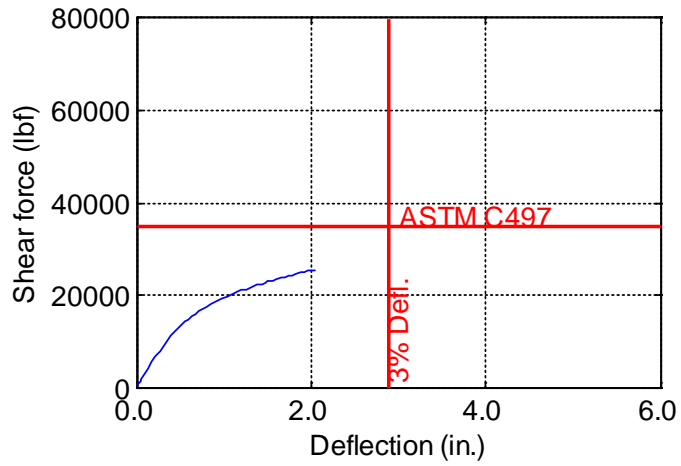


Figure B-165. TW-096-06-0.25

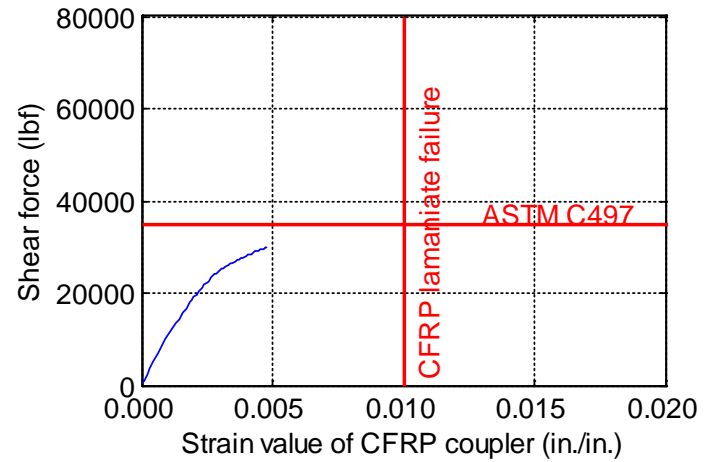
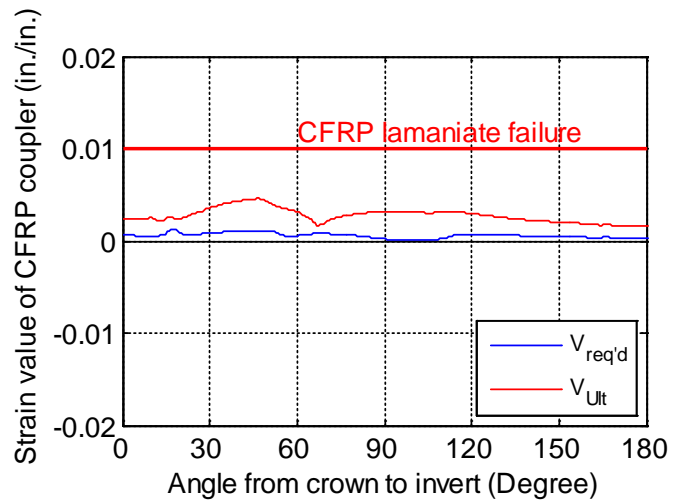
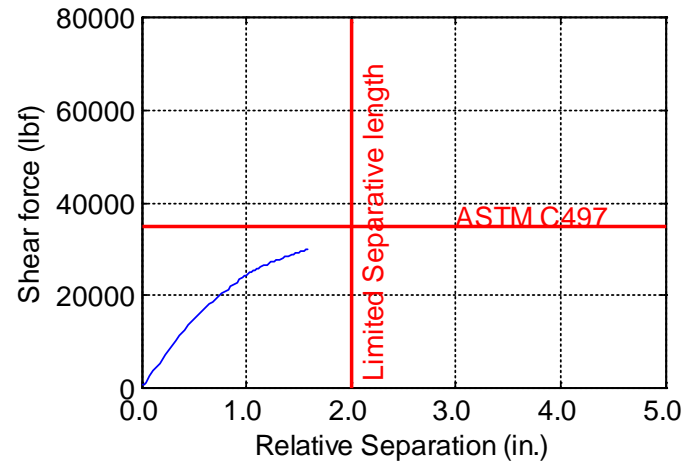
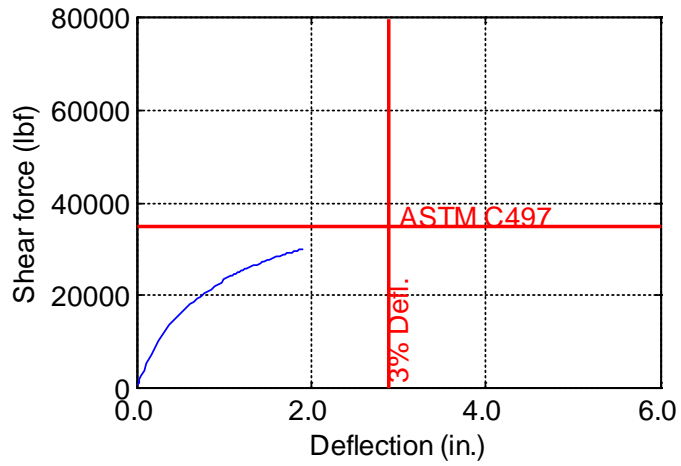


Figure B-166. TW-096-06-0.375

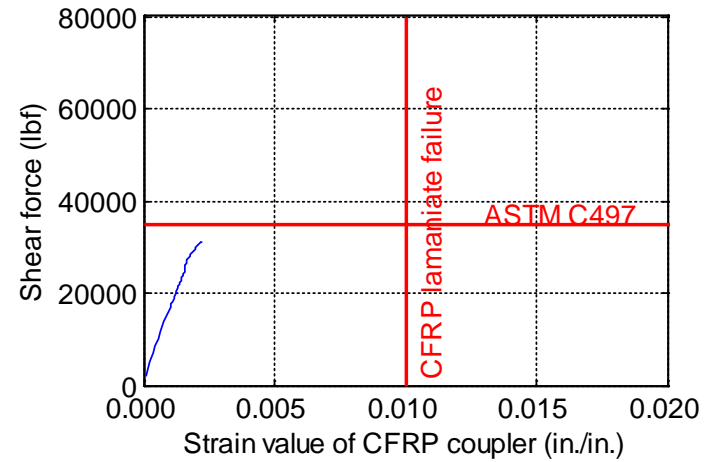
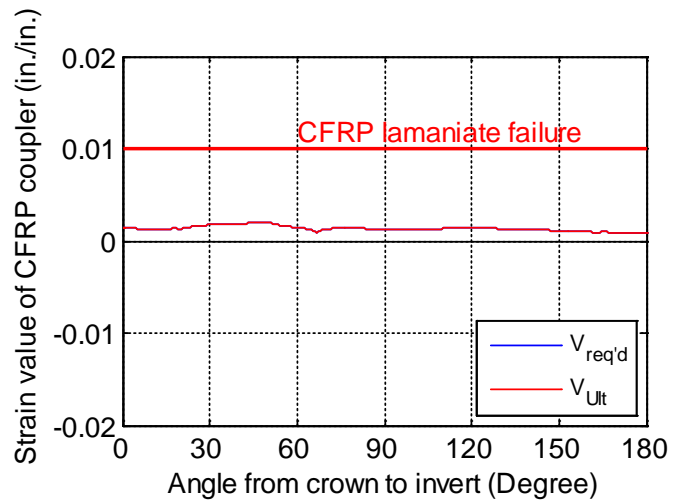
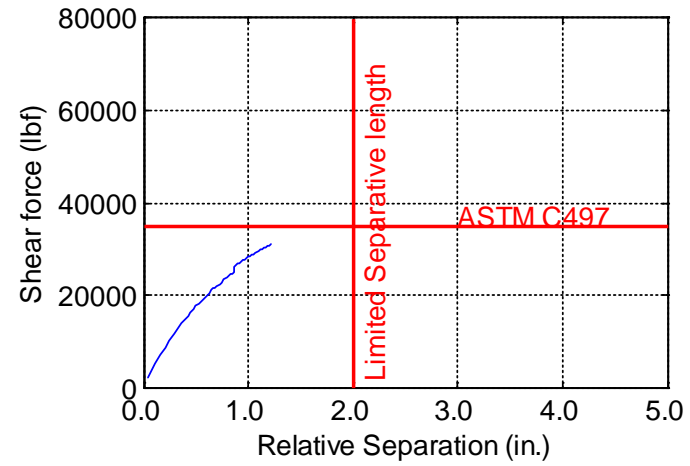
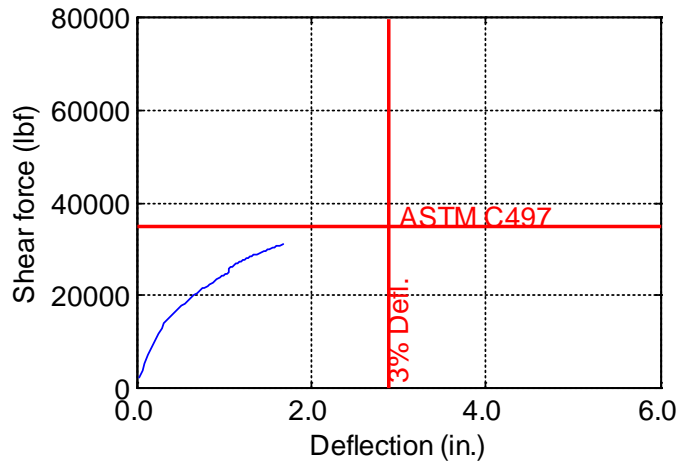


Figure B-167. TW-096-06-0.5

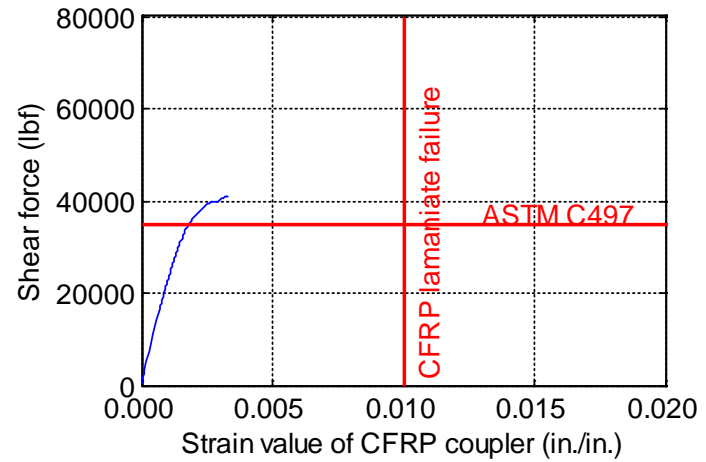
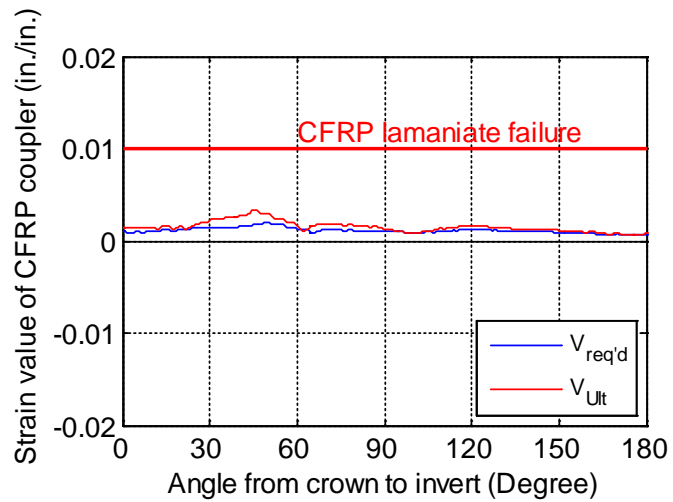
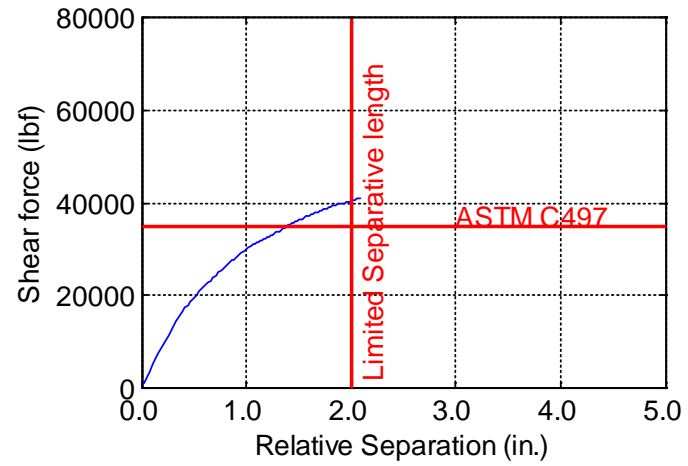
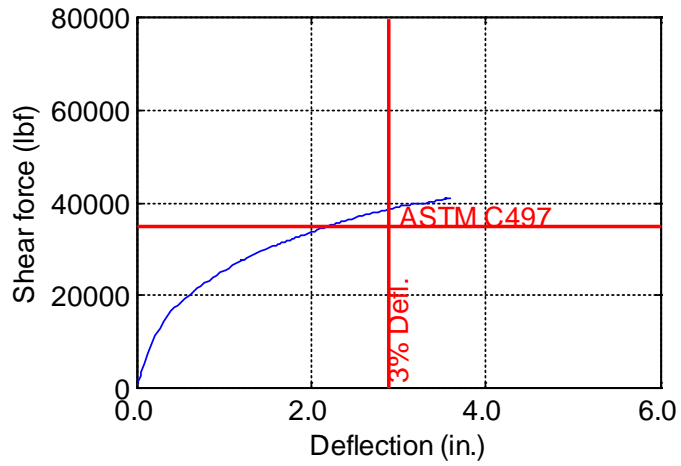


Figure B-168. TW-096-06-0.625

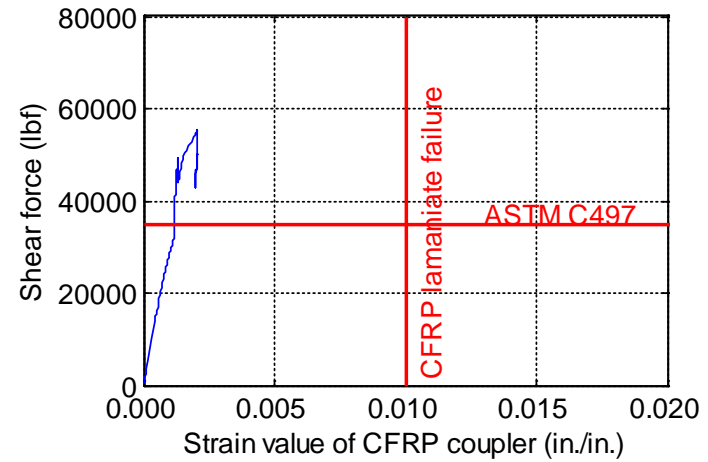
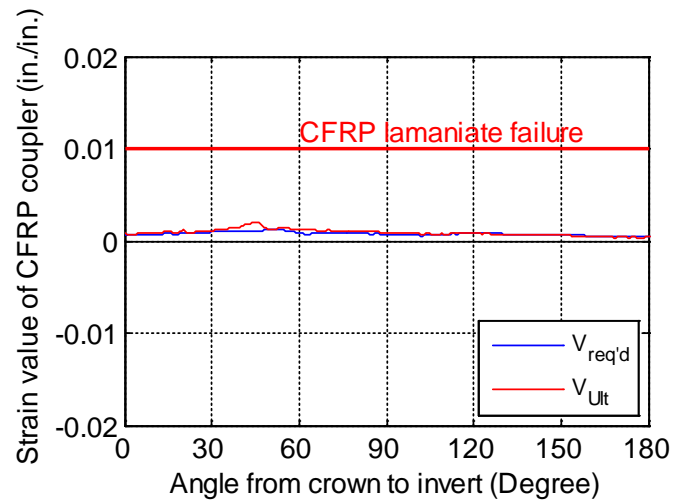
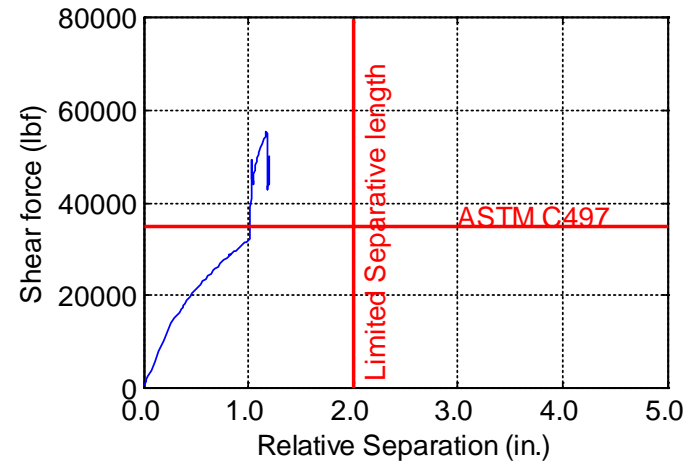
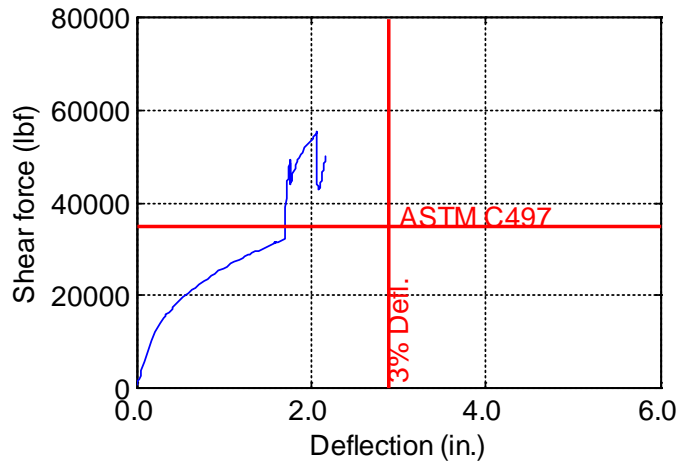


Figure B-169. TW-096-06-0.75

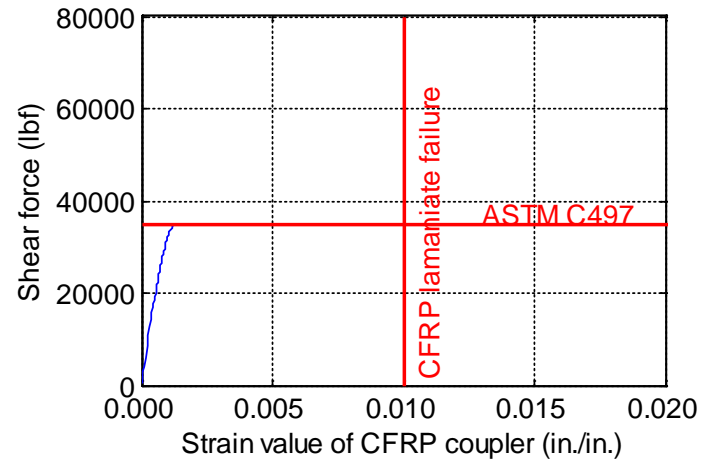
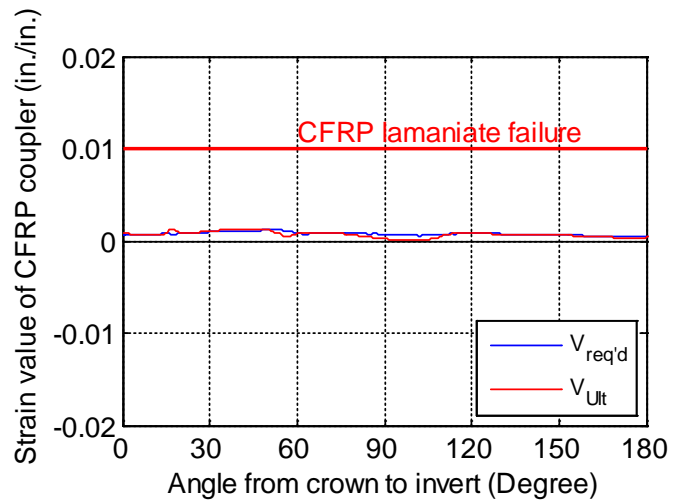
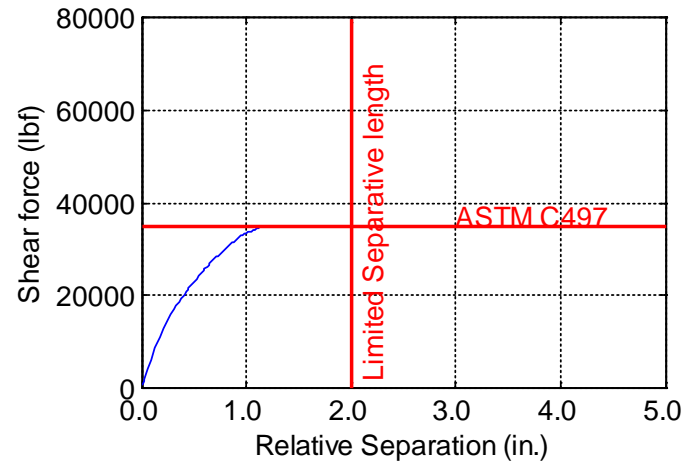
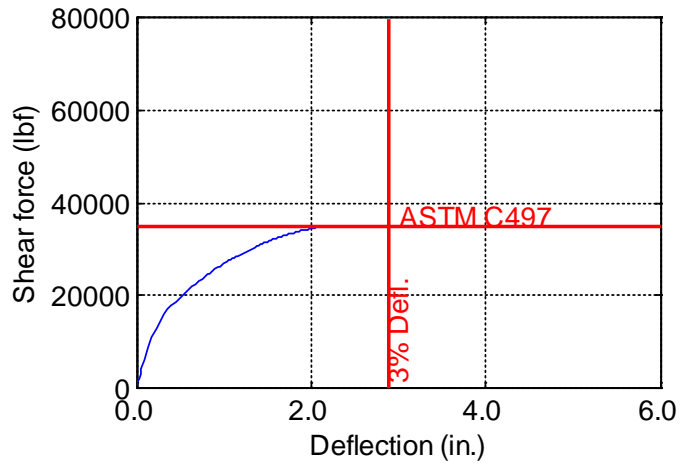


Figure B-170. TW-096-06-0.875

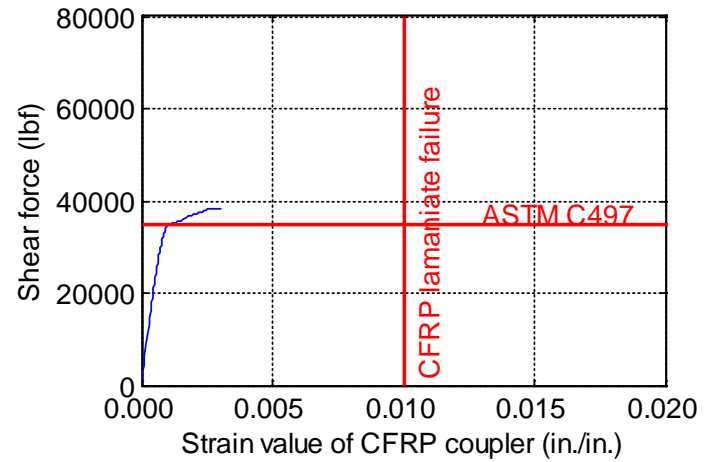
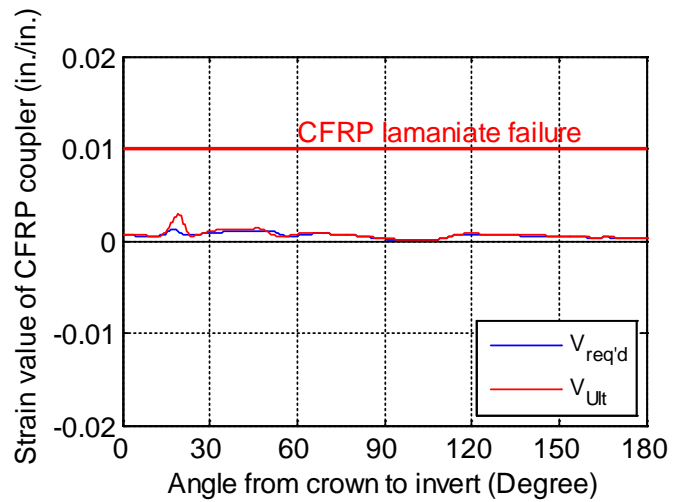
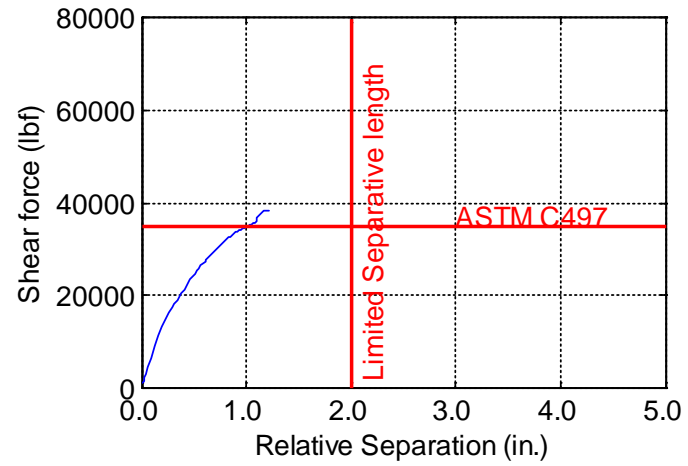
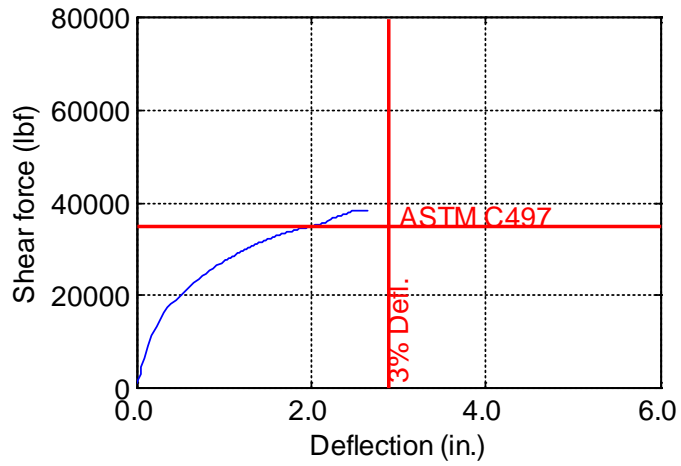


Figure B-171. TW-096-06-1.0

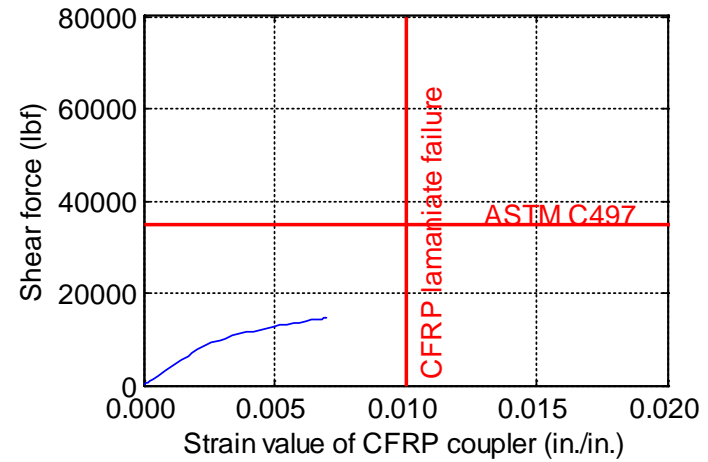
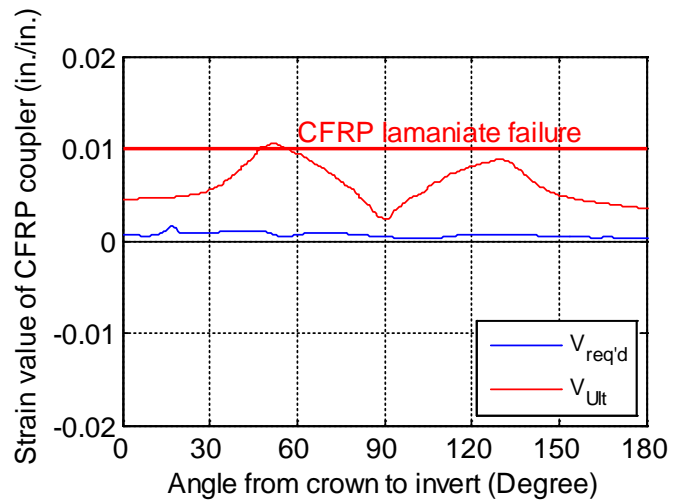
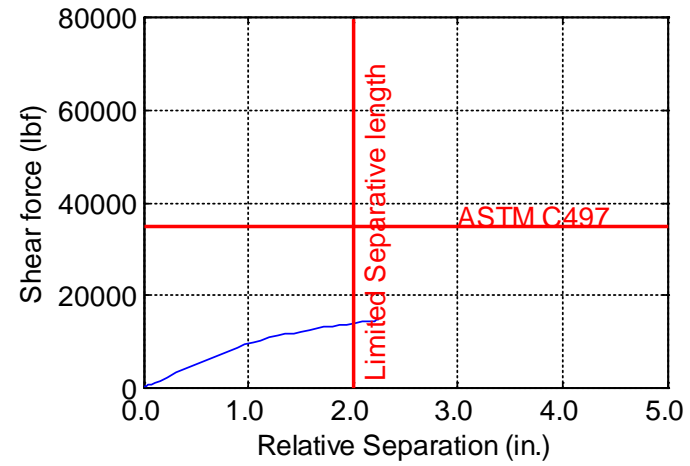
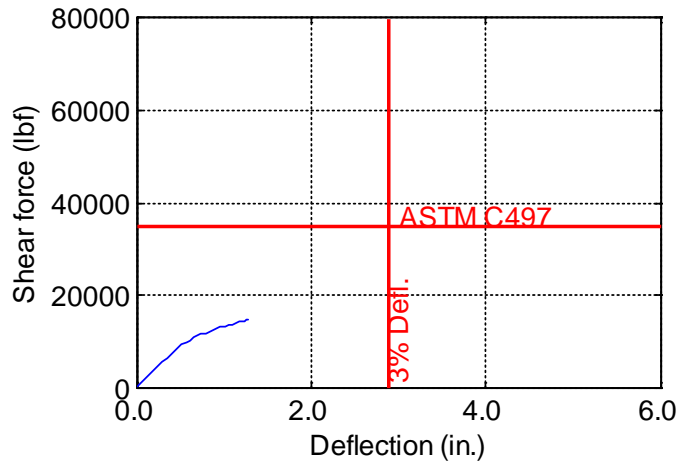


Figure B-172. TW-096-09-0.125

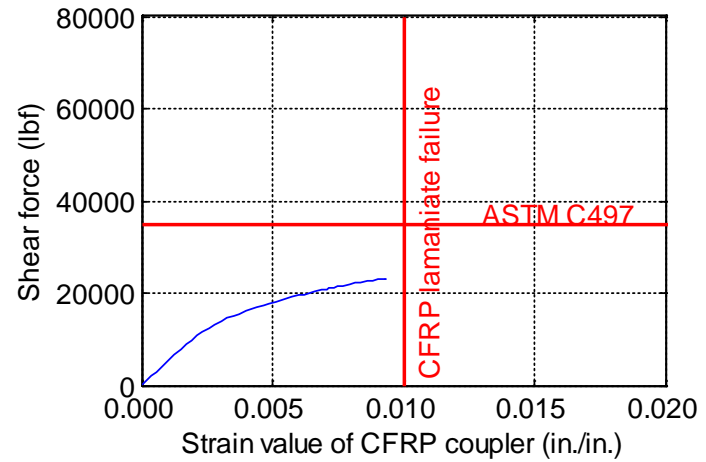
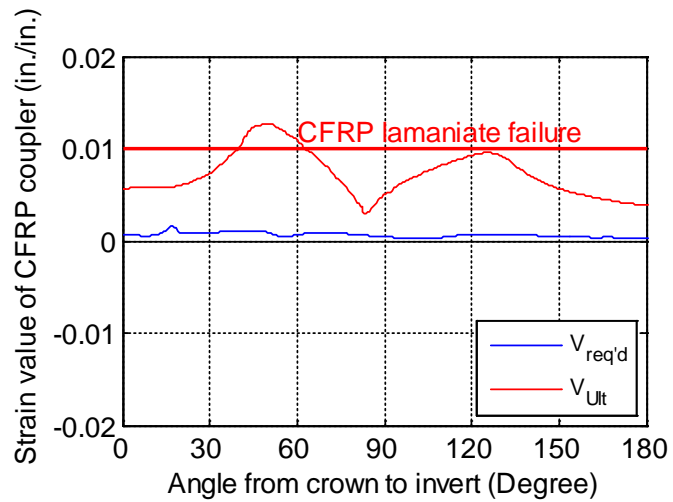
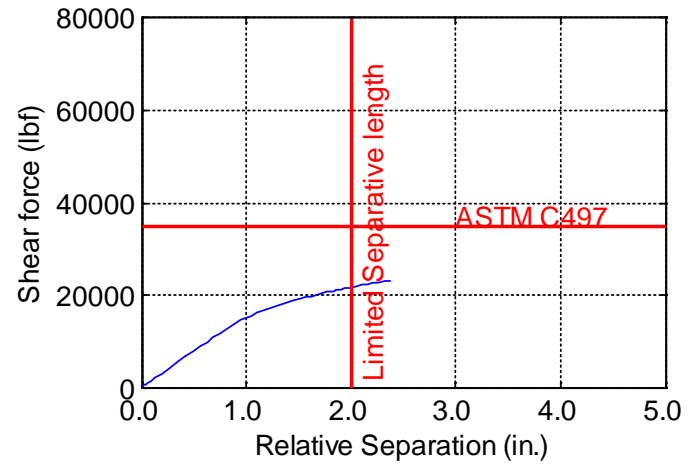
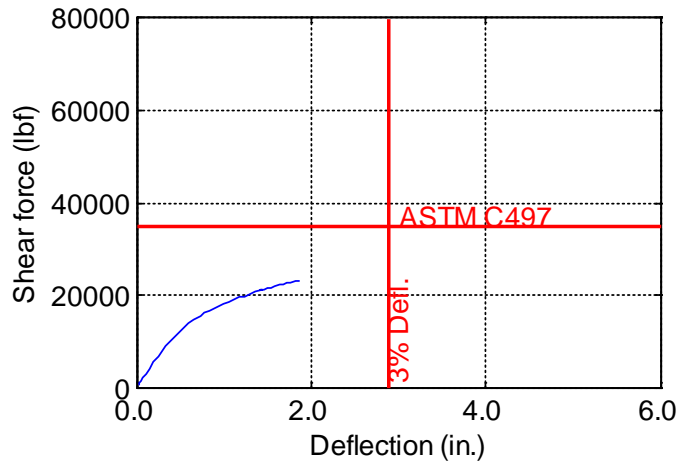


Figure B-173. TW-096-09-0.1875

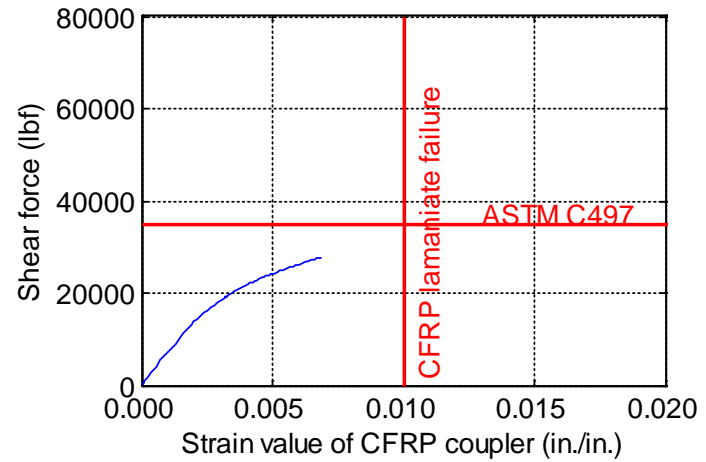
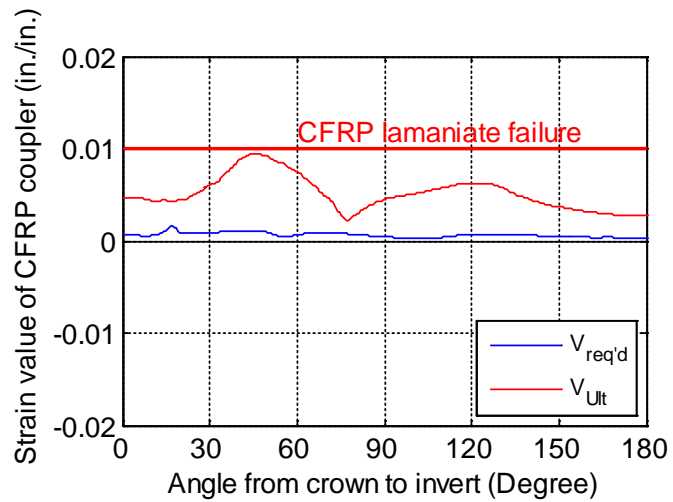
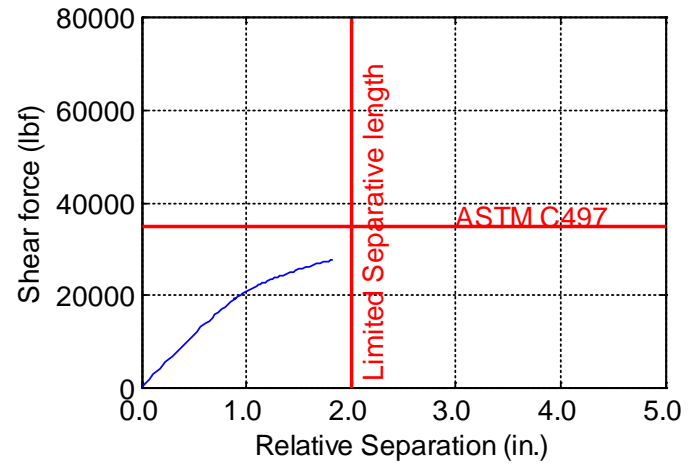
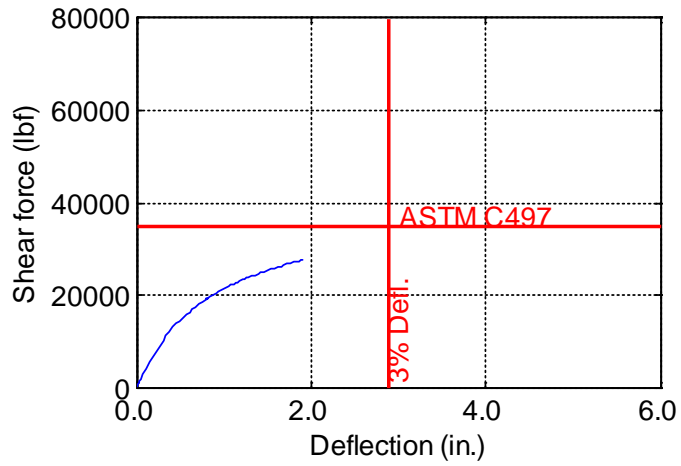


Figure B-174. TW-096-09-0.25

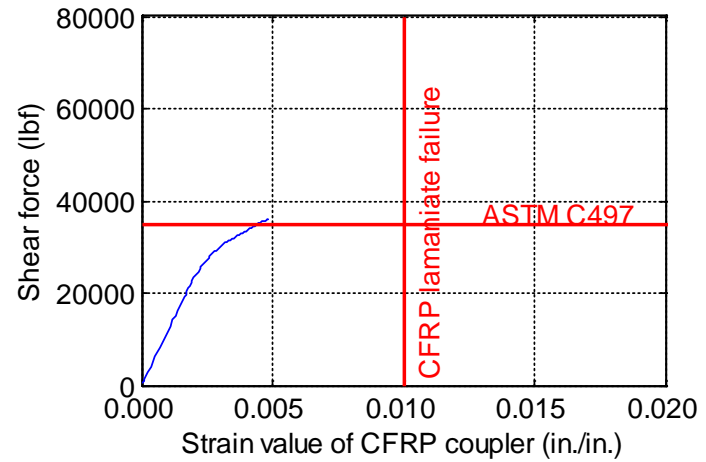
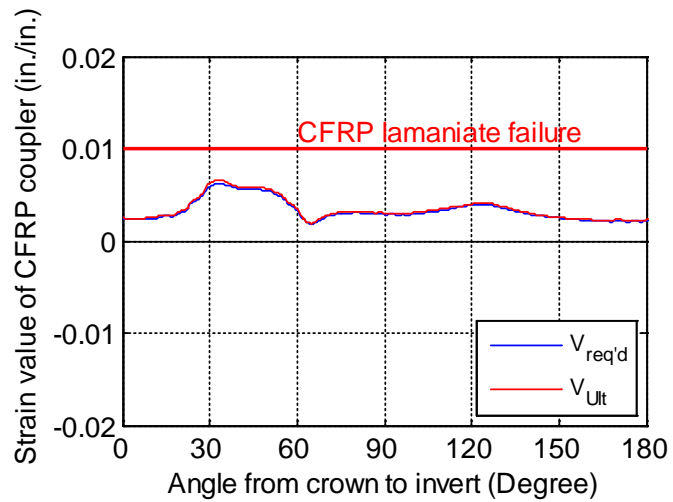
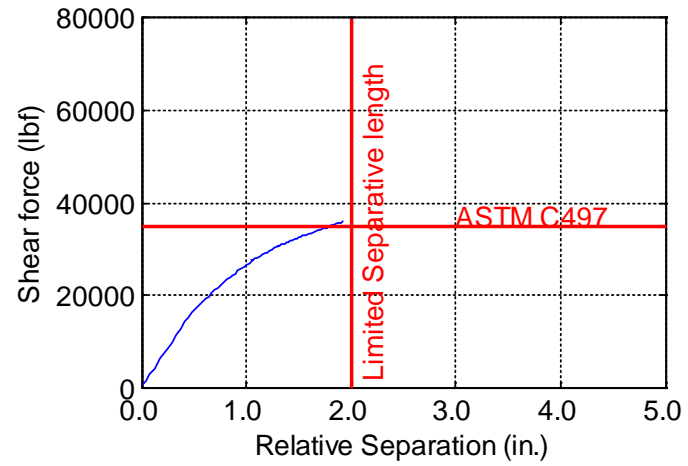
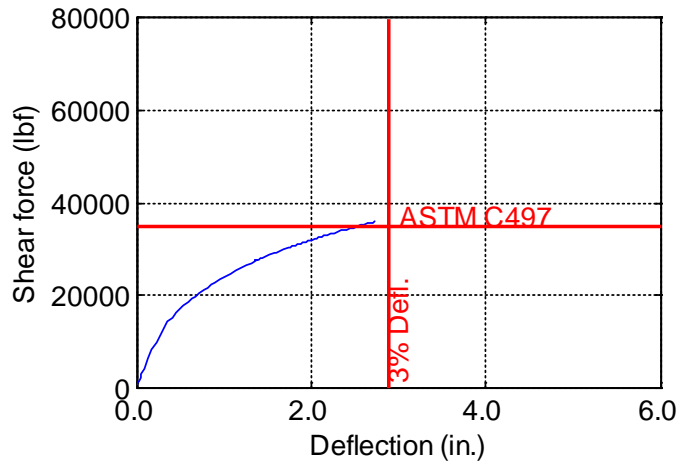


Figure B-175. TW-096-09-0.375

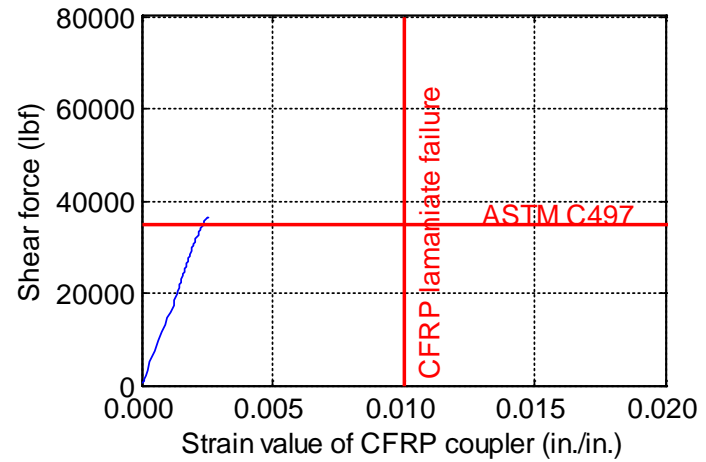
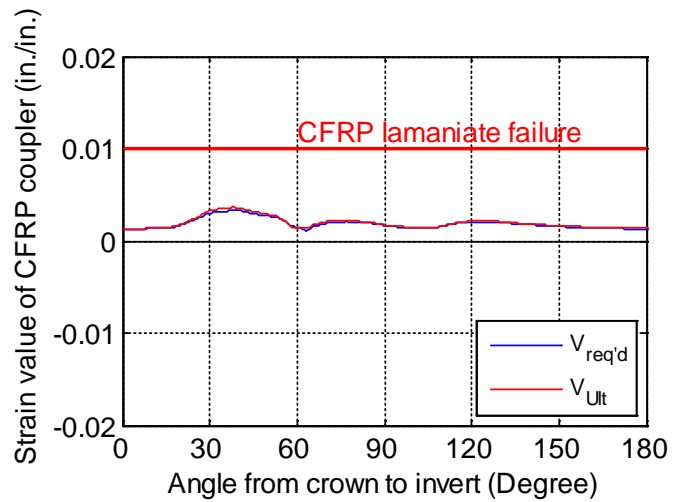
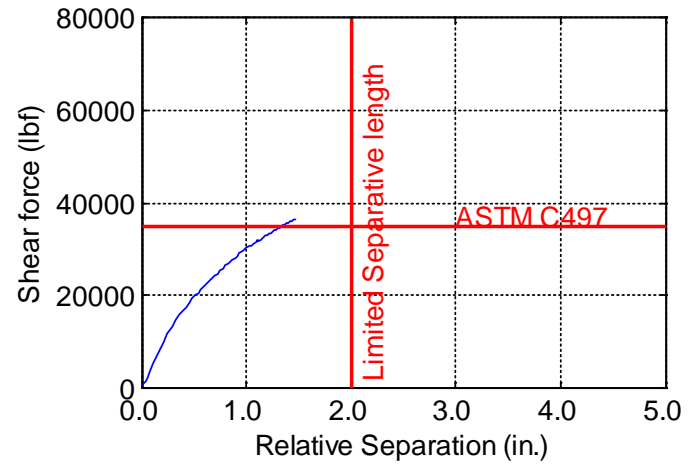
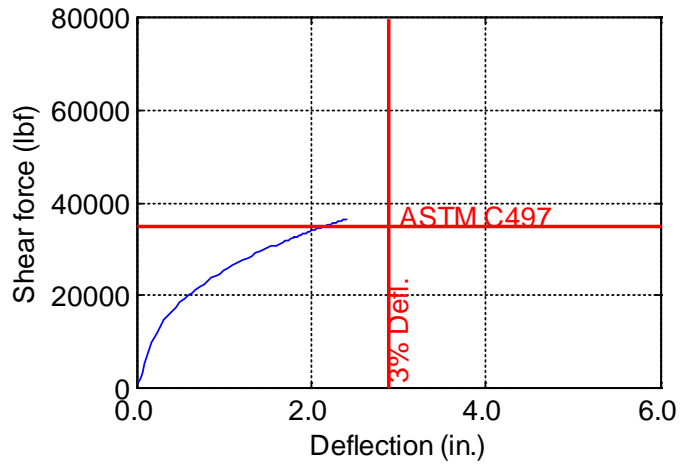


Figure B-176. TW-096-09-0.5

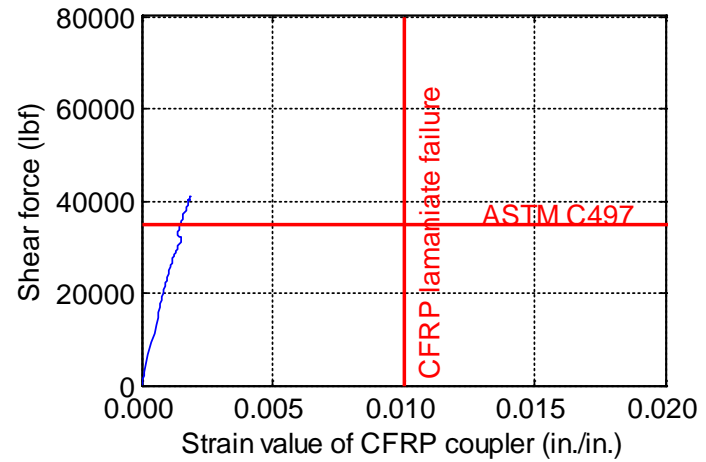
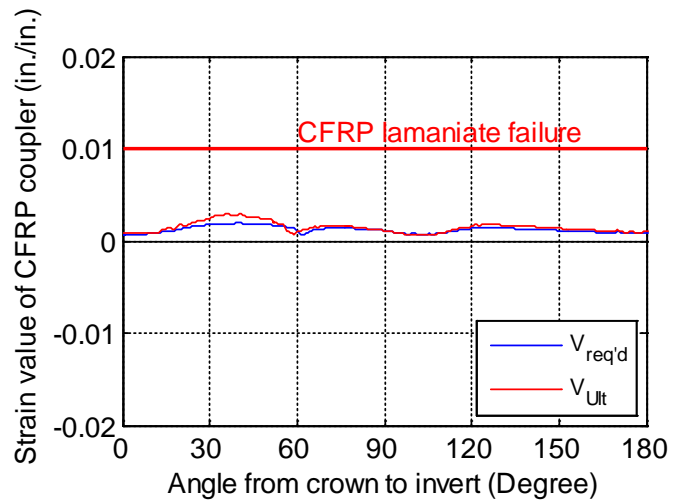
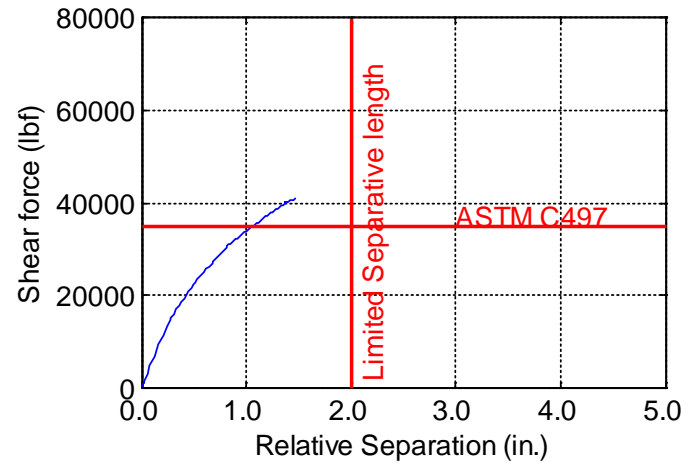
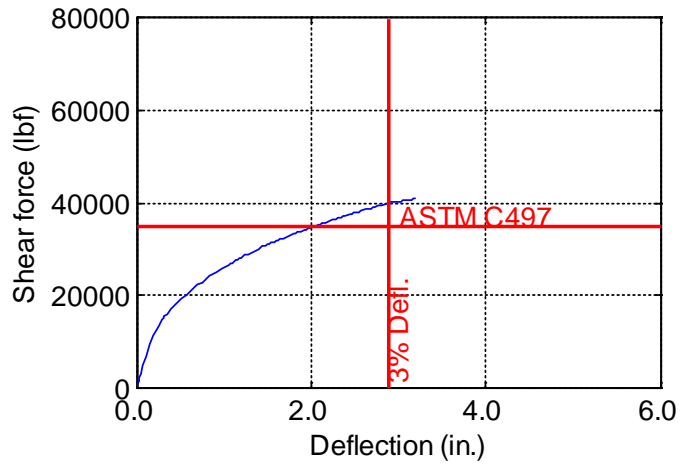


Figure B-177. TW-096-09-0.625

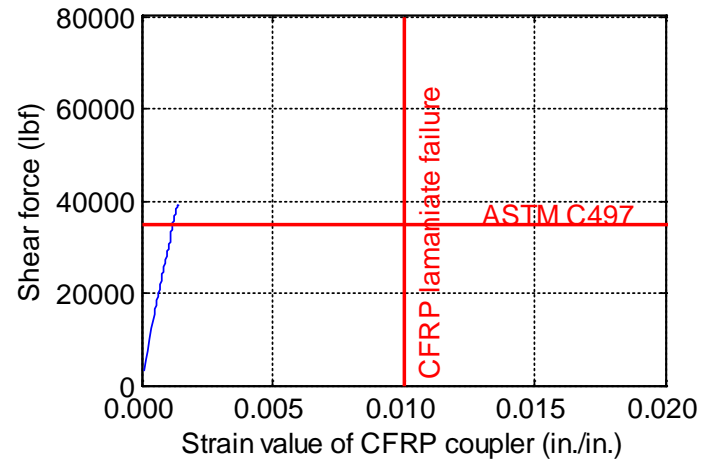
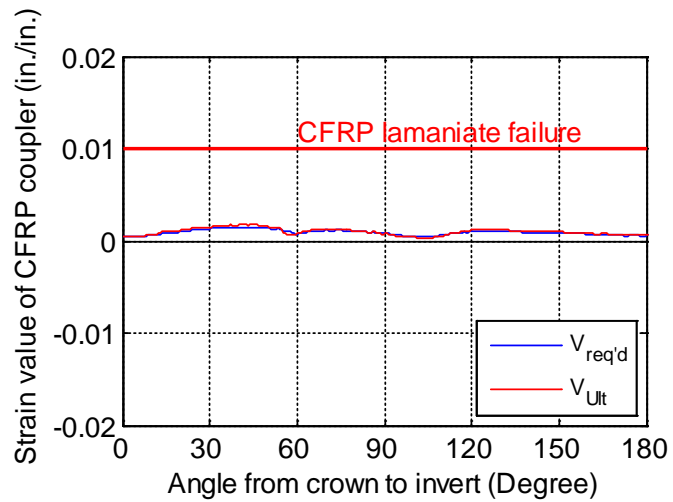
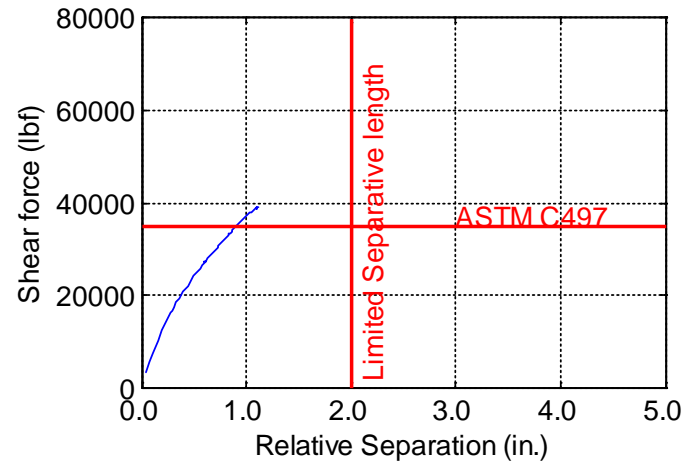
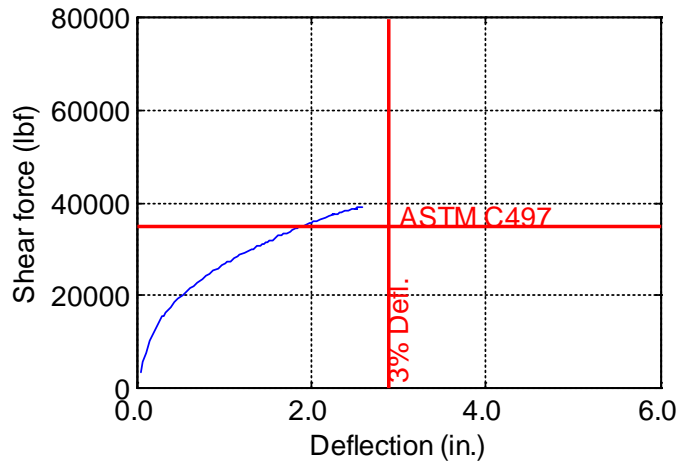


Figure B-178. TW-096-09-0.75

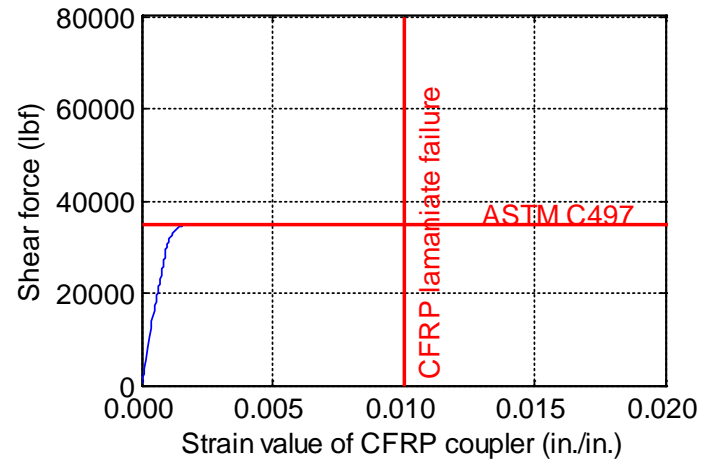
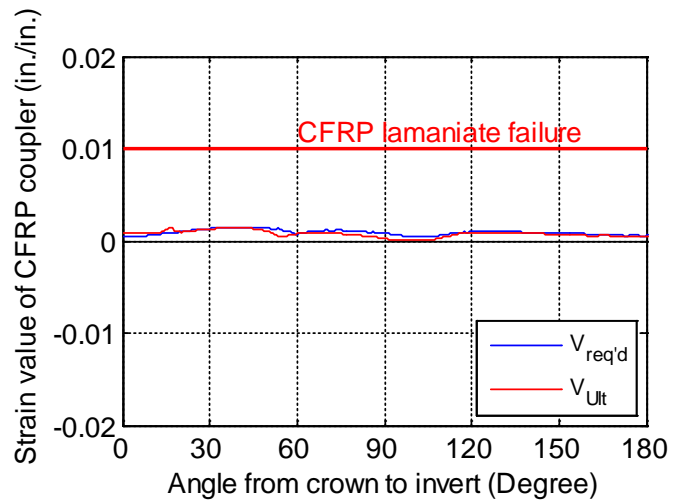
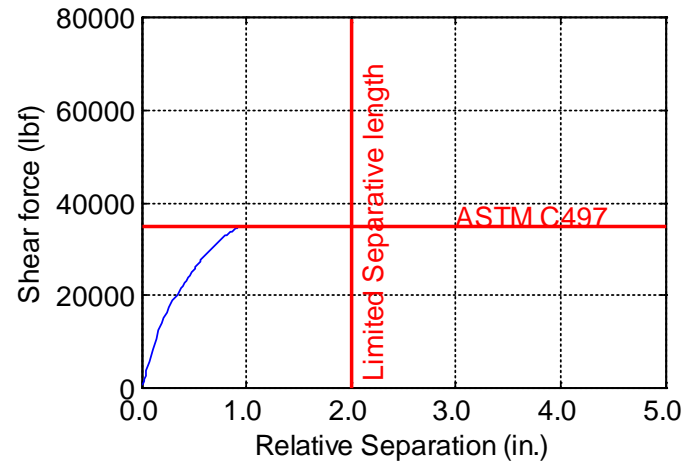
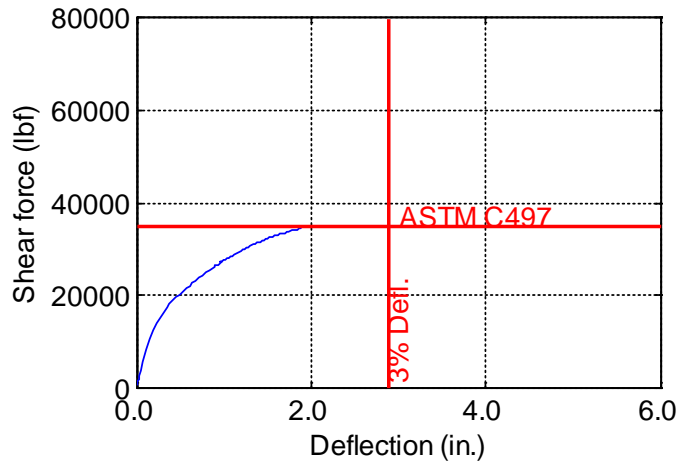


Figure B-179. TW-096-09-0.875

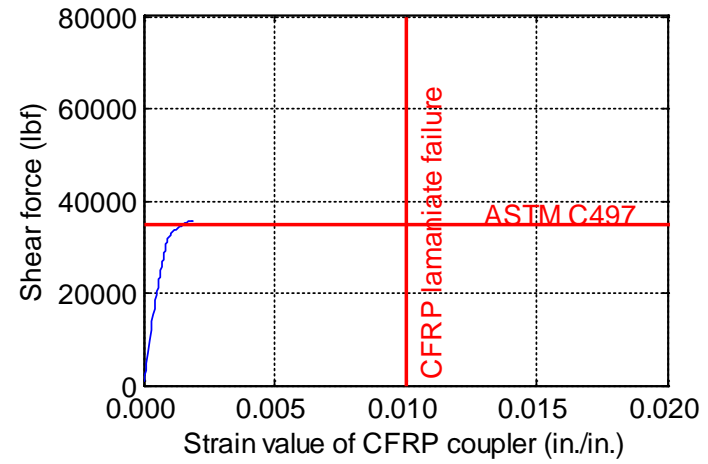
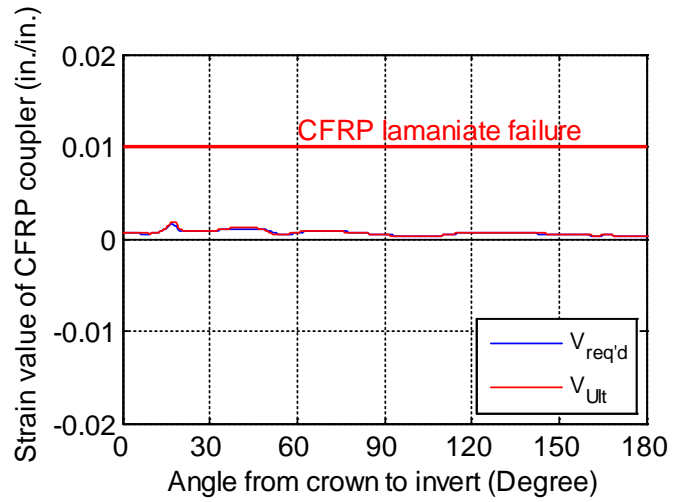
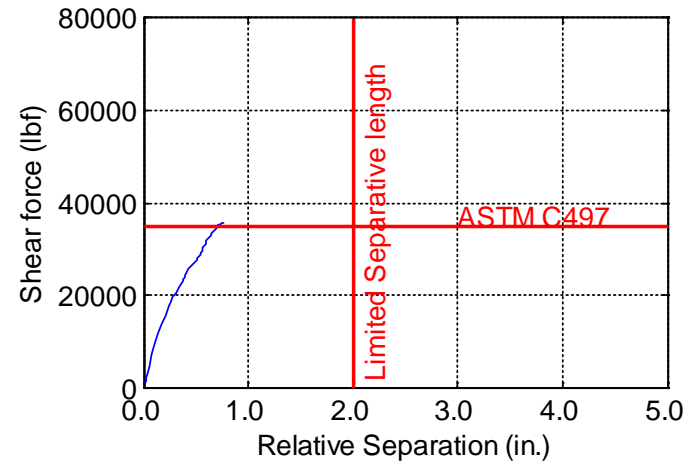
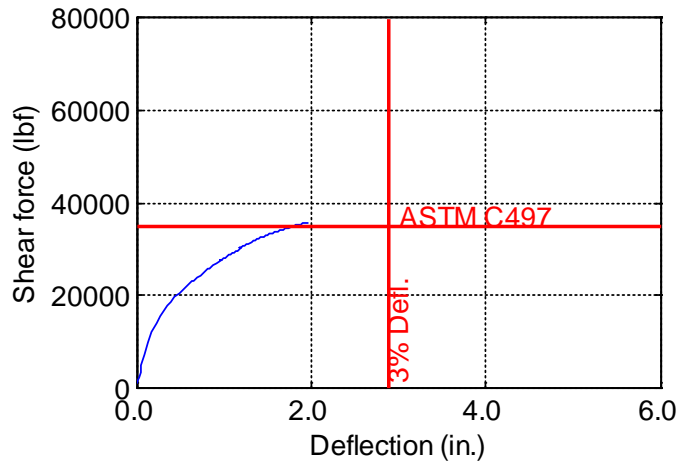


Figure B-180. TW-096-09-1.0

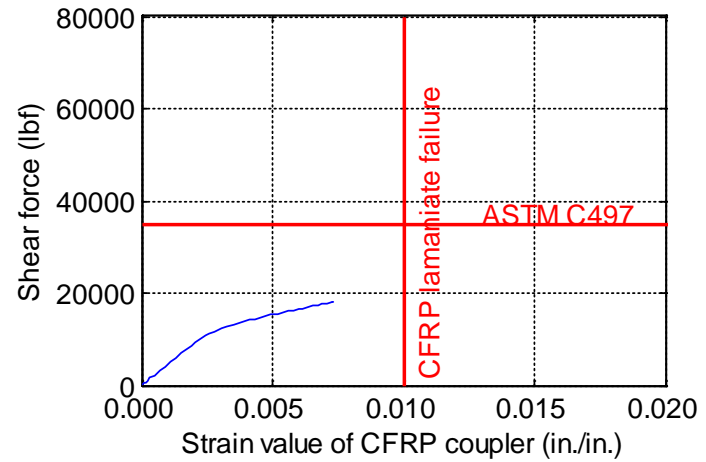
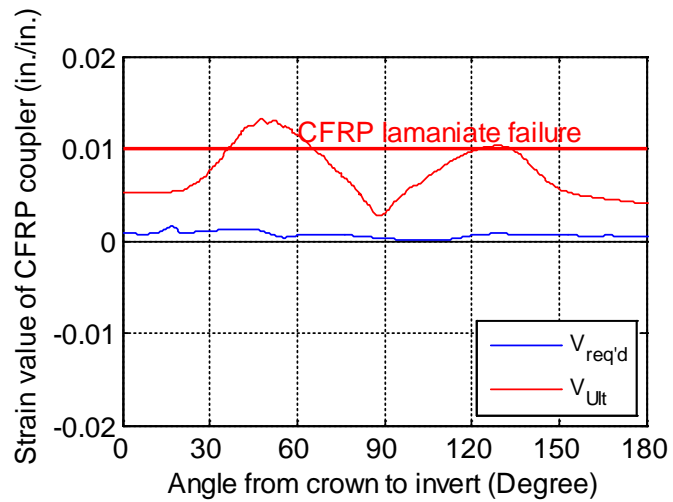
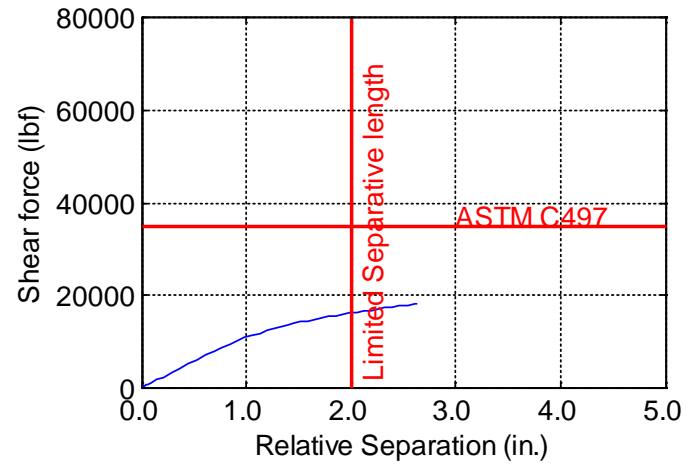
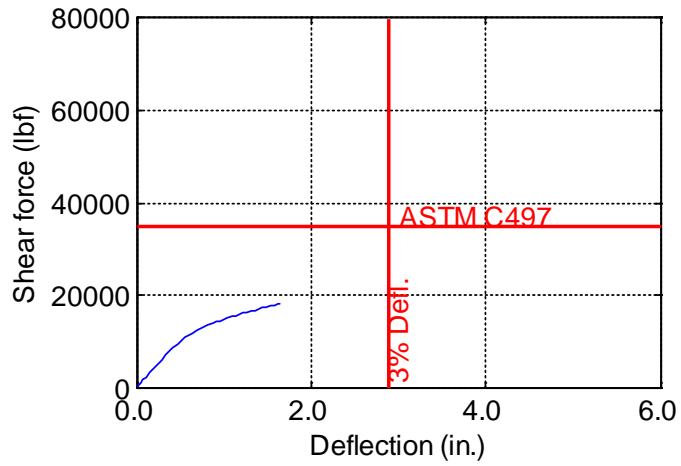


Figure B-181. TW-096-12-0.125

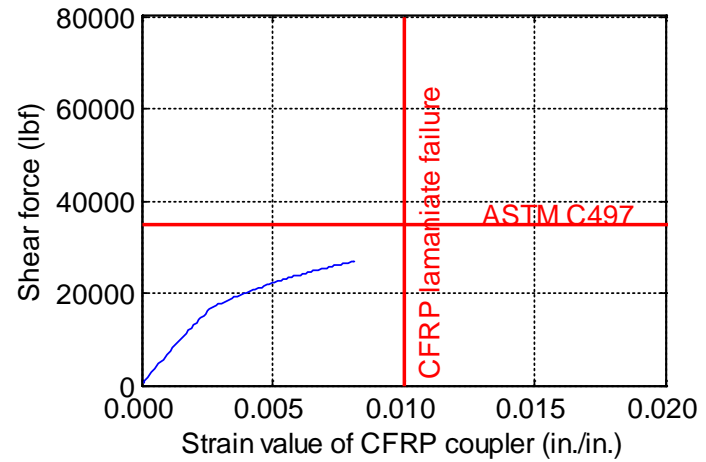
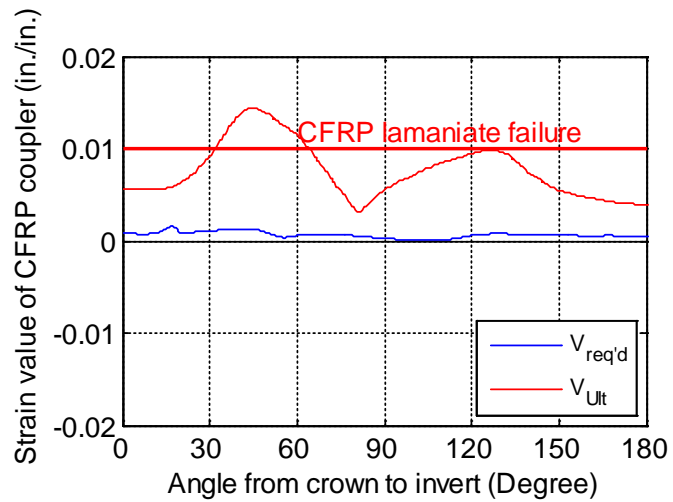
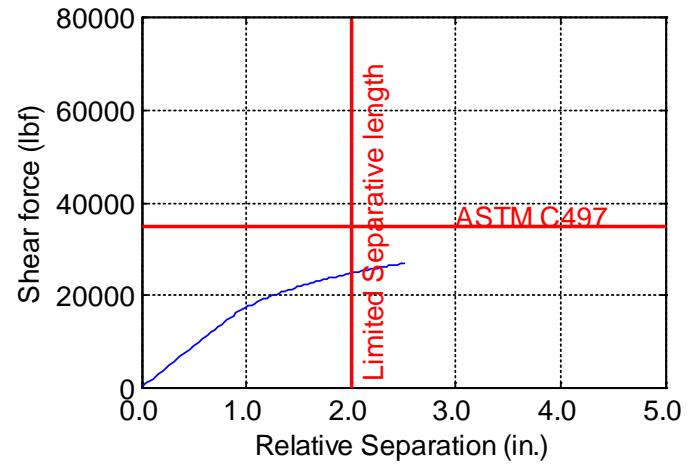
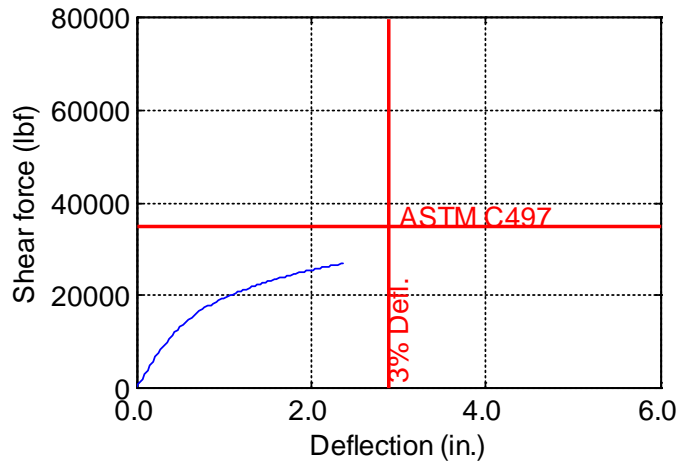


Figure B-182. TW-096-12-0.1875

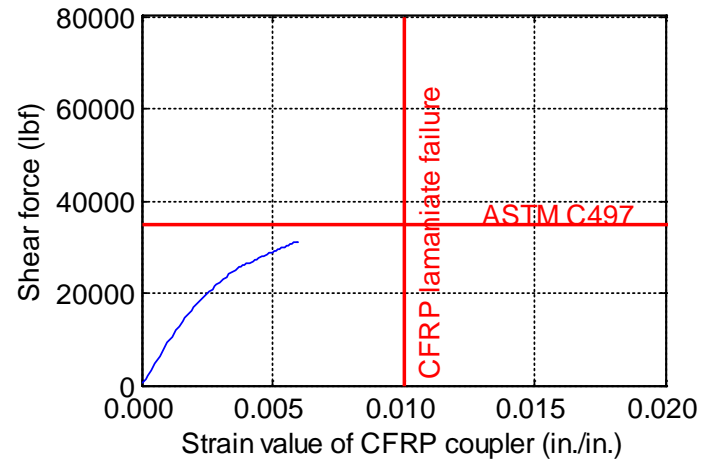
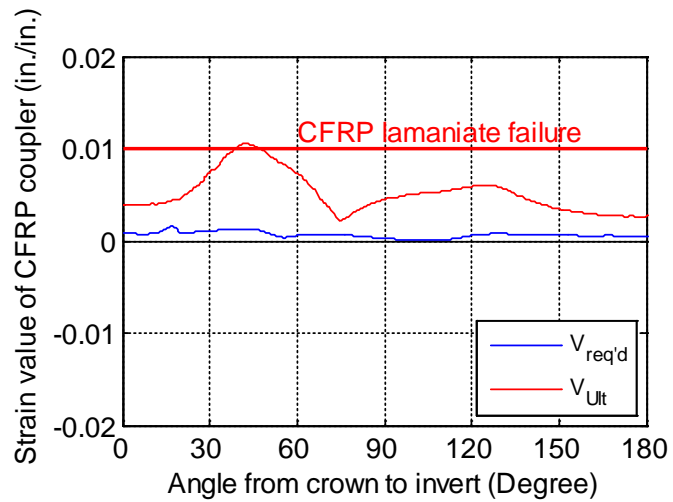
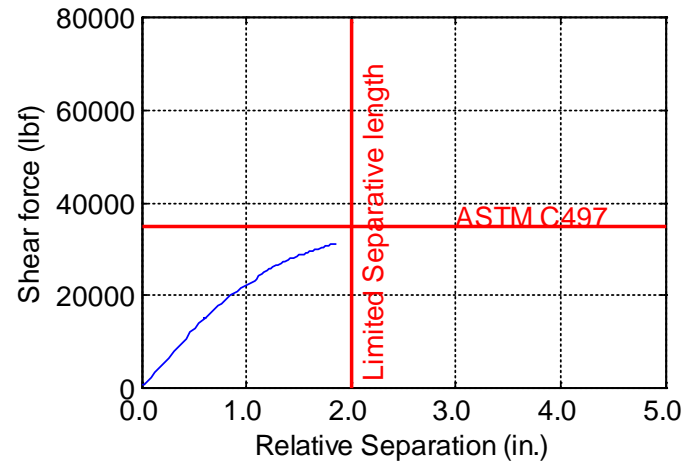
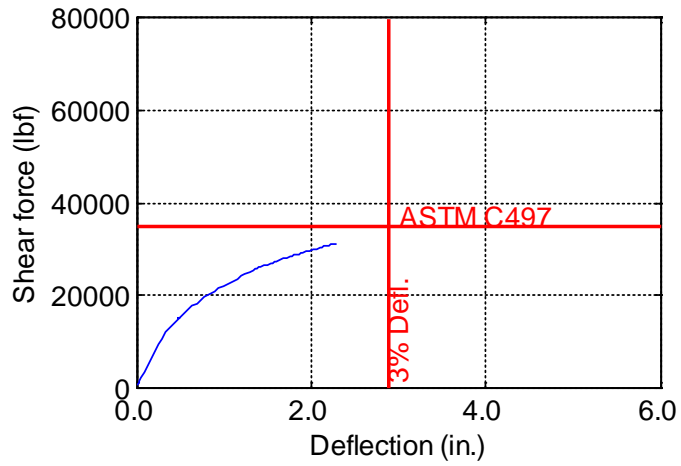


Figure B-183. TW-096-12-0.25

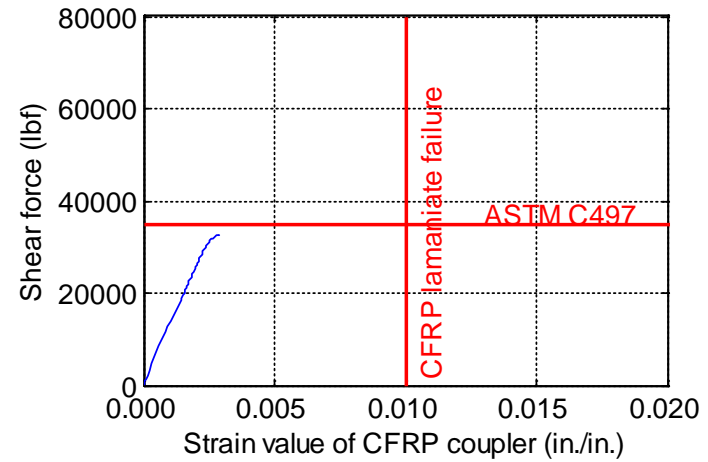
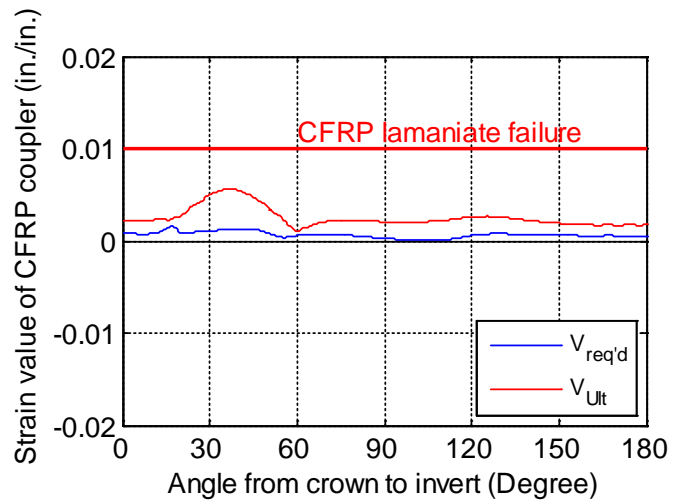
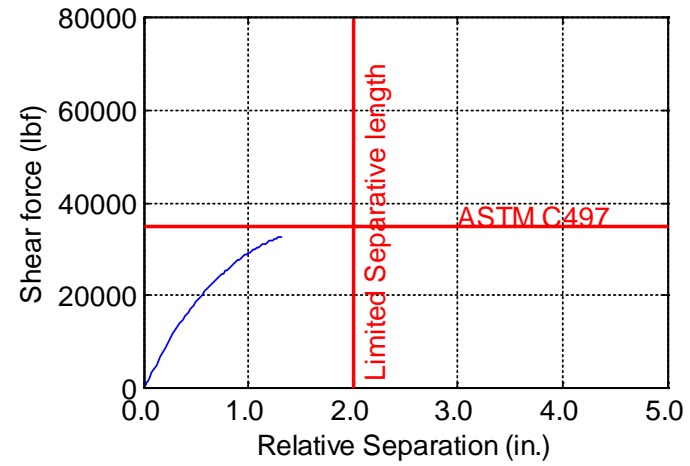
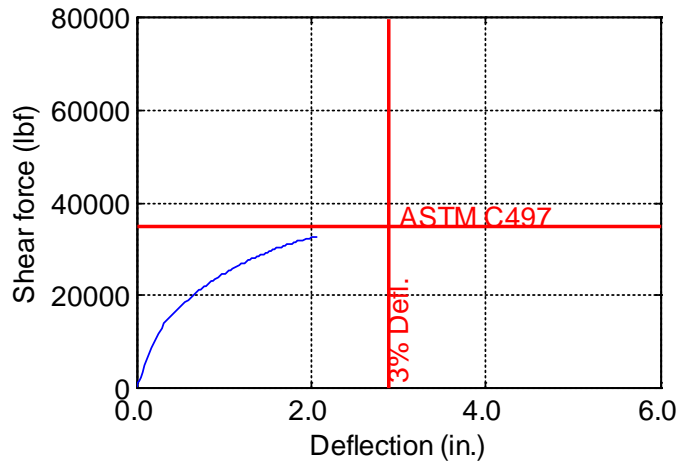


Figure B-184. TW-096-12-0.375

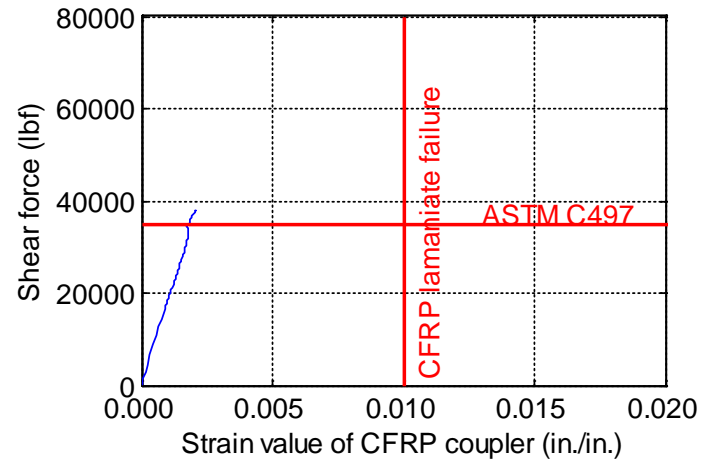
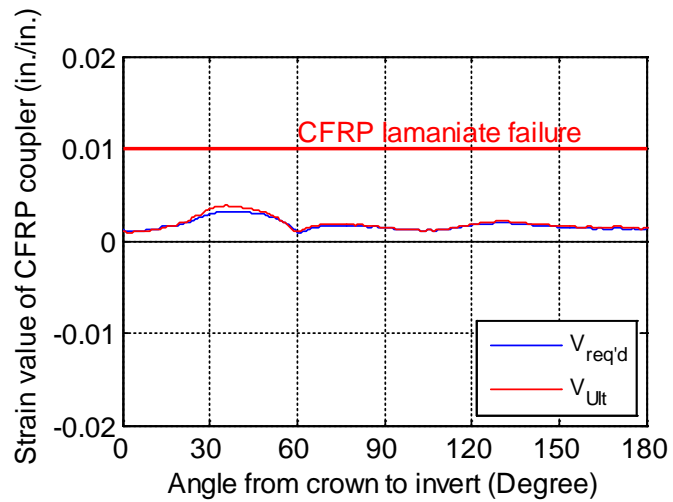
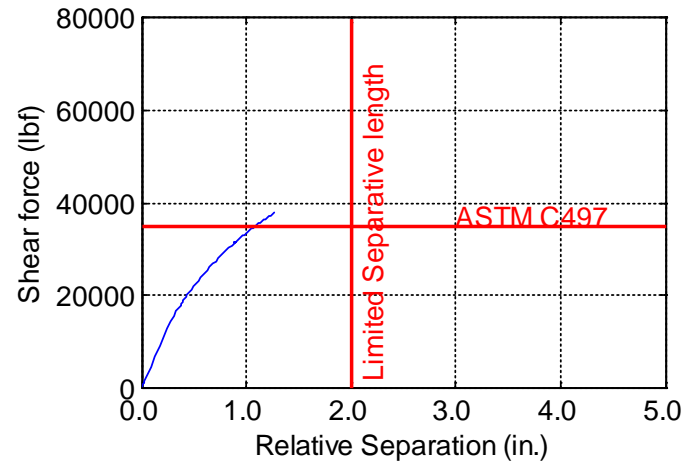
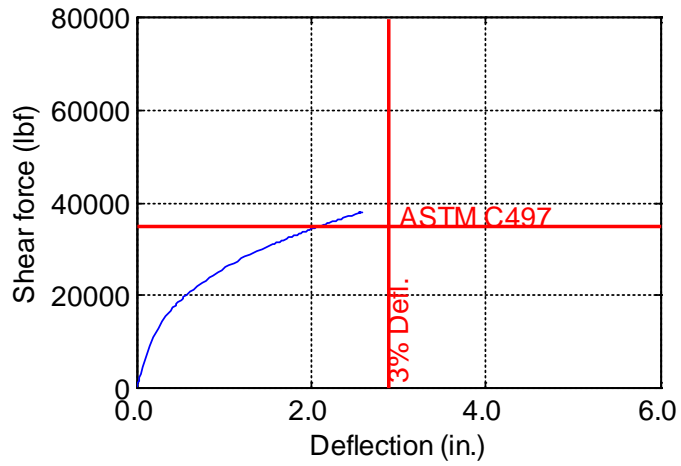


Figure B-185. TW-096-12-0.5

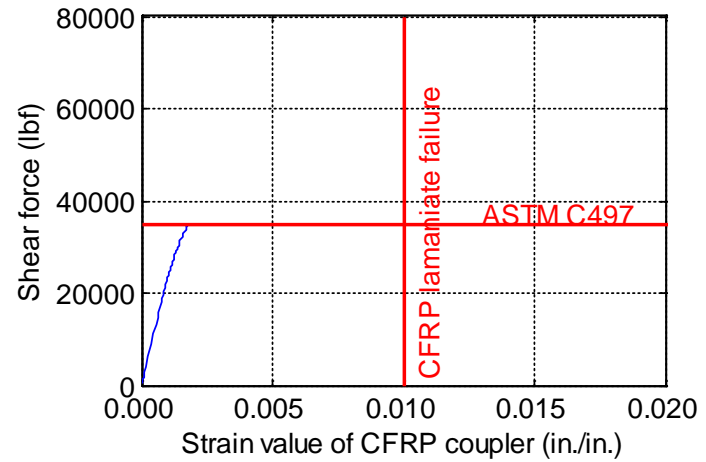
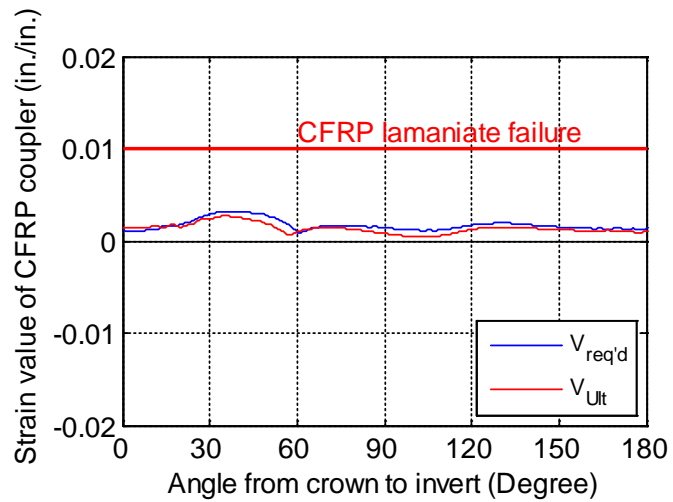
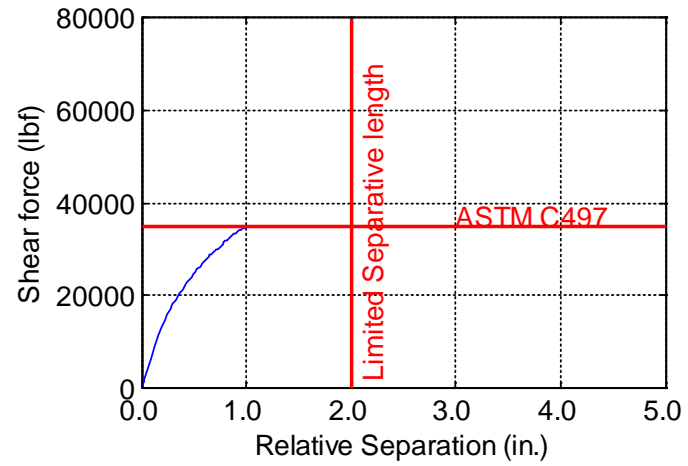
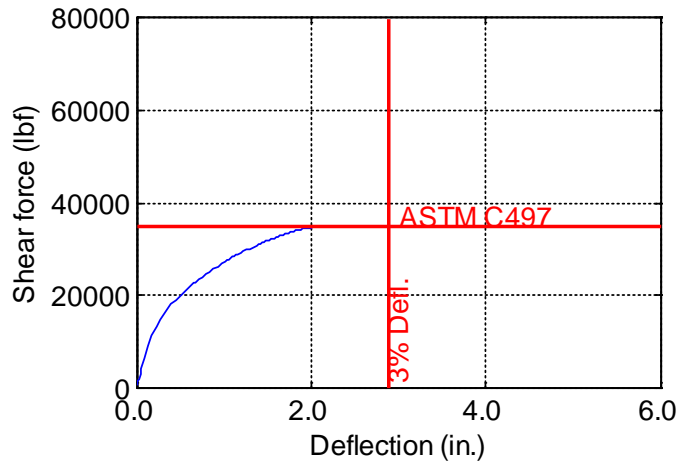


Figure B-186. TW-096-12-0.625

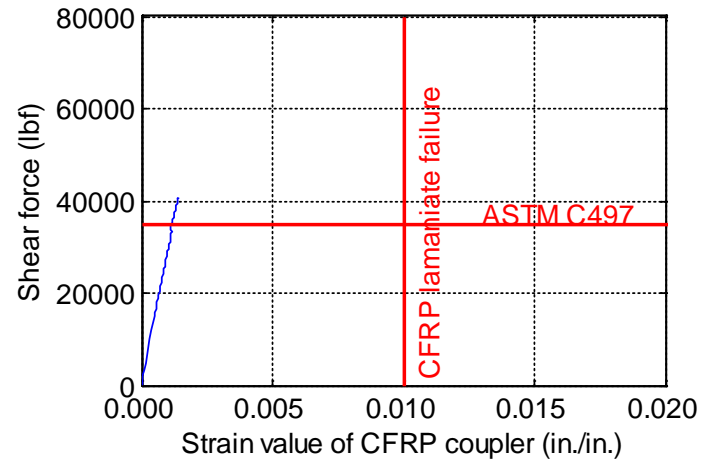
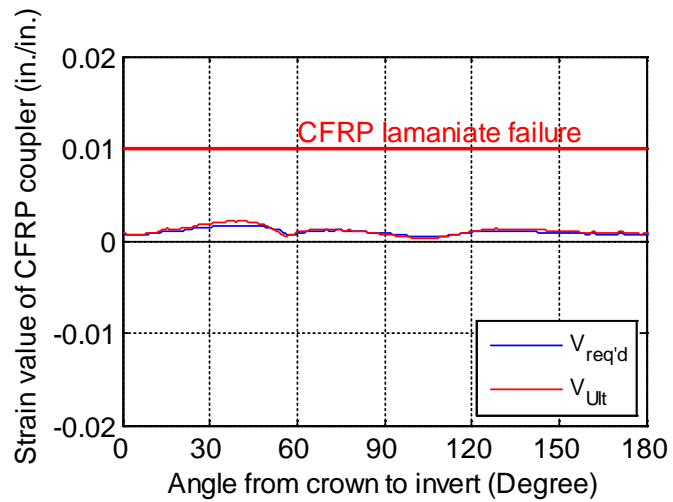
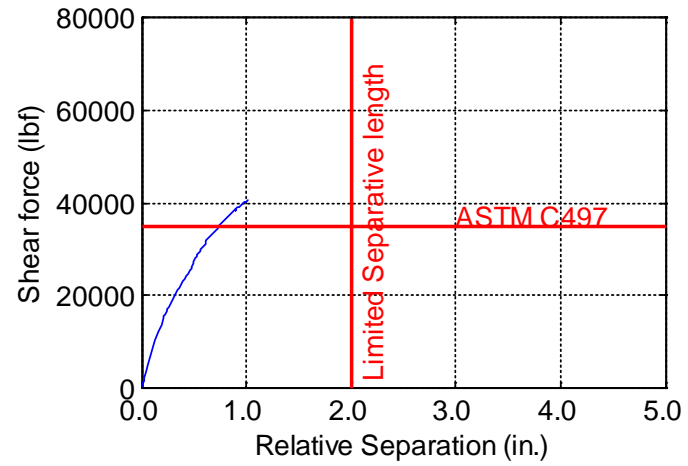
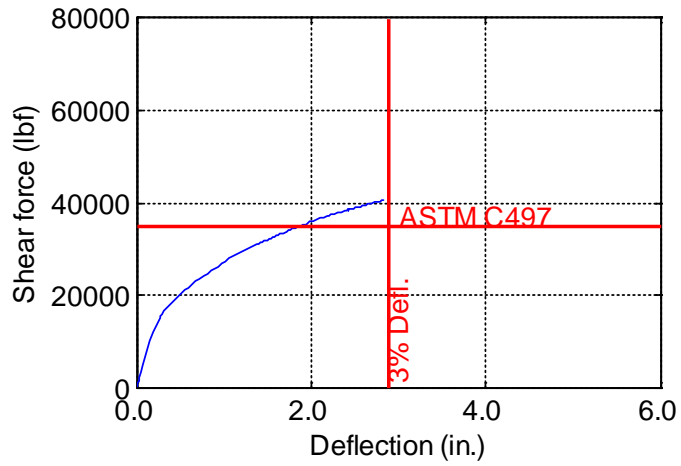


Figure B-187. TW-096-12-0.75

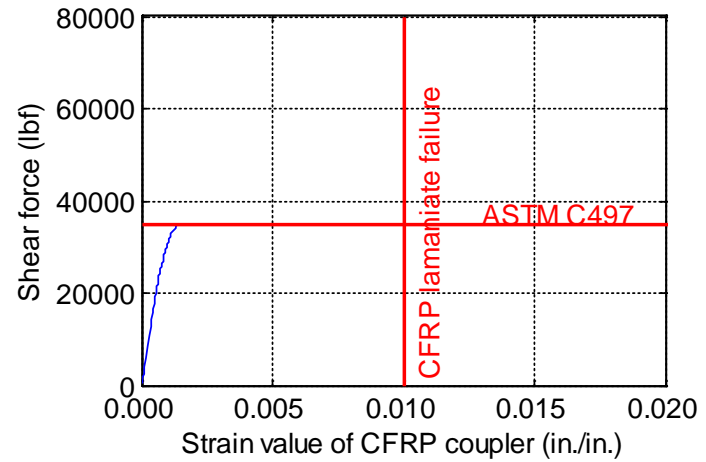
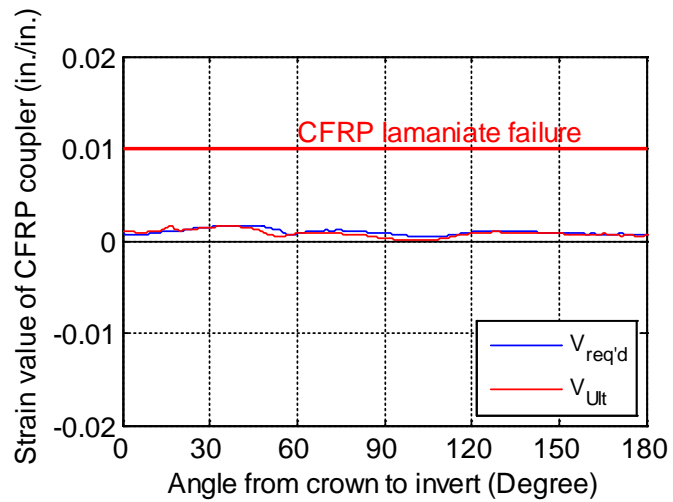
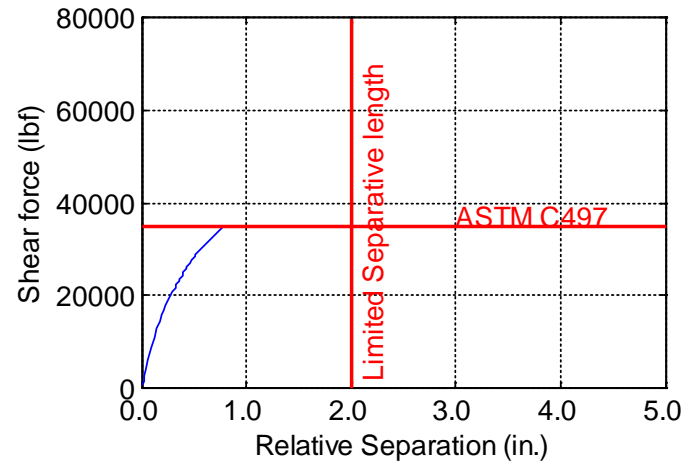
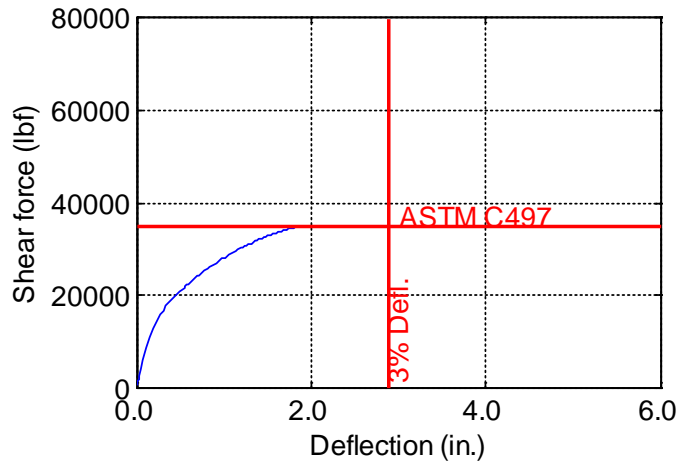


Figure B-188. TW-096-12-0.875

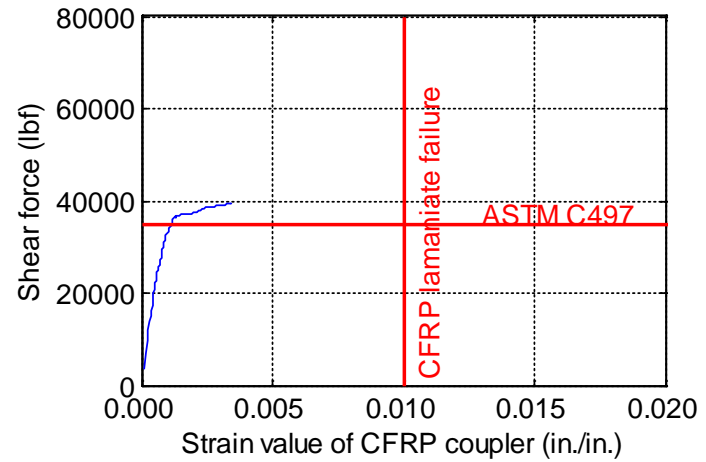
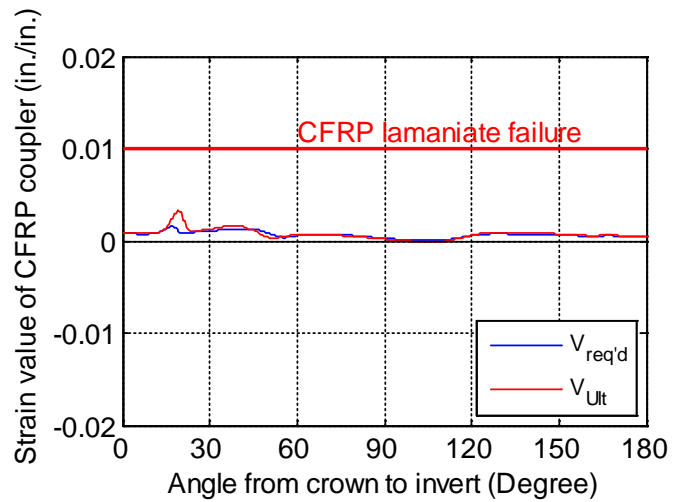
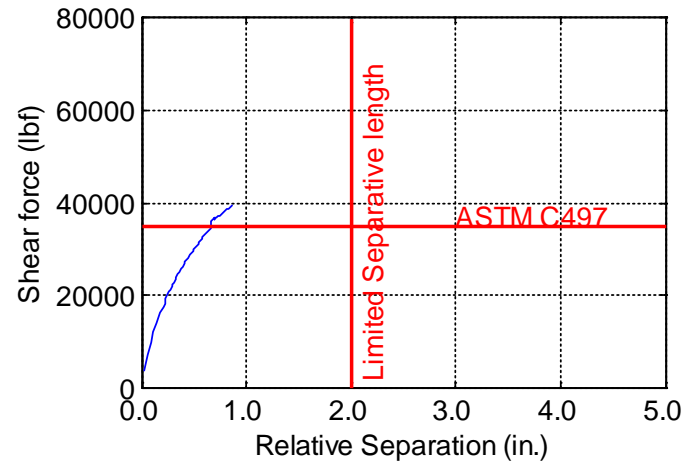
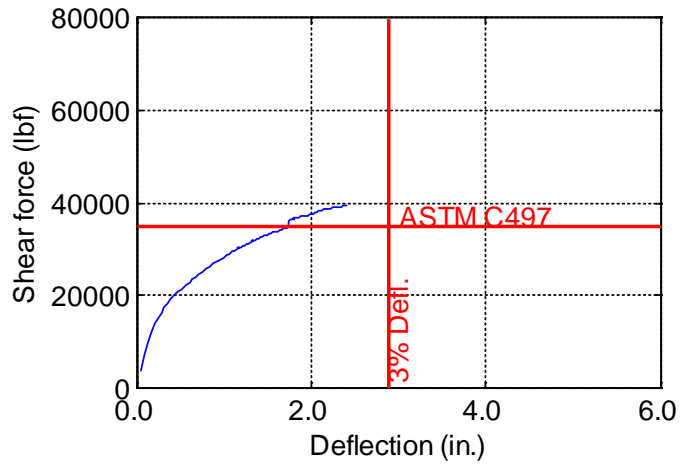


Figure B-189. TW-096-12-1.0

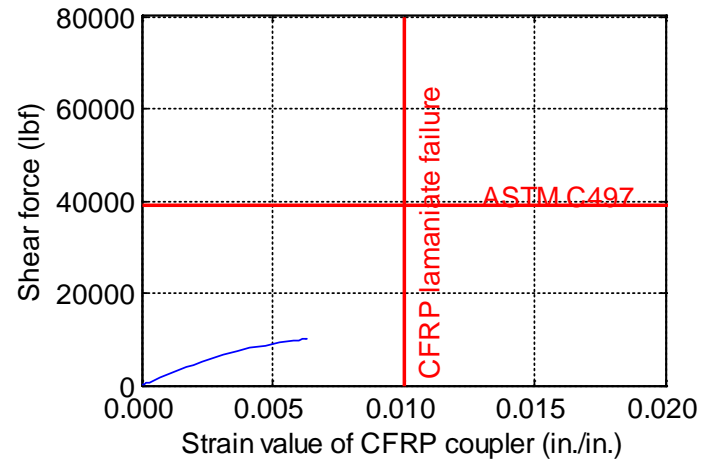
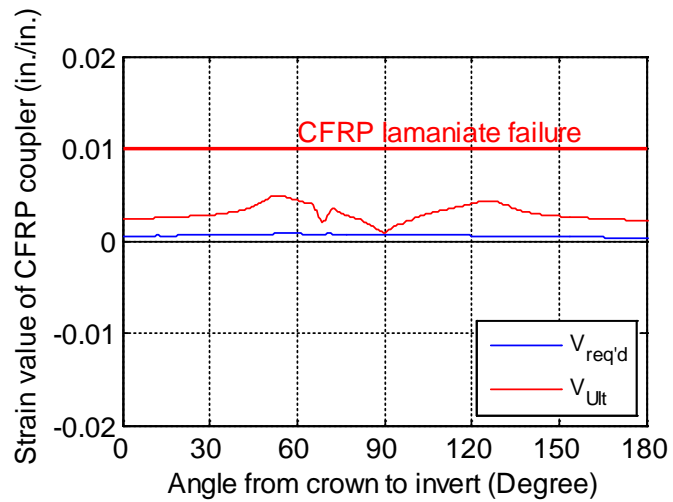
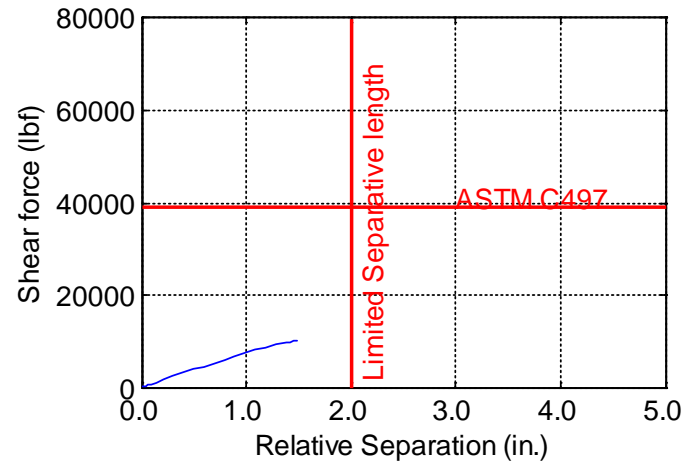
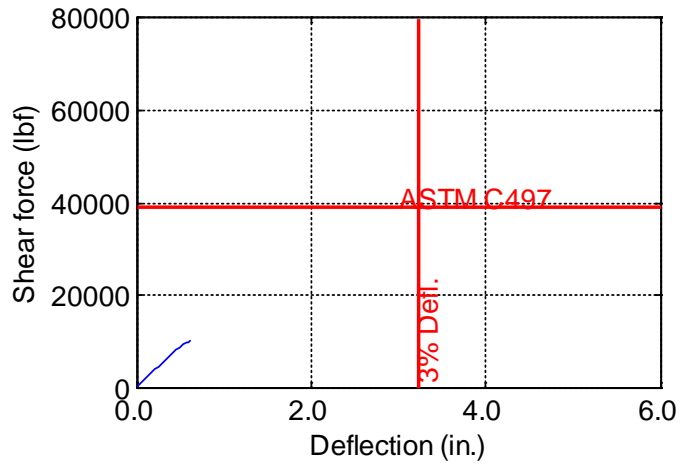


Figure B-190. TW-108-06-0.125

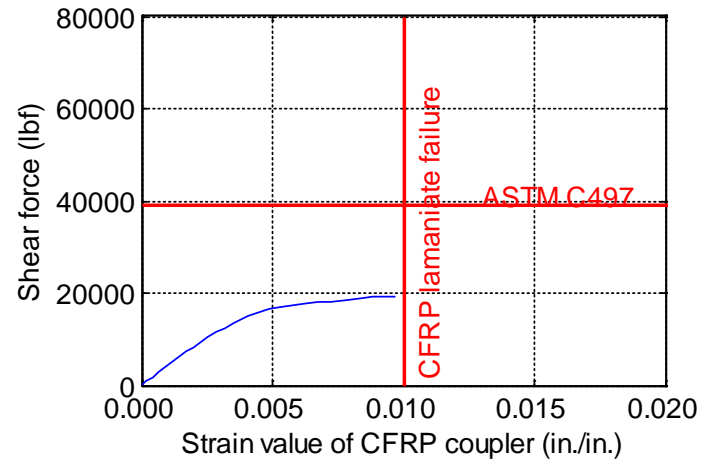
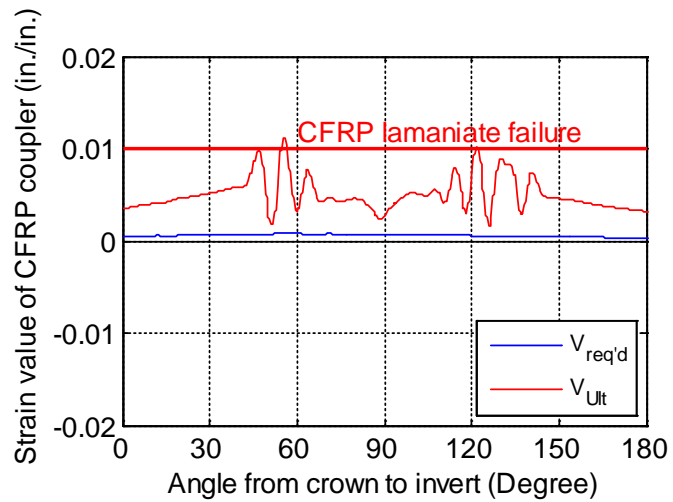
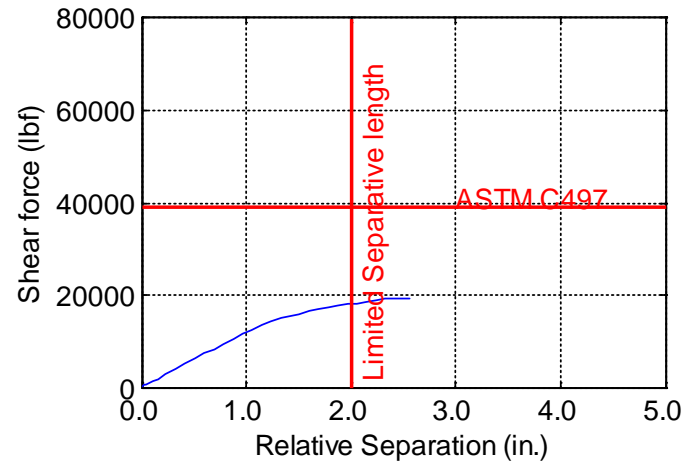
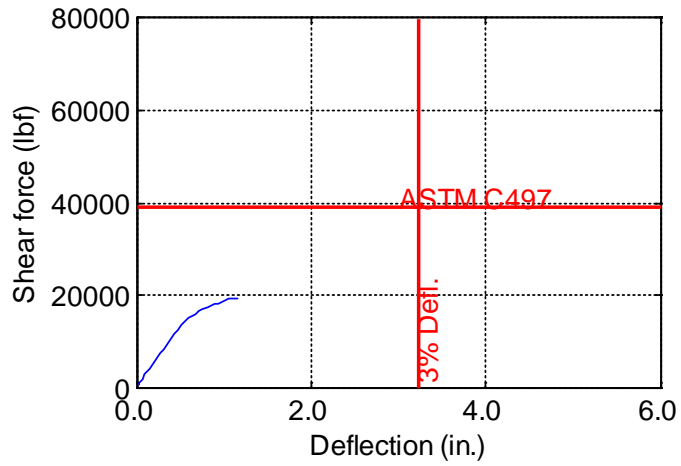


Figure B-191. TW-108-06-0.1875

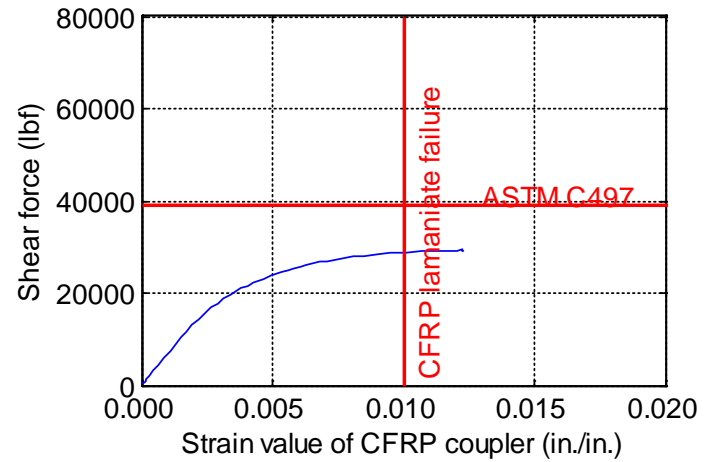
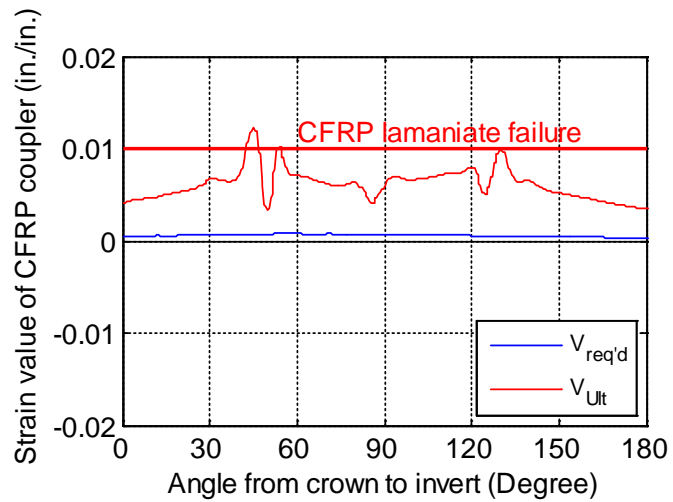
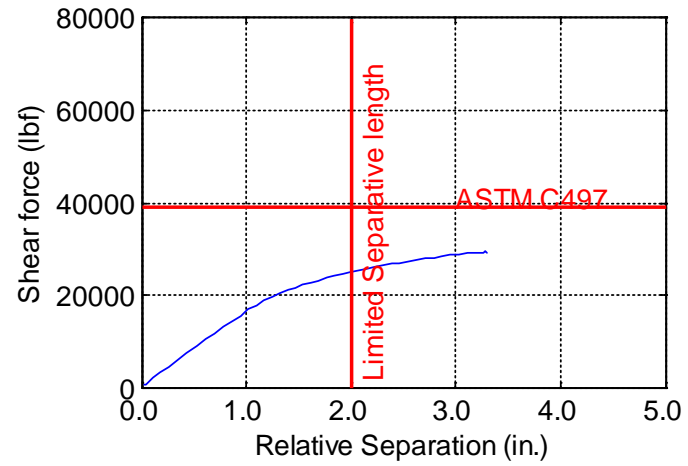
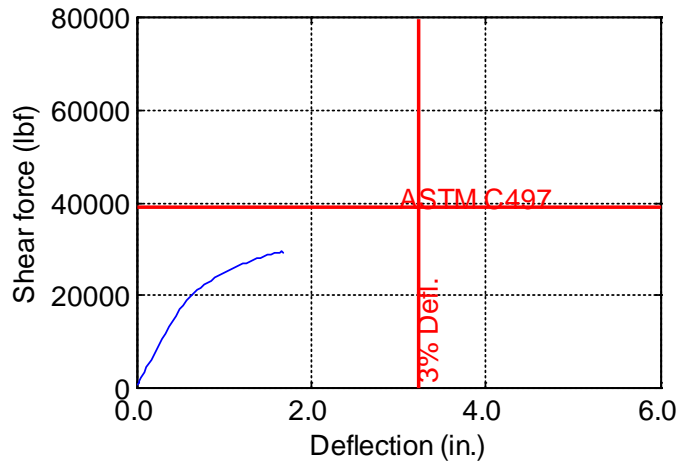


Figure B-192. TW-108-06-0.25

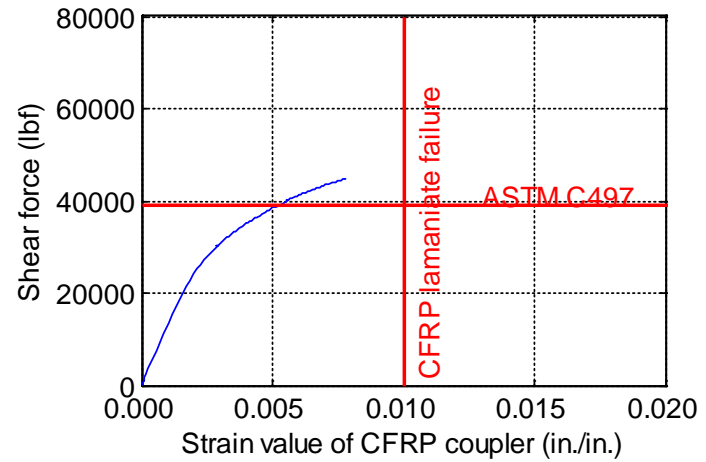
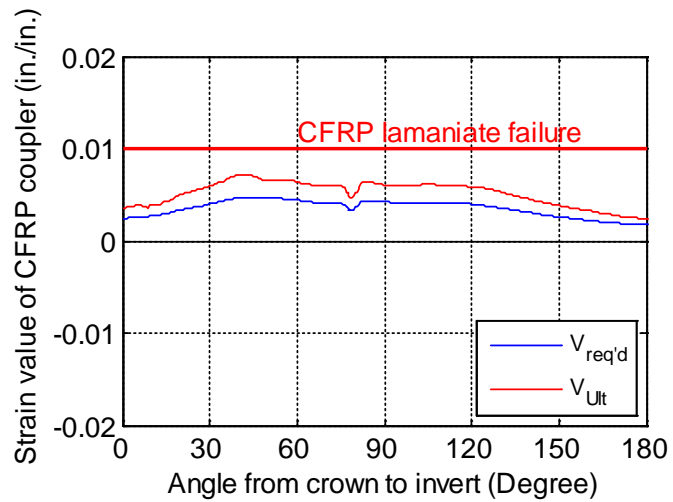
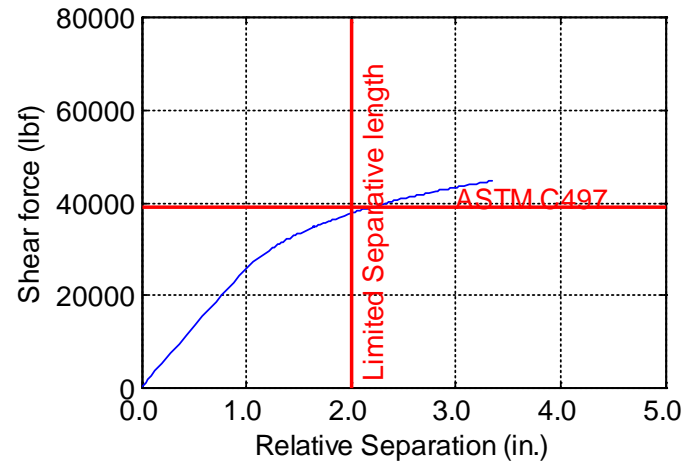
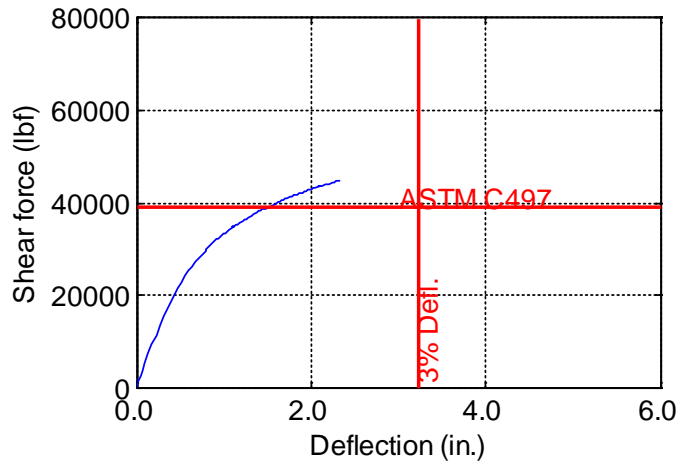


Figure B-193. TW-108-06-0.375

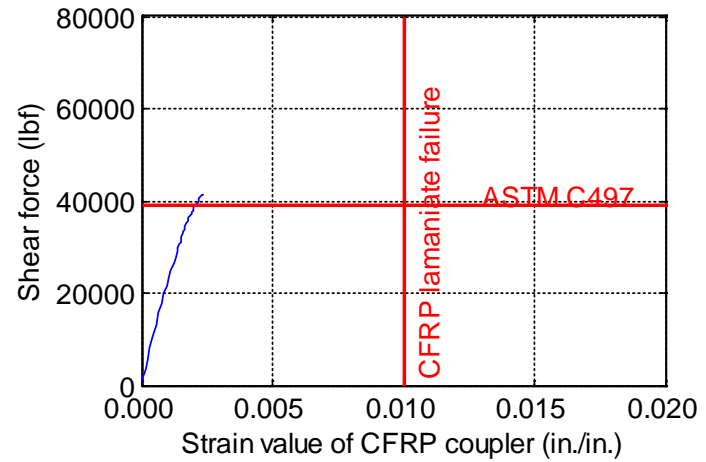
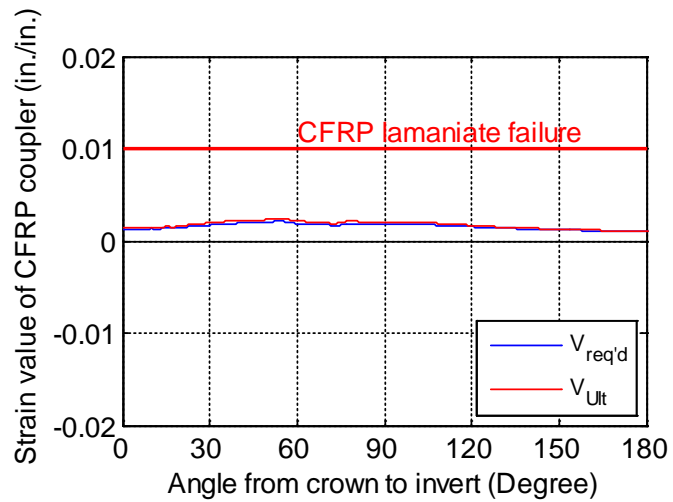
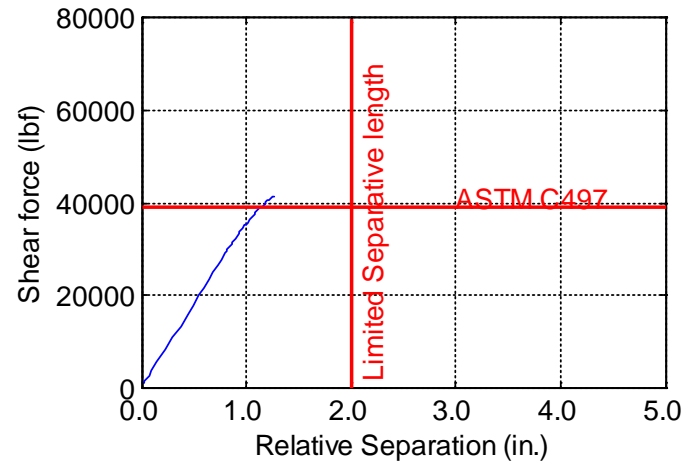
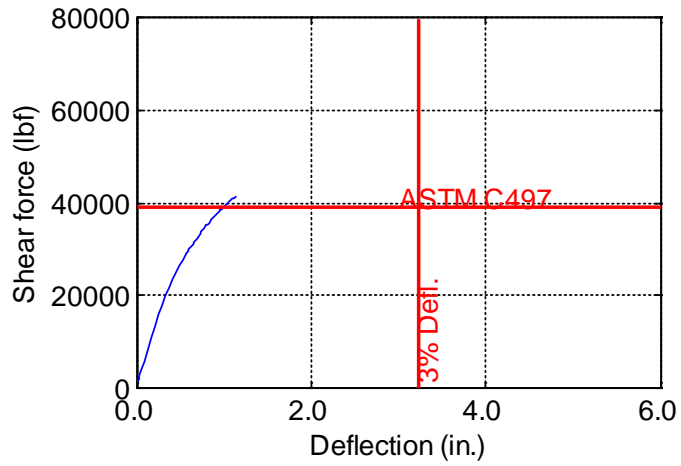


Figure B-194. TW-108-06-0.5

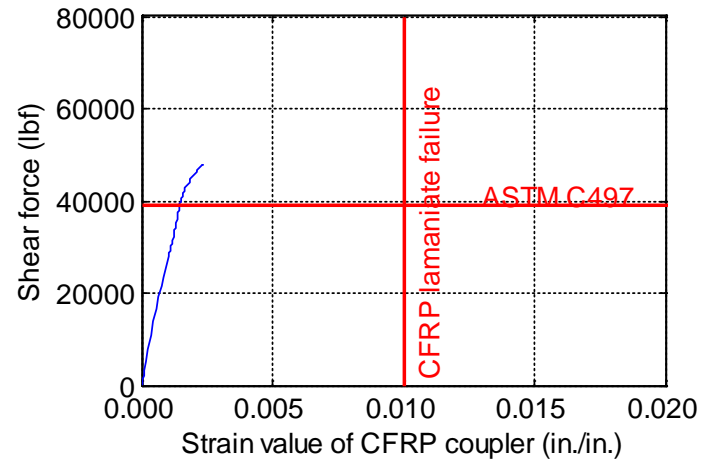
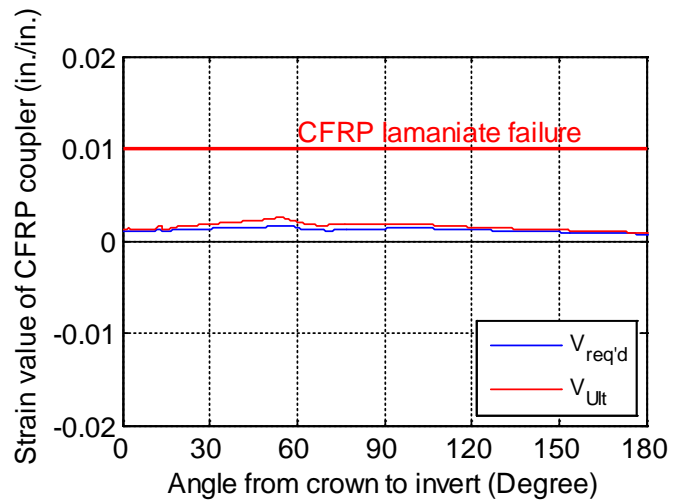
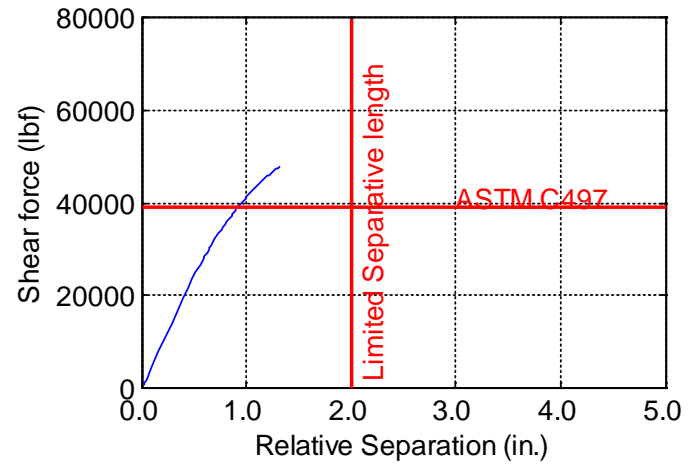
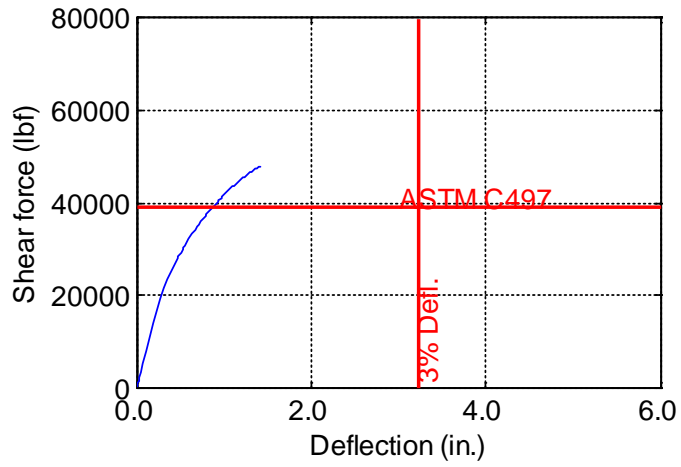


Figure B-195. TW-108-06-0.625

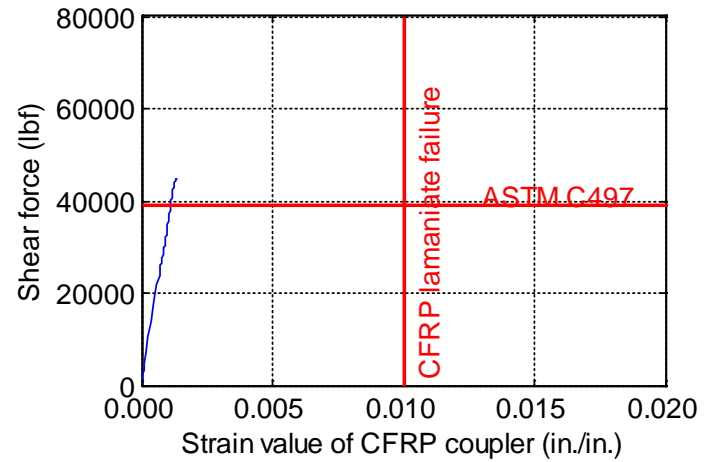
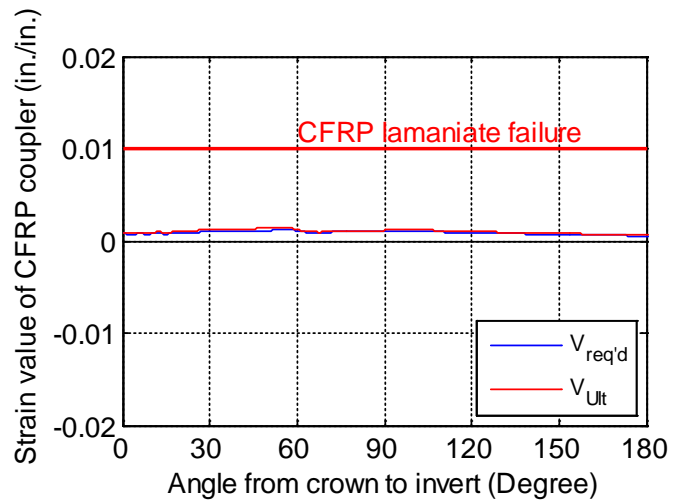
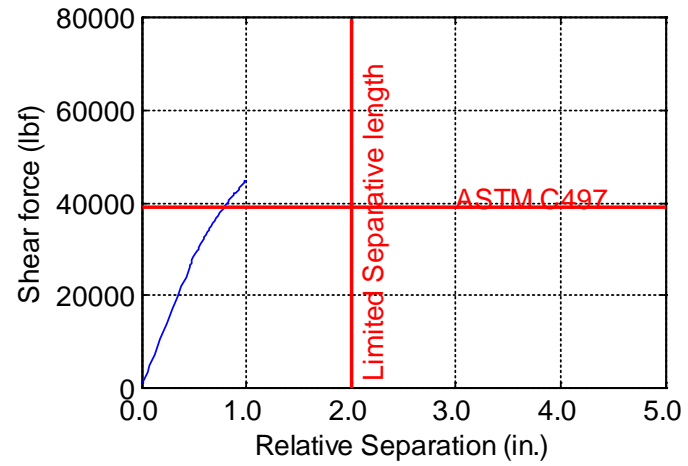
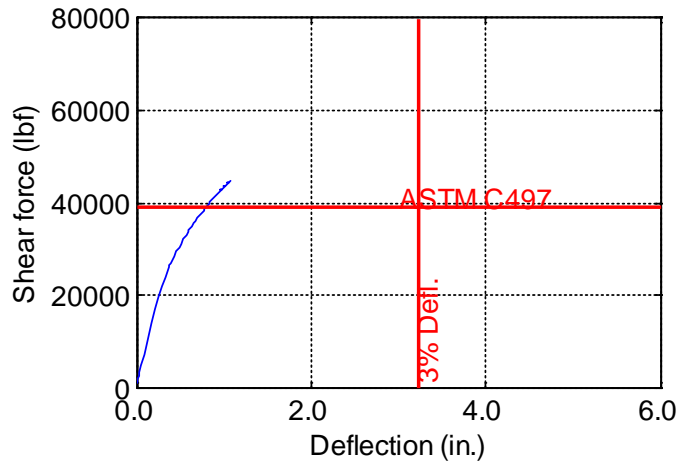


Figure B-196. TW-108-06-0.75

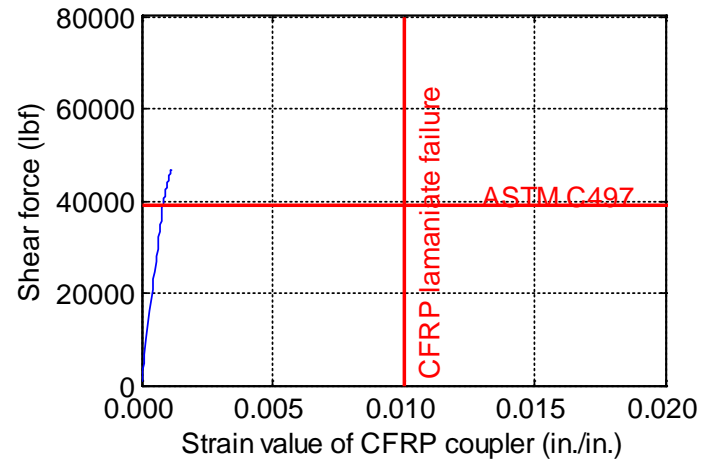
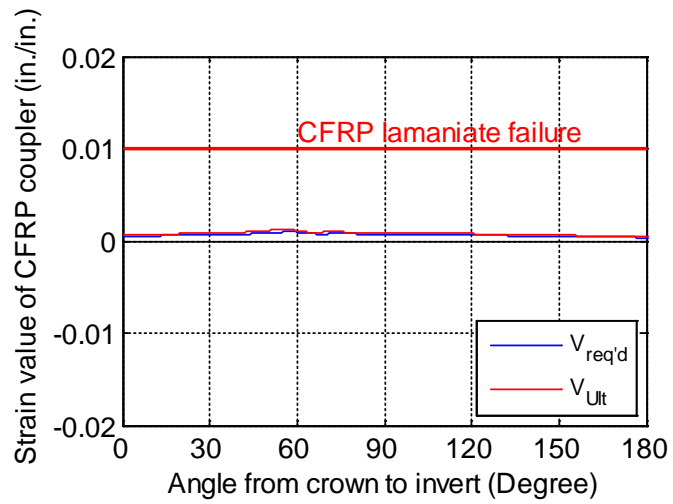
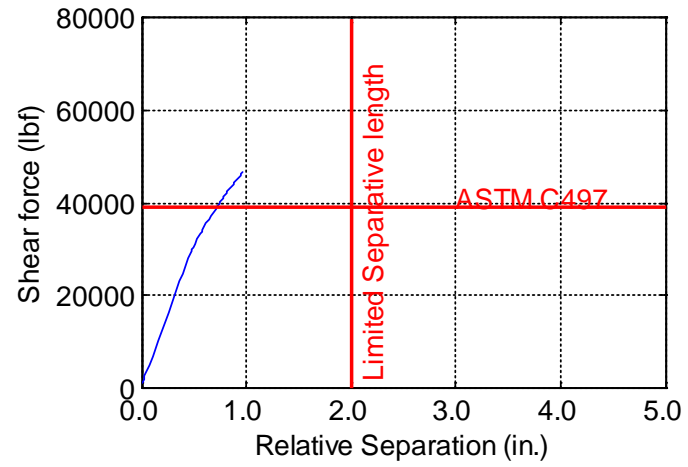
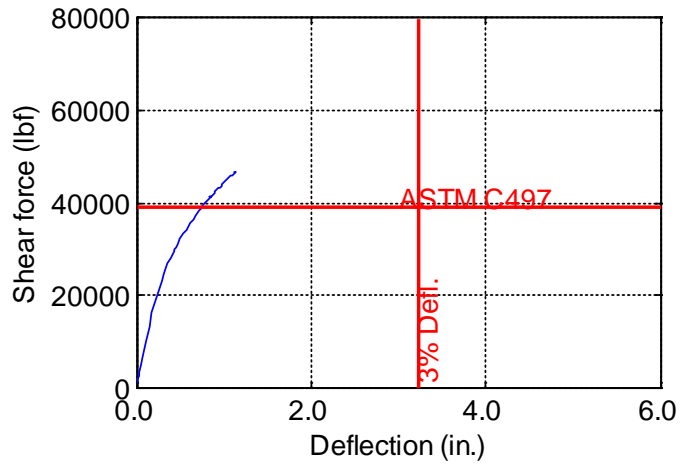


Figure B-197. TW-108-06-0.875

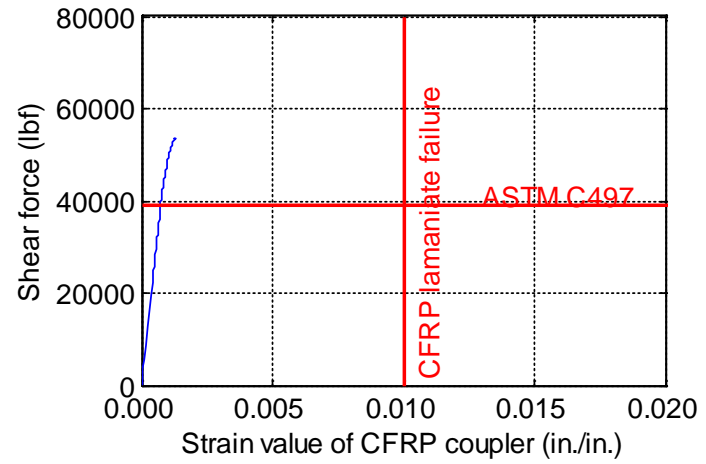
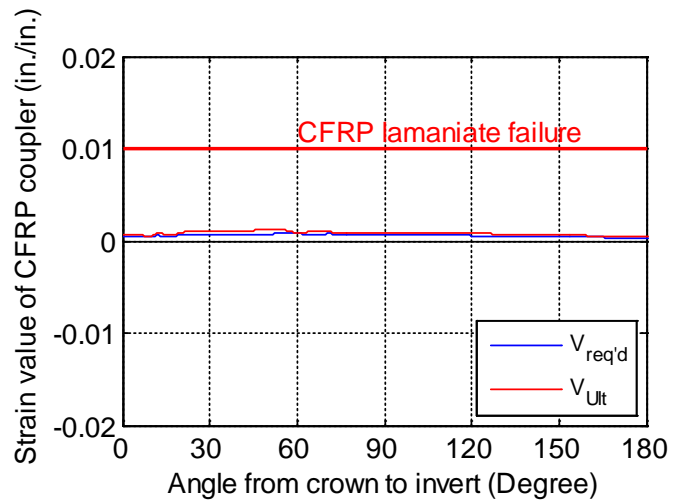
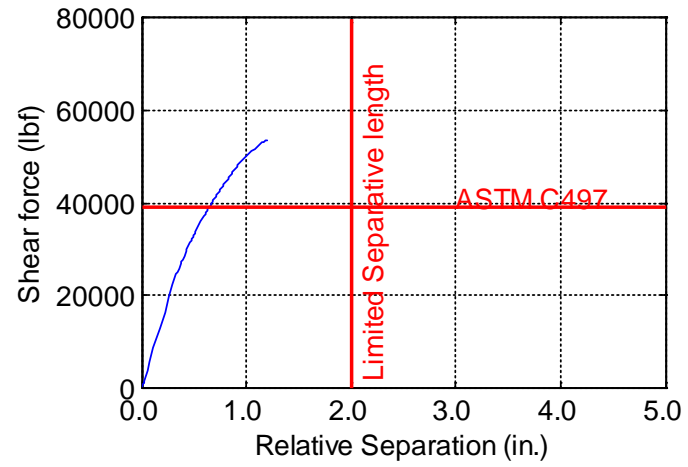
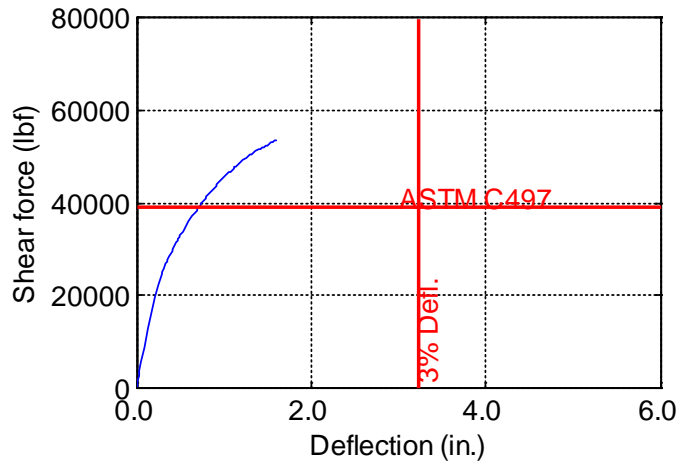


Figure B-198. TW-108-06-1.0

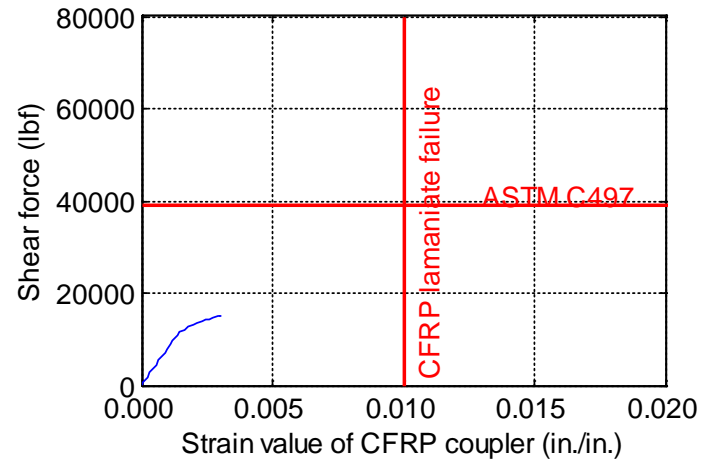
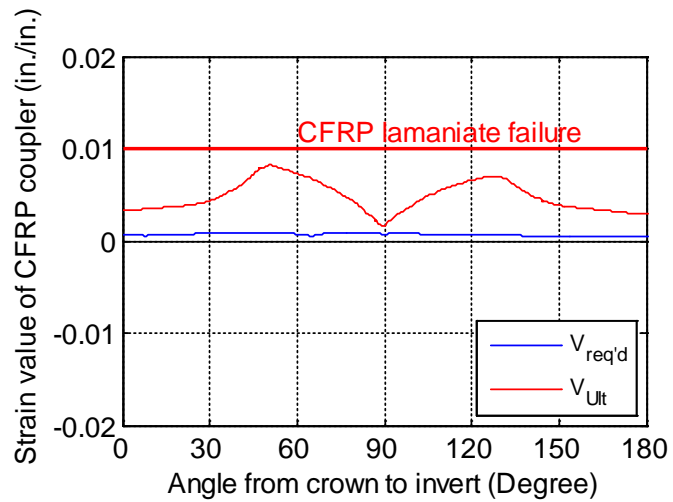
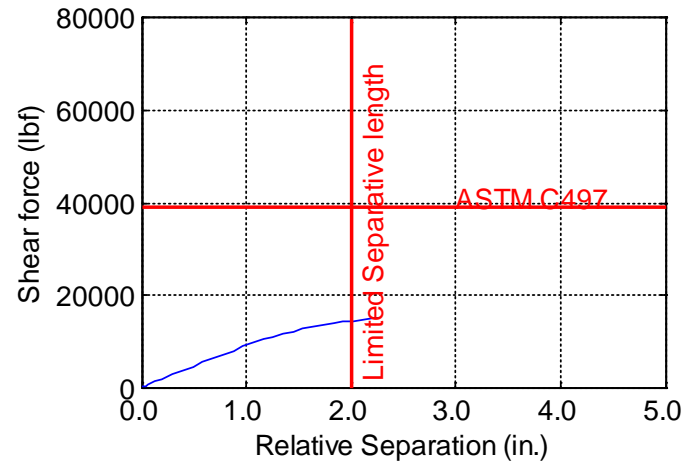
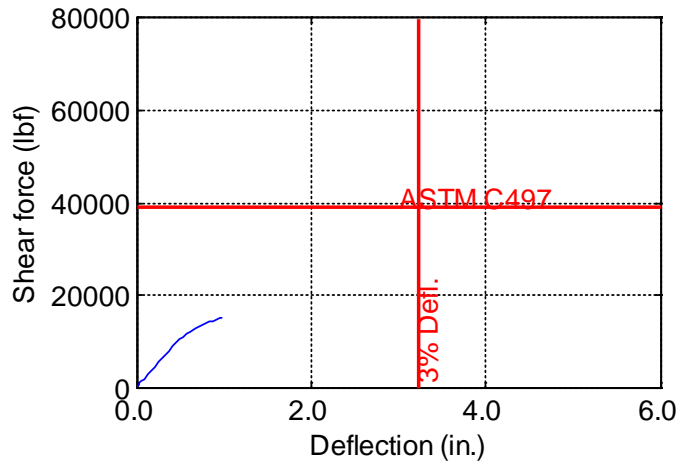


Figure B-199. TW-108-09-0.125

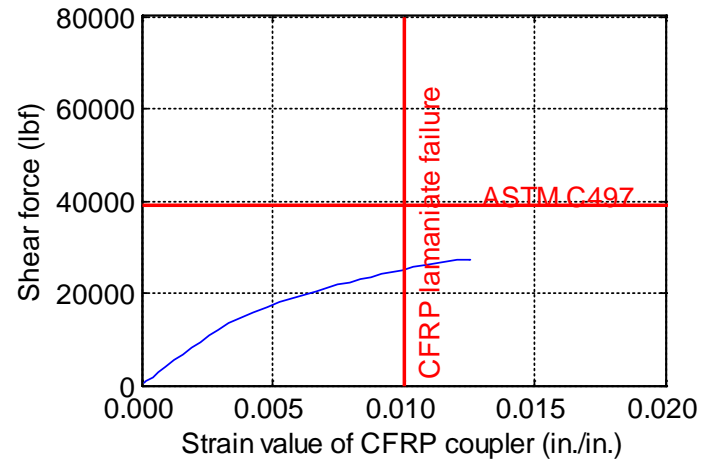
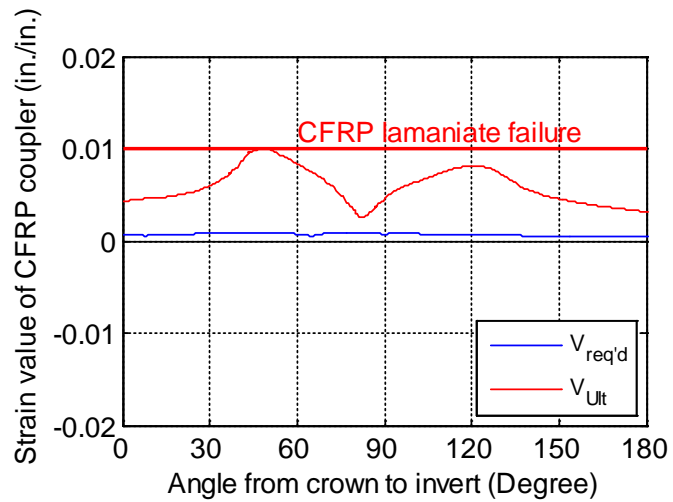
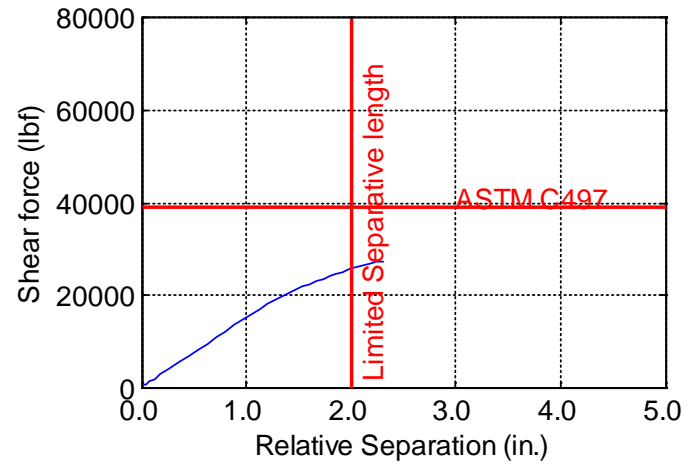
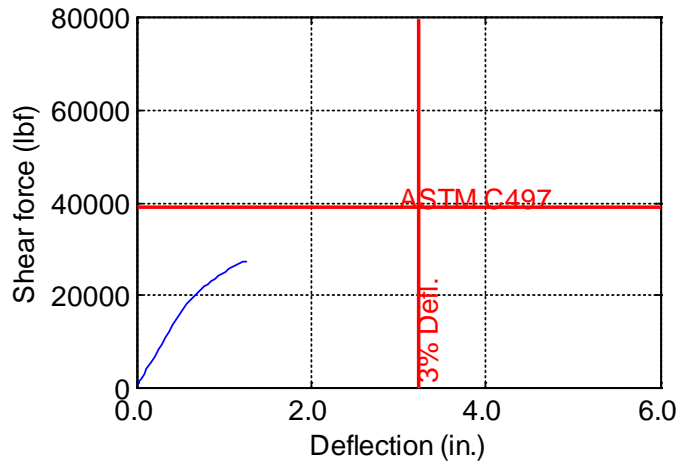


Figure B-200. TW-108-09-0.1875

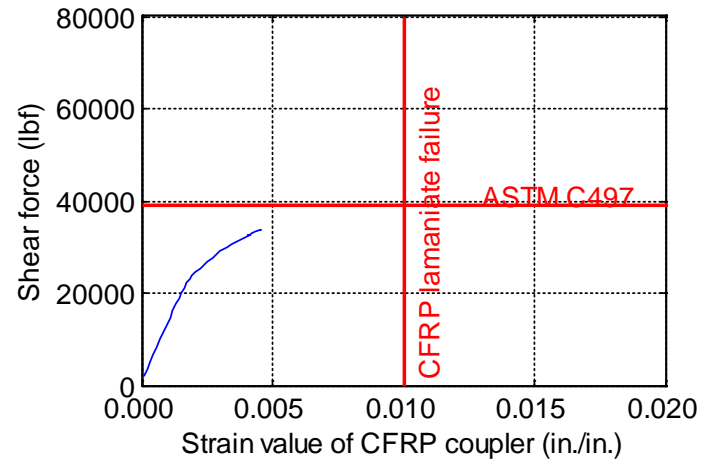
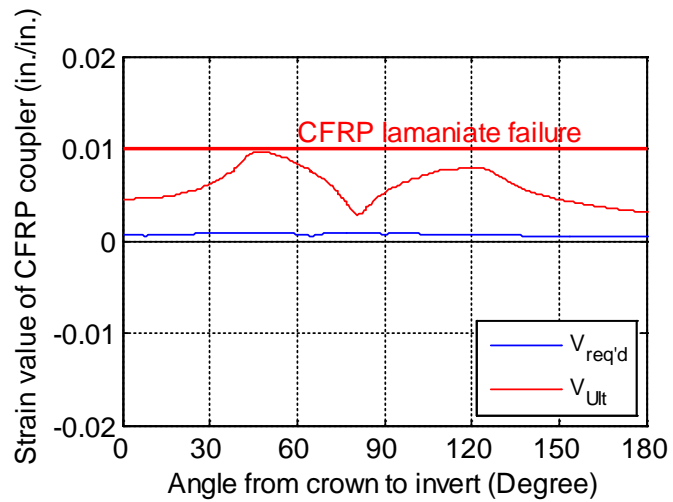
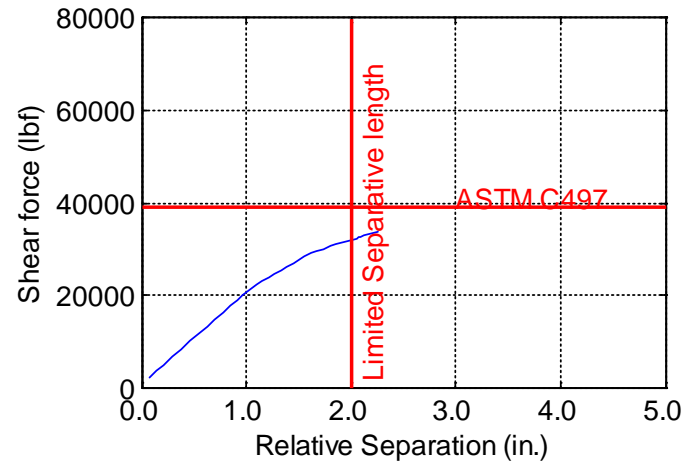
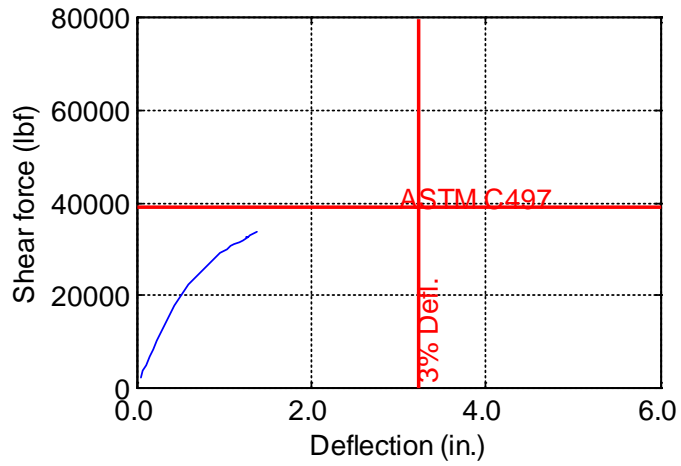


Figure B-201. TW-108-09-0.25

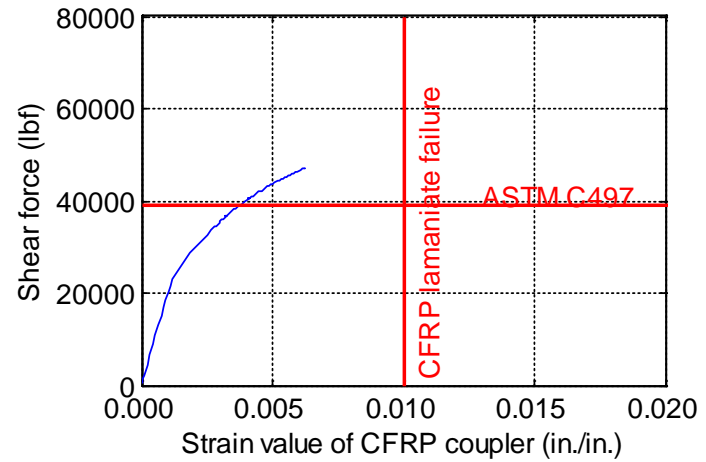
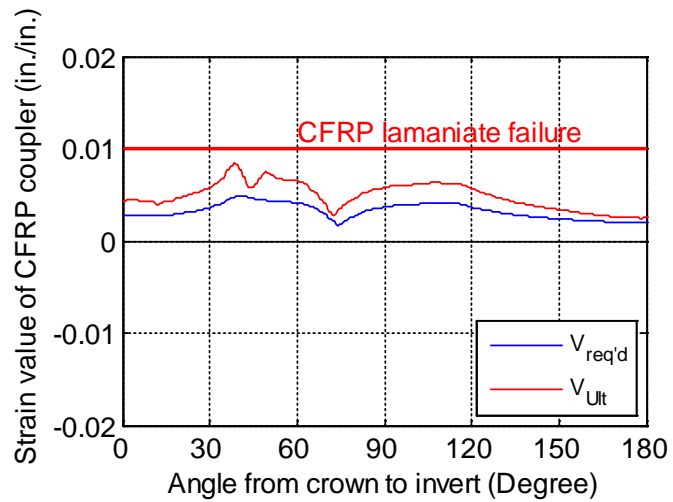
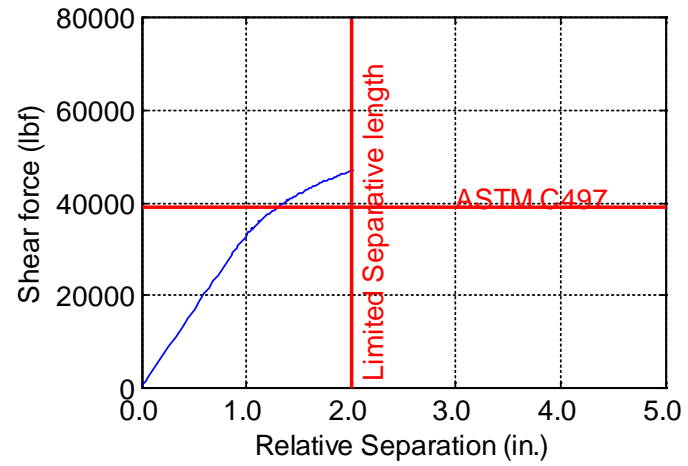
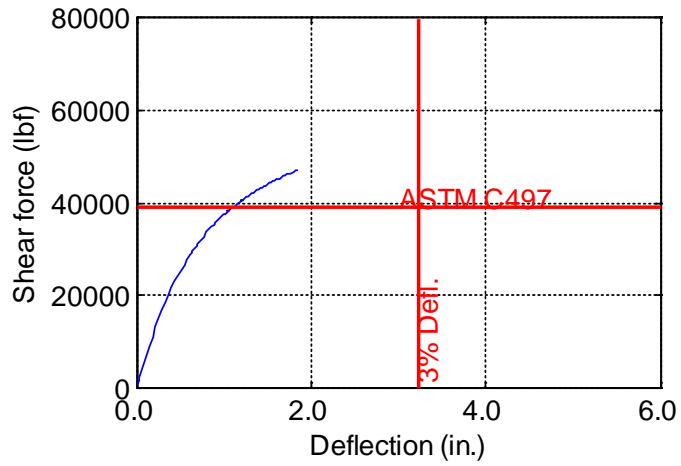


Figure B-202. TW-108-09-0.375

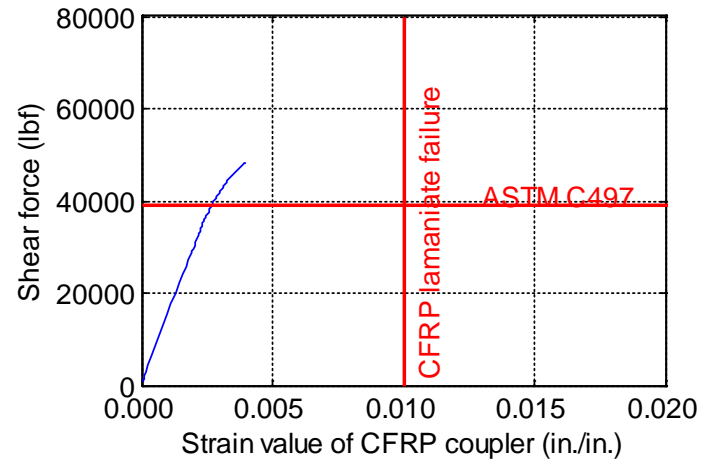
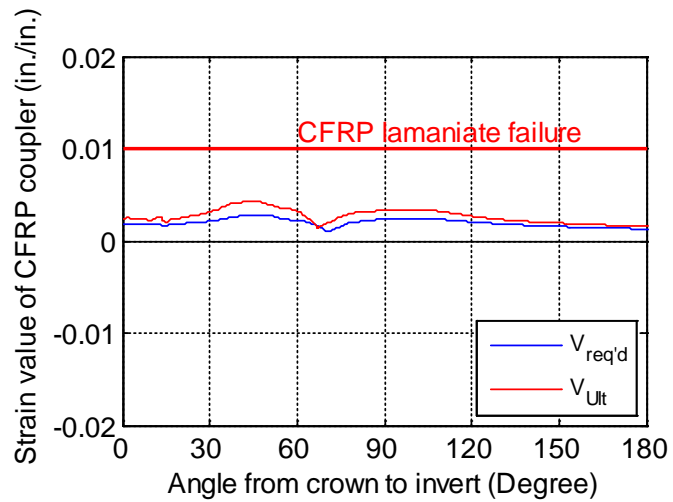
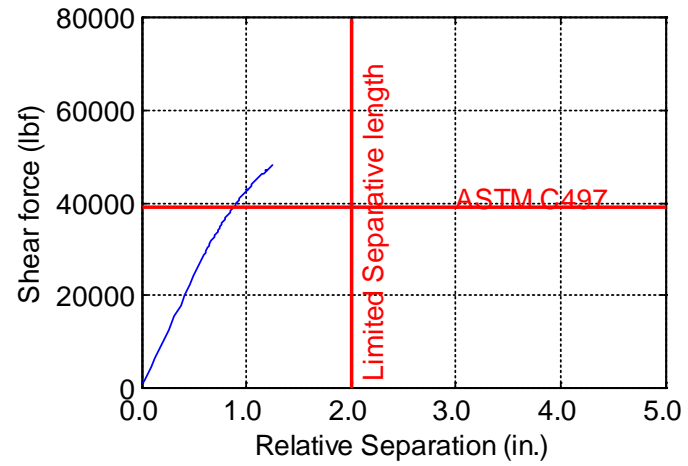
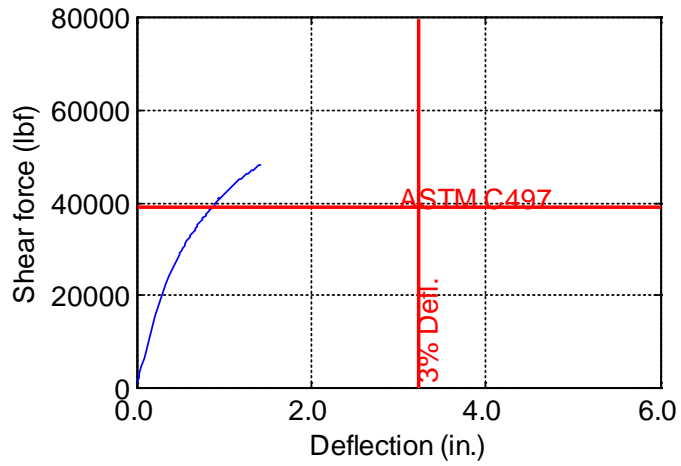


Figure B-203. TW-108-09-0.5

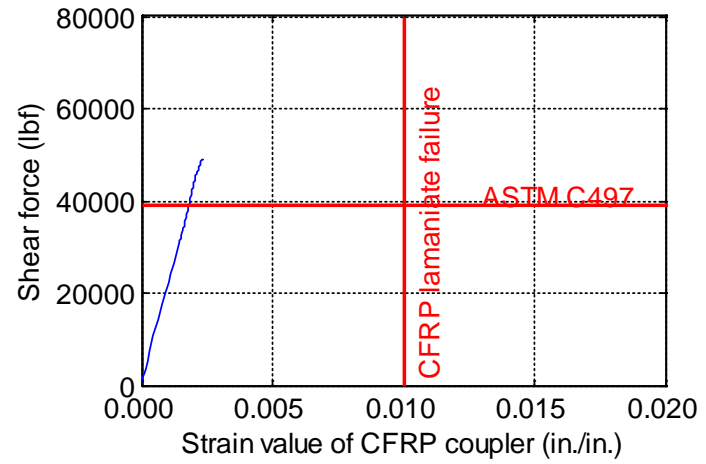
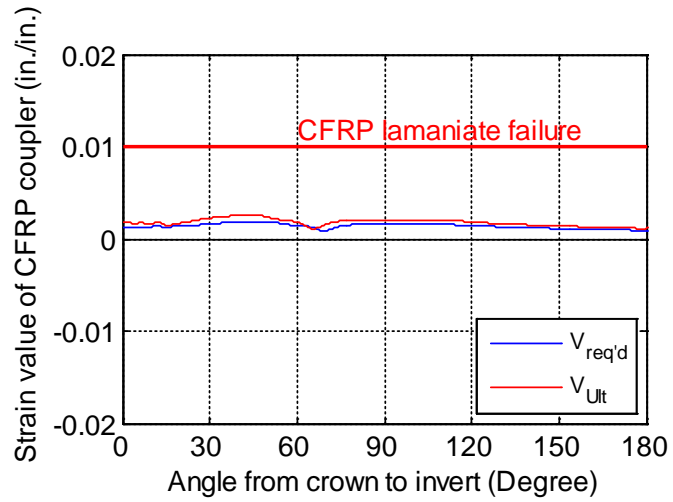
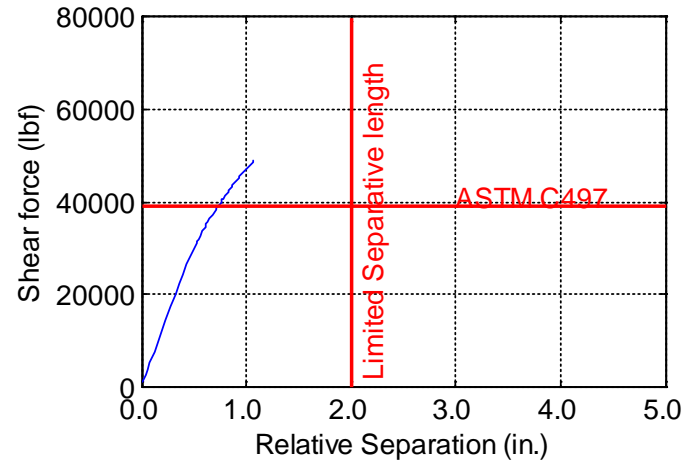
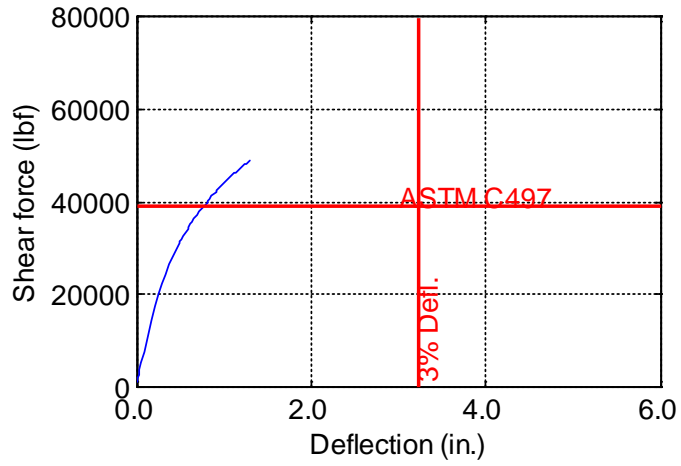


Figure B-204. TW-108-09-0.625

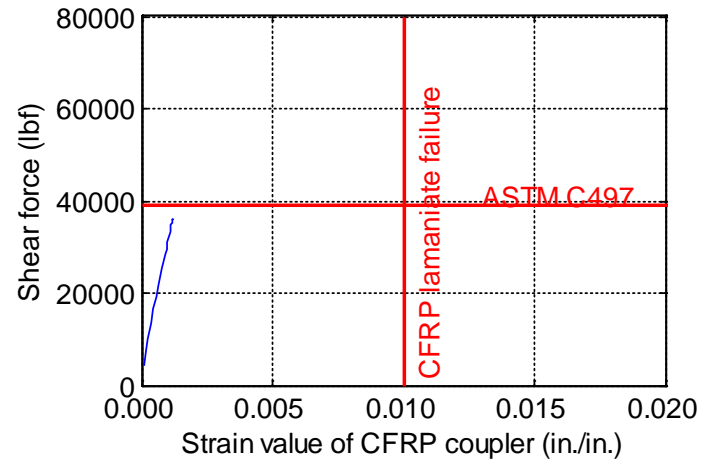
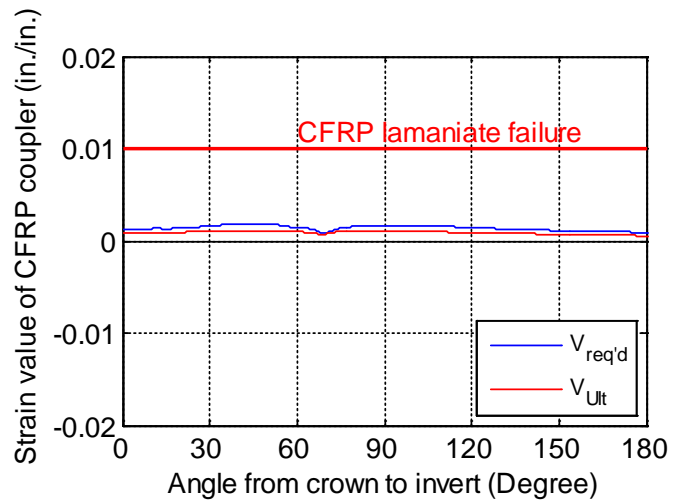
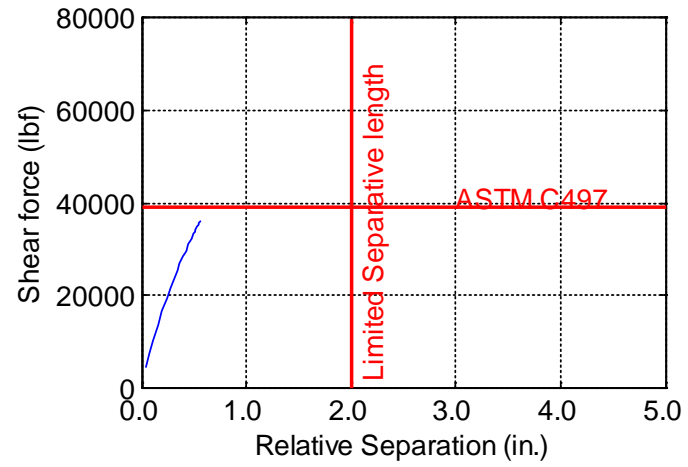
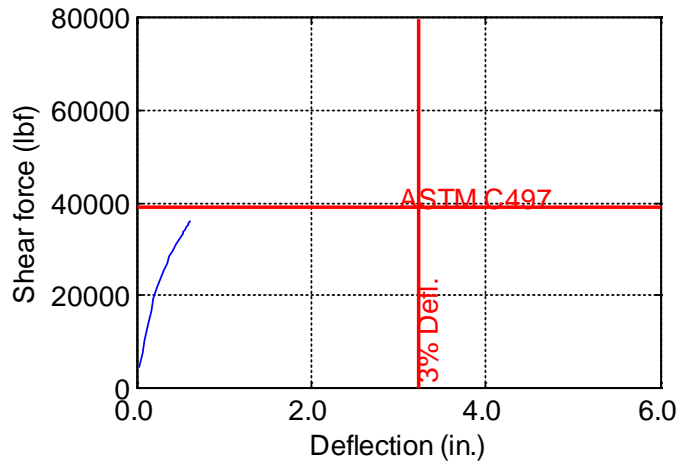


Figure B-205. TW-108-09-0.75

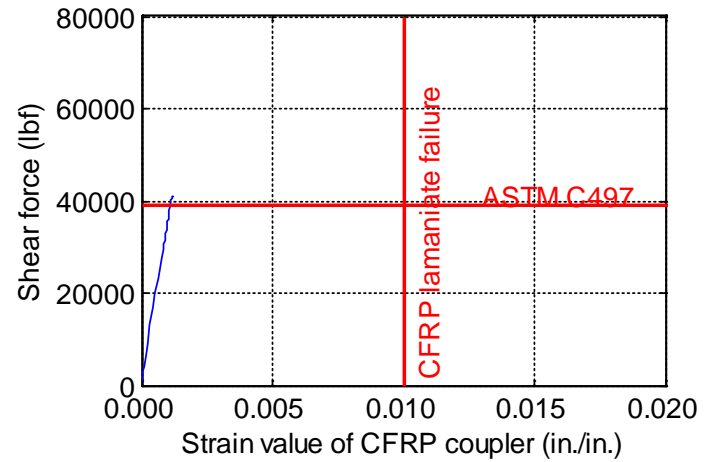
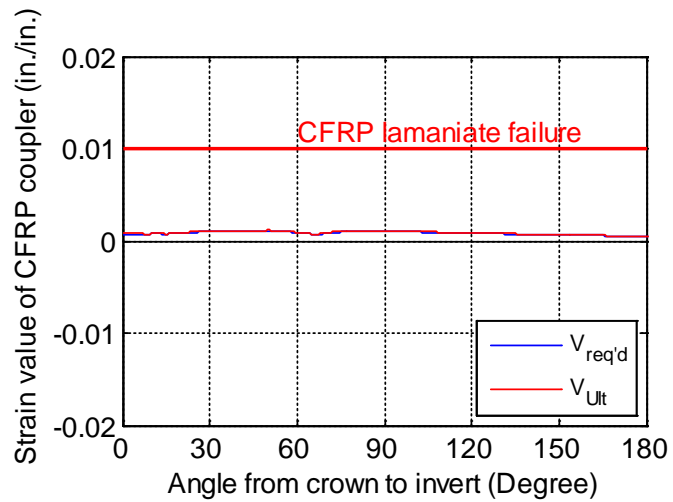
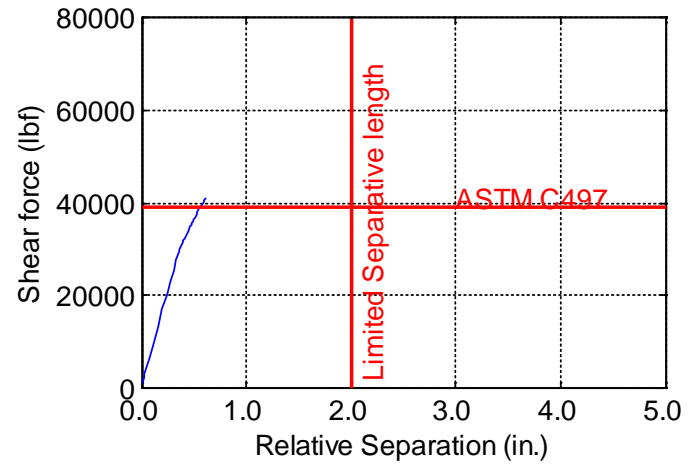
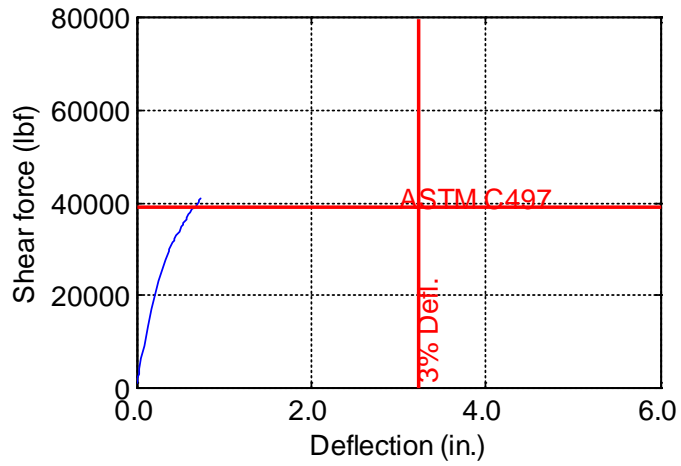


Figure B-206. TW-108-09-0.875

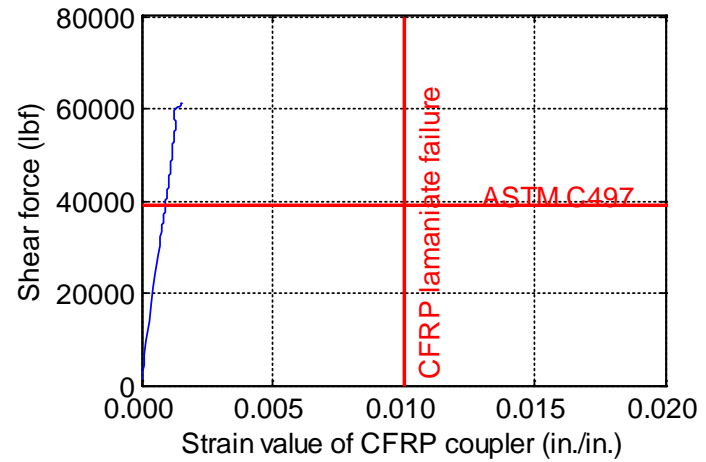
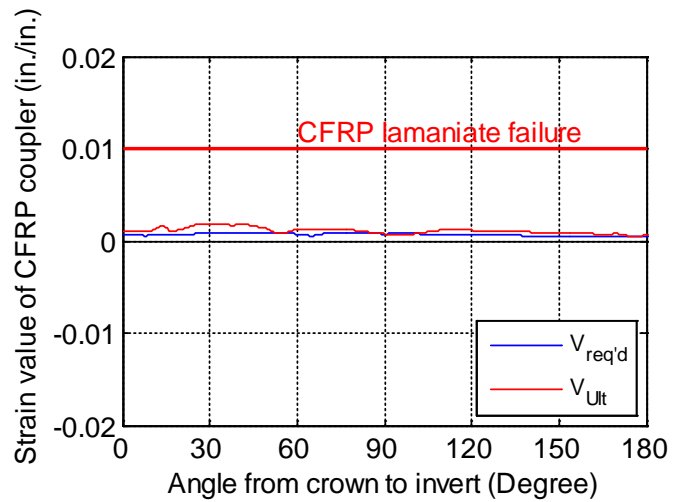
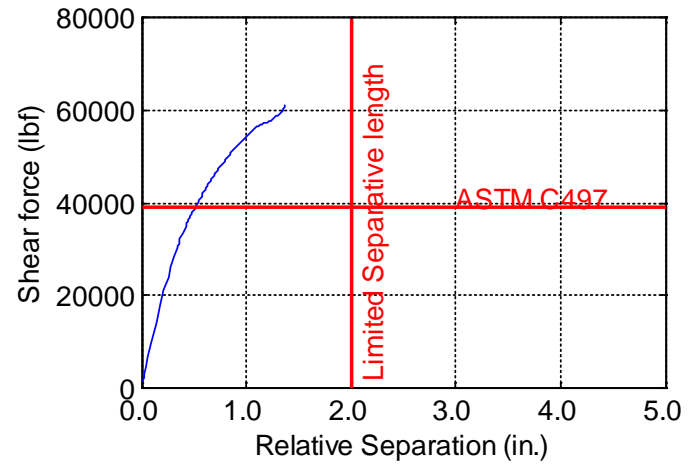
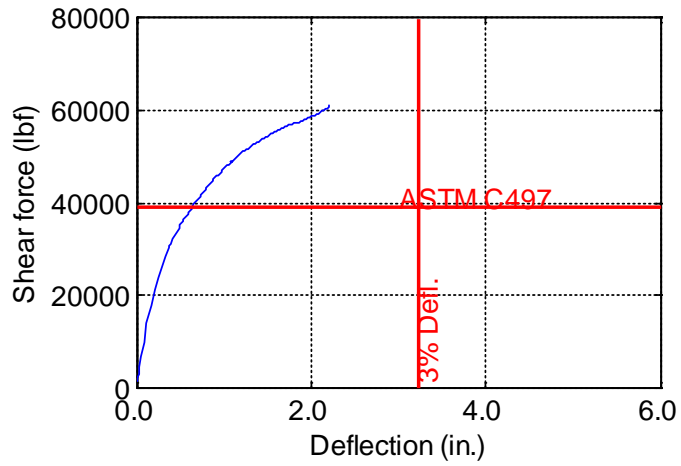


Figure B-207. TW-108-09-1.0

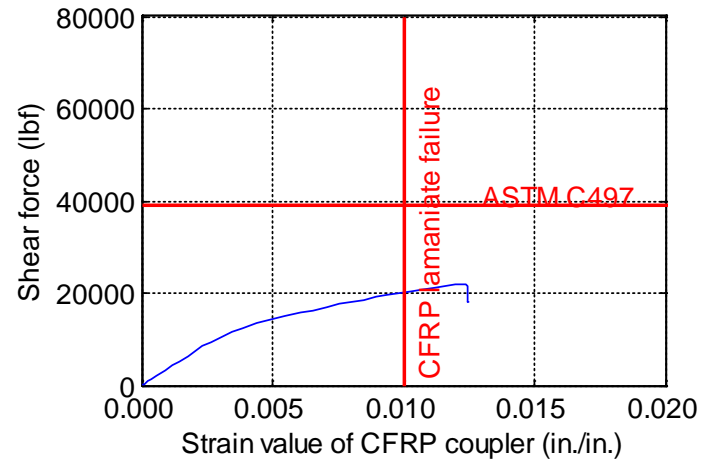
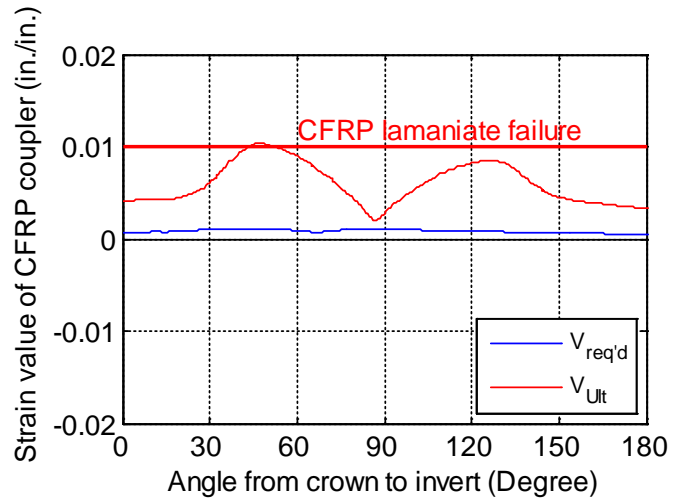
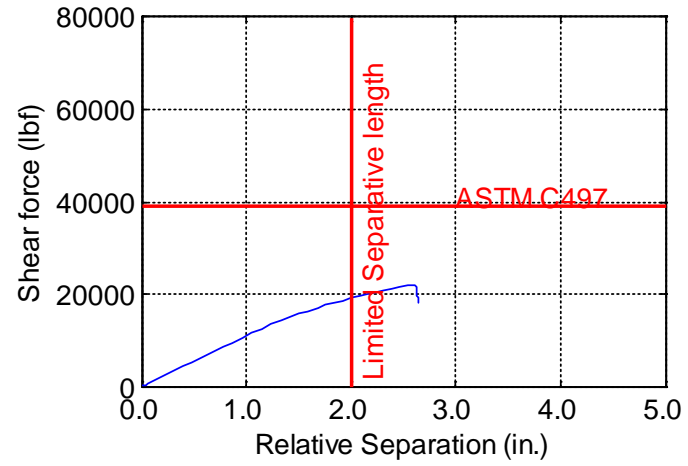
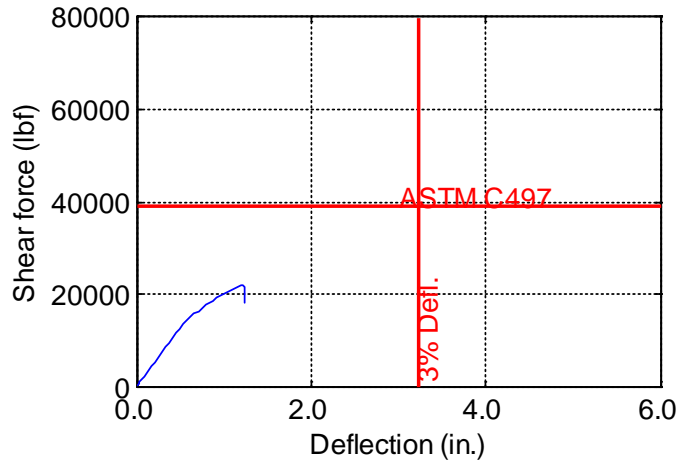


Figure B-208. TW-108-12-0.125

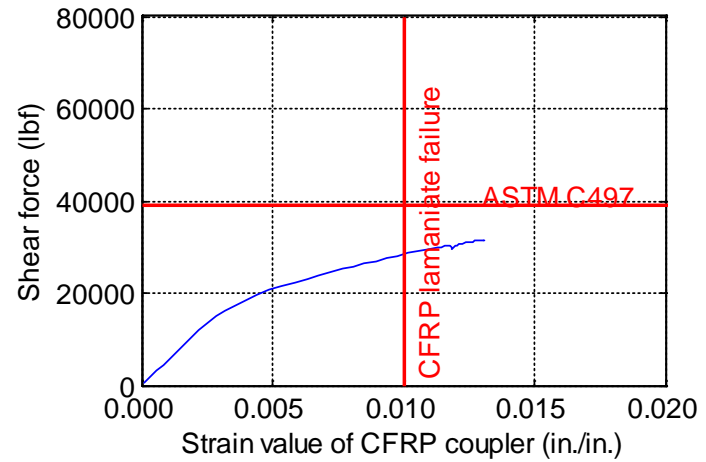
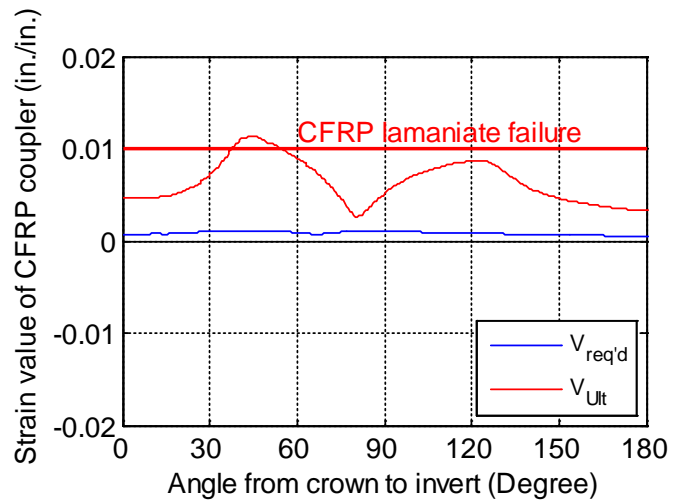
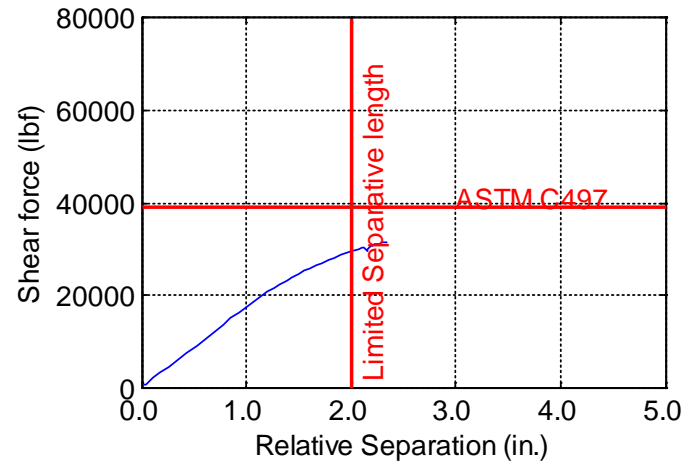
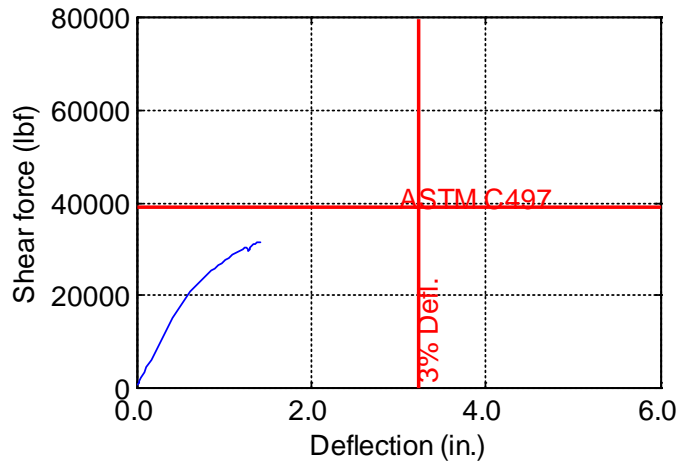


Figure B-209. TW-108-12-0.1875

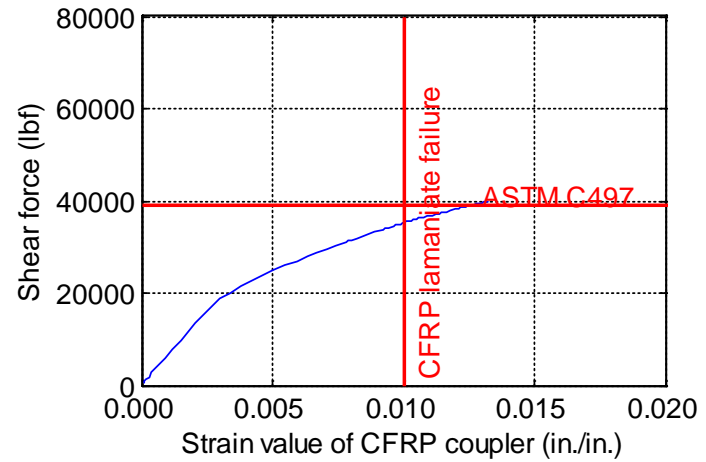
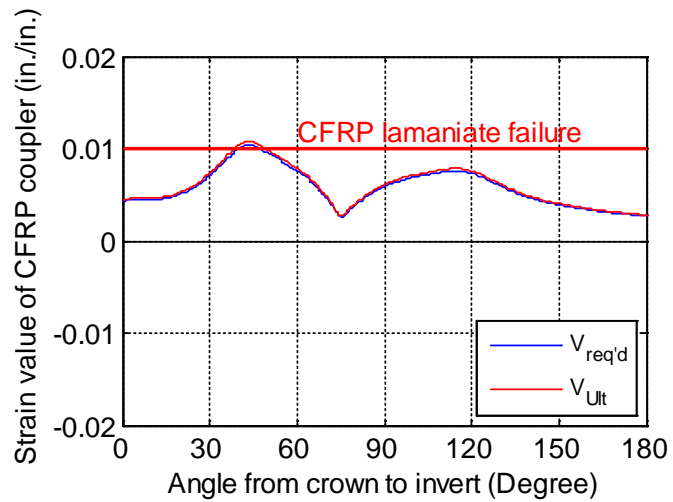
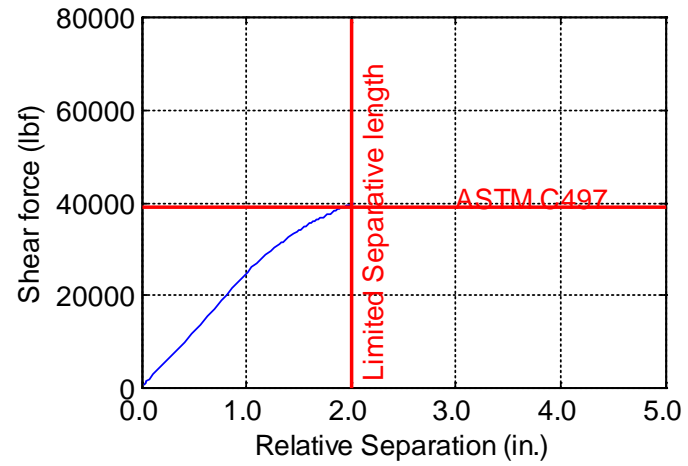
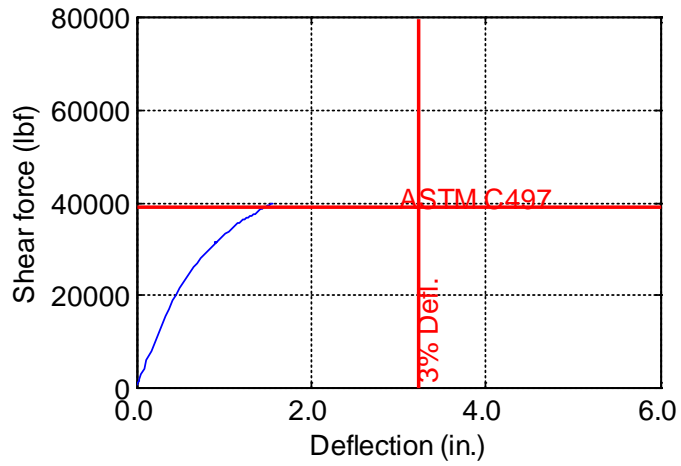


Figure B-210. TW-108-12-0.25

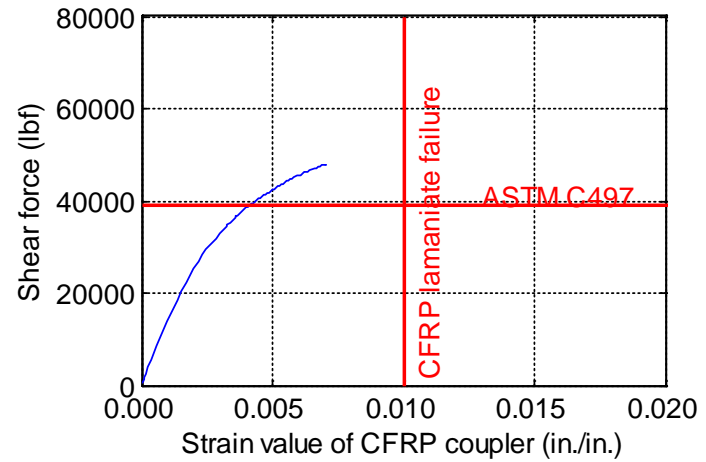
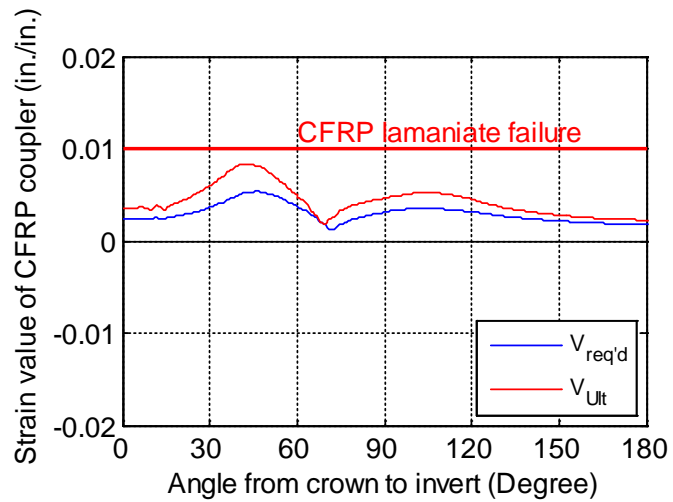
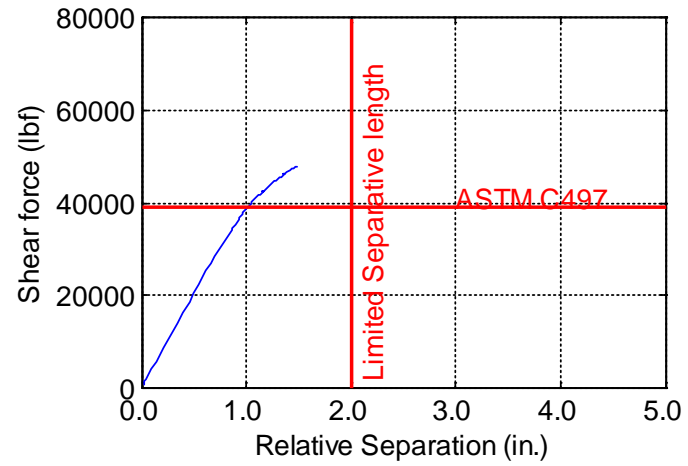
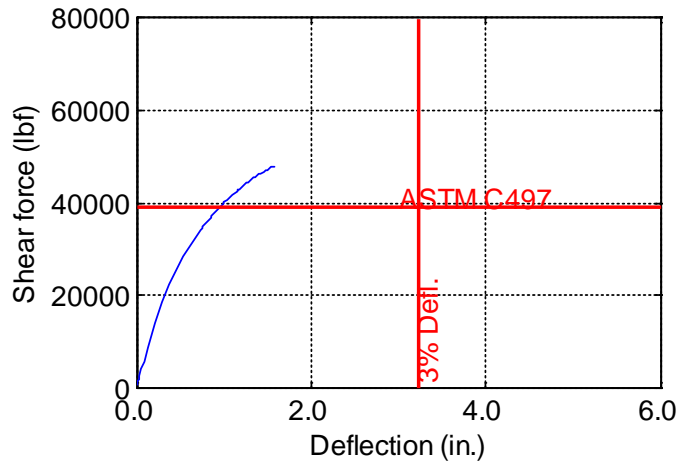


Figure B-211. TW-108-12-0.375

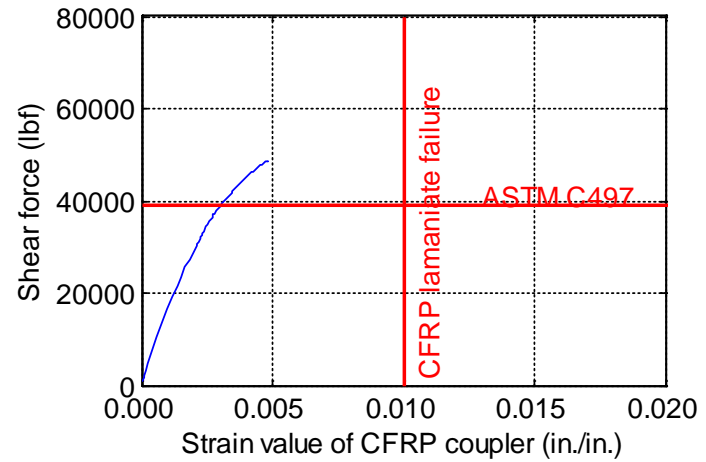
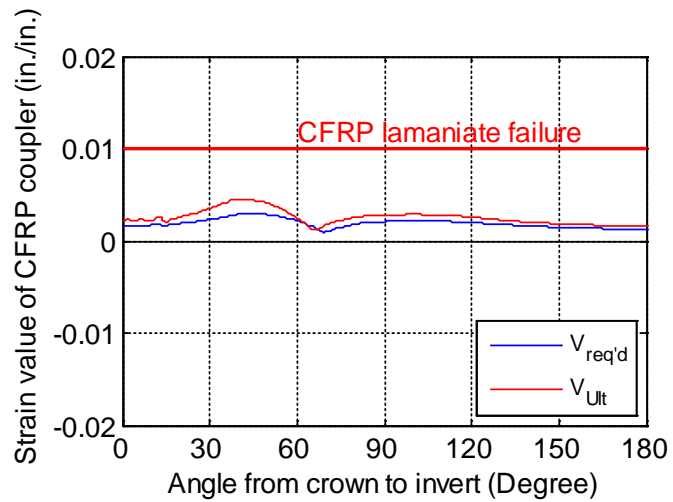
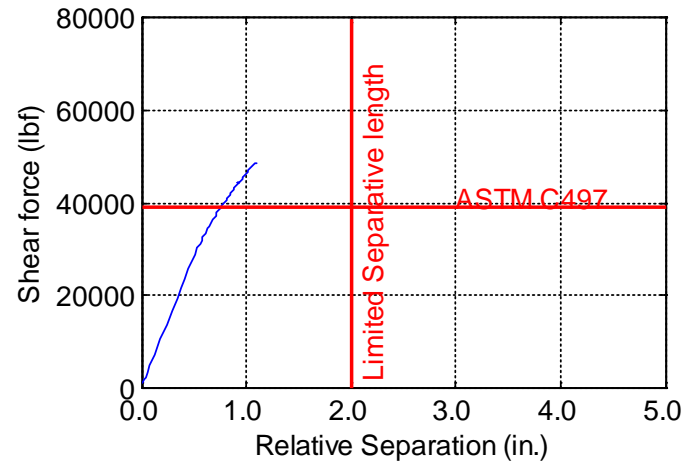
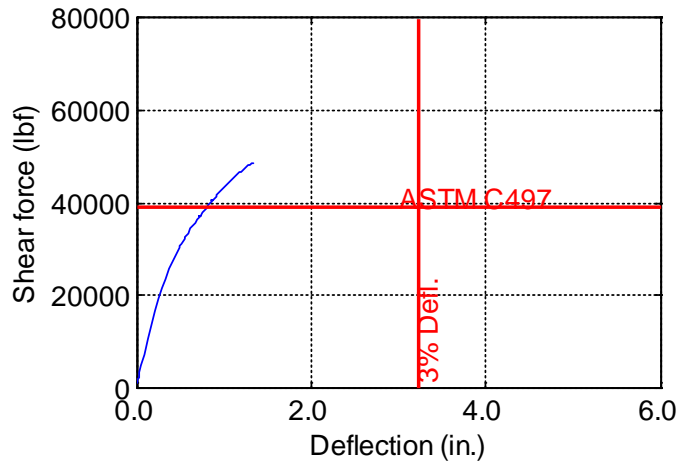


Figure B-212. TW-108-12-0.5

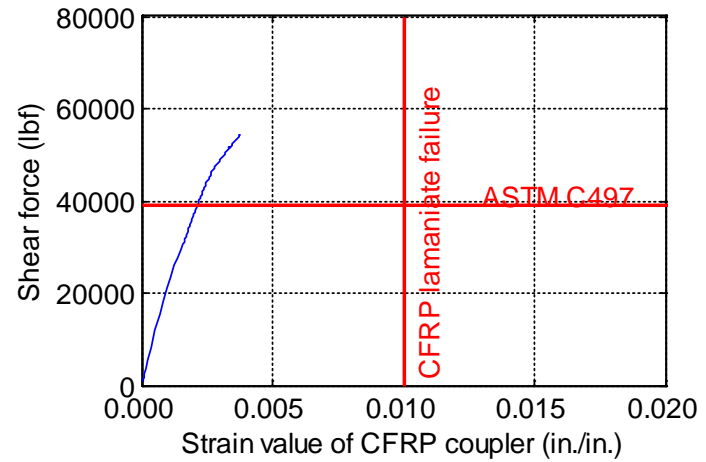
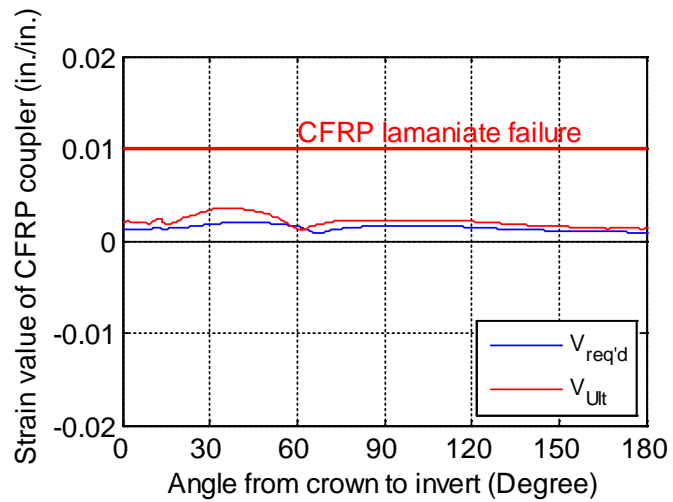
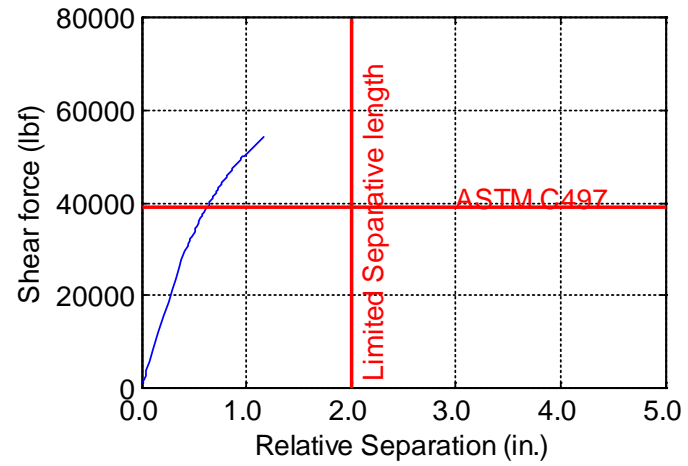
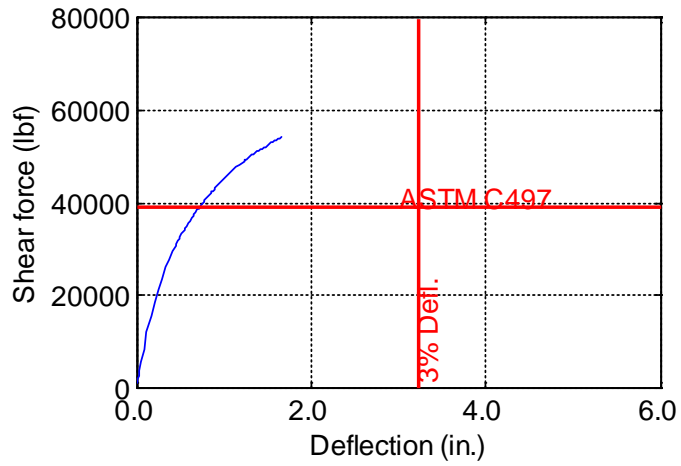


Figure B-213. TW-108-12-0.625

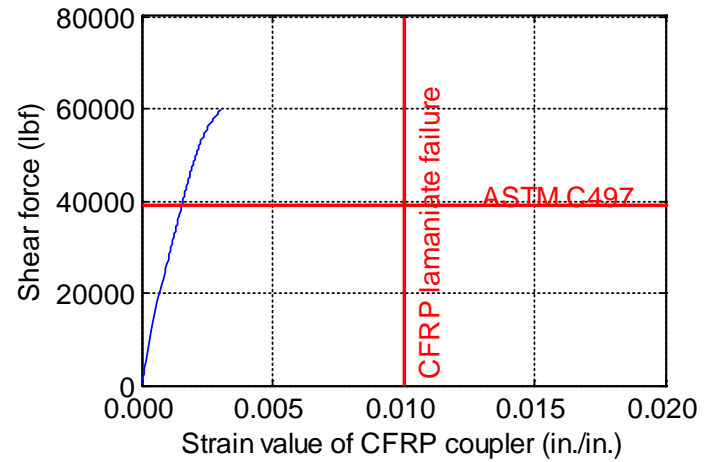
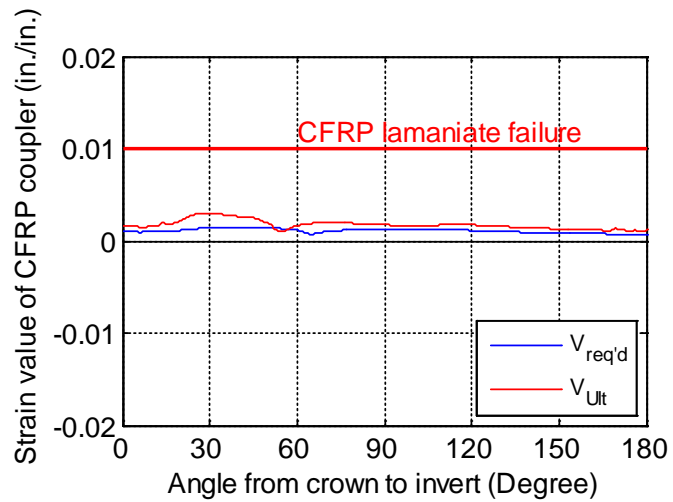
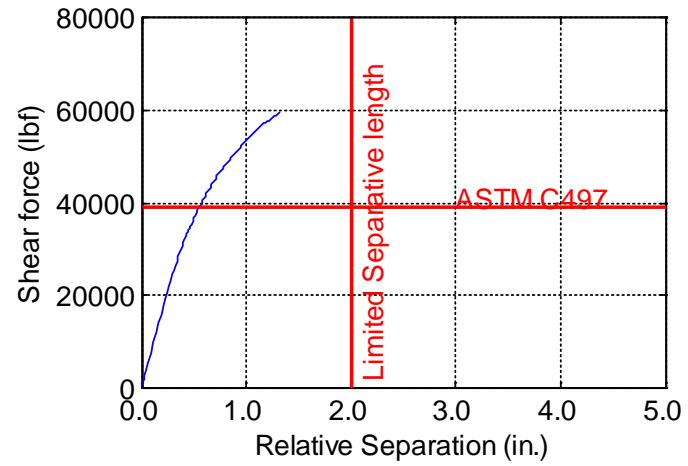
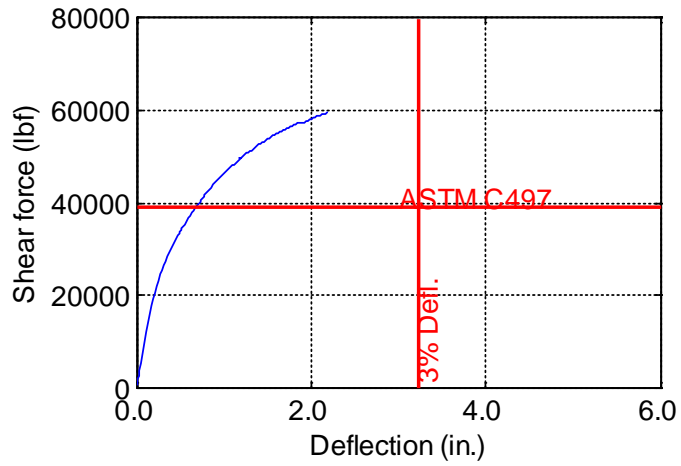


Figure B-214. TW-108-12-0.75

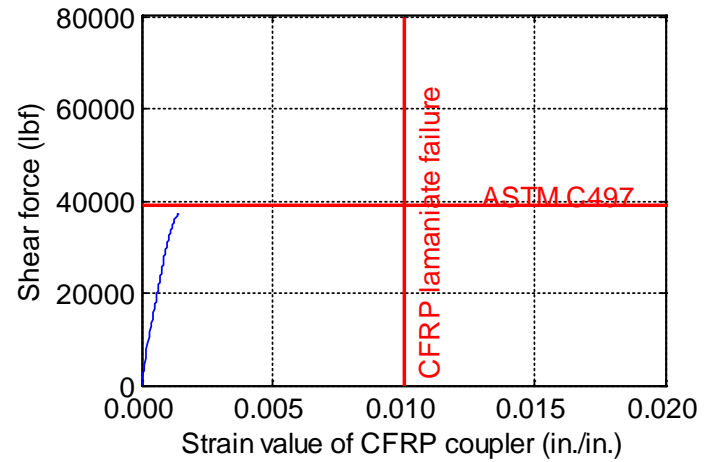
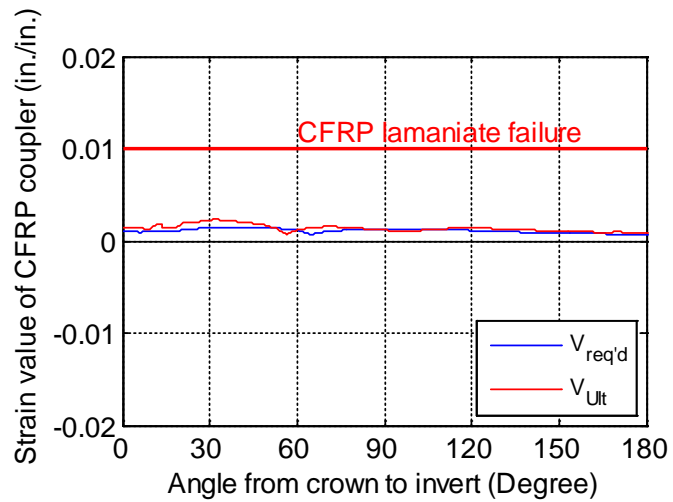
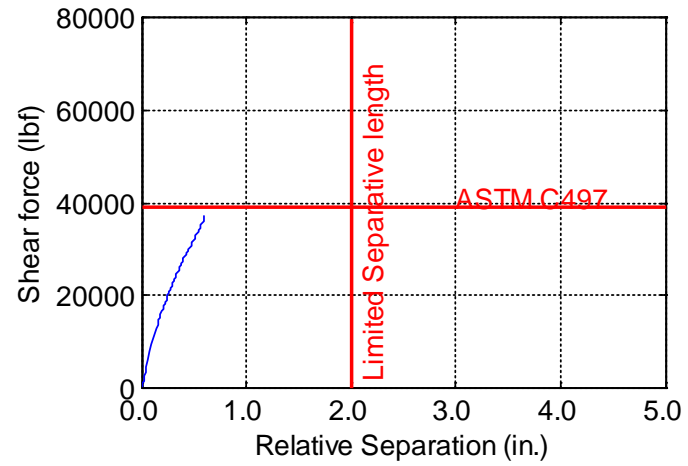
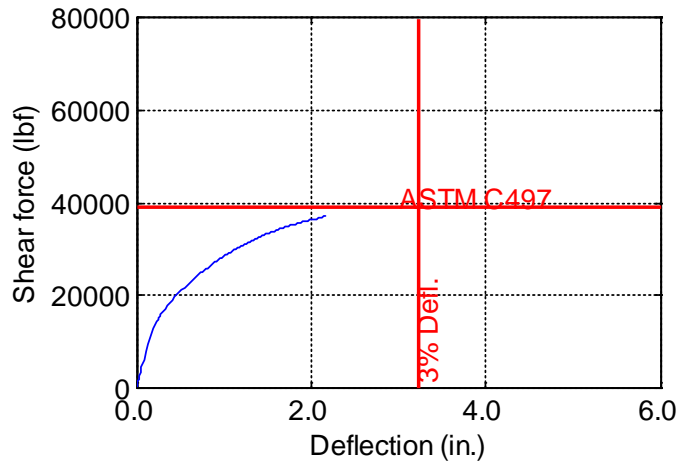


Figure B-215. TW-108-12-0.875

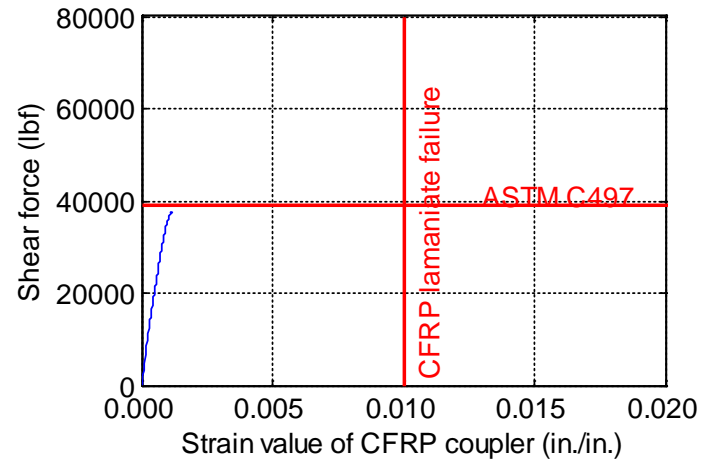
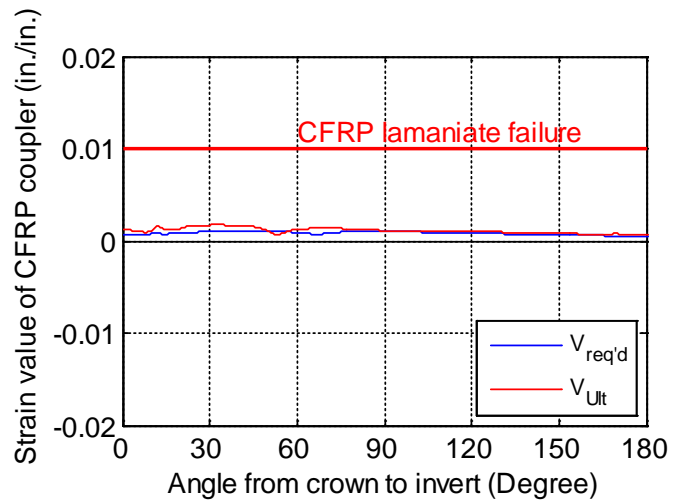
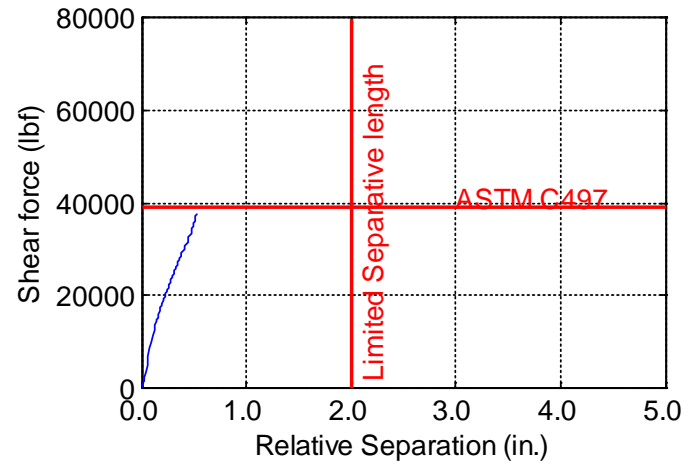
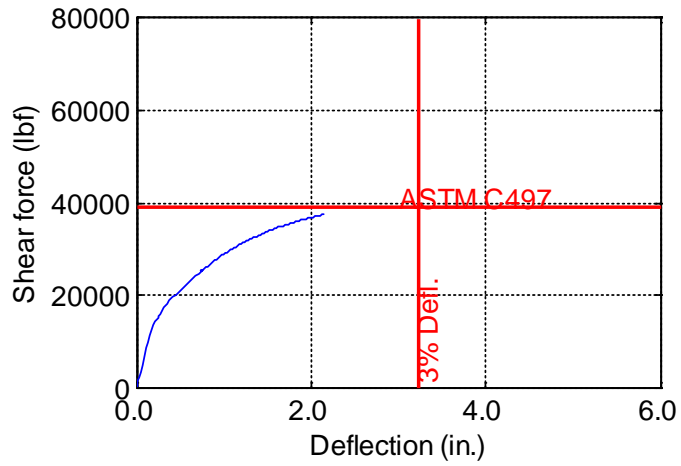


Figure B-216. TW-108-12-1.0

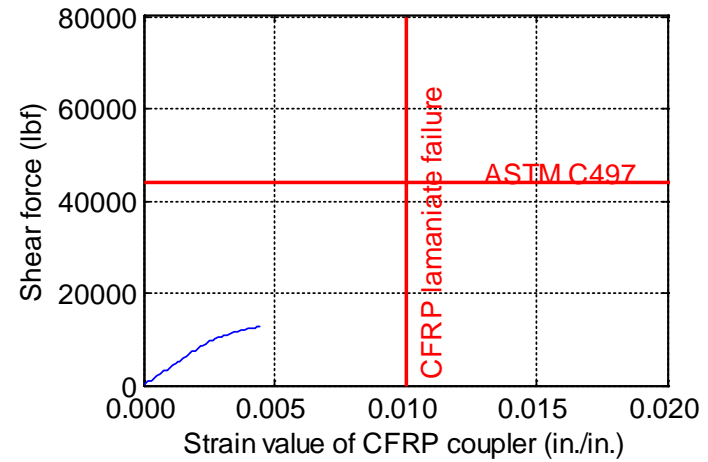
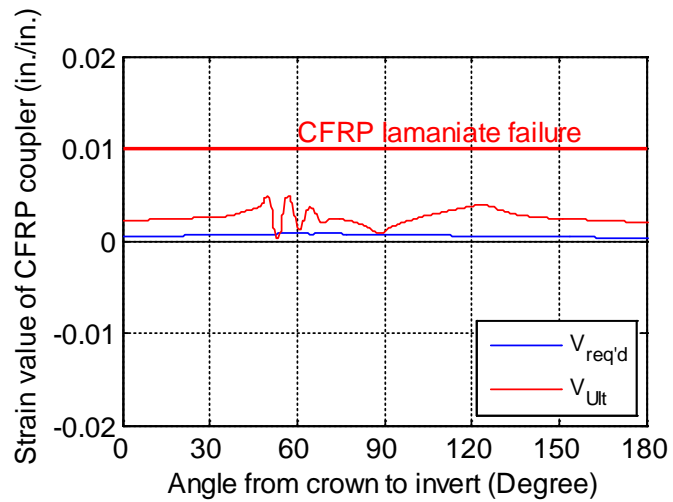
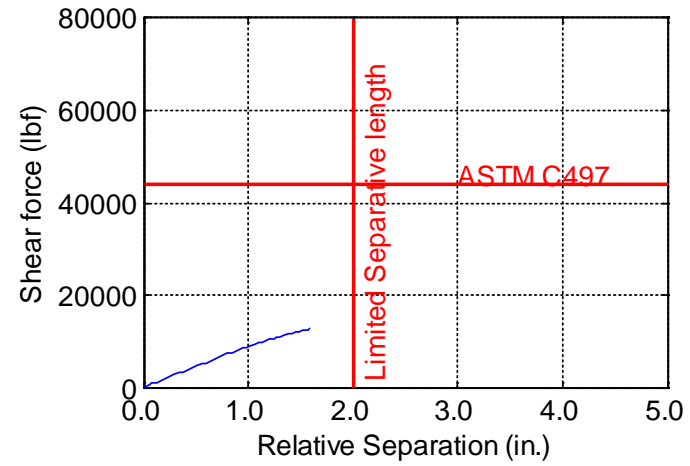
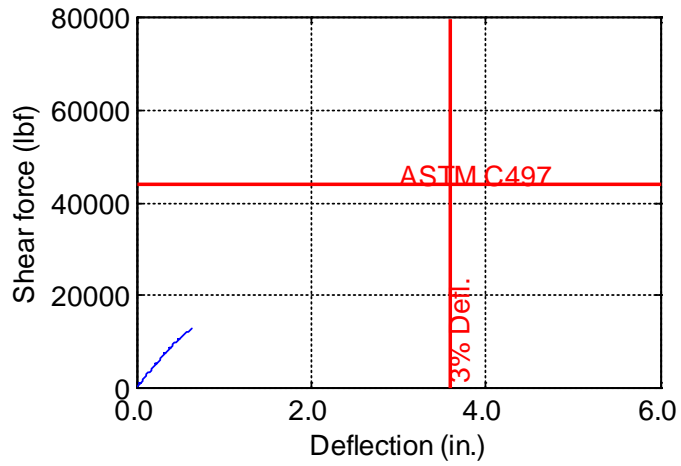


Figure B-217. TW-120-06-0.125

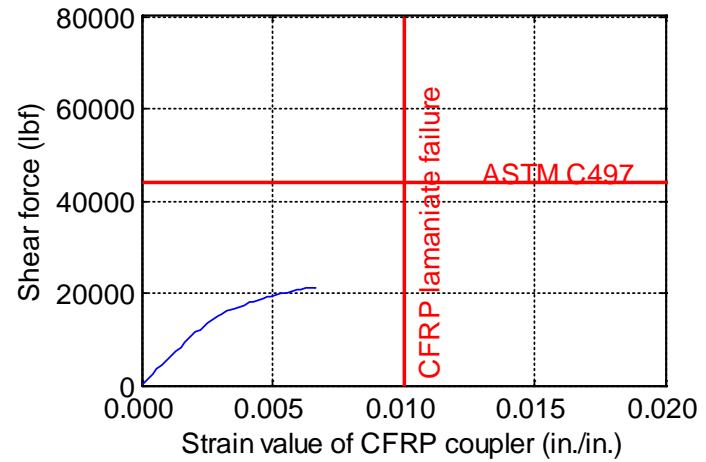
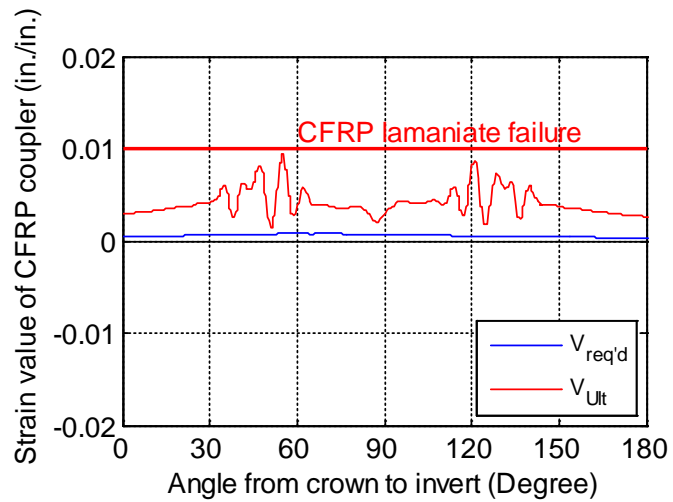
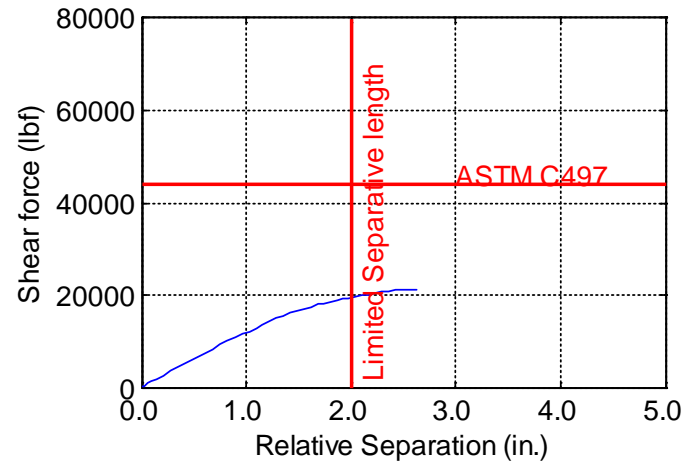
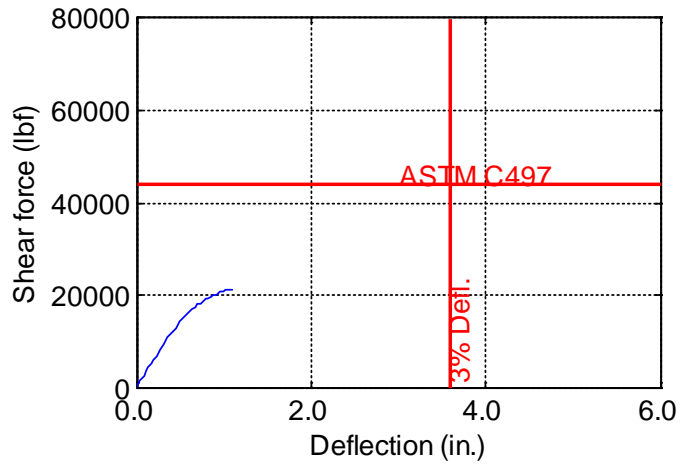


Figure B-218. TW-120-06-0.1875

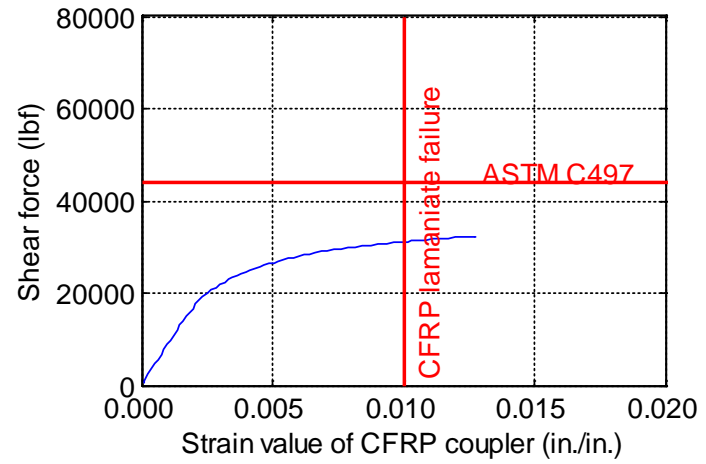
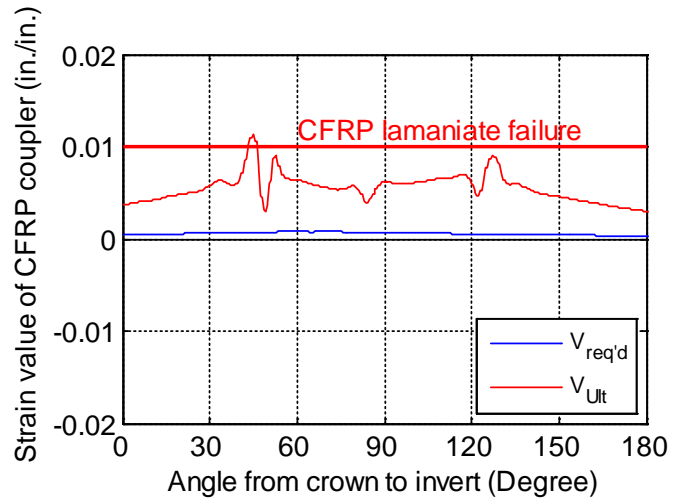
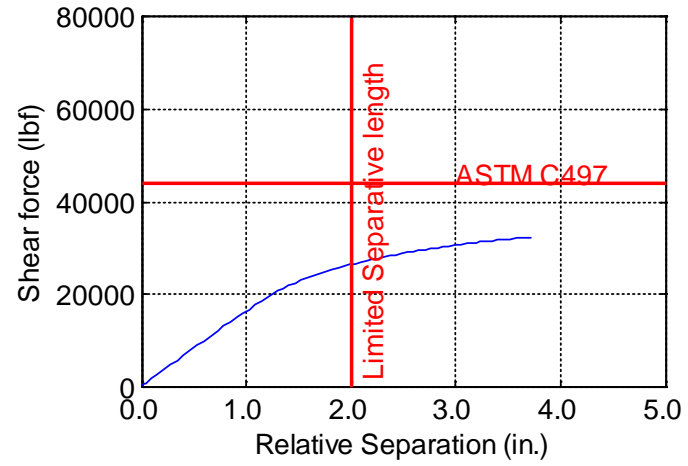
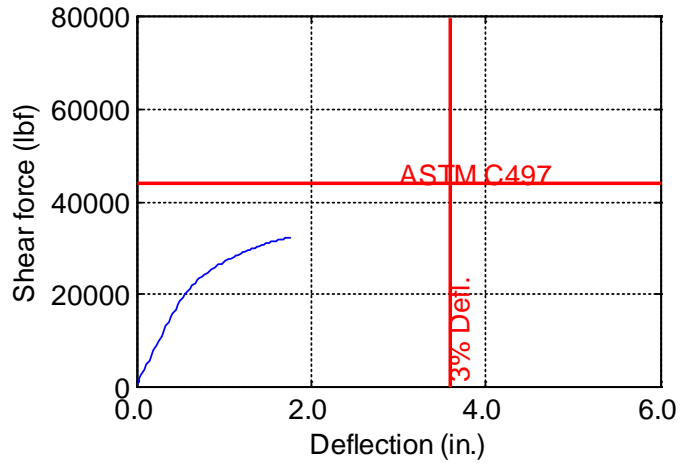


Figure B-219. TW-120-06-0.25

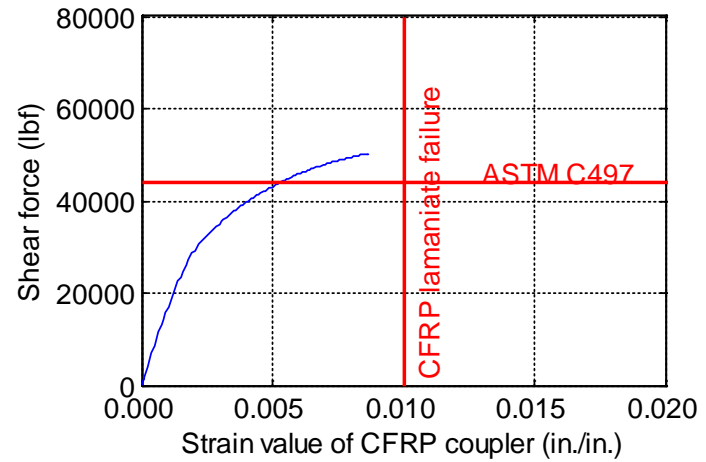
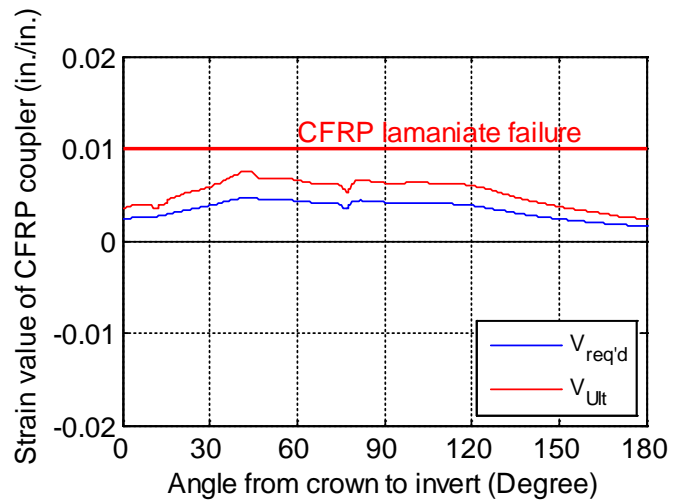
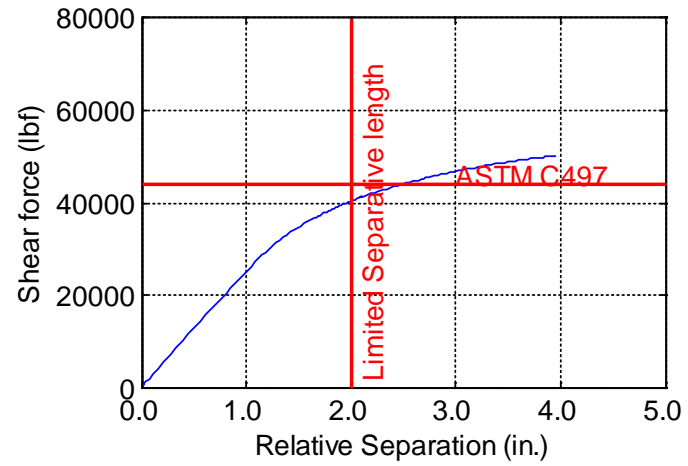
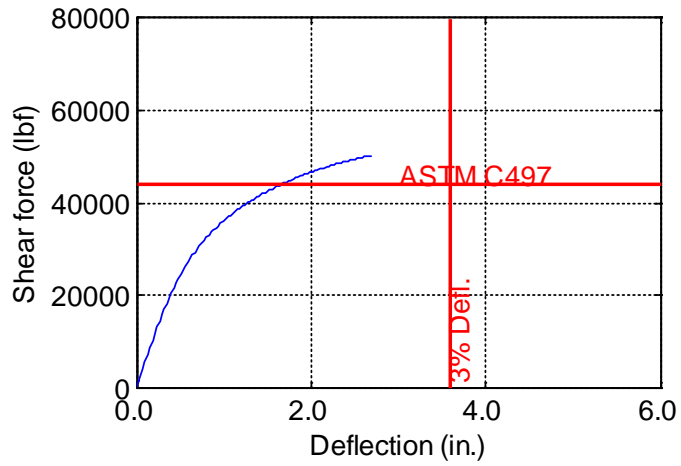


Figure B-220. TW-120-06-0.375

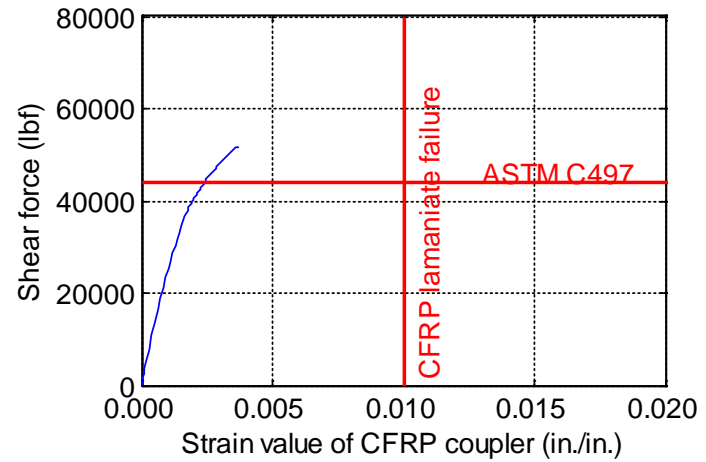
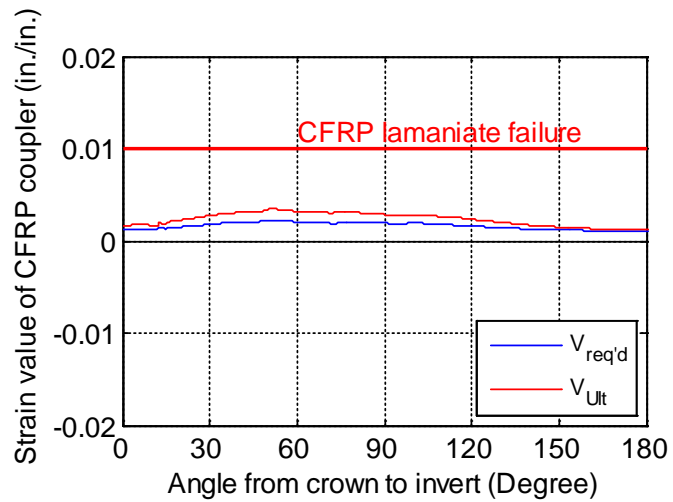
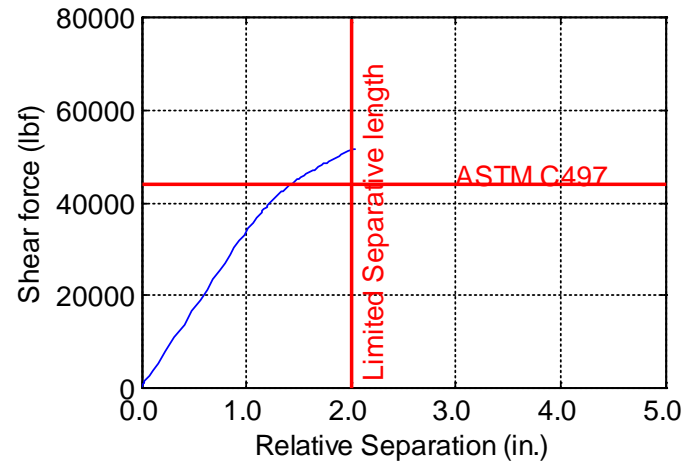
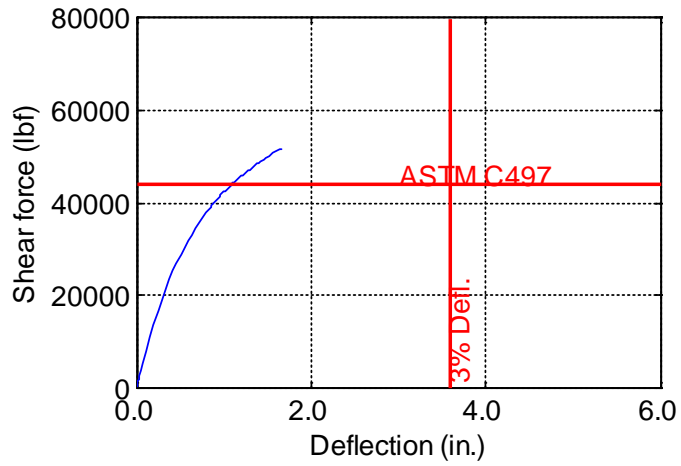


Figure B-221. TW-120-06-0.5

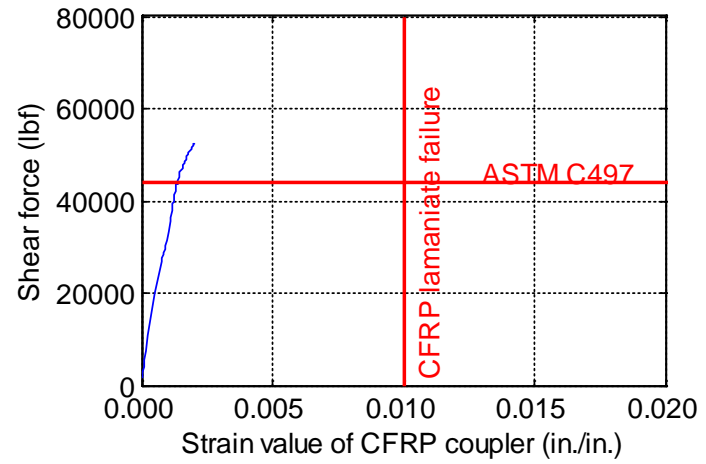
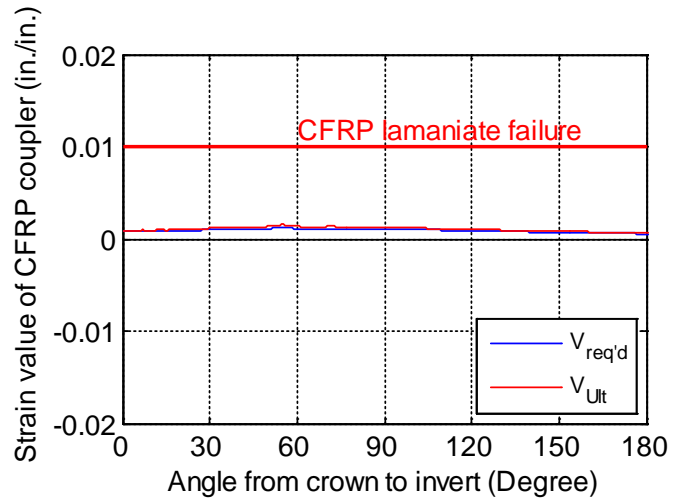
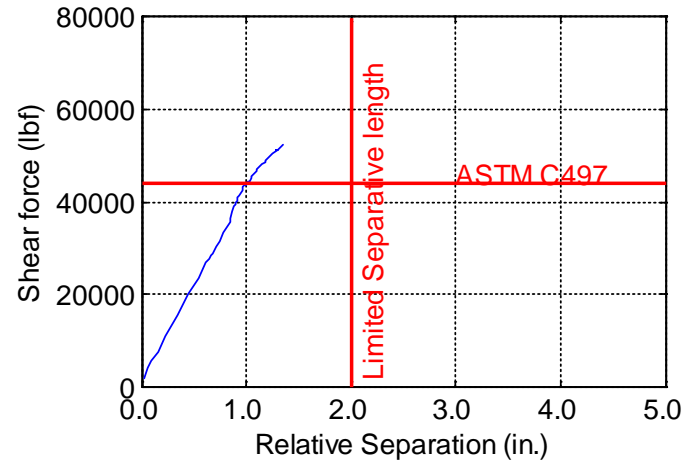
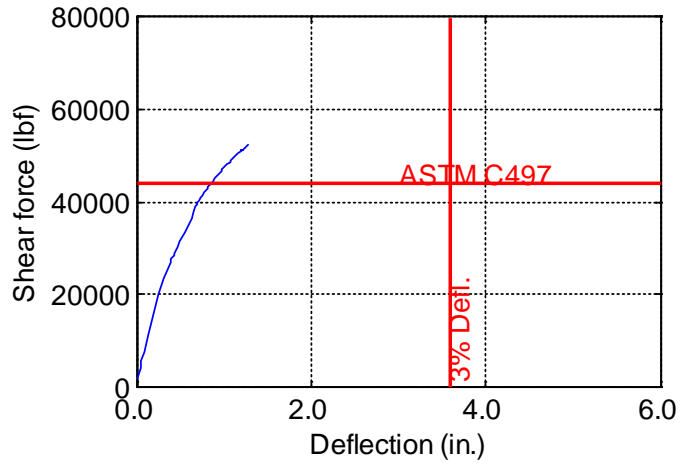


Figure B-222. TW-120-06-0.625

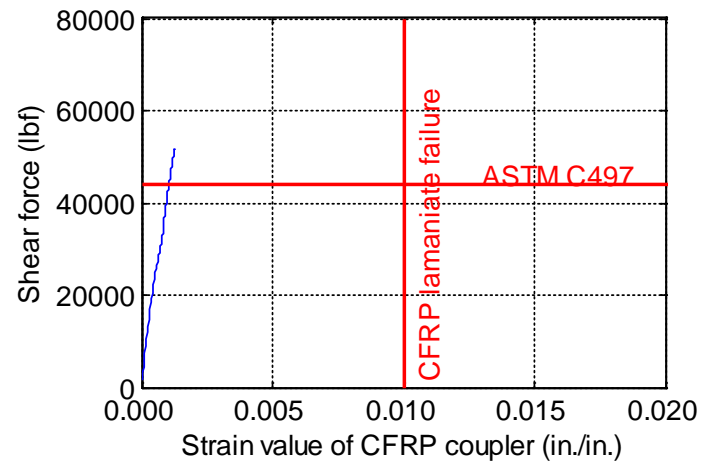
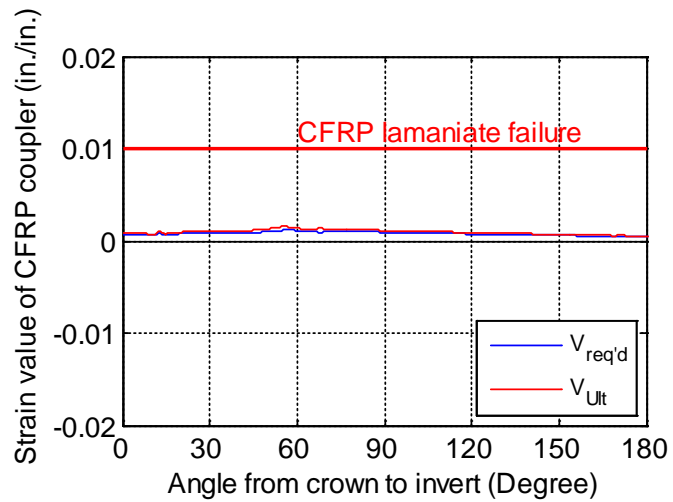
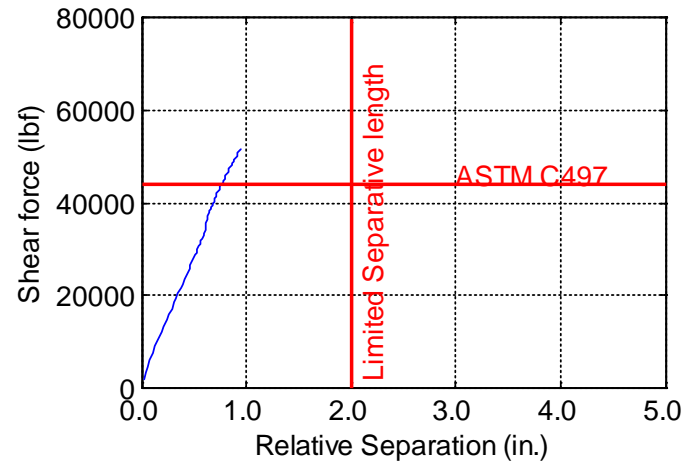
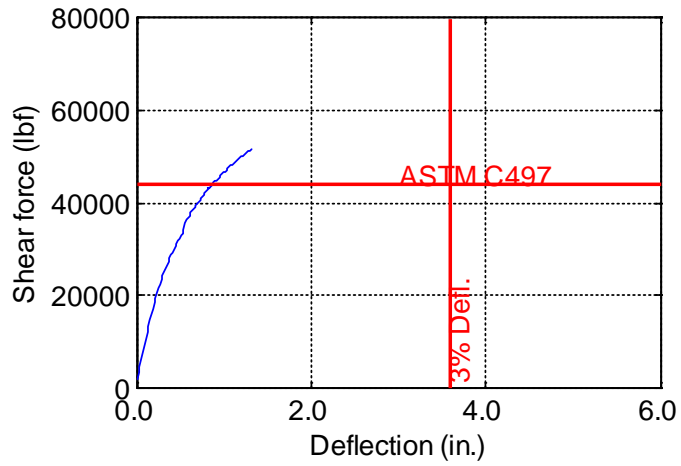


Figure B-223. TW-120-06-0.75

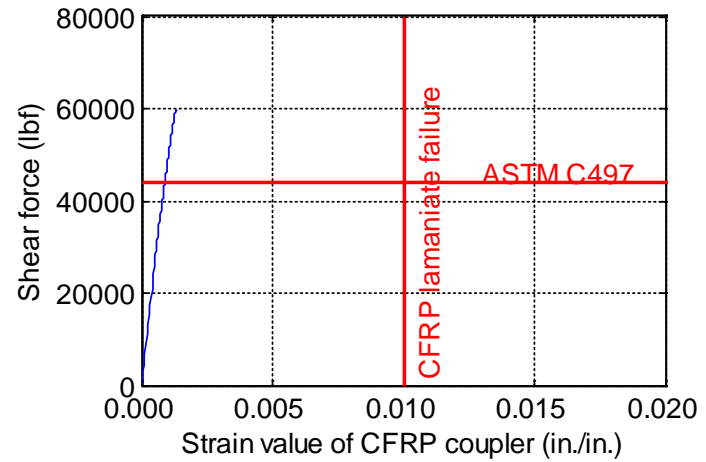
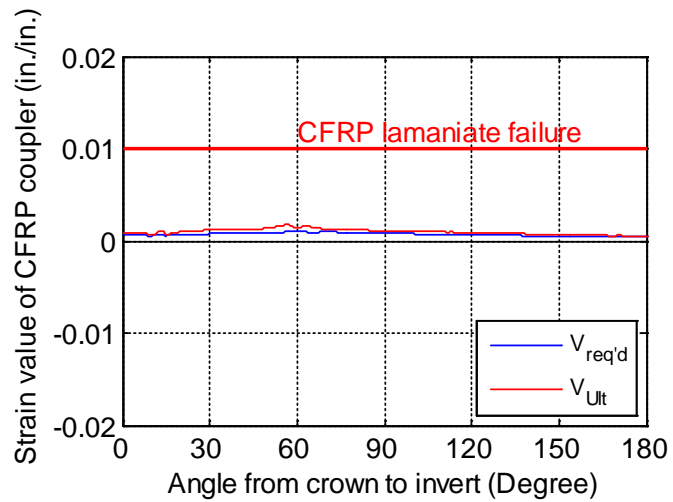
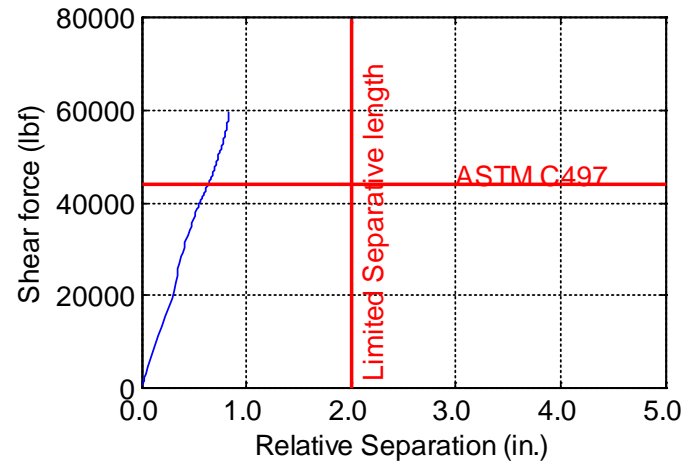
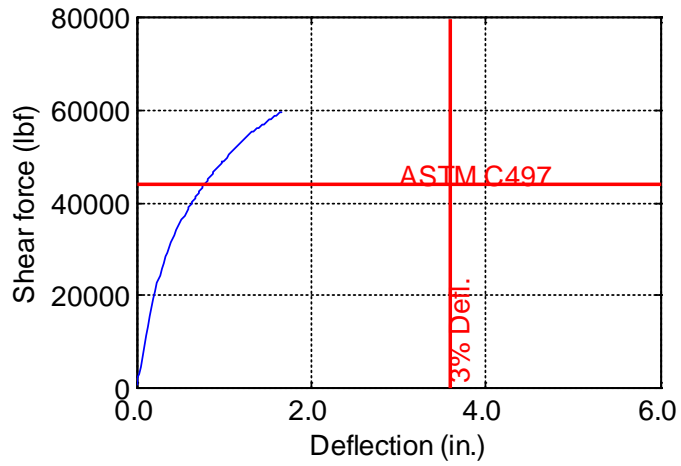


Figure B-224. TW-120-06-0.875

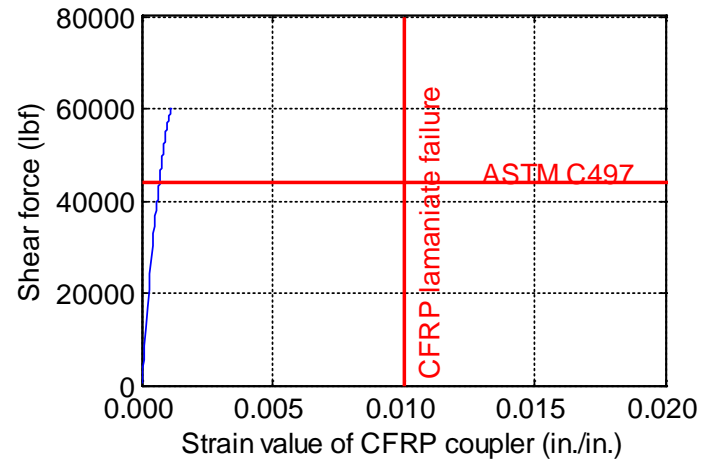
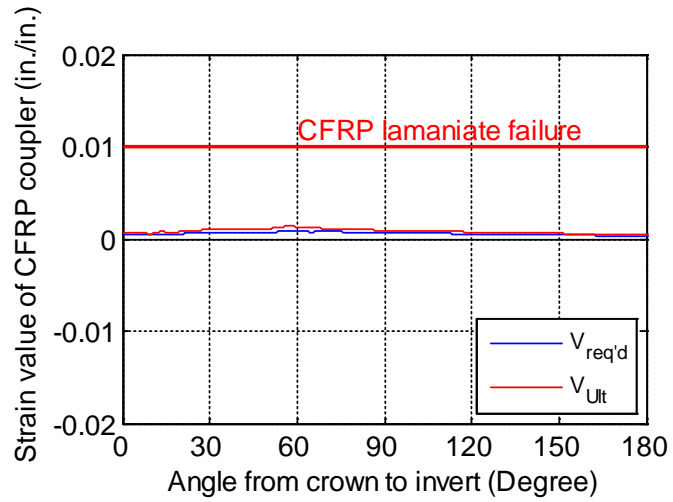
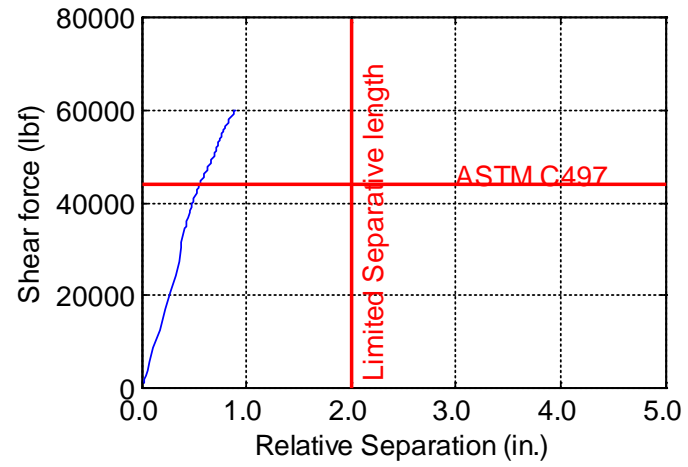
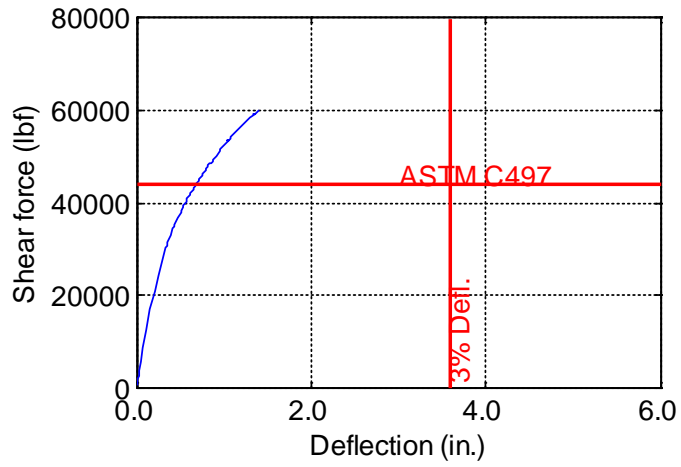


Figure B-225. TW-120-06-1.0

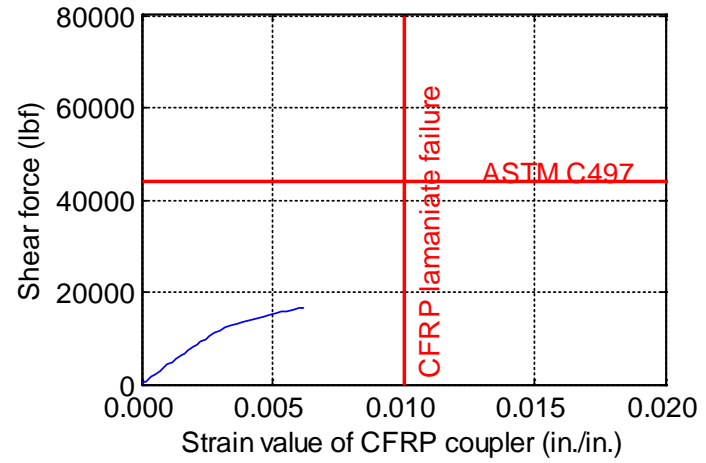
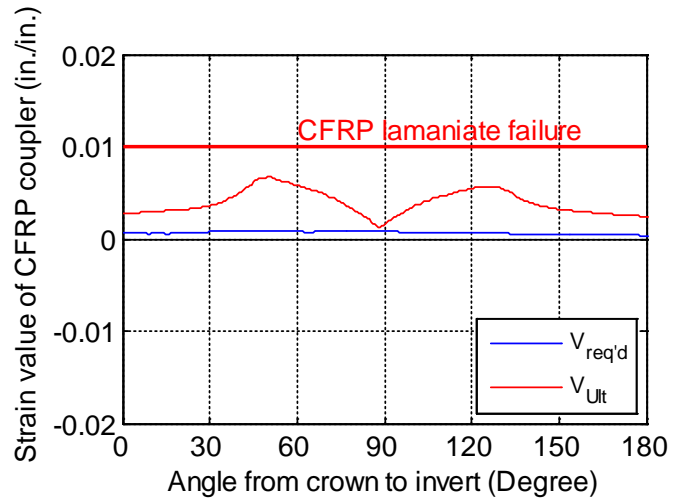
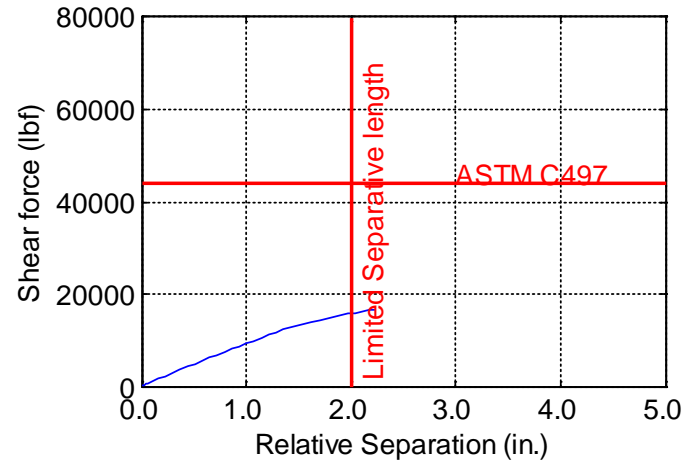
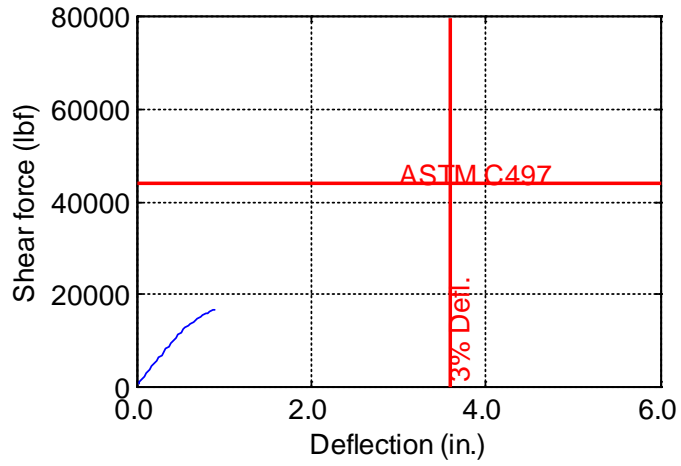


Figure B-226. TW-120-09-0.125

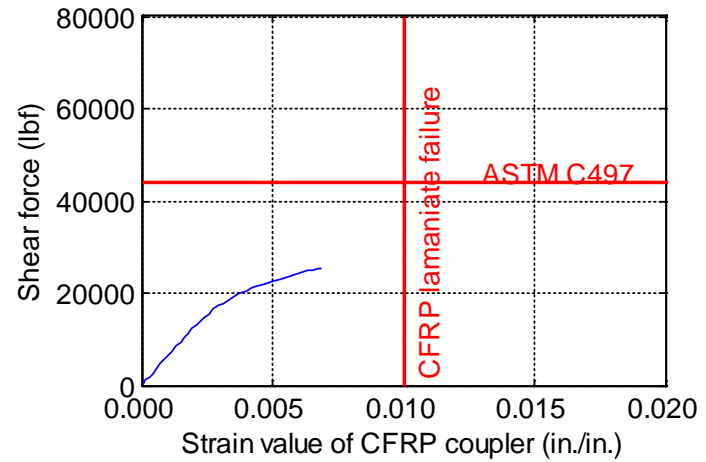
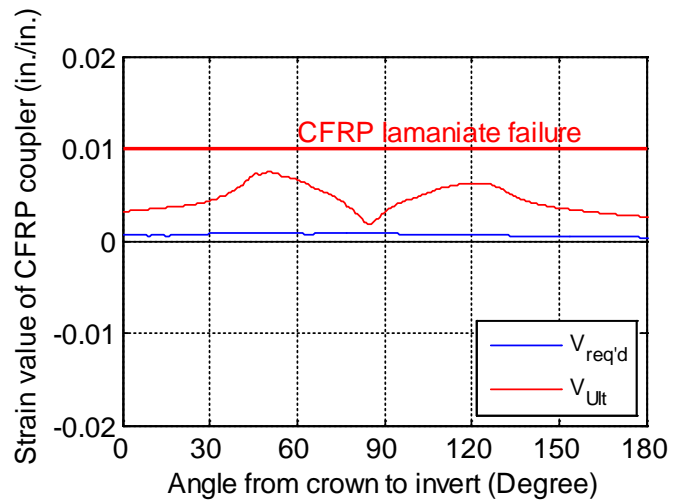
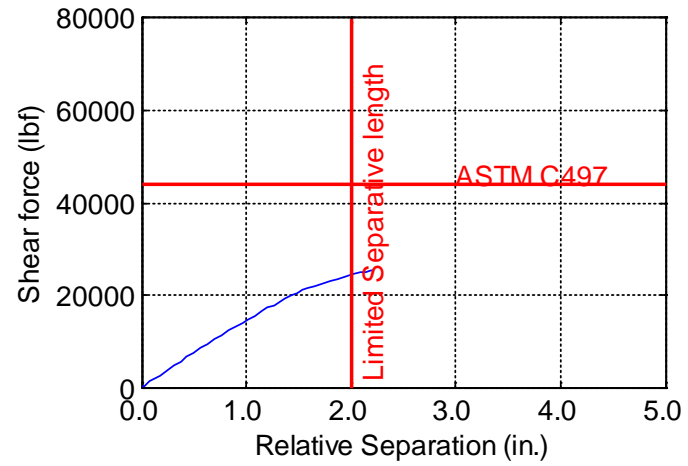
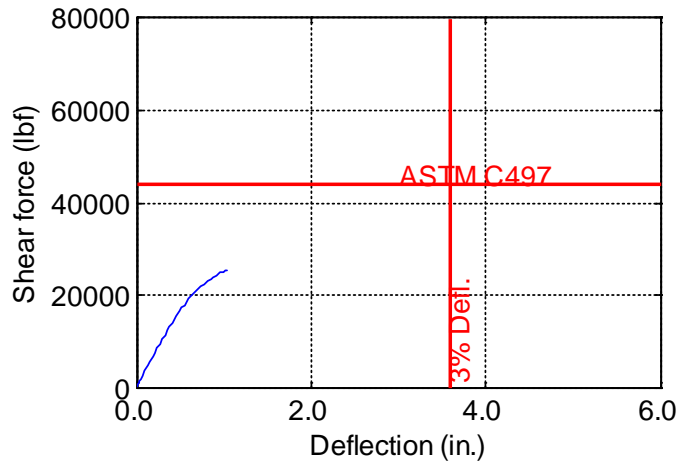


Figure B-227. TW-120-09-0.1875

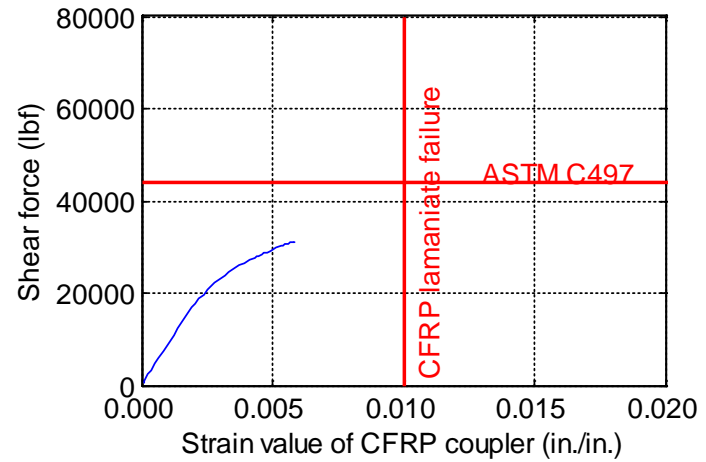
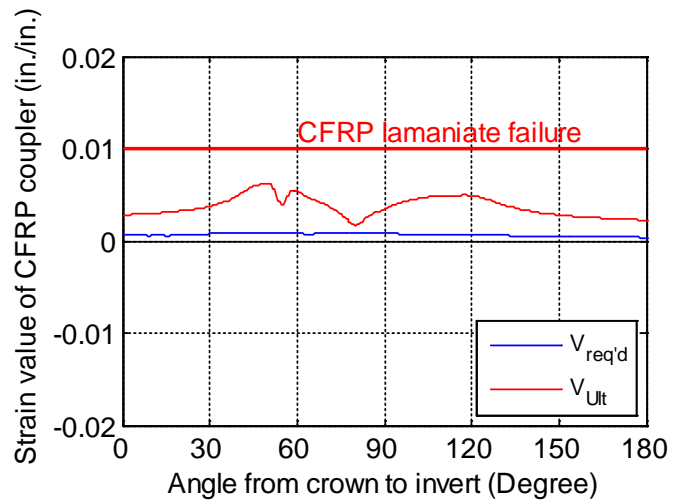
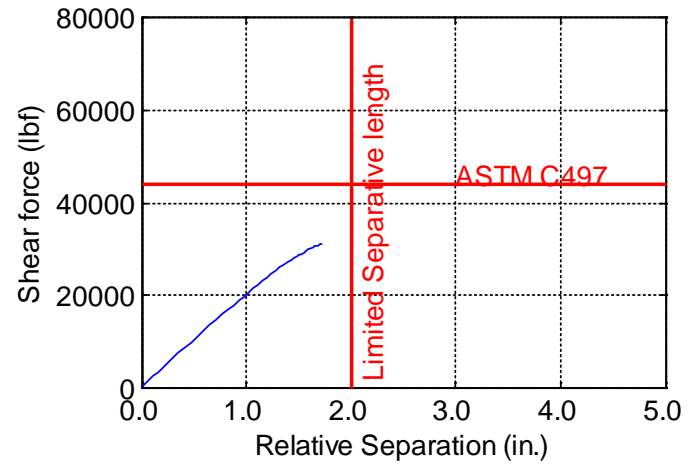
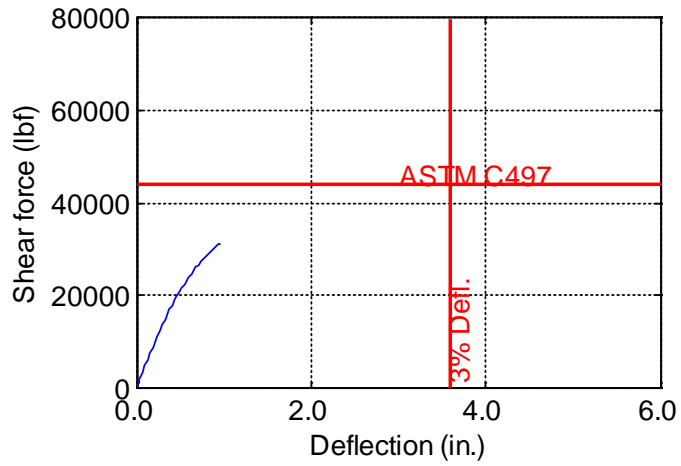


Figure B-228. TW-120-09-0.25

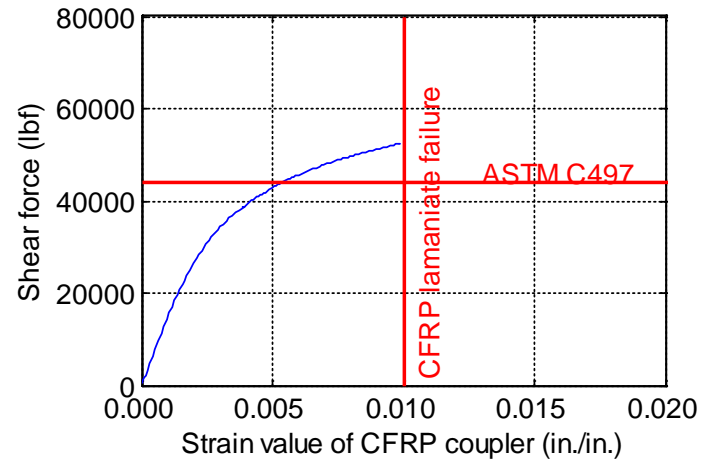
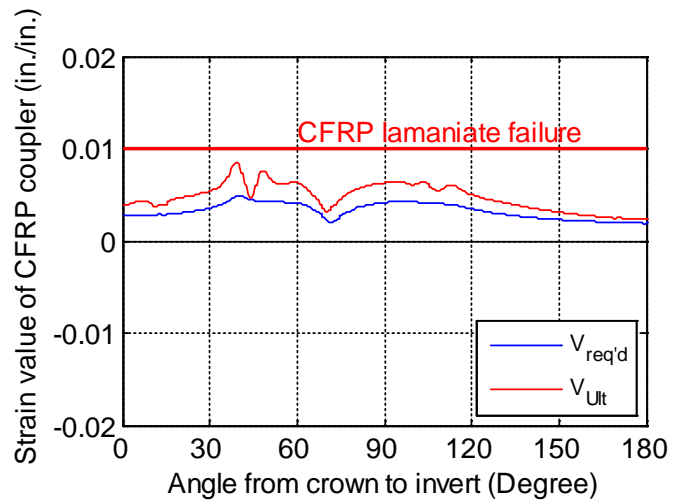
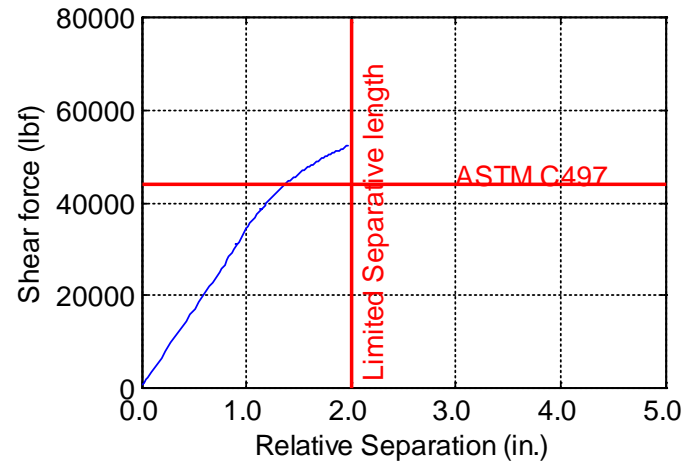
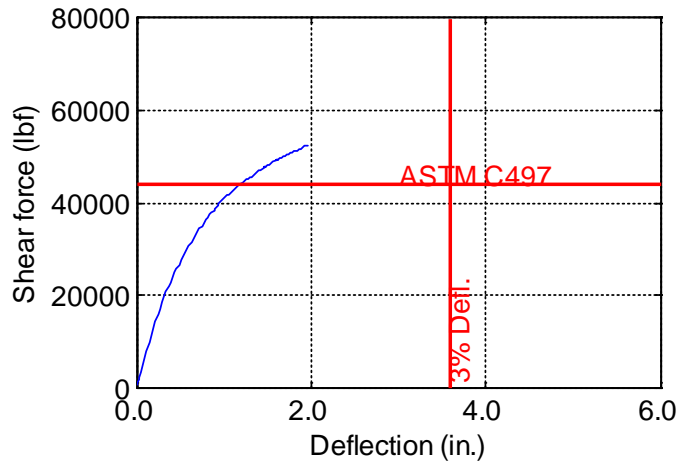


Figure B-229. TW-120-09-0.375

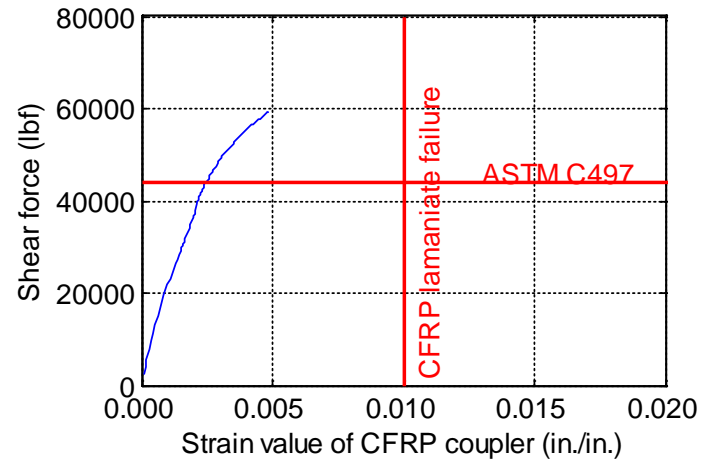
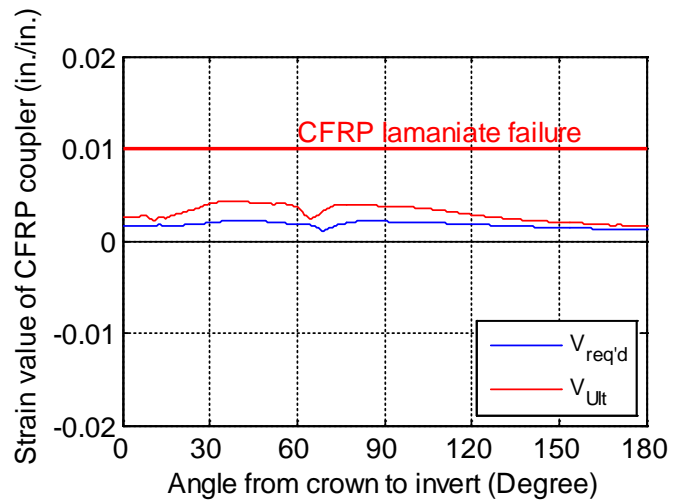
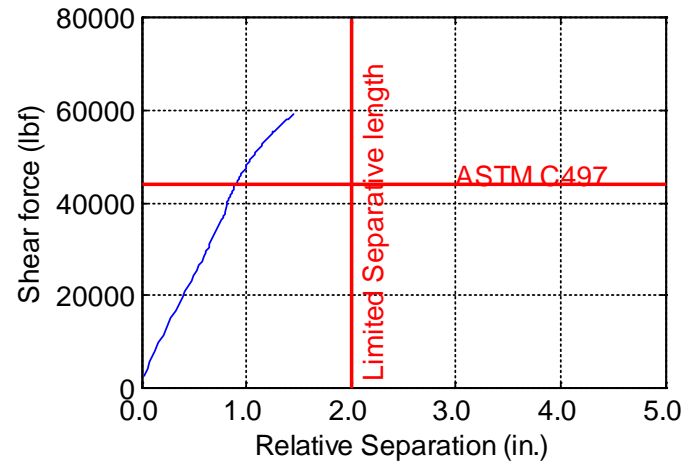
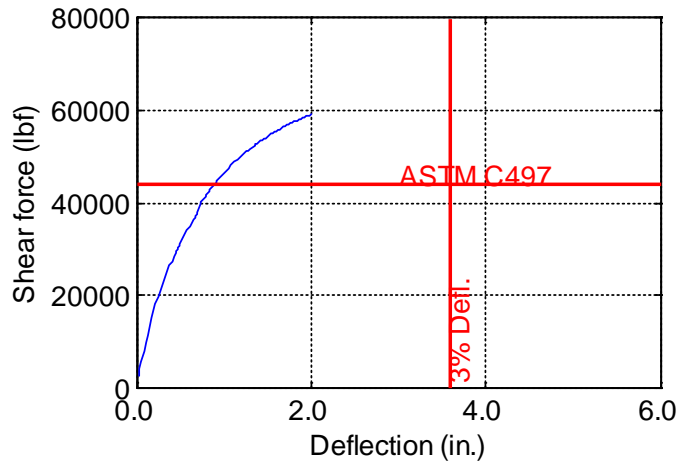


Figure B-230. TW-120-09-0.5

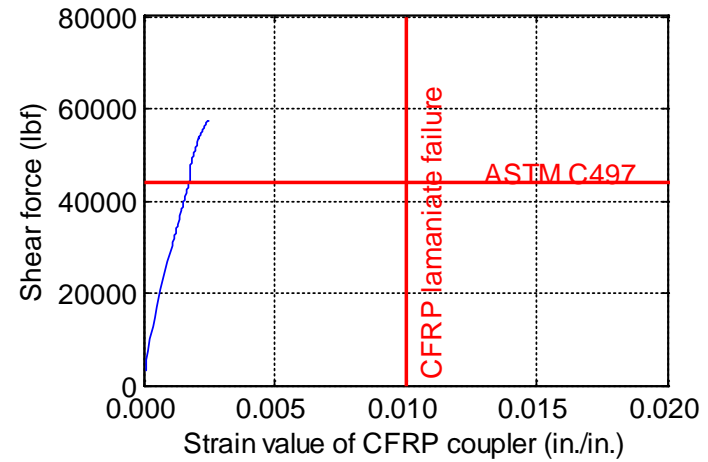
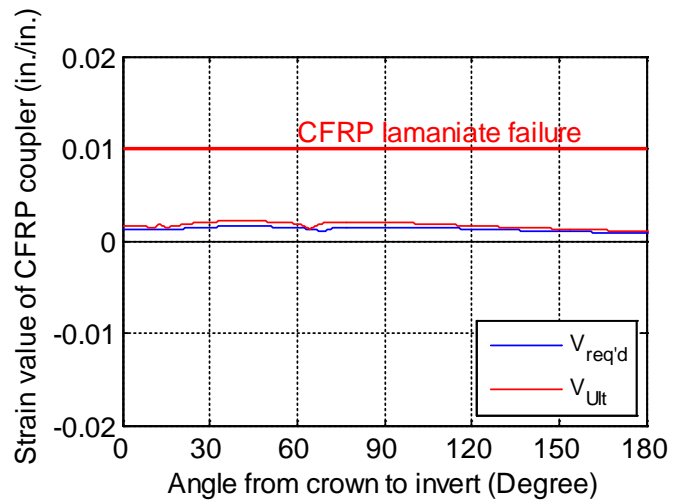
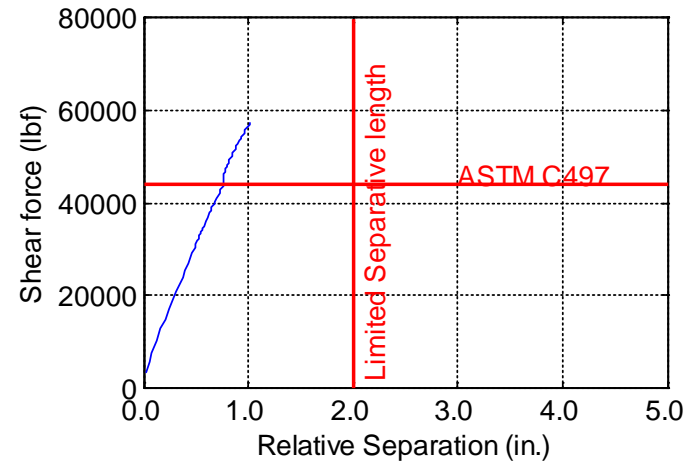
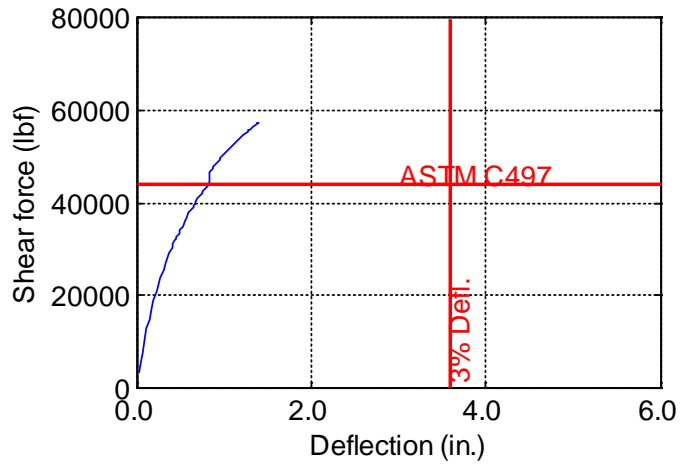


Figure B-231. TW-120-09-0.625

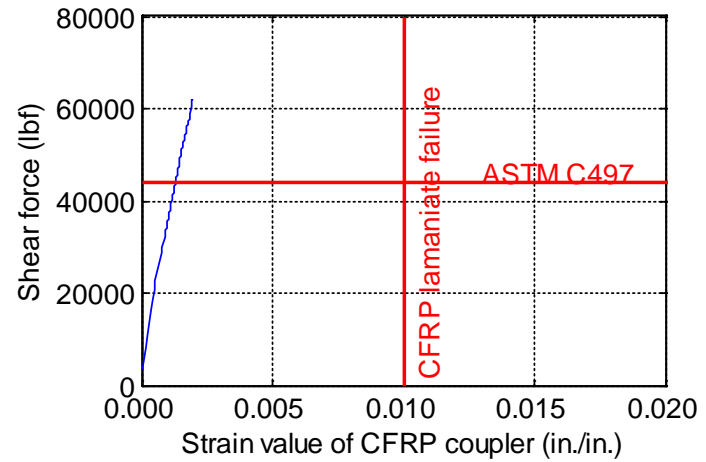
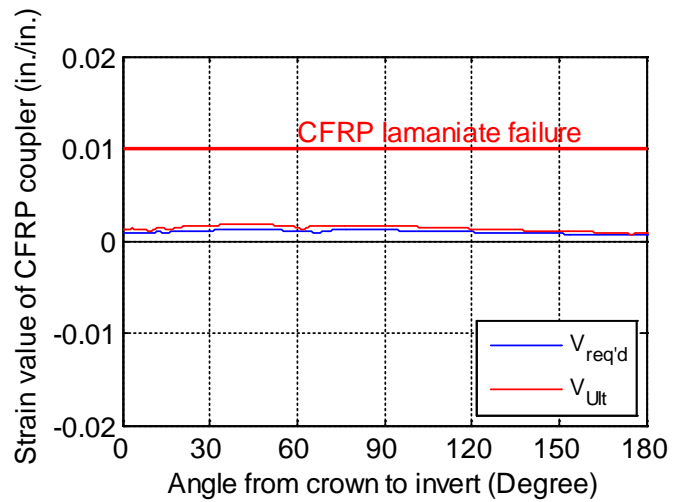
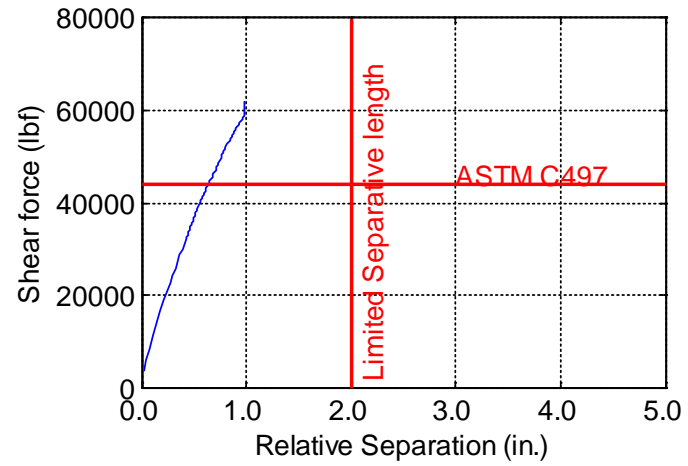
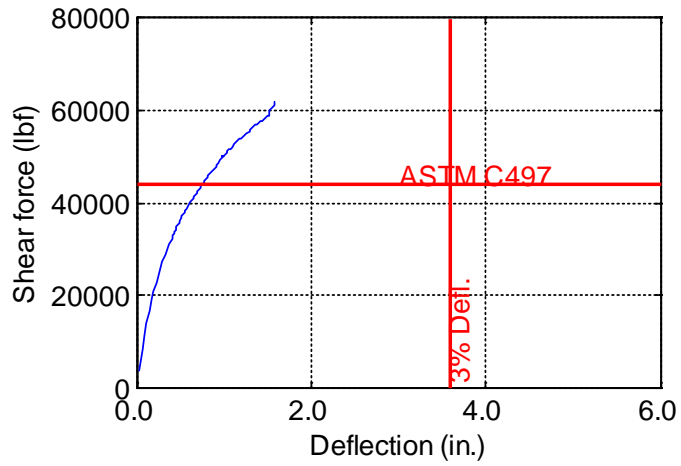


Figure B-232. TW-120-09-0.75

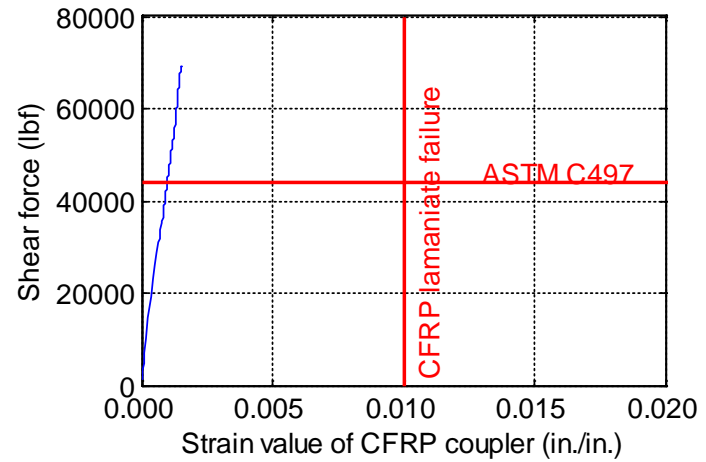
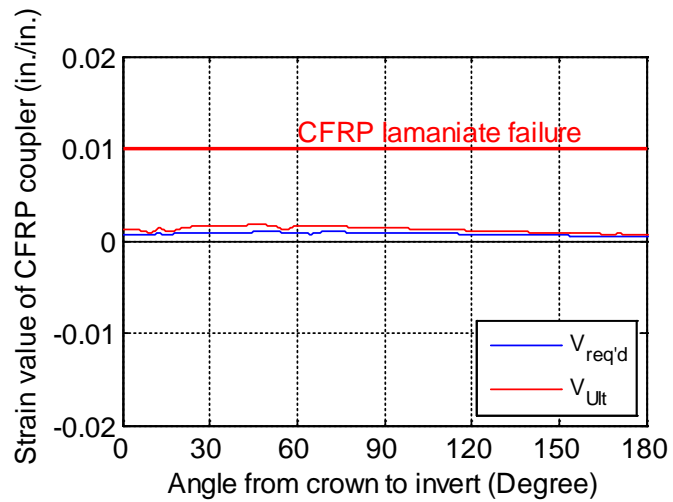
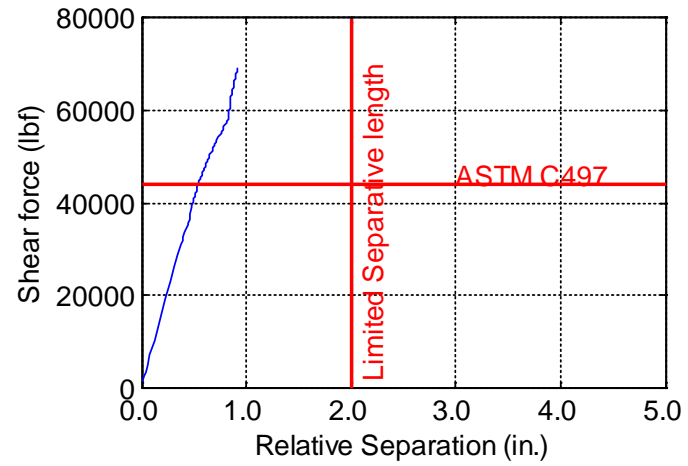
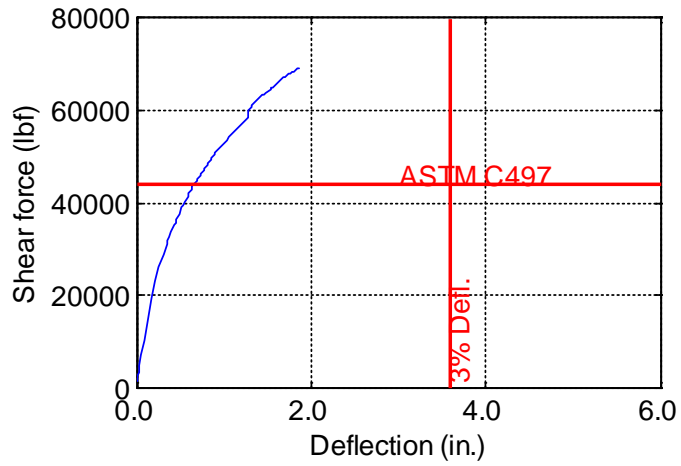


Figure B-233. TW-120-09-0.875

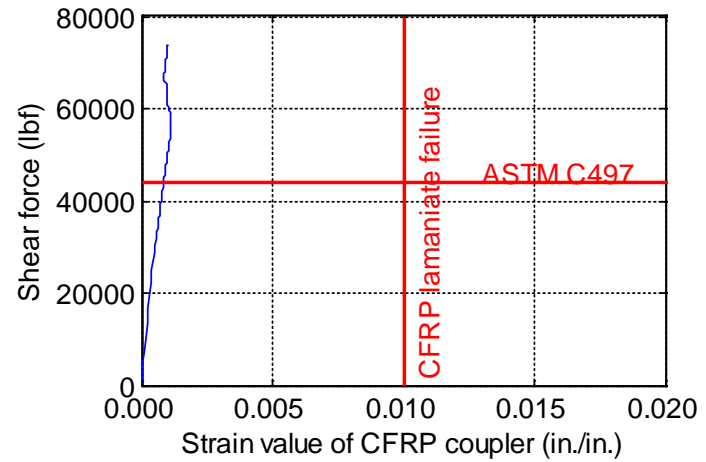
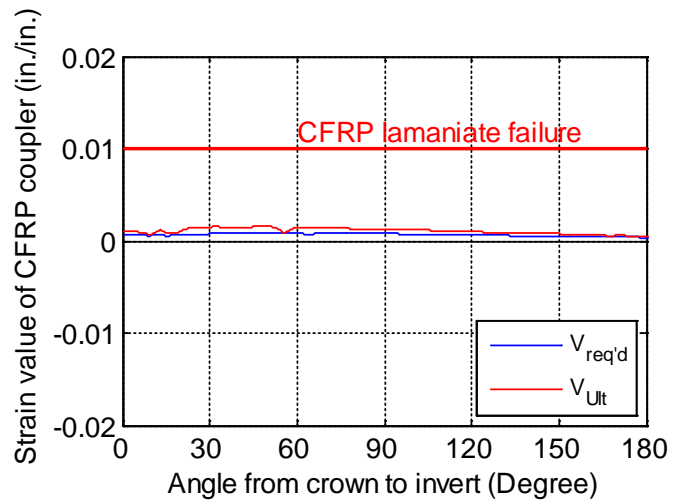
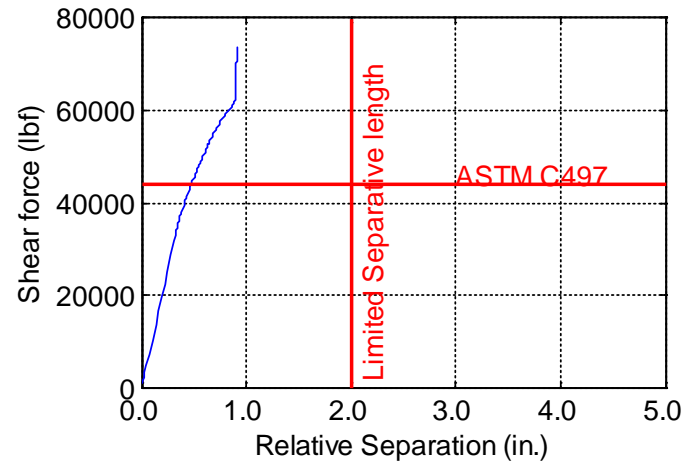
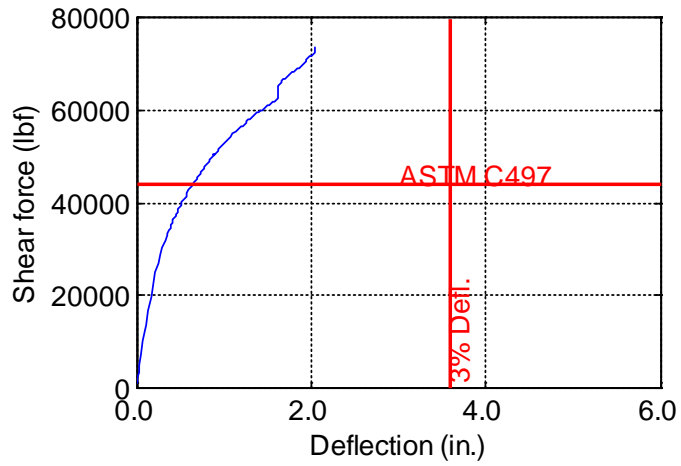


Figure B-234. TW-120-09-1.0

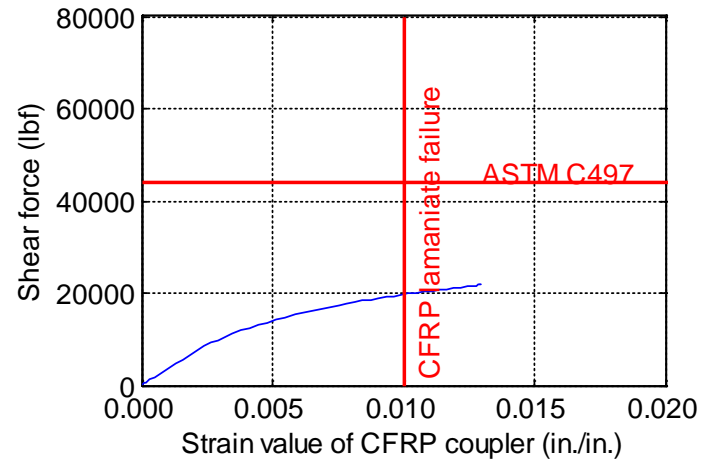
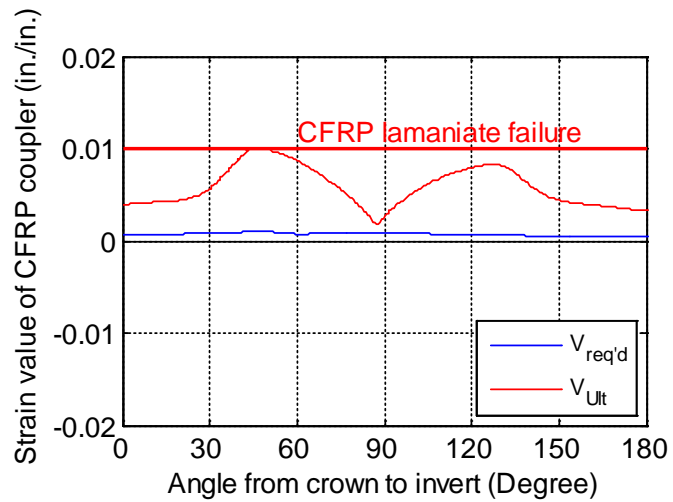
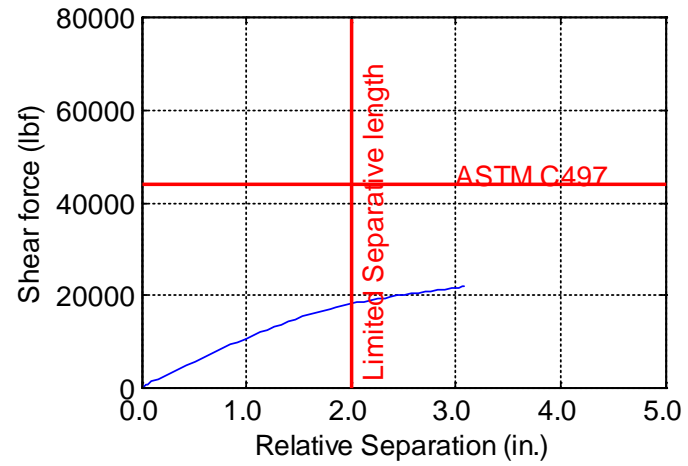
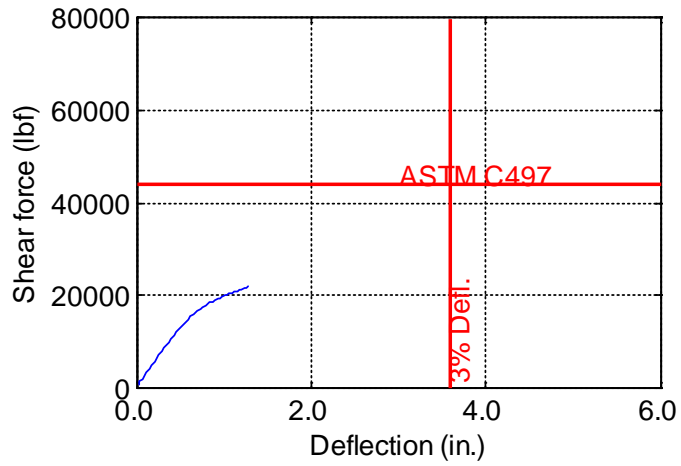


Figure B-235. TW-120-12-0.125

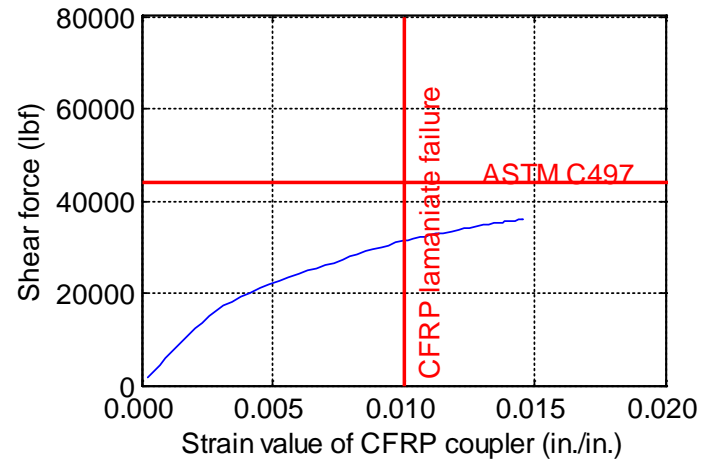
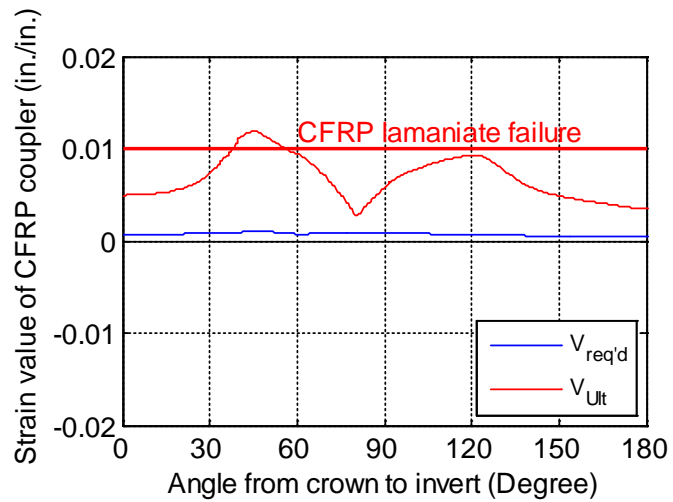
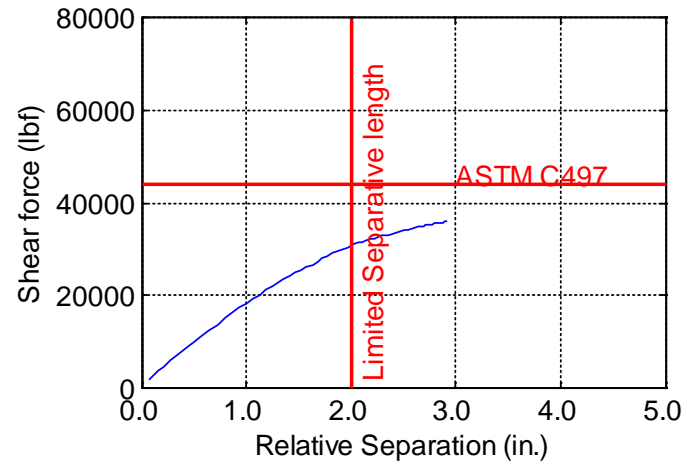
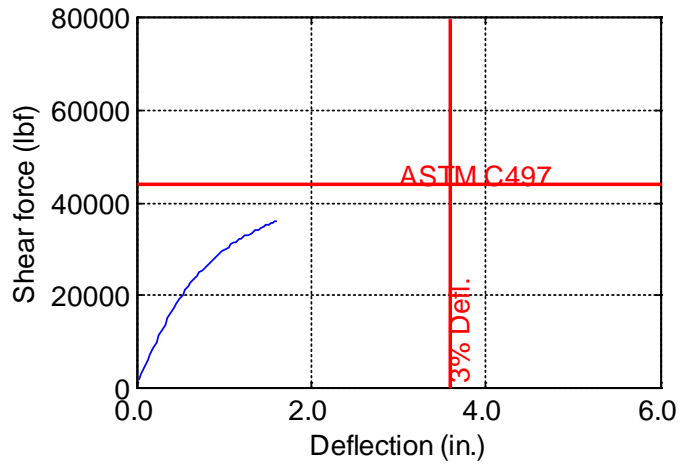


Figure B-236. TW-120-12-0.1875

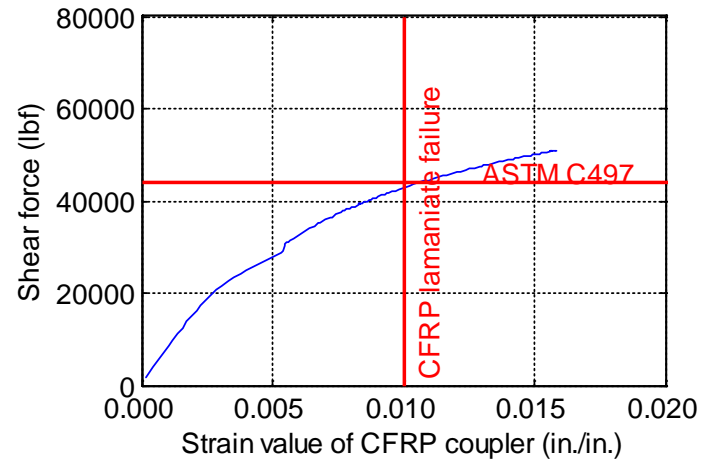
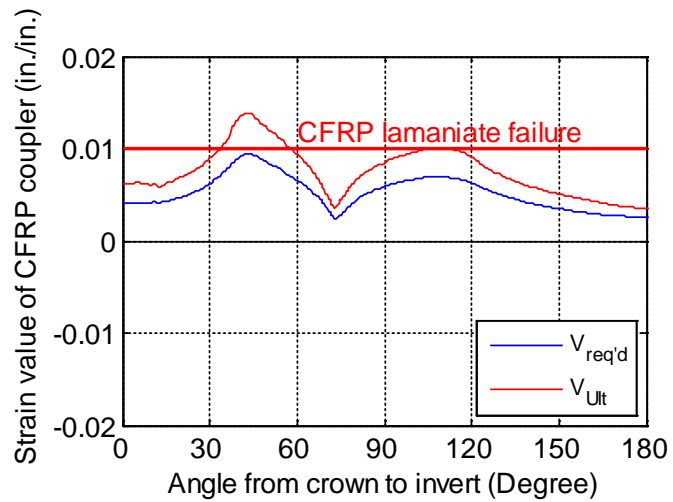
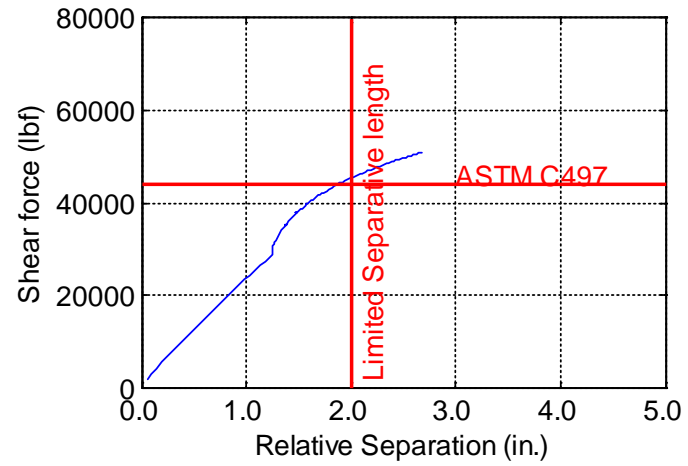
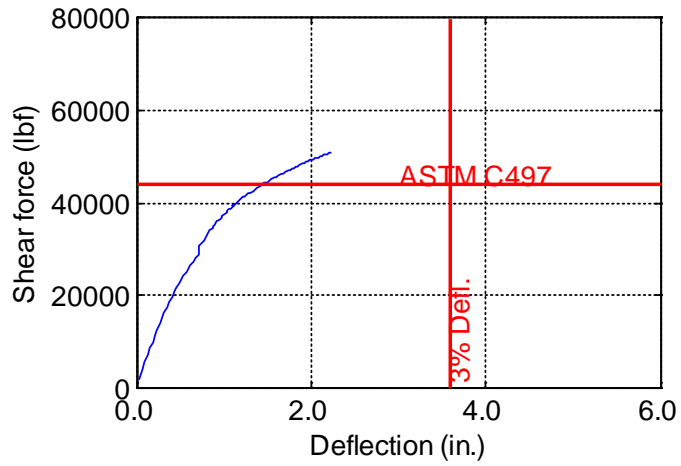


Figure B-237. TW-120-12-0.25

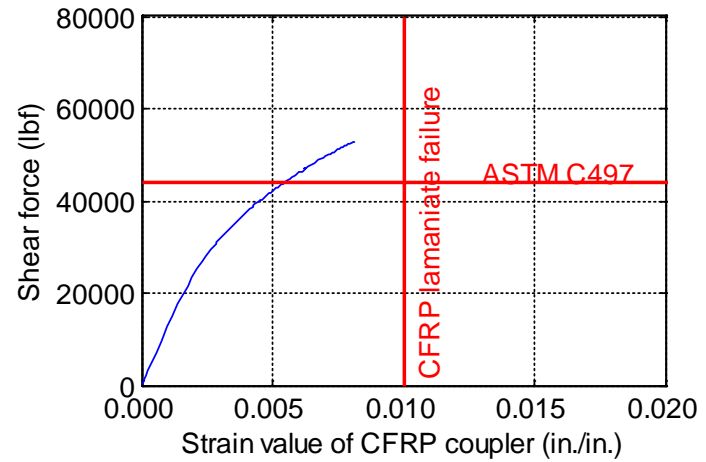
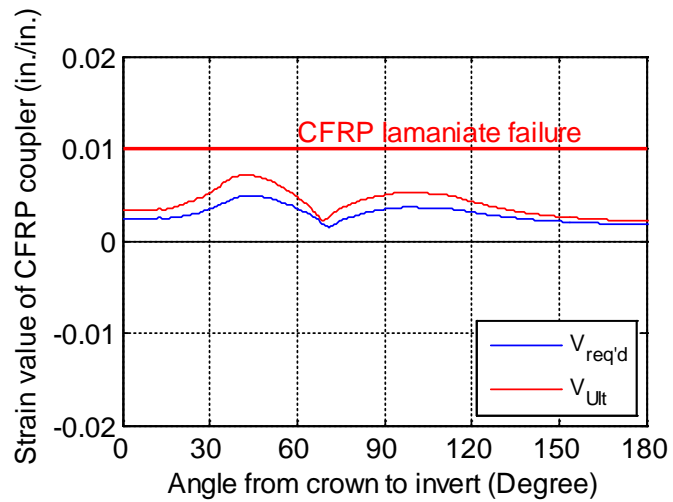
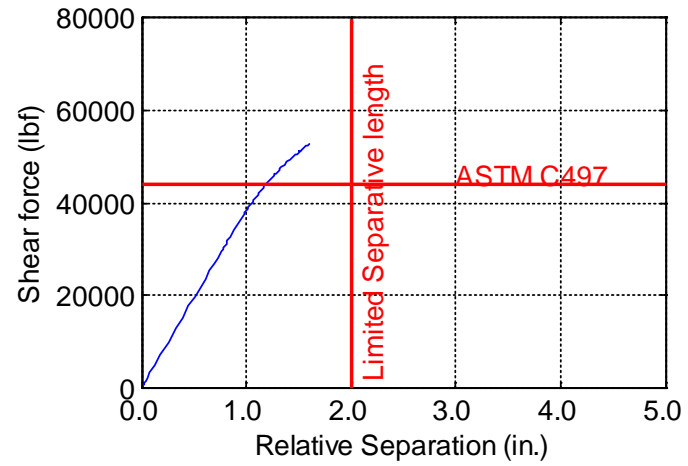
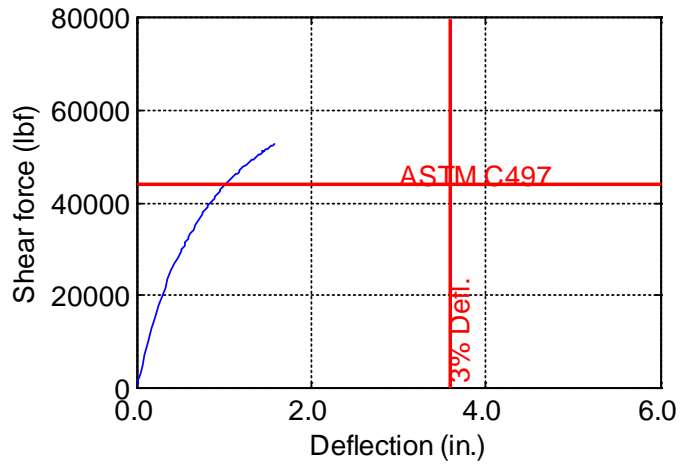


Figure B-238. TW-120-12-0.375

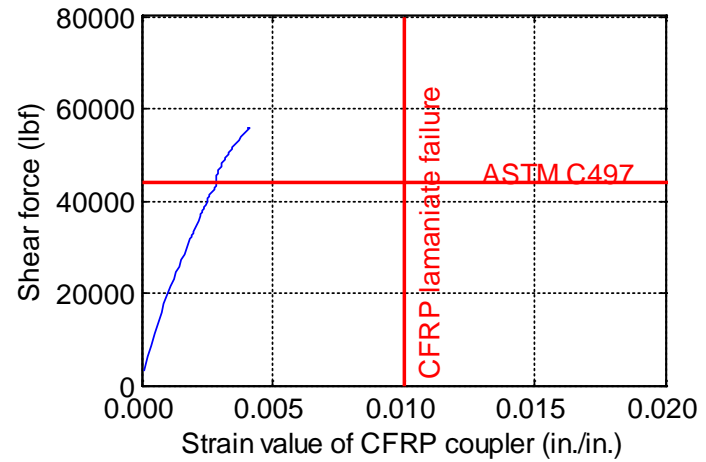
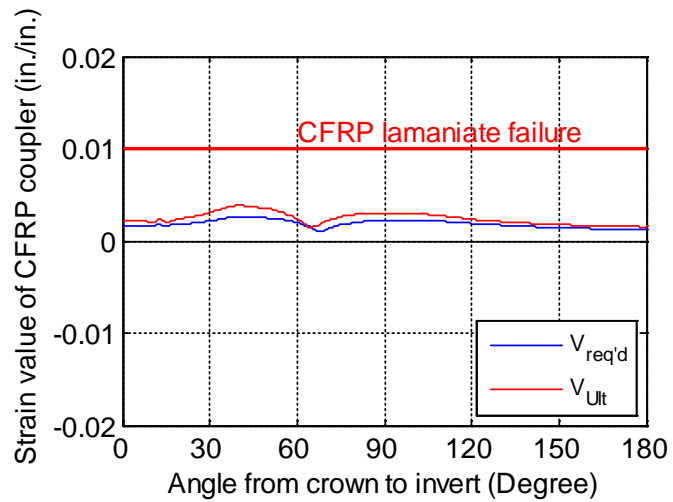
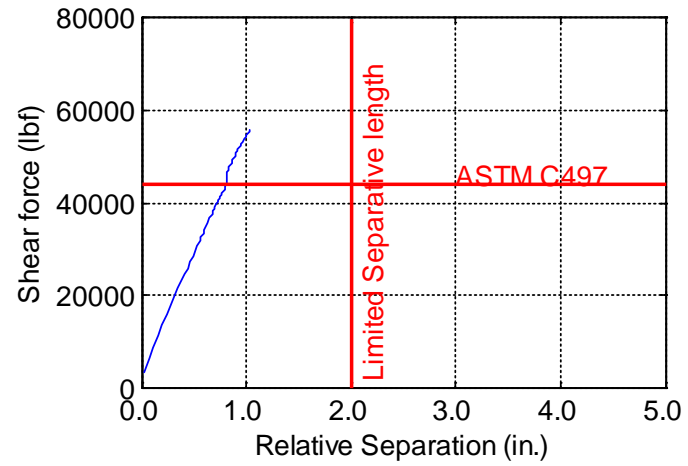
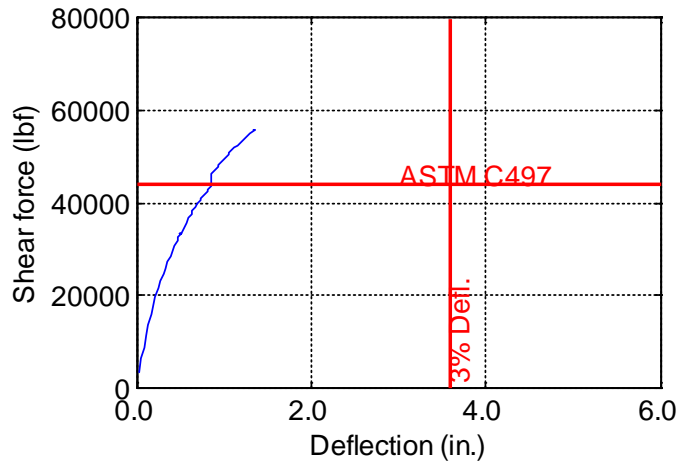


Figure B-239. TW-120-12-0.5

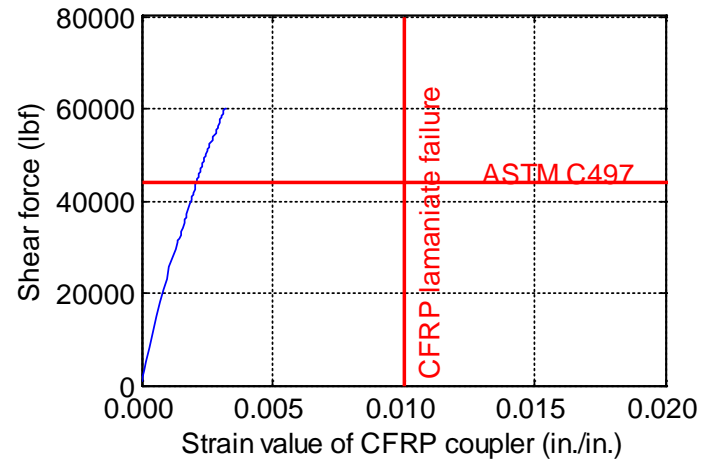
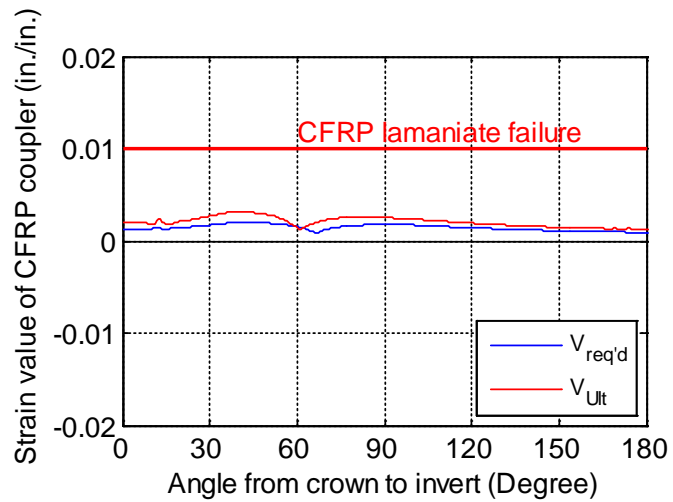
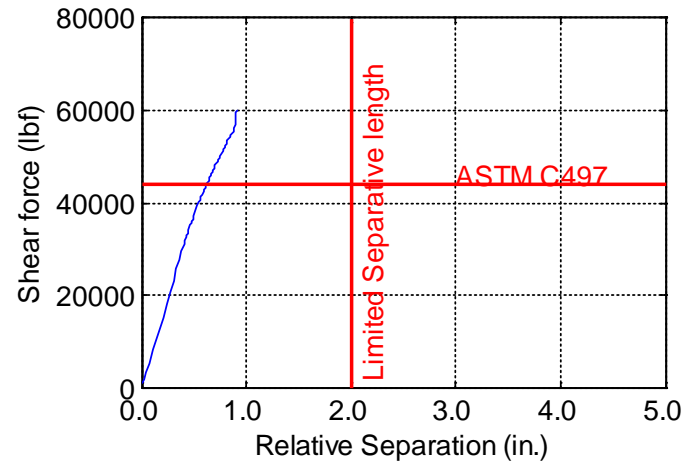
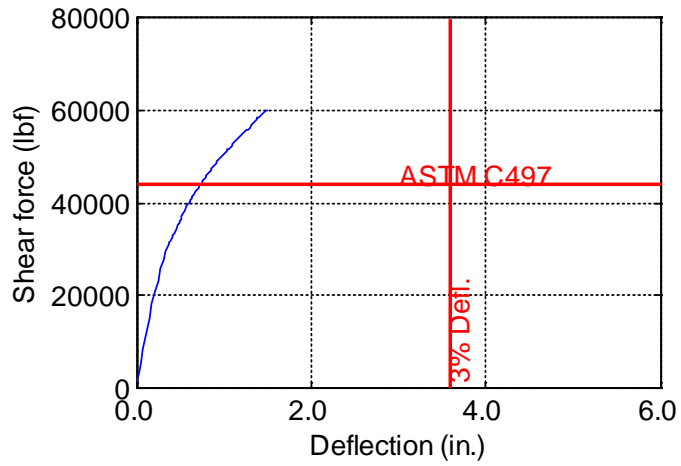


Figure B-240. TW-120-12-0.625

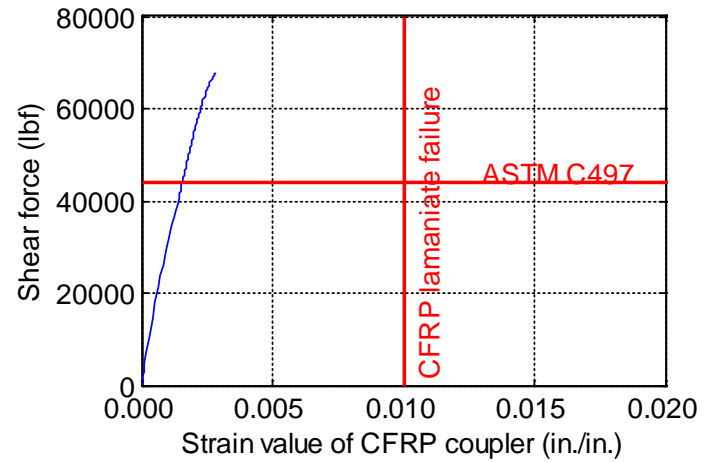
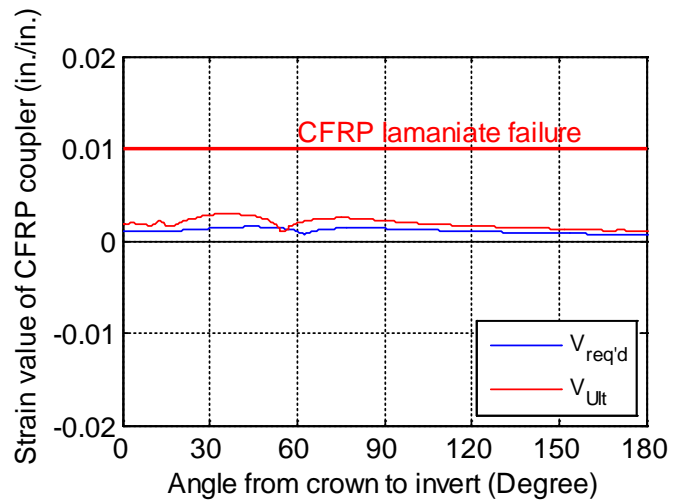
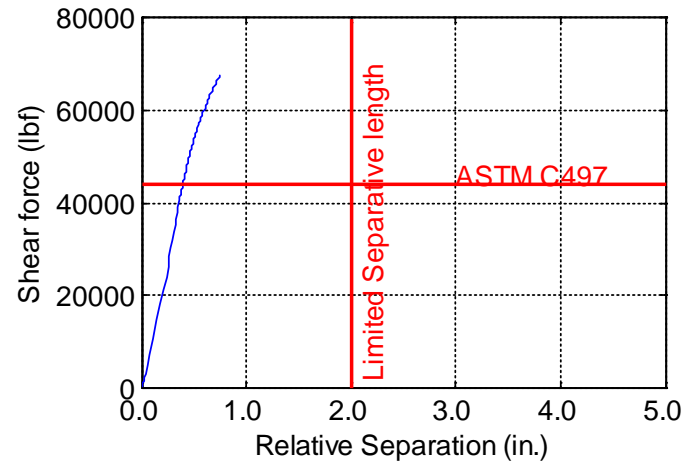
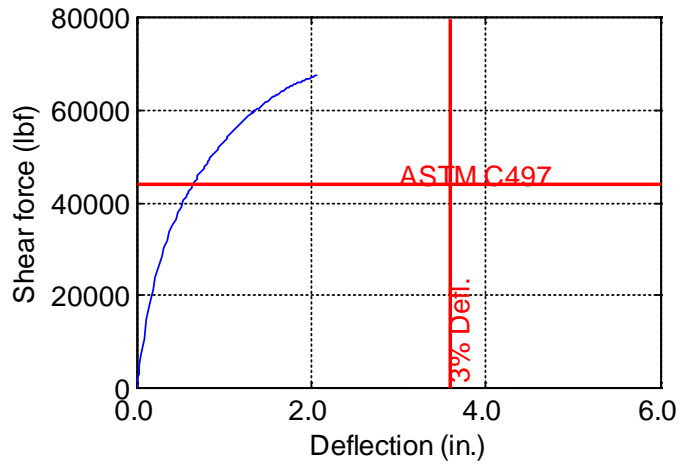


Figure B-241. TW-120-12-0.75

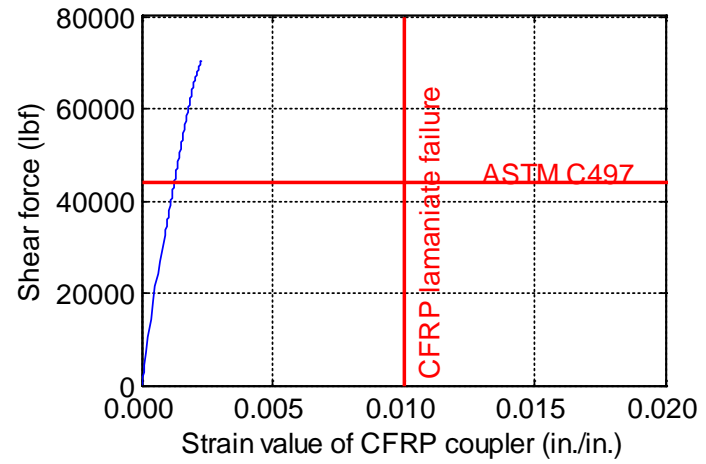
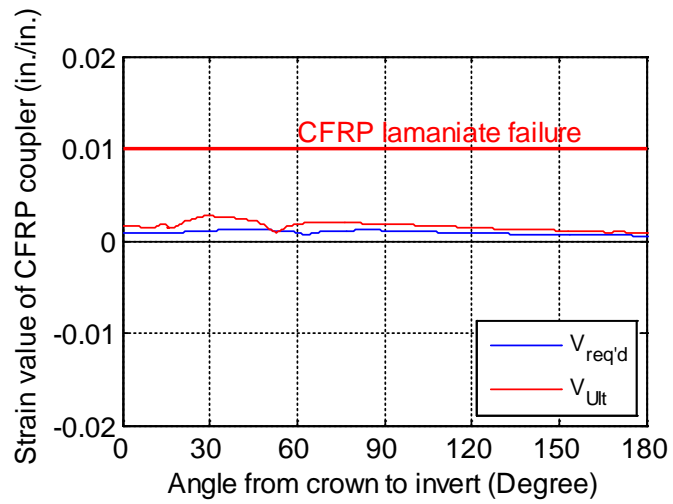
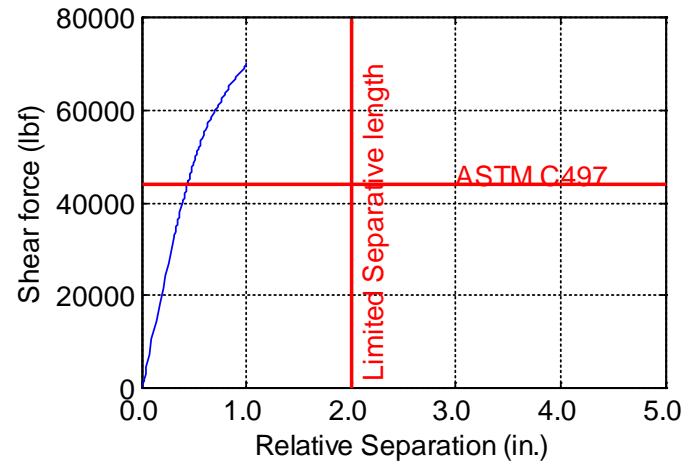
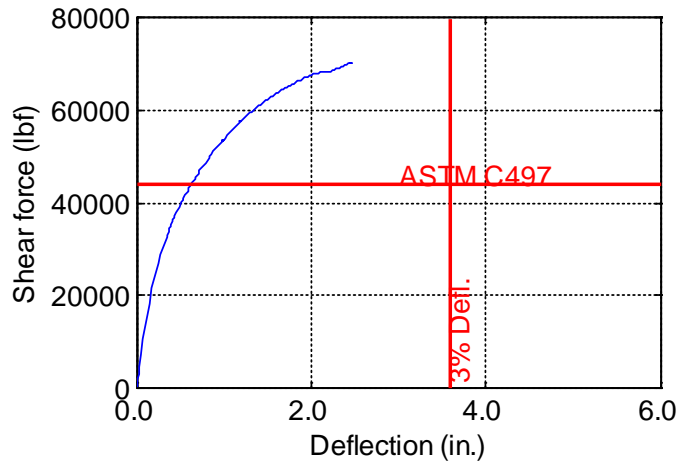


Figure B-242. TW-120-12-0.875

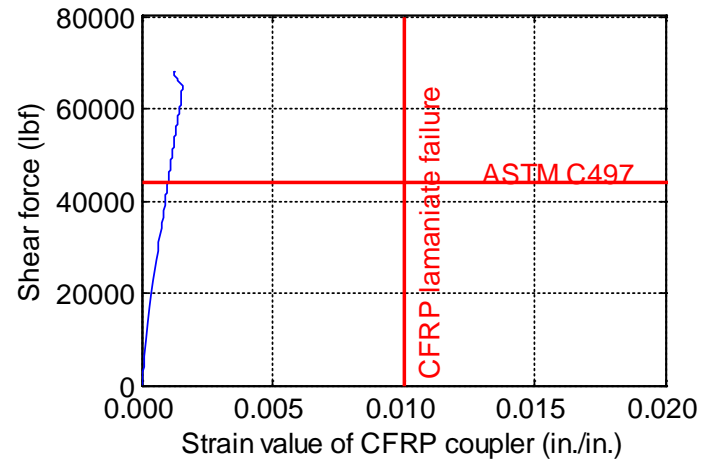
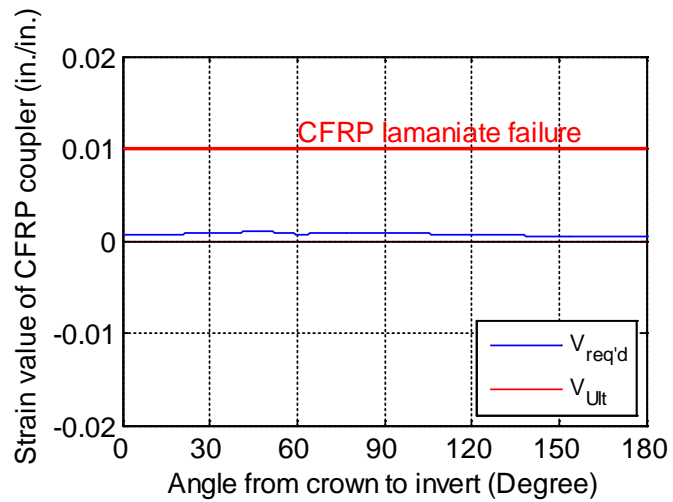
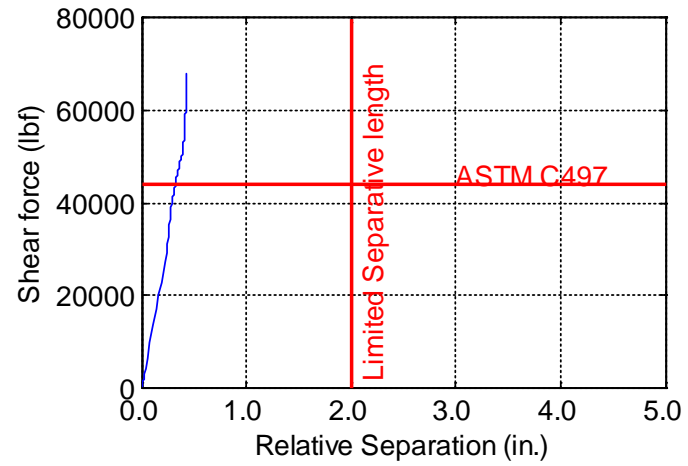
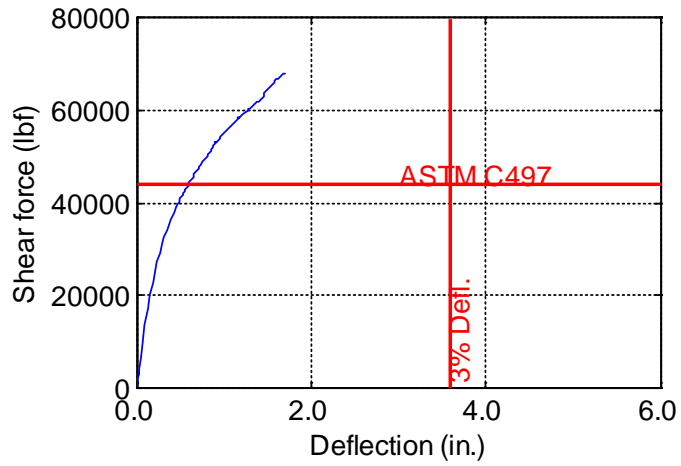


Figure B-243. TW-120-12-1.0

Appendix C
Statistical Analysis Results

Table C-1. Results of investigation of X- and Y- Outliers for ultimate shear force

Obs	Residual	RStudent	H	Ratio	DFFITS	-----DFBETAS-----					
						Obs	Intercept	IDP	Width	THK	tpipe
1	0.1507	1.0362	0.0505	1.0515	0.239	1	0.1824	-0.1531	-0.0878	-0.1219	0.1104
2	0.082	0.5606	0.0432	1.0604	0.1192	2	0.1	-0.0825	-0.0473	-0.0439	0.0595
3	0.1466	1.0022	0.0398	1.0414	0.2041	3	0.1806	-0.1472	-0.0845	-0.0508	0.1062
4	0.0429	0.2921	0.0375	1.0591	0.0576	4	0.0534	-0.0429	-0.0246	-0.0035	0.0309
5	-0.00853	-0.0581	0.0376	1.0611	-0.0115	5	-0.0108	0.0085	0.0049	-0.0009	-0.0062
6	0.003614	0.0246	0.0387	1.0623	0.0049	6	0.0046	-0.0036	-0.0021	0.0009	0.0026
7	-0.0153	-0.1041	0.0402	1.0638	-0.0213	7	-0.0196	0.0153	0.0088	-0.0057	-0.011
8	-0.0368	-0.2516	0.0419	1.0646	-0.0526	8	-0.0477	0.037	0.0212	-0.0174	-0.0267
9	-0.0446	-0.3052	0.0438	1.0659	-0.0653	9	-0.0582	0.0449	0.0258	-0.0251	-0.0324
10	0.0693	0.4709	0.0299	1.0478	0.0826	10	0.0271	-0.0048	-0.0395	-0.0548	-0.0094
11	0.003616	0.0245	0.0226	1.0449	0.0037	11	0.0015	-0.0003	-0.002	-0.0019	-0.0005
12	-0.0268	-0.1807	0.0192	1.0405	-0.0253	12	-0.0112	0.0018	0.0151	0.0091	0.0036
13	-0.0975	-0.6579	0.0169	1.0294	-0.0862	13	-0.0428	0.0067	0.0548	0.0078	0.0131
14	-0.0759	-0.5119	0.017	1.0332	-0.0672	14	-0.0344	0.0052	0.0426	-0.0079	0.0102
15	-0.0917	-0.6194	0.018	1.0317	-0.0839	15	-0.0427	0.0063	0.0516	-0.0226	0.0123
16	-0.1186	-0.8019	0.0196	1.0276	-0.1133	16	-0.0563	0.0082	0.0669	-0.0431	0.0159
17	-0.1502	-1.0171	0.0213	1.021	-0.1501	17	-0.0727	0.0104	0.0849	-0.0696	0.0202
18	-0.177	-1.2008	0.0232	1.0143	-0.1849	18	-0.087	0.0123	0.1004	-0.0975	0.0239
19	0.115	0.7813	0.0298	1.0392	0.1368	19	0.0041	0.0367	-0.0655	-0.0909	-0.052
20	-0.0128	-0.0863	0.0225	1.0446	-0.0131	20	-0.0007	-0.004	0.0072	0.0067	0.0057
21	0.0609	0.4109	0.0191	1.0374	0.0573	21	0.0042	0.0192	-0.0343	-0.0206	-0.0272
22	0.1201	0.811	0.0168	1.0244	0.1059	22	0.0107	0.0379	-0.0676	-0.0096	-0.0537

Obs	Residual	RStudent	H	Ratio	DFFITS	-----DFBETAS-----					
						Obs	Intercept	IDP	Width	THK	tpipe
23	0.0587	0.3962	0.0169	1.0353	0.0519	23	0.0061	0.0185	-0.033	0.0061	-0.0262
24	0.0279	0.1881	0.0179	1.0391	0.0254	24	0.0032	0.0088	-0.0157	0.0069	-0.0125
25	-0.028	-0.189	0.0195	1.0408	-0.0266	25	-0.0035	-0.0088	0.0158	-0.0102	0.0125
26	-0.0166	-0.1119	0.0212	1.0431	-0.0165	26	-0.0022	-0.0052	0.0093	-0.0077	0.0074
27	-0.0554	-0.3746	0.0231	1.0423	-0.0576	27	-0.0076	-0.0175	0.0313	-0.0304	0.0249
28	0.0153	0.1035	0.0279	1.0504	0.0175	28	-0.0006	0.0056	-0.0087	-0.012	-0.0064
29	0.1215	0.8222	0.0207	1.0281	0.1194	29	-0.0026	0.0442	-0.0686	-0.0637	-0.051
30	0.2232	1.5121	0.0172	0.9905	0.2003	30	-0.0016	0.0812	-0.126	-0.0758	-0.0936
31	0.1884	1.2735	0.0149	1.002	0.1567	31	0.0024	0.0683	-0.106	-0.015	-0.0787
32	0.098	0.661	0.015	1.0273	0.0816	32	0.0026	0.0355	-0.055	0.0102	-0.0409
33	0.0352	0.2372	0.0161	1.0367	0.0303	33	0.0013	0.0127	-0.0197	0.0087	-0.0147
34	-0.0397	-0.2677	0.0176	1.038	-0.0358	34	-0.0019	-0.0144	0.0223	-0.0144	0.0166
35	-0.0443	-0.2989	0.0194	1.0395	-0.042	35	-0.0024	-0.0161	0.0249	-0.0204	0.0185
36	-0.0601	-0.406	0.0212	1.0398	-0.0598	36	-0.0037	-0.0218	0.0339	-0.0329	0.0252
37	-0.2933	-2.0051	0.0275	0.9654	-0.337	37	0.0288	-0.117	0.1679	0.2331	0.1145
38	-0.061	-0.4123	0.0202	1.0386	-0.0592	38	0.0047	-0.024	0.0344	0.0319	0.0235
39	0.2146	1.4532	0.0168	0.9936	0.1899	39	-0.0135	0.0843	-0.1211	-0.0728	-0.0825
40	0.2189	1.4807	0.0145	0.9896	0.1793	40	-0.0093	0.0858	-0.1232	-0.0175	-0.084
41	0.1635	1.1038	0.0146	1.0101	0.1341	41	-0.0047	0.064	-0.0918	0.017	-0.0626
42	0.1166	0.7868	0.0156	1.024	0.0991	42	-0.002	0.0456	-0.0655	0.0287	-0.0447
43	0.0768	0.5179	0.0172	1.0332	0.0684	43	-0.0007	0.0301	-0.0431	0.0278	-0.0294
44	0.0162	0.1092	0.0189	1.0407	0.0152	44	0	0.0063	-0.0091	0.0075	-0.0062
45	-0.00563	-0.038	0.0208	1.0429	-0.0055	45	0	-0.0022	0.0032	-0.0031	0.0022

						-----DFBETAS-----					
Obs	Residual	RStudent	H	Ratio	DFFITS	Obs	Intercept	IDP	Width	THK	tpipe
46	-0.1063	-0.7214	0.0278	1.039	-0.122	46	0.0147	-0.0439	0.0604	0.0839	0.0371
47	-0.1	-0.6762	0.0205	1.0327	-0.0979	47	0.0117	-0.041	0.0564	0.0524	0.0347
48	0.1826	1.2354	0.0171	1.0063	0.1631	48	-0.0188	0.0747	-0.1029	-0.0619	-0.0633
49	0.0589	0.3967	0.0148	1.0332	0.0486	49	-0.0049	0.024	-0.033	-0.0047	-0.0203
50	-0.0175	-0.1179	0.0149	1.0364	-0.0145	50	0.0012	-0.0071	0.0098	-0.0018	0.006
51	0.0806	0.5438	0.016	1.0314	0.0693	51	-0.0046	0.0329	-0.0453	0.0198	-0.0278
52	0.0618	0.4168	0.0175	1.0357	0.0556	52	-0.003	0.0252	-0.0347	0.0224	-0.0213
53	0.0552	0.3727	0.0193	1.0383	0.0522	53	-0.0023	0.0226	-0.0311	0.0255	-0.0191
54	0.0324	0.2189	0.0211	1.0422	0.0321	54	-0.0011	0.0133	-0.0183	0.0178	-0.0112
55	-0.5615	-3.9268	0.0267	0.7656	-0.6502	55	-0.0219	-0.0902	0.3288	0.4563	0.0133
56	-0.1442	-0.9757	0.0194	1.0208	-0.1373	56	-0.0083	-0.0223	0.0814	0.0756	0.0033
57	-0.00461	-0.0311	0.016	1.0379	-0.004	57	-0.0003	-0.0007	0.0026	0.0016	0.0001
58	-0.0183	-0.1235	0.0137	1.0351	-0.0145	58	-0.0017	-0.0028	0.0103	0.0015	0.0004
59	0.1213	0.8176	0.0138	1.0211	0.0966	59	0.0128	0.0187	-0.068	0.0126	-0.0027
60	0.0724	0.488	0.0148	1.0315	0.0599	60	0.0084	0.0111	-0.0406	0.0178	-0.0016
61	0.0525	0.3543	0.0164	1.0355	0.0457	61	0.0066	0.0081	-0.0295	0.019	-0.0012
62	0.057	0.3845	0.0181	1.0369	0.0522	62	0.0076	0.0088	-0.032	0.0263	-0.0013
63	0.0322	0.2172	0.02	1.0411	0.031	63	0.0045	0.005	-0.0181	0.0176	-0.0007
64	-0.748	-5.3862	0.0326	0.5926	-0.9882	64	-0.2555	0.1867	0.4523	0.6278	-0.3527
65	-0.2687	-1.8324	0.0253	0.9766	-0.2952	65	-0.092	0.0633	0.1533	0.1423	-0.1195
66	0.0179	0.1211	0.0219	1.0438	0.0181	66	0.0063	-0.0042	-0.0101	-0.0061	0.0079
67	0.007183	0.0485	0.0196	1.0416	0.0068	67	0.0027	-0.0017	-0.004	-0.0006	0.0032
68	0.0598	0.4039	0.0197	1.0382	0.0572	68	0.0231	-0.0139	-0.0337	0.0062	0.0263

Obs	Residual	RStudent	H	Ratio	DFFITS	-----DFBETAS-----					
						Obs	Intercept	IDP	Width	THK	tpipe
69	0.0169	0.1144	0.0207	1.0426	0.0167	69	0.0067	-0.0039	-0.0096	0.0042	0.0074
70	-0.0379	-0.2565	0.0223	1.0431	-0.0387	70	-0.0154	0.0088	0.0214	-0.0138	-0.0167
71	-0.0685	-0.4638	0.024	1.0417	-0.0727	71	-0.0285	0.016	0.0388	-0.0318	-0.0302
72	0.0137	0.0927	0.0259	1.0482	0.0151	72	0.0058	-0.0032	-0.0078	0.0075	0.0061
73	-0.5972	-4.2216	0.0382	0.739	-0.8418	73	-0.2474	0.2217	0.3556	0.4935	-0.3824
74	-0.253	-1.7287	0.031	0.9899	-0.3091	74	-0.106	0.0904	0.1451	0.1347	-0.156
75	0.0347	0.235	0.0276	1.049	0.0396	75	0.0149	-0.0123	-0.0197	-0.0118	0.0212
76	0.3009	2.0558	0.0252	0.9591	0.3308	76	0.1361	-0.1072	-0.172	-0.0244	0.185
77	0.2036	1.384	0.0253	1.0065	0.2231	77	0.0946	-0.0722	-0.1158	0.0214	0.1245
78	0.1157	0.7849	0.0264	1.0354	0.1293	78	0.0549	-0.041	-0.0657	0.0288	0.0707
79	0.0988	0.6708	0.0279	1.0407	0.1137	79	0.0479	-0.035	-0.0562	0.0362	0.0604
80	0.1002	0.681	0.0297	1.0423	0.1191	80	0.0494	-0.0356	-0.0571	0.0468	0.0614
81	0.0484	0.3292	0.0315	1.0521	0.0594	81	0.0242	-0.0172	-0.0276	0.0268	0.0297
82	0.2197	1.5089	0.0437	1.0181	0.3227	82	0.1989	-0.2221	0.0136	-0.1769	0.1602
83	0.1709	1.1675	0.0365	1.03	0.2272	83	0.1568	-0.1712	0.0105	-0.0912	0.1235
84	0.1206	0.8208	0.0331	1.0413	0.1518	84	0.1118	-0.1202	0.0073	-0.0415	0.0867
85	0.0228	0.155	0.0307	1.0531	0.0276	85	0.0215	-0.0227	0.0014	-0.0018	0.0163
86	0.0124	0.0845	0.0308	1.0536	0.0151	86	0.0119	-0.0124	0.0008	0.0013	0.0089
87	0.002582	0.0175	0.0319	1.0549	0.0032	87	0.0025	-0.0026	0.0002	0.0006	0.0019
88	-0.0323	-0.2196	0.0334	1.0555	-0.0408	88	-0.0317	0.0322	-0.002	-0.0119	-0.0232
89	-0.0539	-0.3667	0.0352	1.0555	-0.07	89	-0.0534	0.0537	-0.0033	-0.0253	-0.0388
90	-0.0337	-0.2294	0.037	1.0594	-0.045	90	-0.0336	0.0337	-0.0021	-0.0188	-0.0243
91	0.1853	1.2576	0.0231	1.0113	0.1935	91	0.0179	-0.0129	0.0112	-0.1459	-0.025

Obs	Residual	RStudent	H	Ratio	DFFITS	-----DFBETAS-----					
						Obs	Intercept	IDP	Width	THK	tpipe
92	0.1266	0.8544	0.0159	1.0219	0.1085	92	0.0146	-0.0087	0.0076	-0.066	-0.017
93	0.0762	0.5129	0.0124	1.0284	0.0576	93	0.0098	-0.0052	0.0045	-0.0256	-0.0102
94	-0.0305	-0.2051	0.0101	1.0308	-0.0207	94	-0.0045	0.0021	-0.0018	0.0024	0.0041
95	-0.1059	-0.7124	0.0102	1.0208	-0.0724	95	-0.0172	0.0073	-0.0063	-0.011	0.0141
96	-0.1498	-1.0091	0.0113	1.011	-0.1078	96	-0.026	0.0103	-0.0089	-0.0367	0.02
97	-0.1826	-1.2328	0.0128	1.002	-0.1405	97	-0.0334	0.0126	-0.0109	-0.0661	0.0244
98	-0.2162	-1.4627	0.0146	0.9908	-0.1778	98	-0.0413	0.0149	-0.013	-0.0998	0.029
99	-0.23	-1.5585	0.0164	0.9867	-0.2014	99	-0.0456	0.0159	-0.0138	-0.1261	0.0309
100	0.0329	0.2227	0.023	1.0442	0.0342	100	-0.0084	0.0104	0.002	-0.0258	-0.0148
101	-0.0398	-0.2682	0.0158	1.036	-0.0339	101	0.0093	-0.0125	-0.0024	0.0207	0.0177
102	-0.0702	-0.4723	0.0123	1.0292	-0.0528	102	0.0154	-0.022	-0.0042	0.0236	0.0312
103	-0.1219	-0.8203	0.01	1.0171	-0.0825	103	0.0243	-0.0382	-0.0073	0.0097	0.0541
104	-0.1213	-0.8162	0.0101	1.0173	-0.0825	104	0.0225	-0.038	-0.0072	-0.0125	0.0538
105	-0.0642	-0.4315	0.0112	1.0288	-0.0459	105	0.0112	-0.0201	-0.0038	-0.0157	0.0285
106	-0.061	-0.4107	0.0127	1.0307	-0.0466	106	0.0101	-0.0191	-0.0036	-0.022	0.0271
107	-0.0306	-0.2061	0.0145	1.0353	-0.025	107	0.0049	-0.0096	-0.0018	-0.0141	0.0136
108	-0.0704	-0.4748	0.0163	1.0333	-0.0611	108	0.0107	-0.0222	-0.0042	-0.0384	0.0314
109	-0.1258	-0.8512	0.0212	1.0276	-0.1252	109	0.0419	-0.0458	-0.0076	0.0986	0.0528
110	-0.0935	-0.63	0.0139	1.0271	-0.0748	110	0.029	-0.0338	-0.0056	0.0486	0.0389
111	0.0201	0.1352	0.0105	1.0317	0.0139	111	-0.0059	0.0072	0.0012	-0.0068	-0.0083
112	0.0374	0.2511	0.0082	1.0283	0.0228	112	-0.0103	0.0134	0.0022	-0.003	-0.0155
113	0.004012	0.0269	0.0083	1.0298	0.0025	113	-0.001	0.0014	0.0002	0.0004	-0.0017
114	0.005153	0.0346	0.0093	1.0309	0.0034	114	-0.0013	0.0019	0.0003	0.0013	-0.0021

Obs	Residual	RStudent	H	Ratio	DFFITS	-----DFBETAS-----					
						Obs	Intercept	IDP	Width	THK	tpipe
115	-0.0347	-0.2334	0.0109	1.0313	-0.0245	115	0.0084	-0.0125	-0.0021	-0.0125	0.0144
116	-0.0403	-0.2711	0.0126	1.0327	-0.0306	116	0.0095	-0.0145	-0.0024	-0.0185	0.0167
117	-0.0581	-0.3914	0.0145	1.0329	-0.0474	117	0.0133	-0.021	-0.0035	-0.0316	0.0242
118	0.007667	0.0518	0.0207	1.0428	0.0075	118	-0.003	0.003	0.0005	-0.006	-0.0029
119	0.2289	1.5487	0.0135	0.9844	0.1809	119	-0.084	0.0897	0.0137	-0.1196	-0.0878
120	0.3216	2.1822	0.01	0.934	0.2198	120	-0.1136	0.1262	0.0193	-0.109	-0.1235
121	0.2578	1.7414	0.0077	0.9658	0.1535	121	-0.0854	0.1006	0.0154	-0.0205	-0.0985
122	0.1734	1.1675	0.0078	1.0002	0.1036	122	-0.0549	0.0674	0.0103	0.0179	-0.066
123	0.0946	0.6357	0.0089	1.0217	0.0602	123	-0.0289	0.0367	0.0056	0.0231	-0.036
124	0.0737	0.4957	0.0104	1.0267	0.0508	124	-0.0219	0.0287	0.0044	0.0265	-0.0281
125	0.0251	0.1691	0.0122	1.0332	0.0188	125	-0.0073	0.0098	0.0015	0.0115	-0.0096
126	-0.00366	-0.0247	0.014	1.0358	-0.0029	126	0.001	-0.0014	-0.0002	-0.002	0.0014
127	-0.1433	-0.9703	0.0211	1.0228	-0.1423	127	0.0615	-0.0588	-0.0086	0.1124	0.0498
128	0.179	1.2085	0.0138	1.0042	0.143	128	-0.0727	0.0729	0.0107	-0.0933	-0.0618
129	0.2916	1.9756	0.0104	0.9511	0.2025	129	-0.1145	0.119	0.0175	-0.0987	-0.1008
130	0.1529	1.0283	0.0081	1.0069	0.0927	130	-0.0565	0.0619	0.0091	-0.0121	-0.0524
131	0.1575	1.0596	0.0082	1.0056	0.0961	131	-0.0561	0.0638	0.0094	0.0163	-0.054
132	0.0946	0.636	0.0092	1.022	0.0614	132	-0.0326	0.0383	0.0056	0.0231	-0.0324
133	0.0477	0.321	0.0108	1.0301	0.0335	133	-0.0161	0.0193	0.0028	0.0172	-0.0164
134	0.0672	0.452	0.0125	1.0298	0.0509	134	-0.0221	0.0273	0.004	0.0308	-0.0231
135	0.0264	0.1775	0.0144	1.0355	0.0214	135	-0.0085	0.0107	0.0016	0.0144	-0.0091
136	-0.3395	-2.3188	0.0199	0.9315	-0.3307	136	0.0869	-0.0531	-0.0206	0.2685	0.0078
137	-0.0503	-0.3383	0.0127	1.0319	-0.0383	137	0.0116	-0.0077	-0.003	0.0261	0.0011

Obs	Residual	RStudent	H	Ratio	DFFITS	-----DFBETAS-----					
						Obs	Intercept	IDP	Width	THK	tpipe
138	-0.00365	-0.0245	0.0093	1.0308	-0.0024	138	0.0008	-0.0006	-0.0002	0.0012	0.0001
139	0.0796	0.5345	0.0069	1.0222	0.0446	139	-0.0157	0.0122	0.0047	-0.0063	-0.0018
140	-0.0298	-0.1997	0.007	1.0276	-0.0168	140	0.0054	-0.0045	-0.0018	-0.0031	0.0007
141	-0.0136	-0.0914	0.0081	1.0294	-0.0083	141	0.0023	-0.0021	-0.0008	-0.0033	0.0003
142	-0.1365	-0.9185	0.0096	1.013	-0.0906	142	0.0223	-0.0209	-0.0081	-0.0492	0.0031
143	-0.3331	-2.2635	0.0114	0.9283	-0.2428	143	0.0526	-0.0516	-0.02	-0.1541	0.0076
144	-0.3559	-2.4245	0.0132	0.9156	-0.2808	144	0.054	-0.0553	-0.0215	-0.1959	0.0082
145	-0.422	-2.9091	0.0258	0.8797	-0.4736	145	-0.0119	0.1005	-0.0259	0.3379	-0.1898
146	-0.00774	-0.0522	0.0186	1.0405	-0.0072	146	-0.0004	0.0018	-0.0005	0.004	-0.0034
147	0.0709	0.4777	0.0151	1.032	0.0592	147	0.0043	-0.0164	0.0042	-0.0239	0.031
148	0.2302	1.5565	0.0128	0.9832	0.1773	148	0.0187	-0.0534	0.0138	-0.0183	0.1009
149	0.1268	0.8543	0.0129	1.0188	0.0977	149	0.0121	-0.0293	0.0076	0.0131	0.0554
150	0.0419	0.2822	0.014	1.034	0.0336	150	0.0044	-0.0097	0.0025	0.0103	0.0183
151	0.042	0.2833	0.0155	1.0356	0.0356	151	0.0048	-0.0097	0.0025	0.0152	0.0184
152	-0.00254	-0.0171	0.0173	1.0392	-0.0023	152	-0.0003	0.0006	-0.0002	-0.0012	-0.0011
153	0.0597	0.4028	0.0191	1.0376	0.0562	153	0.0077	-0.0139	0.0036	0.0326	0.0262
154	-0.4053	-2.7981	0.0315	0.8963	-0.5046	154	-0.0422	0.1464	-0.025	0.326	-0.2525
155	-0.156	-1.0582	0.0242	1.0223	-0.1667	155	-0.019	0.0552	-0.0094	0.0821	-0.0952
156	-0.0794	-0.5365	0.0208	1.0367	-0.0782	156	-0.0108	0.0279	-0.0048	0.0269	-0.0482
157	0.2619	1.7791	0.0185	0.9737	0.2442	157	0.0409	-0.0925	0.0158	-0.021	0.1595
158	0.1685	1.1404	0.0186	1.0125	0.1569	158	0.0286	-0.0593	0.0101	0.0176	0.1022
159	0.1277	0.8633	0.0197	1.0255	0.1223	159	0.0231	-0.0449	0.0077	0.0316	0.0774
160	0.1248	0.8446	0.0212	1.0278	0.1243	160	0.0237	-0.044	0.0075	0.0455	0.0758

Obs	Residual	RStudent	H	Ratio	DFFITS	-----DFBETAS-----					
						Obs	Intercept	IDP	Width	THK	tpipe
161	0.1672	1.134	0.0229	1.0173	0.1737	161	0.0331	-0.0591	0.0101	0.0777	0.1019
162	0.1714	1.1637	0.0248	1.0178	0.1856	162	0.0352	-0.0607	0.0104	0.0946	0.1047
163	0.2463	1.699	0.0491	1.0109	0.3861	163	0.1718	-0.2508	0.1286	-0.1998	0.1809
164	0.1706	1.1685	0.0419	1.0357	0.2442	164	0.1212	-0.1719	0.0881	-0.0915	0.124
165	0.1882	1.2877	0.0384	1.0257	0.2575	165	0.1361	-0.189	0.0969	-0.0652	0.1364
166	0.0995	0.6781	0.0361	1.0493	0.1313	166	0.0736	-0.0994	0.051	-0.0081	0.0717
167	0.0341	0.2323	0.0362	1.0584	0.045	167	0.0257	-0.0341	0.0175	0.0036	0.0246
168	-0.00375	-0.0256	0.0373	1.0608	-0.005	168	-0.0029	0.0038	-0.0019	-0.0009	-0.0027
169	-0.0336	-0.2293	0.0388	1.0613	-0.0461	169	-0.0261	0.0337	-0.0173	-0.0125	-0.0243
170	-0.0142	-0.0969	0.0406	1.0642	-0.0199	170	-0.0111	0.0142	-0.0073	-0.0067	-0.0103
171	-0.044	-0.3007	0.0424	1.0645	-0.0633	171	-0.0349	0.0442	-0.0227	-0.0247	-0.0319
172	-0.099	-0.6723	0.0285	1.0413	-0.1151	172	0.0111	0.0069	-0.0503	0.0782	0.0134
173	0.1202	0.8137	0.0212	1.029	0.1198	173	-0.011	-0.0083	0.0607	-0.0631	-0.0162
174	0.0879	0.5932	0.0178	1.0321	0.0799	174	-0.0067	-0.0061	0.0442	-0.0297	-0.0118
175	-0.0569	-0.3832	0.0155	1.0341	-0.0481	175	0.0032	0.0039	-0.0285	0.0045	0.0076
176	-0.1292	-0.8722	0.0156	1.0209	-0.1097	176	0.0055	0.0089	-0.0649	-0.0134	0.0173
177	-0.1721	-1.1636	0.0167	1.0094	-0.1515	177	0.0055	0.0119	-0.0866	-0.0425	0.0231
178	-0.19	-1.2862	0.0182	1.0046	-0.1751	178	0.0044	0.0131	-0.0958	-0.0691	0.0256
179	-0.2095	-1.4211	0.0199	0.9988	-0.2027	179	0.0032	0.0145	-0.1059	-0.0972	0.0283
180	-0.2534	-1.7232	0.0218	0.981	-0.2572	180	0.0022	0.0176	-0.1286	-0.1398	0.0343
181	-0.0224	-0.152	0.0284	1.0506	-0.026	181	0.0104	-0.0071	-0.0114	0.0177	0.0101
182	-0.1491	-1.0099	0.0211	1.0212	-0.1483	182	0.0661	-0.0472	-0.0753	0.0783	0.067
183	-0.0165	-0.1114	0.0177	1.0394	-0.015	183	0.0071	-0.0052	-0.0083	0.0056	0.0074

Obs	Residual	RStudent	H	Ratio	DFFITS	-----DFBETAS-----					
						Obs	Intercept	IDP	Width	THK	tpipe
184	-0.0862	-0.5815	0.0154	1.0299	-0.0727	184	0.035	-0.0271	-0.0432	0.0069	0.0385
185	-0.0936	-0.6314	0.0155	1.0286	-0.0792	185	0.0367	-0.0295	-0.047	-0.0097	0.0418
186	-0.0725	-0.4889	0.0166	1.0332	-0.0634	186	0.0277	-0.0228	-0.0364	-0.0178	0.0323
187	-0.1234	-0.8334	0.0181	1.025	-0.1131	187	0.0461	-0.0389	-0.0621	-0.0448	0.0552
188	-0.1279	-0.8652	0.0198	1.0256	-0.1231	188	0.0469	-0.0405	-0.0645	-0.0592	0.0573
189	-0.1127	-0.7629	0.0217	1.0312	-0.1136	189	0.0407	-0.0357	-0.0569	-0.0619	0.0506
190	-0.0661	-0.4481	0.0265	1.0447	-0.074	190	0.0359	-0.0242	-0.0335	0.0521	0.0279
191	-0.0138	-0.0934	0.0193	1.0412	-0.0131	191	0.0072	-0.005	-0.007	0.0072	0.0058
192	0.007788	0.0525	0.0159	1.0377	0.0067	192	-0.0039	0.0028	0.0039	-0.0026	-0.0032
193	0.0141	0.0946	0.0135	1.0351	0.0111	193	-0.0068	0.0051	0.007	-0.0011	-0.0058
194	-0.0483	-0.3253	0.0136	1.0331	-0.0383	194	0.0226	-0.0174	-0.0242	-0.005	0.0201
195	-0.0852	-0.5741	0.0147	1.0293	-0.0702	195	0.039	-0.0308	-0.0427	-0.0209	0.0355
196	-0.106	-0.7156	0.0162	1.027	-0.0919	196	0.0477	-0.0384	-0.0532	-0.0384	0.0443
197	-0.0846	-0.5713	0.018	1.0328	-0.0773	197	0.0374	-0.0307	-0.0425	-0.039	0.0354
198	-0.0954	-0.645	0.0198	1.0329	-0.0918	198	0.0417	-0.0347	-0.0481	-0.0523	0.04
199	0.0123	0.0835	0.0261	1.0485	0.0137	199	-0.0074	0.0049	0.0062	-0.0097	-0.0048
200	0.1986	1.3455	0.0188	1.002	0.1864	200	-0.1143	0.0782	0.1002	-0.1042	-0.0765
201	0.1822	1.2316	0.0154	1.0047	0.1541	201	-0.1019	0.0714	0.0916	-0.0617	-0.0699
202	0.1975	1.334	0.0131	0.9968	0.1536	202	-0.1063	0.0773	0.0991	-0.0157	-0.0756
203	0.0811	0.5462	0.0132	1.0284	0.0631	203	-0.0424	0.0316	0.0406	0.0084	-0.031
204	0.0513	0.3452	0.0143	1.0334	0.0415	204	-0.0263	0.02	0.0257	0.0126	-0.0196
205	0.0144	0.0969	0.0158	1.0374	0.0123	205	-0.0072	0.0056	0.0072	0.0052	-0.0055
206	-0.0462	-0.3116	0.0175	1.0374	-0.0416	206	0.023	-0.0181	-0.0232	-0.0213	0.0177

Obs	Residual	RStudent	H	Ratio	DFFITS	-----DFBETAS-----					
						Obs	Intercept	IDP	Width	THK	tpipe
207	-0.091	-0.6148	0.0194	1.0332	-0.0864	207	0.0448	-0.0357	-0.0458	-0.0498	0.035
208	0.0324	0.2192	0.0264	1.0479	0.0361	208	-0.0207	0.0133	0.0164	-0.0255	-0.0113
209	0.2126	1.4416	0.0192	0.9968	0.2016	209	-0.1311	0.0872	0.1074	-0.1116	-0.0739
210	0.2892	1.9649	0.0158	0.9571	0.2487	210	-0.1743	0.1187	0.1462	-0.0984	-0.1005
211	0.2885	1.9576	0.0134	0.9554	0.2284	211	-0.1677	0.1181	0.1454	-0.0231	-0.1
212	0.1751	1.1823	0.0135	1.0053	0.1385	212	-0.0988	0.0713	0.0878	0.0182	-0.0604
213	0.1293	0.872	0.0146	1.0199	0.1062	213	-0.0715	0.0527	0.0648	0.0318	-0.0446
214	0.0544	0.3668	0.0161	1.0351	0.047	214	-0.0296	0.0222	0.0273	0.0197	-0.0188
215	0.009829	0.0663	0.0179	1.0398	0.0089	215	-0.0053	0.004	0.0049	0.0045	-0.0034
216	-0.056	-0.3781	0.0197	1.0387	-0.0536	216	0.0298	-0.0229	-0.0282	-0.0306	0.0194
217	-0.1369	-0.9285	0.0253	1.0289	-0.1496	217	0.0634	-0.0213	-0.0694	0.1078	0.0031
218	0.0874	0.5901	0.018	1.0324	0.08	218	-0.0384	0.0135	0.0439	-0.0457	-0.002
219	0.109	0.7351	0.0146	1.0247	0.0896	219	-0.0462	0.0168	0.0546	-0.0368	-0.0025
220	-0.0227	-0.1528	0.0123	1.0335	-0.017	220	0.0091	-0.0035	-0.0113	0.0018	0.0005
221	-0.00109	-0.00734	0.0124	1.0341	-0.0008	221	0.0004	-0.0002	-0.0005	-0.0001	0
222	-0.0299	-0.2016	0.0135	1.0343	-0.0236	222	0.0113	-0.0046	-0.015	-0.0073	0.0007
223	-0.0148	-0.0998	0.015	1.0366	-0.0123	223	0.0055	-0.0023	-0.0074	-0.0054	0.0003
224	-0.0454	-0.3061	0.0167	1.0366	-0.0399	224	0.0165	-0.007	-0.0228	-0.0209	0.001
225	-0.0952	-0.643	0.0186	1.0316	-0.0885	225	0.034	-0.0147	-0.0479	-0.0521	0.0022
226	-0.2133	-1.4556	0.0312	1.0083	-0.2612	226	0.0388	0.0504	-0.1091	0.1695	-0.0953
227	-0.0331	-0.2238	0.0239	1.0452	-0.035	227	0.0053	0.0077	-0.0167	0.0174	-0.0146
228	0.0765	0.5173	0.0205	1.0368	0.0749	228	-0.0111	-0.0178	0.0386	-0.026	0.0337
229	0.0858	0.5794	0.0182	1.0329	0.0789	229	-0.0107	-0.0199	0.0432	-0.0068	0.0377

Obs	Residual	RStudent	H	Ratio	DFFITS	-----DFBETAS-----					
						Obs	Intercept	IDP	Width	THK	tpipe
230	-0.0256	-0.1725	0.0183	1.0396	-0.0235	230	0.0028	0.0059	-0.0128	-0.0027	-0.0112
231	-0.0124	-0.0839	0.0194	1.0413	-0.0118	231	0.0012	0.0029	-0.0063	-0.0031	-0.0055
232	-0.0493	-0.3331	0.0209	1.0406	-0.0486	232	0.0045	0.0115	-0.0248	-0.0179	-0.0217
233	-0.0799	-0.5405	0.0226	1.0385	-0.0822	233	0.0067	0.0186	-0.0403	-0.037	-0.0352
234	-0.1137	-0.7704	0.0245	1.0339	-0.1221	234	0.0088	0.0266	-0.0576	-0.0626	-0.0502
235	-0.2986	-2.052	0.0369	0.971	-0.4015	235	0.0323	0.1077	-0.1543	0.2397	-0.1857
236	0.0257	0.1743	0.0296	1.0518	0.0304	236	-0.0022	-0.0091	0.0131	-0.0136	0.0157
237	0.2463	1.6785	0.0262	0.9886	0.2752	237	-0.0178	-0.0876	0.1255	-0.0845	0.1511
238	0.1056	0.7151	0.0239	1.035	0.1118	238	-0.0055	-0.0373	0.0534	-0.0085	0.0643
239	0.0352	0.2381	0.024	1.0451	0.0373	239	-0.0013	-0.0124	0.0178	0.0037	0.0214
240	0.0113	0.0767	0.025	1.0474	0.0123	240	-0.0003	-0.004	0.0057	0.0028	0.0069
241	0.0165	0.1115	0.0266	1.0489	0.0184	241	-0.0003	-0.0058	0.0083	0.006	0.01
242	-0.0211	-0.1432	0.0283	1.0506	-0.0244	242	0.0002	0.0075	-0.0107	-0.0098	-0.0129
243	-0.0699	-0.4749	0.0302	1.048	-0.0837	243	0.0002	0.0248	-0.0356	-0.0387	-0.0428

Table C-2. Results of investigation of X- and Y- Outliers for vertical deflection equation

Obs	Residual	RStudent	H	Ratio	DFFITS	-----DFBETAS-----					
						Obs	Intercept	IDP	Width	THK	tpipe
1	-0.2242	-0.6756	0.0539	1.0744	-0.1613	1	-0.1431	0.1065	0.0563	-0.0794	-0.0697
2	0.7241	2.2561	0.0906	0.9743	0.7121	2	0.3205	-0.1892	-0.3058	-0.5277	0.1143
3	0.1918	0.5813	0.0656	1.0917	0.154	3	0.0897	-0.0567	-0.0721	-0.0946	0.0351
4	0.0423	0.1272	0.0531	1.0877	0.0301	4	0.0208	-0.0137	-0.0148	-0.0145	0.0086
5	-0.057	-0.1704	0.0429	1.0757	-0.0361	5	-0.0301	0.0207	0.0181	0.0078	-0.0132
6	-0.1425	-0.426	0.0409	1.0685	-0.0879	6	-0.0794	0.0561	0.0422	-0.0008	-0.0361
7	-0.1785	-0.5344	0.0423	1.0668	-0.1123	7	-0.1038	0.0747	0.0502	-0.0208	-0.0484
8	-0.1957	-0.5869	0.0454	1.0684	-0.128	8	-0.1179	0.086	0.0527	-0.0406	-0.0559
9	-0.2181	-0.6556	0.0494	1.0701	-0.1495	9	-0.1355	0.0999	0.0566	-0.0622	-0.0652
10	-0.2315	-0.6955	0.0481	1.067	-0.1564	10	-0.1107	0.1147	-0.02	-0.0926	-0.0763
11	0.5288	1.6213	0.0743	1.0291	0.4593	11	0.1427	-0.1475	-0.034	-0.3496	0.0928
12	0.1425	0.4285	0.0514	1.0803	0.0997	12	0.0433	-0.0448	-0.0047	-0.0624	0.0287
13	0.042	0.1256	0.0403	1.0732	0.0257	13	0.0139	-0.0144	-0.0005	-0.0122	0.0093
14	-0.0722	-0.2149	0.0321	1.0632	-0.0392	14	-0.0266	0.0276	-0.0012	0.0064	-0.018
15	-0.1347	-0.4009	0.0316	1.0589	-0.0724	15	-0.0537	0.0556	-0.0049	-0.0071	-0.0366
16	-0.1758	-0.524	0.0341	1.0581	-0.0985	16	-0.0743	0.0769	-0.0092	-0.0286	-0.0508
17	-0.214	-0.6394	0.0382	1.0583	-0.1274	17	-0.0948	0.0983	-0.014	-0.0542	-0.0651
18	-0.2174	-0.6512	0.043	1.0631	-0.138	18	-0.1003	0.1039	-0.0166	-0.072	-0.0691
19	-0.2214	-0.6689	0.0585	1.0799	-0.1668	19	-0.0821	0.1146	-0.0728	-0.0972	-0.0771
20	0.3958	1.2114	0.0772	1.0686	0.3504	20	0.0613	-0.1171	0.0724	-0.2476	0.0755
21	0.1246	0.3754	0.0557	1.0867	0.0912	21	0.0241	-0.0414	0.0258	-0.0505	0.027
22	0.0381	0.1141	0.0457	1.0794	0.025	22	0.0084	-0.0137	0.0086	-0.0098	0.009

Obs	Residual	RStudent	H	Ratio	DFFITS	-----DFBETAS-----					
						Obs	Intercept	IDP	Width	THK	tpipe
23	-0.0642	-0.1916	0.039	1.0711	-0.0386	23	-0.0168	0.0257	-0.0162	0.0036	-0.0171
24	-0.1207	-0.3605	0.0395	1.0686	-0.0731	24	-0.0352	0.0521	-0.033	-0.0105	-0.0348
25	-0.1588	-0.4753	0.0428	1.0693	-0.1005	25	-0.0501	0.0727	-0.046	-0.0314	-0.0486
26	-0.1869	-0.5612	0.0475	1.0717	-0.1254	26	-0.0629	0.0897	-0.0569	-0.0542	-0.0602
27	-0.2063	-0.6213	0.0529	1.0754	-0.1468	27	-0.0731	0.1031	-0.0655	-0.0761	-0.0693
28	-0.2035	-0.6055	0.0306	1.0513	-0.1075	28	-0.0561	0.0078	0.0558	-0.0515	0.0169
29	-0.2497	-0.7412	0.0244	1.0389	-0.1172	29	-0.0508	-0.0089	0.0801	0.0216	0.0336
30	-0.2308	-0.6846	0.0236	1.0406	-0.1065	30	-0.0521	-0.0027	0.0704	-0.0052	0.0272
31	-0.213	-0.632	0.0249	1.0442	-0.101	31	-0.0521	0.0016	0.0623	-0.0237	0.0222
32	-0.2114	-0.628	0.0274	1.047	-0.1054	32	-0.0552	0.005	0.0597	-0.0395	0.0196
33	-0.1407	-0.4169	0.0227	1.0489	-0.0635	33	-0.017	0.0085	-0.0078	-0.0419	0.0087
34	-0.201	-0.5927	0.013	1.0331	-0.068	34	-0.0101	-0.0026	-0.0014	0.0078	0.0227
35	-0.1781	-0.5251	0.0133	1.0358	-0.0611	35	-0.0129	0.0019	-0.0039	-0.0122	0.0172
36	-0.1722	-0.5085	0.0156	1.0387	-0.064	36	-0.0157	0.0051	-0.006	-0.0269	0.0143
37	-0.1476	-0.4365	0.0188	1.0443	-0.0605	37	-0.0158	0.0068	-0.0067	-0.0342	0.0106
38	-0.1397	-0.4157	0.0315	1.0585	-0.075	38	-0.0018	0.0108	-0.0405	-0.0466	0.0067
39	-0.2417	-0.7251	0.0453	1.0625	-0.158	39	0.0389	-0.0249	-0.0424	0.1196	0.0429
40	-0.2632	-0.7845	0.0325	1.0455	-0.1437	40	0.0341	-0.0187	-0.0509	0.0913	0.0404
41	-0.2124	-0.6294	0.0217	1.0409	-0.0938	41	0.0184	-0.0058	-0.0466	0.031	0.0258
42	-0.1869	-0.553	0.0194	1.0412	-0.0777	42	0.0107	0.0006	-0.0446	0.0011	0.0186
43	-0.182	-0.5387	0.0205	1.0429	-0.078	43	0.0063	0.0049	-0.0463	-0.0186	0.0151
44	-0.1382	-0.4095	0.0234	1.0499	-0.0634	44	0.0023	0.0064	-0.037	-0.0264	0.0096
45	-0.1476	-0.4382	0.0272	1.0532	-0.0733	45	0.0001	0.0092	-0.0412	-0.0394	0.0086

Obs	Residual	RStudent	H	Ratio	DFFITS	-----DFBETAS-----					
						Obs	Intercept	IDP	Width	THK	tpipe
46	0.4011	1.1966	0.0291	1.0168	0.2073	46	0.049	0.054	-0.115	0.0841	-0.0864
47	0.3744	1.1182	0.0324	1.0258	0.2046	47	0.008	0.0899	-0.1335	-0.1022	-0.1088
48	0.3839	1.1431	0.0262	1.0175	0.1874	48	0.0195	0.0798	-0.1283	-0.05	-0.1025
49	0.3138	0.9323	0.0244	1.029	0.1474	49	0.023	0.0576	-0.0997	-0.0066	-0.0783
50	0.4566	1.3609	0.0248	0.9997	0.2172	50	0.0421	0.0753	-0.1397	0.0311	-0.108
51	0.3562	1.0603	0.0266	1.0235	0.1752	51	0.0384	0.0529	-0.1051	0.0511	-0.0801
52	0.4489	1.3344	0.0204	0.9973	0.1924	52	-0.0141	0.0498	0.0194	0.1144	-0.0868
53	0.3615	1.0689	0.0132	1.0091	0.1238	53	-0.0284	0.0576	0.0038	0.0093	-0.0819
54	0.4794	1.4219	0.0146	0.9843	0.1732	54	-0.029	0.0674	0.0111	0.0547	-0.1026
55	0.427	1.2666	0.0172	0.9992	0.1673	55	-0.0192	0.0532	0.0144	0.0807	-0.0866
56	0.5019	1.5006	0.0286	0.9917	0.2576	56	-0.0709	0.0481	0.14	0.1461	-0.0907
57	0.2334	0.6969	0.036	1.0535	0.1347	57	-0.0664	0.0571	0.0425	-0.0915	-0.0669
58	0.2402	0.7124	0.0234	1.0392	0.1103	58	-0.0576	0.0477	0.0499	-0.0456	-0.0607
59	0.3467	1.028	0.0197	1.0183	0.1457	59	-0.0728	0.0582	0.0788	-0.0171	-0.0799
60	0.3926	1.1654	0.0198	1.0093	0.1656	60	-0.0736	0.0567	0.0954	0.0232	-0.084
61	0.4234	1.259	0.0218	1.0046	0.1881	61	-0.0717	0.0531	0.1086	0.0627	-0.085
62	0.48	1.4315	0.0249	0.9939	0.2289	62	-0.0741	0.0526	0.1288	0.1076	-0.0912
63	0.5507	1.646	0.0256	0.9753	0.2667	63	0.05	0.0798	-0.1583	0.1084	-0.1
64	0.4169	1.245	0.0302	1.0143	0.2198	64	-0.0042	0.1042	-0.1488	-0.119	-0.1069
65	0.3724	1.1073	0.0236	1.0173	0.1722	65	0.0073	0.081	-0.1244	-0.0531	-0.0867
66	0.4784	1.424	0.0215	0.9911	0.211	66	0.0202	0.0927	-0.1524	-0.0162	-0.1033
67	0.5332	1.5897	0.0217	0.9767	0.2367	67	0.0325	0.0932	-0.1634	0.0294	-0.108
68	0.5528	1.6504	0.0232	0.9725	0.2545	68	0.0425	0.0878	-0.1638	0.0723	-0.1058

Obs	Residual	RStudent	H	Ratio	DFFITS	-----DFBETAS-----					
						Obs	Intercept	IDP	Width	THK	tpipe
69	0.6504	1.9415	0.0168	0.9368	0.2535	69	-0.0407	0.0789	0.0277	0.1579	-0.1042
70	0.4357	1.2922	0.0164	0.9966	0.167	70	-0.0704	0.0976	-0.0113	-0.1023	-0.1014
71	0.4612	1.3651	0.0113	0.9857	0.1458	71	-0.0608	0.0889	-0.0027	-0.0437	-0.0969
72	0.5321	1.5771	0.0103	0.9666	0.1608	72	-0.0582	0.0902	0.0051	0.0069	-0.103
73	0.5749	1.7071	0.0114	0.9555	0.1834	73	-0.0525	0.0866	0.0128	0.0582	-0.1038
74	0.6165	1.8353	0.0137	0.945	0.2166	74	-0.0468	0.0832	0.0204	0.1088	-0.1046
75	0.6735	2.0206	0.025	0.936	0.3234	75	-0.1164	0.0715	0.1876	0.1877	-0.0991
76	0.4357	1.2955	0.0211	1.0011	0.1902	76	-0.1181	0.0911	0.0902	-0.0883	-0.0956
77	0.5132	1.5256	0.017	0.9778	0.2006	77	-0.1237	0.0914	0.1163	-0.0319	-0.1012
78	0.5702	1.6975	0.0168	0.9617	0.2219	78	-0.1247	0.0882	0.1383	0.0265	-0.103
79	0.619	1.8474	0.0186	0.9484	0.2542	79	-0.1243	0.0841	0.1585	0.0839	-0.1037
80	0.6686	2.0019	0.0215	0.9347	0.2965	80	-0.1243	0.0803	0.1793	0.1416	-0.1048
81	-0.5483	-1.6377	0.0243	0.9748	-0.2582	81	-0.0375	-0.0813	0.1576	-0.1025	0.0815
82	-0.2328	-0.699	0.047	1.0656	-0.1553	82	0.0175	-0.0701	0.0911	0.1168	0.06
83	-0.701	-2.111	0.0299	0.9305	-0.3707	83	0.0228	-0.1793	0.2526	0.2087	0.1579
84	-0.6735	-2.0188	0.023	0.9343	-0.3098	84	0.0018	-0.1501	0.2271	0.1034	0.1358
85	-0.6516	-1.9491	0.0206	0.9397	-0.283	85	-0.0132	-0.1293	0.2088	0.0285	0.1199
86	-0.6068	-1.8123	0.0207	0.954	-0.2633	86	-0.0236	-0.1084	0.1864	-0.0276	0.1032
87	-0.5832	-1.7418	0.022	0.9625	-0.2615	87	-0.0319	-0.0947	0.173	-0.0706	0.0924
88	-0.4956	-1.4713	0.0154	0.981	-0.1841	88	0.0417	-0.0616	-0.0207	-0.1148	0.0628
89	-0.4391	-1.3123	0.0312	1.0101	-0.2354	89	0.1002	-0.1206	0.0242	0.1966	0.1027
90	-0.6443	-1.9222	0.0161	0.9382	-0.2459	90	0.119	-0.1475	0.017	0.1585	0.1297
91	-0.6308	-1.8758	0.0106	0.9379	-0.1946	91	0.0974	-0.1244	0.0039	0.0661	0.1126

Obs	Residual	RStudent	H	Ratio	DFFITS	-----DFBETAS-----					
						Obs	Intercept	IDP	Width	THK	tpipe
92	-0.6029	-1.7899	0.0094	0.9455	-0.1746	92	0.0793	-0.1045	-0.0055	-0.0021	0.0974
93	-0.5691	-1.6886	0.0104	0.9563	-0.1728	93	0.0643	-0.0877	-0.0124	-0.0521	0.0842
94	-0.5355	-1.5891	0.0125	0.9677	-0.1789	94	0.0523	-0.074	-0.0174	-0.089	0.0731
95	-0.4755	-1.417	0.0236	0.9938	-0.2203	95	0.0921	-0.0519	-0.1313	-0.1269	0.0539
96	-0.2245	-0.6748	0.0493	1.0692	-0.1537	96	0.0838	-0.0659	-0.0365	0.1267	0.055
97	-0.522	-1.5662	0.0344	0.9917	-0.2955	97	0.1773	-0.1356	-0.0947	0.2174	0.1152
98	-0.6253	-1.8687	0.0208	0.9483	-0.2721	98	0.1842	-0.1337	-0.1299	0.1335	0.1173
99	-0.6028	-1.796	0.0163	0.9515	-0.2315	99	0.1589	-0.1098	-0.1367	0.0434	0.0994
100	-0.5678	-1.6897	0.0159	0.9616	-0.2149	100	0.1366	-0.0899	-0.1374	-0.0209	0.084
101	-0.528	-1.5707	0.0175	0.9743	-0.2097	101	0.1173	-0.0734	-0.1345	-0.0662	0.0709
102	-0.5034	-1.4986	0.0202	0.9834	-0.2153	102	0.1041	-0.0619	-0.1339	-0.1011	0.0619
103	-0.2377	-0.7054	0.0243	1.0405	-0.1113	103	-0.0124	-0.0348	0.0679	-0.0424	0.0275
104	-0.364	-1.0807	0.0211	1.0164	-0.1585	104	-0.0016	-0.0713	0.1158	0.0185	0.0549
105	-0.3222	-0.9557	0.0209	1.024	-0.1398	105	-0.0074	-0.0569	0.0983	-0.0122	0.0441
106	-0.2816	-0.8353	0.0222	1.032	-0.1258	106	-0.0109	-0.0451	0.083	-0.0317	0.0353
107	-0.181	-0.5343	0.0154	1.0377	-0.0669	107	0.018	-0.0222	-0.0075	-0.0404	0.0171
108	-0.1295	-0.3854	0.0323	1.0602	-0.0704	108	0.0315	-0.0353	0.0071	0.0588	0.026
109	-0.3857	-1.1431	0.0169	1.0079	-0.15	109	0.0768	-0.0874	0.0101	0.0971	0.0649
110	-0.3742	-1.1056	0.0112	1.0047	-0.1179	110	0.0632	-0.073	0.0023	0.0417	0.0546
111	-0.3163	-0.9328	0.0098	1.0139	-0.093	111	0.0462	-0.0542	-0.0029	0.0013	0.0408
112	-0.2635	-0.7767	0.0106	1.0228	-0.0805	112	0.0337	-0.0401	-0.0057	-0.022	0.0304
113	-0.2329	-0.687	0.0127	1.029	-0.0778	113	0.0262	-0.0317	-0.0075	-0.0368	0.0242
114	-0.1809	-0.5364	0.0236	1.0463	-0.0835	114	0.0377	-0.0195	-0.0497	-0.0467	0.0146

Obs	Residual	RStudent	H	Ratio	DFFITS	-----DFBETAS-----					
						Obs	Intercept	IDP	Width	THK	tpipe
115	-0.2424	-0.7236	0.0355	1.0517	-0.1389	115	0.0858	-0.0624	-0.0437	0.1023	0.0454
116	-0.3887	-1.1547	0.0216	1.0119	-0.1715	116	0.1199	-0.0822	-0.0803	0.0854	0.0601
117	-0.3232	-0.9566	0.0169	1.0198	-0.1255	117	0.0897	-0.0582	-0.0728	0.0255	0.0427
118	-0.2723	-0.805	0.0163	1.0274	-0.1037	118	0.0693	-0.0425	-0.0654	-0.0079	0.0314
119	-0.2254	-0.6667	0.0178	1.0352	-0.0897	119	0.0533	-0.0309	-0.0571	-0.0264	0.0229
120	-0.1968	-0.5827	0.0204	1.0412	-0.084	120	0.0436	-0.0239	-0.0521	-0.0378	0.0178
121	-0.0933	-0.277	0.0279	1.0576	-0.0469	121	0.0073	-0.0266	0.0317	0.0166	0.0198
122	0.1175	0.3482	0.0245	1.0525	0.0551	122	-0.0044	0.0283	-0.0364	0.0024	-0.0213
123	0.0236	0.0701	0.0249	1.0567	0.0112	123	-0.0013	0.0062	-0.0076	-0.0016	-0.0046
124	0.1321	0.3917	0.0254	1.0525	0.0633	124	-0.0028	0.0297	-0.0396	0.0126	-0.0225
125	0.1321	0.3917	0.0254	1.0525	0.0633	125	-0.0028	0.0297	-0.0396	0.0126	-0.0225
126	0.2487	0.7357	0.0181	1.0325	0.0999	126	-0.0396	0.0465	0.0093	0.0513	-0.0345
127	0.0294	0.0869	0.0152	1.0462	0.0108	127	-0.0067	0.0076	-0.0003	-0.0038	-0.0056
128	0.1762	0.5197	0.0138	1.0365	0.0616	128	-0.033	0.0381	0.003	0.0117	-0.0281
129	-0.0431	-0.1274	0.0215	1.0526	-0.0189	129	0.0112	-0.0125	0.0013	0.0116	0.0091
130	0.0934	0.2752	0.0134	1.0421	0.0321	130	-0.0192	0.022	0.0004	-0.002	-0.0161
131	0.3507	1.0436	0.0261	1.024	0.1707	131	-0.0946	0.0606	0.0952	0.0848	-0.0441
132	0.0605	0.179	0.0207	1.0512	0.026	132	-0.0204	0.0148	0.0134	-0.0058	-0.0107
133	-0.0277	-0.0829	0.0406	1.0738	-0.017	133	0.0115	-0.009	-0.0049	0.0122	0.0065
134	0.2452	0.7265	0.0208	1.0358	0.1058	134	-0.0729	0.0495	0.0612	0.0246	-0.0359
135	-0.014	-0.0415	0.0259	1.0578	-0.0068	135	0.0052	-0.0039	-0.0028	0.0033	0.0028
136	0.1264	0.3739	0.0197	1.0467	0.0529	136	-0.0398	0.0279	0.0299	0.0015	-0.0202
137	0.2758	0.8185	0.0231	1.0338	0.1257	137	-0.0779	0.0514	0.072	0.0484	-0.0373

Obs	Residual	RStudent	H	Ratio	DFFITS	-----DFBETAS-----					
						Obs	Intercept	IDP	Width	THK	tpipe
138	0.129	0.3847	0.0363	1.0645	0.0746	138	0.0339	-0.0237	-0.0344	0.0289	0.0386
139	0.1982	0.5922	0.0381	1.0601	0.1179	139	0.0322	-0.0157	-0.0667	-0.0516	0.0447
140	-0.0143	-0.0425	0.0323	1.0648	-0.0078	140	-0.0027	0.0016	0.0045	0.0017	-0.0035
141	0.007655	0.0228	0.0308	1.0632	0.0041	141	0.0016	-0.001	-0.0023	-0.0001	0.002
142	0.0385	0.1144	0.0315	1.0636	0.0206	142	0.0089	-0.0059	-0.011	0.0031	0.0106
143	0.0871	0.2593	0.0335	1.0641	0.0483	143	0.0216	-0.0147	-0.024	0.0137	0.0251
144	0.1607	0.4776	0.029	1.054	0.0826	144	0.0173	-0.033	0.0104	0.0433	0.0511
145	0.038	0.1126	0.0259	1.0575	0.0184	145	0.0003	-0.0038	-0.0002	-0.008	0.0092
146	-0.00854	-0.0253	0.0216	1.0532	-0.0038	146	-0.0003	0.0011	-0.0001	0.0006	-0.0022
147	0.0314	0.0929	0.0212	1.0525	0.0137	147	0.0019	-0.0048	0.001	0.0012	0.0088
148	0.1038	0.3079	0.0256	1.0545	0.0499	148	0.0097	-0.0198	0.0057	0.0211	0.0318
149	0.1563	0.468	0.0437	1.0705	0.1001	149	-0.0227	-0.0118	0.032	-0.0596	0.0361
150	-0.00299	-0.00889	0.0317	1.0642	-0.0016	150	0.0003	0.0004	-0.0007	0.0005	-0.0008
151	0.0225	0.0668	0.0284	1.0605	0.0114	151	-0.0016	-0.0033	0.0056	-0.0008	0.0063
152	0.0684	0.2033	0.0288	1.0598	0.035	152	-0.0034	-0.0117	0.0182	0.005	0.0203
153	0.1352	0.4024	0.0311	1.0584	0.0721	153	-0.0041	-0.0259	0.0377	0.022	0.0421
154	0.0521	0.1561	0.0455	1.0789	0.0341	154	0.0157	-0.0131	-0.0138	0.0121	0.0206
155	0.2754	0.8272	0.0468	1.0591	0.1833	155	0.0549	-0.0401	-0.0924	-0.0708	0.0886
156	0.0539	0.161	0.0412	1.0739	0.0334	156	0.0123	-0.0095	-0.0168	-0.0061	0.0184
157	0.0758	0.2264	0.0398	1.0716	0.0461	157	0.019	-0.0151	-0.0225	-0.0001	0.0271
158	0.1046	0.3126	0.0407	1.071	0.0644	158	0.0282	-0.0229	-0.0297	0.0092	0.0389
159	0.0952	0.2849	0.0427	1.0739	0.0602	159	0.0272	-0.0225	-0.026	0.0157	0.0366
160	0.1488	0.4445	0.0386	1.0655	0.0891	160	0.0214	-0.0406	0.0103	0.0414	0.0616

Obs	Residual	RStudent	H	Ratio	DFFITS	-----DFBETAS-----					
						Obs	Intercept	IDP	Width	THK	tpipe
161	0.0901	0.2685	0.0349	1.0654	0.0511	161	0.0038	-0.015	0	-0.0186	0.0304
162	0.0916	0.2723	0.0307	1.0608	0.0485	162	0.0066	-0.018	0.0019	-0.0059	0.0328
163	0.0715	0.2126	0.0305	1.0615	0.0377	163	0.0068	-0.0157	0.0026	0.0032	0.0268
164	0.1033	0.3075	0.0323	1.0618	0.0562	164	0.0117	-0.0248	0.005	0.0139	0.0402
165	0.0809	0.2412	0.0351	1.0661	0.046	165	0.0105	-0.0208	0.0048	0.0171	0.0325
166	0.1699	0.51	0.0482	1.0742	0.1147	166	0.0059	-0.0496	0.0525	0.0535	0.0735
167	0.1094	0.3291	0.0527	1.0843	0.0776	167	-0.0121	-0.0155	0.0231	-0.0414	0.0358
168	0.0401	0.12	0.0409	1.074	0.0248	168	-0.0027	-0.0074	0.0095	-0.007	0.0142
169	0.0566	0.169	0.0378	1.0701	0.0335	169	-0.0021	-0.0121	0.0145	-0.0017	0.0213
170	0.0566	0.1689	0.0384	1.0707	0.0337	170	-0.0008	-0.0135	0.0154	0.0045	0.0222
171	0.0584	0.1745	0.0408	1.0733	0.036	171	0.0003	-0.0151	0.0167	0.0099	0.0238
172	0.137	0.4103	0.0442	1.0727	0.0882	172	0.0028	-0.0378	0.0408	0.0338	0.0576

Table C-3. Results of investigation of X- and Y- Outliers for relative separation at bottom of assemblage

Obs	Residual	RStudent	H	Ratio	DFFITS	-----DFBETAS-----					
						Obs	Intercept	IDP	Width	THK	tpipe
1	-0.0196	-0.0697	0.0567	1.0929	-0.0171	1	-0.0152	0.0114	0.006	-0.0086	-0.0078
2	0.3111	1.1291	0.0916	1.0917	0.3586	2	0.1584	-0.0979	-0.1499	-0.2628	0.064
3	-0.1277	-0.4559	0.0665	1.0975	-0.1217	3	-0.0703	0.046	0.0558	0.0733	-0.0305
4	-0.2018	-0.7162	0.054	1.073	-0.1712	4	-0.1176	0.0797	0.0828	0.0795	-0.0532
5	-0.1836	-0.6481	0.0441	1.0648	-0.1392	5	-0.1159	0.0817	0.0691	0.0275	-0.0549
6	-0.2127	-0.7504	0.0424	1.0583	-0.1579	6	-0.1424	0.1026	0.0754	-0.0045	-0.0694
7	-0.1794	-0.6332	0.0442	1.0656	-0.1361	7	-0.1257	0.092	0.0608	-0.0275	-0.0624
8	-0.1406	-0.4967	0.0476	1.0745	-0.1111	8	-0.1023	0.0757	0.0459	-0.0369	-0.0514
9	-0.1022	-0.3618	0.0519	1.0832	-0.0847	9	-0.0768	0.0574	0.0323	-0.0363	-0.0391
10	0.0654	0.2312	0.0503	1.0839	0.0532	10	0.0384	-0.0394	0.0061	0.0316	0.0272
11	0.1831	0.6571	0.0759	1.101	0.1883	11	0.0574	-0.0611	-0.0112	-0.1424	0.0411
12	-0.0947	-0.3355	0.0526	1.0845	-0.079	12	-0.0342	0.0359	0.0028	0.0488	-0.0244
13	-0.1138	-0.4008	0.0414	1.0703	-0.0833	13	-0.045	0.047	0.001	0.0386	-0.0321
14	-0.1296	-0.4546	0.0333	1.0598	-0.0843	14	-0.0579	0.0601	-0.0027	0.0129	-0.0412
15	-0.1047	-0.3671	0.0329	1.0617	-0.0677	15	-0.0507	0.0525	-0.0044	-0.0073	-0.0361
16	-0.0744	-0.2612	0.0356	1.0669	-0.0502	16	-0.0384	0.0396	-0.0043	-0.0149	-0.0272
17	-0.0665	-0.234	0.0399	1.0721	-0.0477	17	-0.0361	0.0371	-0.0048	-0.0206	-0.0256
18	0.001818	0.006412	0.0449	1.0795	0.0014	18	0.001	-0.0011	0.0002	0.0007	0.0007
19	0.1542	0.5486	0.0605	1.0873	0.1392	19	0.0716	-0.0967	0.0589	0.081	0.0674
20	0.1359	0.4883	0.0794	1.1118	0.1434	20	0.0247	-0.0479	0.0315	-0.1011	0.0329
21	-0.0299	-0.1063	0.0574	1.0935	-0.0262	21	-0.007	0.0119	-0.0077	0.0145	-0.0082
22	-0.043	-0.1519	0.0472	1.0813	-0.0338	22	-0.0116	0.0186	-0.0118	0.0132	-0.0129

Obs	Residual	RStudent	H	Ratio	DFFITS	-----DFBETAS-----					
						Obs	Intercept	IDP	Width	THK	tpipe
23	-0.0388	-0.1366	0.0403	1.0738	-0.028	23	-0.0125	0.0188	-0.0117	0.0025	-0.013
24	-0.00394	-0.0138	0.0408	1.075	-0.0029	24	-0.0014	0.0021	-0.0013	-0.0004	-0.0014
25	0.0314	0.1106	0.0443	1.0785	0.0238	25	0.0123	-0.0174	0.0107	0.0074	0.0121
26	0.0673	0.2377	0.0492	1.0825	0.054	26	0.0282	-0.0391	0.024	0.0233	0.0272
27	0.0996	0.3531	0.0546	1.0865	0.0849	27	0.0441	-0.0603	0.0368	0.044	0.042
28	-0.1534	-0.5377	0.0314	1.0551	-0.0968	28	-0.0477	0.0053	0.051	-0.047	0.0157
29	-0.2875	-1.0064	0.0248	1.025	-0.1604	29	-0.0624	-0.0162	0.1095	0.0283	0.0478
30	-0.2382	-0.8327	0.0241	1.0343	-0.1308	30	-0.0587	-0.0064	0.0868	-0.0075	0.0346
31	-0.1964	-0.6864	0.0255	1.0429	-0.111	31	-0.0532	-0.0006	0.069	-0.027	0.0252
32	-0.178	-0.6229	0.0281	1.0483	-0.1059	32	-0.052	0.003	0.0607	-0.0405	0.0204
33	-0.0424	-0.1479	0.023	1.0546	-0.0227	33	-0.0056	0.0025	-0.0025	-0.0149	0.0034
34	-0.1975	-0.6862	0.0132	1.0299	-0.0794	34	-0.0079	-0.0063	-0.0018	0.0098	0.0282
35	-0.1442	-0.5007	0.0135	1.0372	-0.0586	35	-0.01	-0.0005	-0.0036	-0.0113	0.0176
36	-0.1123	-0.3904	0.0158	1.0427	-0.0494	36	-0.0105	0.0023	-0.0043	-0.0206	0.0119
37	-0.067	-0.2331	0.019	1.0493	-0.0325	37	-0.0076	0.0027	-0.0033	-0.0183	0.0061
38	-0.0136	-0.0478	0.0317	1.0647	-0.0086	38	-0.0001	0.001	-0.0046	-0.0053	0.0009
39	-0.3507	-1.244	0.0472	1.0322	-0.2768	39	0.0774	-0.0518	-0.0777	0.2111	0.0793
40	-0.3368	-1.1859	0.0337	1.0222	-0.2216	40	0.0603	-0.0362	-0.0806	0.1428	0.0659
41	-0.2166	-0.7564	0.0224	1.0364	-0.1145	41	0.0266	-0.0115	-0.0574	0.0396	0.0337
42	-0.1527	-0.5321	0.0198	1.0427	-0.0755	42	0.0129	-0.0024	-0.0435	0.0024	0.0196
43	-0.1234	-0.43	0.0208	1.047	-0.0626	43	0.0068	0.0017	-0.0371	-0.014	0.0133
44	-0.0476	-0.1658	0.0236	1.0551	-0.0258	44	0.0015	0.0018	-0.015	-0.0104	0.0043
45	-0.0402	-0.1405	0.0274	1.0594	-0.0236	45	0.0004	0.0023	-0.0131	-0.0124	0.0031

Obs	Residual	RStudent	H	Ratio	DFFITS	-----DFBETAS-----					
						Obs	Intercept	IDP	Width	THK	tpipe
46	0.3541	1.2453	0.0307	1.0145	0.2216	46	0.0407	0.0653	-0.1229	0.0886	-0.098
47	0.3601	1.2688	0.0341	1.0163	0.2384	47	-0.006	0.1134	-0.1512	-0.1177	-0.1333
48	0.381	1.3388	0.0277	1.004	0.226	48	0.0084	0.1048	-0.151	-0.0595	-0.1299
49	0.2943	1.0309	0.0258	1.0246	0.1679	49	0.0152	0.072	-0.1114	-0.0075	-0.0938
50	0.4682	1.6486	0.0263	0.9749	0.2709	50	0.0357	0.104	-0.1721	0.0379	-0.142
51	0.3336	1.1708	0.0281	1.0173	0.199	51	0.0322	0.0672	-0.1186	0.057	-0.0962
52	0.4211	1.4767	0.0214	0.9859	0.2185	52	-0.0263	0.067	0.0194	0.1249	-0.1065
53	0.3443	1.2005	0.0145	1.0011	0.1454	53	-0.0426	0.0753	0.0041	0.0078	-0.1012
54	0.4852	1.7002	0.0157	0.9594	0.215	54	-0.0487	0.0952	0.0122	0.0623	-0.1352
55	0.4076	1.4262	0.0182	0.987	0.1943	55	-0.0326	0.0718	0.0147	0.0887	-0.1077
56	0.4619	1.6289	0.0296	0.9801	0.2844	56	-0.0877	0.0664	0.1509	0.1543	-0.1107
57	0.2027	0.7137	0.0389	1.0562	0.1436	57	-0.0765	0.0665	0.0459	-0.0978	-0.0752
58	0.2109	0.7374	0.0255	1.0405	0.1192	58	-0.0671	0.0571	0.0533	-0.0507	-0.0693
59	0.3268	1.1429	0.0213	1.0123	0.1685	59	-0.0913	0.076	0.0892	-0.0237	-0.0984
60	0.3741	1.3099	0.0211	0.9996	0.1924	60	-0.0936	0.0761	0.1082	0.0213	-0.105
61	0.407	1.4277	0.023	0.9917	0.219	61	-0.0922	0.0734	0.1234	0.0665	-0.1076
62	0.4434	1.5595	0.026	0.983	0.2545	62	-0.0917	0.0712	0.1399	0.1127	-0.1113
63	0.3664	1.2867	0.0272	1.0077	0.2153	63	0.0276	0.0735	-0.1271	0.0848	-0.0894
64	0.3044	1.0701	0.0323	1.0288	0.1954	64	-0.017	0.1007	-0.1277	-0.1046	-0.1026
65	0.2703	0.9462	0.0254	1.0293	0.1527	65	-0.0047	0.0786	-0.1069	-0.0468	-0.0831
66	0.3136	1.0975	0.0232	1.0173	0.169	66	0.0039	0.0819	-0.1188	-0.0136	-0.0898
67	0.3345	1.1713	0.0233	1.0124	0.181	67	0.0123	0.0794	-0.1224	0.021	-0.0902
68	0.3519	1.2336	0.0249	1.0093	0.197	68	0.0201	0.0766	-0.1251	0.0537	-0.09

Obs	Residual	RStudent	H	Ratio	DFFITS	-----DFBETAS-----					
						Obs	Intercept	IDP	Width	THK	tpipe
69	0.4054	1.4184	0.0179	0.9874	0.1915	69	-0.041	0.0711	0.0181	0.1126	-0.0893
70	0.3024	1.0555	0.0185	1.0153	0.145	70	-0.0697	0.0915	-0.0078	-0.0879	-0.0939
71	0.3243	1.1293	0.013	1.0047	0.1294	71	-0.0621	0.0856	-0.0016	-0.04	-0.0916
72	0.3527	1.228	0.0117	0.9963	0.1337	72	-0.0572	0.0828	0.0038	0.0018	-0.0923
73	0.3635	1.2669	0.0127	0.9944	0.1437	73	-0.0503	0.0769	0.0087	0.0399	-0.0892
74	0.3939	1.3754	0.0149	0.988	0.1693	74	-0.0467	0.0757	0.0138	0.0785	-0.0914
75	0.4382	1.5412	0.026	0.9847	0.2519	75	-0.1	0.0701	0.1421	0.138	-0.0906
76	0.2892	1.0117	0.0235	1.0234	0.157	76	-0.1033	0.0831	0.0727	-0.0746	-0.0858
77	0.3391	1.1848	0.0189	1.0068	0.1643	77	-0.1077	0.0843	0.092	-0.0305	-0.0912
78	0.3714	1.2985	0.0183	0.9976	0.1775	78	-0.1071	0.0816	0.1067	0.0146	-0.0922
79	0.3963	1.3876	0.0199	0.992	0.1977	79	-0.1049	0.0778	0.1193	0.0575	-0.0919
80	0.4197	1.4725	0.0226	0.9875	0.224	80	-0.1029	0.0742	0.1314	0.0988	-0.0917
81	-0.4359	-1.533	0.0259	0.9854	-0.25	81	-0.0207	-0.0911	0.1516	-0.0951	0.0924
82	0.0489	0.1728	0.0499	1.0842	0.0396	82	-0.0069	0.0195	-0.0223	-0.0295	-0.017
83	-0.5399	-1.9123	0.0322	0.9534	-0.3486	83	0.0457	-0.1845	0.2285	0.1944	0.1657
84	-0.52	-1.8334	0.0249	0.9548	-0.2932	84	0.0236	-0.1564	0.2073	0.0978	0.1442
85	-0.5267	-1.855	0.0224	0.9501	-0.2809	85	0.0081	-0.1426	0.201	0.0301	0.1347
86	-0.4818	-1.694	0.0224	0.9665	-0.2562	86	-0.0043	-0.1187	0.1772	-0.0238	0.1148
87	-0.4615	-1.6224	0.0237	0.9748	-0.2528	87	-0.0136	-0.1044	0.1647	-0.0643	0.1034
88	-0.4209	-1.4723	0.0165	0.9814	-0.191	88	0.0542	-0.0771	-0.0186	-0.1111	0.0792
89	-0.1841	-0.6464	0.0343	1.0541	-0.1219	89	0.0582	-0.0679	0.0103	0.1006	0.059
90	-0.4789	-1.6801	0.0184	0.964	-0.2301	90	0.1243	-0.1496	0.0126	0.1465	0.1341
91	-0.49	-1.7144	0.0125	0.9548	-0.1926	91	0.1078	-0.1338	0.0027	0.0674	0.1234

Obs	Residual	RStudent	H	Ratio	DFFITS	-----DFBETAS-----					
						Obs	Intercept	IDP	Width	THK	tpipe
92	-0.4767	-1.6657	0.011	0.9581	-0.1753	92	0.0907	-0.1161	-0.005	0.004	0.11
93	-0.4638	-1.6207	0.0117	0.9631	-0.1763	93	0.0771	-0.102	-0.0109	-0.0448	0.0993
94	-0.4395	-1.5359	0.0137	0.9729	-0.1812	94	0.0642	-0.088	-0.0152	-0.0817	0.0879
95	-0.4491	-1.579	0.0246	0.9798	-0.251	95	0.1149	-0.0754	-0.1452	-0.1351	0.0783
96	0.1008	0.3571	0.0538	1.0854	0.0852	96	-0.0495	0.04	0.0208	-0.07	-0.0341
97	-0.2783	-0.9807	0.038	1.0407	-0.1949	97	0.1239	-0.0984	-0.0626	0.1432	0.0853
98	-0.4551	-1.5994	0.0234	0.9766	-0.2474	98	0.1759	-0.135	-0.1147	0.1241	0.1209
99	-0.4692	-1.6455	0.0184	0.9673	-0.225	99	0.1626	-0.1209	-0.1274	0.0488	0.1115
100	-0.4579	-1.6045	0.0175	0.9704	-0.2144	100	0.1449	-0.1045	-0.1316	-0.0118	0.0992
101	-0.438	-1.5349	0.0189	0.9781	-0.2129	101	0.1281	-0.0896	-0.1317	-0.0576	0.0876
102	-0.4697	-1.6497	0.0214	0.9699	-0.2439	102	0.1283	-0.0869	-0.1469	-0.1042	0.0875
103	-0.2753	-0.9638	0.0259	1.0288	-0.1571	103	-0.0076	-0.0577	0.0953	-0.0569	0.0491
104	-0.3381	-1.1835	0.0228	1.011	-0.1809	104	0.0118	-0.0916	0.1283	0.0227	0.0749
105	-0.3172	-1.1097	0.0226	1.0159	-0.1687	105	0.0034	-0.0783	0.1161	-0.0123	0.0649
106	-0.2998	-1.0492	0.0238	1.0212	-0.1638	106	-0.0029	-0.068	0.1065	-0.0385	0.0571
107	-0.2683	-0.9346	0.0165	1.0207	-0.121	107	0.0396	-0.0494	-0.0118	-0.0677	0.0416
108	0.0906	0.3178	0.0356	1.0658	0.0611	108	-0.0304	0.0335	-0.0051	-0.0505	-0.0261
109	-0.3223	-1.1257	0.0193	1.0114	-0.158	109	0.0896	-0.1008	0.0085	0.1016	0.0794
110	-0.3594	-1.2525	0.0131	0.9959	-0.1443	110	0.0858	-0.0984	0.002	0.053	0.0786
111	-0.321	-1.1169	0.0114	1.0039	-0.1197	111	0.067	-0.0784	-0.0033	0.006	0.0634
112	-0.3202	-1.1141	0.0119	1.0047	-0.1224	112	0.0592	-0.0707	-0.0074	-0.0275	0.0579
113	-0.2908	-1.0123	0.0138	1.0132	-0.1198	113	0.048	-0.0585	-0.01	-0.0508	0.0486
114	-0.3035	-1.0625	0.0246	1.0212	-0.1687	114	0.0833	-0.0513	-0.0977	-0.0877	0.0428

Obs	Residual	RStudent	H	Ratio	DFFITS	-----DFBETAS-----					
						Obs	Intercept	IDP	Width	THK	tpipe
115	-0.0617	-0.2168	0.0393	1.0717	-0.0439	115	0.0286	-0.0219	-0.0138	0.0323	0.0168
116	-0.3795	-1.331	0.0243	1.0011	-0.2099	116	0.1539	-0.1131	-0.0955	0.1073	0.0883
117	-0.3256	-1.1371	0.019	1.0103	-0.1581	117	0.1188	-0.0841	-0.0881	0.0371	0.0665
118	-0.3133	-1.0932	0.0179	1.0122	-0.1478	118	0.1049	-0.0717	-0.0896	-0.0048	0.0575
119	-0.3124	-1.0908	0.0191	1.0136	-0.1522	119	0.0972	-0.0642	-0.0935	-0.0377	0.0521
120	-0.295	-1.0311	0.0215	1.02	-0.1527	120	0.0859	-0.0548	-0.0918	-0.0621	0.0451
121	0.3898	1.368	0.0251	0.9989	0.2193	121	0.0511	0.0191	-0.1314	0.0882	0.0105
122	-0.0163	-0.057	0.0235	1.0558	-0.0088	122	-0.0006	-0.0023	0.0063	0.0029	0.0006
123	0.296	1.0343	0.0212	1.0195	0.1522	123	0.0201	0.0326	-0.1092	-0.0142	-0.005
124	0.1349	0.47	0.0213	1.0463	0.0693	124	0.0124	0.0116	-0.0479	0.0078	0
125	0.2298	0.7999	0.0163	1.0278	0.1029	125	-0.0104	0.0057	0.0123	0.0623	0.011
126	0.3328	1.1616	0.0174	1.0069	0.1544	126	-0.0583	0.0508	-0.0055	-0.0983	-0.0141
127	0.2787	0.9687	0.0117	1.0137	0.1052	127	-0.0379	0.0318	0.0011	-0.0357	-0.0044
128	0.234	0.8121	0.0103	1.021	0.0829	128	-0.0249	0.0199	0.0046	0	0.0011
129	0.2219	0.7703	0.0112	1.024	0.082	129	-0.0184	0.0137	0.0073	0.0232	0.0048
130	0.2976	1.0418	0.0248	1.0228	0.1661	130	-0.051	0.0024	0.0987	0.0917	0.0191
131	0.2155	0.7505	0.018	1.032	0.1015	131	-0.0563	0.0211	0.0602	-0.0204	-0.0001
132	0.3198	1.1158	0.0173	1.0101	0.1482	132	-0.0742	0.0221	0.0945	0.011	0.0064
133	0.1717	0.5978	0.0188	1.0394	0.0828	133	-0.0357	0.0078	0.0529	0.0239	0.0063
134	0.383	1.3416	0.0215	0.9974	0.1987	134	-0.0723	0.0098	0.1232	0.0881	0.0197
135	0.0762	0.2675	0.035	1.0661	0.0509	135	0.0226	-0.0147	-0.0247	0.0199	0.0242
136	0.4752	1.6835	0.0374	0.9826	0.3317	136	0.0794	-0.0305	-0.1899	-0.1509	0.1083
137	0.0611	0.2141	0.0313	1.0629	0.0385	137	0.0124	-0.0062	-0.0228	-0.0088	0.0154

Obs	Residual	RStudent	H	Ratio	DFFITS	-----DFBETAS-----					
						Obs	Intercept	IDP	Width	THK	tpipe
138	0.0355	0.124	0.0296	1.0621	0.0217	138	0.0082	-0.0046	-0.0126	-0.0005	0.0096
139	0.0353	0.1236	0.0303	1.0628	0.0219	139	0.0091	-0.0054	-0.0121	0.0033	0.0102
140	0.0647	0.2266	0.0323	1.0637	0.0414	140	0.018	-0.0113	-0.0215	0.0118	0.0197
141	0.0503	0.1756	0.0271	1.0588	0.0293	141	0.0059	-0.0108	0.0034	0.0155	0.0169
142	0.1562	0.5458	0.0251	1.048	0.0876	142	-0.0019	-0.0135	-0.0003	-0.0411	0.0383
143	0.002156	0.007507	0.0203	1.0524	0.0011	143	0.0001	-0.0003	0	-0.0002	0.0006
144	0.006469	0.0225	0.0197	1.0517	0.0032	144	0.0004	-0.001	0.0002	0.0002	0.0019
145	0.0237	0.0826	0.0238	1.056	0.0129	145	0.0024	-0.0047	0.0014	0.0054	0.0077
146	0.3568	1.2639	0.0442	1.0274	0.2717	146	-0.0699	-0.0185	0.0898	-0.1696	0.0814
147	0.054	0.1892	0.0312	1.063	0.0339	147	-0.0075	-0.0056	0.0149	-0.0124	0.0142
148	0.004944	0.0173	0.0273	1.06	0.0029	148	-0.0005	-0.0007	0.0015	-0.0003	0.0014
149	-0.00174	-0.00609	0.0273	1.06	-0.001	149	0.0001	0.0003	-0.0005	-0.0001	-0.0005
150	0.0291	0.1019	0.0294	1.0619	0.0177	150	-0.0013	-0.0057	0.0095	0.0051	0.0095
151	-0.1335	-0.4707	0.0437	1.0709	-0.1006	151	-0.0461	0.0365	0.043	-0.0361	-0.0574
152	0.5385	1.9207	0.0455	0.9658	0.4192	152	0.1158	-0.0779	-0.215	-0.1693	0.1839
153	0.2294	0.8082	0.0396	1.0523	0.164	153	0.0575	-0.0414	-0.0854	-0.032	0.0834
154	0.0647	0.2274	0.0381	1.0701	0.0452	154	0.0181	-0.0136	-0.023	-0.0005	0.0248
155	-0.0594	-0.2088	0.0388	1.0713	-0.042	155	-0.0181	0.0139	0.0203	-0.0059	-0.0238
156	-0.1131	-0.398	0.0409	1.0698	-0.0822	156	-0.0369	0.0288	0.0374	-0.0216	-0.047
157	-0.0855	-0.3001	0.0361	1.0667	-0.0581	157	-0.014	0.0252	-0.0063	-0.0271	-0.0383
158	0.1515	0.5315	0.0335	1.0576	0.099	158	0.0049	-0.025	0.0004	-0.0392	0.0539
159	-0.0306	-0.1069	0.0289	1.0614	-0.0184	159	-0.0022	0.0062	-0.0007	0.0027	-0.0116
160	-0.00127	-0.00443	0.0284	1.0612	-0.0008	160	-0.0001	0.0003	-0.0001	-0.0001	-0.0005

						-----DFBETAS-----					
Obs	Residual	RStudent	H	Ratio	DFFITS	Obs	Intercept	IDP	Width	THK	tpipe
161	-0.0334	-0.1168	0.03	1.0625	-0.0205	161	-0.0042	0.0085	-0.0018	-0.0049	-0.014
162	-0.065	-0.2279	0.0327	1.0642	-0.0419	162	-0.0095	0.018	-0.0042	-0.0155	-0.0283
163	-0.3297	-1.1677	0.0455	1.0361	-0.2549	163	-0.0126	0.1044	-0.1183	-0.1176	-0.1551
164	0.2671	0.9482	0.0525	1.0587	0.2233	164	-0.0404	-0.0352	0.069	-0.126	0.091
165	0.1503	0.529	0.0398	1.0646	0.1076	165	-0.0142	-0.0276	0.0427	-0.0339	0.0562
166	0.007208	0.0253	0.0361	1.0696	0.0049	166	-0.0004	-0.0016	0.0022	-0.0004	0.0029
167	-0.0685	-0.2404	0.0363	1.068	-0.0466	167	0.0017	0.0171	-0.0219	-0.0052	-0.0288
168	-0.3726	-1.3163	0.0384	1.017	-0.2631	168	0.0004	0.1029	-0.125	-0.0686	-0.1641
169	-0.1323	-0.4658	0.0416	1.0687	-0.0971	169	-0.0026	0.0392	-0.0458	-0.0363	-0.0601

REFERENCES

- Anklesaria, Y. H. (2012). Structural analysis of microsattellites.
- ASTM C1116 / C1116M-06, Standard Specification for Fiber-Reinforced Concrete, ASTM International, West Conshohocken, PA, 2006.
- ASTM D3518 / D3518M-13, Standard Test Method for In-Plane Shear Response of Polymer Matrix Composite Materials by Tensile Test of a $\pm 45^\circ$ Laminate, ASTM International, West Conshohocken, PA, 2013.
- ASTM D3039 / D3039M-14, Standard Test Method for Tensile Properties of Polymer Matrix Composite Materials, ASTM International, West Conshohocken, PA, 2014.
- ASTM C497-16a, Standard Test Methods for Concrete Pipe, Manhole Sections, or Tile, ASTM International, West Conshohocken, PA, 2016.
- ASTM C76-14, Standard Specification for Reinforced Concrete Culvert, Storm Drain, and Sewer Pipe, ASTM International, West Conshohocken, PA, 2014.
- Alhozaimy, A. M., Soroushian, P., & Mirza, F. (1996). Mechanical properties of polypropylene fiber reinforced concrete and the effects of pozzolanic materials. *Cement and Concrete Composites*, 18(2), 85-92.
- Al-Hammoud, R., Soudki, K., & Topper, T. H. (2010). Fatigue flexural behavior of corroded reinforced concrete beams repaired with CFRP sheets. *Journal of Composites for Construction*, 15(1), 42-51.
- Boot, J. C., Toropova, I. L., & Javadi, A. A. (2003). Predicting the creep lives of thin-walled cylindrical polymeric pipe linings subject to external pressure. *International Journal of Solids and Structures*, 40(26), 7299-7314.
- Banthia, N., Trottier, J. F., Wood, D., & Beaupre, D. (1992). Influence of fiber geometry in steel fiber reinforced dry-mix shotcrete. *Concrete International*, 14(5), 24-28.

- Barr, B. and Noor, M.R. (1985). "The Toughness Index of Steel Fibre Reinforced Concrete." *ACI Journal*, September-October, 1985, pp.622-633.
- Banthia, N., & Trottier, J. F. (1995). Test methods for flexural toughness characterization of fiber reinforced concrete: some concerns and a proposition. *ACI Materials Journal*, 92, 48-48.
- Brockenbrough, R. L. (1990). Strength of bell-and-spigot joints. *Journal of Structural Engineering*, 116(7), 1983-1991.
- Buco, J., Emeriault, F., & Kastner, R. (2008). Full-scale experimental determination of concrete pipe joint behavior and its modeling. *Journal of Infrastructure Systems*, 14(3), 230-240.
- Burlayenko, V. N., & Sadowski, T. (2012). A numerical study of the dynamic response of sandwich plates initially damaged by low-velocity impact. *Computational Materials Science*, 52(1), 212-216.
- Bertram, A., Böhlke, T., Estrin, Y., & Lenz, W. (2003). Effect of geometric nonlinearity on large strain deformation: a case study. In *Proceedings of the 9th International Conference on the Mechanical Behavior of Materials (ICM), Genf*.
- Bae, S. W., & Belarbi, A. (2010). Effects of various environmental conditions on RC columns wrapped with FRP sheets. *Journal of Reinforced Plastics and Composites*, 29(2), 290-309.
- Chajes, M. J., Finch, W. W., Januszka, T. F., & Thomson, T. A. (1996). Bond and force transfer of composite material plates bonded to concrete. *ACI Structural Journal*, 93(2), 208-217.
- Chen, B., & Govindaraj, M. (1995). A physically based model of fabric drape using flexible shell theory. *Textile Research Journal*, 65(6), 324-330.

- Dias, A. M. P. G. (2005). *Mechanical behaviour of timber-concrete joints* (Doctoral dissertation, TU Delft, Delft University of Technology).
- Cicekli, U., Voyiadjis, G. Z., & Al-Rub, R. K. A. (2007). A plasticity and anisotropic damage model for plain concrete. *International Journal of Plasticity*, 23(10), 1874-1900.
- Červenka, J., & Papanikolaou, V. K. (2008). Three-dimensional combined fracture–plastic material model for concrete. *International Journal of Plasticity*, 24(12), 2192-2220.
- Du Pont, E. I. (1936). de Nemours and Co. *UK Patent*, 469518.
- Erki, M. A., & Rizkalla, S. H. (1993). FRP reinforcement for concrete structures. *CONCRETE INTERNATIONAL-DETROIT-*, 15, 48-48.
- Engineering mechanics of composite materials, 2nd Ed, 2006.
- Enochsson, O., Lundqvist, J., Täljsten, B., Rusinowski, P., & Olofsson, T. (2007). CFRP strengthened openings in two-way concrete slabs—An experimental and numerical study. *Construction and Building Materials*, 21(4), 810-826.
- Fanella, D. A., & Naaman, A. E. (1985). Stress-strain properties of fiber reinforced mortar in compression. *Journal of The American Concrete Institute*, 82(4), 475-483.
- García, D. B., & Moore, I. D. (2013). Behavior of coupling band joints in buried corrugated steel pipelines. *Journal of Geotechnical and Geoenvironmental Engineering*, 140(2), 04013014.
- Gutkowski, W., & Kowalewski, T. A. (2005). *Mechanics of the 21st Century*. Springer.
- Games, S. (1938). *U.S. Patent No. 2,117,371*. Washington, DC: U.S. Patent and Trademark Office.
- Grzybowski, M., & Shah, S. P. (1990). Shrinkage cracking of fiber reinforced concrete. *Materials Journal*, 87(2), 138-148.

- Grassl, P., & Jirásek, M. (2006). Damage-plastic model for concrete failure. *International Journal of Solids and Structures*, 43(22), 7166-7196.
- Hillerborg, A., Modéer, M., & Petersson, P. E. (1976). Analysis of crack formation and crack growth in concrete by means of fracture mechanics and finite elements. *Cement and Concrete Research*, 6(6), 773-781.
- Hawileh, R. A., Nawaz, W., Abdalla, J. A., & Saqan, E. I. (2015). Effect of flexural CFRP sheets on shear resistance of reinforced concrete beams. *Composite Structures*, 122, 468-476.
- Hawileh, R. A., et al. Effect of Flexural CFRP Sheets on Shear Resistance of Reinforced Concrete Beams. *Composite Structures* 122 (2015): 468-476.
- Jason, L., Huerta, A., Pijaudier-Cabot, G., & Ghavamian, S. (2006). An elastic plastic damage formulation for concrete: Application to elementary tests and comparison with an isotropic damage model. *Computer methods in applied mechanics and engineering*, 195(52), 7077-7092.
- Lee. Grant (201), Century Concrete Pipe Does Exist. American Concrete Pipe Association. Vol. 63, No. 2, pp. 6.
- Lee, H., Cho, D., An, Z., & Chung, W. (2014). Composite behavior of steel I-girders connected to inverted-T bent cap. *International Journal of Steel Structures*, 14(4), 711-721.
- Meier, U. (1995). Strengthening of structures using carbon fibre/epoxy composites. *Construction and Building Materials*, 9(6), 341-351.
- Mikhaylova, Alena, Non-linear Finite Element-based Material Constitutive Law For Zero Slump Steel Fiber Reinforced Concrete Pipe Structures, *Civil & Environmental Engineering*, UT Arlington, 2014.

- Maekawa, K., Okamura, H., & Pimanmas, A. (2003). *Non-linear mechanics of reinforced concrete*. CRC Press.
- Niu, H., & Wu, Z. (2006). Effects of FRP-concrete interface bond properties on the performance of RC beams strengthened in flexure with externally bonded FRP sheets. *Journal of Materials in Civil Engineering*, 18(5), 723-731.
- Park, Y., Abolmaali, A., Beakley, J., & Attiogbe, E. (2015). Thin-walled flexible concrete pipes with synthetic fibers and reduced traditional steel cage. *Engineering Structures*, 100, 731-741.
- Ramakrishnan, V. And Josifek, C. (1987). Performance Characteristics and Flexural Fatigue Strength of Concrete Steel Fibre Composites. Proc. International Symposium on Fibre Reinforced Concrete, December 16-19, 1987, Madras, pp.2.73-2.84.
- Romuldi, J.P. and Batson, G.B. (1963). Mechanics of Crack Arrest in Concrete. *Journal of Engineering Mechanics Division*, Proceedings of the ASCE, Vol.89, June 1963, pp.147-168.
- Rajani, B., & Abdel-Akher, A. (2012). Performance of cast-iron-pipe bell-spigot joints subjected to overburden pressure and ground movement. *Journal of Pipeline Systems Engineering and Practice*, 4(2), 98-114.
- Schneider, J., & Ferdinand, C. (1999, May). Pipeline behavior prediction for superscalar processors by abstract interpretation. In *ACM SIGPLAN Notices* (Vol. 34, No. 7, pp. 35-44). ACM.
- Shah, S. P., & Rangan, B. V. (1971, February). Fiber reinforced concrete properties. In *Journal Proceedings* (Vol. 68, No. 2, pp. 126-137).
- Song, P. S., & Hwang, S. (2004). Mechanical properties of high-strength steel fiber-reinforced concrete. *Construction and Building Materials*, 18(9), 669-673.

- Soroushian, P., & Lee, C. D. (1990). Distribution and orientation of fibers in steel fiber reinforced concrete. *Materials Journal*, 87(5), 433-439.
- Singhal, A. C., & Benavides, J. C. (1983). Axial and bending behavior of pipeline joints. *Journal (American Water Works Association)*, 572-578.
- Seo, D. C., & Lee, J. J. (1999). Damage detection of CFRP laminates using electrical resistance measurement and neural network. *Composite Structures*, 47(1), 525-530.
- Sam, N. (2012, June). Bond strength evaluation of the sprayed FRP on concrete subjected to different surface conditions. In *The 6th International Conference on FRP Composites in Civil Engineering (CICE 2012)*. The 6th International Conference on FRP Composites in Civil Engineering (CICE 2012).
- Tian, Y., Cassidy, M. J., & Youssef, B. S. (2010, January). Consideration for on-bottom stability of unburied pipelines using force-resultant models. In *The Twentieth International Offshore and Polar Engineering Conference*. International Society of Offshore and Polar Engineers.
- Toutanji, H., & Saafi, M. (2000). Flexural behavior of concrete beams reinforced with glass fiber-reinforced polymer (GFRP) bars. *ACI Structural Journal*, 97(5), 712-719.
- Tang, B., & Podolny, W. (1999). A successful beginning for fiber-reinforced polymer (FRP) composite materials in bridge applications. In *Proceedings of the International Conference on Corrosion and Rehabilitation of Reinforced Concrete Structures held December 1998, Orlando, FL., USA*.
- Toutanji, Houssam, and Gerardo Ortiz. The Effect of Surface Preparation on the Bond Interface between FRP Sheets and Concrete Members. *Composite Structures* 53.4 (2001): 457-462.

- Toutanji, H., & Ortiz, G. (2001). The effect of surface preparation on the bond interface between FRP sheets and concrete members. *Composite Structures*, 53(4), 457-462.
- Vectorply reinforcement fibers, Phenix City, AL (2016)
- Wham, B. P., & O'Rourke, T. D. (2015). Jointed pipeline response to large ground deformation. *Journal of Pipeline Systems Engineering and Practice*, 7(1), 04015009.
- Wang, Y., & Moore, I. D. (2014). Simplified design model for rigid pipe joints based on the two-pipe approximation 1. *Canadian Geotechnical Journal*, 52(5), 626-637.
- Wham, B. P., Argyrou, C., Bouziou, D., O'Rourke, T. D., Stewart, H. E., & Bond, T. K. (2014, July). Jointed pipeline response to earthquake induced ground deformation. In *Proc., 10th National Conf. on Earthquake Engineering, Earthquake Engineering Research Institute, Anchorage, AK*.
- Wilson, A., & Abolmaali, A. (2014). Performance of synthetic fiber-reinforced concrete pipes. *Journal of Pipeline Systems Engineering and Practice*, 5(3), 04014002.
- Wu, J. Y., Li, J., & Faria, R. (2006). An energy release rate-based plastic-damage model for concrete. *International Journal of Solids and Structures*, 43(3), 583-612.
- Yao, W., Li, J., & Wu, K. (2003). Mechanical properties of hybrid fiber-reinforced concrete at low fiber volume fraction. *Cement and Concrete Research*, 33(1), 27-30.
- Yao, J., Teng, J. G., & Chen, J. F. (2005). Experimental study on FRP-to-concrete bonded joints. *Composites Part B: Engineering*, 36(2), 99-113.
- Zhou, Z., Ou, J. P., & Wang, B. (2003, November). Smart FRP-OFGB bars and their application in reinforced concrete beams. In *Proceedings of the First International Conference on Structural Health Monitoring and Intelligent Structure* (pp. 13-15).

BIOGRAPHICAL INFORMATION

Sugyu Lee received his Bachelor of Science degree in Civil Engineering from the Chungbuk National University in Cheonju, South Korea in 2011, graduating with top honors from the Civil Engineering Department. Immediately after graduation, he enrolled at the Bucknell University to pursue a Master of Science (M.S.) degree in Civil Engineering, while researching the stability of steel joist girders. After receiving his master's degree, in August 2013, he continued his education at the University of Texas at Arlington, pursuing a PhD in civil engineering and joining Dr. Ali Abolmaali's research group to study the development of joint systems for underground infrastructures.